UNIVERSITY OF LIVERPOOL

Characterising the function of the mitochondrial deubiquitylase USP30 in mitophagy

Jane Jardine

Thesis submitted in accordance with the requirements of University of Liverpool for the Degree of Doctor in Philosophy

December 2020

Characterising the function of the mitochondrial deubiquitylase USP30 in mitophagy

Jane Jardine

Abstract

Parkinson's disease (PD) is the second most prevalent neurodegenerative disorder after Alzheimer's disease. The causes of this disorder are not fully understood, as 95% of cases are sporadic forms of PD. However, the genes involved in familial forms of the disease have been intensely studied and have highlighted the importance of mitochondrial quality control in PD. Indeed, PARK2/PRKN and PARK6/PINK1 are core regulators of mitophagy.

Mitophagy is triggered by mitochondrial impairment through the engagement of the mitochondrial kinase PINK1. Upon mitochondrial membrane depolarisation, PINK1 promotes both the activation of the ubiquitin E3 ligase PRKN and its recruitment to mitochondria. In turn, PRKN tags mitochondrial proteins with ubiquitin. The ubiquitin-coated mitochondrion is then recognised by autophagy receptors that bind to the autophagosomal membrane for safe disposal of the defective organelle.

My project aims at gaining a deeper understanding of the PINK1-PRKN pathway of mitophagy and finding regulators of this pathway. As described above, mitophagy is regulated through ubiquitylation, which itself is controlled by opposing E3 ligases and deubiquitylating enzymes (DUBs). Those enzymes are of particular interest as they could be chemically targeted to prevent mitochondrial failure. In this thesis I have focussed on USP30, a mitochondrial DUB, that is thought to remove ubiquitin from PRKN substrates. Mitophagy reporters enabled me to measure spontaneously occurring, "basal" or constitutive, mitophagy events in live cell imaging experiments. I found that USP30 regulates both basal and depolarisation-induced mitophagy in cells expressing endogenous PRKN. Serendipitously, I discovered that a pool of USP30 was localised at peroxisomes where it regulates pexophagy. In parallel, I made use of those same reporters to characterise alternative means to induce mitophagy.

I also contributed to the generation and characterisation of a new *in vivo* mitophagy reporter model, the mt-Keima fly. This tool enabled me to study mitophagy events in a genetically tractable organism. Preliminary results show that USP30 knockout induces an increase in mitophagy events occurring in the fly brain.

I further engineered USP30 knockout neuroblastoma cells using the CRISPR-Cas9 technology and found, through western blot analysis that TOMM20 was one of the main substrates of USP30. It thus appeared that USP30 removes ubiquitin from TOMM20 to prevent the Parkin-feedforward loop. Accordingly, I found that USP30 deletion and inhibition results in an increase of pS65-Ub generation by PINK1.

I performed a series of proteomic and ubiquitylomic experiments using SILAC based mass spectrometry to further search for substrates of USP30. I found that many outer mitochondrial membrane (OMM) proteins are more ubiquitylated in the absence of USP30, including members of the translocase outer membrane (TOM) complex, the very abundant VDAC proteins, and other less well characterised OMM proteins, many of which are known Parkin substrates. Although many OMM protein were ubiquitylated, I did not measure a global loss of mitochondrial or peroxisomal proteins. Intriguingly, the ubiquitylome datasets also suggested that USP30 loss or inhibition may impact on ribosomal quality control.

Overall, this thesis discloses new exciting roles of USP30 in the context of pexophagy, basal and induced-mitophagy, and further highlights the relevance of USP30 as a therapeutic target for PD.

Table of Contents

List of Figures

List of Tables

Abbreviations

ABCD3/PMP70	ATP binding cassette subfamily D member 3
ABP	Activity based probe
ACN	Acetonitrile
AMBRA1	Autophagy and beclin 1 regulator 1
AMFR	Autocrine motility factor receptor
AO	Antimycin and oligomycin
APF-1	ATP-dependent proteolysis factor 1
ARIH1	Ariadne RBR E3 ubiquitin protein ligase 1
ATG proteins	Autophagy related proteins
ATP13A2	ATPase cation transporting 13A2
BECN1	Beclin 1
BFP	Blue fluorescent protein
BNIP3	BCL2 interacting protein 3
BNIP3L	BCL2 interacting protein 3 like
BSA	Bovine serum albumin
C14orf142/GON7	GON7 subunit of KEOPS complex
CADM2	Cell adhesion molecule 2
CALCOCO2/ NDP52	Calcium binding and coiled-coil domain 2
Cas genes	CRISPR-associated genes
CCCP	Carbonyl cyanide m-chlorophenyl hydrazone
CDC42EP4	CDC42 effector protein 4
CDDO-Me	2-cyano-3,12-dioxoolean-1,9-dien-28-oic acid Methyl Ester
CDK1, 2	Cyclin dependent kinase 1, 2
CDKN1C	Cyclin dependent kinase inhibitor 1C
CDS	Coding sequence
CEP44	Centrosomal protein 44
CHGA, B	Chromogranin A, B
CI, II, III, IV, V	Electron transport chain complexes I, II, III, IV and V
CISD1, 2	CDGSH iron sulfur domain 1, 2
CKS1B, 2	CDC28 protein kinase regulatory subunit 1B, 2
CLR	Cullin-RING ligases
CMA	Chaperone mediated autophagy
CNS	Central nervous system
CNTFR	Ciliary neurotrophic factor receptor
CNTNAP2, 4	Contactin associated protein 2, 4
COPS5, 6	COP9 signalosome subunit 5, 6
COX VIII	Cytochrome c oxidase subunit 8
CRISPR	Clustered Regularly Interspaced Short Palindromic Repeats
CSRP1	Cysteine and glycine rich protein 1
CYB561	Cytochrome b561
DDC	Dopa decarboxylase
DFP	Deferiprone
DJ-1	Parkinsonism-associated deglycase
DLG1	Discs large MAGUK scaffold protein 1
DMSO	Dimethyl sulfoxide

DNAJ	DnaJ heat shock protein family (Hsp40)
DNM1L	Dynamin 1 like
DOX	Doxorubicin
DRD2, 6	Dopamine receptor D2
DTT	Dithiothreitol
DUB	Deubiquitylating enzyme
DUT	Deoxyuridine triphosphatase
EIF4G1	Eukaryotic translation initiation factor 4 gamma 1
EM	Electron microscopy
Em/Ex	Emission/Excitation wavelengths
EMT	Epithelial to mesenchymal transition
ENO2	Enolase 2
EPS15	Epidermal growth factor receptor pathway substrate 15
EPSIN	Epsin 1
ER	Endoplasmic reticulum
ESCRT	Endosomal sorting complexes required for transport
FACS	Fluorescence-activated cell sorting
FBS	Fetal bovine serum
FBXO7	F-box protein 7
FIP200	FAK family kinase-interacting protein of 200
FKBP8	FKBP prolyl isomerase 8
FUNDC1	FUN14 domain containing 1
G-TPP	Gamitrinib-triphenylphosphonium
GABARAP	GABA type A receptor-associated protein
GAP	GTPase activating protein
GAPDH	Glyceraldehyde-3-phosphate dehydrogenase
GAP	GTPase-activating protein
GBA	Glucosylceramidase beta
GDAP1	Ganglioside induced differentiation associated protein 1
GEF	Guanine nucleotide exchange factor
GFP	Green fluorescent protein
GIGYF2	GRB10 interacting GYF protein 2
GRSF1	G-rich RNA sequence binding factor 1
GSG2/HASPIN	Histone H3 associated protein kinase
GWAS	Genome-wide association study
H2A	Histone 2A
H3F3B	Histone H3.3
HBSS	Hank's Balanced Salt Solution
HDR	Homology directed repair system
HGF	Hepatocyte growth factor
HIF1	Hypoxia Inducible Factor
HIST1H2BD/ H2BC5	H2B clustered histone 5
HNRNPDL	Heterogeneous nuclear ribonucleoprotein D like
HRS	Hepatocyte growth factor regulated tyrosine kinase substrate
HSC70	Heat shock cognate 70
HSP9A, 90	Heat shock protein 9A, 90
HSPD1/HSP60	Heat shock protein family D (Hsp60) member 1
HSPE1	Heat shock protein family E (Hsp10) member 1

HTRA2	HtrA serine peptidase 2
HUWE1	HECT, UBA and WWE domain containing E3 ubiquitin protein ligase 1
IVM	Ivermectin
JAMM	Josephins and JAB1/MPN/MOV34 metalloenzymes
KD	Knockdown
KDM5C	Lysine demethylase 5C
KIDINS220	Kinase D interacting substrate 220
KO	Knockout
LAMP1-2	Lysosomal associated membrane protein 1-2
LAMTOR1	Late endosomal/lysosomal adaptor, MAPK and MTOR activator 1
LC–MS/MS	Liquid chromatography tandem mass spectrometry
LC3A-C	Microtubule associated protein 1 light chain 3 alpha-gamma
LIG1	DNA ligase 1
LIR	LC3-interacting region
LPPR4	Phospholipid phosphatase related 4
LRP10	LDL receptor related protein 10
LRRK2	Leucine rich repeat kinase 2
MAM	Mitochondria-associated membranes
MAP7	Microtubule associated protein 7
MDH2	Malate dehydrogenase 2
MDVs	Mitochondria derived vesicles
MF	Mitochondrial Fraction
MFN1, 2	Mitofusin 1, 2
MINDY	MIU novel Deubiquitylase family
MIRO1	Mitochondrial Rho GTPase 1
MIU	Motif Interacting with ubiquitin
MJD	Machado–Joseph disease proteases
MPI	Mammalian protease inhibitor
MPP2	Membrane palmitoylated protein 2
MRI	Magnetic resonance imaging
MSN	Moesin
MTCH2	Mitochondrial carrier 2
mTORC1	Mammalian target of rapamycin complex 1
MTS	Mitochondrial targeting sequence
MUL1	Mitochondrial E3 ubiquitin protein ligase 1
MYO5C	Myosin VC
NDUFB5	NADH:ubiquinone oxidoreductase subunit B5
NES	Nestin
NEUROD1, 6	Neuronal differentiation 1, 6
NHEJ	Non-homologous end joining repair system
NOVA2	NOVA alternative splicing regulator 2
NPTX2	Neuronal pentraxin 2
NPY	Neuropeptide Y
NRP1	Neuropilin 1
NUF2	NUF2 component of NDC80 kinetochore complex
OMM	Outer mitochondrial membrane

OPTN	Optineurin
OTC	Ornithine transcarbamylase
OTULIN	OTU deubiquitinase with linear linkage specificity
OTUs	Ovarian tumor proteases
OXPHOS	Oxidative phosphorylation
PAGE	polyacrylamide gel electrophoresis
PAM (motif)	Proto-spacer adjacent motif
PAM (protein)	Peptidylglycine alpha-amidating monooxygenase
PBH2	Prohibitin 2
PBR	Polybasic region
PBS	Phosphate-Buffered Saline
PCR	Polymerase chain reaction
PD	Parkinson’s disease
PEX proteins	Peroxisomal biogenesis factors
PFA	paraformaldehyde
PI	Phosphatidylinositol
PINK1	PTEN induced kinase 1
PLA2G6	Phospholipase A2 group VI
PMP34, 70	Peroxisomal Membrane Protein 34, 70
PMS	Post Mitochondrial Supernatant
PNS	Post Nuclear Supernatant
POLE, G	DNA polymerase epsilon, gamma
PPEF2	Protein phosphatase with EF-hand domain 2
PRDX3	Peroxiredoxin 3
PRKN	Parkin RBR E3 ubiquitin protein ligase
PSMC1-6	Proteasome 26S subunit, ATPase 1-6
PSMD3-14	Proteasome 26S subunit, non-ATPase 3-14
PTEN-L	Phosphatase and tensin homolog (PTEN)-long
PTM	post translational modification
PTRH2	Peptidyl-tRNA hydrolase 2
pUb	Phosphorylated ubiquitin
QDPR	Quinoid dihydropteridine reductase
RA	Retinoic acid
RACK1	Receptor for activated C kinase 1
RBFOX3	RNA binding fox-1 homolog 3
RBM3	RNA binding motif protein 3
RBP4	Retinol binding protein 4
RBRs	RING-in-between-RING ubiquitin E3 ligases
RBX1, 2	Ring-box 1, 2
RNF185	Ring finger protein 185
ROBO1, 2	Roundabout guidance receptor 1, 2
ROI	Region of interest
ROS	Reactive oxygen species
RPL19	Ribosomal protein L19
Rpn1-13	Proteasome regulatory particle base subunit Rpn1-13
RPS20	Ribosomal protein S20
RPS27A	Ribosomal protein S27a
Rpt1-6	Proteasome regulatory particle base subunit Rpt1-6

RQC	Ribosome-associated Quality Control
RT	Room temperature
RT-qPCR	Quantitative reverse transcription-polymerase chain reaction
S.O.C	Super Optimal Broth with catabolite repression
SARs	Selective autophagy receptors
SCG2	Secretogranin II
SD	Standard deviation
SDS	Sodium dodecyl sulfate
sgRNA	Single-guide RNA
SILAC	Stable isotope labelling by amino acids in cell culture
SLC proteins	Solute carriers
SLIT1, 2	Slit guidance ligand 1, 2
SMURF1	SMAD specific E3 ubiquitin protein ligase 1
SNAP25	Synaptosome associated protein 25
SNARE	Snap receptor
SNCA	Synuclein alpha
SQSTM1	Sequestosome 1
STAM	Signal transducing adaptor molecule
SUMOs	Small ubiquitin like modifiers
SYNGR2	Synaptogyrin 2
SYNJ1	Synaptojanin 1
SYNJ2BP	Synaptojanin 2 binding protein
SYP	Synaptophysin
SYT1	Synaptotagmin 1
TAX1BP1	Tax1 binding protein 1
TBC1D5, 15, 17	TBC1 domain family member 5, 15, 17
TBK1	TANK binding kinase 1
TBS	Tris-buffered saline
TH	Tyrosine hydroxylase
TIAM1	TIAM Rac1 associated GEF 1
TIM	Translocase of inner membrane
TIMM44	Translocase of inner mitochondrial membrane 44
TM	Transmembrane domain
TMEM230	Transmembrane protein 230
TOM	Translocase of outer membrane
TOMM proteins	Translocase of outer mitochondrial membrane
TPA	12-O-tetradecanoyl-phorbol-13-acetate
TRAF2	TNF receptor associated factor 2
TUBA4A	Tubulin alpha 4a
UAS	Upstream activating sequence
Ub-PA	Ubiquitin-propargylamide
UBA domain	Ubiquitin-associated domain
UBA1	Ubiquitin like modifier activating enzyme 1
UBA52	Ubiquitin A-52 residue ribosomal protein fusion product 1
UBA6	Ubiquitin like modifier activating enzyme 6
UBAN	Ubiquitin Binding in ABIN and NEMO
UBB	Ubiquitin B
UBC	Ubiquitin C

UBC domain	Ubiquitin conjugating domain
UBD	Ubiquitin binding domain
UBL	Ubiquitin like protein
UBP	Ubiquitin binding protein
UBZ	Ubiquitin-binding ZnF
UCHs	Ubiquitin C-terminal hydrolases
UFD	Ubiquitin fold domain
UIM	Ubiquitin Interacting Motif
ULK1, 2	Unc-51 like autophagy activating kinase 1, 2
UPR^{mt}	Mitochondrial unfolded protein response
UPS	Ubiquitin proteasome system
USPs	Ubiquitin specific peptidases
VAMP2	Vesicle associated membrane protein 2
VDAC1-3	Voltage dependent anion channel 1-3
VIM	Vimentin
VNC	Ventral nerve cord
VPS family	Vacuolar protein sorting family
WIPI1-4	WD repeat domain, phosphoinositide interacting 1-4
WT	Wildtype
YFP	Yellow fluorescent protein
ZNF598	Zinc finger protein 598
ZUP1	zinc finger containing ubiquitin peptidase 1

Acknowledgments

I would like to express my sincere gratitude towards my PhD supervisors Sylvie Urbé and Michael Clague for their support, guidance and for giving me the possibility to work in such a stimulating research environment! I would also like to thank Parkinson's UK for funding my PhD (H-1502) and giving me the opportunity to become a scientist.

I would like to thank our collaborators: Matthias Trost, Benedikt Kessler, Michael Ahlijanian and Stephanos Ioannidis for their help in this project.

I would like to address a special thank you to the members of the USP30 team: Andreas Kallinos, Elena Marcassa, Aitor Martinez-Zarate, Emma Rusilowicz-Jones, Francesco Barone, Liam Pollock and Katy McCarron with whom it was a pleasure to work.

I would also like to give a special shoutout to the fly people on the 4th floor and especially to Pilar Okenve-Ramos, Natalia Sanchez-Soriano and Monika Chojnowska-Monga for teaching me all about the wonderful world of *Drosophila melanogaster*! Thanks also to Daimark Bennett for his invaluable input on *Drosophila* genetics and imaging.

Thanks to all of my co-workers, in no particular order: Erithelgi Bertsoulaki, Hannah Elcocks, Douglas Grimes, Joana Gomes Neto, Stephanie Mo, Francesca Querques, Victoria Smith, Anne Clancy, Fiona Hood, Leila Rochin, Hannah Glover, Claire Heride, Leah Wilson, Yasmina Sahraoui, Hannah Warren, Ailbhe Brazel, Zohra Butt, Sarah Barnett, Andrew Fielding, Francesca Frigenti, Ioanna Georgiou, Alice Howarth, Dorota Sabat-Pospiech, Adam Linley, Yvonne Tang, Svetlana Telnova, Pei Yee Tey, for making the 5th floor a great workplace!

And last but not least I would like to thank my wonderful family! To my parents for their love and unconditional support. To Vincent and Adam for being the best brothers ever. To my cousin Adèle with whom I enjoyed sharing our stimulating thesis writing sessions. To my grandfather Jacques for believing in me and always keeping his door open. And of course, to Tom for being a wonderful partner, for always being there for me and making me forget all of my doubts and fears.

Chapter 1: Introduction

1.1 Parkinson's disease

1.1.1 Parkinson's disease and genetic risk factors

Parkinson's disease (PD) is known as the second most prevalent neurodegenerative disorder after Alzheimer's disease and affects 2-3% of the population of over 65 years-old (Lane et al., 2018; Tysnes and Storstein, 2017).The first detailed description of PD was published in 1817 by James Parkinson in "An essay on the shaking Palsy" (Digitised version: (Parkinson, 2002)). In this assay he described the progressive motor symptoms: gradual tremor, rigidity, gait abnormality (walking abnormalities), bradykinesia (slow movement), and the associated complications such as defects in speech, sleep impairment and constipation. He developed the following definition for the diagnosis of the Shaking Palsy (PD; then also known as *Paralysis agitans*):

> "Involuntary tremulous motion, with lessened muscular power, in parts not in action and even when supported; with a propensity to bend the trunk forwards, and to pass from a walking to a running pace: the senses and intellects being uninjured."
> – James Parkinson.

Further histological studies revealed that PD is also characterised by the degeneration of dopaminergic neurons of the *substantia nigra* and by abnormal intraneuronal inclusions of alpha-synuclein.

To date, there is no cure for PD. However, an array of treatments is available to reduce PD symptoms and ameliorate the patients' quality of life. The most commonly used treatment is levodopa (also known as L-DOPA), which is a dopamine precursor. Dopamine availability can also be enhanced using dopamine agonists, monoamine oxidase B inhibitors or catechol-o-methyltransferase inhibitors. Other neurotransmitter systems can also be affected in PD such as serotonin, acetylcholine or norepinephrine and can also be modulated pharmacologically. More severe motor dysfunction can be treated by deep brain stimulation or MRI-guided focussed ultrasound (Armstrong and Okun, 2020).

The genetic causes of this disorder are not fully understood, as only 5-10% of cases are hereditary (review: (Poewe et al., 2017)). Since 1997, strong efforts have been put into identifying the genes involved in PD and their function **(Table 1.1),** (review: (Blauwendraat et al., 2020)). The mutations in the gene coding for alpha-synuclein, SNCA, were the first mutations identified as causative of PD (Polymeropoulos et al., 1997). Currently, mutations in more than 20 genes have been described to cause PD **(Table 1.1),** (review: (Blauwendraat et al., 2020)). Although monogenic forms of PD only count for a small portion of total patients, GWAS studies have revealed that mutations in genes associated with hereditary and monogenic forms of PD, such as SNCA or LRRK2, are also genetic risk factors for sporadic forms of PD (Simón-Sánchez et al., 2009; Michael et al., 2011; Nalls et al., 2014; Chang et al., 2017). This reinforces the relevance and need for understanding the underlying mechanisms involved in hereditary forms of PD.

Table 1.1: List of genes mutated in PD

Table adapted from (Blauwendraat et al., 2020). Shown in brackets are putative PD genes for which confidence is low (genes requiring replication or function validation). Cellular and subcellular location as well as cellular pathways were collected from NCBI gene (https://www.ncbi.nlm.nih.gov/gene/). Early onset = Cases where the signs and symptoms of the disease begin before age 50.

Gene	Year of discovery	Proposed disease mechanism	Inheritance and onset	Frequency	Cellular /Subcellular localisation	Cellular pathway
SNCA	1997, 2003	Gain of function, over expression	Dominant	Very rare	Neuron	Synaptic activity
PRKN	1998	Loss of function	Recessive, often early onset	Rare	Cytosol/ mitochondria	Mitophagy
(UCHL1)	1998	Loss of function?	Dominant	Unclear	Neuronal and Membrane-associated/ cytosolic	Ubiquitin hydrolysing
DJ-1	2003	Loss of function	Recessive, often early onset	Very rare	Cytosol/ mitochondria/ nucleus	Multiple
LRRK2	2004	Gain of function	Dominant	Common	Cytosol/ Mitochondria	Neuronal plasticity, autophagy vesicle trafficking
PINK1	2004	Loss of function	Recessive, often early onset	Rare	Mitochondria	Mitophagy

(HTRA2)	2005	Unclear	Dominant	Unclear	Mitochondria	Apoptosis
POLG	2006	Loss of function?	Dominant	Rare	Mitochondria	Mitochondrial DNA replication
ATP13A2	2006	Loss of function	Recessive	Very rare	Lysosome	Unclear
FBXO7	2008	Loss of function	Recessive, often early onset	Very rare	Cytosol/Mitochondria	Member of SCF E3 ubiquitin-protein ligase complex
(GIGYF2)	2008	Unclear	Dominant	Unclear	Cytosol/ ER/ endosome/ golgi	Translation repression?
GBA	2009	Loss of function?	Dominant	Common	Lysosome	Glycolipid metabolism
PLA2G6	2009	Loss of function	Recessive, often early onset	Rare	Not recorded	Phospholipid metabolism
(EIF4G1)	2011	Unclear	Dominant	Unclear	Not recorded	mRNA translation
VPS35	2011	Loss of function	Dominant	Very rare	Endosome	Retromer complex
DNAJC6	2012	Loss of function	Recessive, Often early onset	Very rare	Cytosol	Regulates chaperones
SYNJ1	2013	Loss of function	Recessive	Very rare	Not recorded	phosphoinositide phosphatase
(DNAJC13)	2014	Unclear	Dominant	Unclear	Endosome	Membrane trafficking
(TMEM230)	2016	Loss of function?	Dominant	Unclear	Endosome	Synaptic vesicles trafficking and recycling?
VPS13C	2016	Loss of function	Recessive	Rare	ER- late endosome/lysosome contact sites	Lipid transport
(LRP10)	2018	Loss of function?	Dominant	Unclear	Not recorded	Not recorded

1.1.2 The case of PINK1 and Parkin

PRKN (encoding the ubiquitin E3 ligase Parkin) was another gene found early on to be mutated in PD (Kitada et al., 1998). Leo Pallanck's group later reported that deleting *parkin* in *Drosophila* flies produced individuals with symptoms reminiscent of PD (Greene et al., 2003). The *parkin* null flies had motor defects, being unable to climb or fly, and histopathological characteristics of PD such as disrupted muscle integrity or degeneration of dorsomedial dopaminergic neurons. Mitochondrial structure was also impaired in sperm cells and in indirect flight muscle tissues. Moreover, the flies had a shortened lifespan and males were sterile (Greene et al., 2003). Other studies by Ming Guo's and Jongkyeong Chung's teams described *pink1* null mutant

flies (Clark et al., 2006; Park et al., 2006). Those flies showed the same physical and histological impairments as *parkin* null flies, with exacerbated degeneration of the indirect flight muscles leading to an indentation of the thorax (Clark et al., 2006; Park et al., 2006). Further epistatic experiments revealed that *pink1* and *parkin* were genetically linked as the overexpression of *parkin* in *pink1* null flies rescued most of the PD-reminiscent phenotypes (Clark et al., 2006; Park et al., 2006). The *pink1* and *parkin* double mutants were not more severely affected than the single mutants and PINK1 overexpression was not able to rescue Parkin null mutant phenotypes. Both research teams concluded that *pink1* and *parkin* proteins were involved in the same process with *pink1* acting upstream of *parkin*. As *pink1* is a mitochondrially localised protein and that both the mitochondrial structure and ATP production of *pink1* and *parkin* mutants were impaired, they suggested that the *pink1 / parkin* pathway maintained mitochondrial integrity and function (Valente et al., 2004; Clark et al., 2006; Park et al., 2006).

Many studies then stemmed from this discovery with the intent of better understanding the PINK1-Parkin pathway.

1.2 Ubiquitin

Ubiquitin is a highly stable 76 amino acid long protein that serves as a post-translational modification **(Figure 1.1),** (Vijay-Kumar et al., 1987). It was identified twice in the 1970's in two unrelated studies before it became clear that these concerned the same protein.

1.2.1 Discovery

Ubiquitin was first purified from bovine thymus by Goldstein and colleagues, who were searching for thymic polypeptide hormones (Goldstein et al., 1975). They found that this particular polypeptide was not restricted to the thymus but was abundant in various mammalian and fish tissues, as well as in human immortalised cell lines, plant extracts and yeast. They also found small amounts of this polypeptide in bacteria, although that turned out to be most likely due to cross contamination (Goldstein et al., 1975).

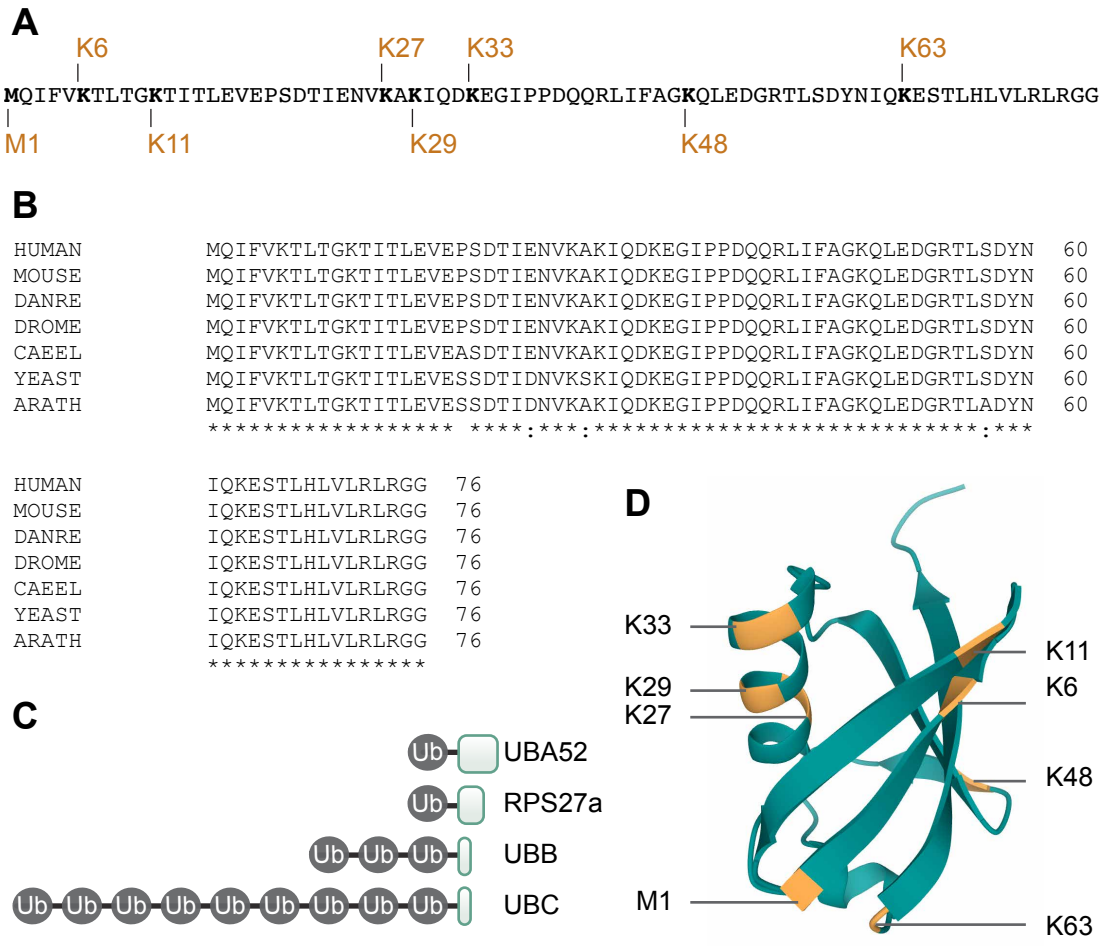

Figure 1.1: Sequence alignments and structure of ubiquitin

A) Amino acid sequence of human ubiquitin. In bold are highlighted ubiquitin's seven lysine residues and amino-terminal methionine. **B)** Ubiquitin is conserved across eukaryotes. The amino sequence of human ubiquitin was aligned to its homologs across six model organisms: *Mus musculus* (MOUSE), *Danio rerio* (DANRE), *Drosophila melanogaster* (DROME), *Caenorhabditis elegans* (CAEEL), *Saccharomyces cerevisiae* (YEAST) and *Arabidopsis thaliana* (ARATH). The sequence alignment was performed using Clustal Omega (EMBL-EBI). "*" indicates perfect alignment. ":" indicates a site belonging to group exhibiting strong similarity. "." indicates a site belonging to a group exhibiting weak similarity. **C)** Schematic representation of the gene product of the four ubiquitin genes (UBA52, RPS27A, UBB and UBC). UBA52 and RPS27A encode for ubiquitin-ribosomal fusion proteins, with a single ubiquitin fused to L40 or S27a, respectively. UBB and UBC encode three and nine ubiquitin repeats, respectively, ended with an additional residue (cysteine and valine). **D)** Ubiquitin 3D structure. The model was generated on PBD (PBD ID: 1UBQ). The seven lysines and the amino-terminal methionine are highlighted in yellow.

Furthermore, they found that its amino acid sequence was conserved between bovine, human and celery (Goldstein et al., 1975). Goldstein and colleagues thus provisionally named this polypeptide UBIP, short for ubiquitous immunopoietic polypeptide, and then renamed it ubiquitin. In 1977, ubiquitin was found to be covalently bound to histone 2A (H2A) at lysine 119, (Goldknopf and Busch, 1977; Hunt and Dayhoff, 1977).

Ubiquitin was rediscovered (then named APF-1) in the context of non-lysosomal proteolysis.

Following the discovery of lysosomes, protein degradation was thought to be solely mediated by those digestive organelles (de Duve, 1959, 1963; de Duve and Wattiaux, 1966). Rabinovitz and Fisher however found that the synthesis of abnormal haemoglobin led to their rapid degradation in rabbit reticulocytes, which were suspected to have little or no lysosomes (Rabinovitz and Fisher, 1964). Etlinger and Goldberg, then used this rabbit reticulocyte system and found that abnormal haemoglobin was broken down by a soluble and ATP-stimulated degradative system, which functioned optimally at pH7.8 contrasting with the acidic pH optimum known to be a feature of degradative activities in the lysosomes (Etlinger and Goldberg, 1977).

Ciechanover, Hershko, Rose and their colleagues then described that this ATP-dependent proteolysis was regulated by APF-1 (ATP-dependent proteolysis factor 1) a ~9kDa protein (Ciechanover et al., 1978). They had dissected the ATP-dependent proteolysis into a two component system with: fraction I (APF-1), a small 9kDa protein and fraction II, which has an APF-1-dependent and ATP-stimulated protease activity (Ciechanover et al., 1978). They further demonstrated that mono-APF-1 and poly-APF-1 chains form complexes with the protein substrates of ATP-dependent proteolysis (Ciechanover et al., 1980; Hershko et al., 1980). Ciechanover, Hershko, Rose and their colleagues further investigated the ATP-dependent proteolysis, nowadays known as the ubiquitin proteasome system (UPS), and went on to identify all of the components involved in this pathway (reviewed in: (Ciechanover, 2005)). They obtained the Nobel Prize of Chemistry in 2004 for their discovery of ubiquitin-mediated protein degradation.

In 1990, Wilkinson and colleagues, revealed that the proteolytic protein APF-1 and the highly conserved protein ubiquitin were one and the same protein (Wilkinson et al., 1980).

1.2.2 Structure and function

Ubiquitin is a modifying protein that is involved in post translational modifications (PTMs). This PTM protein is a member of the ubiquitin like protein family (UBL). UBL proteins share structural similarities and are thought to be evolutionary related. All UBL members have a β-grasp fold which is composed of a five-stranded-β-sheet wrapped around an α-helix and are classified into 9 families: Ubiquitin, SUMO, NEDD8, FAT10, ISG15, URM1, UFM1, ATG12 and ATG8 (Cappadocia and Lima, 2018), (**Figure 1.1D**).

Ubiquitin is expressed as a fusion protein encoded by four different genes: RPS27A, UBA52, UBB and UBC (**Figure 1.1C**). RPS27A (also known as UBA80) and UBA52 code for ubiquitin monomers in frame with a ribosomal protein tail: the 40S protein S27a and the 60S protein L40 respectively (Baker and Board, 1991). UBB and UBC code for ubiquitin repeats comprised of three and nine ubiquitin molecules, respectively (Wiborg et al., 1985). Those repeats are then processed to free ubiquitin and ribosomal subunits by deubiquitylating enzymes such as UCHL1, UCHL3, USP9X, USP7, USP5 and OTULIN (Grou et al., 2015).

1.2.3 Ubiquitylation: The E1-E2-E3 cascade

The entities involved in the ubiquitin conjugation system were first purified by Hershko, Ciechanover, Rose and colleagues (Ciechanover et al., 1982; Hershko et al., 1983). These enzymes are: E1 ubiquitin activating enzymes, E2 ubiquitin conjugating enzymes and E3 ubiquitin ligases (**Figure 1.2**).

1.2.3.1 E1 ubiquitin activating enzymes

In humans, there are two E1 ubiquitin activating enzymes (hereafter referred to as E1): UBA1 and UBA6 (Ciechanover et al., 1982; Jin et al., 2007; Chiu et al., 2007; Pelzer et al., 2007), (reviewed here:(Schulman and Harper, 2009)). E1 ubiquitin catalyse the first step of ubiquitylation. They first adenylate ubiquitin, then bind to ubiquitin's C-terminal end through their catalytic

cysteine, forming a thioester bond, and finally charge E2 ubiquitin conjugating enzymes with ubiquitin (Ciechanover et al., 1981; Haas et al., 1982). E1 enzymes can thus be loaded with two ubiquitin molecules simultaneously: one at the E1's adenylation active site and another via a thioester bond at the E1's catalytic cysteine (Haas et al., 1982).

The E1 activating reaction can be summarised as follow:

$$E1_{SH} + ATP + Ub \overset{Mg2+}{\Longleftrightarrow} E1_{SH}^{AMP-Ub(A)} + PPi \quad (1)$$

$$E1_{SH}^{AMP-Ub(A)} \Longleftrightarrow E1_{S-Ub(T)} + AMP \quad (2)$$

$$E1_{S-Ub(T)} + ATP + Ub \overset{Mg2+}{\Longleftrightarrow} E1_{S-Ub\,(T)}^{AMP-Ub(A)} + PPi \quad (3)$$

$$E1_{S-Ub(T)}^{AMP-Ub(A)} + E2_{SH} \Longleftrightarrow E1_{SH}^{AMP-Ub(A)} + E2_{S-Ub} \quad (4)$$

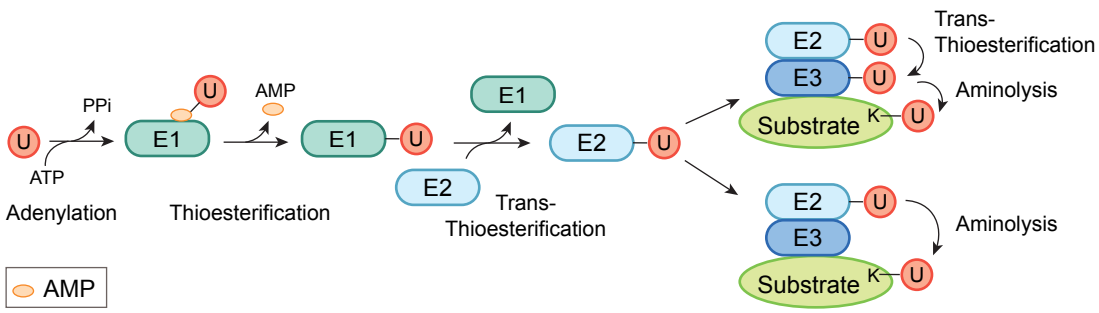

Figure 1.2: The ubiquitylation cascade.

Schematic representation of the E1, E2, E3 ubiquitylation cascade. The E1 activating enzyme first binds ubiquitin through its active adenylation site and adenylates ubiquitin. The E1 catalytic cysteine then forms a thioester bond with ubiquitin. The E1-ubiquitin pair is recognised by an E2 conjugation enzyme and ubiquitin is transferred to the E2's catalytic cysteine by transthioesterification. The E2 then binds to an E3 ligase and its substrates. If the E3 belongs to the RING family, then ubiquitin is directly transferred to its substrate by aminolysis. If the E3 belongs to the HECT or the RBR families then ubiquitin is first transferred to the E3's catalytic cysteine by transthioesterification then conjugated to the substrate by aminolysis.

1.2.3.2 E2 conjugating enzymes

There are ~40 E2s in the human proteome, of which 35 are specific to ubiquitin (Clague et al., 2015).

E2 enzymes have a crucial role in the ubiquitin cascade. They not only permit the transfer of ubiquitin from the E1 to the E3 but also control monoubiquitylation, ubiquitin chain initiation and ubiquitin chain elongation, the processivity of chain formation as well as the topology of the chain linkages (Ye and Rape, 2009).

E2s interact with E1 and E3 enzymes via their ubiquitin conjugating (UBC) domain. The binding of an E1 to ubiquitin, results in a conformational change of the E1 which exposes a negatively charged groove within its ubiquitin fold domain (UFD). This groove is selectively recognised by the E1 interacting helix (α-helix 1) located in the UBC domain of ubiquitin E2. The ubiquitin molecule is then transferred from E1's catalytic cysteine to E2's own catalytic cysteine by a transthioesterification reaction (Ye and Rape, 2009). Finally, E2s select E3 ligases via their unique E3 interacting loops (L1 and L2 loop) residing in the UBC domain (Zheng et al., 2000). An example of well characterised E2/E3 pairs are Cdc34 and SCF (Skowyra et al., 1997).

1.2.3.3 E3 ligases

There are more than 600 E3 ubiquitin ligases which are distributed across three major E3 families: HECT, RING and RING-in-between-RING (RBR), (Heride et al., 2014; Zheng and Shabek, 2017). HECT and RBR E3 ligases have a catalytic cysteine in their HECT and RING2 domains respectively (**Figure 1.3A-B**). They are thus able to form covalent intermediates with ubiquitin. Ubiquitin is transferred from the E2's catalytic cysteine to these E3's catalytic cysteine by transthioesterification and then conjugated to its substrate (Rotin and Kumar, 2009; Smit and Sixma, 2014).

RING E3 ligases are the most abundant E3 ligases in the human proteome. These enzymes either have a zinc- containing RING domain or U-box catalytic domain. RING and U-box domains are structurally similar and do not possess a catalytic cysteine. Thus, unlike HECT and RBR, RING E3s do not form a covalent bond with ubiquitin **(Figure 1.3C)**. Instead, they direct E2s to their substrate and activate the E2-mediated ubiquitin-substrate conjugation via

their RING domain (Budhidarmo et al., 2012; Metzger et al., 2014). RING E3 ligases also include the multimeric Cullin-RING ligases (CLR) ligase complexes **(Figure 1.3D)**. These complexes are arranged around a cullin scaffold protein, of which there are 7 encoded in the human genome (CUL1, 2, 3, 4, 4B, 5 or 7). The cullin scaffold is bound to an E2 interacting RING protein (RBX1 or RBX2) at its C-terminus and to an adaptor protein (ex: Skp1) and substrate recognition protein (e.g.: F-box proteins) at its N-terminus (Zimmerman et al., 2010).

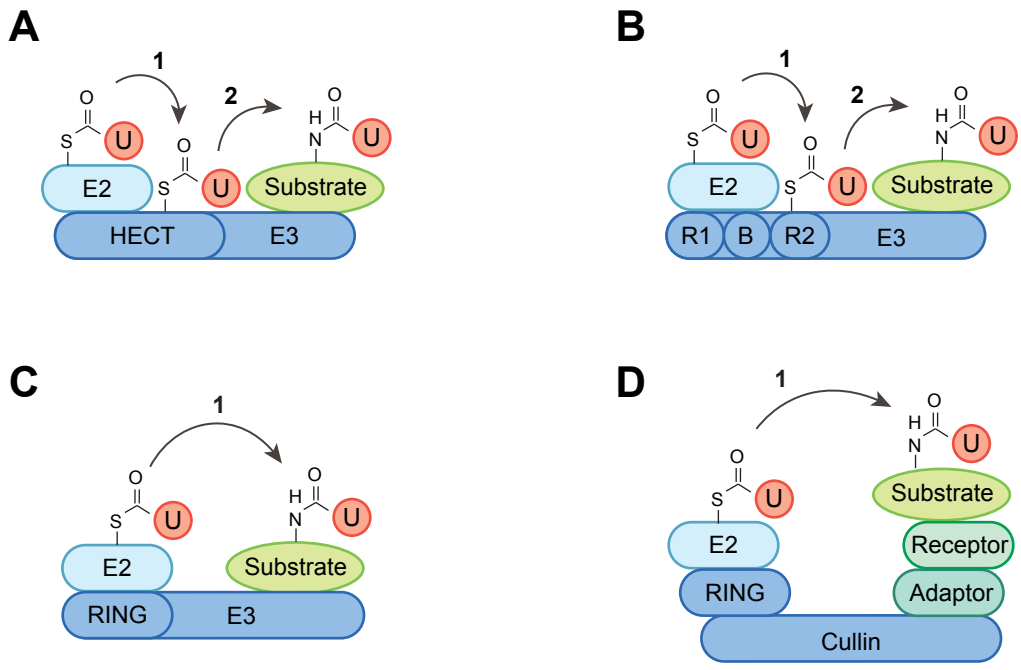

Figure 1.3: E3 ubiquitin ligases

There are three families of E3 ubiquitin ligases: HECT E3, RING-in-between-RING (RBR) E3 and RING E3 ligases. **A-B)** HECT E3 and RBR ligases both possess a catalytic cysteine which mediates substrate ubiquitylation. Ubiquitin is transferred from the E2 to the substrate in a 2-step process: 1) Ubiquitin is first transferred to the catalytic cysteine on the E3 by transthioesterification, 2) then the ubiquitin is conjugated to the substrate. **A)** HECT E3 ligases possess a HECT domain. The amino terminal end of the HECT domain interacts with the E2 enzyme, whilst the catalytic cysteine is located at the carboxy-terminal end. **B)** RBRs have two RING domains, RING1 (R1) and RING2 (R2) separated by an in-between-RING domain (B). The RING1 domain binds the E2s enzyme and the RING2 domain possesses the catalytic cysteine. **C)** RING E3 ligases are the most abundant ligases and lack an active cysteine. The ubiquitin transfer is thus a one-step process: the ubiquitin is directly added by the E2 to the substrate. The RING E3 ligases are characterised by the presence of a RING or a U-box domain. Those two domains adopt a similar structure with the exception that RING domains are arranged around two zinc ions. RING and U-box domains bind to the ubiquitin charged E2 and activate substrate ubiquitylation. **D)** Cullin-RING ligases (CLR) are a subfamily of RING ligases. These are multimeric

E3 ligase complexes composed of an E2 binding RING protein (RBX1 or RBX2), a cullin scaffold protein, a substrate recognition protein (receptor) and an adaptor protein.

1.2.4 The ubiquitin code

Ubiquitin modifications exist in multiple forms: mono-ubiquitylation or poly-ubiquitylation, with various chain linkages and possible post-translational modifications.

1.2.4.1 Ubiquitin linkage

Ubiquitin is attached to substrates by an isopeptide bond formed between its C-terminal glycine residue and the substrate's lysine ε-amine group (Goldknopf and Busch, 1977; Hunt and Dayhoff, 1977; Clague et al., 2015). Ubiquitin can thus be conjugated to other ubiquitin molecules on each of its seven lysines. Ubiquitin's amino-terminal methionine can also be ubiquitylated and form linear chains. In mammalian cells, common chain linkages include Lys48 and Lys63-linked chains. Met1, Lys6, Lys11, Lys27, Lys29 and Lys33)-linked chains are more atypical ubiquitin chains (**Figure 1.4A**), (Akutsu et al., 2016).

Broadly speaking, each chain-linkage type is associated with specific cellular pathways. Lys48 (K48)-linked chains are well known to target proteins for proteasomal degradation. In contrast, Lys63 (K63)-linked chains are involved in a broader range of pathways such as autophagy or endosomal sorting via the ESCRT complex (Komander and Rape, 2012; Swatek and Komander, 2016). Interestingly, Lys6 (K6) along with K63, K48, K11-linked chains decorate outer mitochondrial membrane (OMM) proteins following mitophagy induction with mitochondria depolarising agents (Cunningham et al., 2015).

1.2.4.2 Ubiquitin and ubiquitin chain types

Most of the cellular ubiquitin pool is conjugated to substrates as single molecules (mono-ubiquitylation). In HEK293 cells monoubiquitylation represents more than 60% of total ubiquitin (Kaiser et al., 2011; Clague et al., 2015). Up to 50% of cellular monoubiquitylation is on histones, such as the aforementioned monoubiquitylation of H2A at K119 (Goldknopf and Busch,

1977; Hunt and Dayhoff, 1977). Histone monoubiquitylation regulates chromatin organisation, gene expression and DNA damage repair (Cao and Yan, 2012; Clague et al., 2019).

The next biggest ubiquitin reservoir is free ubiquitin (>20% of total ubiquitin in HEK293 cells) whilst polyubiquitin chains represent roughly 10% of total ubiquitin (Heride et al., 2014; Kaiser et al., 2011). These ubiquitin chains can be homogenic (single linkage type), heterogenic (mixed chain linkages) or branched when one ubiquitin is ubiquitylated a several sites (**Figure 1.4B**), (Swatek and Komander, 2016).

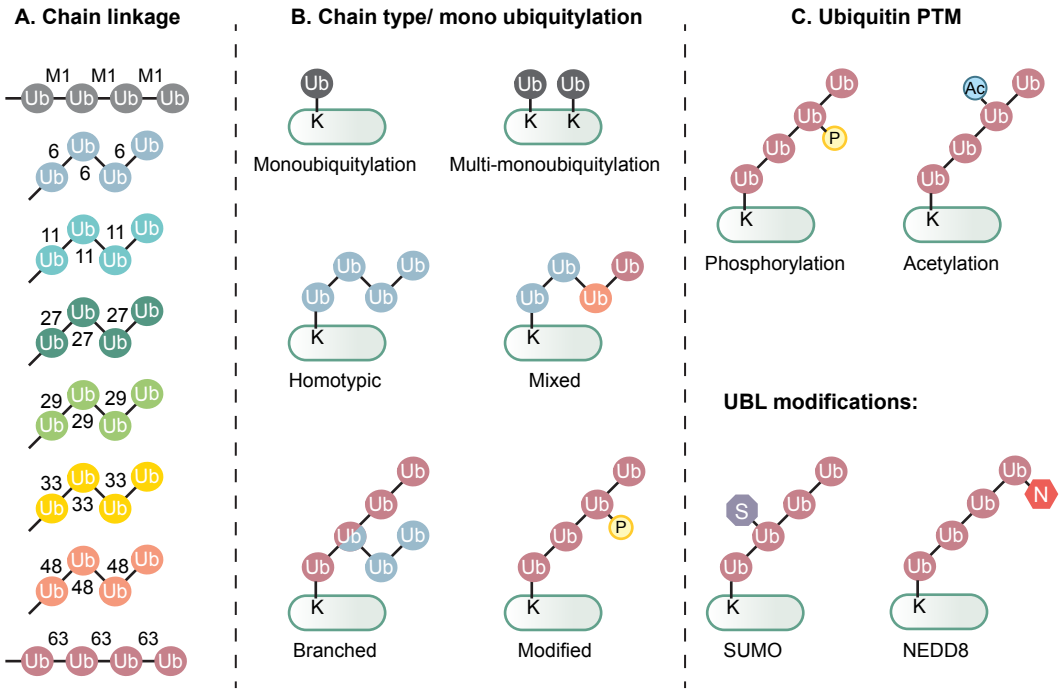

Figure 1.4: The ubiquitin code.

A) Ubiquitin can be linked to other ubiquitin moieties by its methionine (Met1, M1) or any of its seven lysine residues (Lys6, Lys11, Lys27, Lys29, Lys33, Lys48 or Lys63). Methionine chains are linear and are linked by a peptide bond between the carboxyl terminal glycine and the amino-terminal methionine (Met1, M1). Lysine linked chains have various topologies and are linked by isopeptide bonds formed between the carboxyl terminal glycine and the specific lysine. **B)** Substrates can be modified by a single ubiquitin molecule (monoubiquitylation), by multiple ubiquitin molecules (multi-monoubiquitylation) or by ubiquitin chains. Those ubiquitin chains can be made of one particular linkage (homotypic) or made of several linkages (mixed). Within ubiquitin chains, some ubiquitin moieties can be ubiquitylated at multiple lysine residues and thus form ubiquitin ramifications (branched). Finally, ubiquitin moieties amongst ubiquitin chains can be modified post-translationally. **C)** Ubiquitin post-translational modifications: ubiquitin can be phosphorylated at serine, threonine and tyrosine residues; ubiquitin's lysine residues also get acetylated; on top of this, ubiquitin can also be modified by two UBLs, SUMO and NEDD8.

1.2.4.3 Ubiquitin modification

The ubiquitin code can be further complexified by the addition of post-translational modifications (PTMs). Ubiquitin can be modified by small chemical PTMs such as acetylation and phosphorylation, or modified by UBLs (sumoylation and neddylation) (Swatek and Komander, 2016), (**Figure 1.4C**).

1.2.5 Reading the ubiquitin code

Ubiquitylated substrates are recognised by ubiquitin binding proteins which possess ubiquitin binding domains (UBDs). More than 20 UBDs have been identified in the human genome (Heride et al., 2014). UBDs are classified by their structure into five categories, (Husnjak and Dikic, 2012):

- α-helical (UBA, UIM, DUIM, MIU, CUE, GAT, VH8, UBAN)
- zinc finger (NZF, ZnF UBP, ZnF A20, UB2)
- pleckstrin-homology (PH) fold (GLUE, PRU)
- ubiquitin conjugating-like (UEV, UBC)
- Others (SH3, UBM, PFU, Jab1/MPN)

The ubiquitin-associated (UBA) domain was the first identified UBD. Hofmann and Bucher had observed, by using sequence alignments, that a ~55 aa long motif was common to a subset of E2, E3, DUBs, kinases and other proteins involved in ubiquitylation and was also conserved across species (Hofmann and Bucher, 1996). They found that UBAs were present in those proteins as single copies or tandem repeats.

The majority of UBDs were shown to bind the hydrophobic residues of ubiquitin: around Ile44 (with the surrounding Leu8, Val70 residues), and more rarely at Ile36 (Husnjak and Dikic, 2012).

Ubiquitin binding proteins can have multiple UBDs which enhances binding affinity and specificity. As an example, the DUB USP5, which recognises free ubiquitin chains, has one N-terminal ZnF-UBP and two C-terminal UBA domains. It's ZnF-UBP domain specially recognises the C-terminal GlyGly tail of ubiquitin as well as its hydrophobic Leu8. USP5 thus cleaves unanchored ubiquitin chains to replenish the free monoubiquitin pool (Reyes-Turcu et al., 2006, 2008; Komander et al., 2009; Husnjak and Dikic, 2012).

The organisation of UBDs within proteins also affects their affinity for specific chain linkages. The BRCA1-A subunit RAP80 and the DUB ATXN3 both possess a tandem of Ubiquitin Interacting Motifs (UIM) but are specific for Lys63 and Lys48-linked chains respectively (Sims and Cohen, 2009). One difference lies in the length and nature of their UIM linkers. RAP80 has a rather long linker (7 aa) when compared to ATXN3 (2 aa), which is thus more adapted to the extended conformation of Lys63-linked and less efficient for binding the closed conformation Lys48-linked ubiquitin chains (Sims and Cohen, 2009).

UBDs have been identified in hundreds of proteins in the human genome. Those proteins are not only found in ubiquitin conjugating (E1, E2, E3) and ubiquitin hydrolysing enzyme (DUBs) but also ubiquitin receptor proteins such as autophagy adaptors (SQSTM1, NDP52, NBR1, TAX1BP1, OPTN), proteasome ubiquitin receptors (Rpn10/PSMD4 and Rpn13/ADRM1), other members of the UPS system, endocytosis adapters and regulators (EPS15, EPSIN, STAM, Hrs, RABGEF1, …) and many others (Husnjak and Dikic, 2012).

1.2.6 Deubiquitylation: Deubiquitylating enzymes (DUBs)

Deubiquitylating enzymes (DUB) are ubiquitin proteases which cleave peptide or isopeptide bonds formed between ubiquitin molecules or between ubiquitin molecules and a substrate protein.

DUBs are involved in a plethora of pathways. Some of their major functions include: 1) regenerating the cellular pool of free ubiquitin through the recycling of ubiquitin chains and processing of ubiquitin-fusion proteins produced by RPS27s, UBA52, UBB and UBC; 2) protecting proteins from proteasomal or lysosomal degradation (removal of degradative ubiquitin); 3) controlling protein function or protein complex assembly (removal of non-degradative ubiquitin), (Clague et al., 2012, 2019).

1.2.6.1 DUB families

To date, 99 deubiquitylating enzymes (DUBs) have been identified in the human genome (**Figure 1.5**). Those proteins are categorised into 7 families

based on the conformation of their catalytic domains: USP, UCH, OTU, MJD, MINDY, ZUP1 and JAMM (Clague et al., 2019).

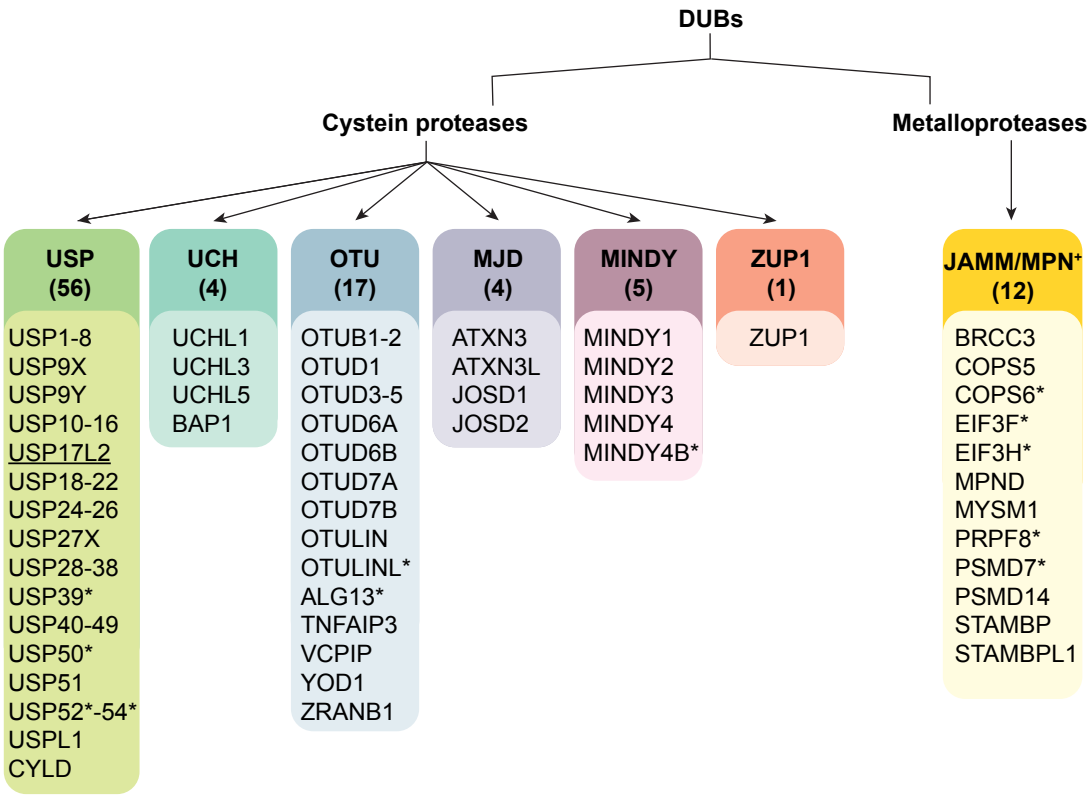

Figure 1.5: Deubiquitylating enzyme families.

There are 99 DUBs in the human genome classified into seven families: USP, UCH, OTU, MJD, MINDY, ZUP1 and JAMM (also known as MPN). USP, UCH, OTU, MJD, MINDY and ZUP1 are cysteine proteases whilst JAMMs are metalloproteases. In total, there are 11 inactive DUBs (pseudo-DUBs) distributed across USPs, OTUs, MINDYs, and more abundantly in JAMMs (5 out of 12 DUBs). A single member of the USP17 clade is shown (The USP17 group results from gene duplication). Asterisks indicate pseudoDUBs.

Six of those seven families are cysteine proteases whereas the JAMMs are zinc-dependent metalloproteases (Clague et al., 2013). Cysteine proteases possess a catalytic triad formed of a catalytic cysteine, a histidine and a 3rd residue, usually asparagine or aspartic acid, which catalyse deubiquitylation. DUBs are able to recognise and bind ubiquitin thanks to their catalytic domains and more specifically to their primary recognition site (S1) (Mevissen and Komander, 2017).

MINDYs (MIU novel Deubiquitylase family) were discovered by Yogesh Kulathu's and Kay Hofmann's groups while investigating the small UBD Motif Interacting with Ub (MIU) (Abdul Rehman et al., 2016). The biological function of MINDYs is still unknown. However, one striking observation is that all analysed members of the MINDY family are highly specific for K48-linked chains (Abdul Rehman et al., 2016; Kristariyanto et al., 2017). The ZUP1 family was co-discovered in 2018 by four research teams. Currently this new DUB family is only composed of one member: ZUP1. Similar to MINDY proteins, ZUP1 has a MIU motif and multiple other UBDs. ZUP1 was reported to preferentially cleave long K63-linked chains, to localise to the nucleus and is thought to prevent DNA damage (Haahr et al., 2018; Hermanns et al., 2018; Hewings et al., 2018; Kwasna et al., 2018).

Amongst the 99 identified DUBs, 11 are predicted to be catalytically inactive. These DUBs are qualified as pseudo-DUBs (**Figure 1.5**). Pseudo-DUBs are found amongst USPs, OTUs, MINDYs and are abundant among JAMMs (Walden et al., 2018). Albeit being inactive DUBs, pseudo-DUBs remain essential (**Figure 1.6**). They have the ability to activate competent DUBs and other enzymes. Well characterised DUB-pseudo-DUB heterodimers include COPS5-COPS6 involved in the COP9 signalosome (de-neddylating complex) and PSMD14-PSMD7 regulating the removal of ubiquitin from proteins committed to proteasomal degradation (19S proteasome) (**Figure 1.6A-B**) (Clague et al., 2019; Walden et al., 2018). Pseudo-DUBs can also act as scaffold proteins for the assembly of large protein complexes: PRPF8 coordinates the assembly of the spliceosome (pre-mRNA splicing) (**Figure 1.6C**) (Clague et al., 2019; Walden et al., 2018).

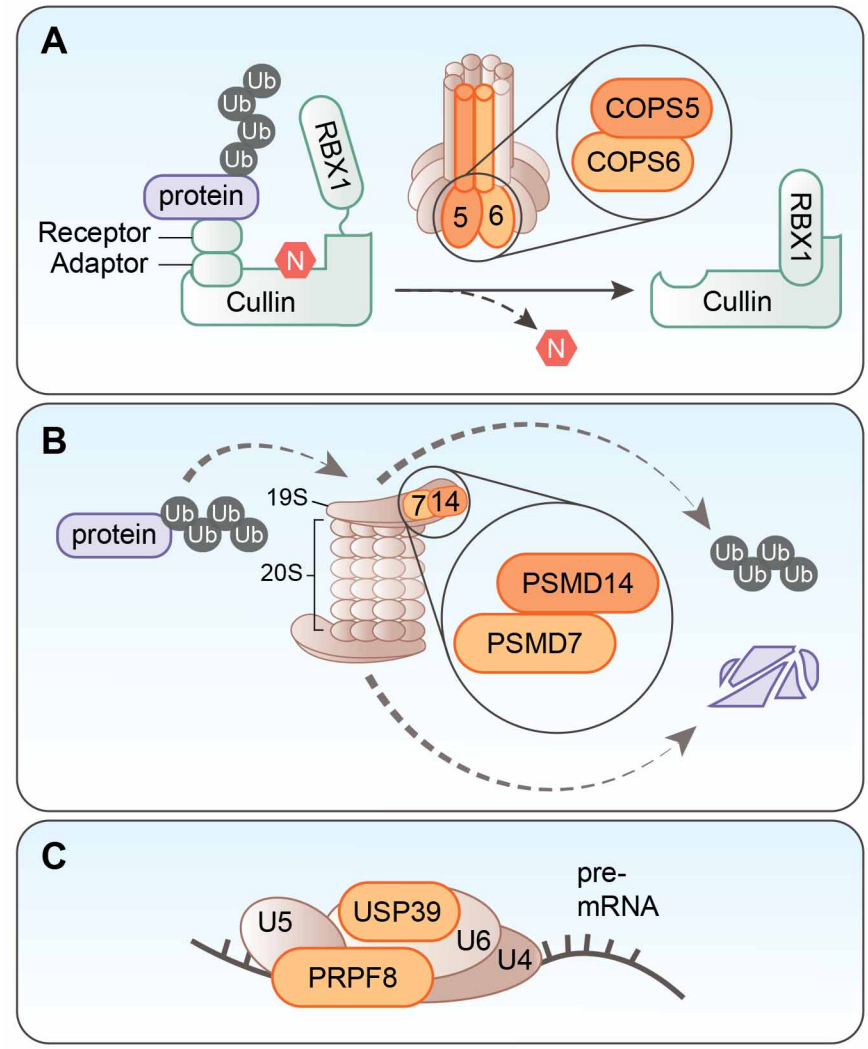

Figure 1.6: Essential cellular functions regulated by pseudoDUBs.

A) The JAMM DUB-pseudoDUB heterodimer COPS5 (active)-COPS6 (inactive) form the catalytic core of the COP9 signalosome that is responsible for removing NEDD8 from Cullin-RINGLigases (CLR). **B)** Another JAMM DUB-pseudoDUB heterodimer, PSMD14 (active)- PSMD7 (inactive) found at the 19S proteasome deubiquitylate proteins targeted for degradation. **C)** The pseudoDUBs USP39 and PRPF8 control pre-mRNA splicing. PRPF8 coordinates the assembly of the spliceosome whilst USP39 is an integral part of the triple small nuclear ribonuclearprotein (tri-snRNP, U4/U6.U5) a building block of the spliceosome. PseudoDUBs are shown in light orange and active DUBs are shown in dark orange.

1.2.6.2 Cleavage type

To respond to the diversity of the ubiquitin code, DUBs have developed a variety of cleavage modes and affinities for specific chain linkages (**Figure 1.7**).

Overall, most USPs are not specific for a particular ubiquitin chain linkage whereas most OTUs have a preference for one to three ubiquitin chain linkages (**Figure 1.7A**). ZUP1 and most JAMMs have a preference for K63 chain linkages whilst MINDYs are highly specific for K48 chains; MJDs were reported to prefer K48- and K63-linked chains (McCullough et al., 2004; Abdul Rehman et al., 2016; Kristariyanto et al., 2017; Mevissen and Komander, 2017).

As described earlier, the affinity of DUBs for certain chain linkages can be dictated by specific UBDs as well as their spatial arrangement. Deletion of UIM and ZnF motifs in OTUD1 and OTUD2, respectively, significantly decreases their chain linkages preferences (Mevissen et al., 2013). However, other factors contribute to chain specificity. As an example, the deletion of OTUD3's UBA domain does not reduce its affinity for K6- and K11-linked ubiquitin chains (Mevissen et al., 2013).

It is also worthwhile to note that only ~30% of DUBs possess UBDs (Komander et al., 2009). The ubiquitin binding sites within the DUBs' catalytic domains thus also play a crucial role in cleavage specificity. USP30 which does not present any supplementary domains outside of its catalytic domain cleaves preferentially K6 chains (Clague et al., 2013; Gersch et al., 2017). In this case the chain selectivity is encoded in the catalytic domain itself. Other examples illustrating the involvement of ubiquitin binding sites within the DUBs catalytic domain in chain selectivity include OTUD2 and OTUD3. The secondary ubiquitin binding site (S1') of OTUD3 contributes to its ability to act on K11 chains. OTUD2 possesses another ubiquitin binding site (S2) which enhances its affinity for longer K11 chains (Mevissen et al., 2013). Overall, chain linkage specificity is thus mediated by UBDs and by the catalytic domains' ubiquitin binding sites.

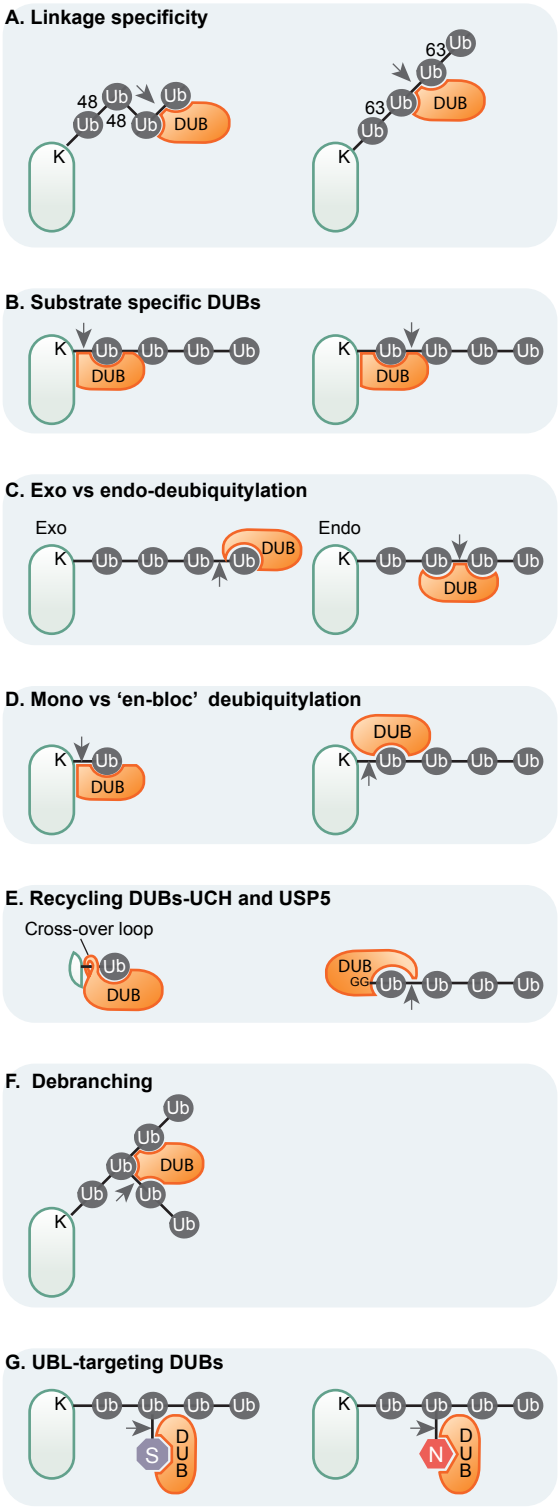

Figure 1.7: Array of DUB-mediated ubiquitin-cleavage modes.

Deubiquitylating enzymes have a wide array of cleavage modes to deal with the various chain linkages. **A)** DUBs can be specific for certain chain linkages. These chain preferences rely on the structural arrangement of their ubiquitin binding domains (UBDs) and on their specific ubiquitin binding sites (S1, S1', S2) located within their catalytic domain. **B)** Some DUBs are substrate specific and thus directly bind their target protein and then cleave off the ubiquitin residues. **C)** Depending on the arrangement of the ubiquitin binding sites, ubiquitin chain cleavage can occur within the chain (endo) or at the distal end of the chain (exo). **D)** Most of the cellular ubiquitin is conjugated through monoubiquitylation. Thus, some DUBs specifically recognise mono-ubiquitylated substrates (left). Others can cleave a whole chain at once, "en bloc" cleavage (right). **E)** UCHs have been reported to cleave small residues adjacent to the ubiquitin C-terminus, such as peptide left-overs from proteasomal degradation. They have a crossover loop which is thought to restrict them from binding large or folded ubiquitin conjugates (left). USP5 possesses a ZnF-UBP domain which recognises the C-terminal GlyGly residues of unanchored ubiquitin chains (right). It can thus process unattached chains into free ubiquitin. Both UCHs and USP5 are essential for ubiquitin recycling. **F)** Branched ubiquitin chains have been reported to be processed by DUBs. However, it is not yet known if there exist specific modes of ubiquitin chain debranching such as the direct targeting of branching points. **G)** Up to date, three DUBs (COPS5, USPL1 and USP18) have been identified as UBL proteases (targeting NEDD8, SUMO and ISG15, respectively). Those could potentially cleave off UBLs from ubiquitin chains. Arrows indicate cleavage site.

Several DUBs show substrate specificity rather than chain linkage affinity (**Figure 1.7B**). This is exemplified by the USP family. Most USPs show no chain specificity but instead have additional motifs directing their localisation and promoting protein-protein interaction (Faesen et al., 2011; Mevissen and Komander, 2017).

Ubiquitin chains can be cleaved from the extremities (exo) or within the chain (endo) (**Figure 1.7C**). MINDY-1 is an example of exo-deubiquitylating DUB. Due to its MIU arrangement, it can only strip off ubiquitin from the C-terminal end of chains in a stepwise manner (Abdul Rehman et al., 2016). Conversely, OTUD2 and OTUD3 have an additional S2 site which promotes endo-cleavage (Mevissen and Komander, 2017; Mevissen et al., 2013).

Deubiquitylases can also be sensitive to the length of the ubiquitin chains. Due to the arrangement of their MIU tandem motif, MINDY-1 and MINDY-2 preferentially cleave long poly-ubiquitin chains. MINDY-1 was shown to have no catalytic activity against mono-ubiquitin (Abdul Rehman et al., 2016; Kristariyanto et al., 2017).

Although several DUBs have no affinity for monoubiquitylation, cellular ubiquitin is mostly found in form of monoubiquitylation (**Figure 1.7D, left**). Roughly 50% of monoubiquitylation occurs at histones (Kaiser et al., 2011). DUBs such as MYSM1, USP3, USP16, USP22 and BAP1, are involved in histone deubiquitylation (reviewed in (Clague et al., 2019)).

Another mode of chain cleavage is the “en bloc” cleavage (**Figure 1.7D, right**). Such cleavage is observed in proteins committed to proteasomal cleavage. The DUB-pseudo-DUB heterodimer PSMD14-PSMD7 and USP14 mediated “en bloc” cleavage at the 19S proteasome (the “lid” of the proteasome).

Other cleavage particularities have also been observed in UCH enzymes. Those enzymes have a unique cross over loop (also known as active site loop) which restricts the access to the catalytic core (**Figure 1.7E, left)**. Thus, UCHs with a short cross over loop, such as UCHL1, cannot cleave bound-ubiquitin molecules unless they are attached to short and unfolded C-terminal extensions (Less than 10 aa long). UCHL1 can therefore remove short peptide remnants from ubiquitin such as those left-over from proteasomal degradation (Bishop et al., 2016).

Certain DUBs are also able to recognise detached ubiquitin chains, such as chains removed by en-bloc cleavage or endo-cleavage (**Figure 1.7E, right**). Those DUBs, like USP5, mentioned above, possess a ZnF-UBP domain that recognises the C-terminal GlyGly. ZnF-UBP containing DUBs include USP3, USP5, USP13, USP16, USP22, USP33, USP44, USP45 and USP49. Currently, only USP3, USP5 and USP16 were reported to recognise and cleave unanchored ubiquitin chains (Bonnet et al., 2008; Reyes-Turcu et al., 2006). Both ZnF-UBP, containing DUBs, and UCH play an important role in the recycling of cellular ubiquitin and replenishing of the free ubiquitin pool.

Further layers of ubiquitin code complexity are added by chain branching and PTMs. The cleavage of branched chains is not yet understood. However, it is hypothesised that some DUBs have the capacity of directly cleaving branching points (Mevissen and Komander, 2017), (**Figure 1.7F**).

Small chemical PTMs (phosphorylation, acetylation) and UBLs (SUMO, NEDD8) can be tackled by specific proteases (**Figure 1.7G**). Three DUBs have been reported to selectively cleave UBLs: COPS5 is part of the COP9 signalosome and removes NEDD8 moieties; USPL1 is a SUMO protease and USP18 targets ISG15 (Cavadini et al., 2016; Schulz et al., 2012; Malakhov et al., 2002). Those UBL specific DUBs thus also have the potential to remove SUMO or NEDD8 from ubiquitin chains.

Two ubiquitin phosphatases, PTEN-L and PPEF2, were recently shown to specifically oppose the phosphorylation of ubiquitin at Ser65 by the mitochondrial kinase PINK1 (Wall et al., 2019; Wang et al., 2018). The removal of phosphoryl groups enables deubiquitylation by DUBs. Indeed, a large portion of DUBs appear to poorly hydrolyse Ser65-phosphorylated ubiquitin (Wauer et al., 2015a).

1.2.6.3 Subcellular localisation of DUBs

Most human DUBs, ~80%, are either cytosolic or nuclear. This was first assayed by systematically tagging a large cohort of DUBs with GFP in HeLa cells and mapping them by immunofluorescence microscopy (Urbé et al., 2012). Later, global mass spectrometry screens from subcellular fractionations shed light on the abundance and localisation of most of HeLa cell proteins,

including DUBs (Itzhak et al., 2016). Roughly 20% of DUBs are associated with specific cellular structures (Reviewed in (Clague et al., 2019)). As an example, USP21 was found to be restricted to centrosomes and microtubules (Urbé et al., 2012).

Several DUBs possess splicing variants which localise to distinct organelles (**Figure 1.8**). Splice variants 1, 2 and 3 of USP33 are found in ER and on COPII-coated vesicles (Thorne et al., 2011). USP33 variant 3 (USP33V3), which is missing an 8 amino acid sequence in its catalytic domain, predominantly resides at the Golgi apparatus (Thorne et al., 2011). Similarly, USP35 has multiple isoforms. Yogesh Kulathu's group characterised two USP35 isoforms with isoform 1 (full length) being cytosolic and isoform 2 (N-terminal truncation of 269 residues) being restricted to the ER and lipid droplets (Leznicki et al., 2018).

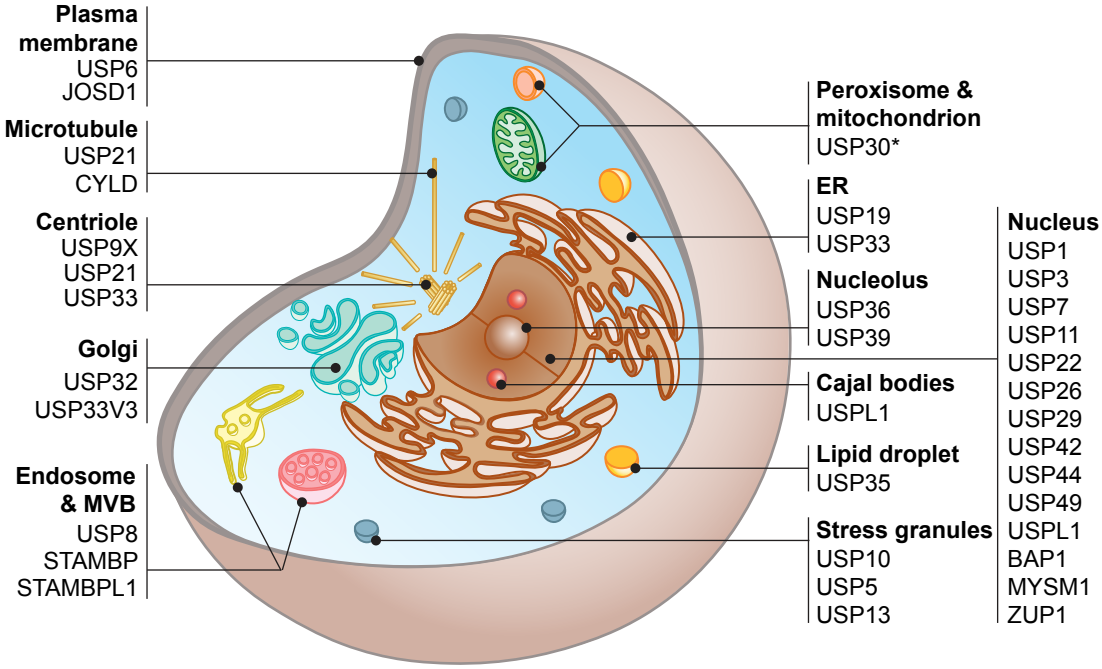

Figure 1.8: Subcellular localisation of DUBs.

Mammalian DUBs are predominantly localised to the cytosol (not shown) or to the nucleus. However, a subset of DUBs (~20%) are associated with particular cellular structures. Some DUBs localise to microtubules (USP9X, USP21, CYLD), others to selective organelles. This is exemplified by USP33V3 and USP32 which are Golgi-specific DUBs. USP30 and USP19 are the only DUBs to have a transmembrane domain which enables them to anchor themselves to the ER or to mitochondria and peroxisomes, respectively. USP30*: We discovered that endogenous USP30 is localised to both mitochondria and peroxisomes. The details are described in Chapter IV and Marcassa et al., 2018.

1.3 Protein degradation pathways

In eukaryotes, proteolysis is primarily mediated by the Ubiquitin Proteasome System (UPS), the endo-lysosomal pathway and autophagy (Ciechanover, 2005) (**Figure 1.9**).

The UPS degrades ubiquitylated proteins via the proteasome whilst autophagy and the endosomal pathways of degradation require the lysosome.

All three pathways are tightly regulated by ubiquitin and each involves specific ubiquitin receptors, which recognise ubiquitylated cargoes thanks to their ubiquitin binding domains, and target them to one of the degradation pathways: UPS (Rpn1, Rpn10, Rpn13), endo-lysosomal pathway (ESCRT-0 members, HRS and STAM; ESCRT-I, TGS101 and UBAP1; ESCRT-II, VPS36) and autophagy (> 30 autophagy receptors, such as SQSTM1, NBR1, NDP52, TAX1BP1, or OPTN), (Clague and Urbé, 2010).

1.3.1 Endo-lysosomal pathway

The endo-lysosomal pathway targets cell surface membrane proteins captured in endocytic vesicles such as receptors, ion channels and nutrient transporters. Endosomes are sorting facilities, which can recycle endocytosed cargoes to the plasma membrane, recycling endosomes or Golgi thanks to the retromer complex (VPS35, VPS26 and VPS29) and other complexes (eg: retriever complex). Alternatively, cargoes are incorporated into intralumenal vesicles of multivesicular bodies for subsequent degradation thanks to the ESCRT complex (Endosomal Sorting Complexes Required for Transport). These multivesicular bodies, also sometimes referred to as late endosomes, ultimately fuse with the lysosome (Cullen and Steinberg, 2018; Norris and Grant, 2020).

1.3.2 Ubiquitin Proteasome System (UPS)

The UPS system was first described by Aaron Ciechanover, Avram Hershko, Irwin Rose and colleagues (Ciechanover, 2005). In this system proteins are tagged with ubiquitin and sent for degradation in the proteasome, a multi-protein complex.

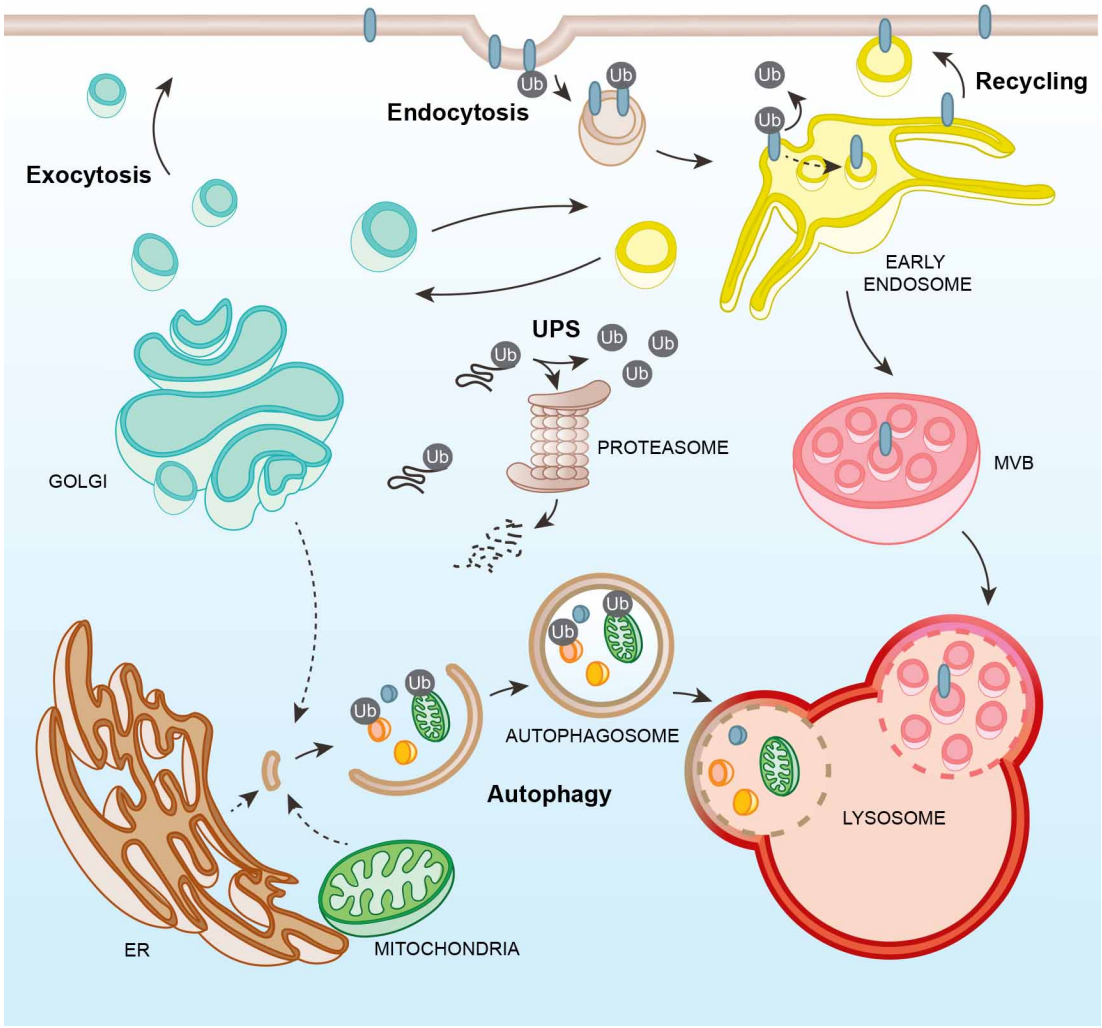

Figure 1.9: The major proteolysis pathways, UPS, endo-lysosomal degradation and autophagy are interconnected.

Endosomes are sorting facilities which either internalise endocytosed cargoes into intralumenal vesicles for degradation or recycle them from the tubular regions back to the plasma membrane (in some cases via perinuclear recycling endosomes, not shown) or to the Golgi apparatus. Internalisation into intralumenal vesicles is controlled by the ESCRT complex that recognises ubiquitylated cargoes. Recycling is controlled by the retromer or retriever complexes following the recognition of the sorting motif. Degradation occurs when the late endosome or multivesicular body fuses with the lysosome. Macro-autophagy (autophagy) requires the formation of an autophagosome which captures cytoplasmic content and ultimately fuses with the lysosome to form an autoplysosome where degradation takes place. Autophagy can be non-selective or selective. In selective autophagy, autophagy receptors target the autophagosome to specific protein or organelle cargoes either by binding to ubiquitin-tags or to the cargo itself. The UPS degrades ubiquitylated proteins through the proteasome. Ubiquitin itself is recycled by DUBs associated with the proteasome and endosome respectively.

ER: Endoplasmic reticulum; MVB: Multi-vesicular body.

1.3.2.1 The 26S proteasome

The 26S proteasome is a 2.5MDa complex composed of a 20S core particle (CP) and one or two 19S regulatory particles (RP). The 20S CP is a barrel shaped proteolytic complex formed of two heptameric α-rings and two heptameric β-rings organised as follows: α_{1-7}/ β_{1-7}/ β_{1-7}/ α_{1-7}. The α-rings form a gate with their N-terminal tails to regulate the entry of proteins within the proteolytic chamber. The β-rings contain the three proteases (β_1, β_2 and β_5) (Rousseau and Bertolotti, 2018; Yu and Matouschek, 2017).

The 19S RP is involved in substrate recognition, unfolding and translocation into the CP catalytic chamber. It consists of a base complex and lid complex.

Protein unfolding is mediated by a hexameric AAA-ATPase (Rpt1-6 in yeast/ PSMC1-6 in humans) ring located in the base which mechanically unfold proteins by ATP hydrolysis and engages the substrate to the proteolytic core of the CP (Bard et al., 2018; Schweitzer et al., 2016). The base also contains four non-ATPase RP proteins (Rpn1, Rpn2, Rpn10 and Rpn13 in yeast/ PSMD2, PSMD1, PSMD4 and ADRM1 in human). Rpn1, Rpn10 and Rpn13 are ubiquitin receptors that recognise ubiquitylated proteins thanks to their UBD domains (Yu and Matouschek, 2017). Rpn1, Rpn2 and Rpn13 also serve as interacting platforms for proteasome substrate recognising proteins and substrate modifiers such as DUBs and ubiquitin E3 ligases. Protein recognition is also managed by shuttle substrate adaptors which possess a UBL domain to bind to the proteasome and UBA domains to bind ubiquitin such as Rad23 (RAD23A-B) and Dsk2 (UBQLN1-2) in yeast (Bard et al., 2018; Yu and Matouschek, 2017).

The lid is a horseshoe structure that organises the base/lid association and also regulates the deubiquitylation of proteasome substrates. It contains nine Rpn proteins: Rpn3, Rpn5, Rpn6, Rpn7, Rpn8, Rpn9, Rpn11, Rpn12 and Sem1 (PSMD3, PSMD12, PSMD11, PSMD6, PSMD7, PSMD13, PSMD14, PSMD8, PSMD9 in humans) (Rousseau and Bertolotti, 2018). PSDM14/PSMD7 form a DUB-pseudo-DUB heterodimer that sits at the entry of the AAA-ATPase ring and removes ubiquitin from substrates engaged for proteasomal degradation by “en bloc” cleavage (Clague et al., 2019). Two other DUBs, Ubp6 (USP14) and UCHL5 (only in humans), associate with the proteasome by binding Rpn1 (PSMD2) and Rpn13 (ADRM1) respectively, and

control the fate of proteasome targeted proteins (de Poot et al., 2017). USP14 and UCHL5 can remove ubiquitin from substrate prior to their engagement in the AAA-ATPase ring and prevent their degradation. USP14 has also been shown to cooperate with PSMD14. Indeed, USP14 has a higher affinity for multi-ubiquitylated proteins (Lee et al., 2016). It can therefore work in unison with PSMD14 in a 2-step deubiquitylation process: USP14 first removes supernumerary ubiquitin chain from proteasomal substrate and PSMD14 secondly cleaves off the remain ubiquitin chains once the substrate is engaged in the proteasome.

1.3.2.2 Proteasome degradation signal

The targeting of a protein to the proteasome usually requires that : 1) it is ubiquitylated for it to be recruited and 2) that it contains a disordered region (also known as initiation region) to become engaged by the RP and translocated into the CP (Roberts and Pruneda, 2020).

1.3.2.2.1 Ubiquitin signal

Long (> tetraUb) K48-linked chains are the best characterised proteasome targeting signal. However other poly ubiquitin chains such as K11 or K63, as well as branched chains have been found capable of targeting substrates to the proteasome (Meyer and Rape, 2014; Yu and Matouschek, 2017). Although long polyUb chains are more efficient than mono-ubiquitin, multi-monoubiquitylation and multi-diUb were reported to efficiently target the proteasome (Lu et al., 2015).

Interestingly, a few proteins, such as ornithine decarboxylase, can be degraded without ubiquitylation. However, the underlying targeting mechanisms are not fully understood (Yu and Matouschek, 2017).

1.3.2.2.2 Initiation region

The initiation region is a >20 amino-acid long disordered region of proteasome substrates that enables their engagement (Yu and Matouschek, 2017). Not all proteasome substrates possess an initiation region, however ubiquitin modification is able to induce localised protein destabilisation which exposes these disordered regions (Carroll et al., 2020; Roberts and Pruneda, 2020).

1.4 Autophagy

Autophagy, meaning “self-eating” in Greek, is a term coined by Christian de Duve in 1963. This term englobes pathways where intracellular content is targeted for lysosomal (or vacuolar in yeast and plants) degradation. Autophagy includes macroautophagy, microautophagy and chaperone mediated autophagy (CMA) (**Figure 1.10**) (Yim and Mizushima, 2020). Microautophagy and CMA occur directly at the lysosome. During microautophagy, the lysosomal membrane invaginates to engulf cytoplasmic content. The mechanisms underlying microautophagy are yet unknown. CMA involves the cytosolic chaperone HSC70. HSC70 recognises a five amino acid sequence on target proteins, KFERQ or variants, and recruits those proteins to LAMP2A, a lysosomal membrane protein. The cargo:HSC70:LAMP2A binding favours LAMP2A oligomerisation and enables the import of the cargo protein into the lysosomal lumen (Yim and Mizushima, 2020).

Macroautophagy is the best characterised pathway of autophagy and will be hereafter referred to as autophagy. In this pathway, double-membrane vesicles (autophagosomes) engulf cytoplasmic components and then fuse with the lysosome. Autophagy recycles intracellular components in case of nutrient shortage. Other functions of autophagy include degrading damaged or impaired organelles, alleviating cellular stress (hypoxia, oxidative stress, ER stress, …), removing abnormal protein aggregates and eliminating pathogens. Autophagy can be non-selective or selective.

1.4.1 Mechanism of mammalian autophagy

The steps of autophagy can be briefly summarised as follow: 1) autophagy induction signal, 2) nucleation of the autophagosome precursor (isolation membrane), 3) extension and shaping of the isolation membrane, 4) closure of the autophagosome, 5) fusion with a lysosome (autophagolysosome formation), 6) degradation of the autophagolysosome content by hydrolases.

The ATG genes are the core genes regulating autophagy. They were first identified by Yoshinori Ohsumi in 1993 using the yeast *Saccharomyces cerevisiae* (Tsukada and Ohsumi, 1993; Ohsumi, 2014). The ATG genes can be categorised into 6 functional groups: 1) the ULK kinase complex (ULK1 or ULK2, FIP200, ATG13, ATG101), 2) ATG9-containing vesicles, 3) Class III

PI3K complex I (VPS34, p150, BECN1, ATG14L and NRBF2), 4) the ATG2-WIPI complexes (WIPI1-4) , 5) the ATG16L1 complex (ATG12-ATG5-ATG16L1) and 6) the Atg8-family members (LC3A, LC3B, LC3C, GABARAP, GABARAPL1, GABARAPL2) (Nakatogawa, 2020).

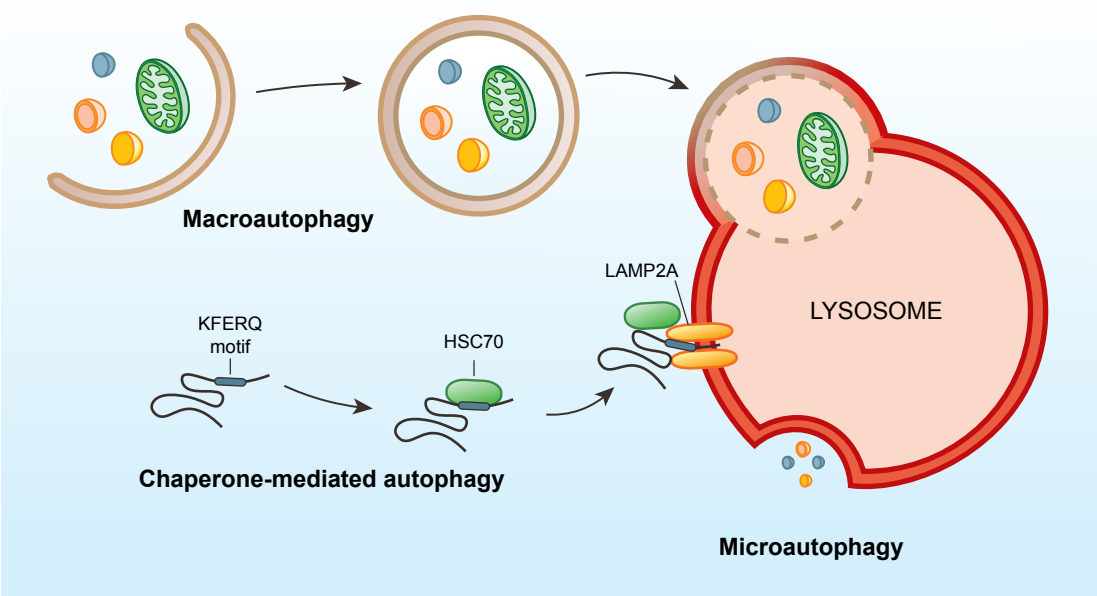

Figure 1.10: Autophagy subtypes: Macro-, micro- and chaperone-mediated autophagy.

All autophagy pathways target cytoplasmic content for degradation in the lysosome. These pathways include macroautophagy, microautophagy and chaperone mediated autophagy (CMA). In macroautophagy, the cytoplasmic content is captured by a double membrane vesicle called the autophagosome, which then fuses with the lysosome. Both microautophagy and CMA occur directly at the lysosome. In CMA, a cytosolic chaperone protein, HSC70, binds to the KFERQ motif of the target protein and brings it to LAMP2A, a lysosomal membrane protein. This enables the formation of a multimeric LAMP2A complex and promotes the translocation of the cargo protein to the lysosomal lumen. Microautophagy is the direct invagination of the lysosomal membrane to engulf cytoplasmic content.

1.4.1.1 Autophagy induction and the ULK complex:

As briefly mentioned earlier, autophagy is induced by a wide range of triggers. All of these initiating pathways are unique but often converge on TORC1. TORC1 constitutively inhibits autophagy by phosphorylating ULK1 and ATG13. TORC1 inactivation enables the assembly of multiple ULK complexes, also known as initiator complexes, that recruit and activate the ATG cascade through phosphorylation of ATG proteins (He and Klionsky, 2009; Zachari and Ganley, 2017; Velazquez and Jackson, 2018).

1.4.1.2 Isolation membrane and ATG9-vesicles

In mammals, autophagosome formation was reported to occur at ER subdomains and specifically at ER-mitochondrial contact sites (Hamasaki et al., 2013). The ULK complexes have been described to accumulate at ER subdomains rich in phosphatidylinositol (PI) synthase (Nishimura et al., 2017). There the ULK complexes initiate autophagosome formation.

ATG9 containing vesicles are recruited to the site of autophagosome formation and are thought to be involved in the generation of the isolation membrane. In mammals, those vesicles cycle between the ER, the Golgi, the plasma membrane (through clathrin mediated-endocytosis) and recycling endosomes (Mercer et al., 2018; Nakatogawa, 2020).

The PI3K-complexes I are then targeted to the autophagosome precursor and phosphorylate PI to produce phosphatidylinositol-3-phosphate (PI3P). PI3P-binding proteins, such as the members of the WIPI family ($WIPI_{1-4}$), then accumulate on pre-autophagic membrane (Mercer et al., 2018; Polson et al., 2010).

1.4.1.3 Membrane extension and lipidation

The WIPI proteins bind to ATG2 and form ATG2-WIPI complexes. Those complexes are able to tether ER-associated membranes to the autophagosome precursor and promote membrane expansion (Bakula et al., 2017; Chowdhury et al., 2018).

In mammals, the membrane required for the expansion of the autophagosome can originate from the ER, Golgi, plasma membrane and recycling

endosomes. Lipids can originate from the ER directly through the omegasome, a ring shape ER-structure surrounding the isolation membrane, or through COPII vesicles and possibly via ER-mitochondria contact sites (Nakatogawa, 2020).

Another important process in autophagosomal membrane expansion is the lipidation of Atg8-family proteins. This 2-step process requires 1) ATG16L1 complex formation and 2) conjugation of Atg8-family proteins to phosphatidylethanolamine (Hanada et al., 2007; Fujita et al., 2008; Lane and Nakatogawa, 2013). ATG12 is a UBL which is conjugated to ATG5 lysines by the E1 ATG7 and the E2 ATG10. ATG12-ATG5 can then bind ATG16L1 and form the ATG16L1 E3 ligase complex. The ATG16L1 complex is responsible for Atg8-lipidation. All Atg8-family members are UBLs and are conjugated to phosphatidylethanolamine's amino group (Hanada et al., 2007; Fujita et al., 2008; Lane and Nakatogawa, 2013).

1.4.1.4 Autophagosome closure, fusion with the lysosome and lysosomal degradation

Closure is thought to require membrane fission and the ESCRT machinery (Nakatogawa, 2020). Finally, the tethering and fusion of the autophagosome to/with lysosomes is mediated by SNARES (STX17, SNAP29) and is supported by the HOPS complex. The autophagosome content is then degraded by lysosomal hydrolases (Dikic and Elazar, 2018; Zhao and Zhang, 2019).

1.4.2 Mechanism of selective autophagy

In the case of nutrient starvation, autophagy is thought to be non-selective and engulfs part of the cytoplasm with organelles, membranes and proteins, and recycles them. Autophagy can also be directed towards the degradation of specific (or part of) organelles, protein aggregates or pathogens. In mammals, characterised pathways of selective autophagy include: mitophagy (mitochondria), pexophagy (peroxisomes), reticulophagy (ER), ribophagy (ribosomes), lipophagy (lipid droplets), lysophagy (lysosomes), aggregophagy (proteins aggregates), xenophagy (bacteria and viruses). Autophagy can also

target nutrients and proteins: glycophagy (glycogen), ferritinophagy (ferritin) (Gatica et al., 2018).

In selective autophagy, autophagosome assembly around the autophagy cargo requires autophagy receptors. These autophagy receptors possess an LC3-interacting region (LIR) which binds the Atg8-family members LC3 and GABARAPs and recruits them to the autophagy cargo (Kirkin and Rogov, 2019). This was discovered by the Johansen lab, which found that the ubiquitin binding protein SQSTM1/p62 could interact with LC3s and GABARAPs via a 22 a.a. conserved motif and mediate the autophagic degradation of polyubiquitylated protein aggregates (Bjørkøy et al., 2005; Pankiv et al., 2007). Several selective autophagy receptors (SARs) can also bind to FIP200, such as SQSTM1 and NDP52, and thus have the ability to recruit ULK complexes to initiate autophagosome formation around the cargo. SARs can bind ubiquitin on ubiquitylated cargo or directly bind the cargoes themselves. In mammals, many SARs have ubiquitin binding domains (UBDs) which enables them to bind ubiquitylated substrates and recruit an autophagosome to ubiquitylated regions (Husnjak and Dikic, 2012). Other SARs function independently of ubiquitin binding. Such examples include membrane bound mitochondrial SARs: BNIP3 (OMM), BNIP3L (OMM), FUNDC1 (OMM), and BCL2L13 (OMM), NIPSNAPs (Matrix), PHB2 (IMM), which have transmembrane domains as well as a LIR domain (Kirkin and Rogov, 2019).

1.4.3 Mitophagy pathways

Mitophagy is the selective autophagic degradation of mitochondria. It can be induced by various stimuli, such as oxidative stress, mitochondrial impairment or damage, ion starvation (iron chelation), hypoxia or abnormal protein aggregation in mitochondria (Allen et al., 2013; Ashrafi et al., 2014; Jin and Youle, 2013; Liu et al., 2012; Pimenta de Castro et al., 2012; Yang and Yang, 2013; Zhang et al., 2008).

Mitophagy can also be developmentally programmed. This includes the removal of all mitochondria from erythroblasts during erythrocyte maturation, the degradation of paternal mitochondria following fusion of sperm with the egg in mammals, as well as the elimination of glycolytic mitochondria during

cardiomyocyte maturation to favour a metabolic switch towards mitochondria adapted to a fatty acid metabolism.

The best characterised pathway of mitophagy is regulated by the kinase PINK1 and the ubiquitin E3 ligase Parkin. This pathway has been extensively studied due to its link to Parkinson's disease. However, not all pathways of mitophagy require PINK1 and Parkin.

Other E3 ligases were found to be involved in mitophagy instead of Parkin or in parallel with Parkin such as HUWE1, MUL1, MARCH5, ARIH1 (See Chapter V), (Koyano et al., 2019a; Rojansky et al., 2016; Strappazzon et al., 2015; Villa et al., 2017; Yun et al., 2014)

There are also ubiquitin-independent pathways employing the mitophagy receptors mentioned above that do not possess ubiquitin binding domains. Hypoxia was reported to induce mitophagy through two autophagy receptor pathways. Firstly hypoxia promotes the expression of the mitochondrial autophagy receptor BNIP3L (also known as NIX) in a HIF1 (Hypoxia Inducible Factor)-dependent manner (Bellot et al., 2009; Zhang et al., 2008). Secondly hypoxia activates FUNDC1, an integral OMM protein and mitophagy receptor, by promoting the dephosphorylation of its LIR domain. This enables the direct binding of FUNDC1 to autophagosomal membranes (Chen et al., 2017; Liu et al., 2012).

Although programmed mitophagy or acute stress, such as the complete depolarisation of the mitochondrial network, can lead to global mitophagy causing the complete removal of mitochondria from cells, localised damage was shown to promote bit-by-bit (also known as piecemeal) mitophagy, where only a portion of the network is eliminated. The mitochondrially targeted photosensitiser KillerRed (Mt-KR) probe can induce ROS at focal points of the mitochondrial network when stimulated by light. This promotes the local recruitment of Parkin, focal ubiquitin deposition and recruitment of LC3 and LAMP1 to specific puncta on mitochondria in both mammalian cells and murine hippocampal neurons (Yang and Yang, 2013; Ashrafi et al., 2014). Similarly, overexpressing a mutant form of ornithine transcarbamylase (ΔOTC) promotes the accumulation of misfolded ΔOTC on mitochondria and induces PINK1

accumulation to focal ΔOTC aggregates. This leads to the recruitment of Parkin to mitochondria containing ΔOTC and induces mitophagy following Drp1-mediated fission (Burman et al., 2017; Jin and Youle, 2013).

1.4.4 Mitochondria derived vesicles (MDVs): an alternative to mitophagy

An alternative pathway to piecemeal mitophagy are mitochondria derived vesicles (MDVs). MDVs were first observed in 2008 by Heidi McBride's group (Neuspiel et al., 2008). By confocal and electron microscopy, they observed small vesicles (~100nm) budding off from mitochondria independently of DRP1 (Neuspiel et al., 2008). These vesicles contained the E3 ligase MUL1, colocalised with the retromer complex (VPS35) and fused with peroxisomes (Braschi et al., 2010). The transport of MUL1 to peroxisomes via the MDVs appeared to be dependent on the retromer complex as knocking-down VPS35 decreased the pool of MUL1-positive peroxisomes (Braschi et al., 2010).

Sucrose gradients, subcellular fractionations and microscopy performed *in vitro* and *in vivo* revealed that MDVs carry only selective mitochondrial cargo and exist as single membrane bound vesicles with OMM proteins such as VDAC or double-membrane bound vesicles (McLelland et al., 2014; Soubannier et al., 2012a).

McBride's team reported on a subset of double membrane MDVs containing the matrix protein pyruvate dehydrogenase (PDH) that fuse with the lysosome independently of ATG5, BECN1, RAB9 and LC3 (McLelland et al., 2014; Soubannier et al., 2012b). These MDVs were enriched in oxidised cargoes and their formation was stimulated following oxidative stress (ex: Complex III inhibitor Antimycin A treatment), (Soubannier et al., 2012a). Interestingly, the generation of this subset of MDVs was dependent on PINK1 and Parkin function and their fusion with late-endosome/lysosomes required the mitochondrial SNARE Stx17, SNAP29 and VAMP7 as well as the HOPS tethering complex (Vps39, Vps41), (McLelland et al., 2014, 2016). MDVs thus constitute an alternative quality control mechanism which sends oxidised mitochondrial content for lysosomal degradation independently of the autophagy machinery.

1.4.5 Rabs and mitochondria clearance

Rabs, Rab GTPase activating proteins (GAP) and Rab Guanine nucleotide exchange factor (GEF) are involved in canonical and alternative pathways of mitophagy.

The mitochondrial Rab7-specific GAPs TBC1D15 and TBC1D17 were shown to regulate autophagosome biogenesis and prevent excessive expansion of the autophagosomal membrane on mitochondria (Yamano et al., 2014). Following the ubiquitylation of OMM proteins during PINK1/Parkin mitophagy, RABGEF1 is recruited to damaged mitochondria through ubiquitin binding and recruits Rab5 and Rab7 which in turn bring ATG9 vesicles to mitochondria (Yamano et al., 2018). The retromer associated Rab7-specific GAP TBC1D5 and the retromer itself were also shown to modulate the cycling of Rab7 between the endolysosomal and mitochondrial compartments (Jimenez-Orgaz et al., 2018). The activity of Rab7 towards ATG9 vesicle was reported to be positively regulated by the phosphorylation of Rab7 at S72 by TBK1 (Heo et al., 2018).

Another pathway of mitochondrial degradation involves the Parkin-dependent sequestration of mitochondria within Rab5-positive vesicles (Hammerling et al., 2017a, 2017b). The autophagic protein BECN1 mediates the activation of Rab5 and enables the engulfment of mitochondria in endosomes by the ESCRT complexes. These vesicles are then degraded in lysosomes (Hammerling et al., 2017a). The autophagy adapter BNIP3 was shown to enhance the sequestration of mitochondria in Rab5 vesicles (Hammerling et al., 2017b).

During ischemia or nutrient starvation induced mitophagy, Rab9-positive trans-Golgi membranes were described to be recruited to damaged mitochondria following the phosphorylation of Rab9 at S179 by ULK1 (Saito et al., 2019). This pathway was shown to be BECN1 dependent and Parkin-independent.

1.4.6 The PINK1/Parkin pathway of mitophagy

As described in **section 1.2**, PINK1 and Parkin are two PD risk genes which were found to be involved in a joint mitochondrial quality control pathway (Greene et al., 2003; Clark et al., 2006; Park et al., 2006). In 2008, Richard Youle's lab revealed that triggering mitochondrial depolarisation with the

protonophore Carbonyl cyanide m-chlorophenyl hydrazone (CCCP) provoked the redistribution of Parkin from the cytosol to depolarised mitochondria and promoted their autophagic degradation in mouse embryonic fibroblasts (MEF) and HeLa cells overexpressing Parkin (Narendra et al., 2008).

1.4.6.1 Mitochondrial damage sensing by PINK1

Genetic manipulations in *Drosophila* demonstrated that *Pink1* acts upstream of *Parkin* **(see section 1.2)** (Clark et al., 2006; Park et al., 2006). This mitochondrial kinase serves as a sensor of damaged mitochondria and initiates mitophagy.

In healthy mitochondria, the 63 kDa long PINK1 precursor is continually under proteolytic control (**Figure 1.11**). PINK1 first bind to the OMM translocase (TOM) complex and is imported in the IMM translocase (TIM) complex possibly through its N-term mitochondrial targeting signal (MTS) and in a mitochondrial membrane potential (Δψm)-dependent manner. Its N-terminal segment is cleaved by the matrix proteases MPP (mitochondrial processing protease) which removes the MTS, and then by PARL (presenilin-associated rhomboid-like protein) which cleaves within the transmembrane domain (TMD) at Ala103 into a 52 kDa protein. Finally, PINK1 is retro-translocated to the cytosol to be fully degraded by the proteasome (Jin et al., 2010; Deas et al., 2011; Yamano and Youle, 2013; Bayne and Trempe, 2019). In healthy mitochondria PINK1 thus has a short half-life. In HeLa cells overexpressing PINK1, its half-life was estimated to last ~27 min (Lin and Kang, 2008).

In dysfunctional and depolarised mitochondria, PINK1 is no longer imported in the TIM complex. PINK1 therefore accumulates at the TOM complex (Matsuda et al., 2010; Narendra et al., 2010a). This anchorage at the OMM is stabilised by PINK1's OMM localisation signal and by a negatively charged triad of glutamic acid (112E, 113E and 117E), both flanking PINK1's transmembrane domain (Okatsu et al., 2015a; Sekine et al., 2019). PINK1 stabilisation at the OMM upon depolarisation was also reported to be TOMM7-dependent (Sekine et al., 2019). PINK1 that fails to accumulate at the OMM of depolarised mitochondria is imported in the IMM and cleaved by the protease OMA1 (Sekine et al., 2019).

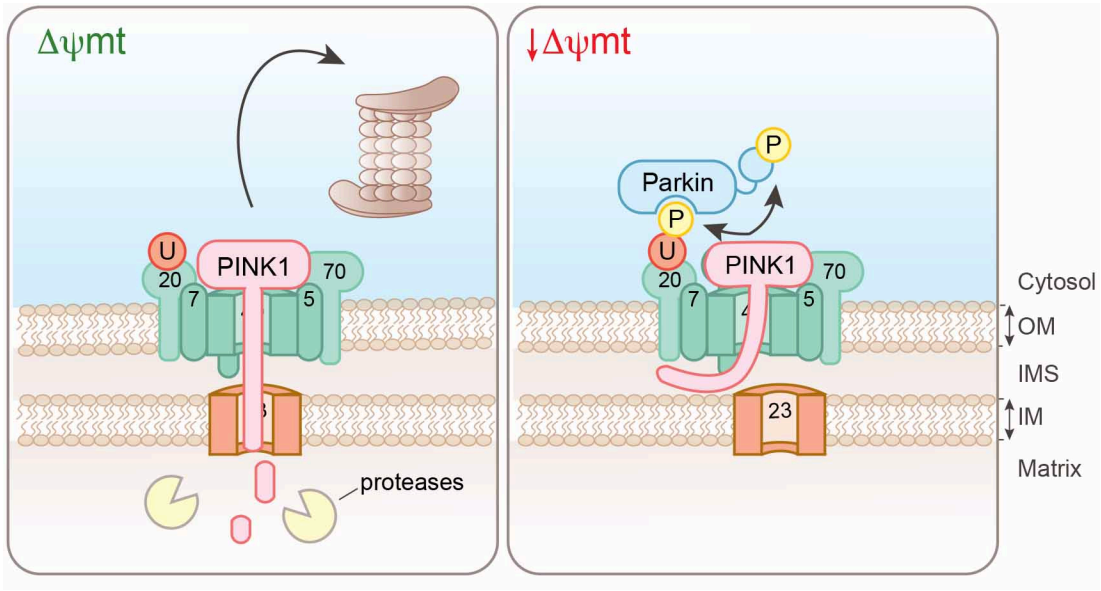

Figure 1.11: PINK1, a sensor of mitochondrial damage.

At steady state, PINK1 is rapidly degraded by the proteasome (left). PINK1's N-terminal segment is imported in the mitochondrial matrix through the TOM and TIM complexes and cleaved by the proteases PARL and MPP. The 52kDa cleaved PINK1 is then retrotranslocated to the cytosol and degraded by the proteasome.

When mitochondria are impaired and depolarised, PINK1 can no longer be imported into the matrix and accumulates at the OMM (right). Stabilised PINK1 activates mitophagy by phosphorylating nearby ubiquitin at Ser65, which recruits Parkin. PINK1 then fully activates Parkin by phosphorylating its Ubl domain at Ser65.

Once stabilised at the OMM, PINK1 auto-phosphorylates at Ser228 and Ser402, and is thought to dimerise to be fully active (Aerts et al., 2015; Okatsu et al., 2012, 2013; Rasool et al., 2018).

Once activated, PINK1 starts phosphorylating nearby ubiquitin at Ser65 to promote Parkin recruitment and activation (Kane et al., 2014; Kazlauskaite et al., 2014; Koyano et al., 2014). Parkin binds pS65-Ubquitin via its RING1 domain and this releases the Ubl which was occluding its E2 binding site located at the RING1 **(Figure 1.12),** (Gladkova et al., 2018; Sauvé et al., 2018). PINK1 is then able to phosphorylate Parkin at the Ubl domain, which both liberates the catalytic RING2 domain and releases the REP element which was inhibiting the E2 binding site. Parkin is then fully active (Gladkova et al., 2018; Sauvé et al., 2018; Kumar et al., 2015; Wauer et al., 2015b).

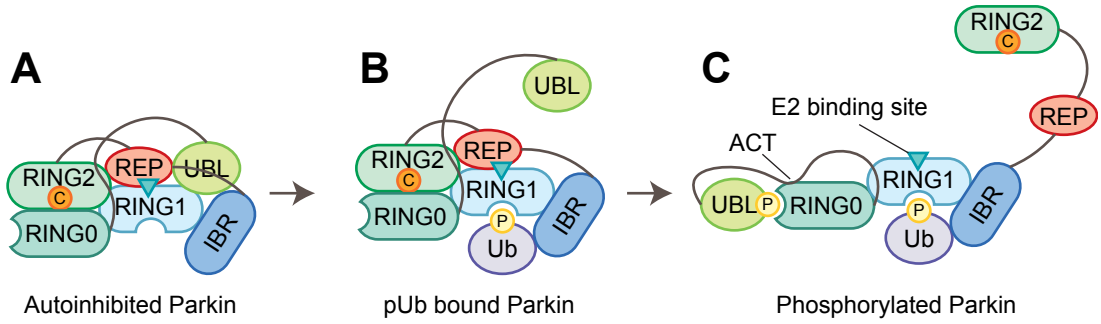

Figure 1.12: Parkin activation by PINK1

A) Parkin is an RBR E3 ligase which is autoinhibited at steady state. Its RING0 domain occludes the catalytic cysteine located in the RING2 domain while both the repressor element (REP) and the UBL domain obstruct the E2 binding site situated at the RING1 domain. **B)** PINK1 phosphorylates nearby mitochondrial ubiquitin at Ser65 (pUb). Parkin is recruited to mitochondria due to its affinity for pUb and binds pUb through its RING1 domain. Parkin then undergoes conformational changes: it releases the UBL domain and thereby partially liberates the E2 binding site. **C)** PINK1 is then able to phosphorylate Parkin's UBL domain at Ser65. In response to this, p-Parkin undergoes additional conformational changes. First, the RING2 domain and REP are released from the RING0 and RING1 domains, respectively. Those events expose the catalytic cysteine and the E2 binding domain. Secondly, the p-UBL binds RING0 at its phosphate binding pocket. The linker region between p-UBL and RING0 binds RING0's hydrophobic groove and acts as an activating element (ATC) by promoting the full release of RING2. Parkin is then fully active.

Figure adapted from Sauvé et al., 2018 and Gladkova et al., 2018.

1.4.6.2 Parkin-mediated ubiquitylation and feed-forward amplification of mitophagy

Once recruited to mitochondria, Parkin ubiquitylates OMM proteins (**Figure 1.13**). Absolute quantification (AQUA)-based proteomics have revealed that Parkin is able to generate most ubiquitin-linkages (Ordureau et al., 2014). Upon mitochondrial depolarisation, Parkin produces mainly canonical K48- and K63-linked ubiquitin chains and non-canonical K11- and K6-linked ubiquitin chains to a lesser extent in HeLa Flp-In Parkin (Ordureau et al., 2014). Although less abundant than canonical ubiquitin chains, K6-linked chains were reported to undergo the highest fold-increase following mitochondrial depolarisation in HEK293 and SH-SY5Y cells overexpressing Parkin (Cunningham et al., 2015).

Known substrates of Parkin Include proteins of the TOM complex (TOMM5, TOMM20, TOMM40 TOMM70) which regulate mitochondrial protein import; VDAC ion channel proteins (VDAC1, VDAC2, VDAC3); proteins orchestrating

mitochondrial fusion and fission such as: MFN2, DNM1L or FIS1; proteins mediating mitochondrial transport such as MIRO1, and many others (Sarraf et al., 2013; Bingol et al., 2014; Cunningham et al., 2015; Rose et al., 2016; Martinez et al., 2017). Some of these ubiquitylated species are sent for proteasomal degradation (e.g.:MIRO1, TOMM20) in cell overexpressing Parkin (Liang et al., 2015).

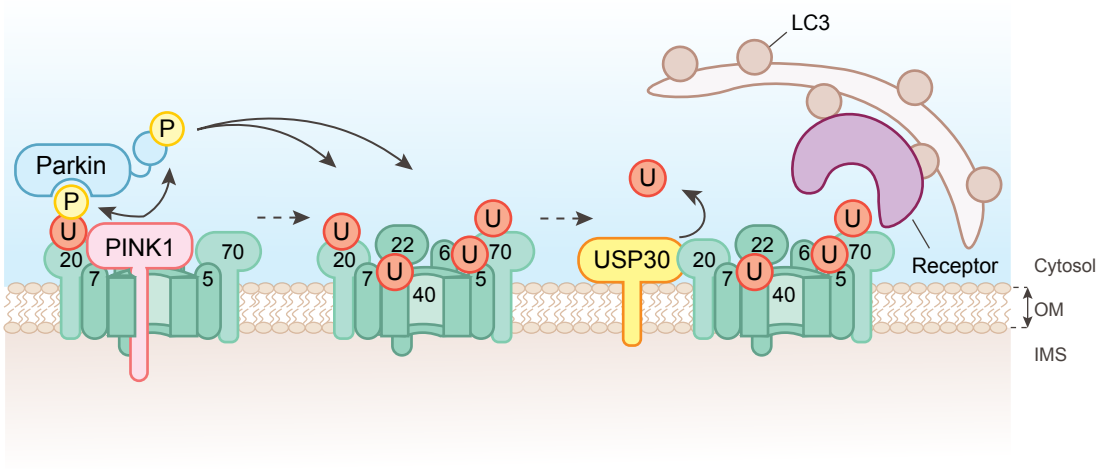

Figure 1.13: Model detailing the mechanism of mitophagy activation.

PINK1 initiates mitophagy by phosphorylating surrounding mitochondrial ubiquitin at Ser65 (pUb). This enables the recruitment of Parkin to the OMM due to its affinity for pUb. PINK1 can then activate Parkin by phosphorylating its Ubl domain at Ser65. Activated Parkin ubiquitylates OMM proteins such as members of the TOM complex (TOMM5, TOMM20, TOMM40, TOMM70). This serves as a platform for the recruitment of autophagy receptors (NDP52, OPTN, TAX1BP1, NBR1 or SQSTM1). Those receptor proteins bind ubiquitin via their UBDs and bind to the LC3-containing autophagosomal membrane through their LIR domain. The mitochondrion is then enveloped in the autophagosomal membrane and subsequently undergoes lysosomal degradation. USP30 is thought to oppose mitophagy by deubiquitylating Parkin substrates, although more recent models suggest a role for USP30 upstream of PINK1 (detailed in Chapter VII and Figure 7.1).

The remaining ubiquitylated substrates enable the recruitment of the autophagosome thanks to autophagy receptors (NDP52/CALCOCO2, OPTN, TAX1BP1, NBR1 and SQSTM1/p62) (Heo et al., 2015; Lazarou et al., 2015; Moore and Holzbaur, 2016). As described above, these receptor proteins bind ubiquitin via their UBDs (UBA for SQSTM1 and NBR1, UBAN for OPTN and UBZ for both NDP52 and TAX1BP1) and also possess LC3-interacting regions (LIR) with which they attach to LC3-containing autophagosomes (Husnjak and Dikic, 2012). SQSTM1 has been reported by various research teams to accumulate on depolarised mitochondria (Geisler et al., 2010; Narendra et al., 2010b; Okatsu et al., 2010; Wong and Holzbaur, 2014). However, the binding of SQSTM1 to ubiquitin was described as non-essential for mitophagy (Narendra et al., 2010b; Wong and Holzbaur, 2014). Youle's group tested if any of the five autophagy adaptors cited above were essential for mitophagy by engineering pentaKO HeLa cells (Lazarou et al., 2015). They found that only NDP52 and OPTN overexpression could alone rescue mitophagy. The single KO of any of the adaptors did not affect mitophagy. The doubleKO of NDP52 and OPTN strongly inhibited mitophagy and more so when combined with TAX1BP1 KO (Lazarou et al., 2015). Intriguingly, Noriyuki Matsuda's group found that OPTN and NDP52 had a lower affinity than NBR1 and SQSTM1 for all ATG8 proteins (Yamano et al., 2020). Instead, OPTN could bind efficiently to ATG9A via its leucin zipper domain and recruits ATG9A-containing vesicles to ubiquitylated mitochondria during mitophagy (Yamano et al., 2020). Richard Youle's team found that NDP52 binds to FIP200, a member of the ULK autophagy initiating complex, via its SKIP carboxyl homology (SKICH) domain and directs the ULK complex to mitochondria to induce mitophagy (Vargas et al., 2019). The OPTN-ATG9A and NDP52-FIP200 axes thus enable *de novo* biogenesis of autophagosome to mitochondria (Yamano and Youle, 2020).

The kinase TBK1 is also recruited to mitochondria during mitophagy and phosphorylates NDP52, OPTN and SQSTM1 (Heo et al., 2015; Moore and Holzbaur, 2016; Richter et al., 2016). The phosphorylation of OPTN and NDP52 enhances their affinity for ubiquitin and therefore increases mitophagy efficiency (Heo et al., 2015). Furthermore, TBK1 facilitates the interaction between NDP52 and FIP200 (Vargas et al., 2019), but does not affect the

binding of OPTN to ATG9A (Yamano et al., 2020). Thanks to the autophagy adaptors the ubiquitylated mitochondrion is then wrapped in the autophagosomal membrane which then fuses with the lysosome to proceed with mitochondrial degradation (Bayne and Trempe, 2019).

1.4.6.3 USP30 opposes Parkin

As mitophagy is a process regulated by ubiquitin our team and others have searched for DUBs opposing Parkin. Bingol and colleagues screened Flag-tagged DUBs and found that the overexpression of USP30 antagonised mitophagy in SH-SY5Y and HeLa cells treated with CCCP (Bingol et al., 2014). At the time, USP30 was known to be a mitochondrial DUB, anchored at the OMM and facing the cytosol (Nakamura and Hirose, 2008). Its function was still poorly understood and it was associated with mitochondrial fusion and fission dynamics and HGF-dependent cell scattering (Buus et al., 2009; Nakamura and Hirose, 2008). Baris Bingol and his team discovered that USP30 delayed mitophagy by opposing the ubiquitylation of Parkin substrates (TOMM20 and MIRO1), in Parkin overexpressing cells (Bingol et al., 2014). They also performed ubiquitylomic experiments in HEK293 cells either overexpressing Parkin or expressing USP30 shRNA. These mass spectrometry experiments suggested that FKBP8, MUL1, PTRH2 (also called PTH2) and PRDX3 were common mitochondrial substrates of Parkin and USP30 (Bingol et al., 2014). Shortly after, our lab and others confirmed that TOMM20 was a bona fide substrate of USP30 and that USP30 opposed the autophagic degradation of mitochondrial content (Liang et al., 2015; Wang et al., 2015). Amos further demonstrated that CCCP-mediated ubiquitylation of OMM proteins lead to both their lysosomal and proteasomal degradation, in Parkin overexpressing cells. In those cells, mitophagy induction with CCCP was also accompanied by high levels of apoptosis which could be antagonised by PINK1 KD or proteasome inhibition. Excessive OMM protein ubiquitylation and their subsequent extraction for degradation possibly disrupts mitochondrial membranes and causes apoptosis. Interestingly, Amos revealed that USP30 opposed this CCCP-mediated BAX/BAK independent apoptosis whilst its depletion could sensitise a variety of mammalian cells to BH3

mimetics (Liang et al., 2015). USP30 thus potentially has anti-apoptotic functions independently of its role in mitophagy.

Jacob Corn and colleagues assessed whether USP30 presented ubiquitin chain preferences. They found that in vitro, USP30 efficiently cleaved K6 and K11 ubiquitin chains. Moreover, in HEK293 overexpressing Parkin, USP30 KO specifically enriched K6 ubiquitin chains by 5-fold (Cunningham et al., 2015). Malte Gersch, in David Komander's lab, confirmed these observations *in vitro*, used K6-affimers to show that USP30 could remove K6-linked ubiquitin from TOMM20 in HeLa expressing Parkin and further expanded on USP30's affinity for K6-linked chains by providing the crystal structure of USP30 in complex with K6-diUb (Gersch et al., 2017).

1.4.6.4 Alternative DUBs involved in mitophagy

To date, USP30 is the only DUB known to constitutively localise at mitochondria. However other deubiquitylating enzymes were reported to affect mitophagy.

Several members of the USP family modulate the localisation of Parkin. USP33, which shuttles between the ER and the Golgi, was found to overlap with mitochondrial staining and to deubiquitylate Parkin at K435 (Niu et al., 2019). USP33 likely controls Parkin ubiquitylation from mitochondria-associated membranes in the ER and hinders the recruitment of Parkin to mitochondria. Likewise, the endosomal DUB USP8 was shown to deubiquitylate Parkin (Durcan et al., 2014). Unlike USP33, USP8 accelerated the recruitment of Parkin to mitochondria by removing K6-linked ubiquitin chains from Parkin (Durcan et al., 2014). USP36, a nucleolus residing DUB, was also reported to facilitate the relocation of Parkin from the cytosol to mitochondria, possibly through transcriptional regulation (Geisler et al., 2019).

A small pool of USP15, which is a predominantly cytosolic DUB (Urbé et al., 2012), was found to be enriched in mitochondrial fractions (Cornelissen et al., 2014). USP15 was shown to decrease the deposition of ubiquitin on mitochondrial fractions and to oppose the degradation of damaged mitochondria in cells overexpressing Parkin. Interestingly, the Vandenberghe group found that mitophagy is enhanced in the flight muscles of WT aged flies

(4-week-old) compared to young flies (1-week-old). This increase in mitophagy with age was not observed in *Parkin* RNAi or *Pink1* mutants. They find that knocking-down *CG8334*, which they describe as "*Drosophila Usp15*", rescues this impairment (Cornelissen et al., 2018a). It is however important to note that *CG8334* is more homologous to human USP32 rather than USP15 (see FlyBase; (Clague et al., 2013, 2019)).

Finally, McQuibban's team reported on a putative short isoform of USP35 (N-terminal truncation of 468 residues) localising on polarised mitochondria with its unique N-terminal mitochondrial targeting sequence (Wang et al., 2015). Depleting USP35 (all USP35 isoforms) was shown to increase the ubiquitylation and degradation of OMM proteins as well as raise mitolysosome density during CCCP-induced mitophagy. However, the short-USP35 variant is missing part of the catalytic domain and the catalytic cysteine (Wang et al., 2015). Thus, mitophagy inhibition could have been mediated by the non-mitochondrial USP35 variants (located at the ER, lipid droplets and cytosol) or could be caused by a scaffolding function of short-USP35.

1.5 Drosophila melanogaster

1.5.1 Major breakthrough discoveries made using *Drosophila melanogaster*

Drosophila melanogaster is a model organism which has been used for over a century.

Charles William Woodworth was the first scientist to breed and recommend the use of *Drosophila* for research purposes in the early 1900's (Markow, 2015). Using *Drosophila*, Thomas H. Morgan described the role played by chromosomes in heredity, work for which he earned a Nobel prize in 1933 (First book published on the subject: (Morgan et al., 1915)), (Morgan, 1933). His success brought much attention to this model, which became the most employed model organism in that era. In 1946 his colleague Hermann Muller, received a Nobel prize "for the discovery of the production of mutations by means of X-ray irradiation" (Muller, 1946, 1927). Both bodies of work had an immense impact on modern genetics. Subsequently, Nobel prizes were awarded to Edward B. Lewis, Christiane Nüsslein-Volhard, Eric F. Wieschaus

for their discoveries on “the genetic control of early embryonic development” in 1995, then to Richard Axel for his “discovery of odorant receptors and the organization of the olfactory system”, next to Jules A. Hoffmann for his insight in ”the activation of innate immunity” in 2011 and then recently to Jeffrey C Hall, Michael Rosbash and Michael W Young for “discoveries of molecular mechanisms controlling the circadian rhythm” in 2017 (Hall et al., 2017; Hoffmann, 2011; Lemaitre et al., 1996; Lewis, 1978; Lewis et al., 1995; Nüsslein-Volhard and Wieschaus, 1980; Axel, 2004; Vosshall et al., 1999).

1.5.2 Advantages:

The success of *Drosophila* as a model organism is based on the following key points: they have a rapid life cycle, produce many progenies, can easily be genetically manipulated, are affordable and are low maintenance.

1.5.3 Life cycle of *Drosophila melanogaster*

Drosophila melanogaster have a rapid life cycle. It takes roughly 10 days from fertilisation to obtain a mature adult (**Figure 1.14**), (Ashburner and Thompson, 1978). Key stages of *Drosophila* development include: the embryonic stage, followed by three larval stages (1st instar, 2nd instar and 3rd instar larvae), the pupal stage and finally the adult stage.

Embryogenesis comprises 17 *Drosophila* embryonic stages and lasts for ~24h at 25ºC (Campos-Ortega and Hartenstein, 1997), (see also: The Interactive Fly website). The eggs then hatch into a 1st instar larva which molts 25h later into a 2nd instar larva and then molts a second time, after 24h, into a 3rd instar larva (Tyler, 2000). The 1st, 2nd and early 3rd stage instar larvae feed on and burrow into the substrate they were laid on (foraging behaviour). The 3rd instar larva is the largest larval stage; once mature the larva stops feeding and crawls out of the medium (wandering” behaviour), and prepares itself for pupation (Sokolowski et al., 1984). Pupation occurs ~120h after fertilisation. During pupation the *Drosophila* undergoes morphogenesis until it ecloses, ~9-10 days later, into an adult fly (Bainbridge and Bownes, 1981). Adult females start mating ~12h following eclosion (Ashburner and Thompson, 1978). At their peak of fertility (4-7 day-old adults) females lay 50-70 eggs per day (Tyler, 2000). In total, adult *Drosophila* can live up to 10 weeks (Tyler, 2000).

As *Drosophila* are ectotherms, their development fluctuates with temperature. As stated above, at 25ºC the development to an adult can take 9-10 days whilst at 10ºC it can take up to 57days. Conversely, high temperature accelerate their development which then only lasts 8 days (Tyler, 2000).

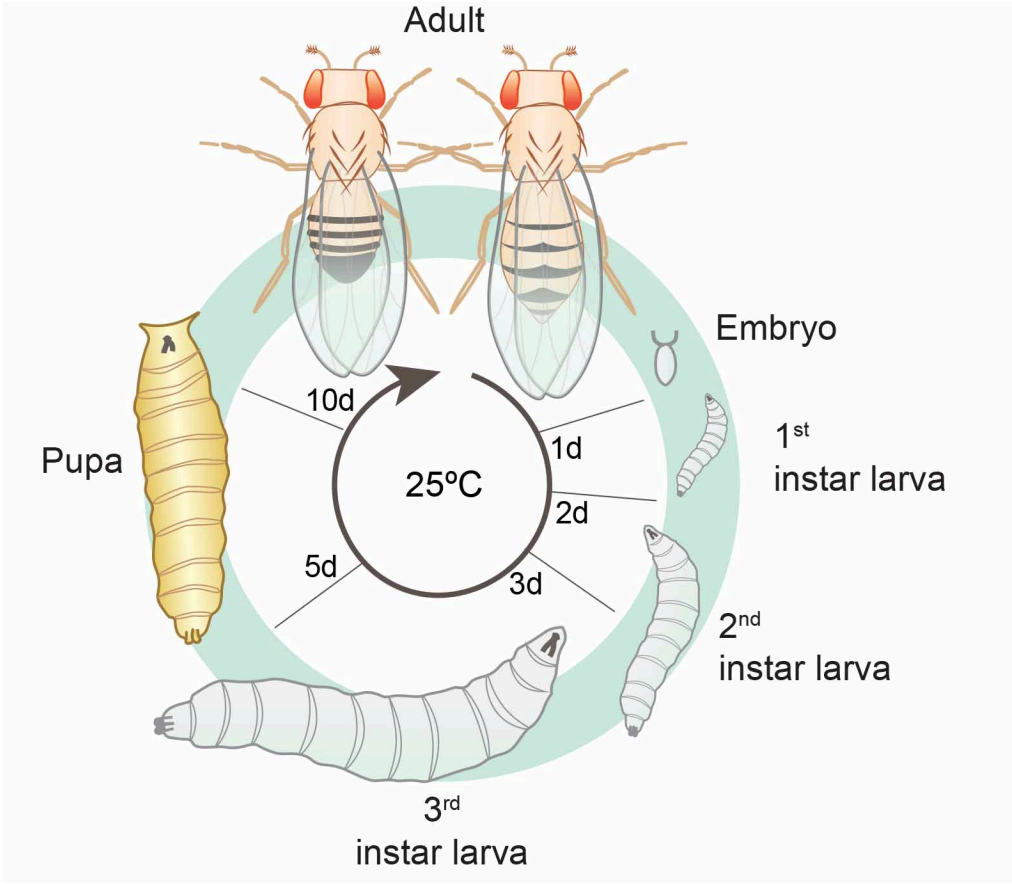

Figure 1.14: Life cycle of *Drosophila melanogaster*

At 25ºC, embryogenesis lasts for ~24h. The egg hatches into a larva which undergoes two molts (first, second and third instar larva). Five days post fertilisation, the third instar larva forms a pupa and undergoes morphogenesis. Eclosion happens on average ten days after fertilisation of the egg and produces a mature adult fly.

1.5.4 *Drosophila* genome

The genome of *Drosophila melanogaster* is ~180 Mb long with 1/3 of heterochromatin. Their genome is distributed in four pairs of chromosomes containing ~13,600 genes **(Figure 1.15)**. They have a pair of sex chromosomes (XX for females and XY for males) and three pairs of autosome chromosomes (Adams et al., 2000). The Y chromosome is mostly constituted of heterochromatin and Y-linked genes are believed to result from autosomal-to-Y transposition. Indeed, the few protein coding genes it contains have paralogs in autosomal genes. These Y-linked genes were reported to be involved in male fertility (Carvalho et al., 2015). Approximatively 80% of the euchromatin is located on the autosomal chromosomes I and II (Adams et al., 2000). Chromosome IV is much smaller than its counterparts and contains only 1.2 Mb of euchromatin. As protein coding genes are mainly located on two pairs of chromosomes and are less redundant than in mammals this greatly facilitates genetic studies.

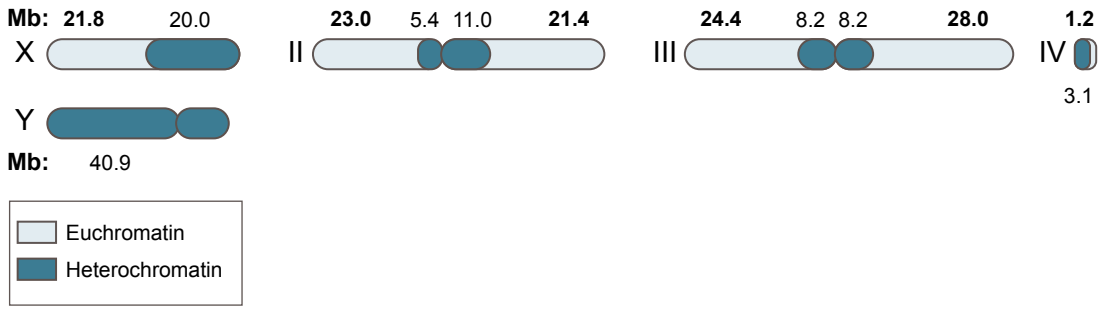

Figure 1.15: Chromosomes of Drosophila melanogaster.

Schematic representation of D. melanogaster's sexual (X and Y) and autosomal chromosomes (II, III and IV). The length of euchromatin and heterochromatin are labelled in bold and regular font respectively. Schematic adapter from Adams *et al.*, 2000.

1.5.5 *Drosophila*, a model to study disease

Although the *Drosophila* genome is simpler than the human genome, it is estimated that 77% of human disease associated genes have orthologues in *Drosophila* (Reiter et al., 2001). As an example, *Drosophila* possess orthologues of the PD-causing genes PARK2/PRKN (*park*/*CG10523* in *Drosophila*) and PINK1/Park6 (*Pink1*/*CG4523*). Mutations in those genes promote disease-phenotypes reminiscent of human PD in *Drosophila* such as locomotor defects or neurodegeneration (Greene et al., 2003; Clark et al., 2006; Park et al., 2006). These early *Drosophila* studies were key to understand the role of PINK1 and Parkin. They revealed that PINK1 and Parkin were genetically linked and paved the way for all of the subsequent studies on the PINK1/Parkin pathway of mitophagy. Interestingly, drosophila also express the mitochondrial DUB *Usp30* (*CG3016* for drosophila), (Tsou et al., 2012).

1.5.6 UAS-GAL4 system in *Drosophila*:

The UAS-GAL4 system enables the targeted expression of a gene of interest. It was first developed for mammalian cells by Hitoshi Kakidani and Mark Ptashne and by Nicolas Webster and Pierre Chambon (Kakidani and Ptashne, 1988; Webster et al., 1988). Andrea Brand and Norbert Perrimon then adapted it to *Drosophila melanogaster* (Brand and Perrimon, 1993). GAL4 is a yeast regulatory protein which binds to upstream activating sequences (UAS) to activate the expression of genes linked to UAS. Mark Ptashne's group showed that the yeast GAL4 could similarly activate transcription in *Drosophila melanogaster* (Fischer et al., 1988). Andrea Brand and Norbert Perrimon developed a two-piece system with "GAL4-driver" lines and "UAS-reporter" lines (**Figure 1.16**), (Brand and Perrimon, 1993). The GAL4-driver lines have the GAL4 encoding gene in the vicinity of tissue-specific enhancer or promoter whilst the UAS-reporter line has the UAS sequence followed by at gene of interest. When the GAL4 and UAS lines are crossed they produced F1 progenies expressing the gene of interest in the selected tissues. Interestingly this method also enables temporal regulation of gene expression as GAL4-drivers' expression can be restricted to specific developmental stages. Further development of the UAS-GAL4 system allows a more refined gene expression with temperature sensitive GAL4 (TARGET system), ligand inducible GAL4

(GAL-ER or Geneswitch) or split-GAL4 (Caygill and Brand, 2016). Maintaining the UAS and GAL4 in separate strains allows to maintain healthy stocks in cases where the gene of interests produces lethal or deleterious gene products. This system also allows the rapid generation of a variety strains each expressing the gene of interest in different tissues.

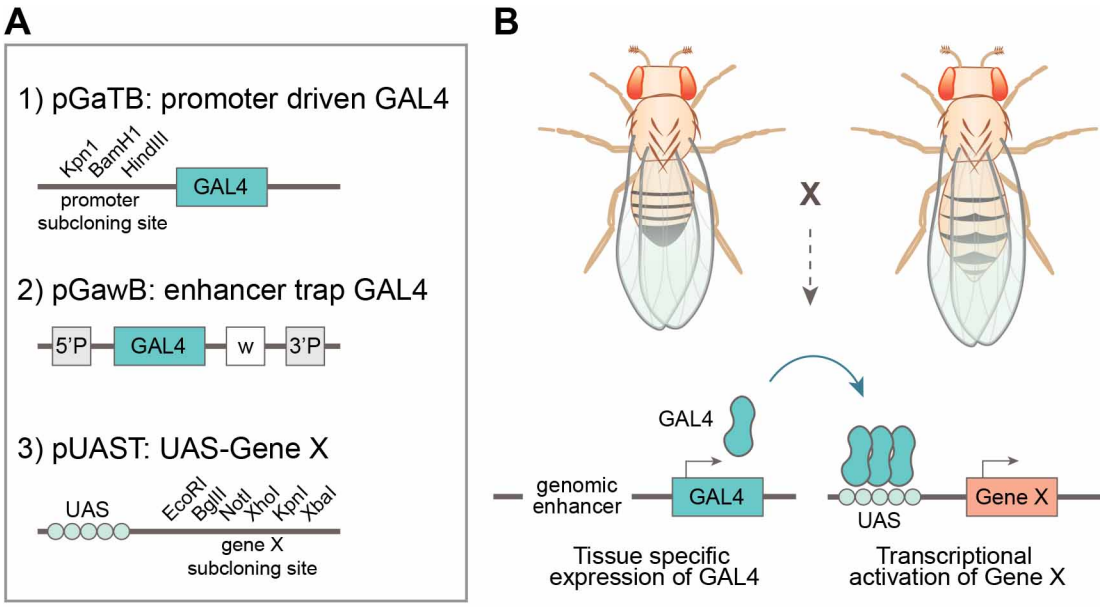

Figure 1.16: The UAS/GAL4 system to target gene expression in *Drosophila.*

A) Simplified representation of vectors used to generate UAS and GAL4 *Drosophila* lines by Brand and Perrimon. **A1)** pGaTB: the gene encoding GAL4 is preceded by a cloning insertion site for the subcloning of promoter sequences; **A2)** pGawB is an enhancer trap vector. It is inserted randomly into the fly genome thanks to P-element sequences (5'P and 3'P) driving GAL4 expression from various genomic enhancers. The presence of an enhancer is visualised thanks to the co-expression of the white eye reporter gene. **A3)** pUAST consists of the upstream activating sequence (UAS) to which GAL4 binds followed by a cloning site for the gene of interest. **B)** Schematic representation of the UAS/GAL4 system in *Drosophila*. To promote the tissue-specific expression of a gene of interest, a GAL4-"driver" fly is crossed with a UAS fly. The resulting F1 progeny will express GAL4 under the control of a genomic enhancer which will specifically drive the expression of the gene X. Figure adapted from (Brand and Perrimon, 1993).

1.5.7 Conclusion on the use of *Drosophila*:

Drosophila melanogaster is a highly interesting model for the study of USP30 and mitophagy *in vivo*. It expresses orthologues of mitophagy and PD genes such as *Pink1*, *park* or *Usp30*, and genetic manipulations are straightforward. *Pink1* and *park* mutants present phenotypes reminiscent of PD which means that it is possible to assess the effect of USP30 towards PD symptoms. Moreover, its small size simplifies imaging and enables the observation of the entire organism.

1.6 Aims of the study and summary of chapters

It is possible that mitophagy is disrupted not just in patients suffering from hereditary PINK1 and PARKIN loss function mutations. Mitochondrial dysfunctions were recorded in patients with additional hereditary mutations and this also extends to sporadic forms of Parkinson's disease (Chen et al., 2019). I thus aimed at better understanding mitophagy and finding pharmacological means to stimulate this pathway. Here were my three main objectives during this thesis:

1. Unravel the mechanisms of mitophagy in a "physiological context" (basal mitophagy)
2. Shed light on the array of functions and substrates of USP30
3. Characterise a tool compound specifically inhibiting USP30
4. Generate animal models to study mitophagy

In Chapter III, I will define cellular and chemical tools available to study mitophagy. In chapter IV, I will describe how USP30 regulates basal mitophagy and pexophagy in SH-SY5Y mito-QC cells. In Chapter V, I will report on USP30 specific inhibitors and on USP30 knock-out cells and use those tools to perform ubiquitylomic and proteomic analysis of USP30 substrates. Finally, in Chapter VI, I will characterise novel USP30 knock-out and mt-Keima expressing *Drosophila melanogaster* models.

Chapter 2: Materials and methods

2.1 Cell biology

2.1.1 Materials and reagents

The reagents employed in the cell biology experiments detailed in this thesis are listed in Tables 1.1, 1.2 and 1.3.

Table 2.1: Cell biology reagents and resources

REAGENT or RESOURCE	SOURCE	IDENTIFIER
Experimental Models: Cell Lines		
HCT116	ATCC	#CCL-247™
HEK293T	ECACC	# 12022001
HeLa	ECACC	# 93021013
hTERT-RPE1	Gifted by Francis Barr (University of Oxford)	
hTERT-RPE1-YFP-Parkin	Gifted by Jon Lane (University of Bristol)	
SH-SY5Y	ECACC-Sigma	Cat#94030304
SH-SY5Y mito-QC	Gifted by Ian Ganley (MRC-PPU, Dundee)	
SKN-BE2(c)	Gifted by Violaine See (University of Liverpool)	
U2OS	ECACC	Cat# 92022711
U2OS mito-QC	Gifted by Ian Ganley (MRC-PPU, Dundee)	
U2OS SKL-Keima	Made by Aitor Martinez-Zarate	
Medium and additives		
Dulbecco's Modified Eagle's Medium (DMEM)	Thermo Fischer Scientific	#31966-021
DMEM-F12	Thermo Fischer Scientific	#31331-028
Non-essential amino acids (MEM/NEAA)	Thermo Fischer Scientific	#11140-035
Penicillin/streptomycin	Thermo Fischer Scientific	#15070-063
Fetal bovine serum (FBS)	Gibco	#10270106
trypsin-EDTA	Invitrogen	#15400
Retinoic acid	Sigma	#R2625
12-O-Tetradecanoylphorbol 13-acetate	Sigma	#P1585
Neurobasal™ Medium	Fischer Scientific-Gibco	#11570556
N-2 Supplement	Fischer Scientific-Gibco	# 11520536
Glutamax-100X	Fischer Scientific-Gibco	# 35050038
Transfection reagents		
Lipofectamine™ RNAiMAX	Invitrogen	#13778150
Lipofectamine 2000	Invitrogen	#11668019

Lipofectamine 3000	Invitrogen	#L3000015
Opti-MEM	Invitrogen	#409864
GeneJuice® Transfection reagent	EMD Millipore	#70967
Imaging reagents		
Methanol-free formaldehyde ampoules	Thermo Fischer Scientific	#28908
Triton TX-100		
Bovine serum albumin (BSA)		
Mowiol	Merck Millipore	#475904
DAPI	Invitrogen	#D1306
µ-Dish 35mm high	Ibidi	# 81156
Plasmids		
pEGFP-N3-USP30	Clague-Urbé lab	
pEGFP-N3-USP30-C77S	Clague-Urbé lab	
pRFP-N3-hmUSP30	Clague-Urbé lab	
pRFP-N3-hC77S-mUSP30	Clague-Urbé lab	
pCMV6-myc-ddk-hmUSP30	Clague-Urbé lab	
pCMV6-myc-ddk-hC77S-mUSP30	Clague-Urbé lab	
pcDNA3.1(+)	Invitrogen	#V79020
mCherry-Peroxisome (SKL-mCherry)	Addgene	#54520
pCDNA3.1 TagBFP-SKL	Clague-Urbé lab	
Kits		
CellTiter-Glo Assay	Promega	#G7571

Table 2.2: siRNA list

siRNA Dharmacon / Horizon		
TARGET (siRNA ID)	IDENTIFIER	SEQUENCE
FBXO7 (SMARTpool)	L-013606-00-0005	GAAUGACGACAGUAUGUUA, CUGAGUCAAUUCAAGAUAA, CAUUAGAGACCUUGUAUCA, UAGCCAACAUAUACAAAGA
HUWE1 (SMARTpool)	L-007185-00-0005	GCUUUGGGCUGGCCUAAUA, GCAGUUGGCGGCUUUCUUA, GAGCCCAGAUGACUAAGUA, UAACAUCAAUUGUCCACUU
MARCH5 (SMARTpool)	L-007001-00-0005	GUAAAUUGAUGUUCAGUAG, GCUGAAUACCUAAUAGUUU, GCGCAAAUACUCGAAUAAA, GAAUAAUGGUCGGCUCUAU
MUL1 (SMARTpool)	L-007062-00-0005	GGAGCUGUGCGGGUUA, GGCAUGCAGUACCUAA, UAACAGCCAGUUUGUGGAA, GUACAACAGCUAAUAGUUU

PINK1 (SMARTpool)	L-004030-00	GCAAAUGUGCUUCAUCUAA, GCUUUCGGCUGGAGGAGUA, GGACGUUGUUCCUCGUUAU, GGAGACCAUCUGCCCGAGUA
PRKN (SMARTpool)	L-003603-00-0002	GUAAAAGAAGCGUACCAUGA, GAACAUCACUUGCAUUACG, GAUAGUGUUUGUCAGGUUC, UUAAAGAGCUCCAUCACUU
USP30 (D1)	Custom order	CAAAUUACCUGCCGCACAAUU
USP30 (D3)	D-021294-03	ACAGGATGCTCACGAATTA

Table 2.3: List of Antibodies used in Immunofluorescence assays

Primary Antibodies for Immunofluorescence			
TARGET (Species)	SOURCE	IDENTIFIER	Incubation condition
Catalase (Rb)	Abcam	#ab1877	1:750, 1h
USP30 (Rb)	Gifted by Baris Bingol (Genetech, USA)		1:100, 1h
PMP70 (Ms)	Sigma	#SAB4200181	1:500, 1h
TIMM44 (Rb)	Sigma	#HPA043052	1:250* or 1:500, 1h
Myc (Ms)	BD Biosciences	#51826	1:500, 1h
pUb S65 (Rb)	Millipore	#ABS1513-I	1:500, 1h
TOMM20 (Rb)	Sigma	#HPA011562	1:250* or 1:500, 1h
TOMM20 (Ms)	BD Biosciences	#612278	1:500, 1h
Secondary Antibodies			
TARGET (Species)	SOURCE	IDENTIFIER	Incubation condition
Donkey anti-rabbit AF488	Invitrogen	#A21206	1:500, 45min
Donkey anti-mouse AF488	Invitrogen	#A21202	1:500, 45min
Donkey anti-rabbit AF594	Invitrogen	#A21207	1:500, 45min
Donkey anti-mouse AF594	Invitrogen	#A21203	1:500, 45min
Donkey anti-rabbit AF647	Invitrogen	#A32795	1:250, 45min
Donkey anti-mouse AF647	Invitrogen	#A32787	1:500, 45min

*Higher antibody concentration (1:250) were used when conjugated with Far red secondary antibodies

2.1.2 Cell culture

SH-SY5Y, hTERT-RPE1 YFP-Parkin and hTERT-RPE1 cells were grown in DMEM-F12 whilst U2OS and HeLa cells were grown in DMEM. Both media were supplemented with 10% heat-inactivated FBS, 1% NEAA and 1% Penicillin/streptomycin. The cells were cultured in a humidified incubator at 5%

CO_2 atmosphere maintained at 37ºC and split upon confluency at concentrations ranging from 1:2 to 1:8 as required.

2.1.3 siRNA transfection

Cells were seeded in 6-well plates: $3x10^5$ cells per well for SH-SY5Y cells and $2.5x10^5$ cells per well for hTERT-RPE1 YFP-Parkin cells. 24h later the medium was exchanged in each well for 830µl of fresh medium without additives. The RNAi transfection reagent (RNAiMAX) and siRNA oligonucleotides were separately incubated with Opti-MEM for 5 min at RT as shown in table 1.4. Solutions A and B were then mixed at a 1:1 ratio, incubated further for 20min at RT and then added to the cells to obtain a final siRNA oligo concentration of 40nM. The medium was exchanged 24h later for 2ml of fresh medium with additives (10% FBS, 1% NEAA, 1% Penicillin/Streptomycin) and the transfected cells analysed after 72h of transfection, unless otherwise specified in the figure legends. In the specified experiments performed in the SH-SY5Y cells, cells were split at 24 hours following the first siRNA transfection at a 1:3 ratio into fresh 6-well plates and a second siRNA transfection was performed as above (72h after the first transfection) for a total of 144 hours of depletion prior to analysis.

Table 2.4: siRNA transfection procedure

Solution A		**Solution B**	
Reagent	Volume	Reagent	Volume
RNAiMAX	2µl	Oligonucleotide (20µM)	2µl
Opti-MEM	83µl	Opti-MEM	83µl

2.1.4 plasmid DNA transfection

Cells were seeded into 6-well plates, left to recover overnight and transfected the following day. U2OS and hTERT-RPE1 cells were transfected using the GeneJuice transfection reagent at a 3:1 ratio (3µl reagent for 1µg plasmid DNA) whilst SH-SY5Y cells were transfected with Lipofectamine 2000 at a 24:5 ratio (12µl reagent for 2.5µg plasmid DNA). The transfection procedures were performed according to the manufacturers' instructions. Briefly, GeneJuice and Opti-MEM were mixed together for 5 min then the mixture was supplemented

with the plasmid DNA and was finally left to incubate at RT for 20 min (see table 1.5). When using Lipofectamine two solution were first made: Lipofectamine diluted in Opti-MEM (A) and plasmid DNA diluted in Opti-MEM (B) (see table 1.5). The solutions were left to incubate for 5 min, they were then mixed at a 1:1 ratio and finally incubated at room temperature for 20 min. In both cases, the resulting mixtures were directly added to the cells and incubated for 24h.

Table 2.5: Plasmid DNA transfection procedure

RPE1, U2OS		**SH-SY5Y**		
Reagent	Volume/ Mass		Reagent	Volume/ Mass
GeneJuice	3µl	**A**	Lipofectamine 2000	12µl
Opti-MEM	100µl		Opti-MEM	238µl
Plasmid DNA	1µg	**B**	Plasmid DNA	2.5µg
			Opti-MEM	247.5µl

2.1.5 Microscopes

Confocal microscopes: a) 3i Marianas spinning disk confocal microscope with 10x dry, 40x NA 1.3 oil and 63x NA 1.4 oil objectives. The microscope is equipped with a Hamamatsu Flash 4 sCMOS camera and a Photometrics Evolve EMCCD camera. The acquisition software used is the Slide Book 3i v3. b) Zeiss LSM800 with Airyscan confocal microscope equipped with 63x NA 1.4 oil objective and using the Zen acquisition software.

Epifluorescence microscopes: a) Leica MZ10 F modular stereo microscope with 8x-80x magnification (used to screen *Drosophilas*).
b) Nikon Ti-Eclipse inverted microscope equipped with 10x dry N.A. 0.3, 20x dry N.A. 0.45, 40x dry N.A. 0.95 and 60x oil N.A. 1.4 objectives. This microscope was used in combination with the NIS-elements imaging software.

2.1.6 Immunofluorescence

Cells were seeded into 6-well plates containing 22x22mm coverslips. For immunofluorescence they were first rinsed twice in PBS and then fixed using 4% paraformaldehyde (PFA) in PBS for 15min. Once the PFA was discarded,

they were washed twice in PBS and the remaining free aldehyde groups were quenched by a 5min incubation in 50mM ammonium chloride in PBS. The coverslips were again washed twice in PBS and then permeabilised using 0.2% Triton X-100 in PBS for 5min. Following two PBS washes, the coverslips were blocked for 30min in 3% bovine serum albumin (BSA) in PBS. The primary antibodies were diluted in 3% BSA/PBS as described in Table 1.3 and added to the cells for 1h at RT. Following two PBS washes the coverslips were incubated with the secondary antibodies for 45min. Finally, the coverslips were washes three times in PBS, then once in Millipore water and mounted onto glass slides using Mowiol, supplemented with DAPI (1:200) where indicated.

2.1.7 Live cell imaging

Live cell imaging experiments were performed using the 3i Marianas spinning disk confocal microscope, the EMCDD camera and the 40x or 63x oil objectives (see section 1.1.5). Cells were grown in 35mm µ-Dishes (Ibidi) and the imaging was performed in a humidified chamber at 37ºC supplied with 5% CO_2.

2.1.8 Mitophagy analysis in mito-QC expressing cells

2.1.8.1 Quantitation using Fiji

The images were acquired randomly and analysed using Fiji (Image J) v2.0.0. A region of interest (ROI) was drawn around each cell and saved using the "ROI manager" function. Then the GFP signal was subtracted from the mCherry signal using the "Image Calculator" function. The image obtained from the subtraction was then processed into a binary image, showing only the mitolysosomes ("red-only" dots), using the Threshold tool. The number and area of mitolysosomes per ROI was measured with the "Analyse Particles" function.

2.1.8.2 Manual quantitation

All images were processed using Fiji (Image J) v2.0.0. Then the number of cells undergoing mitophagy (= cells with more than three mitolysosomes) were visually assessed and counted over the total number of cells per image.

2.1.9 SH-SY5Y cell differentiation into dopaminergic-like neurons

2.1.9.1 Protocol#1 (RA and TPA)

SH-SY5Y cells were grown in 6-well plates or Ibidi dishes to a confluence of 70%. The medium was exchanged for “low FBS medium” (1% FBS, 1% NEAA, 1%P/S) and supplemented with 10µM retinoic acid (RA). The cells were treated with RA up to 72h (with media/RA exchange at 48h). The cells were then grown in “low FBS medium” supplemented with 80nM 12-O-tetradecanoyl-phorbol-13-acetate (TPA) for another 72h (with media/TPA exchange at 48h).

2.1.9.2 Protocol#2 (RA and N2 differentiation media)

This protocol was provided by Heather Mortiboys (SITraN, Sheffield). SH-SY5Y cells were seeded at a density of $6x10^3$ cells/cm^2. They were cultured for 48h before switching to N2 differentiation media (49.5% DMEM-F12 Medium, 49.5% Neurobasal Medium, 0.5% N2 supplement, 0.5% GlutaMax) supplemented with 10µM RA. The cells were incubated in this media for 7days with 50% of the media being replaced every 2-3 days.

2.1.10 Keima pH titration

U2OS-SKL-Keima cells were grown in DMEM, the medium was then exchanged for buffers with pH ranging from pH8 to pH4 (143mM KCl, 1.17mM $MgCl_2$, 1.3mM $CaCl_2$, 5mM Glucose). The K+/H+ ionophore nigericin was added at 10µM to each buffer in order to equalises the extra- and intra-cellular pH. Finally, the cells were incubated with 50mM NH_4Cl (Adapted from: (Despras et al., 2015)).The cells were equilibrated for 5min and imaged in between each buffer exchange using a 3i spinning disk confocal microscope (Em445/Ex610 then Em561/Ex610). Images were analysed using “pixelAnalysis” plugin coded by Dave Mason (CCI, University of Liverpool) for the FIJI.

2.1.11 Image processing

Images were processed either in Adobe Photoshop CC (2019) or in Omero.web version 5.5. Figures were assembled on Adobe Illustrator (2019).

2.1.12 CellTitre-Glo Luminescence assay

Cells were seeded in the wells of a black clear bottom 96-well plate (Corning) at a density of 3 x10^5 cells per well. The following day, the medium was exchanged and replaced with 100µl media with 1.5 µM oligomycin or 50 mM 2-deoxyglucose or the combination of both or untreated. After 30min, 100µl of assay solution (CellTitre-Glo Reagent) was added to each well. The plate was shaken at 250 rpm for 2 min to induce cell lysis then incubated at RT for 10 min covered in foil. Luminescence was measured on a GloMax®-Multi Detection System (Promega) with the built-in Promega protocol.

2.2 Biochemistry

2.2.1 Materials and reagents

The reagents employed in the biochemistry experiments detailed in this thesis are listed in Tables 1.6 and 1.7.

Table 2.6: Biochemistry reagents and resources

REAGENT or RESOURCE	SOURCE	IDENTIFIER
Commercial Assays		
BCA Protein Assay (Pierce)	Pierce Biotechnology	#23225
Bovine IgG	Sigma-Aldrich	#I9640
2-mercaptoethanol	Sigma-Aldrich	#M6250
Inhibitors		
Protease inhibitor cocktail	Sigma-Aldrich	P8340
PhosSTOP (phosphatase inhibitor tablets)	Roche-Sigma	#4906837001
Tools		
Cell cracker homogeniser	EMBL, Heidelberg	
XCell SureLock Mini-Cell System	Thermo Fischer Scientific	#EI0001
XCell SureLock Midi-Cell System	Thermo Fischer Scientific	#WR0100
Genie Blotter with Platinized Titanium Anode, 15 x 17 cm	IDEA Scientific company (MN, USA)	#4003
Buffers		
Tris- Acetate SDS running buffer	Invitrogen	#LA0041
NuPAGE MOPS	Invitrogen	#NP0001-02
NuPAGE MES	Invitrogen	#NP0002-02
Precast gels and molecular weight markers		
NuPAGE Bis-Tris 4-12% gels 10 wells 1mm	Invitrogen	#NP0321BOX

NuPAGE Bis-Tris 4-12% gels 10 wells 1.5mm	Invitrogen	#NP0303BOX
NuPAGE Bis-Tris 4-12% gels 20 wells 1mm	Invitrogen	#W61402A
NuPAGE 3-8% Tris-Acetate gels 20 wells 1mm	Invitrogen	#EA0375BOX
Prestained broad range molecular weight marker	New England Biolabs	#P7708S
Full range molecular weight marker rainbow	Invitrogen	#11580684
Unstained broad range molecular weight marker	New England Biolabs	#P7702S
Other		
Marvel skimmed milk powder	Marvel	
Amersham Protran 0.45µm nitrocellulose membrane	GE healthcare	#10600002
Ponceau S	Sigma-Aldrich	#P7170
Gelatin from cold water fish skin	Sigma-Aldrich	#G7765

Table 2.7: Antibodies used for western blotting analysis

Primary Antibodies for western blotting			
TARGET (Species)	SOURCE	IDENTIFIER	Incubation condition
Actin (Ms)	Abcam	Ab6276	1:10 000, 30 mins
Actin (Rb)	Sigma	A2266	1:10 000, 30min
Actin (Ms)	ProteinTech	66009-1-Ig	1:10 000, 30min
Actin (Rb)	ProteinTech	20536-1-AP	1:10 000, 30min
Catalase (Rb)	Abcam	ab1877	1:2000, O/N
Cullin1 (Rb)	Invitrogen	71-8700	1:1000, O/N
Cullin3 (Rb)	Bethyl	A301-109A	1:2000, 1h
FBXO7 (Rb)	Aviva	OAAN03680	1:1000, O/N
FIS1 (Rb)	Proteintech	10956-1-AP	1:1000, O/N
FKBP8 (Ms)	RD systems	MAB3580	1:1000, O/N
GFP (Sheep)	gift from Prof. Ian Prior (University of Liverpool)		1:5000, 1h
HSP60 (Goat)	Santa cruz	sc-1052	1: 2000, O/N
HUWE1 (Rb)	Bethyl	A300-486A	1:2000, O/N
Keima (Ms)	MBL	M126-3	1/500, O/N
MAGEA10 (Rb)	Proteintech	15295-1-AP	1:1000, O/N
MARCH5 (Rb)	Milipore	06-1036	1:1000, O/N
MIRO1 (Rb)	Sigma	HPA010687	1:1000, 1h
Mitofusin 1 and 2 (Ms)	Abcam	ab57602	1:1000, O/N
Mitofusin 2 (Ms)	Abcam	ab5688	1:1000, O/N
Mul1 (Rb)	Invitrogen	PA5-29550	1:1000, O/N
OPA1 (Rb)	Abcam	ab42364	1:1000, O/N
Optineurin C-term (Rb)	Cayman Chemical	100000	1:1000, O/N
p62 (Ms)	BD Transduction Lab	610833	1:1000, O/N

Parkin (Ms)	Santa Cruz	sc32282	1:250, O/N
Parkin S65 (Rb)	Miratul Muquit (University of Dundee)		1:1000, O/N
PARP p85 fragment (Ms)	Cell Signalling	9546	1:2000, O/N
PEX19 (Rb)	Invitrogen	PA5-22129	1:1000, O/N
PEX5 (Rb)	Novus Biologicals	NBP-87185	1:1000, O/N
PINK1 (Rb)	Cell Signalling	6946S	1:1000, O/N
PMP70 (Ms)	Sigma	SAB4200181	1:1000, O/N
PRDX3 (Ms)	Sigma	SAB1407075	1:1000, O/N
pUb S65 (Rb)	Millipore	ABS1513-I	1:1000, O/N
SYNGR3 (Rb)	Abcam	ab113712	1:1000, O/N
TOMM22 (Ms)	Sigma	sc-58308	1:1000,1h
TOMM20 (Rb)	Sigma	HPA011562	1:1000,1h
TOMM20 (Rb)	ProteinTech	11802-1-AP	1:2000, O/N
TOMM7 (Rb)	ProteinTech	15071-1-AP	Try 1:500, O/N
α-Tubulin (Ms)	Sigma	T5168	1:10 000, O/N
Ubiquitin "VU-1" (Ms)	LifeSensor	VU101	1:2000, O/N
USP30 (Rb)	Sigma-Atlas	HPA016952	1:500, O/N
USP30 (Sheep)	MRC Dundee	N/A	1:1000, O/N
USP33 (Ms)	Sigma	WH0023032M1	1:1000, 1h
VDAC (Rb)	Cell Signaling	4866	1:1000, O/N
VDAC1 (Ms)	Abcam	ab14734	1:1000, O/N
Vps35 (Goat)	Abcam	ab10099	1:1000, O/N

Secondary Antibodies			
TARGET (Species)	SOURCE	IDENTIFIER	Incubation condition
Donkey anti-mouse IRDye 800CW	LICOR	926-32212	1:10 000, 1h RT
Donkey anti-mouse IRDye 680CW	LICOR	926-32222	1:10 000, 1h RT
Donkey anti-rabbit IRDye 800CW	LICOR	926-32213	1:10 000, 1h RT
Donkey anti-rabbit IRDye 680CW	LICOR	926-32223	1:10 000, 1h RT
Donkey anti-sheep IRDye 800CW	LICOR	926-32214	1:10 000, 1h RT
Donkey anti-sheep IRDye 680CW	LICOR	926-32224	1:10 000, 1h RT

2.2.2 Mammalian cell lysis

Regular lysis was performed on a metal plate on ice to maintain the cells ice-cold. The cells were washed twice in 4ºC PBS and were further incubated with either RIPA buffer (10mM Tris-Cl pH 7.5, 150mM NaCl, 1% triton X-100, 0.1% SDS, 1% sodium deoxycholate) or NP40 buffer (25mM Tris-Cl pH 7.5, 100mM NaCl, 0.5% NP40, 50mM NaF) and rocked on ice for 10min. Both buffers were supplemented with mammalian protease inhibitors (1:250) and phosphatase

inhibitors tablets (Roche) where indicated. The lysates were then clarified by centrifuging at 14,000g for 5min at 4ºC in a table-top centrifuge to pellet out any cell debris.

For hot lysis, cells were washed twice in PBS at 37ºC and then incubated with boiling lysis buffer (2% SDS, 1mM EDTA, 50mM NaF) on a dry-heat block at 110ºC. The lysates were then scraped with a cell scraper (Greiner), collected into 2ml screw-cap tubes (Corning) and further boiled at 110ºC for 10min with intermittent harsh vortexing every 2 min.

2.2.3 Protein assay and sample preparation

Protein concentration was determined using the Pierce BCA Analysis kit following manufacturer's instructions. Briefly, a 6-point standard curve was generated using bovine IgG (Sigma) (1mg.ml^{-1}) in a 96 well plate, (see Table 1.8). The samples were loaded as triplicates and each standard curve point as duplicates. The BCA Reagents A and B were mixed together (50:1 ratio) and added to all of the wells. The plate was then incubated for 30min at 37ºC and then scanned at OD_{562} on a Thermo Labsystems Multiskan spectrum plate reader.

The samples were all adjusted to a common concentration using the same lysis buffer used in the lysis and prepared in 5X sample buffer (15% SDS, 321.5mM Tris-HCl pH6.8, 50% Glycerol, 16% 2-Mercaptoethanol, 1.25% Bromophenol blue) for regular lysis or 5X hot lysis sample buffer (7% SDS, 312.5mM Tris-HCl pH6.8, 50% Glycerol, 16% 2-Mercaptoethanol, 1.25% Bromophenol blue) and boiled for 5min at 95ºC.

Table 2.8: Typical BCA protein assay

	IgG (µl)	H_2O (µl)	Lysis Buffer (µl)	Lysate (µl)	BCA Mix (µl)
Standard curve	0	10	3	-	200
	2	8	3	-	200
	4	6	3	-	200
	6	4	3	-	200
	8	2	3	-	200
	10	0	3	-	200
Sample	0	10	-	3	200

2.2.4 Mitochondria enrichment

Two 15cm dishes of cells were used per condition. The whole protocol was performed on ice or at 4ºC and all solutions were pre-cooled at 4ºC. Cells were rinsed twice with PBS and then scraped in 5ml PBS using a silicon cell scraper. The cells obtained from duplicate dishes were combined and centrifuged for 2min at 1,000g. The cell pellets were resuspended in 5ml HIM buffer (200mM mannitol, 70mM sucrose, 1mM EGTA, 10mM HEPES pH 7.4) and centrifuged 1,000g for 5min. The cells were resuspended in 1ml HIM buffer supplemented with mammalian protease inhibitors, then mechanically broken by shearing through at 23G needle 3-times and then homogenised by passing 3-times through a cell cracker (8.02mm diameter) and using 8.01mm steel ball (As described in (Aubry and Klein, 2006)). The homogenates were centrifuged 10min at 600g to pellet out the nuclei and thus obtaining the Post Nuclear Supernatant (PNS). The PNS was further separated into a Post Mitochondrial Supernatant (PMS) and a Mitochondrial Fraction (MF) by centrifugation at 7,000g for 15min. The MF pellet was resuspended in HIM buffer supplemented with mammalian protease inhibitors. Protein concentration of all samples was determined using the BCA assay (Pierce) and all fractions were adjusted to the same final concentration. Equal amounts of PNS, MF and PMS were analysed by western blotting.

2.2.5 Western blotting

2.2.5.1 SDS-PAGE Electrophoresis

Protein lysates were resolved by Sodium dodecyl sulphate (SDS)-polyacrylamide gel electrophoresis (PAGE). The lysates were loaded into 4-12% Bis-tris (low and medium molecular weight proteins) or 3-8% Tris-Acetate (high molecular weight proteins) precast NuPAGE gels using the XCell SureLock gel tank systems. Typically, MOPS running buffer was used to resolve proteins ranging 30-200kDa and MES running buffer for <30kDa proteins in the 4-12% Bis-Tris gels while Tris-Acetate running buffer in the 3-8% Tris-Acetate gels for >250kDa proteins. In general, gels were ran 15min at 80V then 60min at 150V.

2.2.5.2 Electrophoretic transfer and protein immunostaining

The resolved proteins were then transferred onto 0.45µm pore-size nitrocellulose membranes using the Genie blotter system (IDEA Scientific, MN, USA). The transfer tanks were filled with transfer buffer (3.03g Tris, 14.4g Glycine, 200ml methanol, topped up to 1L with distilled H_20) and the transfers were set at a constant current of 0.9A and 24V for 1h at RT, or 2h on ice when transferring high molecular weight proteins (>200kDa). The nitrocellulose membranes were then stained in Ponceau to verify equal protein loading and transfer, and then washed 3-times in TBS-T (made from a 20x TBS stock solution: 3M NaCl and 0.2M Tris-HCl pH7.6; then supplemented with 0,1% w/v Tween-20). The membranes were further blocked 1h at RT in 5% powder milk in TBS-T and then incubated with primary antibodies diluted in 5% milk in TBS-T. For details on the incubation conditions see Table 1.7. The membranes were next washed three times in TBS-T and probed for 1h with secondary antibodies labelled with IRDye 800CW or IRDye 680CW diluted at 1:10 000 in 5% milk in TBS-T. Finally, the membranes were washes twice in TBS-T then in TBS and scanned on the LICOR Odyssey CLx imaging system. Images where analysed using the ImageStudio and ImageStudioLight quantification software.

2.2.6 Ubiquitin gels

To specifically probe for ubiquitin, the western blotting protocol was slightly modified. SDS-PAGE and transfer were performed as indicated in section 1.2.5.1 and 1.2.5.2. However, following Ponceau staining, the membranes were briefly rinsed in TBS-T and then boiled for 30 min in Millipore water in between two glass plates. This was reported to enhance ubiquitin detection by possibly exposing hidden antigenic sites (Swerdlow et al., 1986).

Following heat-inactivation, the membrane were rinsed 3-times in TBS-T then blocked in 0.5% Cold Water Fish skin gelatin (Sigma) in TBS-T. Antibody incubations and scanning were performed as in section 1.2.5.2, with the exception that antibodies were diluted into 0.5% Cold Water Fish skin gelatine instead of Milk.

2.3 Molecular biology

2.3.1 Materials and reagents

The reagents employed in the molecular biology experiments detailed in this thesis are listed in Tables 1.9.

Table 2.9: Molecular biology resources and reagents

REAGENT or RESOURCE	SOURCE	IDENTIFIER
Enzymes		
PfuUltra II Fusion HS DNA polymerase	Agilent	#600670
Medium		
S.O.C. Medium	Invitrogen	#15544034
Cells		
TOP10 competent cells	Fisher Scientific	#C404003
DH5α competent cells	Invitrogen	#18265-017
Buffers		
TAE buffer	National Diagnostics	#EC-872
Ethidium Bromide	Sigma-Aldrich	#E1510
Kits		
Zero Blunt® TOPO® PCR Cloning Kit for Sequencing	Invitrogen	#K2875
MinElute Gel extraction Kit	Qiagen	#28604
QiaPrep Spin Miniprep kit	Qiagen	#27106
HiSpeed Plasmid Midi kit	Qiagen	#12643
HiSpeed Plasmid Max kit	Qiagen	#12663
Quick Ligation kit	New England Biolabs	#M2200S
Quick-DNA Miniprep	Zymo Research	#D3025
Plasmids		
pTagBFP-H2B vector	Evrogen	#FP176
pcDNA3.1(+)	Invitrogen	#V79020
pSpCas9(BB)-2A-GFP (PX458)	Addgene	#48138
PX330-Puro	Gifted by Prof Ciaran Morrison (NUI Galway)	
Primers		
NAME	SEQUENCE	IDENTIFIER
USP30-Ko-1-pcrUP-FW	GTGCCTGGCCTTGTTAATTTAG	#2225
USP30-Ko-1-pcrUP-RV	CAGGCATGAGCCACTGCAC	#2226
USP30-Ko-2-pcrUP-FW	CACAGCGCAGGAACTCTGGGTC	#2227
USP30-Ko-2-pcrUP-RV	TTGGCCTCCTAAAGTACTGG	#2228
USP30-Ko-2-pcrUP-FW	GAACACCTGCTTCATGAACTC	#2229
USP30-Ko-2-pcrUP-RV	CTGTCATCTGGACTTCTTTG	#2230

JJ-TagBFP-C1-NheI-F1	GAGCTAGCGCCACCATGAGC-GAGCTGATTAAGGAGAACATGC	#2255
JJ-TagBFP-SKL-XhoI-R1	CACTCGAGTTACAGCTTGGATGA-ACCATTAAGCTTG	#2256
Tools		
Horizontal midi electrophoresis tank	Scie-Plas	# HU13

2.3.2 Polymerase Chain Reaction (PCR)

DNA was amplified by PCR using the PfuUltra II Fusion HS DNA polymerase. The primers are listed in Table 1.9. The PCR mix was prepared as in Table 1.10 and the PCR program is detailed in Table 1.11.

Table 2.10: PCR Mix

	pTagBFP-SKL PCR	Control PCR
H2O	40 µl	41 µl
10x Pfu Buffer Ulta II	5 µl	5 µl
dNTPs (25 mM)	0.5 µl	0.5 µl
Primer	1.25 µl	1.25 µl
Primer	1.25 µl	1.25 µl
Template	50 ng (1ul)	-
HS Ultra Pfu II	1 µl	1 µl
Total	50 µl	50 µl

Table 2.11: PCR program

Segment	Step	n. of cycles	Temperatures	Duration
1	Denaturation	1	95°C	2 min
2	Denaturation	25	95°C	30 sec
	Annealing		Tm-5°C	30 sec
	Extension		68°C	1 min/kb
3	Final extension	1	68°C	15 min
4	hold	1	10°C	∞

2.3.3 Agarose gel electrophoresis

PCR or restriction digest products were resolved by gel electrophoresis in 0.8 or 1.0 % Agarose gels were made from electrophoresis grade agarose (Invitrogen) melted in TAE buffer (National Diagnostics) and supplemented with 0.5 µg.ml^{-1} ethidium bromide (Invitrogen). Ethidium bromide enabled the visualisation of DNA when using UV light. 6x loading dye (NEB) was added to

the DNA samples prior to loading. The DNA gels were resolved at 120 V for 30 to 60 min in electrophoresis tanks filled with TAE buffer and then visualised using a UV light source. The DNA was extracted from the gels using the Quiagen gel extraction kit following the manufacturer's instructions.

2.3.4 TOPO blunt-end cloning

To further amplify PCR products, these were inserted into pCR4Blunt-TOPO sub-cloning vector (from Zero Blunt® TOPO® PCR Cloning Kit). This kit enables an efficient one-step cloning mediated by topoisomerase I. Topoisomerase I is covalently bound to both ends of linearised pCR4Blunt-TOPO vectors and catalyses blunt-end ligations. The ligation mix is described in Table 1.12 and was incubated for 15min at room temperature. The resulting vectors were transformed into TOP10 *Escherichia coli* bacteria (see details in section 1.3.5).

Table 2.12: pCR4Blunt-TOPO and PCR product ligation mix

H_2O	2 µl
6x Salt-solution	1 µl
PCR-product	2* µl
pCR4 TOPO-vector	1 µl
Total	**6 µl**

*4 µl for larger constructs (>2 kb), 2 µl for 1-2 kb, 1 µl for 0.5 kb-1kb.

2.3.5 Bacterial transformation

Bacterial transformations were induced by heat shock. The bacterial strain used were either TOP10 or DH5α cells. For each transformation, 2-6µl of ligated vector were added to 50µl of chemically competent bacteria and left for 20min on ice. The mix was then incubated at 42ºC for 45s in a water bath and cooled back down on ice for 5 min. Finally, the bacteria were supplemented with 200µl of S.O.C Medium and left to recover 1h at 37ºC in a shaking incubator.

The transformed bacteria were plated on LB agar plates with the appropriate antibiotic (Kanamycin: 10mg.ml ml^{-1} or Ampicillin: 100mg.ml^{-1}) and incubated for 16h at 37ºC. On average, six TOP10 colonies were picked per transformation and expanded in LB medium with antibiotics. The plasmid DNA

was extracted using the Quiagen Miniprep, Midi or Max kit following the manufacturer's protocol.

2.3.6 Glycerol stocks

Glycerol stocks were made from 5ml overnight DH5α cultures. The cultures were pelleted 5min at 4,000 rpm. The pellets were then resuspended in 1.5ml 40% Glycerol/LB medium solution and aliquoted in cryovial (0.75ml per cryovial). The aliquots were stored at -80ºC.

2.3.7 Restriction digest

Restriction digests were set up as indicated in Table 1.13. For diagnostic digests 500ng of plasmid DNA were incubated for 1h in the presence of restriction enzymes at the appropriate temperature (37ºC for most enzymes). For restriction cloning, 4µg of DNA were used and the reactions were left to incubate for 3h at the recommended temperature (37ºC for most enzymes). The digests were resolved on agarose gel (see section 1.3.3). All restriction enzymes and buffers were supplied from New England Biolads (NEB).

Table 2.13: Test digests:

	Diagnostic digest	Vector/ insert digest for cloning
Restriction enzyme (NEB)	0.5 µl	1µl
10x Reaction buffer (NEB)	1 µl	3µl
Plasmid	3-8 µl (0.5 to 2µg)	4-10µl (~4µg)
ddH_2O	Up to 10µl	Up to 30µl

2.3.8 Quick ligation

DNA ligations were performed using the Quick ligation kit (NEB). For each ligation, 50 ng of vector were combined with a 3-fold molar excess of insert (average molecular weight of a DNA base pair ~620g.mol^{-1}). The reaction mix is detailed in Table 1.14. The reaction was incubated 5min at room temperature and 2 µl were then used to transform 50 µl of chemically competent cells as described above (2.3.5).

Table 2.14: Quick ligation

	Ligation	Insert control	Vector control
Vector	50ng	50ng	-
Insert	3-fold molar excess	-	3-fold molar excess
ddH_2O	Up to 10 µl	Up to 10 µl	Up to 10 µl
2x Quick buffer	10 µl	10 µl	10 µl
Quick ligase	1 µl	1 µl	1 µl
Total	20	20	20

2.3.9 Generation of USP30 knockout cells

SH-SY5Y USP30 KO cells were generated using the CRISPR-Cas9 editing system with sgRNAs targeting exon 3 of USP30 isoform 1 (sgRNA1: AGTTCACCTCCCAGTACTCC, sgRNA2: GTCTGCCTGTCCTGCTTTCA). The sgRNAs were cloned into the pSpCas9(BB)-2A-GFP (PX458) vector and the PX330-Puro and sequence verified by Elena Marcassa. KOC and KOD were engineered by transfecting SH-SY5Y cells with PX458-sgRNA#1. The positive cells were selected by FACS 24h later (selection of GFP positive cells; central FACS facility on the University of Liverpool campus) and were single cell diluted. KO11 were generated by transfecting SH-SY5Y mito-QC cells with PX330-puro and were selected 24h later with 1-1.5 µg.ml^{-1} puromycin over 72h. Individual clones were amplified, and their alleles sequenced at Dundee's DNA sequencing service.

The genomic DNA from each clone was extracted using Quick-DNA Miniprep kit (Zymo Research) following the manufacturer's instructions. The edited region of USP30 was amplified by PCR (see section 1.3.1) using the following sets of primers: 2225/2226 (KO11), 2227/2228 (KO11) & 2229/2230 (KO7, KOC and KOD) (Table 1.9). The PCR products were then inserted into pCR4-TOPO plasmids and transformed into TOP10 bacteria (see sections 1.3.4 and 1.3.5). Between 6-10 colonies per clone and sets of primer were expanded and their plasmid DNA extracted (section 1.3.5). A diagnostic restriction digest with EcoRI was performed to checked whether the plasmids contained an

insert (section 1.3.7). All plasmids positive for the insert were sent for Sanger sequencing at the Dundee's DNA Sequencing and Services Unit.

2.3.10 TagBFP-SKL plasmid

The pTagBFP sequence from the pTagBFP-H2B expression vector was amplified by PCR using the 2255 and 2256 primers (see section 1.3.2). These primers were also used to add a sequence coding for SKL adjacent to the amplified sequence, and flanked pTagBFP-SKL with restrictions sites (NheI and XhoI restriction sites for 2255 and 2256 respectively). The PCR product was resolved on an 1% agarose gel, then gel extracted and subcloned in pCR4Blunt-TOPO vector (see sections 1.3.3, 1.3.4 and 1.3.5). The vector was then transformed in TOP10 cells, expanded in LB supplemented with Kanamycin and extracted by using the Qiagen Miniprep (see section 1.3.5). The plasmid DNA was analysed for the presence of an insert by EcoRI digestion (pCR4Blunt-TOPO's insertion site is flanked by EcoRI restriction sites), the NheI and XhoI double digest was also tested and SpeI was used to linearise the vector (single restriction site in pCR4 TOPO vector), (see section 1.3.7).

One positive colony was further expanded in LB with Kanamycin and extracted using the Qiagen Midi kit. The pTagBFP-SKL sequence was then subcloned into the mammalian expression vector pCDNA3.1+. The vector and the pTagBFP-SKL insert were digested with NheI and XhoI then ligated using the Quick Ligase kit (see sections 1.3.7 and 1.3.8). The ligation products were transformed in DH5α cells then test digested with the following restrictions enzymes: NheI/XhoI (insert test), Bsu361/NdeI (inside/outside), Bsu361 (linearisation) (see sections 1.3.5 and 1.3.7). The positive plasmids were sent for sequencing at Dundee's DNA sequencing service.

The primers are detailed below:

JJ-TagBFP-SKL-For (2255): 5'-GAGCTAGCGCCACC ATG AGC GAG CTG ATT AAG GAG AAC ATG C -3'

JJ-TagBFP-SKL-Rev (2256): 5'- CACTCGAGTTACAGCTTGGATGAACC ATT AAG CTT G-3'

Primer colour legend: Restriction sites (NheI and XhoI for 2255 and 2256 respectively), Kozak sequence, STOP, SKL, pTagBFP ORF, linker

2.4 Mass spectrometry

2.4.1 Materials and reagents

The reagents employed in the mass spectrometry experiments detailed in this thesis are listed in Tables 1.15.

Table 2.15: Mass spectrometry reagents

REAGENT or RESOURCE	SOURCE	IDENTIFIER
SILAC Amino Acids and medium		
SILAC DMEM-F12 media lacking L-Arginine and L-Lysine	DC Biosciences LTD	-
DMEM-F12 for SILAC	Life Technologies Limited	#88370
Dialysed FBS	Biosera	#FB-1001/500
L-Lysine monohydrochloride (Lys0)	Sigma-Aldrich	#L8662
L-Lysine-4,4,5,5-d_4 hydrochloride (Lys4)	Sigma-Aldrich	#616192
L-Lysine-$^{13}C_6$,$^{15}N_2$ hydrochloride (Lys8)	Sigma-Aldrich	#608041
L-Arginine (Arg0)	Sigma-Aldrich	#A8094
L-Arginine-$^{13}C_6$ hydrochloride (Arg6)	Sigma-Aldrich	#643440
L-Arginine-$^{13}C_6$,$^{15}N_4$ hydrochloride (Arg10)	Sigma-Aldrich	#608033
L-Proline (Pro0)	Sigma-Aldrich	#P5607
Other		
DNA Lobind 1.5 ml tube	Eppendorf	# EP0030108051
Trypsin Gold	Promega	# V5280

2.4.2 SILAC labelling

SHSY5Y, SHSY5Y-KOD and SHSY5Y-KO11 cells were grown for at least 8 passages in SILAC DMEM/F12 supplemented with 10% dialysed FBS, 200 mg/L L-proline and either L-lysine (Lys0) together with L-arginine (Arg0), L-lysine-$_2H_4$ (Lys4) with L-arginine-U-$_{13}C_6$ (Arg6) or L-lysine-U-$_{13}C_6$-$_{15}N_2$ (Lys8) with L-arginine-U-$_{13}C_6$-$_{15}N_4$ (Arg10) at final concentrations of 28 mg.L^{-1} arginine and 146 mg.L^{-1} lysine.

2.4.3 Label test

2.4.3.1 In gel digest

2.4.3.1.1 Gel preparation

SILAC-labelled SH-SY5Y, SHSY5Y-KOD and SHSY5Y-KO11 cells were grown in 6cm dishes until confluency then lysed in NP40 buffer with MPI as described previously. The lysates were resolved in NuPage 4-12% 10 well (1.5mm) gels. The gel was then fixed with acetic acid and methanol (10% acetic acid, 50% methanol in H_2O) for 10mins. Identical gel slices (~ 5 x 2 mm) were cut out from each sample lanes using a scalpel, divided further into 1 x 1 mm pieces and placed into 1.5 ml Lobind Eppendorf tubes. The gel pieces were dehydrated with 100µl of 50mM Ammonium bicarbonate (Ambic) in Acetonitrile (ACN) for 5 min (900 rpm, RT) and the supernatant discarded. The samples were further dried out using SpeedVac Concentrator Plus (Eppendorf) at 60°C for 5 min.

2.4.3.1.2 Sample reduction and alkylation

The dried out-samples were reduced in 50 µl/band of 10mM Dithiothreitol (DTT) in 100mM Ambic at 56ºC and shaken at 900rpm for 1h. The supernatant was discarded, and the samples left to cool for 5 min. The samples were alkylated using 50µl/ band of 50mM iodoacetamide in 100 mM ambic and incubated at 30min at RT on a shaker (900 rpm). The supernatant was discarded. The samples were washed twice consecutively in 300 µl of 100 mM ambic then in 300 µl of 20 mM Ambic / ACN for 15 min each on a shaker (900 rpm). The supernatants were discarded.

The gel pieces were dehydrated with 100µl of ACN for 5 min (900 rpm, RT) and the supernatant discarded. The samples were further dried out using SpeedVac Concentrator Plus (Eppendorf) at 60°C for 5 min.

2.4.3.1.3 Trypsin digestion

Trypsin Gold was added to the protein samples at a ~1:25-1:50 trypsin to protein ratio and diluted in the reaction buffer (40µl per band, 40mM Ambic, 9% ACN). The gel bands were left to rehydrate in the digestion buffer for 30min at RT then incubated overnight at 37ºC.

2.4.3.1.4 Peptide extraction

The digest was supplemented with 40µl of ACN and incubated for 30min at 30ºC at 900rpm. The supernatant was collected into Eppendorf Lobind tubes and the gel pieces were mixed with 50µl of 1% formic acid in water for 20min. The supernatant of the gel pieces was added into the precedent Eppendorf Lobind tube. This was repeated once more.

The gel pieces were dehydrated using 150µl ACN and incubated for 10min at 900rpm. The supernatant was added to the same Lobind tube. The Lobind collection tubes containing the peptide samples were placed in the speed vacuum until all the liquid had evaporated. Dried peptides were stored at -20C until further processing. Peptide samples were re-suspended in 25µl of 1% formic acid prior to mass spectrometry analysis.

2.4.3.2 Mass spectrometry analysis

5µl of each sample was loaded on a high performance liquid chromatography column coupled to an LTQ-Orbitrap XL (Thermo Fisher) fitted with a Proxeon nanoelectrospray source. Samples were resolved on a 1-62% linear ACN gradient over 21mins. MS spectra were acquired by the Orbitrap at a resolution of 30,000 and MS/MS was performed on the TOP 5 ions. All spectra were acquired using Xcalibur software (version 2.0.7; Thermo Fisher Scientific). MS spectra were analysed using MaxQuant (version 1.5.3.8), (Cox and Mann, 2008).

2.4.4 Proteomics and ubiquitylomics analysis

Proteomic and ubiquitylomic (diGly immunoprecipitation using the PTMScan Ubiquitin Remnant Motif [K-GG] Kit #5562; Cell Signalling Technology) sample preparation and analysis by liquid chromatography tandem mass spectrometry (LC-MS/MS) were performed by Emma Rusilowicz-Jones in collaboration with both Benedikt Kessler's (University of Oxford, UK) and Matthias Trost's (Newcastle University, UK) groups as detailed in our manuscript (Rusilowicz-Jones et al., 2020). For the proteome, samples were analysed on an Orbitrap Q Exactive HF. For the ubiquitylome, samples were analysed on an Orbitrap Fusion Lumos (one replicate of the total ubiquitylome) and Orbitrap Q Exactive HF (mito-ubiquitylome and three replicates of the total ubiquitylome).

The proteomics data files were analysed using MaxQuant (version 1.6.7.0) (Cox and Mann, 2008). Statistical analysis was performed using Perseus (version 1.6.10.0) (Tyanova et al., 2016a). Scatter plots and heatmaps were made using JMP (version 15.0) and Morpheus (Broad Institute, https://software.broadinstitute.org/morpheus), respectively.

2.5 *Drosophila* biology

2.5.1 Materials and reagents

The reagents employed in the drosophila biology experiments detailed in this thesis are listed in Tables 1.16.

Table 2.16: *Drosophila* biology reagents

REAGENT or RESOURCE	SOURCE	IDENTIFIER
Experimental Models: Organisms/Strains		
Usp30 KO	Generated by WellGenetics Inc.	
UAS-Mt-Keima M2 (III)	Generated by Aitor Martinez-Zarate in collaboration with Ugo Mayor	
UAS-Mt-Keima M3 (II)	Generated by Aitor Martinez-Zarate in collaboration with Ugo Mayor	
UAS-Mt-Keima M4 (III)	Generated by Aitor Martinez-Zarate in collaboration with Ugo Mayor	
UAS-Mt-Keima M7 (II)	Generated by Aitor Martinez-Zarate in collaboration with Ugo Mayor	
UAS-mitoGFP (III)	Bloomington, gift by Natalia Sanchez-Soriano (University of Liverpool)	BL8443
UAS-*Parkin* (II)	Bloomington	BL37509
UAS-*Pink1* (II)	VDRC	#21859
tub-GAL4 (III)	Bloomington, gift by Natalia Sanchez-Soriano (University of Liverpool)	BL5138
elav-GAL4 (III)	Bloomington, gift by Natalia Sanchez-Soriano (University of Liverpool)	BL8760
Antibodies		
Mouse Anti-Keima-Red mAb	MBL	M126-3
Sheep Anti-GFP Ab	gift from Prof. Ian Prior (University of Liverpool)	
Mouse Anti-beta Actin mAb	Abcam	Ab6276
Chemicals		

Antimycin A	Sigma	#75351
Oligomycin A	Sigma	#A8674
Deferiprone	Sigma	#379409
Trizol Reagent	Thermo Fischer Scientific	#15596026
Fluorescent dyes		
Mitotracker™ Deep Red	Thermo Fischer Scientific	M22426
Lysotracker™ Blue DND-22	Thermo Fischer Scientific	L7525
Lysotracker™ Blue DND-22	Thermo Fischer Scientific	L7525
Plasmids		
mt-mKeima (h)-pIND(SP1)	Gift by Atsushi Miyawaki (RIKEN, Japan)	
pCASPER-Tubulin-QF7m1	Addgene, gifted by Daimark Bennett (University of Liverpool)	#46128
pUAST-mt-Keima	Clague-Urbé and Ugo Mayor labs	
Dissection and homogenization tools		
Pellet pestles	Sigma	Z359947-100EA
Dumont No.5 Forceps	InterFocus	#11252-30
Dumont HP Tweezers 5	AgarScientific	AGT5034
Microscopy		
MatTek dish 35mm	MatTek	P35G-1.5-14-C
Halocarbon oil 700	Sigma	H8898
Coverslips No2 22x64mm	Scientific Laboratory Supplies Limited	MIC3268
Coverslips No1.5 22x22mm	Scientific Laboratory Supplies Limited	MIC3124
Coverslips No1 13mm Dia	Scientific Laboratory Supplies Limited	MIC3306
Molecular biology Kits and enzymes		
RNeasy Mini Kit	Qiagen	#74106
Reverse Transcription Syst.	Promega	A3500
RevertAid H minus M-MuLV Reverse Transcriptase	Thermo Fischer Scientific	EP0451
iTaq Universal SYBR Green Supermix	Biorad	1725120
Others		
Nuclease free water	Sigma-Aldrich	#W4502

2.5.2 *Drosophila* maintenance

Drosophila stocks were kept at 18ºC and expanded at 25ºC for experimental use. All flies were fed with the standard fly food (provided by the Manchester Fly Facility, UK).

2.5.3 Climbing assay (also known as negative geotaxis assay)

Motor function was assessed using the climbing assay (= negative geotaxis assays). Up to ten males or females aged 12-days-old were placed in 19cm graduated tubes closed at both ends (Different sexes and genotypes were kept separated) and left to rest for 5min, with the tube lying horizontally. Each tube was then set upright and taped 5 times to stimulate climbing. Meanwhile, the flies were filmed for 1min using a smartphone camera. Three technical replicates were performed per tube and were spaced at 5min intervals. The videos were analysed on QuickTime Player v10.5. The height climbed by each fly, 20s after stimulation, was recorded for each replicate. The graphs were produced using GraphPad Prism v6.0.

2.5.4 Survival curve

50 new-born flies for each sex and genotype were grown in their regular food tubes (16-17 fly per tube) at 27ºC. The number of live flies per vials was counted every 2-3 days (Mon-Wed-Fri) for 44 days and the flies were exchanged to new tubes every 7days. The experiment was repeated 3 times. Graphs were produced using GraphPad Prism v6.0.

2.5.5 *Drosophila* lysis

In preparation of immunoblotting, flies were snap-frozen in liquid nitrogen. Either whole organism or heads-only were lysed in Laemmli buffer (250mM Tris pH 7.5, 4% SDS, 40% Glycerol, 100mM DTT, w/v 0.05 Bromophenol Blue) in 1.5ml Eppendorf tubes. The tissues were homogenised using homogenisation pestles. The samples were then boiled 10min at 95ºC.

2.5.6 *Drosophila* neuronal embryonic culture

Male and female *Drosophila* of the selected cross were incubated in a fresh vial for 14h to stimulate reproduction and were then discarded from the vial. Embryos were dechorionated for 90s in 50% bleach and the reaction was

ended by adding two volumes of water. They were then transferred onto agar plates and stage E11 embryo were visually selected using a Leica fluorescence microscope; each neuronal culture was derived from 10 stage E11 embryos. Selected embryos were collected into a 1.5ml Eppendorf tube and rinsed in 70% ethanol, then rinsed in neuronal media (25% FBS, 2µg.ml-1 Insulin, 1% Penicillin/Streptomycin, in Schneider's *Drosophila* Media at pH 6.8-6.9, provided by Natalia Sanchez-Soriano, University of Liverpool) and subsequently gently homogenised in 100µl dispersion media (1% penicillin/streptomycin, 50µg.ml-1 phenylthiourea, 1 mg.ml-1 collagenase and 5 mg.ml-1 Dispase II in HBSS, provided by Natalia Sanchez-Soriano, University of Liverpool) using pestles. The homogenates were incubated for 3.30min at 37ºC. The reaction was ended by the addition of 200µl neuronal media and the homogenates were centrifugated for 5min at 900g. The supernatant was discarded, and the pellet resuspended in 30µl neuronal media. The homogenate was deposited onto a microscopy slide coated with Concavalin A (provided by Natalia Sanchez-Soriano, University of Liverpool) and covered by a coverslip. The cultured cells were incubated in the dark at 26ºC first upside down for 2h, then flipped back and grown for 48h.

2.5.7 Live imaging of whole larvae

Stage 3 larvae were anesthetised in 10% chloroform mixed in Halocarbon oil for 5min. The larvae were then mounted in between two 22x64 coverslips coated in the 10% chloroform/Halocarbon oil mixture and separated by 22x22 coverslips. The larvae were imaged straight after mounting for 30min maximum. For all anatomical analysis, images were acquired on the 3i spinning disk confocal with the sCMOS camera (higher resolution); the EMCCD camera was required for mitophagy analysis (greater sensitivity). z-stack (100 planes, 1µM step size) were taken using the 10x objective lens and single plane images using the 63x objective lens. Mt-Keima: sequential imaging, Ex445/Em620nm then Ex561/Em620nm. Mito-GFP: Ex445/ Em510nm.

2.5.8 Lysotracker and Mitotracker assay

Drosophila embryonic neuronal culture grown for 48h on Concavalin A coated slides were incubated for 30 min with 100nM Mitotracker Deep Red or with 5μM Lysotracker Blue. Images were captured using a spinning disk confocal microscope, a 63X objective lens and the sCMOS camera. Mitotracker Deep Red: Ex640/Em665nm and 100ms exposure time; Lysotracker Blue Ex405/Em422nm and 300ms exposure time.

2.5.9 Adult *Drosophila* tissue dissection and imaging.

Adult *Drosophilas* were anesthetised in ice for 5min. The flies were then dissected in PBS using Dumont No.5 Forceps and Dumont HP Tweezers 5. The dissected tissues were mounted in PBS into MatTek 35mm dishes and tightly covered with a 13mm diameter coverslip attached to the dish using double sided tape. z-stack (70 planes, 1μM step size) or single plane images were acquired with a spinning disk confocal, a sCMOS camera and a 10x objective lens. Mt-Keima: sequential imaging, Ex445/Em620nm then Ex561/Em620nm.

The brain dissections were performed with the assistance of Natalia Sanchez-Soriano's and Pilar Okenve-Ramos (University of Liverpool).

2.5.10 Mt-Keima analysis

The mitophagy index and corresponding mitophagy index plots were generated using the pixelAnalysis function in ImageJ/FIJI from single plane images. This plugin was coded by Dave Mason (CCI, Liverpool, UK), (Adapted from (Sun et al., 2015)). The pixel intensity values in Ex561 images were plotted over the pixel intensity value of Ex445 images. The plots were divided in 4 quadrants to obtain: pixels originating from the mitochondria in acidic compartments "b" and pixels from the rest of the network "a", "c" and "d". The mitophagy index (M.I.) was calculated as follow: pixels b/ (pixels (a - BG) + b + c + d). BG: Background signal, which was measured in the nucleus. Graphs were produced using GraphPad Prism v6.0.

2.5.11 Fly mutagenesis

2.5.11.1 Mt-Keima fly engineering

The fly mt-Keima plasmid was engineered by Aitor Martinez-Zarate (Ugo Mayor, BioGUNE, Bilbao, Spain; Sylvie Urbé and Michael Clague, University of Liverpool, UK). Briefly, the mt-Keima sequence from the mammalian plasmid mt-mKeima (h)-pIND(SP1), kindly provided by Atsushi Miyawaki (RIKEN, Japan), was amplified and cloned into a *Drosophila* expression vector pUAST (Katayama et al., 2011). The mt-Keima-pUAST construct was then injected in wildtype (*w1118*) *Drosophila* embryo by Bestgene Inc. (California, USA). The resulting positive strains were screened by Aitor Martinez-Zarate and Juanma Ramirez (UPV-EHU, Spain) by detecting mt-Keima's expression and fluorescence in the *Drosophila* eye after being crossed with *GMR*-GAL4 flies. Four independent UAS-mt-Keima strains were selected: M3 and M7 (insertion in the 2nd chromosome) and M2 and M4 (insertion in the 3rd chromosome).

2.5.11.2 CRISPR/Cas9-mediated *Usp30* KO in *Drosophila*

CRISPR-mediated mutagenesis was done by WellGenetics Inc. using modified methods of Kondo and Ueda (2013). In brief, two gRNA sequences, CGAAGGACCCCAGAAAACGA[AGG] and GTGACCGCTGTTTGCCTCCC-[CGG], were cloned into U6 promoter plasmid(s). Cassette Stop-w containing 3-frame stop codons and *hs-w* (eye marker) and two 1kb homology arms were cloned into pUC57-Kan as donor template for repair. *Usp30*-targeting gRNAs and hs-Cas9 were supplied in DNA plasmids, together with donor plasmid for microinjection into embryos of control strain *w1118*. F1 flies carrying selection marker of *hs-w* were further validated by genomic PCR and sequencing. CRISPR generates a 1742-bp deletion allele of *Usp30*, deleting most of CDS region of *Usp30* (*CG3016*) gene and is replaced by cassette *hs-w*.

2.5.12 mRNA extraction from whole *Drosophila*

Protocol from Kevin Bogart and Justen Andrews (Bogart and Andrews, 2006). 50 mg of frozen flies were homogenized in 1 ml Trizol with a disposable plastic pestle in a 1.5 ml microcentrifuge tube and then incubated at RT for 5 min. The homogenate was centrifugated at 12,000 rcf for 10 min at 4ºC to pellet insoluble debris. The supernatant was transferred to a new microcentrifuge tube, mixed with 200 µl of Chloroform and then incubated at RT for 3 min. The

sample was centrifugated for 15min at 10,000 rcf, 4ºC. The upper aqueous phase (~0.6 ml) was transferred to a fresh RNAse-free microcentrifuge tube, mixed with 0.5 ml isopropanol, incubated for 10 min at RT and centrifugated at 12,000 rcf for 10 min at 4ºC. The supernatant was discarded, the pellet washed in 1ml 75% ethanol and re-spun at 7,500 rcf for 5 min at 4ºC. The supernatant was discarded, and the pellet left to air dry for 10min. Finally, the pellet was resuspended in 100µl RNase-free water.

The concentration and quality of the extracted mRNA were assessed using a NanoDrop Spectrophotometer ND100 at 260nM and taking into account the A260/A280 and A260/A230 ratios.

2.5.13 Reverse transcription

Drosophila total RNA, extracted as in section 1.5.12, was reversed transcribed to cDNA using the Promega's Reverse Transcription System and RevertAid H minus M-MuLV Reverse Transcriptase (ThermoFisher) as follows. Total RNA was mixed with Oligo(dT) primers (RNA Mix, Table 1.17), and incubated for 5min at 70ºC to prime the RNA polyA tails for reverse transcription. The reverse transcription mix, detailed in the Table 1.18, was then added to the RNA Mix, incubated for 5min at 37ºC and finally supplemented with 1µl of reverse transcriptase. The mix was incubated for 1h at 42ºC and the synthesis was then arrested by heating the cDNA samples at 70ºC for 10min. They were finally cooled on ice for 5 min and diluted in H_2O up to 100µl.

Table 2.17: Total *Drosophila* RNA and primer Mix

Reagent	Volume per reaction
Total RNA	1µg
Nuclease free ddH2O	Up to 10µl
Oligo(dT) primer	1µl

Table 2.18: Reverse transcription Mix

Reagent	Volume per reaction
5x reverse transcription buffer	4µl
PCR nucleotide mix (Promega)	2µl
RNasin (Promega)	0.5µl
Nuclease free ddH2O	1.5µl

2.5.14 Quantitative real-time polymerase chain reaction qRT-PCR

The primers used for qRT-PCR are detailed in Table 1.19. The qRT-PCR reaction buffer was prepared as in Table 1.20 and plated into a 96well qPCR plates (6µl per well). Finally, 4µl of cDNA, prepared as in section 1.5.13, was added to each well. qRT-PCR was performed using BioRad's CFX Connect Real-Time PCR Detection System and monitored with CFX Manager™ Version: 3.1.1517.0823. The cDNA samples were denatured at 95ºC for 3 min, amplified for 40 cycles using a 2-step protocol: 10s at 95ºC followed by 30s at 60ºC and then incubated at 72ºC for 10min.

The cycle threshold values (Ct, also known as Cq), indicating the number of PCR cycle at which the samples' reaction curve intersected the threshold line, were calculated by the CFX Manager Analysis software. No reverse transcriptase samples and no cDNA (water only) samples were included as controls. The mean Ct was then calculated for each condition (3 replicates per condition) and normalised to the house keeping gene αtub84B (ΔCt). The relative expression of test samples to their calibrator sample (eg: USP30 KO cDNA over *w1118* cDNA) was indicated as $2^{-\Delta\Delta Ct}$.

Table 2.19: qPCR primers

Primers	Sequence
Forward USP30#1	AGCCGCATCTCAATAGCCAG
Reverse USP30#1	GCACATCGGTGGTACTACAC
Forward USP30#2	TTTCTGGGGTCCTTCGGGTT
Reverse USP30#2	GGTCAGTCCAAAGTTGTGGAGA
Forward αTub84B	CACACCACCCTGGAGCATTC
Reverse αTub84B	CCAATCAGACGGTTCAGGTTG

Table 2.20: qRT-PCR Mix

Reagent	Volume per reaction
SyBrGreen Biorad supermix	5.0µl
H_2O	0.7µl
Forward primer (20µM)	0.15µl
Reverse primer (20µM)	0.15µl

Chapter 3: Monitoring mitophagy: the toolbox

3.1 Introduction

Microscopy has been one of the favoured techniques to observe mitophagy. In particular, electron microscopy has greatly helped the field. In 1957, researchers started reporting on mitochondria found in “vesicles” (Clark, 1957; Ashford and Porter, 1962; Novikoff and Essner, 1962). Then in the early 2000s, John Lemasters and colleagues stained rat hepatocytes with mitochondrial and lysosomal dyes, and observed that upon nutrient starvation, depolarised mitochondria were colocalising with lysosomes (Lemasters et al., 1998; Elmore et al., 2001, 2004), [see review: (Rodriguez-Enriquez et al., 2004)]. Youle and colleagues followed up on that discovery and popularised the use of depolarising agents to induce and amplify mitophagy (Narendra et al., 2008). Alongside others, they discovered that Parkin and PINK1 regulate mitophagy (Narendra et al., 2008, 2010a; Matsuda et al., 2010; Vives-Bauza et al., 2010). Since then, the field has been moving swiftly and is now in search of efficient and reliable means to study mitophagy.

In this chapter my aim is to answer the following questions:
What means are available to amplify the mitophagy signal in human cells? How can we visualise spontaneous mitophagy events *in vivo*? Can we induce mitophagy independently of depolarisation?

I will start by presenting the hTERT-RPE1-YFP-Parkin cells, a cell model introduced by Jon Lane’s group, that is used in combination with uncoupling agents to magnify mitophagy processes (Liang et al., 2015; MacVicar and Lane, 2014). Next, I will describe mitophagy probes, which permit the visualisation of mitophagy events by microscopy. Finally, I will introduce new mitophagy triggers.

3.2 Combining depolarisation with Parkin overexpression: A powerful cocktail to amplify and observe mitophagy.

Mitophagy can be artificially triggered using agents that depolarise the inner mitochondrial membrane. Depolarisation prevents PINK1 cleavage at the inner mitochondrial membrane and causes its accumulation at the outer mitochondrial membrane (Jin et al., 2010). PINK1 then proceeds to phosphorylate ubiquitin and the E3 ligase Parkin, which triggers mitophagy [Reviewed in: (Bingol and Sheng, 2016; Harper et al., 2018; Pickles et al., 2018)].

The most commonly used tool to depolarise mitochondria is the protonophore Carbonyl cyanide *m*-chlorophenyl hydrazone (CCCP) (Narendra et al., 2008; Poole et al., 2010; MacVicar and Lane, 2014; Liang et al., 2015). CCCP increases the proton conductance across bilayer membranes (Kasianowicz et al., 1984). At mitochondria, this causes a collapse of the membrane potential and leads to the uncoupling of oxidative phosphorylation (Heytler and Prichard, 1962; Heytler, 1963; Liberman et al., 1969). However, CCCP is not specific for mitochondrial membranes and has been reported to uncouple proton gradients at other organelles such as lysosomes or the Golgi apparatus, and thus disrupts the intraluminal pH of these organelles (Llopis et al., 1998; Padman et al., 2013).

I have instead been using an inhibitor cocktail, composed of Antimycin A and Oligomycin A (AO), which directly targets constituents of the mitochondrial electron transport chain and thus induces a mitochondria-specific membrane depolarisation. Antimycin A inhibits complex III (CIII) of the respiratory chain which collapses the proton gradient (Alexandre and Lehninger, 1984). This however forces the F_1F_0-ATP synthase to work in reverse and produces reactive oxygen species (ROS) (Ivanes et al., 2014; Ksenzenko et al., 1983; Starkov and Fiskum, 2001). To prevent this compensatory mechanism, I have used Antimycin A in combination with Oligomycin A, an inhibitor of the F_1F_0-ATP synthase [for review see: (Georgakopoulos et al., 2017)]. Individually those inhibitors can induce mitophagy in mammalian cells but are much more potent when combined together (Allen et al., 2013).

Depolarising agents are often used in combination with Parkin overexpression. Overexpressing this E3 ligase increases the ubiquitylation of mitochondrial proteins up to an easily detectable level and accelerates mitochondria clearance (Narendra et al., 2008; Bingol et al., 2014; MacVicar and Lane, 2014; Liang et al., 2015). Overexpression of tagged Parkin also allows one to follow Parkin's translocation from the cytosol to the mitochondria (Narendra et al., 2008, 2010a; Matsuda et al., 2010; Liang et al., 2015). hTERT-RPE1-YFP-Parkin cells have been reported to be highly sensitive to depolarisation, clearing close to 90% of their mitochondria following 24h incubation with CCCP (MacVicar and Lane, 2014; Marcassa et al., 2018). I therefore started to study mitophagy in this highly dynamic model.

3.2.1 Parkin translocates to mitochondria upon depolarisation

I first characterised mitophagy in hTERT-RPE1-YFP-Parkin cells by immunofluorescence and assessed the effect of depolarisation on the cellular distribution of Parkin (**Figure 3.1**). I treated the cells with high doses of AO (5μM each) for 1, 8 and 10 hours and stained them for TOMM20, an outer mitochondrial membrane (OMM) protein. Within one hour, I observed a redistribution of Parkin from a diffuse to a punctate pattern, colocalising with fragmented mitochondria. Indeed, potent stressors such as depolarisation promotes mitochondrial fission to facilitate the autophagic degradation of defective mitochondrial fragments (Twig et al., 2008; Frank et al., 2012). In parallel, depolarisation promotes the PINK1-dependent recruitment of Parkin to mitochondria which initiates mitophagy (Matsuda et al., 2010; Narendra et al., 2010a; Vives-Bauza et al., 2010). After eight hours of treatment, the mitochondrial network appeared disrupted, partially degraded and retracted to few sites in the cytosol. At this point, all of the cytosolic Parkin had translocated to the mitochondria. At the ten hour time point, most of the OMM protein were degraded.

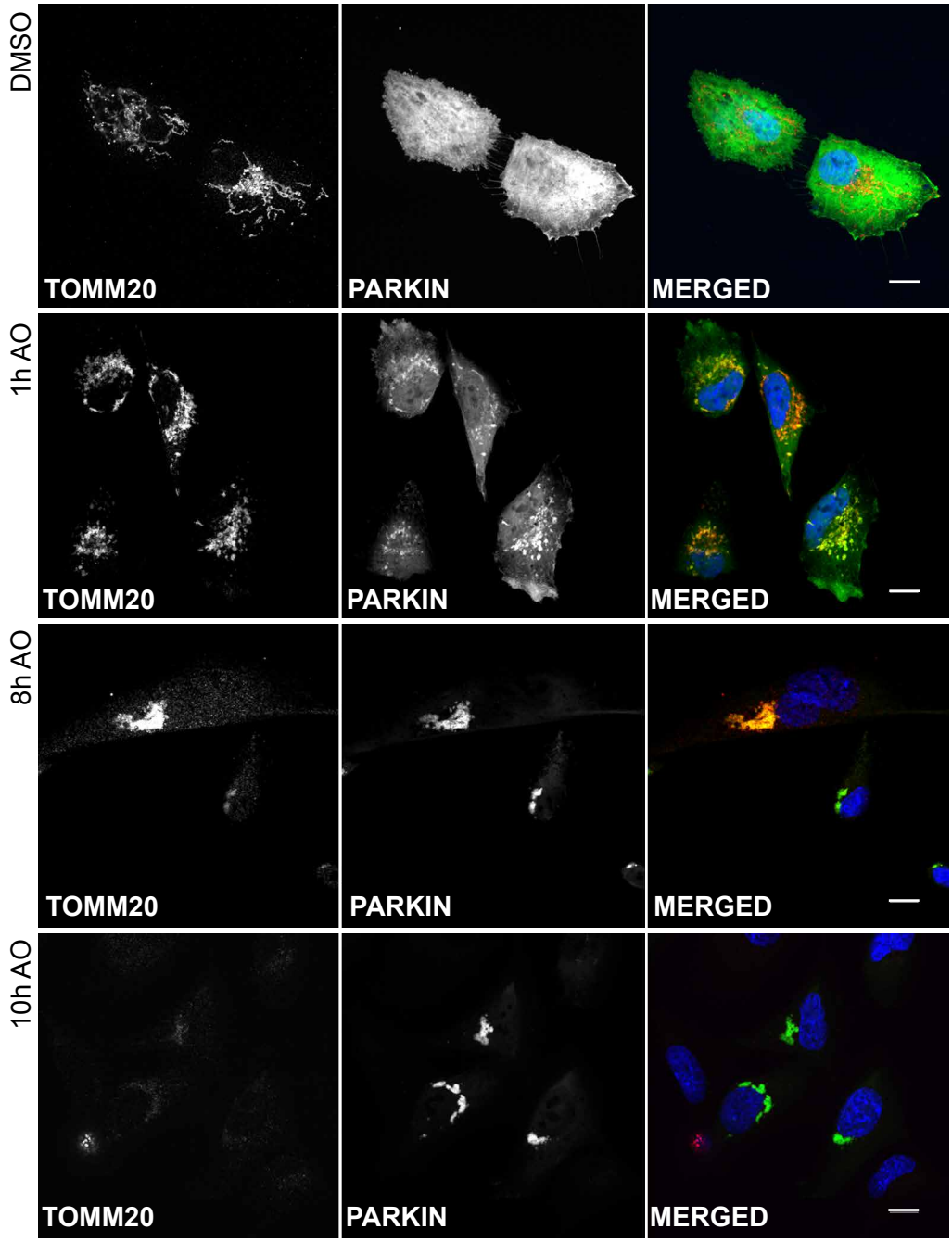

Figure 3.1: Depolarisation induced by Antimycin A and Oligomycin A initiates mitochondrial degradation and Parkin recruitment to mitochondria.

hTERT-RPE1-YFP-Parkin cells were treated with DMSO or Antimycin A and Oligomycin A (AO, 5μM each) for 1h, 8h and 10h. The cells where then fixed with PFA and stained with anti-TOMM20 antibody. The coverslips were mounted using mowiol mixed with DAPI. Images were taken using a 3i spinning disk confocal microscope. Scale bar: 10μm. Data from a single experiment.

I repeated this experiment with another mitochondrial marker, TIMM44 (**Figure 3.2**). Unlike TOMM20, TIMM44 is an inner membrane protein and is therefore degraded in the lysosome, whereas TOMM20 is also at least partially degraded by the proteasome (Chan et al., 2011; Yoshii et al., 2011; Sarraf et al., 2013; Liang et al., 2015; Rose et al., 2016). As observed previously, Parkin started accumulating on mitochondria one hour after depolarisation and fully localised to mitochondria after 4h (**Figure 3.2A-D**). After 24h, OMM and IMM proteins were cleared and the whole mitochondrial network had been sent for proteasomal and autophagic degradation.
This observation is in agreement with the literature and showed that depolarisation in Parkin-overexpressing cells can promote the full clearance of the mitochondrial network (Narendra et al., 2008; Allen et al., 2013; Marcassa et al., 2018). With the loss of mitochondria, newly synthesised Parkin was distributed to the cytosol (**Figure 3.2A-B**).

In parallel, I assessed whether lower doses of AO would be sufficient to promote Parkin translocation to mitochondria (**Figure 3.2D**). When using the drugs at 1μM, 78% and 92% of cells had mitochondrial Parkin after 2h and 4h of treatment respectively. When I lowered those concentrations to 0.1μM, Parkin's recruitment to mitochondria, which was seen in 76% of the cells, was delayed up to the 8h timepoint. When further reducing the concentrations of depolarisation agents to 0.01μM, the percentage of cells with mitochondrial Parkin did not exceed 22%.

It was previously reported that depletion of the mitochondrial deubiquitylase USP30 increases Parkin-dependent ubiquitylation of mitochondrial proteins (Bingol et al., 2014; Cunningham et al., 2015; Liang et al., 2015). The question remained whether USP30 inhibits Parkin recruitment to mitochondria or if it merely removes ubiquitin from Parkin substrates.

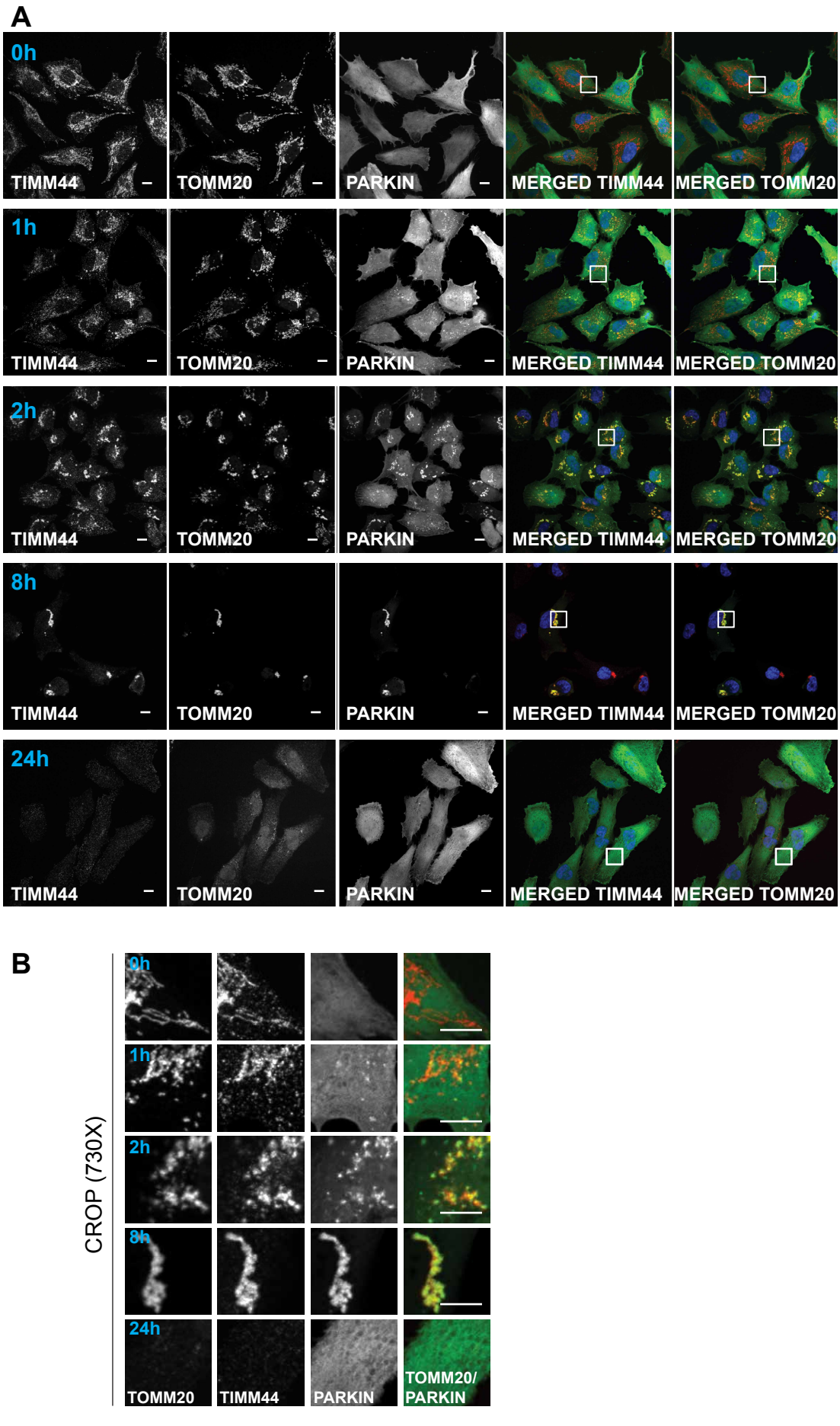
A
0h
1h
2h
8h
24h
TIMM44
TOMM20
PARKIN
MERGED TIMM44
MERGED TOMM20
B
CROP (730X)
9h
1h
2h
8h
24h
TOMM20
TIMM44
PARKIN
TOMM20/
PARKIN

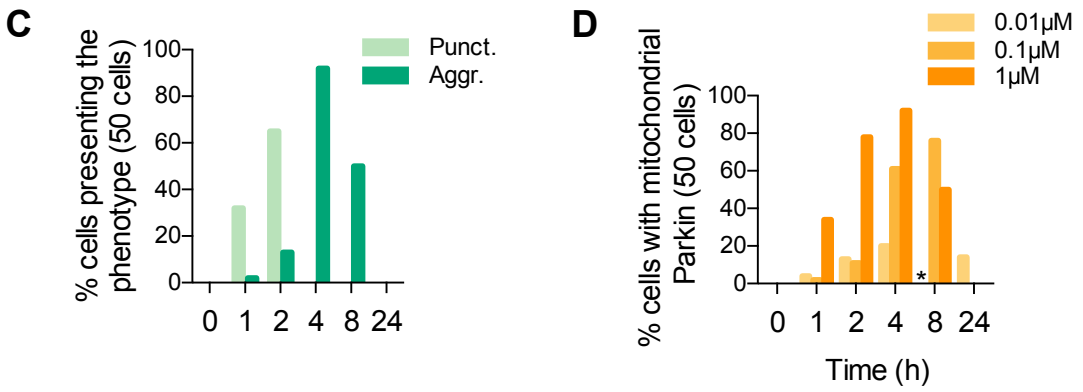

Figure 3.2: Antimycin A and Oligomycin A induce Parkin translocation to mitochondria.

hTERT-RPE1-YFP-Parkin cells were treated with DMSO 0.01µM, 0.1µM and 1µM of Antimycin A and Oligomycin A for 1h, 2h, 8h and 24h. The cells where then fixed with PFA and stained with both anti-TOMM20 and anti-TIMM44 antibodies. The coverslips were mounted using mowiol mixed with DAPI. Images were taken using a 3i spinning disk confocal microscope. **A)** Images show hTERT-RPE1-YFP-Parkin cells treated with 1µM of Antimycin A and Oligomycin A over time. Scale bar: 10µm. **B)** Cropped and enlarged images from panel A. Scale bar: 10µM. **C)** Panel A quantification: The translocation of Parkin to mitochondria was sorted into 3 categories (Diffused, Puncta and Aggregates). The graph depicts the percentage of cells with either Parkin puncta (Punct.) or aggregates (Aggr.) on mitochondria. **D)** The percentage of cell with mitochondrial Parkin (aggregates + puncta) was plotted over time. *8h time point, 0.01µM AO: Parkin was cytosolic in all of the cells quantified. Data from a single experiment

3.2.2 USP30 depletion does not affect the recruitment of overexpressed Parkin to mitochondria

I transfected hTERT-RPE1-YFP-Parkin cells with either non-targeting (NT1) or USP30-targeting (D1 and D3) siRNA oligos for 72h and depolarised mitochondria for 1h with increasing amounts of AO (0.01, 0.1 and 1µM each), (**Figure 3.3**). The knockdown process appeared to have sensitised the cells to the AO treatments. After 1h with 1µM AO, 67% of cells transfected with non-targeting (NT1) siRNA oligos had Parkin puncta on their mitochondria against 32% of untransfected cells in the previous experiment (**Figure 3.3D and 3.2C**). The additive stress caused by the transfection might have lowered the threshold for mitophagy induction. However, USP30 depletion itself did not consistently affect Parkin relocation (**Figure 3.3D**). With 1µM AO treatment, ~70% of cells presented mitochondrial Parkin puncta independently on USP30 depletion. One could argue that with 1µM, mitophagy and Parkin recruitment

occured too rapidly to detect a further enhancement upon USP30 knockdown. At a lower concentration (0.1µM), one siRNA oligo appeared to enhance Parkin recruitment (D3; 53% of cells with Parkin punctae compared to 30% for NT1), while the second oligo had the opposite effect (D1: 16%); although both siRNA oligos efficiently depleted USP30 (**Figure 3.3D and Figure 3.5**).

A genome-wide siRNA screen performed in HeLa cells overexpressing YFP-Parkin similarly revealed that upon CCCP treatment USP30 knockdown did not affect Parkin recruitment to mitochondria (Hasson et al., 2013).
In agreement with my observation, a genome-wide siRNA screen performed in HeLa cells overexpressing YFP-Parkin and aiming at identifying regulators of CCCP-induced mitophagy also failed to isolate USP30 as a regulator of Parkin recruitment (Hasson et al., 2013).

These results indicate that in Parkin-overexpressing cells, USP30 does not oppose mitophagy by preventing the recruitment of Parkin to mitochondria.

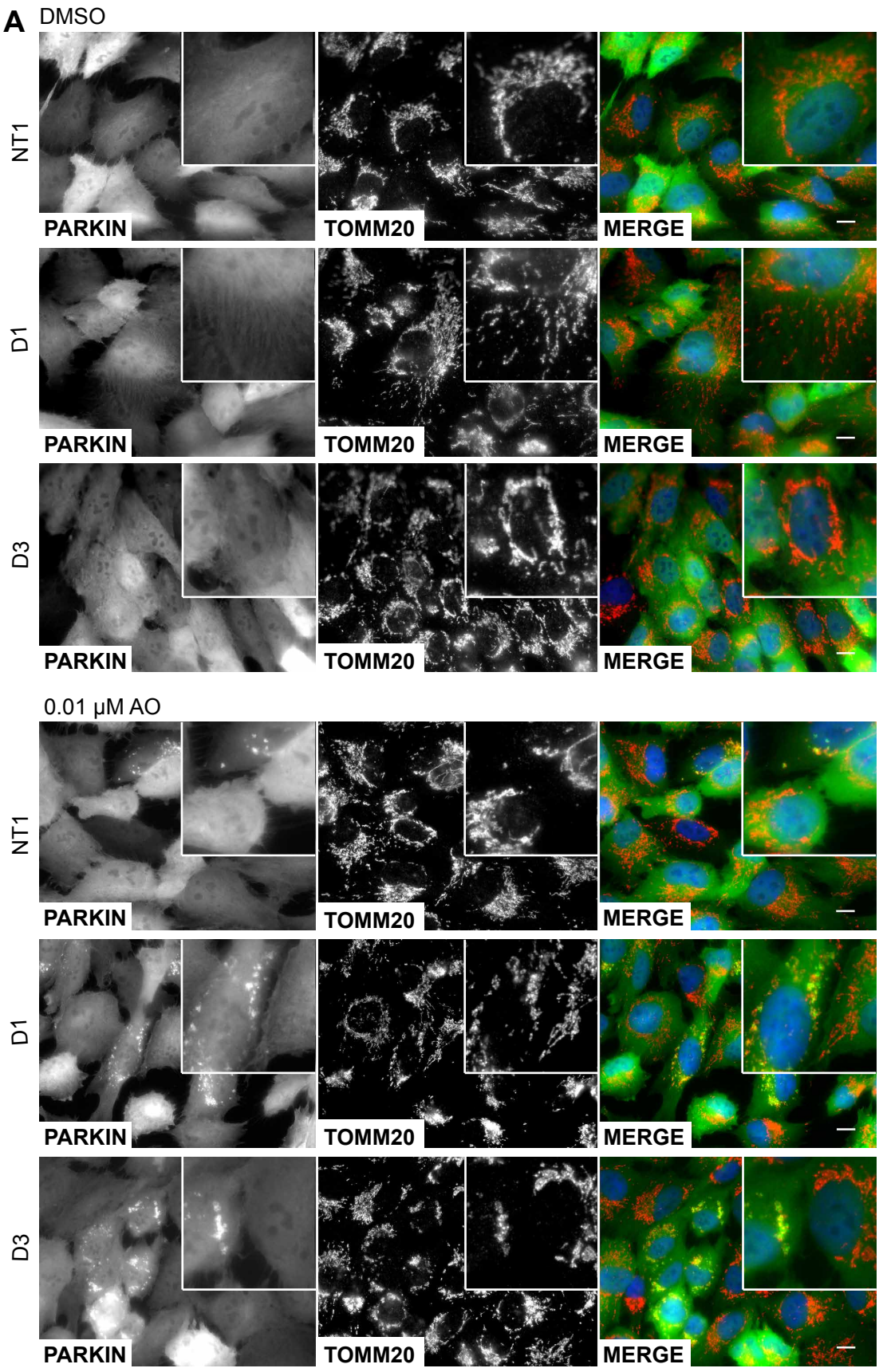
A
DMSO
NT1
D1
D3
PARKIN
TOMM20
MERGE
0.01 µM AO
NT1
D1
D3
PARKIN
TOMM20
MERGE

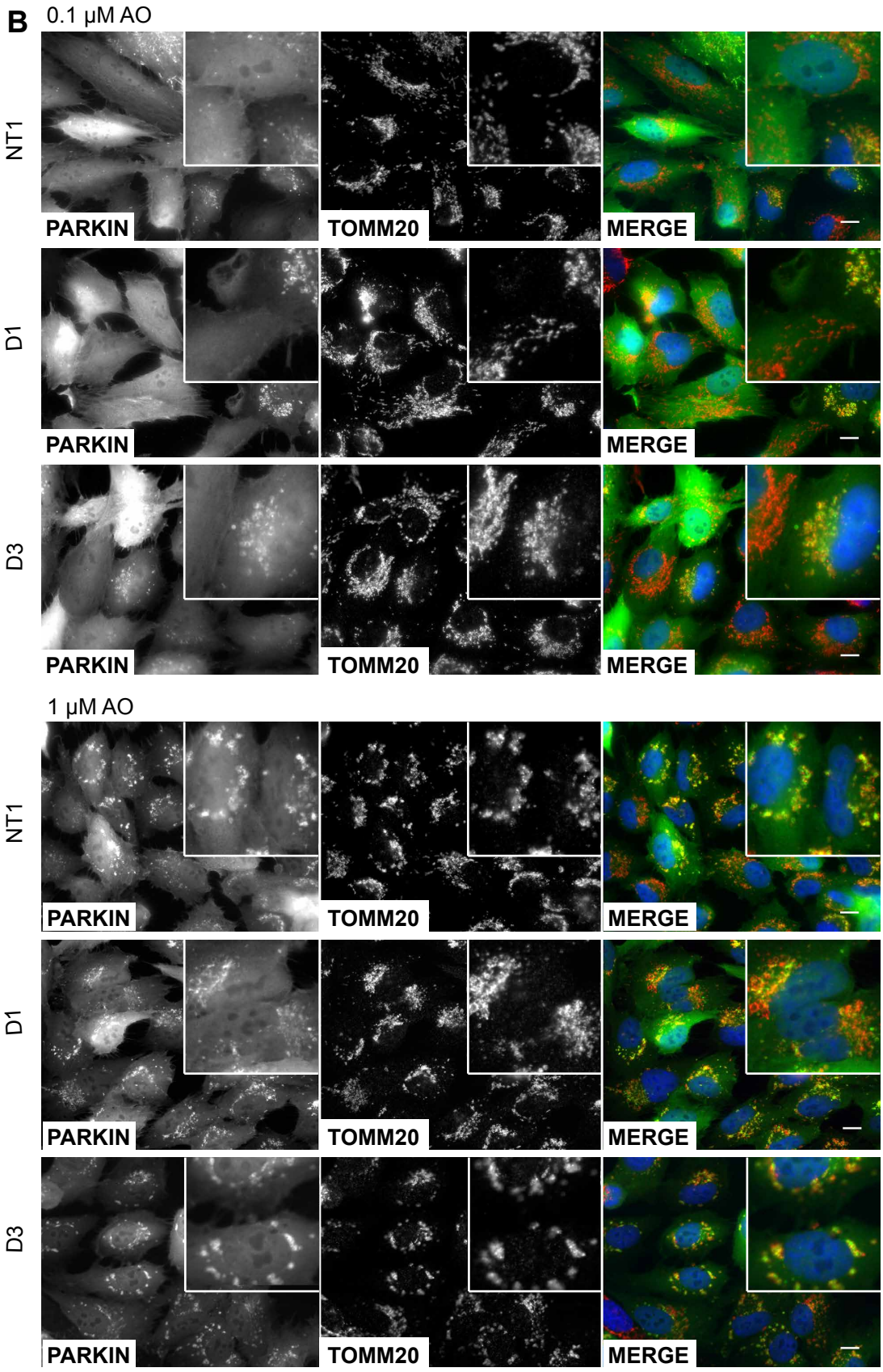
B
0.1 μM AO
NT1
D1
D3
PARKIN
TOMM20
MERGE
1 μM AO
NT1
D1
D3
PARKIN
TOMM20
MERGE

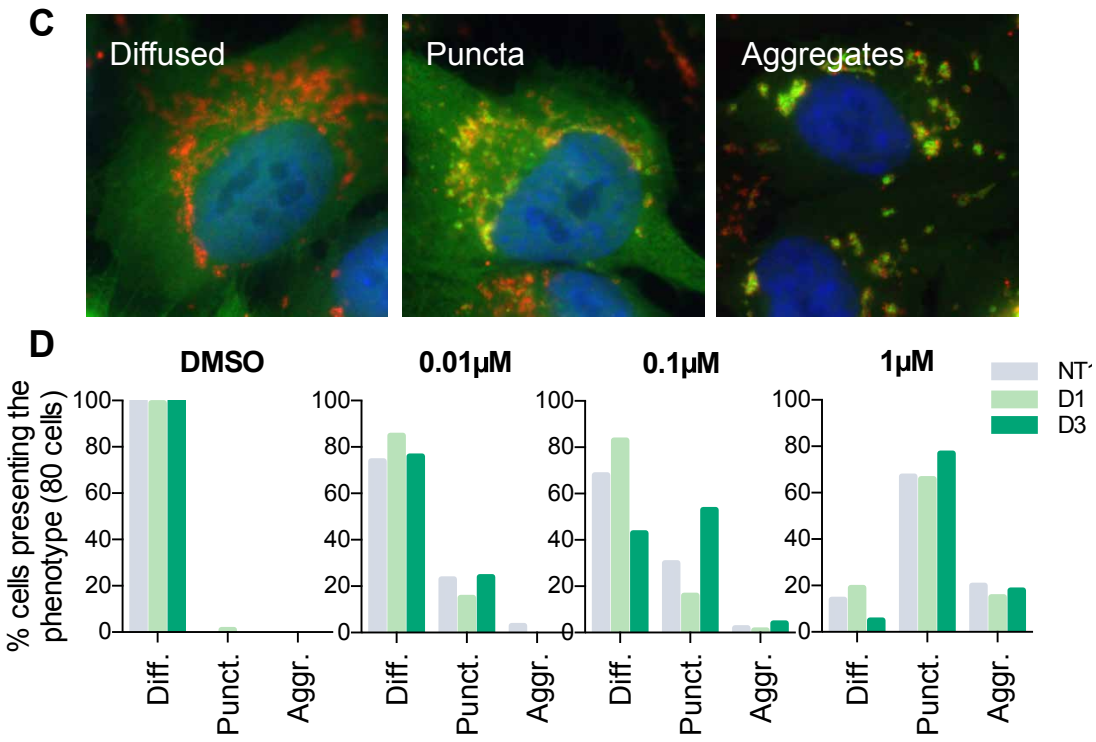

Figure 3.3: USP30 knockdown does not affect Parkin translocation to mitochondria.

A and B) hTERT-RPE1-YFP-Parkin cells were transfected with either non-targeting (NT1) or individual oligos targeting USP30 (D1 and D3) for 72h and treated with 0.01, 0.1 or 1µM Antimycin A and Oligomycin A (AO) for 1h. The cells where then fixed with PFA and stained with anti-TOMM20 antibody. The coverslips were mounted using mowiol mixed with DAPI. Scale bar: 10µm. **C)** The translocation of Parkin to mitochondria was monitored on a NIKON Ti-Eclipse microscope and sorted into 3 categories: Diffused, Puncta and Aggregates. **D)** Graph describing Parkin's translocation stages upon depolarisation and depletion of USP30. Data from a single experiment.

3.2.3 USP30 depletion accelerates depolarisation induced ubiquitylation and degradation of the outer mitochondrial membrane protein TOMM20.

Western blot analysis is another powerful approach to study mitophagy in the hTERT-RPE1-YFP-Parkin cells. Jin Rui Liang, aka “Amos”, a former PhD student in the Clague-Urbé lab, has shown that USP30 binds to TOMM20, one of Parkin’s substrates. He further discovered that USP30 depletion strongly enhanced CCCP-induced degradation of TOMM20 in hTERT-RPE1-YFP-Parkin cells (Liang et al., 2015).

First, I set out to reproduce his results and assess whether AO-induced ubiquitylation was regulated by USP30. To observe ubiquitylation and early OMM degradation events, I treated hTERT-RPE1-YFP-Parkin cells for 4h with CCCP (10µM) and AO (1µM each), (**Figure 3.4**). After 4h of mitophagy induction, the pool of the OMM protein MIRO1 was nearly fully degraded (~20% left) and the levels of other OMM proteins, TOMM20 and TOMM22, were decreasing.

In agreement with Amos’ results, USP30 knockdown specifically enhanced the elimination of TOMM20 and TOMM22 upon CCCP treatment without affecting PINK1 stability, Parkin ubiquitylation or other OMM and IMM proteins (Liang et al., 2015). All of those results were also reproduced with AO treatment.

To better observe the ubiquitylation events preceding the proteasomal degradation of OMM proteins, I treated hTERT-RPE1-YFP-Parkin cells for only 1h and with varying concentrations of AO (0.01, 0.1 and 1µM), (**Figure 3.5**). I also probed for OPA1 to have an indication of the depolarisation status of the mitochondrial network. OPA1 is a core regulator of mitochondrial membrane fusion and can interfere with mitophagy (MacVicar and Lane, 2014). This protein has eight splice variants which can be cleaved at S1 and S2 sites. S1 cleavage is mediated by OMA1, a mitochondrial protease, and gives rise to short OPA1 (S-OPA1) species which are unable to support mitochondria fusion (Ishihara et al., 2006), [for review see: (McBride and Soubannier, 2010)].

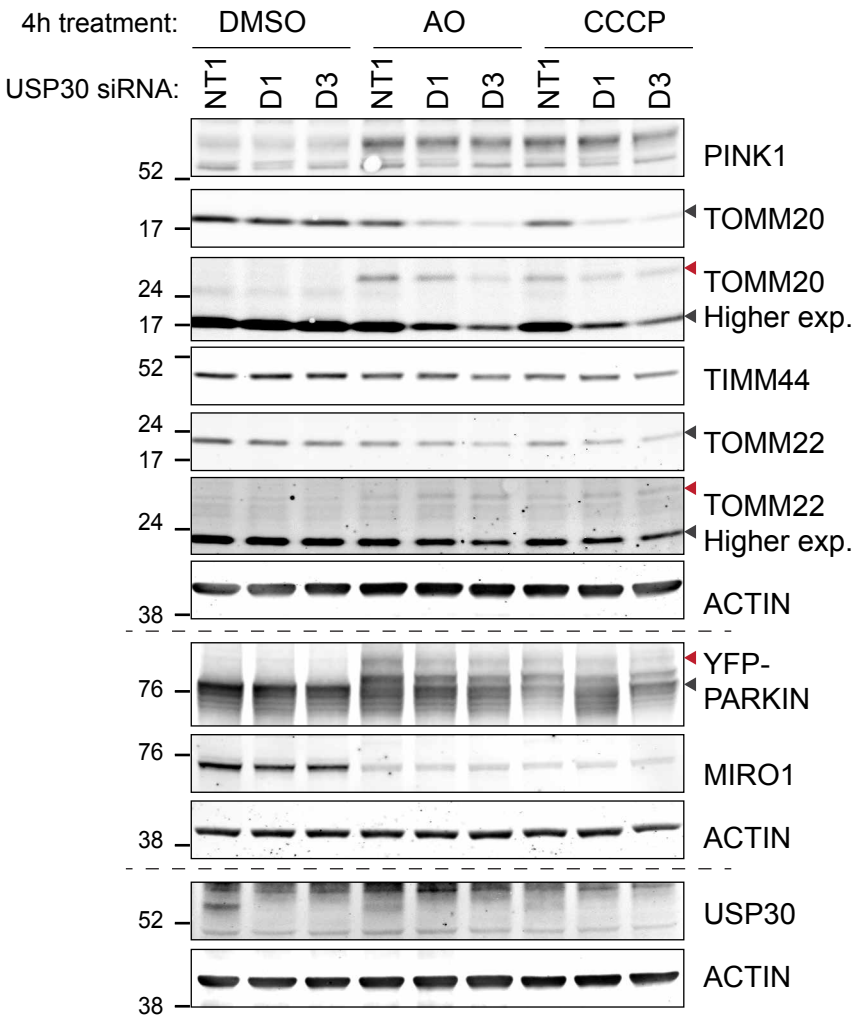

Figure 3.4: USP30 knockdown increases depolarisation-induced degradation of mitochondrial proteins.

hTERT-RPE1-YFP-Parkin cells were transfected with either non-targeting (NT1) or individual oligos targeting USP30 (D1 and D3) for 72h and treated with DMSO, Antimycin A and Oligomycin A (AO, 1μM each) or CCCP (10 μM) for 4h then lysed in RIPA buffer. The lysates where probed for mitochondrial proteins. Higher exp.: higher exposure. The black arrows indicate unmodified-proteins; the red arrows point towards ubiquitylated-proteins. Data from a single experiment.

Depolarisation promotes the OMA1-dependent cleavage of long forms of OPA1 (L-OPA1) to enable fission of the mitochondrial network (Ishihara et al., 2006),(MacVicar and Lane, 2014). I found that with a one-hour treatment, only the 1μM concentration was sufficient to promote the full cleavage of L-OPA1; suggesting that 0.1 and 0.01 μM AO result in an incomplete depolarisation of the mitochondrial network (**Figure 3.5**). In agreement with this, I observed that the MFN2 pool was only partially degraded with 0.1μM AO whilst only a small fraction remained intact with 1 μM AO.

With 1μM AO, TOMM20 was poly- or multiply mono ubiquitylated: mono-, di- and tri-ubiquitylated species of TOMM20 were distinguishable by western blot analysis. Interestingly, knocking down USP30 clearly enhanced TOMM20 ubiquitylation.

Amos made a similar finding. He treated hTERT-RPE1-YFP-Parkin cells with 10μM CCCP for 5h and blocked the proteasomal degradation of OMM proteins using the proteasome inhibitor epoxomicin. He was then able visualise an enhancement of mono- and di- TOMM20 ubiquitylation species in USP30 knockdown cells that were absent in the control cells at that timepoint (Liang et al., 2015).

My results with the more selective depolarising agents AO further confirm that TOMM20 is a bona-fide substrate of USP30 in hTERT-RPE1-YFP-Parkin cells.

As is clear from the above, overexpression of YFP-Parkin is clearly a useful tool to amplify mitophagy and easily assess the involvement of proposed mitophagy players. Yet, in the cells I used here, Parkin is overexpressed at very high and non-physiological levels and this might have affected the data I was collecting: by saturating the cells with Parkin, this E3 may ubiquitylate nearby proteins non-specifically.

Hence, I decided to turn to a cell model expressing endogenous Parkin and USP30 to further study mitophagy.

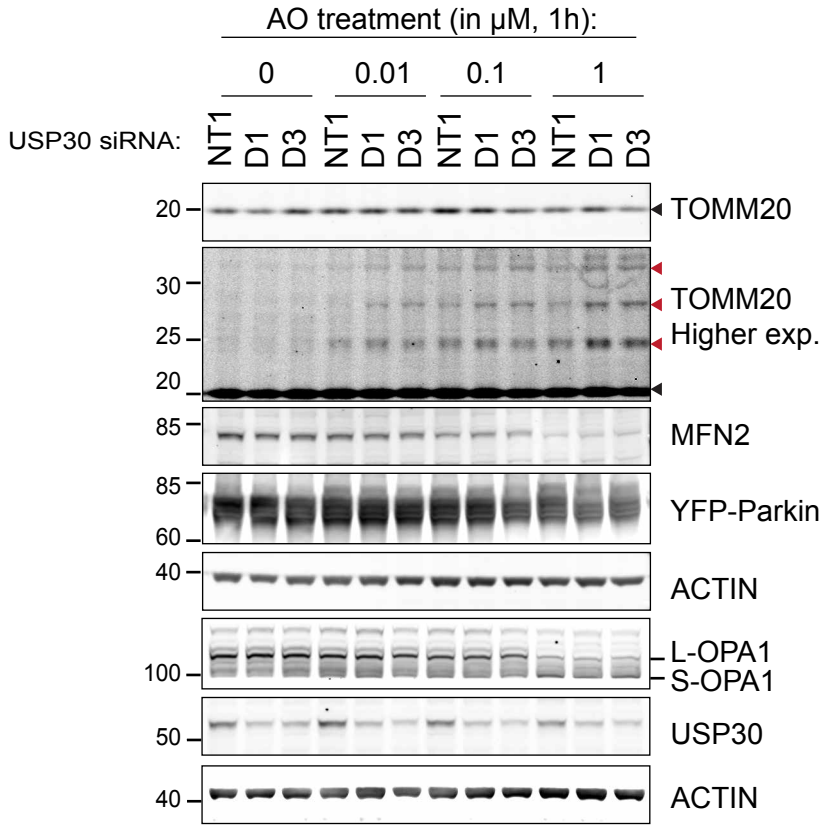

Figure 3.5: USP30 knockdown increases depolarisation induced ubiquitylation and degradation of mitochondrial proteins.

hTERT-RPE1-YFP-Parkin cells were transfected with either non-targeting (NT1) or individual oligos targeting USP30 (D1 and D3) for 72h and treated with DMSO or 0.01, 0.1 or 1µM Antimycin A and Oligomycin A (AO) for 1h. The cells were lysed in RIPA buffer and immunoblotted for mitochondrial proteins. Black arrow: unmodified TOMM20; Red arrow: Ubiquiylated species of TOMM20. Note that the 3rd ubiquitin band from the bottom appears as a double band, which may result from the ubiquitylation of different lysines. Data from a single experiment.

3.3 SH-SY5Y cells stably expressing mCherry-GFP-FIS1101-152: A cell model to monitor endogenous mitophagy.

3.3.1 SH-SY5Y cells: A neuroblastoma cell line expressing endogenous Parkin and USP30

I first assessed the expression levels of Parkin, USP30 and other mitochondrial proteins across cell lines that were readily available to me (**Figure 3.6A**). Neuroblastoma cells such as SH-SY5Y and SKN-BE2(c) expressed Parkin strikingly higher than other immortalised cell lines in the panel. The embryonic kidney derived cell line, HEK293T also expressed reasonably large amounts of Parkin. On the contrary, HCT116, MCF7 and U2OS cells appeared to express much lower levels, whilst Parkin was undetectable in HeLa and hTERT-RPE1 cells. It should be noted though that the HCT116 sample appeared to be underloaded.

An expanding body of work suggests that Parkin is a tumour suppressor. Indeed, the PARK2 gene is deleted in a plethora of human cancers (Gong et al., 2014; Veeriah et al., 2010a, 2010b). This could explain the absence of Parkin form HeLa cells. Interestingly, USP30 expression appeared to correlate with TOMM20 across cells: the USP30/TOMM20 ratio was relatively constant whether the cells expressed USP30 highly or not (**Figure 3.6B**). Parkin expression did neither correlate with USP30 or TOMM20 (**Figure 3.6C-D**).

As I was interested in proteins involved in familial forms of Parkinson's disease, I decided to focus on cells that would be the closest to neuronal cells such as neuroblastoma. I chose the SH-SY5Y cells as these have been well documented to share neuronal features such as tyrosine hydroxylase and dopamine-β-hydroxylase activity and have the ability to differentiate into neuronal-like cells (Kovalevich and Langford, 2013; Presgraves et al., 2004).

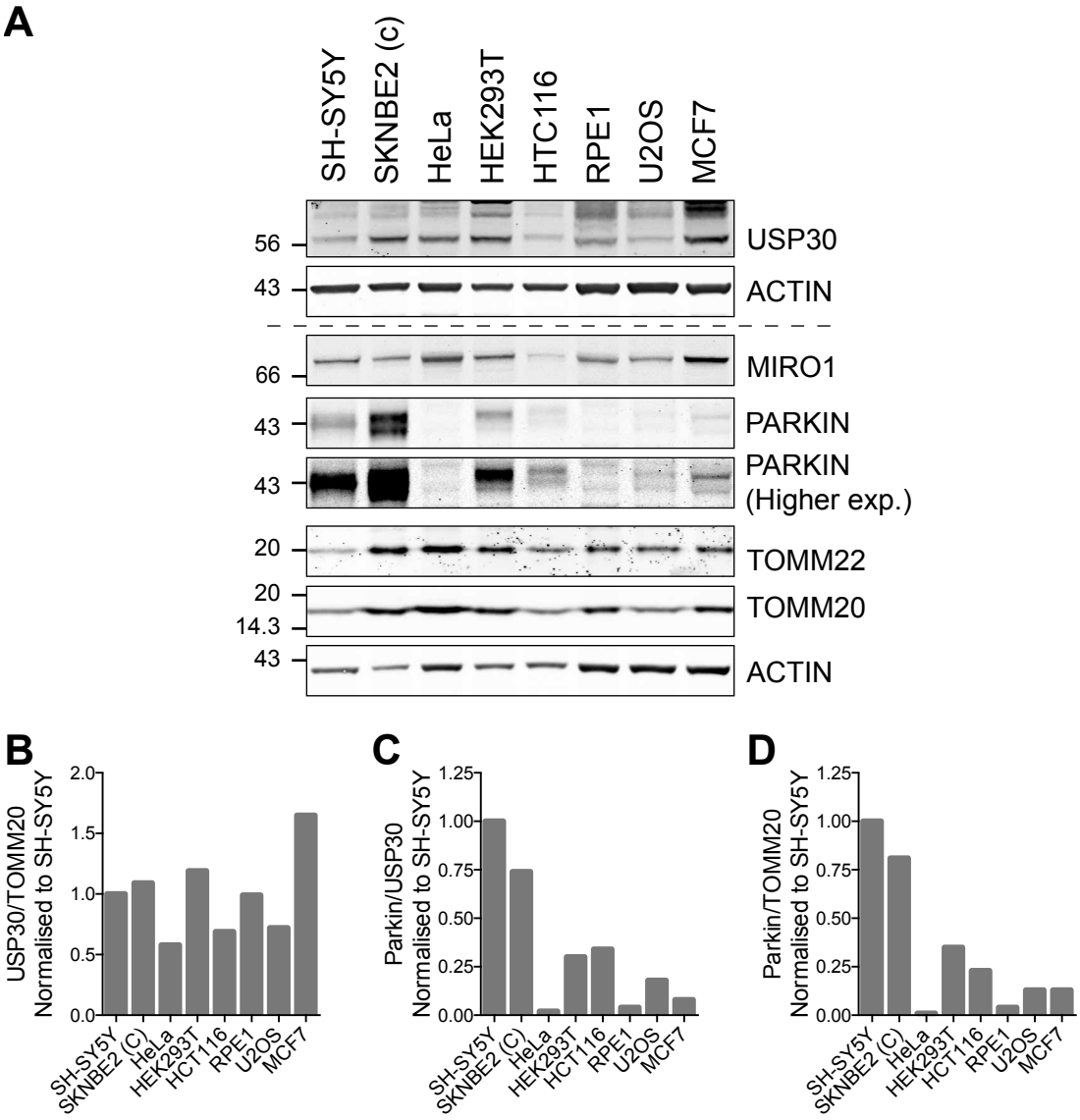

Figure 3.6: Expression levels of key mitophagy players across neuroblastoma-derived, and non-neuroblastoma cells.

A) SH-SY5Y, SKNBE2(c), HeLa, HEK293T, HCT116, RPE1, U2OS and MCF7 cell lysates were probed for mitophagy markers as shown on the figure. **B-D)** Graphs representing the relative expression of **B)** USP30 or **C-D)** Parkin over **B&D)** TOMM20 or **C)** USP30 and normalised to SH-SY5Y cells. The images were acquired using a LICOR Odyssey CLx infrared imaging platform and analysed using the ImageStudio quantification software. Higher exp. = higher exposure. Data from a single experiment.

3.3.2 Mitochondrial fraction enrichment: Amplifying the signal.

Western blot analysis is a powerful approach to monitor global mitophagy as seen in YFP-Parkin overexpressing hTERT-RPE1 cells. However, SHSY5Y cells express a much lower amount of endogenous Parkin and thus the number of mitophagy events is expected to be lower. In order to pick up the mitophagy signal more efficiently by immunoblotting, I adopted a cell fractionation and mitochondrial enrichment protocol (**Figure 3.7**).

After homogenising SH-SY5Y (mito-QC, a variant described in section 2.3) cells in a hypotonic buffer, I centrifuged the homogenates at 600g to spin out the nucleus. I then fractionated the post nuclear supernatant (PNS) at 7,000g to obtain a mitochondria enriched pellet (MF). It should be noted that this pellet also contains other heavy membranes such as ER and some peroxisomes. I loaded equal amounts of protein in each fraction (7µg protein) and quantified the MF over PNS band intensity ratio using the ImageStudio software. I found that in the MF, USP30 was enriched 6-fold, TOMM20 2.5-fold and PMP70 2.2-fold.

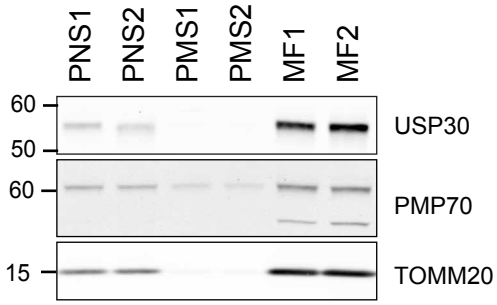

Figure 3.7: Mitochondrial enrichment by differential centrifugation.

Two dishes of SH-SY5Y mito-QC cells were homogenised in HIM buffer (1 and 2). The nuclei were spun down at 600g to collect the Post Nuclear Supernatant (PNS). The PNS was spun a second time at 7,000g. The resulting pellet was labelled Mitochondria Fraction (MF) and the supernatant the Post Mitochondrial Supernatant (PMS). Data from a single experiment.

I next used this technique to analyse mitochondrial fractions enriched from SH-SY5Y cells treated for 1 or 4h with AO (1μM each) (**Figure 3.8**).

Upon depolarisation, PINK1 gradually accumulated over time exclusively in the mitochondrial fraction. This was accompanied by the apparent poly- or multiple mono ubiquitylation of MFN1 and MFN2 as evidenced by multiple higher molecular weight species. In contrast, the fission protein FIS1 was strongly mono- and possibly di-ubiquitylated. Surprisingly, whilst TOMM20 was one of the most clearly ubiquitylated proteins in hTERT-RPE1-YFP-Parkin cells, I could not pick up any ubiquitylated species of TOMM20 in SH-SY5Y cells. The only bands I could observe at this molecular weight were most likely non-specific as they were also seen in the absence of depolarisation.

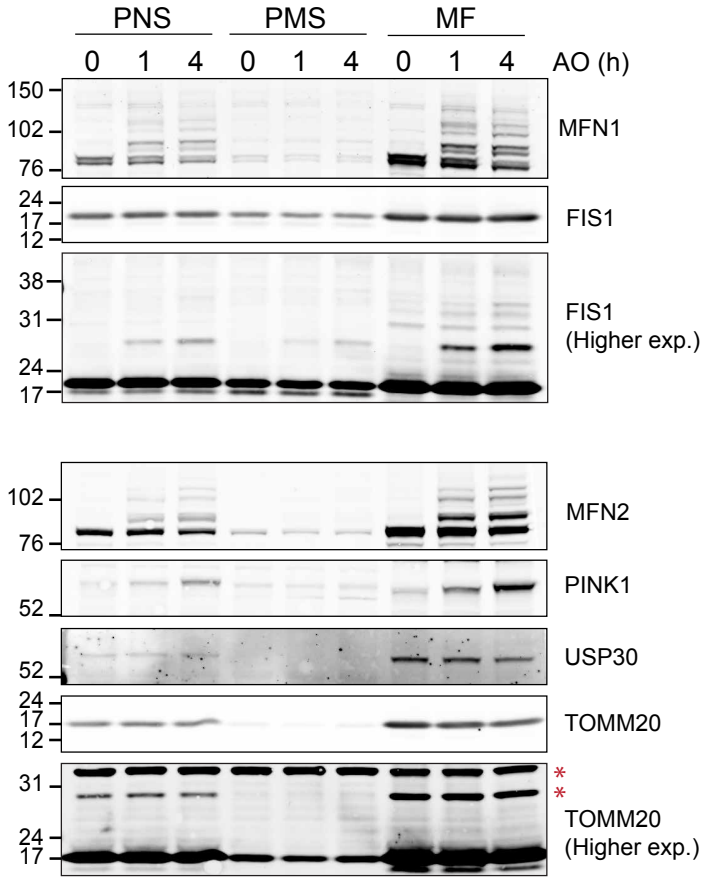

Figure 3.8: Antimycin A and Oligomycin A induce the ubiquitylation of mitochondrial proteins in SH-SY5Y mito-QC cells.

SH-SY5Y MGFIS cells were treated with Antimycin A and Oligomycin A (AO; 1μM each) for 0, 1 and 4h and homogenised. The homogenates were then fractionated by centrifugation to obtain a Post Nuclear Supernatant (PNS), a Post Mitochondrial Supernatant (PMS) and a Mitochondrial Fraction (MF). The fractions were then resolved by western blotting and probed as annotated. Red asterisk: non-specific band. Data from a single experiment.

3.3.3 Mitophagy probes for in vivo imaging

In recent years, a variety of reporters and dyes have been generated to specifically observe mitophagy (**Table 3.1**). I chose to use the mCherry-GFP-$FIS1_{101-152}$ reporter, also known as mito-QC, which had been characterised and introduced into SHSY5Y and U2OS cells by the Ganley lab (MRC-PPU, Dundee). This fluorescent probe consists of tandem fluorophores (mCherry and GFP) attached to the mitochondrial targeting sequence (MTS) of FIS1 (aa 101 to 152), which targets it to the OMM (**Figure 3.9**) (Allen et al., 2013).

This type of Cherry/RFP and GFP tandem tagged reporters have been widely used to study autophagy flux (when coupled to LC3 or p62/SQSTM1) and were first introduced by Tamotsu Yoshimori and Terje Johansen (Kimura et al., 2007; Pankiv et al., 2007). The GFP fluorescence is quenched in acidic compartments such as lysosomes. Hence, healthy and cytosolic mitochondria appear as both “green” and “red” whilst fragments that are engulfed in autolysosomes appear as “red”-only puncta.

I treated SH-SY5Y mito-QC cells, kindly gifted by the Ganley lab, for 24h with 1 μM Antimycin A and either with 1μM (low) or 10 μM (high) Oligomycin A and then measured the number of mitophagy events occurring in those cells (**Figure 3.10A-C**). The “low AO” (1μM each) condition was sufficient to promote the ubiquitylation of OMM proteins in SH-SY5Y mito-QC cells and thus had the potential to trigger mitophagy (**Figure 3.8**). The “high AO” (1 and 10μM respectively), was optimised by the Ganley lab to specifically observe mitophagy in SH-SY5Y mito-QC cells (Allen et al., 2013). I observed the cells using a 3i spinning disk microscope and sequentially imaged the GFP and mCherry fluorophores (Ex488/Em507 then Ex561/Em610) with either a 60X or 40X oil objective lens (**Figures 3.10A-C and 3.10D respectively**).

I considered that each “red-only” punctum corresponded to a mitolysosome. To obtain a binary image showing only the mitolysosomes, I used the “Image Calculator” plugin on Fiji and subtracted the image obtained with the green laser (Ex488/Em507) from the one taken in the red channel (Ex561/Em610). I then used the threshold tool to obtain a binary image and counted the number of dots per cell using the “Analyze Particles” function in Fiji (**Figure 3.10B**).

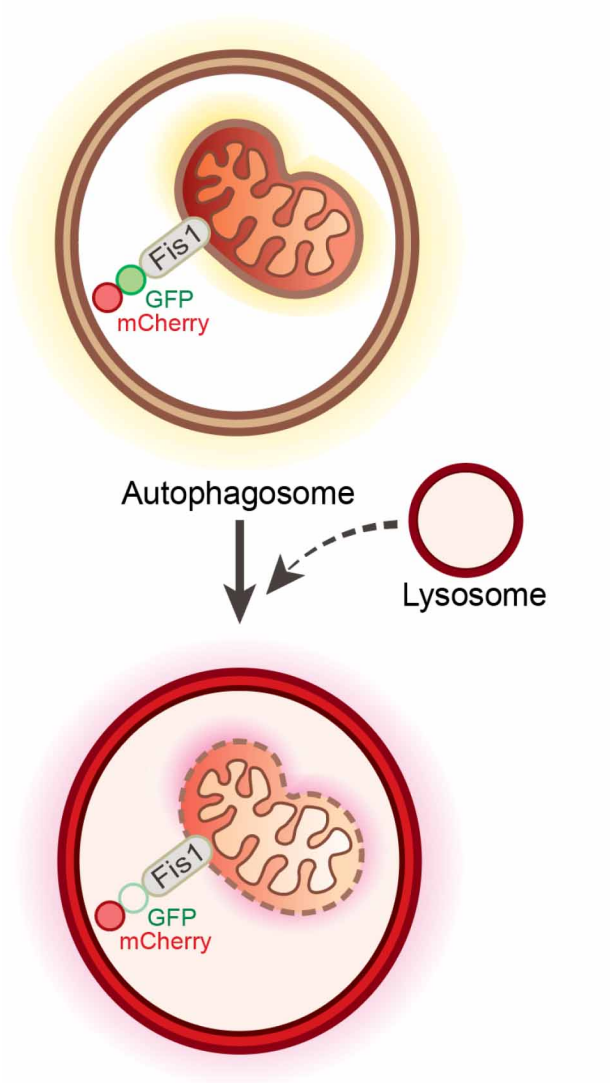

Figure 3.9: Schematic representation of the mCherry-GFP-FIS1$_{101-152}$ mitophagy reporter.

This probe is comprised of a fluorophore tandem, mCherry and GFP, which is tagged to the mitochondrial targeting sequence of FIS1 (residues 101–152), an outer mitochondrial membrane protein. Upon mitophagy, mitochondria fragments are engulfed in autophagosomes which then fuse with lysosomes for their degradation. The resulting mitolysosomes are acidic and thus quench the GFP fluorophore, revealing red only puncta.

I found that “low AO” promoted mitochondrial fragmentation but was insufficient to induce the formation of detectable mitolysosomes within 24h (**Figure 3.10C**). When using the “high AO” treatment, I triggered a clear and significant rise in mitophagy: on average the control DMSO and “low AO” treated cells had 0.8 mitolysosomes per cells against 5 mitolysosomes per cells with “high AO” (**Figure 3.10C-D**). I then used the “high AO” combination as a standard for all of the following imaging experiments.

It is interesting to note that the “basal” (uninduced) mitophagy rate of SH-SY5Y mito-QC cells was strikingly low: they had on average 10-fold less mitolysosomes than U2OS mito-QC cells (Marcassa et al., 2018).

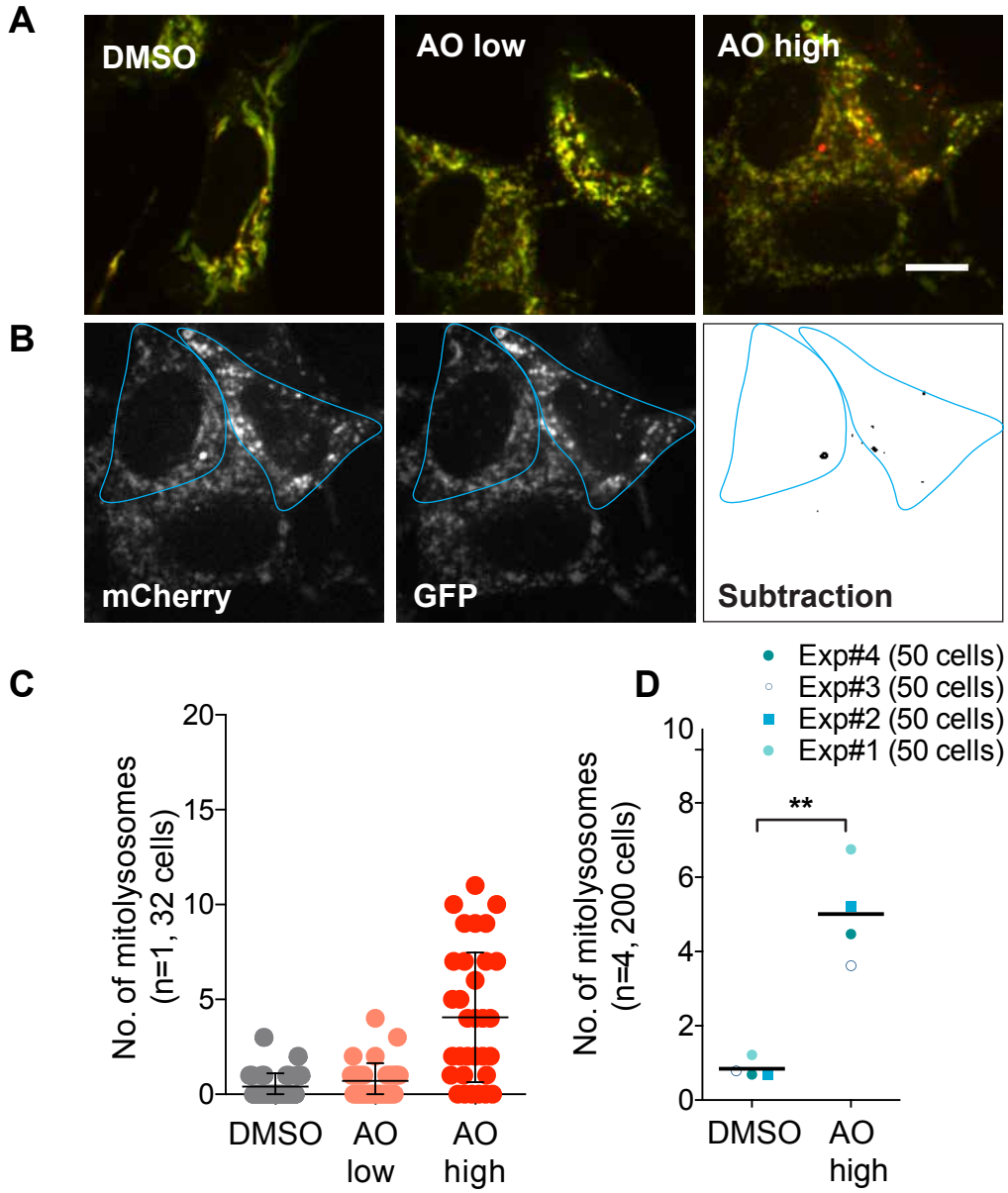

Figure 3.10: Antimycin A and Oligomycin A promote the formation of mitolysosomes in SH-SY5Y mito-QC cells.

A) SH-SY5Y mito-QC cells were treated for 24h with Antimycin A and Oligomycin A at either low dose (AO low; 1µM each) or high dose (AO high; 1µM and 10µM respectively). The cells were imaged by confocal using a 63X objective lens. Scale bar: 10µm. **B)** Panel demonstrating the image analysis method: A ROI is drawn around each cell (in blue). Then using the Image Calculator plugin on Fiji, the green (GFP) channel is subtracted from the red channel (mCherry) to obtain the mCherry-only stained mitolysosomes. The number of mitolysosmes per ROI (cell) is counted using the Analyze Particles function of Fiji. **C)** Graph representing the number of mitolysosomes per cell (spread of data in a single experiment). Error bars: mean ± SD. **D)** SH-SY5Y mito-QC cells were treated with high doses of Antimycin A and Oligomycin A (AO; 1 and 10µM respectively). The images were taken using a 40X confocal objective lens then analysed as in B). Average of four experiments. The statistical significance of the results was assessed using a t-test; ** indicates p-value <0.01, p =0.0053.

Allen and colleagues had previously arbitrarily set a threshold of 3 or more mitolysosomes per cell to determine the number of cells undergoing mitophagy (Allen et al., 2013). I used this as an alternative approach to quantitate mitophagy. After processing all the images in the same manner, I manually counted SH-SY5Y mito-QC cells that had 3 or more “red”-only punctate (**Figure 3.11**). This quantitation process was faster and enabled me to quantify a greater number of cells. Using this technique, I found that 24h AO induced mitophagy in 27% of SH-SY5Y mito-QC cells (**Figure 3.11B**). Those results were in good agreement with the Ganley lab, which report an induction of mitophagy in 33% of SH-SY5Y mito-QC cells with 24h AO. I also tested the efficiency of Deferiprone (DFP), an iron chelator, to promote mitophagy in this cell line (**Figure 3.11A-B**). Indeed, Ganley and colleagues have shown that DFP promotes mitolysosome formation in SH-SY5Y mito-QC cells independently of PINK1 stabilisation or Parkin activity, with 42% of cells having more than 3 mitolysosomes (Allen et al., 2013). In my hands, 1mM DFP was twice as potent as AO: promoting mitophagy in 61% of SH-SY5Y mito-QC cells following a 24h treatment (**Figure 3.11B)**.

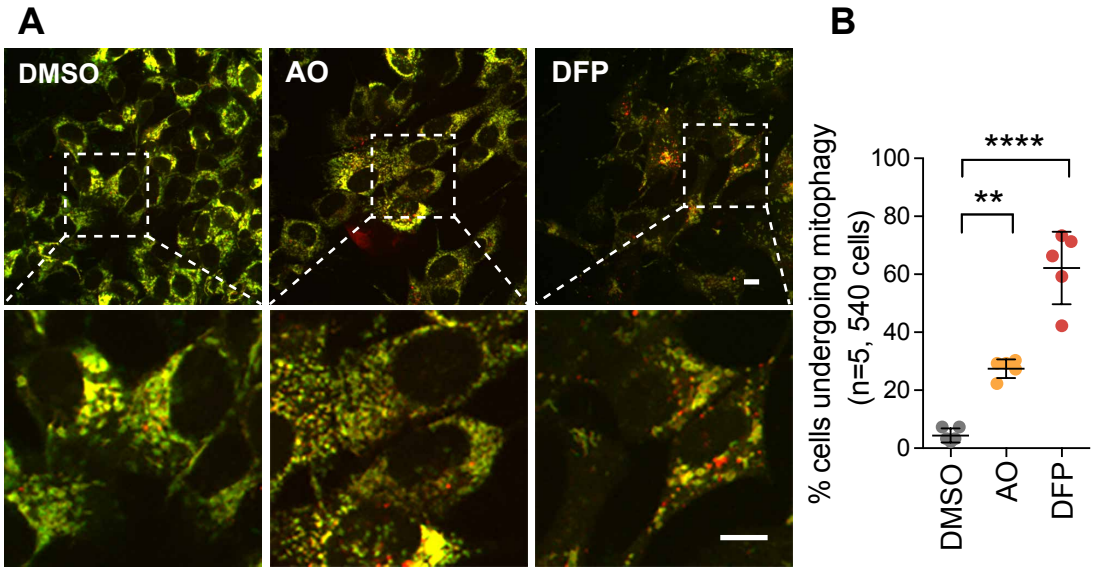

Figure 3.11: Deferiprone induces mitophagy in SH-SY5Y mito-QC cells.

A) SH-SY5Y mito-QC cells were treated with Antimycin A and Oligomycin A (AO; 1 and 10μM respectively) or Deferiprone (DFP; 1mM) for 24h. Mitophagy was measured by live cell imaging using a confocal microscope. Scale bar: 10 μm. **B)** Manual quantitation: all images were leveled identically then merged. The cells undergoing mitophagy (= cells with more than 3 mitolysosomes) were then counted and expressed as a percentage of total cell number. Shown is the average of 5 experiments. Error bars: mean ± SD. Statistical analysis was performed using the one-way ANOVA test. (** $p<0.01$; **** $p<0.0001$).

3.4 Exploring novel mitophagy triggers

As I was interested in expanding the current knowledge on depolarisation-dependent and independent means of inducing mitophagy in SH-SY5Y cells, I performed a mini-compound screen using both imaging and western blotting. I chose drugs that had previously been shown to target mitochondrial proteins or mitophagy. I selected Gamitrinib-triphenylphosphonium (G-TPP), 2-cyano-3,12-dioxoolean-1,9-dien-28-oic acid Methyl Ester (CDDO-Me), Ivermectin (IVM) and Doxorubicin (DOX).

G-TPP, a derivative of Geldanamycin, is an HSP90 inhibitor that is exclusively targeted to mitochondria via its TPP moiety (Siegelin et al., 2011). Through the inhibition of the chaperone, G-TPP induces the accumulation of misfolded protein and activates the mitochondrial Unfolded Protein Response (UPR). In HeLa over-expressing Parkin, G-TPP has been reported to promote PINK1 stabilisation and the subsequent recruitment of Parkin to trigger the mitophagy cascade (Fiesel et al., 2017). G-TPP has also been shown to promote PINK1 and pS65-ubiquitin accumulation in both human primary fibroblasts and in iNeurons (Fiesel et al., 2017).

CDDO-Me is a Lon protease inhibitor (Bernstein et al., 2012). Lon is a mitochondrial matrix protease essential for mitochondrial quality control. It mediates the proteolysis of oxidised proteins and can selectively degrade key proteins during stress conditions (for example during respiratory chain remodelling). It also serves as a mitochondrial chaperone and can directly bind mitochondrial DNA to regulate its maintenance (Pinti et al., 2016). The Cossarizza lab found that in RKO cells, CDDO-Me impairs the mitochondrial network structure and promotes mitochondrial depolarisation, mitochondrial ROS production, degradation of mitochondrial proteins (MFN2, DNM1L, TOMM20) and apoptosis. Interestingly, below 1μM, apoptosis is not induced but there still remains a trend towards reduction of MFN2 and TOMM20 levels (Gibellini et al., 2015). In a similar fashion to G-TPP, CDDO-Me could potentially induce mitophagy by interfering with protein degradation and folding.

IVM is an antiparasitic drug that has been reported to have anti-cancer properties (Zhu et al., 2017). Mechanistically, IVM is thought to target mitochondrial respiration and to decrease the mitochondrial membrane potential. This promotes the generation of reactive oxygens species and mitochondrial fragmentation (Zachari et al., 2019; Zhu et al., 2017). Employing microscopy, Ktistakis's group have discovered that IVM promotes the accumulation of ubiquitin structures and autophagosomes around mitochondria in HEK293T and MEF cells. They reported that this pathway involves members of the canonical autophagic machinery (FIP200, ATG13, ULK1/2, NDP52) and is accompanied by a reduction in TOMM20 and MFN2 levels after 3h of IVM treatment (Zachari et al., 2019).

Finally, DOX is a potent chemotherapeutic drug affecting a broad spectrum of malignancies. DOX can mediate cell death through DNA intercalation and Topoisomerase II arrest. Through its quinone structure, DOX has also the ability to produce ROS and subsequent DNA damage [review: (Yang et al., 2014)]. One of the main downfalls of DOX is that it promotes cardiotoxicity. A body of work suggest that cardiotoxicity is linked to a deregulation of autophagy or mitophagy.
The individual studies disagree with each other: some report that DOX induces the accumulation of both autophagosomes as well as accumulation of PINK1 and Parkin at mitochondria in rat and human cardiomyocytes, respectively (Kobayashi et al., 2010; Yin et al., 2018). In contrast others demonstrate, that in mouse heart DOX inhibits the recruitment of Parkin to mitochondria and reduces the engulfment of mitochondria into autophagosomes in a p53-dependent manner (Hoshino et al., 2013).

3.4.1 Preliminary screen in hTERT-RPE1-YFP-Parkin cells

I first performed a mini-imaging screen in hTERT-RPE1-YFP-Parkin cells (**Figure 3.12**). In this screen, I treated the cells for 1h and 6h with IVM (20μM), DOX (62.5nM and 250nM), CDDO-Me (100nM), and G-TPP (10μM). I used AO (1 and 10μM respectively) and DFP (1mM) as positive controls for the induction of the PINK1/Parkin canonical pathway and non-canonical mitophagy pathways. I first focussed on Parkin recruitment to mitochondria and classified the mitochondrial Parkin phenotype into two categories: puncta and aggregates (**as in Figure 3.3C**).

The only condition that showed translocation of Parkin to mitochondria after only one hour of treatment was the AO treatment, with 81% of cells having mitochondrial Parkin puncta (**Figure 3.12A-B**). After 6h, all AO-induced cells had Parkin aggregates (**Figure 3.12C**). At this time point, G-TPP induced near complete translocation of Parkin to mitochondria: 74% of cells had Parkin aggregates and 12% of cells had Parkin puncta. In the case of Ivermectin, 60% of cells had Parkin puncta and the mitochondrial network appeared fragmented.
Consistent with the fact that DFP was reported to induce mitophagy independently on PINK1 and Parkin, I did not observe any effect of DFP on the cellular localisation of Parkin in hTERT-RPE1-YFP-Parkin cells (Allen et al., 2013). Similarly, CDDO-Me and DOX did not promote the relocalisation of Parkin.

G-TPP and Ivermectin emerged as interesting candidates to induce Parkin recruitment in cell models that overexpress Parkin. I therefore went on to assess their ability to induce mitophagy in a model expressing endogenous Parkin.

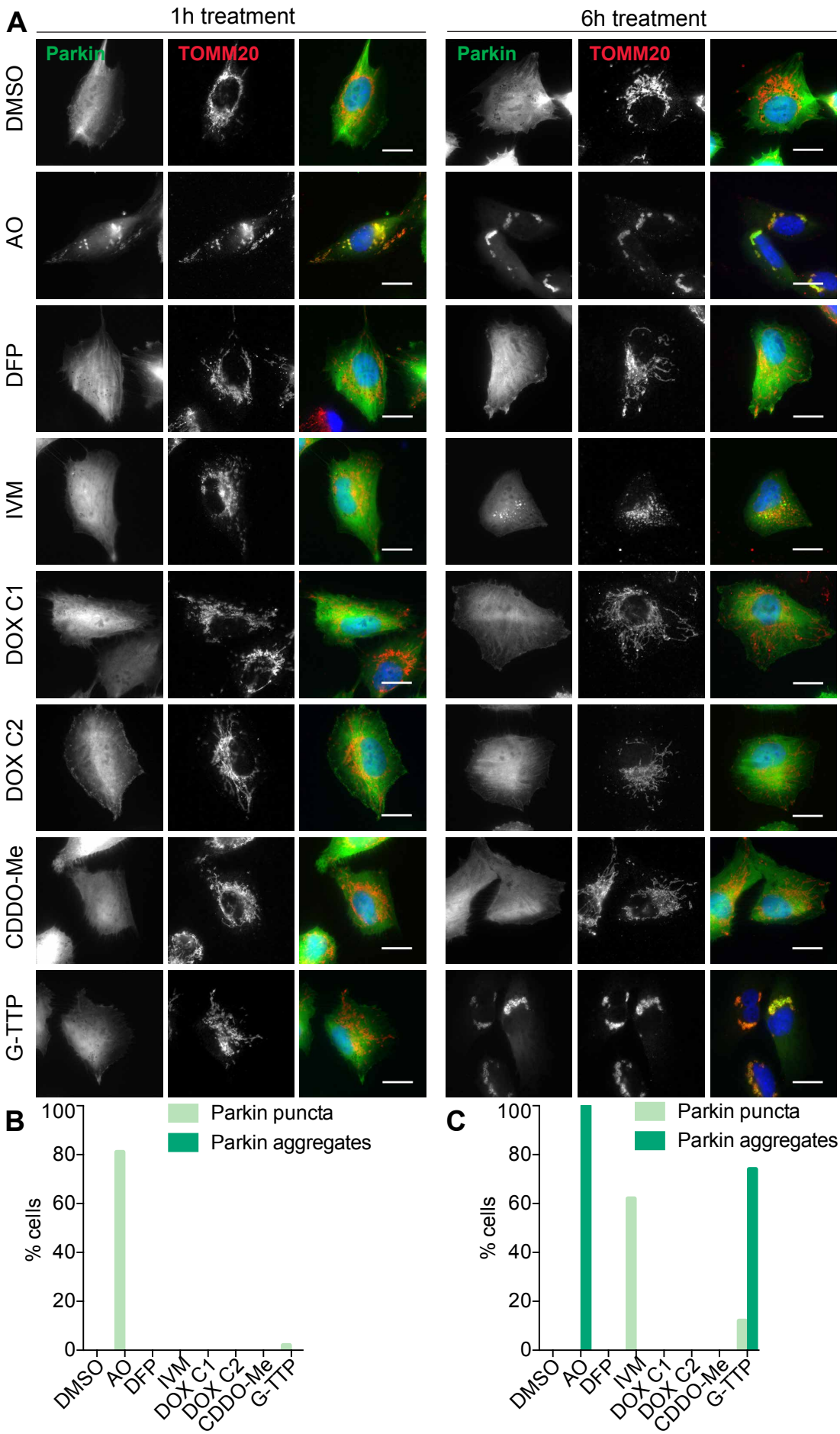
A
1h treatment
6h treatment
Parkin
TOMM20
DMSO
AO
DFP
IVM
DOX C1
DOX C2
CDDO-Me
G-TTP
B
C
Parkin puncta
Parkin aggregates
% cells
100
80
60
40
20
0
DMSO
AO
DFP
IVM
DOX C1
DOX C2
CDDO-Me
G-TTP

Figure 3.12: Mini-imaging screen for alternative mitophagy inducers in hTERT-RPE1-YFP-Parkin cells.

A) hTERT-RPE1-YFP-Parkin cells were treated for both 1 and 6h with Antimycin A and Oligomycin A (AO; 1 and 10μM respectively), Deferiprone (DFP; 1mM), Ivermectin (IVM; 20μM), Doxorubicin (DOX; C1: 62.5nM, C2: 250nM), CDDO Methyl Ester (CDDO-Me; 100nM) or Gamitrinibtriphenylphosphonium (G-TPP; 10μM). The cells were then fixed with PFA, permeabilised and stained with a TOMM20 antibody. The coverslips were finally mounted with mowiol containing DAPI. Scale bar: 10μm. **B and C)** Quantification of the percentage of cells presenting either Parkin puncta or Parkin aggregates on mitochondria. Data from a single experiment (50 cells analysed). **B)** 1h treatment. **C)** 6h treatment.

3.4.2 Mini-screen in SH-SY5Y mito-QC cells

I treated SH-SY5Y mito-QC cells for 24h with AO (1 and 10μM each), DOX (250nM), CDDO-Me (1μM) and G-TPP (10μM) and imaged the cells by live microscopy (**Figure 3.13A-B**). AO induced mitophagy in 33% percent of cells compared to the 2% basal mitophagy levels (> 3 mitolysosomes per cell). Interestingly, whilst DOX and CDDO-Me did not trigger Parkin accumulation in hTERT-RPE1-YFP-Parkin cells, these compounds did stimulate mitophagy in SH-SY5Y mito-QC cells: 21% of DOX and 53% of CDDO-Me treated SH-SY5Y mito-QC cells had more than 3 mitolysosomes. Contrary to my observations in hTERT-RPE1-YFP-Parkin cells, G-TPP promoted little or no increase in mitophagy: 6% of G-TPP against 2% of DMSO treated cells were undergoing mitophagy following the 24h treatment.

In parallel I immunoblotted a duplicate set of cells and assessed the levels of mitochondrial depolarisation (OPA1 cleavage), apoptosis induction (PARP cleavage), PINK1 accumulation, Parkin modification and mitochondrial ubiquitylation (MFN2, FIS1, TOMM20, and pS65-Ubiquitylation) (**Figure 3.13C-D**).

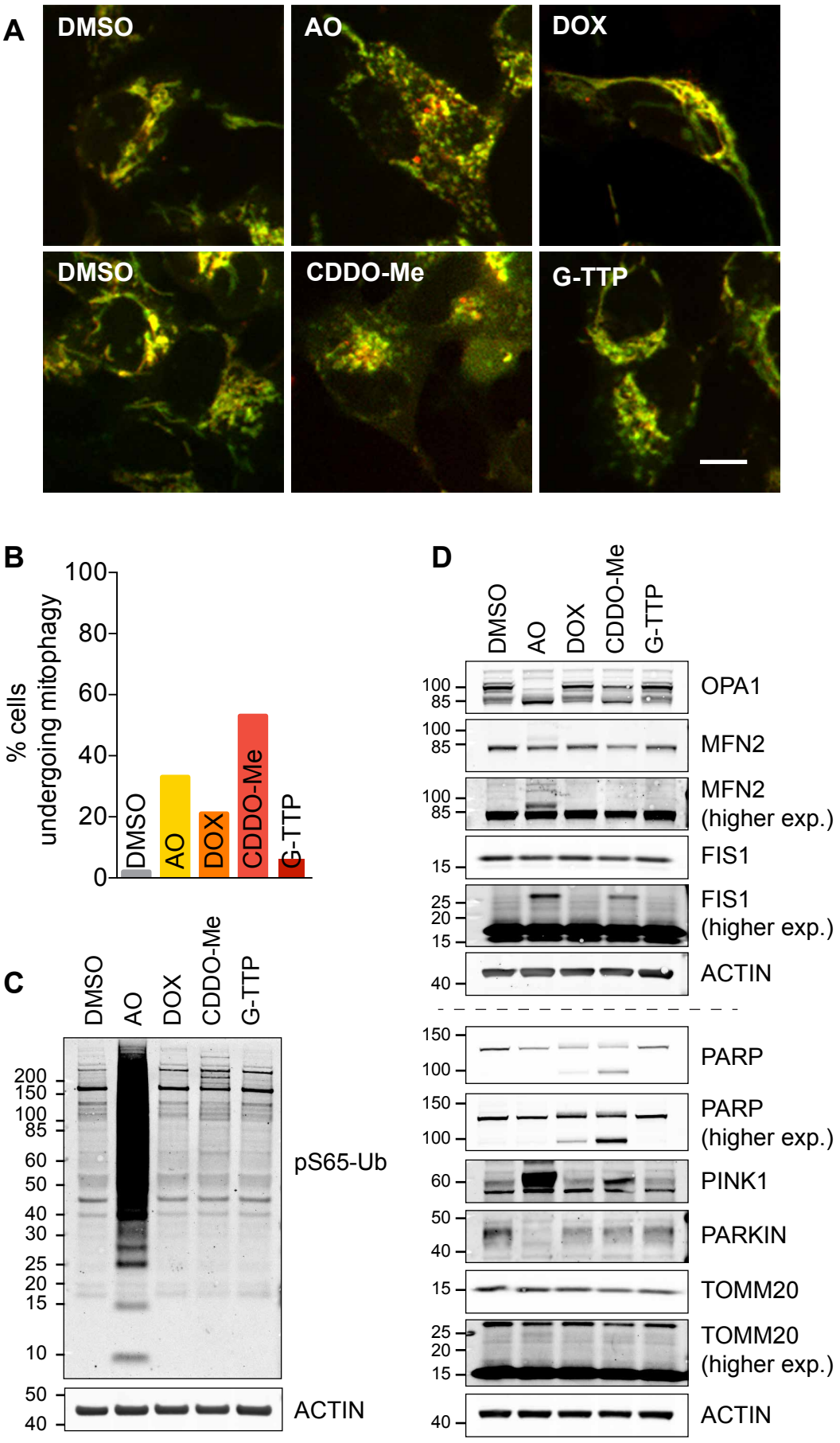
A
DMSO
AO
DOX
DMSO
CDDO-Me
G-TTP
B
% cells undergoing mitophagy
100
80
60
40
20
0
DMSO
AO
DOX
CDDO-Me
G-TTP
C
DMSO
AO
DOX
CDDO-Me
G-TTP
200
150
100
85
60
50
40
30
25
20
15
10
pS65-Ub
50
40
ACTIN
D
DMSO
AO
DOX
CDDO-Me
G-TTP
OPA1
MFN2
MFN2 (higher exp.)
FIS1
FIS1 (higher exp.)
ACTIN
PARP
PARP (higher exp.)
PINK1
PARKIN
TOMM20
TOMM20 (higher exp.)
ACTIN

Figure 3.13: Imaging and western blotting mini-screen for alternative mitophagy triggers in SH-SY5Y mito-QC cells.

A) SH-SY5Y mito-QC cells were treated for 24 with Antimycin A and Oligomycin A (AO; 1 and 10μM each), Doxorubicin (DOX; 250nM), CDDO Methyl Ester (CDDO-Me; 1μM) or Gamitrinib-triphenylphosphonium (G-TPP; 10μM) then imaged by live cell imaging. Scale bar: 10μm. **B)** Manual quantification of the percentage of cells undergoing mitophagy (= cells with more than 3 mitolysosomes). Data from a single experiment (100 cells analysed). **C and D)** SH-SY5Y MGFIS cells were treated as in A and harvested in NP40 lysis buffer. The lysates were immunoblotted as indicated in the figure.

I probed for a marker of apoptosis firstly to verify if the drugs were toxic in SH-SY5Y cells and secondly because it has been reported that Parkin sensitises cell to apoptosis following depolarisation in Parkin overexpressing cells. Parkin is thought to trigger apoptosis through the direct ubiquitylation and degradation of MCL1 or by a ubiquitylation and proteasomal degradation of OMM proteins leading to the rupture of the OMM (Yoshii et al., 2011; Carroll et al., 2014; Liang et al., 2015). In SH-SY5Y cells expressing endogenous Parkin, AO did not promote PARP cleavage. As expected, treating those cells with AO for 24h triggered depolarisation, as seen by the accumulation of S-OPA1, and promoted the accumulation of PINK1, phosphorylation of ubiquitin on Ser65 and ubiquitylation of OMM proteins (MFN2, FIS1). Interestingly, Parkin itself was depleted after 24h of depolarisations, presumably along with the mitochondria it was recruited to.

Similar to induction of mitophagy with OA, CCDO-Me treatment induced OPA1 cleavage, albeit to a lesser extent, and thus mitochondrial depolarisation, PINK1 accumulation and FIS1 ubiquitylation. Interestingly in contrast to AO, CDDO-Me did not induce ubiquitylation of MFN2. The levels of pS65-Ub were also slightly elevated with CDDO-Me and could result from the stabilisation of a small amount of PINK1. In RKO cells, 1μM CDDO-Me was shown to promotes Caspase 9 cleavage and apoptosis (Gibellini et al., 2015). I confirmed in SH-SY5Y cells where I observed the cleavage of PARP.

I also observed a small induction of PARP cleavage with DOX but did not measure any changes in accumulation of PINK1 or protein ubiquitylation or turnover in SH-SY5Y cells. Likewise, G-TPP treatment neither triggered PINK1 accumulation nor promoted ubiquitylation of outer mitochondrial membrane proteins.

In hTERT-RPE1-YFP-Parkin cells, the induction of Parkin recruitment to mitochondria by G-TPP had appeared delayed in comparison with AO (**Figure 3.12**). I thus wondered if the ubiquitylation of OMM proteins and subsequent autophagic engulfment of mitochondria was also delayed. I thus treated SH-SY5Y mito-QC cells for 48h with 10μM G-TPP but did not observe any increase in the percentage of cells undergoing mitophagy compared to the DMSO condition (**Figure 3.14A-B**).
Likewise, also treating the cells with higher doses (15 and 20 μM) G-TPP for either 24 or 48h did not result in the appearance of ubiquitylated species of MFN2 and FIS1 nor did I measure the generation of pS65-Ub (**Figure 3.14C-D**). I used AO as a positive control and found that after 48h of treatment, an even greater amount of PINK1 is stabilised than after 24h, whilst MFN2 and FIS1 are still equally ubiquitylated and the pS65-Ub signal remains stable.

In contrast to G-TPP, IVM, used at 5 and 10 μM, promoted mitophagy in 27% and 59% of SH-SY5Y mito-QC cells respectively (**Figure 3.15A-B**). IVM-induced mitophagy was also accompanied by the ubiquitylation of FIS1 and the generation of phospho-ubiquitin (**Figure 3.15C).** The western blot analysis also suggested the involvement of Parkin in Ivermectin-mediated mitophagy as the Parkin pool was diminished by more than 50% after 24h of IVM treatment. Intriguingly, I did not measure any increase in full length PINK1 at this time point, whilst I did observe pS65-Ub accumulation. PINK1 could possibly be engaged at early stages of IVM-induced mitophagy and then get degraded. This experiment should be repeated and a positive control for PINK1 accumulation included, such as AO treated samples. PINK1 knockdown experiments and IVM time courses would also help shed light on this observation.

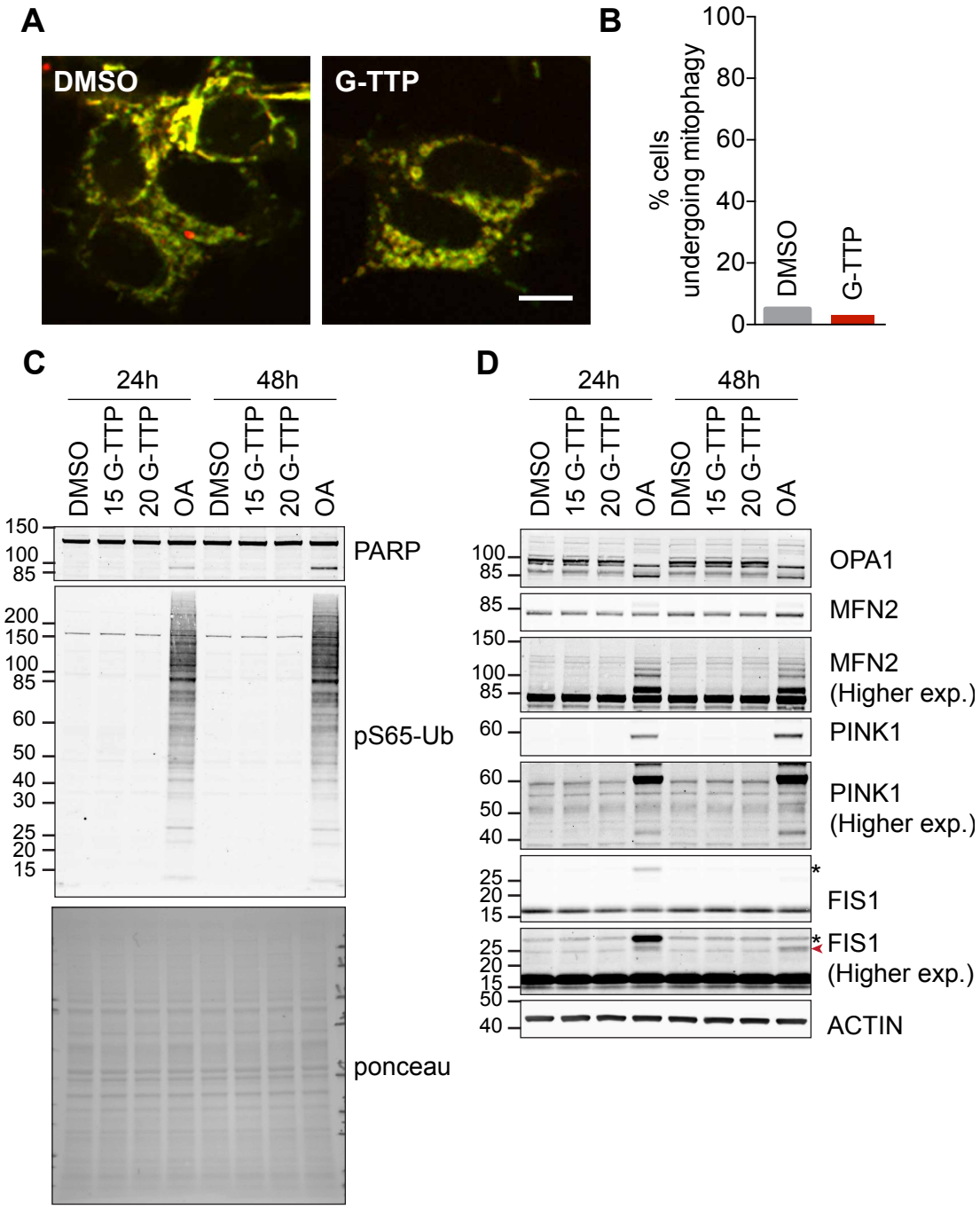

Figure 3.14: Gamitrinib-TPP does not trigger mitophagy in SH-SY5Y mito-QC cells.

A) SH-SY5Y mito-QC cells were treated for 48h with 10μM Gamitrinib-TPP (G-TTP). Mitophagy was assessed by live imaging. Scale bar: 10μm. **B)** Manual quantification of cells undergoing mitophagy (= cells with more than 3 mitolysosomes). Data from a single experiment (100 cells analysed). **C and D)** SH-SY5Y mito-QC cells were treated for both 24h and 48h with either G-TTP (15 and 20μM) or with Antimycin A and Oligomycin A (AO; 1μM each). AO was used as a positive control of mitophagy. The samples were lysed using NP40 lysis buffer and probed as annotated. Red arrow: FIS1 ubiquitylated species. Asterisk: Probable unspecific band that runs slightly

higher than the predicted molecular weight of ubiquitylated FIS1. Higher exp. = Higher exposure.

IVM did not appear to induce OPA1 cleavage suggesting that it may not trigger potent mitochondrial depolarisation, contrary to what has been reported in RCC cells: in RCC cells 5μM IVM is sufficient to significantly decrease the mitochondrial membrane potential and with 15μM the membrane potential was decreased by ~3 fold (Zhu et al., 2017). Ktistakis' group reported that 1 and 10μM ivermectin significantly inhibited mitochondrial oxygen consumption rate of HEK293 cells by 20 and 30% respectively within 25min compared to 60% inhibition with 1μM oligomycin (Zachari et al., 2019).

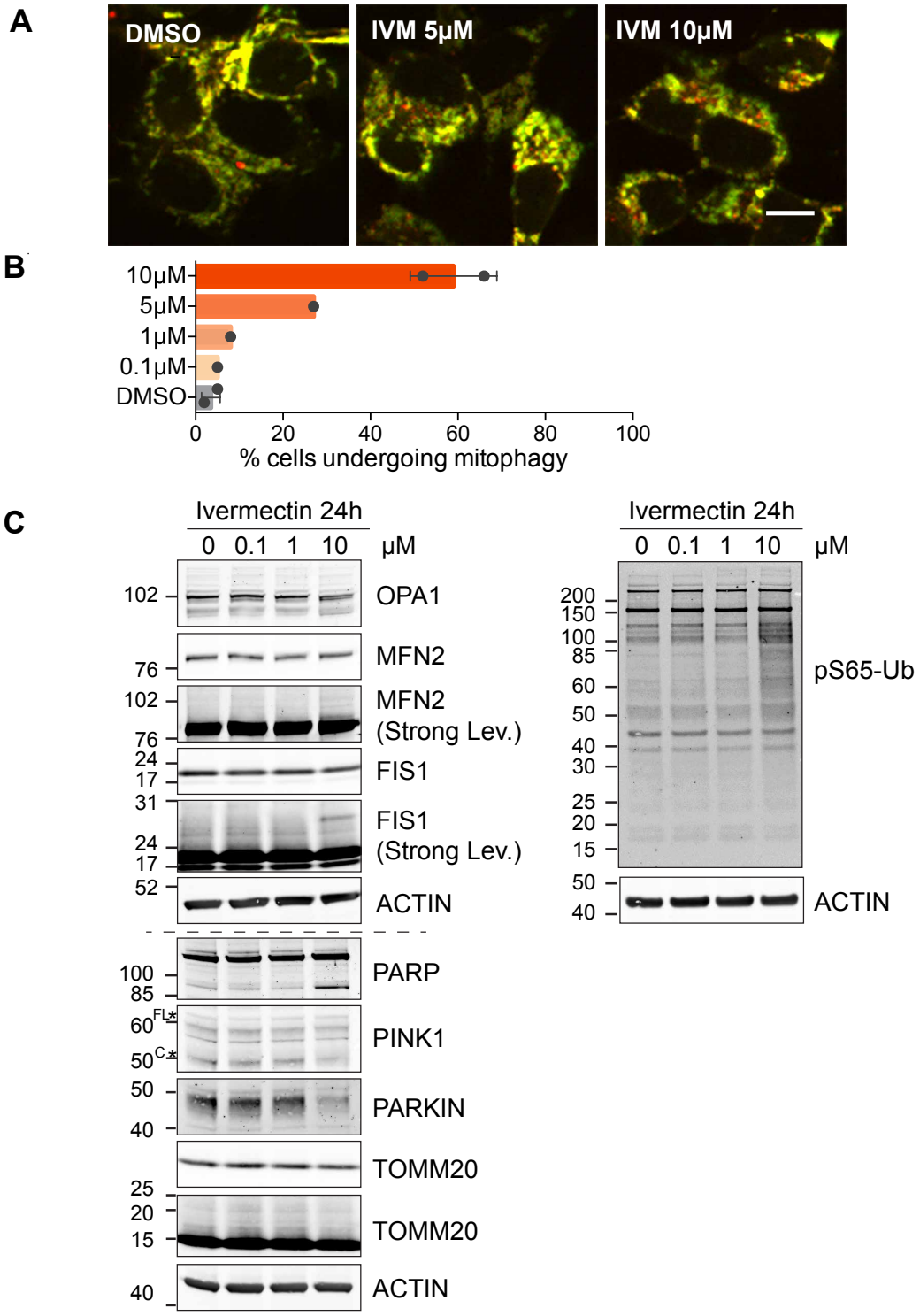

Figure 3.15: Ivermectin induces mitophagy in SH-SY5Y mito-QC cells.

A) SH-SY5Y mito-QC cells were treated with Ivermectin (IVM, 0, 5 or 10μM) for 24h. Mitophagy was measure by live microscopy. Scale bar: 10μm. **B)** Exp#1 cells were treated for 24h with 0, 0.1, 1, 10μM IVM (100 cells analysed). Exp#2 cells were treated for 24h with 0, 5 or 10μM IVM (100 cells analysed). The images were manually quantified (cells undergoing mitophagy = cells with more than 3 mitolysosomes). Error bars: mean ± SD. **C)** SH-SY5Y mito-QC cells treated for 24h with ivermectin (0, 0.1, 1, 10μM) were lysed in NP40 and immunoblotted as depicted.

3.5 Discussion:

3.5.1 Magnifying and amplifying the PINK1/Parkin pathway to reveal core mitophagy regulators.

Using the hTERT-RPE1-YFP-Parkin cells, I found that similar to CCCP, AO triggers mitochondrial fragmentation, mitochondrial depolarisation, accumulation of full-length PINK1 and Parkin recruitment to mitochondria. This was accompanied by the ubiquitylation of OMM proteins such as TOMM20 and their degradation as seen with MFN2.
In these cells, Parkin translocation was highly dependent on the degree of mitochondrial depolarisation. Employing 1μM of AO was sufficient to activate the depolarisation-induced cleavage of OPA1 and efficiently recruit Parkin to mitochondria after only 1h of treatment. However, although Parkin's recruitment relies on preceding ubiquitylation of the OMM that serves as a substrate for PINK1, knocking down the mitochondrial deubiquitylase USP30 did not increase or accelerate Parkin translocation in hTERT-RPE1-YFP-Parkin cells. This suggests that USP30 does not prevent mitophagy by globally removing ubiquitin or pS65-Ub moieties necessary for Parkin recruitment. However, in the YFP-Parkin-hTERT-RPE1 system, the number of USP30 molecule per SH-SY5Y cell is most likely too low to limit the feedforward loop and prevent Parkin recruitment. This could be assessed by monitoring endogenous Parkin or by employing cells overexpressing catalytically inactive Parkin in which the feedforward loop would not be engaged.

In contrast to my observations, overexpressing USP30 in HeLa overexpressing Parkin cells delayed Parkin's recruitment to mitochondria (Geisler et al., 2019; Wang et al., 2015). A genome wide siRNA screen performed in HeLa overexpressing Parkin, specifically assessing modulators of Parkin recruitment, found that Parkin recruitment to mitochondria was enhanced by the knockdown of proteins such as BAG4 or SIAH3 (Hasson et al., 2013). But, congruent with my results and other screens, USP30 knockdown did not affect Parkin translocation following CCCP treatment (Geisler et al., 2019; Hasson et al., 2013). The USP30-dependent regulation

of Parkin recruitment might be concentration dependent. In excess, USP30 appears to have the potential to remove ubiquitin prior to PINK1 phosphorylation and therefore limits Parkin's recruitment. However, our data suggest that the endogenous expression levels of USP30 are too low to efficiently oppose Parkin. This is in agreement with mass spectrometry experiments reporting that USP30 is a low abundance protein (Kulak et al., 2014; Nagaraj et al., 2011; Schwanhäusser et al., 2011).

Other DUBs have been proposed to regulate Parkin recruitment. USP33, originally characterised as an ER and Golgi localising DUB, was recently shown to also localise at mitochondria (Niu et al., 2019; Thorne et al., 2011). It was reported that overexpressed USP33-GFP overlaps with TOMM20 by immunofluorescence in HEK293 cells. The overexpressed protein was also found in mitochondrial fractions following mitochondria enrichment assays (Niu et al., 2019). Using Parkin truncation mutants, Niu and colleagues next showed that overexpressed USP33 binds to full length Parkin, to Parkin's UBL domain and to its RING2 domain (Niu et al., 2019). They further demonstrated that knocking down USP33 accelerates the recruitment of Parkin to mitochondria (TOMM20 staining) in U2OS cells overexpressing GFP-Parkin treated with 20μM CCCP. Concomitantly, they observed an increase in ubiquitylated species of Parkin and suggested that USP33 destabilises Parkin through deubiquitylation (Niu et al., 2019).

Other members of the USP family, instead positively regulate Parkin translocation. USP8 has been reported to remove inhibitory K6-Ubiquitin chains from Parkin and thus oppose Parkin's self-ubiquitylation to accelerate mitophagy (Durcan et al., 2014). An siRNA screen for DUBs regulating Parkin recruitment to mitochondria in HeLa over expressing Parkin cells, revealed that the nucleolus localised DUB, USP36, facilitates the recruitment of Parkin possibly through transcriptional regulation (Geisler et al., 2019).

DUBs, such as short-USP35 isoform that is most likely catalytically inactive (missing the catalytic cysteine present in full length USP35) and USP15 that is cytosolic, were reported instead to oppose Parkin ubiquitylation of OMM

proteins (Cornelissen et al., 2014; Wang et al., 2015). However, USP30 is so far the only active DUB constitutively localising at mitochondria (Urbé et al., 2012; Marcassa et al., 2018).

Whilst my experiments did not reveal a role for USP30 in Parkin recruitment, I did observe that USP30 opposed Parkin ubiquitylation of OMM proteins. In hTERT-RPE1-YFP-Parkin cells, USP30 depletion specifically enhanced TOMM20 ubiquitylation as previously reported by Amos (Liang et al., 2015). By western blotting, I did not observe the enhancement of ubiquitylated species of other OMM proteins (TOMM22, MIRO1 or MFN2). Mass spectrometry experiments performed in HEK293 cells overexpressing Parkin and USP30 or depleted of USP30 revealed that other Parkin substrates of such as GDAP1, VDAC1, VDAC2 and VDAC3 were deubiquitylated by USP30 (Bingol et al., 2014; Cunningham et al., 2015). Likewise, I also observed these additional ubiquitylation events by mass spectrometry using SH-SY5Y USP30 knockout cells. This is further detailed in Chapter V.

3.5.2 The mitophagy probes: Catching spontaneous mitophagy events.

To study mitophagy *in vivo*, multiple research groups have generated pH sensitive reporters (Table 3.1). Rosella and mito-QC are two reporters that contain a tandem fluorophore and are based on the same principle: GFP gets quenched in the acidic environment of the lysosome thus revealing the mitochondrial fragments that are engulfed in autophagolysosomes (Rosado et al., 2008; Allen et al., 2013).
Mt-Keima is a dual-excitation fluorophore: at mitochondrial pH (pH8), Keima is favourably exited by 445nm lasers but when the pH decreases, its excitation shifts towards a peak of 561nm. As for the above reporters, this allows for the discrimination between healthy mitochondria (pH8) and mitolysosomes (pH4) (Katayama et al., 2011). Both mito-QC and Mt-Keima have been used to generate animal models of mitophagy enabling mitophagy to be observed *in vivo:* Whitworth's group and our lab have generated *Drosophila* models whilst Ganley and Finkel's labs have produced mice models (Lee et al., 2018; McWilliams et al., 2018; Sun et al., 2015). The fly models will be further

detailed in Chapter VI, where I will present the generation and characterisation of the mt-Keima fly. One of the key differences between the mito-QC and mt-Keima reporters lies in their targeting: mito-QC is targeted to the OMM via FIS1's MTS whilst mt-Keima is targeted to the Matrix by COX VIII's MTS. Thus, the use of the mito-QC probe could be limited by the proteasomal degradation of OMM proteins during mitophagy. However, unlike mito-QC, mt-Keima is incompatible with fixation and is therefore restricted to live imaging (Allen et al., 2013; McWilliams et al., 2016).

Table 3.1: Commonly used dyes and probes to monitor mitophagy

Probe/ dye	Technique	Reference
mitoQC	mCherry-GFP-FIS1$_{101-152}$ GFP is quenched in acidic pH Targeting sequence: FIS1$_{101-152}$ (OMM)	(Allen et al., 2013)
Mt-Keima	pH dependent shift in excitation of Keima Targeting sequence: MTS of COX VIII (Matrix)	(Katayama et al., 2011)
MitoTimer	Time dependent shift in emission of DsRed1-E5 Targeting sequence: MTS of COX VIII (Matrix)	(Hernandez et al., 2013)
Rosella	DsRed-GFP GFP quenching in acidic pH Targeting sequence: MTS of Citrate Synthase (Matrix)	(Rosado et al., 2008)
Mtphagy Dye	Increased emission and excitation with pH acidification Fluorescent moiety: perylene-3,4-dicarboximide Fluorescence quencher: piperazine group Targeting moiety: triphenylphosphonium (TPP)	(Iwashita et al., 2017; Zielonka et al., 2017)

The Mtphagy Dye is a pH-sensitive small molecule that is directed to mitochondria by its TPP moiety. It contains the fluorescent dye perylene-3,4-dicarboximide that is constantly quenched at neutral pH by another moiety, the piperazine group. Once in acidic compartments, such as lysosomes, Mtphagy's piperazine group gets protonated, thus cancelling its quenching effect and liberating Mtphagy's fluorescence (Iwashita et al., 2017). Mtphagy gives an indication on mitophagy by highly fluorescing in mitolysosomes. To

assess the relative number of mitolysomes with respect to the total mitochondrial mass, Mtphagy can be used in combination with mitochondrial dyes such a MitoTracker. However, this technique is limited as most mitochondrial stains rely on the mitochondrial membrane potential to localise to the mitochondria (Padman et al., 2013).

Finally, MitoTimer is a probe that uses the time depend-shift of emission of DsRed1-E5 also called Fluorescent Timer (Terskikh et al., 2000). It was originally created to follow the biogenesis, ageing and turnover of mitochondria (Hernandez et al., 2013). Unlike the previously discussed reporters, MitoTimer is not pH sensitive but sensitive to oxygen and temperature, thus the emission wavelength of Timer shifts linearly from green to red with time and can be used as a “fluorescent clock” (Terskikh et al., 2000). When tagged to mitochondria, Timer gives indications of mitochondrial turnover, biogenesis and enables the discrimination of “young” and “old” mitochondria (Hernandez et al., 2013).
The Yan lab proposed that mitochondrial ROS can oxidise MitoTimer and trigger a radical shift of emission that creates red only puncta for damaged mitochondria (Laker et al., 2014). In *Drosophila* and mice models of MitoTimer, those red puncta have been shown to colocalise partially with mitochondria, LC3 and LAMP1 therefore suggesting that these are mitolysosomes (Laker et al., 2014, 2017; Stotland and Gottlieb, 2016). Thus, Laker and colleagues suggested the use the MitoTimer as a reporter of mitophagy. However, more studies have to be conducted to use this probe as such. Indeed, Hernandez and colleagues, reported that MitoTimer is denatured at pH 4.5 and loses its fluorescence (Hernandez et al., 2013). Hence it would not be possible to track mitochondrial delivery to lysosomes. It is instead recommended to measure the loss of red fluorescence as a readout of lysosomal degradation of mitochondria rather than counting the number of red puncta.

All of the aforementioned assays are endpoint assays. They thus only report on lysosomal degradation of mitochondrial content and not on the progress of mitophagy itself.
I chose to use the mito-QC reporter to follow mitophagy in the SH-SY5Y cells. The read-out is clear and a stable SH-SY5Y mito-QC cell line had already been

generated and was generously provided by the Ganley lab (Allen et al., 2013). Moreover, the mCherry and GFP fluorescence are compatible with the lasers on most microscopes.

3.5.3 Moving away from Oxidative phosphorylation uncouplers?

Using the hTERT-RPE1-YFP-Parkin and SH-SY5Y mito-QC cell lines, I selected few potential mitophagy triggers: DOX, CDDO-Me, IVM and G-TTP. IVM and CDDO-Me induced mitochondrial ubiquitylation and mitophagy in SH-SY5Y mito-QC and DOX promoted mitophagy without FIS1 and MFN2 ubiquitylation.

IVM was one of the most potent triggers of mitophagy in both screens: 20μM IVM promoted the recruitment of Parkin to mitochondria in 60% cells within 6h in hTERT-RPE1-YFP-Parkin cells and a 24h treatment with 5μM was sufficient to promote mitophagy in 27% of SH-SY5Y mito-QC cells. Using 10μM IVM for 24h I also detected ubiquitylated species of FIS1 and accumulation of pS65-Ub but also PARP cleavage.
Ktistakis's lab, had suggested that Ivermectin induced mitophagy was independent on Parkin. They compared CCCP and IVM and found that unlike CCCP, treating cells with 15μM IVM for 90 min did not trigger Parkin recruitment to mitochondria in HEK293 cells expressing mCherry-Parkin. Although Parkin was not present at mitochondria after 90min, they observed by microscopy the recruitment of the autophagic machinery to mitochondria: LC3, WIPI2, ATG13, NDP52, OPTN, p-TBK1 and ubiquitin formed aggregates around TOMM20 puncta in both HEK293 and MEF cells. After 2h of IVM treatment, they observed the degradation of TOMM20 by western blot analysis. The IVM-induced LC3 puncta were dependent on the canonical autophagy machinery (FIP200, ATG13 and ULK1/2). They also observed the mitochondrial ubiquitin puncta appearing with IVM were reduced by 50% with the combined knockout of the cytosolic E3 ligases TRAF2, CIAP1 and CIAP2 (Zachari et al., 2019).

We could therefore hypothesise that in response to IVM treatment, TRAF2, CIAP1 and CIAP2 are engaged in the early stages of mitochondrial ubiquitylation which enables the recruitment of the autophagy machinery. Parkin may then be recruited at a later stage to amplify the ubiquitylation signal and subsequent mitophagy events. This would lead to the potent mitophagy induction that I have measured after 24h using the mito-QC probe in SH-SY5Y cells.

Another potent trigger was CDDO-Me, the Lon protease inhibitor: 24h of 1μM CDDO-Me in SH-SY5Y mito-QC cells led to mitochondrial depolarisation (visualised by OPA1 cleavage), PINK1 stabilisation, a slight increase in pS65-Ubiquitin, FIS1 ubiquitylation and promoted the autophagic degradation of mitochondria in 53% of SH-SY5Y mito-QC cells.

Gibellini and colleagues have shown that Lon knockdown leads to impaired mitochondrial structure, degradation of selective mitochondrial proteins, defective mitochondrial function and further apoptotic cells death in colon cancer cells (Gibellini et al., 2014). Subsequently, they made use of the Lon inhibitor CDDO-Me in colon cancer cells and found similar results. As mentioned earlier on, below 1μM, apoptosis was not induced but reduction in MFN2 and TOMM20 levels were still observed (Gibellini et al., 2015). In SH-SY5Y mito-QC cells treated with 1μM CDDO-Me for 24h, I did not observe any clear degradation of either TOMM20 or MFN2 but I instead discerned ubiquitylated species of FIS1. CDDO-Me potentially induces mitophagy by interfering with the degradation of mitochondrial misfolded proteins. EM imaging revealed that 24h treatment of 2.5μM CDDO in Granta cells promotes the accumulation of electron dense inclusion within mitochondria, which are most likely misfolded protein aggregates (Bernstein et al., 2012). This accumulation of misfolded protein in the matrix could affect PINK1 import through the TIMM complex and thus enable PINK1 accumulation without the need for depolarisation.

The hypothesis that misfolded proteins can induce mitophagy was tested and proven by Richard Youle's lab. They over-expressed a deletion mutant of ornithine carbamoyltransferase (ΔOTC, first introduced by Nicholas Hoogenraad), which generates insoluble protein aggregates in the

mitochondrial matrix and found that it induced mitophagy in a depolarisation-independent manner (Burman et al., 2017; Jin and Youle, 2013; Zhao et al., 2002). ΔOTC expression for 48h induced the mitochondrial Unfolded Protein Response (UPR^{mt}) as well as accumulation of PINK1 and Parkin at mitochondria (Jin and Youle, 2013). ΔOTC accumulated at mitochondrial subdomains and promoted localised mitophagy. ΔOTC foci colocalised with TOMM20 and mitochondrial dyes, as well as Parkin, ubiquitin, OPTN and LC3. Those foci then dissociated from the rest of the network in a DRP1 dependent manner. Using PINK1 KO cells, Youle and colleagues reported that this misfolded protein-induced mitophagy was dependent on PINK1 and that it was accelerated by Parkin overexpression (Burman et al., 2017).

Actinonin, a drug promoting mito-ribosome stalling and thus protein misfolding at mitochondria, reproduced the effects of ΔOTC expression confirming that overwhelming the UPR^{mt} quality control promotes PINK1-dependent mitophagy (Burman et al., 2017).

Interestingly knocking down Lon but not CLPP, another matrix protease, enhanced PINK1 accumulation, Parkin recruitment and mitochondria clearance in response to ΔOTC expression (Jin and Youle, 2013). This would suggest that Lon is essential in degrading misfolded proteins in the matrix and delays the involvement of mitophagy as a backup quality control system. This supports the use of Lon inhibitors, such as CDDO-Me, to trigger mitophagy.

However, CDDO-Me does not only affect the UPRmt and mitophagy. CDDO-Me directly targets Keap1 and IKKβ, which activates Nrf2 and supresses NF-κB (Ahmad et al., 2006; Yates et al., 2006; Wang et al., 2014). Other targets of CDDO-Me include cyclins (Wang et al., 2017b). As CDDO-Me lacks specificity, I would not recommend it for the study of mitophagy.

The HSP90 inhibitor, G-TTP (a Geldanamycin derivative), is another compound promoting the accumulation of misfolded proteins at mitochondria and subsequent UPR^{mt}. This compound had contradictory effects in SH-SY5Y cells and hTERT-RPE1-YFP-Parkin cells.

When I used G-TPP at 10μM, it induced the recruitment of Parkin to mitochondria in close to 90% of hTERT-RPE1-YFP-Parkin cells after 6h but

had no effect on mitochondrial protein ubiquitylation or mitophagy events in SH-SY5Y mito-QC cells after 24h and 48h.
A study performed in HeLa cells overexpressing Parkin and mt-Keima, showed that 10μM G-TPP, was sufficient to induce a significant shift towards mitophagy fluorescence from 4h onwards. The induction was however less efficient than CCCP: after 12h with G-TPP the mitophagy index was ~80% weaker than with 10μM CCCP (Fiesel et al., 2017). Such weak mitophagy induction might not be detectable in SH-SY5Y mito-QC cells whereas in the YFP-Parkin overexpressing RPE1 cells, the Parkin amplification loop would allow even this weak trigger to initiate a clear mitophagy signal.

They further observed that 10μM G-TPP induced the stabilisation of PINK1, the accumulation of pS65-ubiquitin and the recruitment of Parkin to mitochondria within 4h in HeLa cells overexpressing Parkin (Fiesel et al., 2017). They also observed PINK1 stabilisation and pS65-Ubiquitin accumulation in human primary fibroblast and in iNeurons treated with 15μM G-TPP for 8h (Fiesel et al., 2017).
This was confirmed in hTERT-RPE1-YFP-Parkin cells by my colleague Liam Pollock. He treated these cells with either G-TPP (10 and 20μM) or 17-AAG, a Geldanamycin derivative that is not targeted to mitochondria, for 4h and 24h. He found that both concentrations of G-TPP but not 17-AAG promoted OPA1 cleavage, PINK1 and pS65-Ubiquitin accumulation as well as FIS1 poly ubiquitylation and degradation of MFN1 and MFN2 at 4h. Interestingly, he also observed PINK1 and pS65-Ub accumulation, to a lesser extent, in the parental hTERT-RPE1 cells which lack Parkin. This suggests that G-TPP mediated mitophagy does not require Parkin.

Intriguingly, silencing another mitochondrial chaperone HSP9A, also known as GRP75, mt-HSP70 or mortalin, was reported to promote mitophagy in SH-SY5Y cells (Burbulla et al., 2014). This chaperone is involved in the import and proper folding of mitochondrial proteins in the matrix (review: (Wiedemann and Pfanner, 2017)). Knocking down HSP9A promoted the accumulation of misfolded proteins, fragmentation of the mitochondrial network and the formation of LC3 and WIPI2 puncta in SH-SY5Y cells. Moreover, silencing of

HSP9A resulted in the colocalisation of TOMM20 with LAMP1 and a reduction in TOMM20 protein levels (Burbulla et al., 2014).
Treating HCC cells with the 17-AAG HSP90 inhibitor over 24h increases the mRNA levels of HSPA9 and the protein levels of HSP9A possibly as a compensatory mechanism (Guo et al., 2014). Thus, in my experiments, SH-SY5Y mito-QC cells might have upregulated HSPA9 in response to G-TPP, to compensate for the loss of HSP90 activity. This might have prevented the accumulation of misfolded proteins and the stabilisation of PINK1. It would thus be of interest to measure the influence of HSPA9 directed inhibitors, such as MTK-077, on mitophagy induction.

The DNA intercalator and inhibitor of Topoisomerase II, DOX, was another drug able to induce mitophagy in SH-SY5Y mito-QC cells: a 24h treatment with 250nM DOX induced mitophagy in 21% of cells. This mitophagy induction did not correlate with PINK1 accumulation, pS65-Ubiquitylation or with the ubiquitylation or degradation of MFN2 and FIS1. Likewise, 250nM of DOX did not promote the recruitment of Parkin to mitochondria in hTERT-RPE1-YFP-Parkin. In contrast to my observations, DOX (62.5 and 250 nM) had previously been shown to induce PINK1 and Parkin accumulation, LC3-II formation as well as MFN2, VDAC, COXIV loss in AC16 human cardiomyocyte cells (Yin et al., 2018). Another study showed that treating HCT116 and HL-1 with 20nM-1μM DOX for 24h downregulated CCCP mediated mitophagy: the accumulation of PINK1 and Parkin, as well as mitochondrial ubiquitylation was significantly reduced. Similarly injecting mice with DOX, decreased CCCP-induced Parkin accumulation mice hearts (Hoshino et al., 2013).
In vivo work in mice suggested that both acute and chronic DOX injection promote the accumulation of autophagosomes in mouse heart. Abdullah and colleagues hypothesised that this accumulation was the result of defective lysosomal degradation rather than due to an increase in autophagy (Abdullah et al., 2019). Indeed, co-treatment with chloroquine, which raises lysosomal pH and thus inhibits the degradation of autophagosomal content, did not further enhance autophagosome accumulation in mice heart.

It would thus be essential to verify if the rise in mitolysosomes that I was observing after 24h of DOX in SH-SY5Y mito-QC cells results from impaired autophagosomal flux or from a genuine induction of mitophagy.

Mitophagy can also be induced independently of drug treatment. Optogenetics have been repurposed to trigger phototoxic fluorescent proteins. KillerRed (KR) is one of those phototoxic fluorophores and has been linked to a mitochondrial targeting sequence to specifically trigger mitochondrial ROS (Bulina et al., 2006). Ashrafi and colleagues have used the mt-KR to activate mitophagy in rat and mice hippocampal neurons. Following the photoactivation of KR (Ex585/Em610nm), mitochondria become fragmented, swollen and finally are sent for autophagic degradation: 20min post-photoactivation, YFP-Parkin and LC3 puncta colocalise with mitochondrial fragments and those disappear within 40min (Ashrafi et al., 2014). The benefit of such a technique is that mitophagy can be triggered in both a spatially and temporally manner. The disadvantage of this system is that it requires overexpression of the Killer Red protein prior to any experiment.

In this chapter I have highlighted the efficacy of AO and Parkin overexpression to amplify mitophagy. I then discussed novel triggers and probes that can be used to study alternative pathways of mitophagy. In the next chapter, I will use those tools to specifically look at USP30-mediated mitophagy in SH-SY5Y cells.

Chapter 4: USP30-regulates mitophagy in SH-SY5Y cells

4.1 Introduction.

USP30 was first studied for its putative role in the regulation of mitochondrial fusion and fission dynamics. Early publications have correlated USP30 depletion and inhibition with mitochondrial elongation (Nakamura and Hirose, 2008; Yue et al., 2014).

It was only in 2014 that the link between USP30 and mitophagy was made. Bingol and colleagues performed a microscopy screen in HeLa and SH-SY5Y cells over-expressing Parkin to look for DUBs preventing CCCP-mediated degradation of mitochondria, visualised then by the loss of TOMM20 staining. USP30 and OTUD6A were the only two hits emerging from this study (Bingol et al., 2014). Complementary studies confirmed that USP30 deubiquitylates Parkin substrates, has a preference for K6 chains and opposes BH3 mimetic induced apoptosis (Cunningham et al., 2015; Liang et al., 2015; Wang et al., 2015).

The majority of studies analysing the role of USP30 in mitophagy, were conducted in cells that over-express Parkin and made use of depolarisation agents. The field has thus little information on firstly whether USP30 could oppose mitophagy in cells that do not overexpress Parkin and secondly if USP30 could regulate spontaneous mitophagy events occurring independently from mitophagy triggers, also known as basal mitophagy. Finally, the question remained whether USP30 functions were restricted to mitochondria.

To answer those questions, I have studied USP30 in cells that endogenously express Parkin. Serendipitously I discovered that a pool of USP30 was localising to peroxisomes and I contributed to elucidating its role at peroxisomes. I have used of the mito-QC probe to look at basal mitophagy in SH-SY5Y cells and will briefly describe the work done in parallel by my colleagues in cells that do not express detectable levels of Parkin.

4.2 USP30 localises at both mitochondria and peroxisomes in SH-SY5Y cells

4.2.1 USP30 copy number in SH-SY5Y cells

I first characterised the expression levels and the localisation of USP30 in SH-SY5Y cells, prior to conducting functional studies.

I used western blotting to quantify the USP30 copy number in SH-SY5Y cells (**Figure 4.1**). Malte Gersch (then a post-doctoral fellow in David Komander's laboratory at the LMB in Cambridge and now an independent group leader at the Max Planck Institute in Dortmund, Germany) kindly provided us with a recombinant protein comprising the sequence encompassing amino acids 64-502 of human USP30 (475 $\mu g.ml^{-1}$). I used known amounts of USP30(64-502) to generate a protein standard curve by western blotting. On the same gel, I loaded 10, 20 and 30µg of SH-SY5Y RIPA lysates (**Figure 4.1A**). I employed an antibody targeting the residues 290-433 in human USP30, to detect both endogenous and recombinant USP30 (**Figure 4.1B**). I analysed the western blot with an infrared imager (Odyssey CLx, LICOR) and ensured that signals were not saturated. I then used the signals for the recombinant protein to generate a standard curve (**Figure 4.1C**). The number of USP30 molecules per µg was determined by converting USP30(64-502)'s molecular mass (49.75 kDa) into its metric mass ($8.26x10^{-11}$ng) which allowed me to infer the number of USP30 molecules present in each standard curve point. Finally, I used a linear regression to obtain the number of USP30 molecules present in each SH-SY5Y lysate lane (**Figure 4.1D**). Counting the number of cells present in a duplicate dish allowed me to deduce the number of USP30 molecules per cell. I estimated that each SH-SY5Y cell contained molecules of 9.5×10^4 USP30.

Using the same technique I teamed up with my colleague Andreas Kallinos to compare the number of USP30 proteins found in all four of the cell lines we use to study mitophagy: SH-SY5Y cells, the osteosarcoma U2OS cells, the retinal pigment epithelial hTERT-RPE1 cells, and the colorectal carcinoma HCT116 cells (**Figure 4.2**).

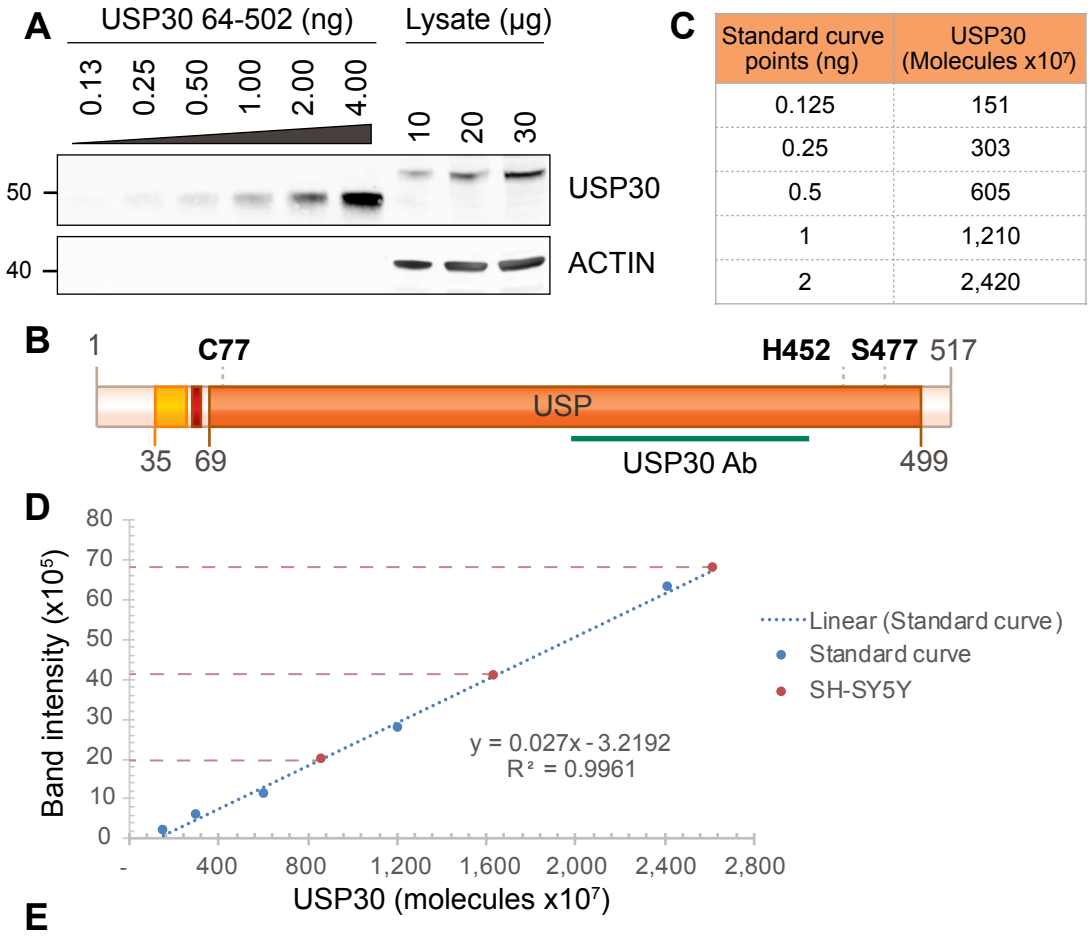

C

Standard curve points (ng)	USP30 (Molecules x10⁷)
0.125	151
0.25	303
0.5	605
1	1,210
2	2,420

E

Lysate (ng)	Volume of lysate (µl)	Band intensity	USP30 (Molecules)	USP30 per µl
10	7	20 x10⁵	860 x10⁷	1,2 x10⁹
20	14	41 x10⁵	1,634 x10⁷	1,2 x10⁹

Mean USP30 per µl	Cell per µl	USP30 per cell
6 x10⁸	1.26 x 10⁴	95,100

Figure 4.1: Quantifying the number of USP30 molecules per SH-SY5Y cells.

A) The USP30 copy number in SH-SY5Y cells was measured by western blotting. A standard curve was generated using known amounts of recombinant USP30[64-502] protein. SH-SY5Y cells were lysed in RIPA then 10, 20 and 30µg of lysates were run next to the standard curve. **B)** USP30 was detected using an antibody targeting a segment of the USP domain (290-433 aa) and scanned on an Odyssey CLx imaging system. **C-D)** The intensity of the protein bands was determined using Image Studio. The graph represents the intensity plotted against the number of USP30[64-502] molecules present in each point of the standard curve point. The number of molecules per µg was calculated by converting USP30[64-502]'s molecular mass (49,75 kDa) into metric mass (8.26 x10^{-11} ng) using Avogadro's constant (6.02214086 Å~ 1023 mol^{-1}). **E)** The linear function describing the standard curve (y = 0.539x – 3.2192), provided the number of USP30 molecules present in each lysate lane, which was further translated into the number of USP30 molecules per µl. The number of cells per µl of lysate was established using a cell counter and was used to determine, by

correlation, the number of USP30 molecules contained in one SH-SY5Y cell (4.76 x10_4). Data from a single experiment.

We loaded all lysates on the same gel and using the same standard curve quantified their USP30 copy number (**Figure 4.2A, 2B and 2C**). We discovered that SH-SY5Y cells express 2.9- and 1.4-fold more USP30 molecules per cell than U2OS and HCT116 cells respectively. Interestingly, hTERT-RPE1 cells showed the highest level of USP30 expression, 2.2-fold more USP30 than SH-SY5Y cells (**Figure 4.2C**). In this second experiment the USP30 band intensity and the resulting copy number per cell was lower by 3-4-fold in comparison to Figure 4.1, whilst the standard curve remained identical: 2.6 x10^4 versus 9.5 x10^4 in the first experiment for SH-SY5Y cells and 5.7 x10^4 versus 17.1 x$10^{4.}$ (not shown) RPE1 cells. The samples used in this second experiment were the same ones as in Figure 4.1, it is possible that despite storage at -20°C in sample buffer, some protein was lost due to precipitation or aggregation as a result of multiple freeze thaw cycles. However, the relative abundance between the cells remain equivalent: RPE1 have on average ~2-fold more USP30 proteins than SH-SY5Y cells.

I next looked up for USP30 transcript datasets in the Broad Institute Cancer Cell Line Encyclopedia (CCLE) database. I used the associated Affymetrix microarray rather than their RNA sequencing dataset as the later had no entry for SH-SY5Y cells. hTERT-RPE1 cells were not captured in either datasets as they are immortalised but are not transformed. The USP30 mRNA abundance in SH-SY5Y, U2OS and HCT116 cells followed a similar trend to the protein copy number. SH-SY5Y cells contain between 1.6 and 1.9-fold more USP30 mRNA than U2OS and HCT116 cells (**Figure 4.2D**). As SH-SY5Y cells express high amounts of USP30, they are ideal for the assessment of the localisation of endogenous USP30.

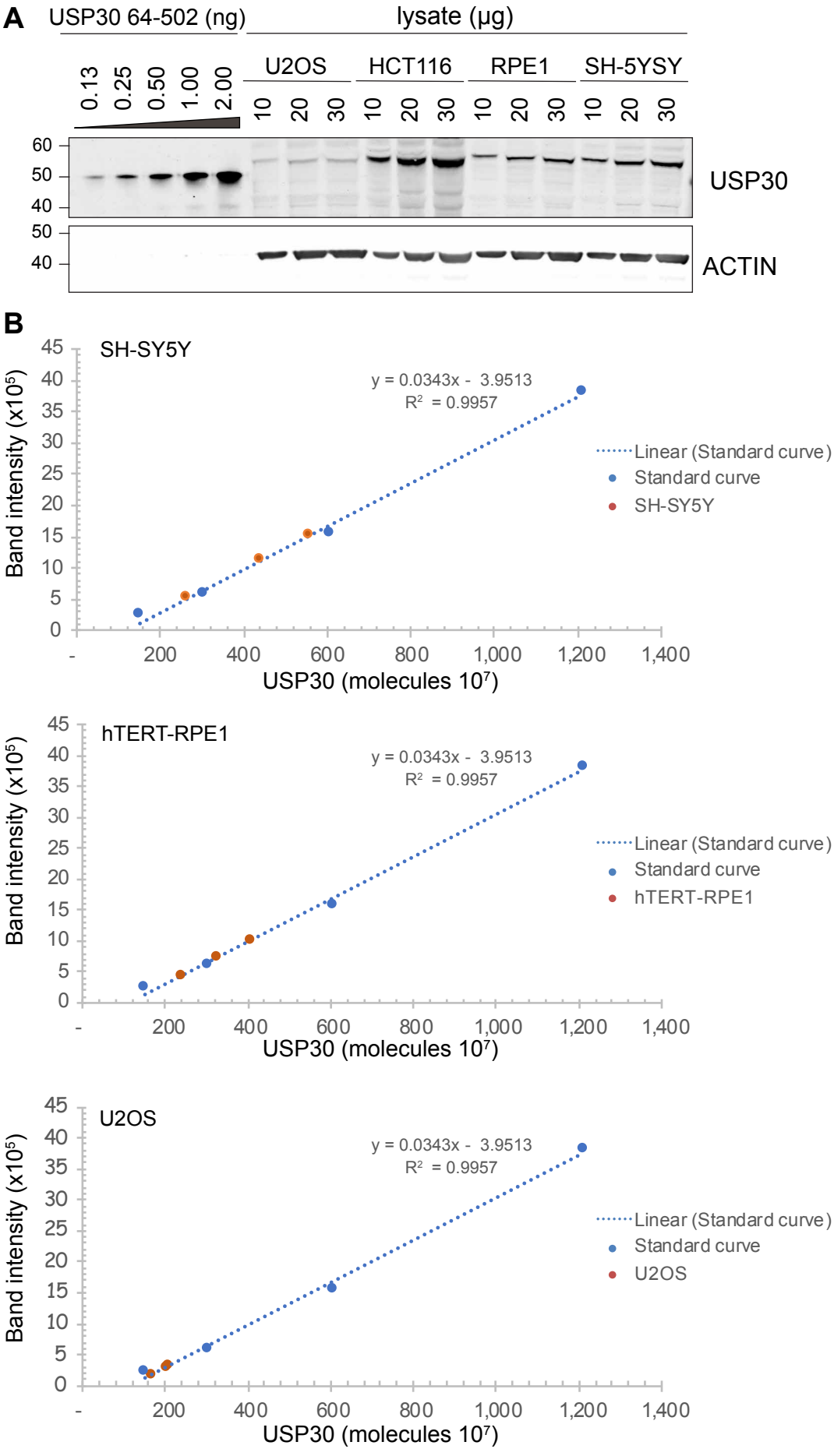
A
USP30 64-502 (ng)
lysate (µg)
0.13
0.25
0.50
1.00
2.00
U2OS
HCT116
RPE1
SH-5YSY
10
20
30
60
50
40
USP30
ACTIN
B
SH-SY5Y
y = 0.0343x - 3.9513
R² = 0.9957
Linear (Standard curve)
Standard curve
SH-SY5Y
Band intensity (x10⁵)
USP30 (molecules 10⁷)
hTERT-RPE1
U2OS

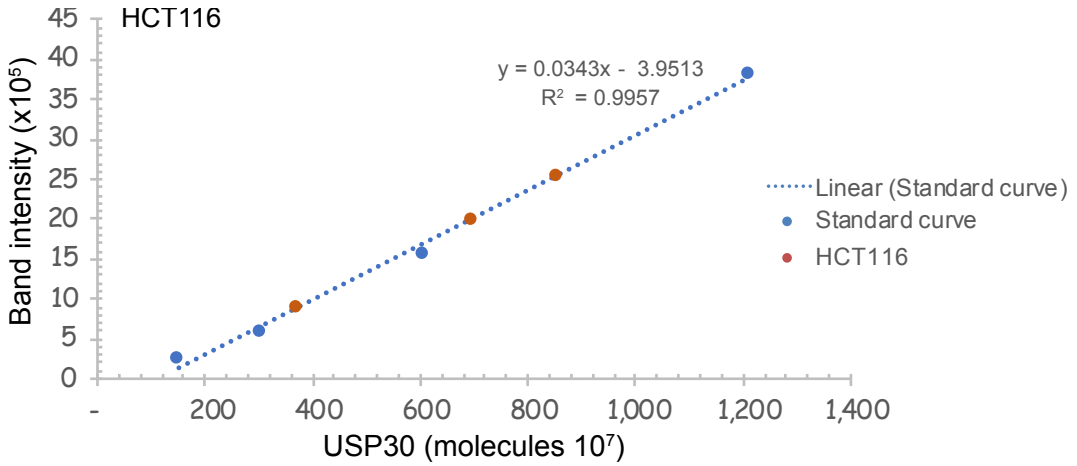

C

Cell line	Lysate (µg)	Band intensity	USP30 (Molecules)	USP30 per µl	Average USP30 per µl
SH-SY5Y	10	5.12 x10^5	264 x10^7	3.8 x10^8	3.3 x10^8
	20	11.10 x10^5	439 x10^7	3.2 x10^8	
	30	15.10 x10^5	555 x10^7	2.7 x10^8	
hTERT-RPE1	10	4.21 x10^5	238 x10^7	3.9 x10^8	2.9 x10^8
	20	7.25 x10^5	327 x10^7	2.7 x10^8	
	30	10.00 x10^5	407 x10^7	2.2 x10^8	
HCT1116	10	8.76 x10^5	371 x10^7	8.6 x10^8	7.7 x10^8
	20	19.9 x10^5	695 x10^7	8.0 x10^8	
	30	25.40 x10^5	856 x10^7	6.6 x10^8	
U2OS	20	2.96 x10^5	202 x10^7	1.0 x10^8	0.9 x10^8
	30	3.15 x10^5	207 x10^7	0.7 x10^8	

D

Cell line	Cell per µl	USP30 per cell
SH-SY5Y	1.26 x10^4	26,000
hTERT-RPE1	0.51 x10^4	57,000
HCT116	4.34 x10^4	17,700
U2OS	0.94 x10^4	9,070

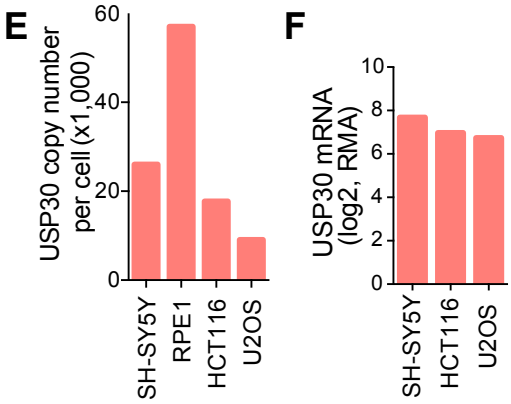

Figure 4.2: Evaluating the USP30 copy number in mammalian cells.

A) The USP30 copy number in SH-SY5Y, hTERT-RPE1 (RPE1), HCT116 and U2OS cells was measured by western blotting. A standard curve was generated using known amounts of recombinant USP30[64-502] protein. Cells were lysed in RIPA then 10, 20 and 30µg of lysates were run next to the standard curve. **B)** The intensity of the protein bands was quantified using Image Studio. The graph represents the intensity plotted against the number of USP30[64-502] molecules present in each point of the standard curve point. The number of molecules per µg was calculated by converting USP30[64-502]'s molecular mass (49,75 kDa) into metric mass (8.26 x10-11 ng) using Avogadro's constant (6.02214086 -1). **C-D)** The linear function describing the

standard curve (y = 0.539x – 3.2192), provided the number of USP30 molecules present in each lysate lane, which was further translated into the number of USP30 molecules per µl. The number of cells per µl of lysate was established using a cell counter and was used to determine, by correlation, the number of USP30 molecules contained in one cell. **E)** Graph representing the USP30 protein copy number in SH-SY5Y, RPE1, HCT116 and U2OS cells. Data from a single experiment. **F)** Graph indicating USP30 mRNA levels in SH-SY5Y, RPE1, HCT116 and U2OS cells. The data was collected from the Broad Institute Cancer Cell Line Encyclopedia (CCLE) and its associated Affymetrix microarray database with Robust Multichip Average (RMA) normalisation.

I compared the copy number of both USP30 and known mitochondrial USP30 substrates (TOMM20, VDACs, CISD1) (Bingol et al., 2014; Cunningham et al., 2015) using two genome wide mass spectrometry datasets from HeLa human cancer cells and 3T3 mouse fibroblasts (Kulak et al., 2014; Schwanhäusser et al., 2011). The copy number for USP30 was of 4.9 $x10^3$ and 2.3 $x10^2$ in HeLa and 3T3 cells respectively, whilst VDACs, CISD1 and TOMM20 all have a copy number ranging between 1.5 $x10^5$ and 3 x 10^6 in those cells (Kulak et al., 2014; Schwanhäusser et al., 2011). Overall USP30 is largely inferior in terms of copy number compared to its substrates. Therefore, USP30 most likely does not globally deubiquitylate mitochondria but rather acts on discrete ubiquitylation events. Amos Liang had discovered that USP30 binds to TOMM20 and TOMM22 independently on its catalytic activity and thus potentially localises to the TOM complex (Liang et al., 2015). The low copy number of USP30 suggests that it only docks to a subset of TOM complexes.

4.2.2 USP30 knockdown optimisation in SH-SY5Y cells

As I was going to use siRNA mediated depletion of USP30 in SH-SY5Y cells to assess the function and location of USP30, I started by optimising siRNA transfection in those cells (**Figure 4.3**). I used a non-targeting siRNA oligo (NT1) as a negative control and used two distinct oligos to target USP30 (D1 and D3) that had previously been characterised by Amos Liang and had been shown to efficiently deplete USP30 in multiple cell types (Liang et al., 2015; Marcassa et al., 2018). I transfected the cells by lipofection using Lipofectamine RNAiMax. This transfection reagent was optimised for the delivery of siRNA in most human cell lines, including neuroblastoma cells. My co-workers had previously established 40nM siRNA as the standard

concentration used for transfection of a variety of cell lines. I thus adopted this concentration for my experiments and focussed my optimisation on two parameters: media composition and length of transfection (**Figure 4.3A**).

I first assessed whether the media additives which I routinely use to culture SH-SY5Y cells such as fetal bovine serum (FBS) or the antibiotic mixture Penicillin/Streptomycin (P/S) affected the knockdown efficiency. I performed the siRNA transfection in medium with no additives, in medium with 10% FBS or in medium with 10% FBS and 1% P/S. For transfections completed in medium with no additives, I either supplemented the medium with 10% FBS 6h after transfection or not. In all conditions, USP30 expression was approximatively decreased by 60%. The addition of P/S appeared to slightly worsen the knockdown efficiency.

Overall, these results could either reveal a suboptimal transfection efficiency, meaning that only 60% of the cells are transfected, or that USP30 is incompletely silenced in all of the cells. This is an unsatisfactory result as the remaining wildtype cells or residual USP30 would be able to mask effects resulting from the knockdown.

I decided to increase the length of the knockdown to try to improve its efficiency. Schwanhäusser *et al.*, have reported that USP30 has a half-life of 57.54h in 3T3 cells (Schwanhäusser et al., 2011). Arresting the production of newly synthesised USP30 for 72h might not be sufficient to see a complete loss of the protein. Thus, I compared the standard 72h single hit protocol with a protocol including two transfection hits over a 144h period. For this set I excluded serum and antibiotics during the transfection and supplemented the cells with 10% FBS after 6 hours (**Figure 4.3B**). Increasing the transfection time did not increase further the silencing efficiency. This incomplete silencing was not specific to USP30: A control siRNA oligo targeting USP33 transfected for 72h in medium with no additives similarly resulted in a 59% knockdown efficiency (**Figure 4.3C**). This USP33 siRNA is used as a standard control in my host lab as we have observed very efficient knockdown of USP33 in other cell lines.

As the knockdown efficiency in this cell line appeared poor, I generated USP30 knockout SH-SY5Y cells using the CRISPR/Cas9 system (see Chapter V).

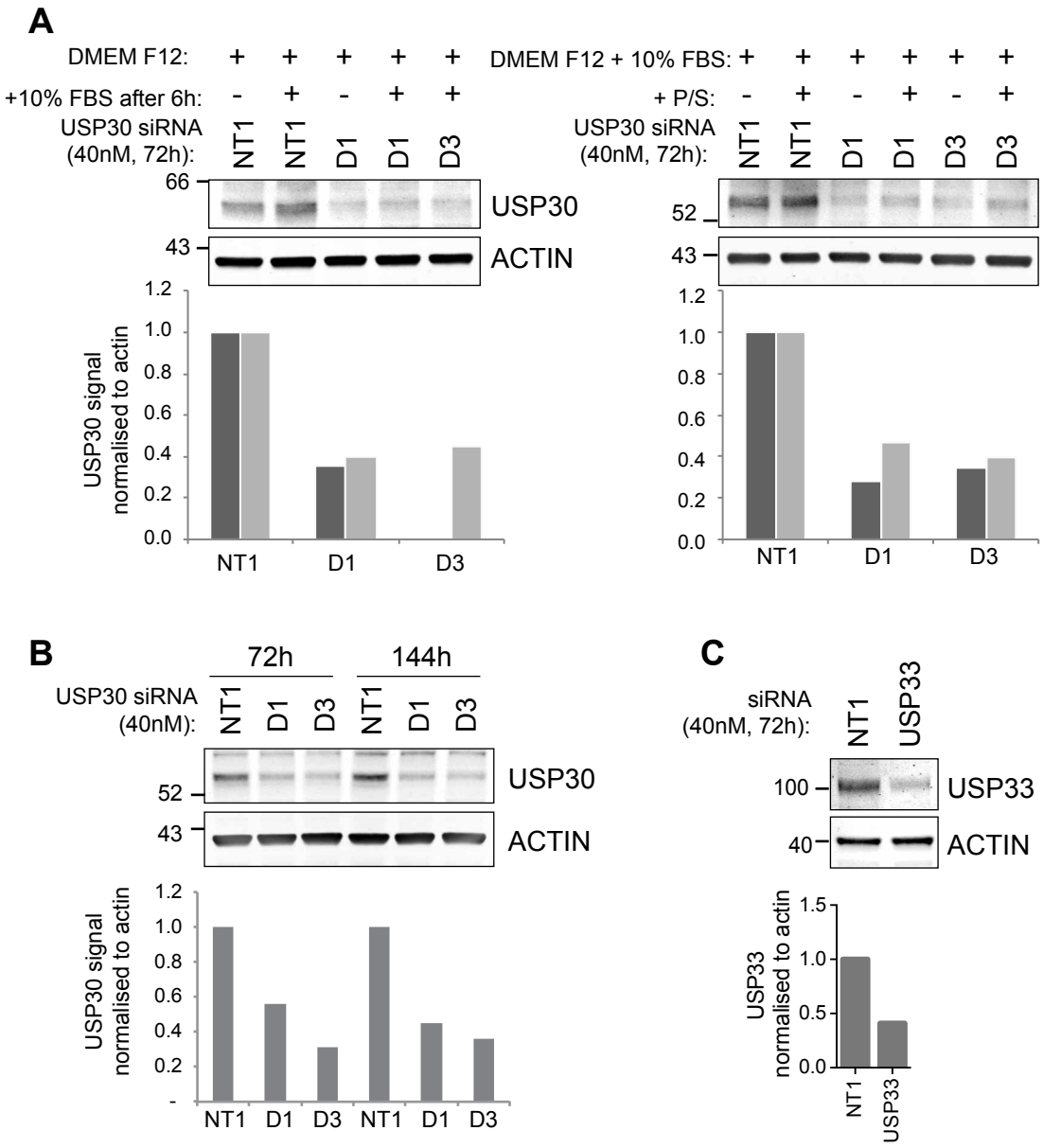

Figure 4.3: Optimising siRNA transfection in SH-SY5Y cells

A) SH-SY5Y cells were transfected with either non-targeting (NT1) or individual oligos targeting USP30 (D1 and D3) for 72h. Four conditions were tested: The cells were (1) transfected in medium with no additives or (2) in medium containing 10% Fetal Bovine Serum (FBS) with or without (3) Penicillin/Streptomycin (P/S). The addition or not of (4) FBS 6h after transfection in media without additives was also tested. In all four conditions, the medium was exchanged for medium with additives (10% Fetal Bovine Serum, 1% Penicillin/Streptomycin, 1% non-essential amino acids) after 24h transfection**. B)** The cells were transfected once for 72h or twice over a 144h period (2 x 72h transfections) in medium without additives. The medium was supplemented with 10% Fetal Bovine Serum 6h after the transfection then was exchanged for medium with additives (10% Fetal Bovine Serum, 1% Penicillin/Streptomycin, 1% non-essential amino acids) after 24h. **C)** SH-SY5Y cells were transfected with either NT1 or an individual oligo targeting USP33 for 72h in medium with no additives. Data from a single experiment.

4.2.3 Endogenous USP30 localises to mitochondria

In the early 2000s, no mammalian deubiquitylases were known to localise at mitochondria. However, the yeast Ubp16 was reported to localise at the outer mitochondrial membrane via an N-terminal hydrophobic domain (Kinner and Kölling, 2003). Hirose and Nakamura searched for a similar membrane topology across mammalian deubiquitylases and found that USP30 had an N-terminal (35-54 aa) hydrophobic region (**Figure 4.4A**),(Nakamura and Hirose, 2008). Although the transmembrane domain protein sequence of mammalian USP30 only weakly aligns with its yeast orthologue, they have a similar hydrophobic pattern on hydropathy plots (**Figure 4.4B-C**) (Nakamura and Hirose, 2008). This transmembrane domain anchors USP30's N-terminal region in the outer mitochondrial membrane with the catalytic C-terminal domain facing the cytosol (**Figure 4.4D**). USP30 is therefore predicted to deubiquitylate outer mitochondrial membrane proteins and potentially other cytosolic or MAM associated proteins. Unlike for Ubp16, the localisation of human USP30 is also dependent on positively charged residues that flank its transmembrane domain (Nakamura and Hirose, 2008). The polybasic region (PBR) that follows the transmembrane domain appears to be conserved in mammals such as mice and humans and an alternative PBR of equal length and position is found in zebrafish. The USP30 fly orthologue's (*CG3016*) transmembrane domain lies upstream of a smaller PBR of four arginine (**Figure 4.4B**). This suggests that in Metazoan, USP30 relies on both the transmembrane domain and a PBR to localise at mitochondria.

As mentioned above, most prior studies looking at USP30 localisation were overexpressing tagged USP30 (Nakamura and Hirose, 2008; Cunningham et al., 2015; Wang et al., 2015). In 2014, the Bingol lab published an antibody able to detect endogenous USP30 by immunofluorescence and that endogenous USP30 co-localised with HSP60 in SH-SY5Y cells (Bingol et al., 2014). I verified the cellular localisation of endogenous USP30 by co-staining mitochondria for TOMM20 and USP30, using this same antibody, kindly provided by Baris Bingol (Genentech, USA) (Bingol et al., 2014). As a negative control for the selectivity of the antibody, I depleted USP30 using the USP30-targeting siRNA oligo D3 (**Figure 4.5**). In the mock transfected set (NT1), the USP30 staining delineated a mitochondrial network overlapping with

TOMM20. USP30 depletion removed all of this TOMM20 positive mitochondrial signal, leaving only a diffuse and punctate background staining that was apparent throughout the cell. Thus, I confirmed that endogenous USP30 localises at mitochondria in SH-SY5Y cells.

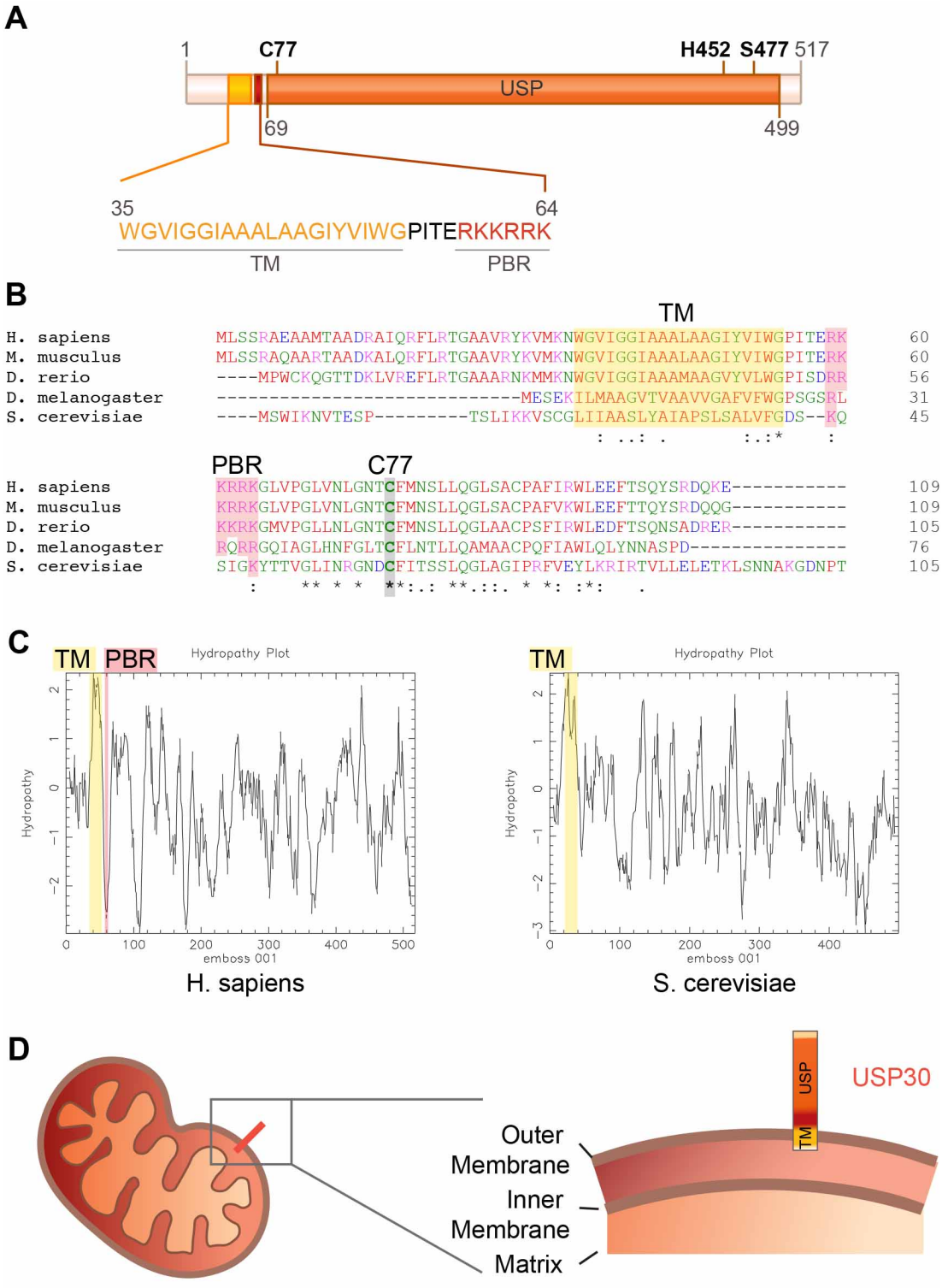

Figure 4.4: Structure and hydrophobic properties of USP30's transmembrane and polybasic regions.

A) Schematic representation of the protein sequence and domains of USP30 isoform 1. The catalytic triad, composed of C77, H452 and S477, is highlighted in bold. Important features of the protein are highlighted: the USP domain, the transmembrane domain (TM) and the polybasic region (PBR) are annotated on this schematic. **B)** ClustalW protein sequence alignment of USP30's transmembrane domain and polybasic residues in H. sapiens, M. musculus, D. rerio, D. melanogaster (*CG3016*) and S. cerevisiae (Ubp16). The transmembrane domain is highlighted in yellow, the polybasic region in pink and the catalytic cysteine in grey. Colour coding: red: Small (small+ hydrophobic (incl.aromatic -Y)), blue: Acidic, magenta: Basic – H, green: Hydroxyl + sulfhydryl + amine + G. Annotations: * single, fully conserved residue; : conservation between groups of strongly similar properties - scoring > 0.5 in the gonnet PAM 250 matrix; . conservation between groups of weakly similar properties - scoring =< 0.5 in the gonnet PAM 250 matrix. **C)** Kyte-Doolittle Hydropathy plot of human and mice USP30 made with "EMBOSS Pepwindow" from EMBL-EBI. Window size: 10. **D)** Schematic representation of USP30 anchorage and orientation at the outer mitochondrial membrane. Figure adapted from Hirose and Nakamura, 2008.

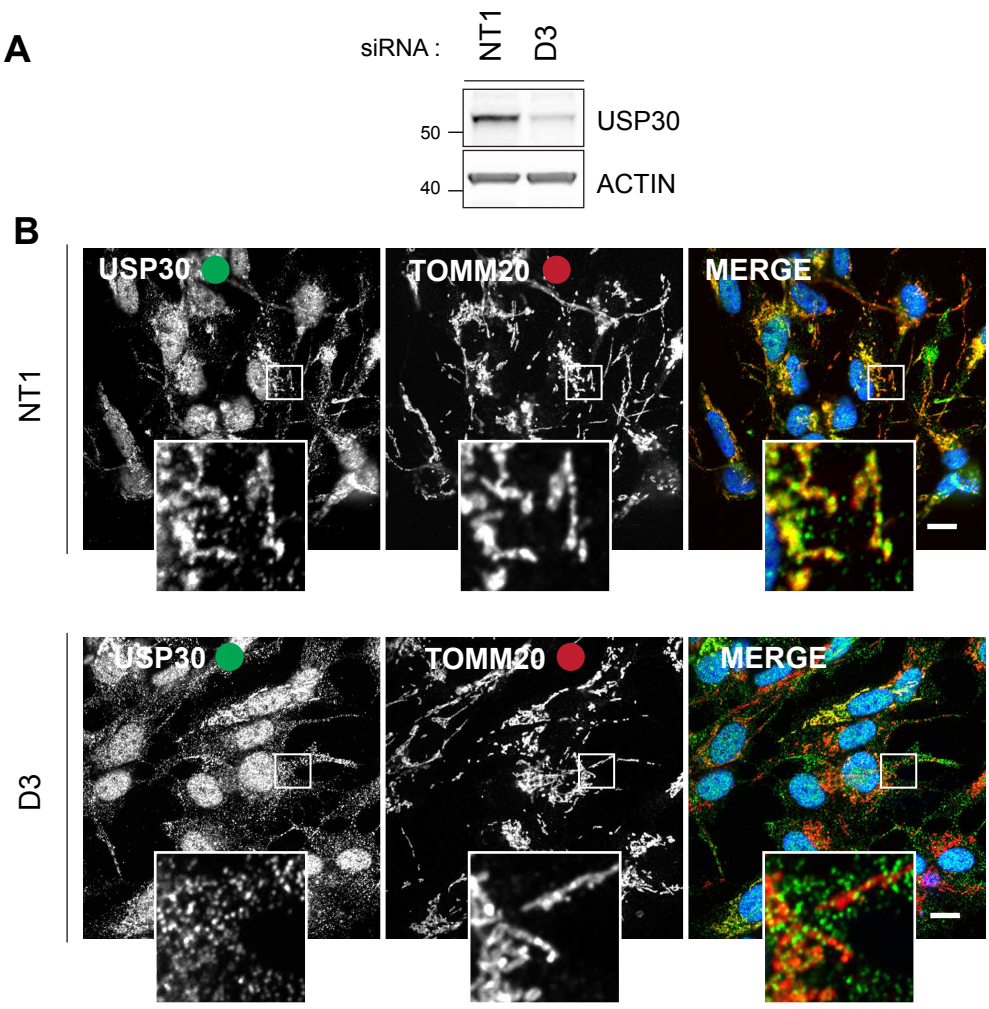

Figure 4.5: Endogenous USP30 localises to mitochondria in SH-SY5Y cells.

SH-SY5Y cells were transfected with non-targeting siRNA (NT1) and with siRNA against USP30 (D3) for 144h (two hit knockdown). **A)** Representative blot. **B)** The cells were then fixed and probed for USP30 and TOMM20 using Alexa Fluor 488 and Alexa Fluor 594-coupled secondary antibodies respectively. The coverslips were mounted in mowiol containing DAPI. Images were acquired sequentially using a 3i spinning disk confocal microscope with a 63x objective and a sCMOS camera. Scale bar: 10µm. Representative images from two experiments.

4.2.4 USP30 also localises to peroxisomes

When overexpressing USP30-GFP in U2OS cells, I observed round puncta that did not colocalise with TOMM20 (**Figure 4.6**). I could also detect similar structures when looking at endogenous USP30 in the SH-SY5Y cells; although some of these were clearly non-specific as they were not affected by USP30 siRNA. (**Figure 4.5**). I wondered whether a pool of USP30 was localising to another organelle. These non-mitochondrial structures were round and roughly the size of fragmented mitochondria. Peroxisomes are single membrane bound organelles that fulfill those criteria. Moreover they have an overlapping proteome with mitochondria and also share common metabolic functions (Islinger et al., 2018; Cipolla and Lodhi, 2017; Schrader et al., 2015; Hartwig et al., 2013). Hence, I decided to focus on this candidate. I overexpressed USP30 in easily transfectable cells, hTERT-RPE1 and U2OS, and co-stained for peroxisomal proteins (**Figure 4.7**), (see also our published article and corresponding commentary: (Marcassa et al., 2018, 2019)). I stained for PMP70, a peroxisomal membrane protein and catalase a peroxisomal matrix protein. As matrix proteins are imported during the final step of peroxisome maturation, Catalase also gives an indication of the maturation stage of the peroxisomes. I observed that USP30-RFP and USP30-MYC positive punctate structures co-localised with PMP70 and Catalase respectively. I concluded that over-expressed USP30 localises to both mitochondria and peroxisomes. Using immunofluorescence, I then verified if endogenous USP30 was also targeted to peroxisomes in SH-SY5Y cells.

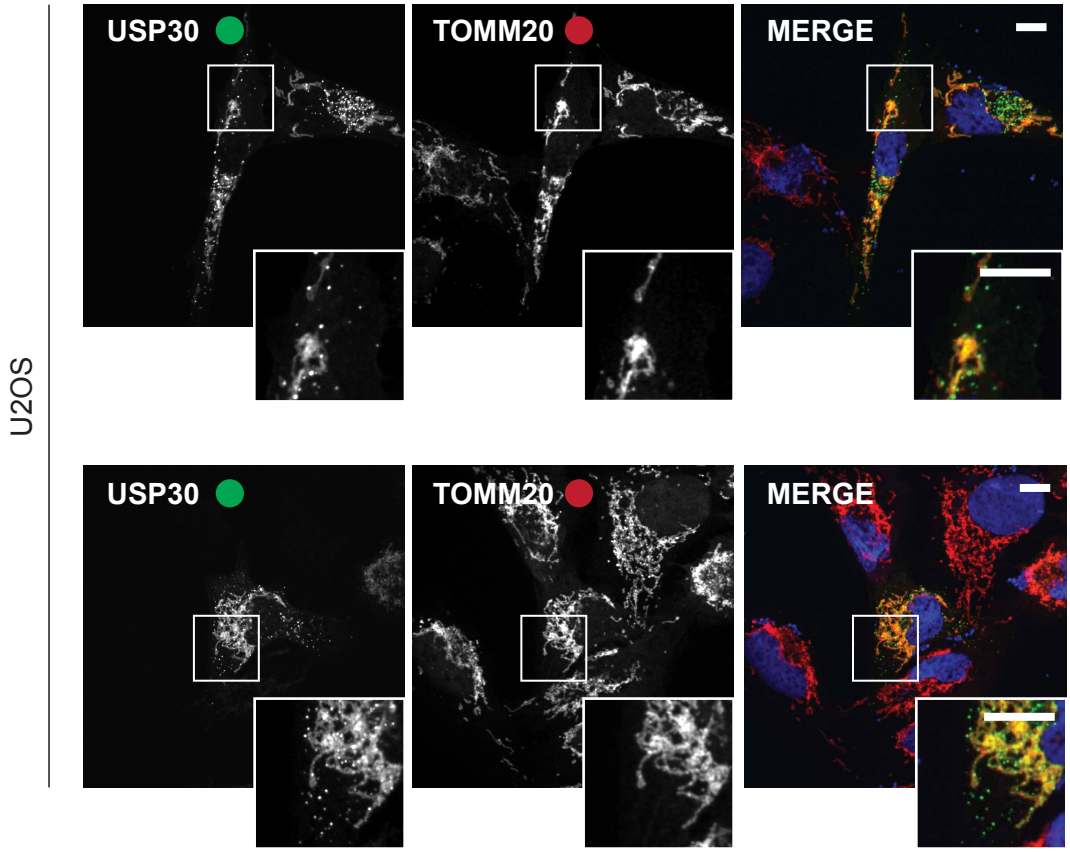

Figure 4.6: USP30-GFP localises to mitochondria in U2OS cells.

U2OS cells were transfected with USP30-GFP for 24h then fixed and stained for TOMM20 using an Alexa Fluor 488-coupled secondary antibody. The coverslips were mounted using Mowiol mixed with DAPI. Images were acquired sequentially using a 3i spinning disk confocal microscope with a 63x objective and a sCMOS camera. Scale bar: 10µm. Data from a single experiment.

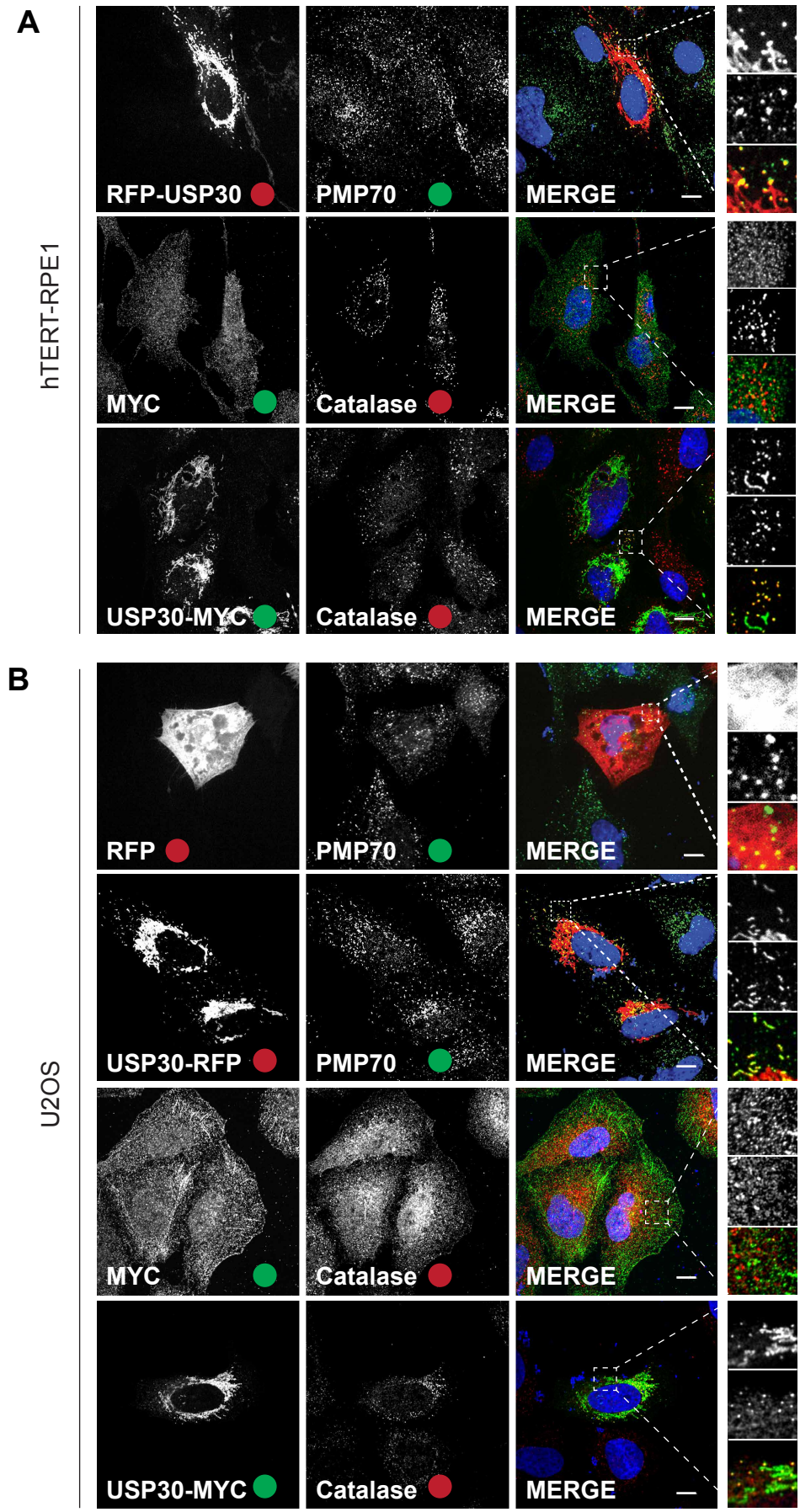
A
hTERT-RPE1
RFP-USP30
PMP70
MERGE
MYC
Catalase
MERGE
USP30-MYC
Catalase
MERGE
B
U2OS
RFP
PMP70
MERGE
USP30-RFP
PMP70
MERGE
MYC
Catalase
MERGE
USP30-MYC
Catalase
MERGE

Figure 4.7: A pool of USP30 localises to peroxisomes in hTERT-RPE1 and U2OS

A) hTRERT-RPE1 cells and **B)** U2OS cells were transfected with RFP, USP30-RFP, pCDNA3.1 and USP30-MYC for 24h then fixed and stained with antibodies targeting MYC with Alexa Fluor 488-coupled secondary antibody and/or peroxisomal proteins: PMP70 or Catalase with Alexa Fluor 488 and Alexa Fluor 594-coupled secondary antibodies respectively. The coverslips were mounted in mowiol containing DAPI. Images were acquired sequentially using a 3i spinning disk confocal microscope equipped of a sCMOS camera and a 63x objective lens. Scale bar: 10µm. Data from a single experiment.

To control for the non-specific punctate staining coming from the USP30 antibody, I seeded two sets of SH-SY5Y cells, one transfected with non-targeting siRNA (NT1) and the other with USP30 targeted siRNA (D3) and then used PMP70 as a peroxisomal marker (**Figure 4.8**),(Marcassa et al., 2018). I discovered that a pool of endogenous USP30 colocalised with PMP70.

I then wondered how USP30 was localised to peroxisome. I assessed whether it was dependent on its catalytic activity. I transfected hTERT-RPE1 cells with either USP30-GFP or with catalytically dead USP30 C77S-GFP and cherry-SKL (**Figure 4.9A**). The SKL sequence is the most common peroxisomal targeting signal involved in peroxisomal matrix import and can be used to target fluorophores to mature peroxisomes. In parallel, I transfected hTERT-RPE1 with USP30-MYC or USP30 C77S-MYC and probed the fixed cells with anti-MYC and Catalase antibodies. I transfected pCDNA3.1 as control for non-specific MYC staining (**Figure 4.8C**),(Marcassa et al., 2018). In both sets of experiments, I found that catalytically inactive USP30 localised to peroxisomes. We thus concluded that USP30 localised to peroxisomes independently on its catalytic activity.

As it is the first time that USP30 has been reported on peroxisomes we went on to characterise its peroxisomal function.

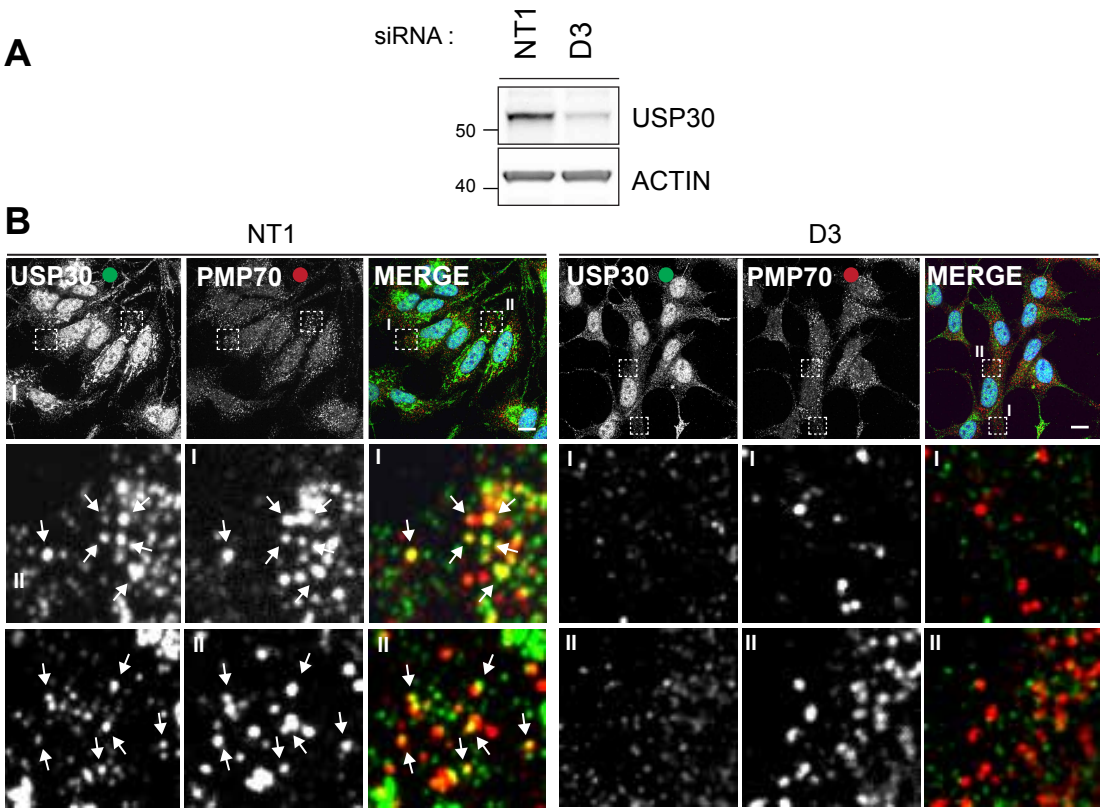

Figure 4.8: Endogenous USP30 localises to peroxisomes in SH-SY5Y cells.

Duplicate samples from the experiment shown in Figure 4.5. SH-SY5Y cells were transfected with non-targeting siRNA (NT1) and with siRNA targeting USP30 (D3) for 144h (two hit knockdown). **A)** Representative blot (reproduced from figure 4.5). **B)** The cells were then fixed and probed for USP30 and PMP70 using Alexa Fluor 488 and Alexa Fluor 594-coupled secondary antibodies respectively. The coverslips were mounted in mowiol containing DAPI. Images were acquired sequentially using a 3i spinning disk confocal microscope with a 63x objective and a sCMOS camera. Scale bar: 10µm. Representative images from two experiments.

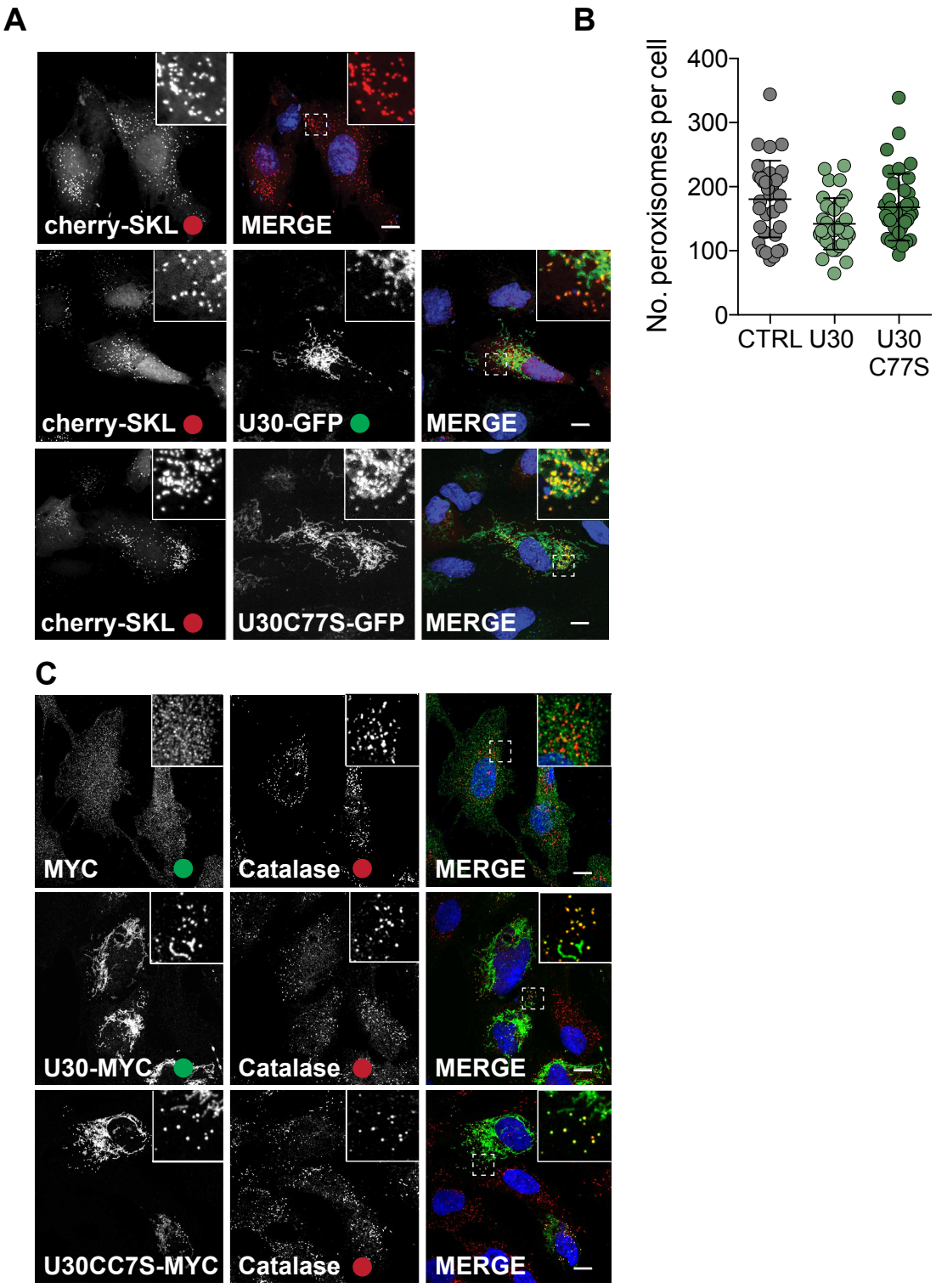

Figure 4.9: USP30 localises to peroxisomes independently of its catalytic activity.

hTRERT-RPE1 cells were transfected with **A)** cherry-SKL alone (UNT) or with USP30 -GFP or USP30 C77S-GFP or **C)** with pCDNA3.1, USP30-MYC and USP30 C77S-MYC for 24h. All cells were fixed and for **C)** probed for MYC and Catalase using Alexa Fluor 488 and Alexa Fluor 594-coupled secondary antibodies respectively. All coverslips were mounted in mowiol containing DAPI. Images were acquired sequentially using a 3i spinning disk confocal microscope with a 63x objective and a sCMOS camera. Scale bar: 10µm. **B)** Quantification of the no. of peroxisomes (SKL

puncta) per cell using the Fiji's Analyse Particles plugin (35 cells analysed). Representative images from two experiments.

4.3 Role of USP30 in SH-SY5Y cells

4.3.1 USP30 regulates pexophagy

As USP30 regulates mitochondrial autophagy, my colleagues and I wondered if analogously USP30 could regulate peroxisomal autophagy (pexophagy). Supporting this theory, Cunningham *et al*., had found that pexophagy in HEK293 cells was decreased by two-fold when overexpressing for two days a PMP34-USP30 chimeric protein, in which the human USP30 DUB domain was subcloned downstream of the peroxisomal membrane protein PMP34 to target it artificially to peroxisomes (Cunningham et al., 2015).

As a preliminary study, I assessed whether the overexpression or depletion of USP30 would affect peroxisome number or mass. I first used the experiment shown in Figure 4.9 to count the number of cherry-SKL positive peroxisomes in hTERT-RPE1 cells transfected with wild-type or catalytically inactive USP30. Surprisingly, I found that overexpressing USP30, but not its catalytic mutant USP30 C77S, reduced by 20% the average number of SKL-cherry bearing peroxisomes per cell (**Figure 4.9B**). On the other hand, depletion of USP30 in both U2OS and hTERT-RPE1 cells, did not induce any obvious change in abundance of peroxisomal proteins by western blotting (**Figure 4.10**).

In order to measure pexophagy in a direct manner, my colleague Aitor Martinez-Zarate generated a pexophagy reporter by flanking the pH sensitive Keima fluorophore with a SKL sequence. Similar to mitophagy, during pexophagy peroxisomal membrane proteins are ubiquitinated by an E3, such as PEX2, and recognised by the LC3-adaptor proteins NBR1 and p62. Peroxisomes are then engulfed in autophagosomes and safely disposed in lysosomes for degradation (Sargent et al., 2016; Zhang et al., 2015). The excitation of the SKL-Keima probe will then shift from 445nm in healthy peroxisomes to 561nm in acidic autolysosomes.

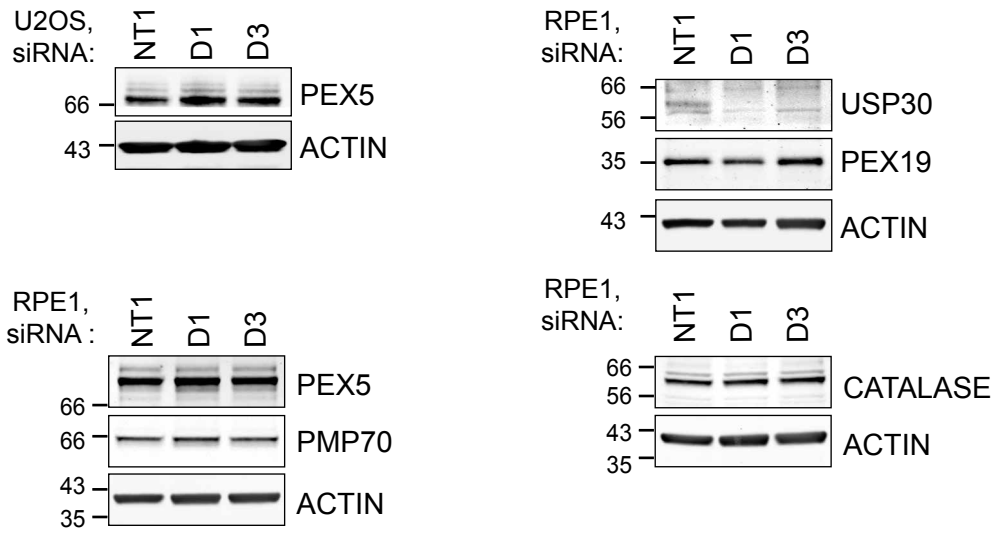

Figure 4.10: USP30 depletion does not affect peroxisomal protein expression.

U2OS and hTERT-RPE1 cells were knocked down for 72h with 40nM siRNA targeting USP30 (D1 and D3); a non-targeting siRNA was used as a control (NT1). The cells were lysed in RIPA and immunoblotted for peroxisomal proteins. Data from a single experiment.

My colleague Elena Marcassa measured a two-fold increase in pexophagy events in hTERT-RPE1 cells depleted of USP30, either by knockdown or knockout (Marcassa et al., 2018). This phenomenon was rescued with the reintroduction of wildtype USP30 but not with catalytically inactive USP30C77S, indicating that pexophagy is repressed by USP30's catalytic activity. Elena further transfected hTERT-RPE1 overexpressing Keima-SKL with ATG7 and USP30-targeting siRNA oligos. She found that the pexophagy increase was dependent on ATG7 and consequently dependent on the autophagy machinery (Marcassa et al., 2018).

4.3.2 Regulation of mitophagy in SHSY5Y mito-QC cells by USP30

Mitophagy has largely been studied in the context of Parkin over-expression and harsh depolarisation, but what is the contribution of PINK1, Parkin and USP30 to basal mitophagy?

4.3.2.1 Preliminary results indicate that USP30, Parkin and PINK1 depletion minimally affects basal mitophagy in SH-SY5Y cells.

I made use of the SH-SY5Y mito-QC cells to quantify the number of mitophagy events occurring after USP30 depletion (**Figure 4.11**). After 144h of siRNA transfection, I achieved 80-87% of depletion of USP30. The knockdown efficiency was increased by seeding two-fold less cells than I previously had. I obtained a ~30% rather than 60% confluency on the day of the transfection. I did not observe any significant changes between the number of mitolysosomes generated with siUSP30 oligos (D1 and D3) and the control siRNA (NT1), (**Figure 4.11.C**). However, I did observe a clear trend towards an increase in the number of cells having more than five mitolysosomes. On average, 1.3% of the control NT1 transfected cells had more 5 mitolysosomes against 6.7 and 5.7% of D1 and D3 transfected cells respectively. The average number of mitolysosomes in SH-SY5Y mito-QC cells is very low with 84% of the cells having zero or one mitolysosome in the absence of a mitophagy trigger. In comparison, hTERT-RPE1 and U2OS cells on average have ten mitolysosomes per cells under basal conditions. In those cells, Elena observed a doubling of the number of mitolysosomes after 72 hours of USP30 depletion (Marcassa et al., 2018).

I had also transfected SH-SY5Y mito-QC cells with siRNAs targeting PINK1 or Parkin with or without co-transfection of USP30-targeted siRNA oligos (**Figure 4.12**). Neither Parkin nor PINK1 depletion significantly affected the number of mitolysosomes present in SH-SY5Y cells (**Figure 4.12C-D**). Again, when looking at the percentage of cells with more than 5 mitolysosomes, I detected a small trend towards an increase of mitophagy with USP30 depletion and no changes with PINK1 or Parkin depletion (NT1: 6%, D1: 11%, Parkin: 7%, PINK1: 7%).

It is possible that basal mitophagy events are too rare in SH-SY5Y cells to be studied by manual image analysis. Moreover, the knockdown efficiency in these cells is rather poor and more so in this experiment (47% for Parkin, 69% for PINK1 and 59% for USP30; Experiment performed prior optimising the cell density); rendering any subtle effect of protein depletion even harder to detect.

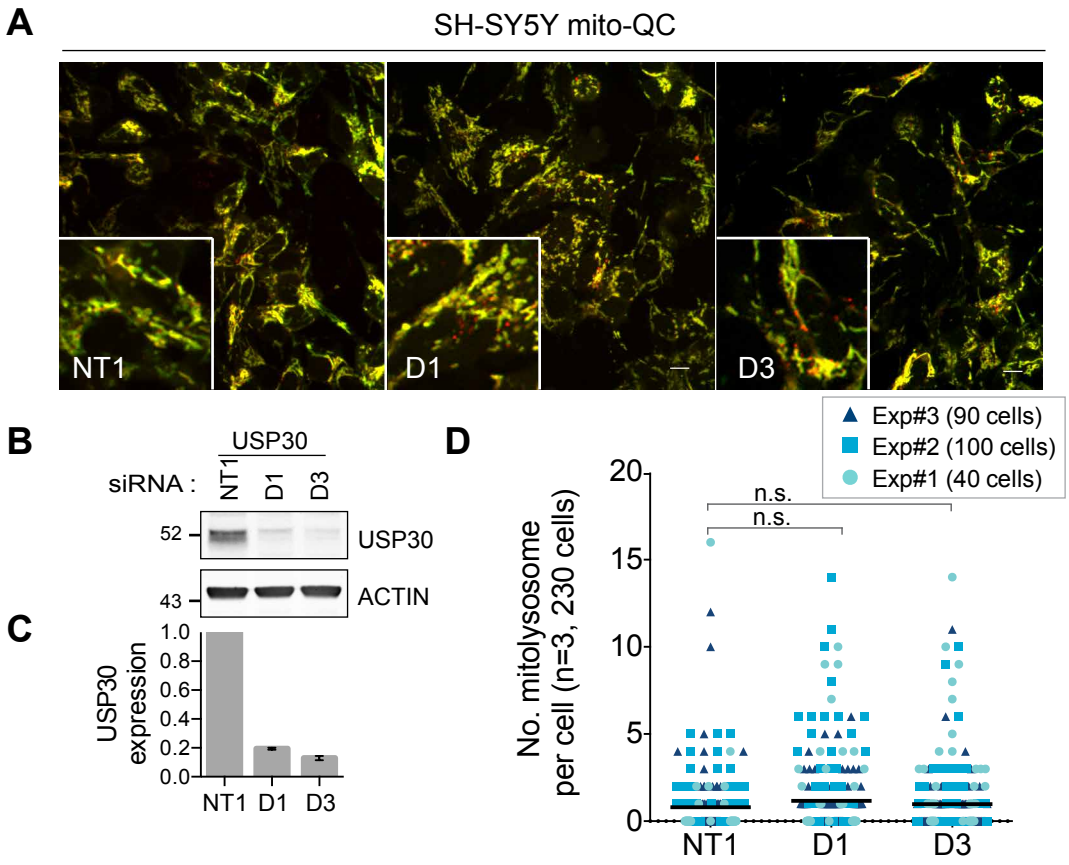

Figure 4.11: USP30 depletion minimally affects basal mitophagy in SH-SY5Y cells.

A) SH-SY5Y mito-QC cells were subjected to a "two hits" transfection protocol over 144h (72h each) using siRNA oligos targeting USP30 (D1 and D3) or non-targeting siRNA (NT1). Images were acquired sequentially using a 3i spinning disk confocal microscope with an EMCCD camera and a 63x objective lens. Scale bar: 10µm. **B)** Representative western blot from RIPA lysates. **C)** USP30 expression was normalised to Actin and to NT1. The analysis was performed using ImageStudio. **D)** Graph representing the number of mitolysosomes per cell. The images were quantified using the Analyse particle plugin on FIJI. Data from three experiments. Analysis: one-way ANOVA with Tukey's multiple comparison test.

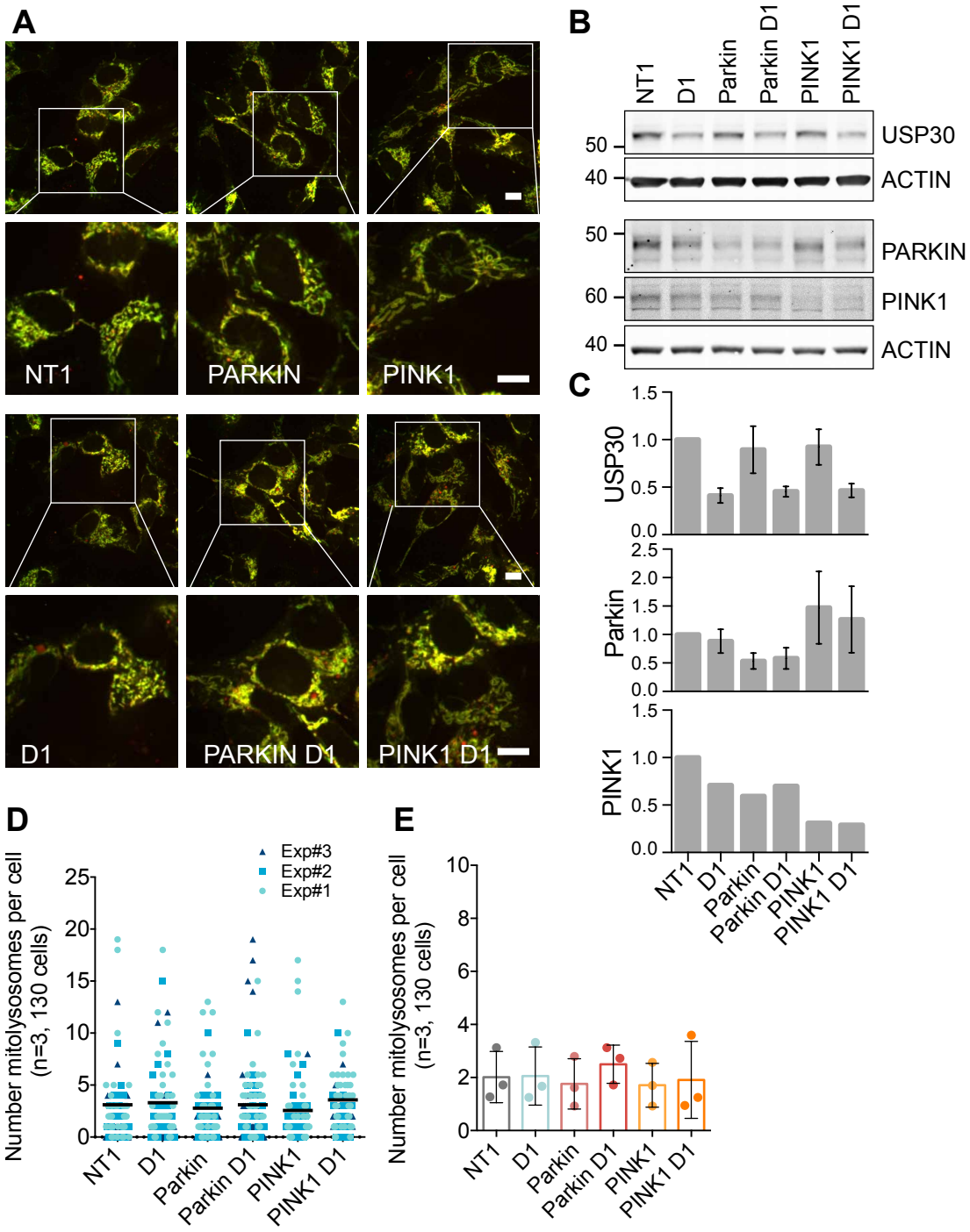

Figure 4.12: PINK1 and PARKIN depletion does not affect basal mitophagy in SH-SY5Y mito-QC cells.

A) SH-SY5Y mito-QC cells were transfected with individual USP30 (D1) and/or PARKIN or PINK1-targeting siRNA oligos for 144h. Non-targeting (NT1) oligos were used as a control. Images were acquired sequentially using a 3i spinning disk confocal microscope with an EMCCD camera and a 63x objective lens. Scale bar: 10µm. **B)** A parallel set of cells was treated for 1h with Antimycin and Oligomycin (AO, 1µM) to induce PINK1 accumulation and reveal the knockdown efficiency. The cells were lysed in NP40 lysis buffer. **C)** The relative protein expression of USP30, Parkin and PINK1 was quantified using ImageStudio and normalised to Actin. Error bars: mean ± SD. **D and E)** The number of mitolysosomes per cell was quantified using the Analyse particle plugin on FIJI. **D)** Graph shows the number of mitolysosomes for

each cell and per experiment. **E)** Graph shows the mean number of mitolysosome per cell (n=3 experiments). Error bars: mean ± SD.

Another potential flaw with this experiment, is the use of the FIS1 targeting sequence for the mito-QC probe. FIS1 localises to and regulates the fission of both mitochondria and peroxisomes, and thus could principally target the mito-QC probe to both organelles (Koch et al., 2005). The Ganley lab, reported that mito-QC is almost exclusively on mitochondria in SH-SY5Y cells, by immunostaining the cells against ATP synthase (Allen et al., 2013). However, a few mito-QC punctate which could correspond to peroxisomes did not appear in the ATP synthase staining. They also stained MEF and mice mito-QC heart tissues against the peroxisomal protein PMP70 and did not detect any overlap between PMP70 and mito-QC. I generated a blue peroxisomal probe, TagBFP-SKL to verify this hypothesis and transfected this construct into SH-SY5Y mito-QC cells (**Figure 4.13**). I found that even though the vast the majority of mitoQC localised to mitochondria, a small proportion of it was co-localising with TagBFP-SKL.

Elena Marcassa took advantage of the better transfection efficiency and the increased levels of basal mitophagy in hTERT-RPE1 and U2OS cells to demonstrate that basal mitophagy was unaffected by PINK1 or Parkin depletion using both the mito-QC and mt-Keima (targeted to the mitochondrial matrix via COX VII's targeting signal) reporters. Elena also revealed that the USP30-dependent enhancement of mitophagy was abolished by PINK1 depletion but unaffected by Parkin (Marcassa et al., 2018).

To circumvent the difficulties I had studying basal mitophagy in SH-SY5Y mito-QC cells, I have generated USP30 knockout cells and characterised USP30-specific inhibitors to use in combination with mass spectrometry. These will be further discussed in Chapter V.

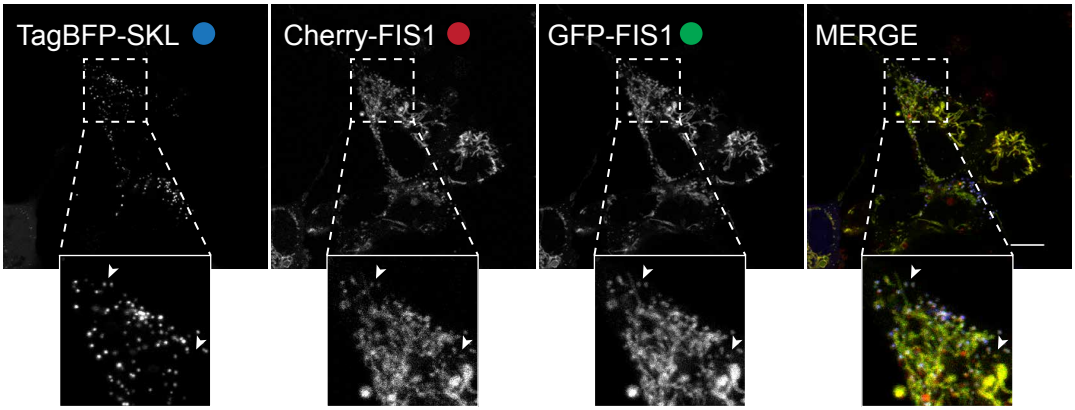

Figure 4.13: The mito-QC reporter also localises to peroxisomes.

SH-SY5Y mito-QC (mCherry-GFP-FIS1$_{101-152}$) cells were transfected for 48h with TagBFP-SKL. The cells were acquired sequentially on a Zeiss LSM 800 confocal. Scale bar: 10µm. Representative images from two experiments.

4.3.2.2 USP30 depletion increases depolarisation induced mitophagy in SH-SY5Y cells

I next assessed whether USP30 was involved in AO or DFP-induced mitophagy in cells expressing endogenous Parkin. I transfected SH-SY5Y mito-QC cells with USP30-targeting (D1) or non-targeting (NT1) oligos and treated them for 24h with AO or DFP (**Figure 4.14**). USP30 depletion significantly increased the number of cells undergoing mitophagy (> 3 mitolysosomes per cell) in the AO condition (**Figure 4.14B**). However, USP30 did not affect DFP-induced mitophagy. We propose that DFP-mediated mitophagy is ubiquitin-independent. An additional indication for this is the fact that we observed MFN2 ubiquitylated species in SH-SY5Y cells treated with AO but not with DFP (**Figure 4.14C**). My colleague Elena Marcassa also found a two-fold increase in the number of mitolysosomes in U2OS mito-QC cells treated with DFP for 24h but likewise she could not detect any ubiquitylated species of MFN1 after 2, 4 or 24 h of treatment (data not shown).

Similarly, in hTERT-RPE1-YFP-Parkin, she did not detect ubiquitylated MFN1, MFN2, FIS1, TOMM20 nor phospho-ubiquitin, nor PINK1 accumulation following 1h, 2h or 6h DFP treatment in comparison to AO induced mitophagy (data not shown). This is consistent with the study by Ganley and colleagues, who generated the SH-SY5Y mito-QC cells and first described that DFP-induced mitophagy is independent of PINK1 and Parkin (Allen et al., 2013).

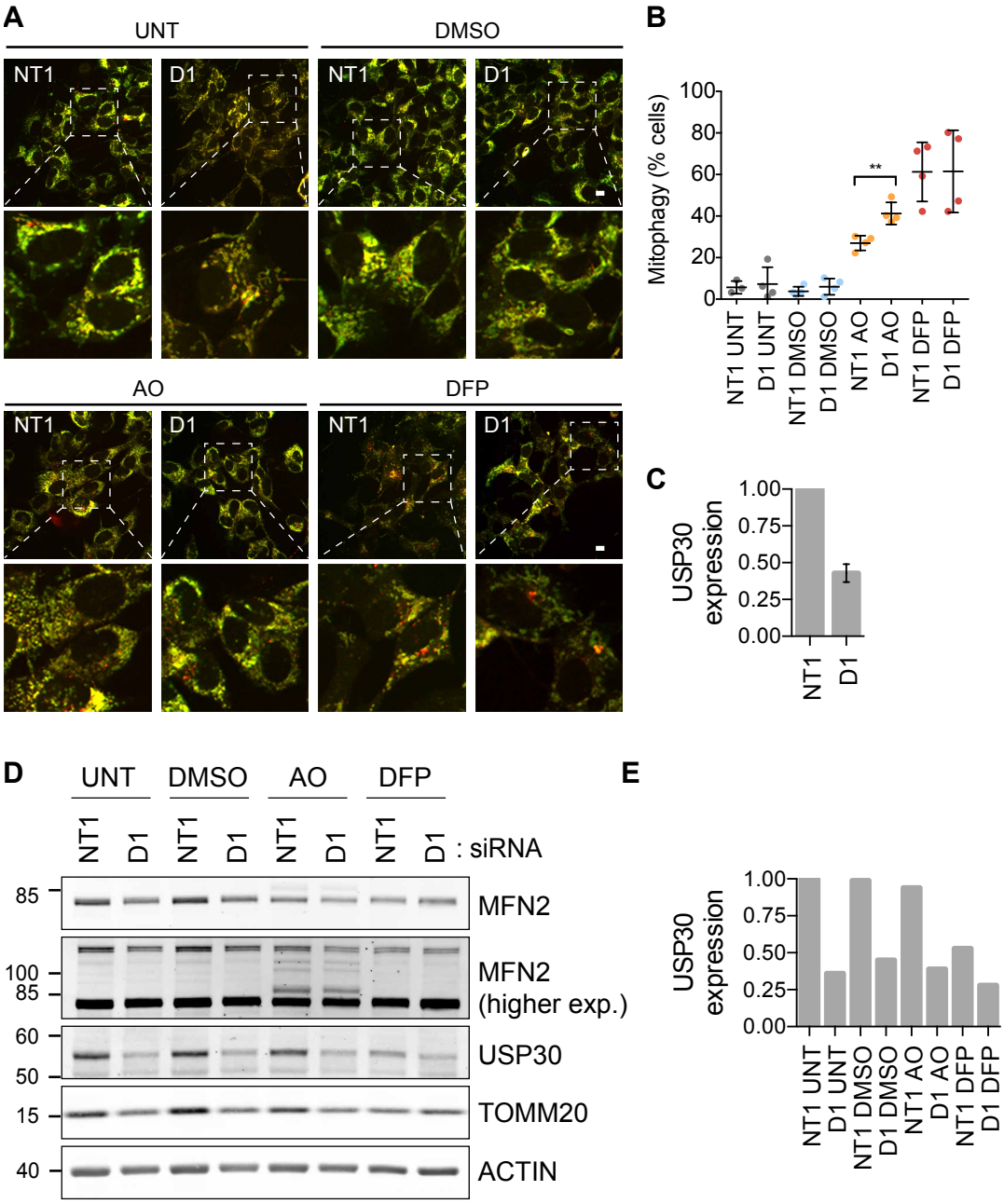

Figure 4.14: USP30 depletion sensitises SH-SY5Y mito-QC cells to AO-induced mitophagy.

A) SH-SY5Y mito-QC cells were transfected with either non-targeting (NT1, 40nM) or USP30-targeted (D1, 40nM) siRNA oligos for 72h. They were then treated for 24h with water (UNT), DMSO, Antimycin and Oligomycin (AO, respectively 1 and 10μM) and Deferiprone (DFP, 1mM). Images were acquired sequentially using a 3i spinning disk confocal microscope with an EMCCD camera and a 40x objective. Scale bar: 10μm. **B)** Graph shows the percentage of cells undergoing mitophagy. A cell having more than 3 mitolysosomes is considered as undergoing mitophagy. Analysis: two-way ANOVA with Bonferroni's multiple comparison test. **: $p < 0.01$. Results from 4 experiments; 110 cells were quantified per experiment. Error bars: mean ± SD. **C)** USP30 knockdown efficiency was assessed by western blotting for each experiment. USP30's expression was normalised to Actin and NT1. **D)** The experiment in A was performed in duplicate and one set was analysed by western blot. **E)** USP30 expression was quantified and normalised to both actin and NT1 UNT.

4.4 Discussion

4.4.1 USP30 localises to peroxisomes

Employing immunofluorescence, I provided the first line of evidence showing that a pool of endogenous USP30 was localised at peroxisomes. I also demonstrated that overexpressed USP30 colocalises with both PMP70 (peroxisome membrane) and Catalase (peroxisome matrix). These observations were further supported by a density gradient analysis performed in HepG2 cells by our colleagues from Markus Islinger's lab (University of Heidelberg, Germany). They found USP30 in both peroxisomal and mitochondrial fractions. USP30 migrated across the gradient in a similar fashion as to glutathione-S-transferase κ (GSTK1), another protein shared between the two organelles (Marcassa et al., 2018).

I reported that USP30's localisation to peroxisomes was independent from its catalytic activity. Employing USP30 truncation mutants, my colleagues Andreas Kallinos and Elena Marcassa assessed whether USP30 had a specific peroxisome targeting sequence. They found that the truncated mutant USP30(1-53) (TM only) was solely localised to peroxisomes (PMP70) and not to mitochondria (TOMM20), whereas USP30(1-68) (TM with its downstream polybasic region) was associated with both organelles and USP30Δ1-53 was diffused in the cytosol. We reasoned that USP30 localisation to peroxisomes required the transmembrane domain (35-54 a.a.) and was independent of the downstream polybasic region (59-64 a.a.). USP30 has therefore distinct targeting motifs for mitochondria and peroxisomes (Marcassa et al., 2018).

Interestingly, the transmembrane domain of USP30 is preceded by three positive residues interspaced by hydrophobic residues (Nakamura and Hirose, 2008). To test whether those positive charges intervene in USP30's localisation, Andreas Kallinos neutralised them by point mutations as described by Nakamura and Hirose (KRmut1),(Nakamura and Hirose, 2008). By immunofluorescence assay he observed a reduced co-localisation between USP30 KRmut1 and PMP70 in comparison with USP30 and PMP70. This could indicate that the basic residues preceding the transmembrane domain are involved in the targeting of USP30 to peroxisomes.

It remains to be elucidated what pathway USP30 follows to be integrated into the peroxisomal membrane. There are two main paths for peroxisomal

membrane sorting: (1) the direct import route (Class I), used by most peroxisomal membrane proteins (PMP), where PEX19 acts as chaperone and forms a soluble complex with PMPs and recruits them to peroxisomes by binding to PEX3, or (2) the indirect import pathway (Class II) where PMPs migrate from the ER to the peroxisome with the help of PEX16 and PEX19 (Farré et al., 2019; Liu et al., 2016).

Many proteins shared between peroxisomes and mitochondria are tail anchored (TA) proteins, with a C-terminal hydrophobic transmembrane domain. Such examples are FIS1, DNM1L, MAVS, MIRO1/2, Bcl-xL, Bcl-2 and others (Koch et al., 2005; Dixit et al., 2010; Costello et al., 2017). Those proteins can either be produced in the cytosol and get directly targeted to peroxisomes via the PEX19-direct pathway or can get integrated into the ER via the GET complex and then sorted to peroxisome using the PEX16-indirect pathway (Schuldiner et al., 2008; Yagita et al., 2013; Mateja et al., 2015; Liu et al., 2016). Characteristics of peroxisomal targeted TA proteins are: a moderately hydrophobic transmembrane domain followed by a highly charged tail (Costello et al., 2017). Although, USP30's transmembrane domain is N-terminal, it is reminiscent of peroxisomal TA proteins'.

Shortly after our publication, Riccio *et al.*, suggested that USP30 uses the PEX16 dependent pathway to translocate to peroxisomes. They demonstrate that overexpressing an ER-targeted PEX16 (sa-PEX16) in COS7 cells relocalises overexpressed USP30 and FIS1 but not TOMM20 to the ER; thus demonstrating that PEX16 can bind to USP30. Endogenous PEX16 could therefore target USP30 to peroxisomes via the ER (Riccio et al., 2019). Intriguingly, it has been reported that neutralising the PBR of USP30 (KRmut2) results in a ER localised protein (Nakamura and Hirose, 2008). Andreas reproduced this experiment and found that USP30 KRmut2 neither co-localised with PMP70 nor with TOMM20 but did overlap with Calreticulin, a protein primarily residing at the ER.

We sought to assess whether USP30 localisation to peroxisomes was dependent on PEX19 by knocking it down in hTERT-RPE1 cells. However, we observed by immunofluorescence that PEX19 knockdown resulted in a diffused catalase staining. We concluded that depleting cells of PEX19 most

likely interfered with peroxisome maturation and thus prevented any further analysis.

MUL1 (also reported as MAPL), another protein shared by mitochondria and peroxisomes can be rerouted from mitochondria to peroxisomes via mitochondria derived vesicles. Those vesicles are transported to peroxisomes by the VPS35-retromer complex (Braschi et al., 2010; Neuspiel et al., 2008). We verified if USP30 was using this pathway by knocking down VPS35 in hTERT-RPE1. In the absence of VPS35, newly transfected USP30 was still distributed on both peroxisomes and mitochondria (Marcassa et al., 2018).

Finally, a recent study described another route for protein redistribution from the mitochondrial network to the peroxisome. Koyano *et al.*, demonstrated that upon mitochondrial stress, MARCH5 (also known as MITOL) gets ubiquitylated by Parkin, then extracted from mitochondria by the p97/VCP complex, and redistributed to peroxisomes via PEX3 and PEX19. They showed that this pathway is dependent on PINK1 and Parkin and that the mitochondrial localisation is a prerequisite for secondary peroxisome targeting (Koyano et al., 2019b). We can rule out this pathway to explain USP30 targeting to peroxisome, as Aitor showed that newly transfected USP30 localises to peroxisomes in the absence of mitochondria in hTERT-RPE1-YFP-Parkin cells treated for 24 h with AO (Marcassa et al., 2018).

From the current data, it seems that USP30 is either directly recruited from the cytosol to the peroxisomes by PEX19 or is targeted to peroxisomes via the ER with the help of PEX16, as proposed by Riccio *et al*.

4.4.2 USP30 prevents the autophagic degradation of peroxisomes

We discovered that peroxisomal USP30 was regulating basal pexophagy. When Elena depleted USP30 from hTERT-RPE1 cells she measured a two-fold increase in pexophagy indicating that USP30 was repressing the process (Marcassa et al., 2018). She found that this process was PINK1 and Parkin-independent but we did not identify the key peroxisome substrates for USP30 nor did we discover the E3 ligase which USP30 opposes in basal pexophagy.

Counterintuitively, I found that overexpressing catalytically active USP30 reduced the number of cherry-SKL (matrix) positive peroxisomes per hTERT-RPE1 cell. USP30 overexpression thus appears to block peroxisome

biogenesis or maturation, which are accompanied by the import of newly synthesised matrix protein (Farré et al., 2019). USP30 could also directly regulate peroxisomal protein import as it was just recently reported to control mitochondrial protein import (Phu et al., 2020) (further discussed in Chapter V). One other possible explanation could be that pexophagy is actively compensated by peroxisome biogenesis. Thus, when pexophagy is inhibited by the over-expression of USP30, peroxisome biogenesis would be downregulated via negative-feed-forward mechanism to maintain the number of peroxisomes per cell relatively stable. One way to assess this would have been to compare by immunofluorescence the number of peroxisomes having imported newly synthesised cherry-SKL against the total number of peroxisome (PMP70 staining), upon USP30 overexpression. In line with this hypothesis, Riccio and colleagues found that overexpressing USP30-FLAG in HeLa cells did not affect the number of PMP70-labeled peroxisomes.

Pexophagy can be triggered by hypoxia, oxidative stress or nutrient deprivation, which also induce global autophagy, and has been broadly studied under those conditions (Eberhart and Kovacs, 2018). Starvation upregulates the expression of the peroxisomal E3 RING E3 ligase PEX2, which then ubiquitylates peroxisomal proteins such as PEX5 and PMP70 to trigger pexophagy (Sargent et al., 2016). ROS triggers the recruitment of the kinase ATM to peroxisomes in a PEX5-dependent manner. ATM then supresses mTORC1 and phosphorylates PEX5, which gets subsequently ubiquitylated and recognised by the adaptor protein p62 causing the autophagosomal engulfment of peroxisomes (Zhang et al., 2015).

PEX2 and PEX5 are also key players in peroxisomal matrix import. PEX5 is the carrier for most matrix proteins and PEX2 is an essential component of the importomer complex (see review: (Farré et al., 2019)). Interfering with either protein would directly affect import of newly synthesised matrix proteins and thus impede peroxisomal maturation. Thus, the depletion of endogenous PEX2 would give inconclusive results as to its function in basal pexophagy.

Neither by straightforward western blotting, nor by immunoprecipitation, could we observe an increase in basal ubiquitylation of PEX5 in USP30 knockout cells (Marcassa et al., 2018). However, Riccio et al. found that in the context of nutrient starvation, USP30 depletion increased PEX5 and PMP70

ubiquitylation. They further demonstrated that USP30 was opposing PEX2 in starvation-induced pexophagy (Riccio et al., 2019).

USP30 may thus suppress both basal and starvation induced pexophagy and deubiquitylate PEX2 substrates. This may then prevent the recruitment of pexophagy adaptors such as NBR1 (Riccio et al., 2019; Sargent et al., 2016; Deosaran et al., 2013). USP30 is thus the first known DUB to regulate pexophagy.

As mitochondria, peroxisomes are fundamental to the health and proper functioning of cells. In mammals, peroxisomes function in many metabolic pathways, such as fatty acid oxidation, phospholipid biosynthesis, oxygen and reactive nitrogen species degradation, amino acid catabolism and many others (Smith and Aitchison, 2013; Wanders and Waterham, 2006). Interestingly, mitochondria and peroxisomes are tightly linked together, both functionally and physically. They co-regulate fatty acid oxidation, scavenge peroxide and reactive oxygen species (Mohanty and McBride, 2013; Wanders, 2013). These organelles also share signalling pathways such as antiviral immunity via MAVS (Dixit et al., 2010). Recently, it was reported that new peroxisomes are hybrids of both ER and mitochondria derived pre-peroxisomes (Sugiura et al., 2017). Now we show that they share similar quality control mechanisms, pexophagy and mitophagy, both regulated by USP30.

Impairment of peroxisome homeostasis is involved in severe developmental brain disorders classified as peroxisome biogenesis disorders (PBD) and single peroxisomal enzymes deficiencies. Although the peroxisome loss observed in this disease was first attributed to defective peroxisome biogenesis mechanisms, Peter Kim's group revealed that the most common mutation in PBD, PEX1-G843D, resulted in an increase of peroxisome degradation by pexophagy (Law et al., 2017). Using various inhibitor of autophagy flux, they were able to reverse the peroxisome loss. Once they discovered that USP30 was a regulator of pexophagy, they assessed its effect in patient derived PEX1-G843D fibroblast and revealed that the overexpression of USP30 was able to recover the peroxisomal pool (Riccio et al., 2019).

Peroxisome dysfunctions are also thought to be involved in ageing and in the progression of age-related neurodegenerative diseases such as Alzheimer's

disease (Islinger et al., 2018; Trompier et al., 2014). This highlights the need to better understand peroxisomal quality control mechanisms such as pexophagy and once more point towards USP30 as an interesting drug target.

4.4.3 USP30 regulates basal and induced mitophagy

My results on basal mitophagy in SH-SY5Y cells were inconclusive due to the poor knockdown efficiency I achieved and the low level of mitophagic flux (= low number of mitophagy events per time period per average cell). However, it is still interesting to note that reducing the levels of PINK1 and Parkin, for which knockdown efficiency was of 69% and 47% respectively, did not decrease the number of basal mitophagy events. My colleague Elena Marcassa made the same observation in U2OS and hTERT cells (Marcassa et al., 2018). This is in agreement with published data showing that PINK1 and Parkin depletion had no effect on basal mitophagy in animal models such as the mito-QC mouse or the mito-QC and the mt-Keima flies (discussed in Chapter VI) (Lee et al., 2018; McWilliams et al., 2018). However, it is also interesting that knockdown of ATG7 in U2OS-mitoQC cells did not deplete cells of all of their mitolysosomes (Marcassa et al., 2018). Those puncta might therefore not originate from the canonical autophagy pathway but could result from direct mitochondria-lysosome or mitochondria-endosome fusion. Such pathways were described by the Fon and McBride labs. They reported on mitochondrial-derived vesicle (MDV) which deliver specific cargoes to endosomes and lysosomes. The formation of those MDV was independent on DNM1L (DRP1) and on the core autophagy machinery, as it occurred in the absence of Atg5, Rab9 or Beclin. Certain MDVs were shown to specifically transport oxidised cargoes. The formation of those oxidised cargo-specialised MDV was dependent of PINK1 and Parkin (McLelland et al., 2014, 2016; Soubannier et al., 2012b, 2012a), (for reviews see: (Roberts et al., 2016; Sugiura et al., 2014)).

In U2OS and hTERT-RPE1 cells, we revealed that USP30 depletion doubled the number of mitophagy events occurring basally in a PINK1-dependent but Parkin-independent manner (Marcassa et al., 2018). This suggests that another E3 ligase might regulate USP30-mediated basal mitophagy. Multiple E3 ligases have been found either on mitochondria or interacting with

mitochondrial proteins such as ARIH1, HUWE1, MUL1, MARCH5 or FBXO7 (Burchell et al., 2013; Chen et al., 2017; Di Rita et al., 2018; Koyano et al., 2019a, 2019b; Strappazzon et al., 2019; Villa et al., 2017; Yun et al., 2014). I will be assessing their involvement in mitophagy in Chapter V, using USP30 knockout SH-SY5Y cells.

Our current discoveries on basal mitophagy indicate that USP30 opposes PINK1 function. The main substrates of PINK1, outside of Parkin, are ubiquitin moieties on outer mitochondrial membrane proteins (Kane et al., 2014; Kazlauskaite et al., 2014; Koyano et al., 2014; Ordureau et al., 2014). Hence, one could speculate that USP30 removes phospho-ubiquitin. However, USP30 has very low affinity for phospho-ubiquitin and distal phosphorylation of ubiquitin chains prevents USP30 hydrolysis (Gersch et al., 2017; Wauer et al., 2015a). We therefore hypothesise that USP30 acts upstream of PINK1 by deubiquitylating its substrates, this would prevent the ubiquitin-mediated recruitment of autophagy adaptor proteins (Heo et al., 2015; Richter et al., 2016), as well as the phospho-ubiquitin-mediated recruitment and activation of Parkin (Gladkova et al., 2018; Sauvé et al., 2018; Okatsu et al., 2015b).

4.4.4 Concluding remarks

In this chapter, I have described a dual role for USP30 in selective autophagy: USP30 regulates both mitophagy and pexophagy. Its role in mitophagy will be further studied and discussed in Chapter V with the generation and characterisation of USP30 knockout cells and USP30 specific inhibitors.

Chapter 5: A selective inhibitor and knock-out cells enable the identification of new players involved in USP30-mediated mitophagy.

5.1 Introduction

In Chapter IV, I described that USP30 regulates both mitophagy and pexophagy. However, a poor knockdown efficiency in SH-SY5Y cells hindered most experiments. I therefore generated USP30 knockout SH-SY5Y cells using Clustered Regularly Interspaced Short Palindromic Repeats (CRISPR). To strengthen the results obtained with the knockout cells, I also utilised and characterised novel USP30 inhibitors. I employed those tools in proteomics and mitochondrial fractionation experiments to find novel substrates of USP30. I confirmed that TOMM20 was one of USP30's main substrates and that USP30 targets most of PRKN's OMM substrates. Potential substrates include the ribosomal protein RPS20, which is ubiquitylated during ribosome quality control and proteins controlling neural structure, function and differentiation. As described by the Harper and Bingol labs, I noticed that USP30's activity was mainly focussed on the mitochondrial protein import complexes, TOM and VDAC complexes, and detected enhanced ubiquitylation of a few matrix and IMS proteins (GRSF1, HSPD1, HSPE1, MDH2, MTCH2, NDUFB5, PRDX3). This suggests that USP30 has a role in mitochondrial protein import via the TOM and VDAC complexes (Ordureau et al., 2020; Phu et al., 2020). Finally, I found that pUb levels are enhanced in USP30 KO cells which fits with a model whereby USP30 activity limits PINK1 substrate availability.

In this Chapter, I will first describe the CRISPR-Cas9 system I have employed to produce USP30 knockout cells. I will then characterise two USP30 inhibitors and finally report on the mass spectrometry experiments I performed using those tools.

5.2 Generation and description of USP30 knockout SH-SY5Y cells

5.2.1 Generation of USP30 knockout SH-SY5Y cells using the CRISPR-Cas9 system

5.2.1.1 Gene editing using the CRISPR/Cas9 system

CRISPR were first discovered in Archea and bacteria (Ishino et al., 1987; Mojica et al., 1993). They were described as short base repeats separated by spacers. In 2005, scientists finally uncovered the role of the CRISPR repeats: they function as an immune adaptive response against virus and plasmid infection (Mojica et al., 2005; Pourcel et al., 2005).

The CRISPR system is an elegant tool to specifically target virus invasion. Following viral infection, bacteria and archaea integrate segments of viral nucleic acid into their genome. They then use those sequences to later recognise the virus and efficiently destroy viral DNA. This system requires CRISPR-associated genes (Cas) that encode proteins such as nucleases or helicases, which orchestrate the DNA cleavage (Rath et al., 2015).

This sophisticated system has been adapted for genome editing; in 2013, the Zhang lab described a three-component system composed of a CRISPR RNA (crRNA), a transactivating crRNA (tracrRNA) and the Streptococcus pyogenes Cas9 (SpCas9 or Cas9) endonuclease. The crRNA is a guide sequence, which directs the Cas endonuclease to the target genomic DNA. In the original bacteria, the tracrRNA enables the processing of the pre-crRNA into its ~20nt mature form. In this system, the tracrRNA is required for correct cleavage by SpCas9; it is thought to serve as a scaffold sequence for Cas9 binding (Cong et al., 2013; Ran et al., 2013). The crRNA and tracrRNA can be fused and the resulting RNA is termed single-guide RNA (sgRNA). The crRNA guide sequence has to be directly followed by a Proto-spacer adjactent motif (PAM). This short motif is essential for the targeting of the Cas9-crRNA complex to dsDNA **(Figure 5.1)**, (Deveau et al., 2008; Gasiunas et al., 2012).

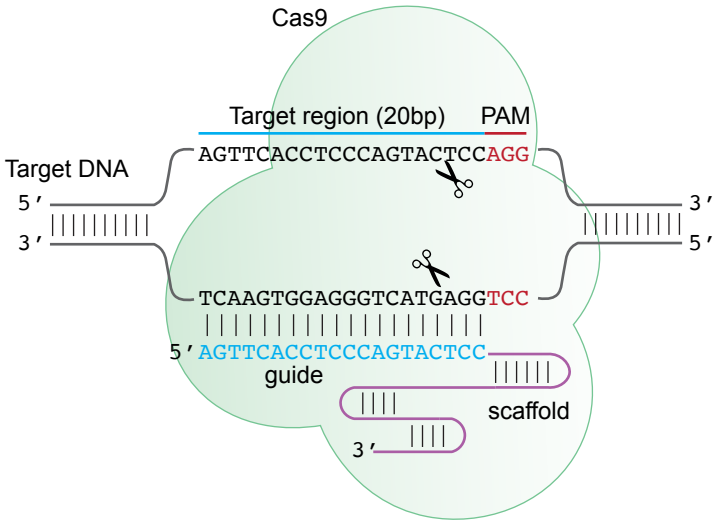

Figure 5.1: Schematic representation of a Cas9 nuclease targeted by its sgRNA.

The S. pyogenes Cas9 nuclease (green) is targeted to genomic DNA by its single-guide RNA (sgRNA). The sgRNA is composed of a 20bp guide sequence (or crRNA, blue), that directs the Cas9 to the target DNA region (overlined in blue), and of a scaffold sequence (or tracrRNA, purple) that enable the Cas9/sgRNA binding. The 3bp PAM sequence (red) adjacent to the target region is required for nuclease activity. Cas9 cleaves both strands of the target DNA ~3bp upstream of the PAM sequence.

Figure adapted from Jinek at al., 2012 and Ran et al., 2013.

Currently, SpCas9 is the most commonly employed Cas endonuclease for genome editing. Indeed, SpCas9 only requires a 3 nucleotide PAM: NGG. This DNA endonuclease contains two nuclease domains, HNH and RuvC. These domains respectively cleave the target- and its antiparallel-DNA strand, to create Double Strand Breaks (DSBs) (Gasiunas et al., 2012; Jinek et al., 2012). These DSBs, trigger two main repair pathways:

- The Non-homologous end joining repair system (NHEJ)
- The homology directed repair system (HDR)

Most DSBs are repaired by the error prone NHEJ system. This repair mechanism directly ligates DNA strands and often causes stochastic insertions or deletions (indels). These indels are of interest when generating knockouts as it causes non-reversible alteration of the gene of interest.

Unlike NHEJ, HDR is highly specific but requires a DNA template to repair DBS. Thus, this system can be used to generate knock-in cells during S-phase (Scully et al., 2019).

5.2.1.2 Targeting Cas9 to USP30's catalytic cysteine

To knockout USP30 in SH-SY5Y cells, I employed Zhang's three component system. I used two sgRNA (sgUSP30-1: 5'-AGTTCACCTCCCAGTACTCC-3'and sgUSP30-2: 5'-TGAAAGCAGGACAGGCAGAC -3') designed by Dr JR Liang. These sgRNA target USP30's USP domain, at exon 3, in the direct vicinity of the catalytic cysteine (C77), **(Figure 5.2)**.

The DSB should then trigger the NHEJ repair pathway and produce indels or a frameshift that will lead to an inactive DUB or cause misfolding and subsequent degradation of the translated protein.

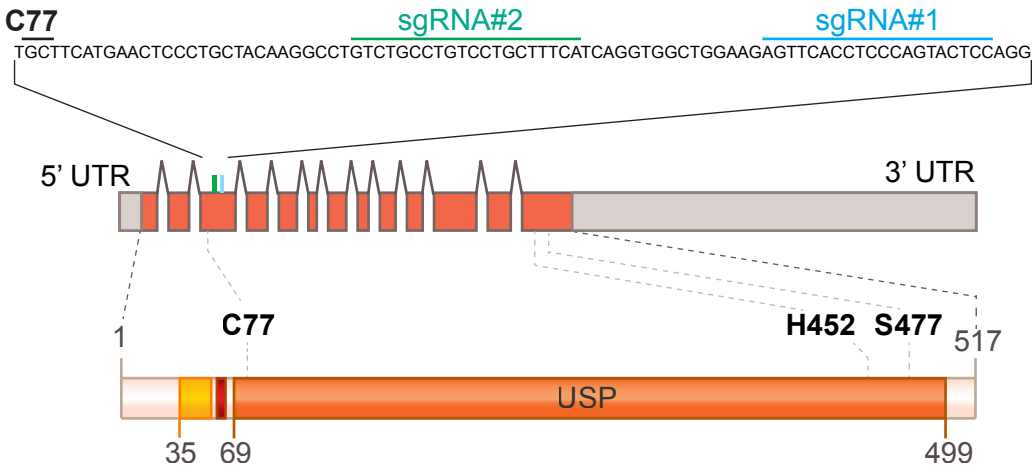

Figure 5.2: Alignment of USP30-targeted sgRNA#1 and #2 with the sequence and exons of USP30 isoform 1.

Schematic representation of the exons of USP30 isoform 1 aligned with the protein domains. The catalytic triad, composed of C77, H452 and S477 is highlighted in bold. Important features of the protein are annotated: the transmembrane domain (yellow), the polybasic region (red) and the USP domain (orange). The regions targeted by sgRNA#1 and 2 are indicated in blue and green respectively.

I employed two plasmids from the Zhang lab to transfect the sgRNAs into SH-SY5Y cells: pX330 and pX458 **(Figure 5.3)**. pX330 contains two cassettes, one encoding for the sgRNA and the other for the Cas9 endonuclease. The Cas9-sgRNA complex is sent to the nucleus by the two nuclear localization signals (NLS) flanking the Cas9. The sgRNA cassette has an insertion site for the guide crRNA and an invariant scaffold tracrRNA **(Figure 5.3A)**. The Morrison lab inserted a puromycin resistance cassette at the 3'end of the Cas9 sequence to select for positively transfected cells (Prof Ciaran Morrison, NUI Galway) **(Figure 5.3B)**. pX458 is a variant of the pX330 plasmid that has an EGFP cassette after the Cas9 sequence **(Figure 5.3C)**. The pX330-puroR and pX458 plasmids containing either sgUSP30-1 or sgUSP30-2 were generated by my colleague Elena Marcassa.

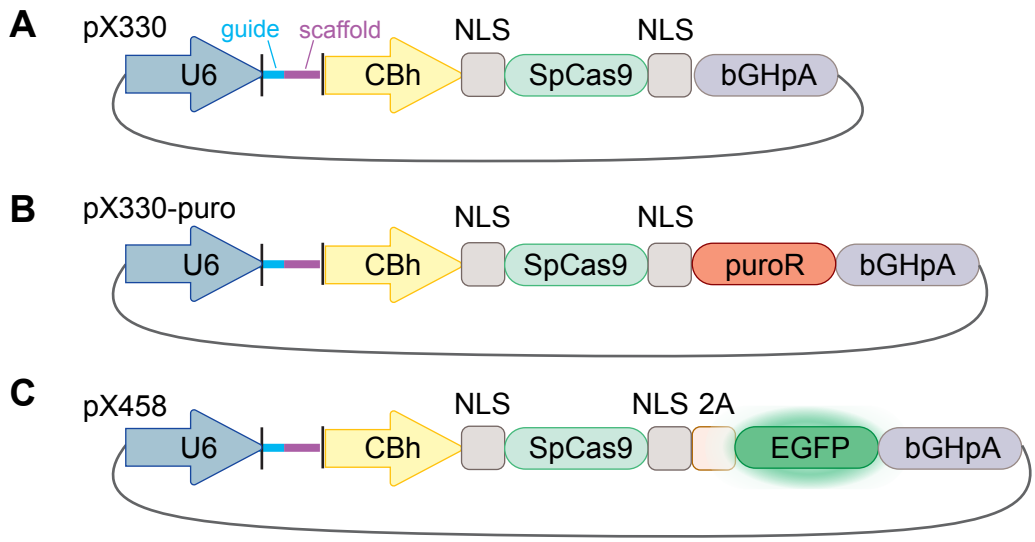

Figure 5.3: Schematic representation of Cas9/sgRNA plasmids used to generate USP30 knockout SH-SY5Y cells.

The two plasmids used to knockout SH-SY5Y cells, **B)** pX330-puro and **C)** pX458, were made from **A)** pX330. pX330 was generated by the Zhang Lab and is formed of two cassettes, one encoding for the sgRNA (blue and purple line) and the other for the S.pyogenes Cas9 nuclease (light green). The sgRNA cassette has an insertion site for the guide RNA sequence (blue) that is followed by the sgRNA scaffold sequence (purple). **B)** pX330-puro contains a puromycin resistance cassette at the 3' end of the Cas9 sequence. **C)** pX458 has an additional EGFP cassette following the Cas9.

Figure adapted from Ran et al., 2013. Abbreviations: U6: U6 promoter; CBh: CMV enhancer + chicken β-actin promoter; NLS: nuclear localisation signal of SV40; SpCas9: S.pyogenes Cas9; 2A: 2A self-cleaving peptide sequence from *Thosea asigna*; bGHpA: bGH poly(A) signal.

5.2.1.3 Generating USP30 knockout SH-SY5Y and SH-SY5Y mito-QC clones.

Ahead of using the pX330-puroR plasmids to knockout USP30, I employed a colorimetric assay to determine the optimal puromycin concentrations required to induce cell death in the non-transfected cells (**Figure 5.4**). I found that 1.5 $\mu g.ml^{-1}$ of puromycin was sufficient to deplete 95% non-resistant cells within 48 hours. Lower doses, such as 1 or 1.25 $\mu g.ml^{-1}$, led to the loss of 75-80% of the population (**Figure 5.5A**). With this assay, I also showed that co-treating with 500$\mu g.ml^{-1}$ of hygromycin did not compromise the cells' sensitivity to puromycin (**Figure 5.4B**).

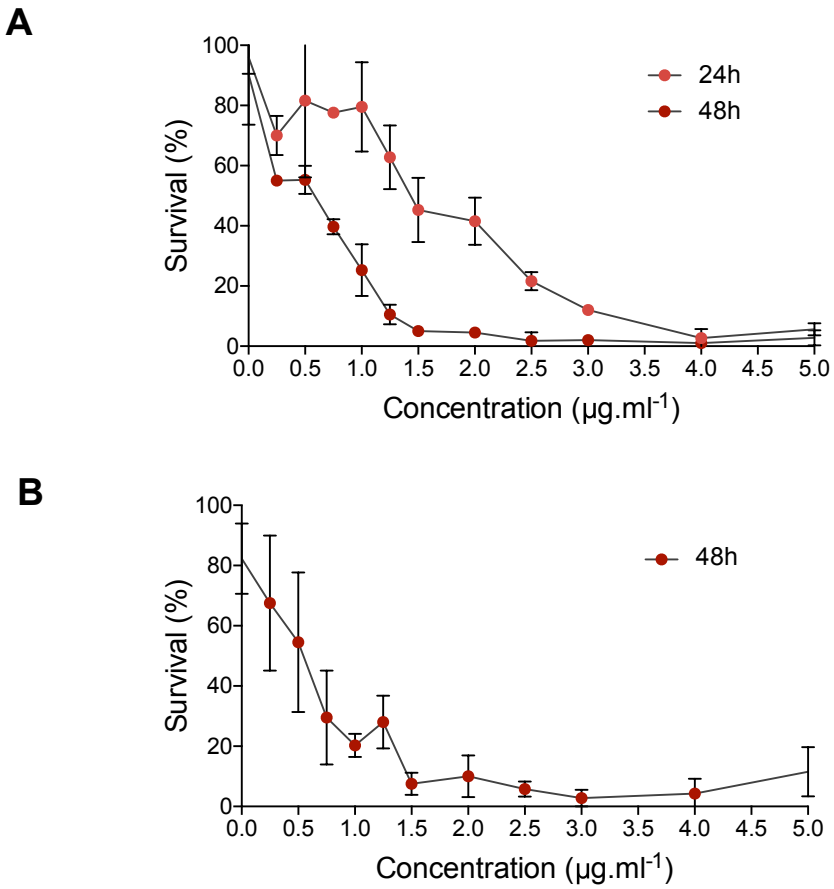

Figure 5.4: Puromycin and hygromycin titration in SH-SY5Y mito-QC cells.

SH-SY5Y mito-QC cells were grown in 96 well plates and treated with increasing concentrations of puromycin. **A)** SH-SY5Y mito-QC cells were treated for 24h or 48h with puromycin. **B)** SH-SY5Y mito-QC cells were co-treated for 48h with 500$\mu g.ml^{-1}$ hygromycin and indicated concentrations of puromycin. The cell viability was assessed using The CellTiter 96® AQueous One Solution Cell Proliferation Assay, a colorimetric analysis. The graphs represent the percentage of cell surviving plotted against puromycin concentration. Error bar = SD, 4 technical replicates.

I transfected SH-SY5Y mito-QC cells with pX330-puroR-sgUSP30#1 and 2 and used pX458-sgUSP30#1 and 2 in SH-SY5Y cells (**Figure 5.5**).
The mito-QC construct is associated with a hygromycin resistance cassette (Allen et al., 2013). As I was aiming to retain this construct in SH-SY5Y mito-QC cells during the knockout process, I performed three distinct experiments with the following transfection conditions: 1- Transfection of pX330-puroR followed by a 72h hygromycin and puromycin treatment. 2- Transfection of pX330-puroR followed by a 72h puromycin treatment. 3- 24h pre-treatment with hygromycin followed by the transfection of pX330-puroR and then combined puromycin and hygromycin treatment for 72h (**Figure 5.5A**). I treated the cells with puromycin concentrations ranging from 0.5 to 1.5 $\mu g.ml^{-1}$ in all three conditions. Once the non-transfected cells had died, I diluted the surviving cells into 10cm dishes to promote the growth of individual colonies. As soon as the colonies were distinguishable by eye and still well separated, I picked single colonies and expanded them for screening.

In a separate approach, I transfected SH-SY5Y cells with pX458-sgUSP30 for 24h, then selected the GFP positive cells by flow cytometry using the FACS AriaIII (central FACS facility on the University of Liverpool campus, operated by Sandra Cachinho) (**Figure 5.5B**).
Under the guidance of Sandra Cachinho, I determined the gates to solely select alive and single cells and to exclude untransfected cells (**Figure 5.6**). The pool of living cells was visualised using granulometry measures, which is determined with Side Scatter values-Area (SSC-A) and Forward Scatter values-Area (FSC-A) (**Figure 5.6A, D and H**). Singlets were discriminated from cell aggregates by their width and height; measures that are performed with the FSC-W (weight) and FSC-H (height) (**Figure 5.6B, E, I**). Finally, using a FITC laser (Ex/Em: 488nm/502-560), I determined the background emission produced by untransfected cells (**Figure 5.6C-D, F-G, J-K**). Using those settings, I determined that ~13% of the population was efficiently transfected with both pX458-sgUSP30#1 and 2 (**Figure 5.6L**). The EGFP+ cells were singled out by the flow cytometer into 96 well plates and expanded for screening.

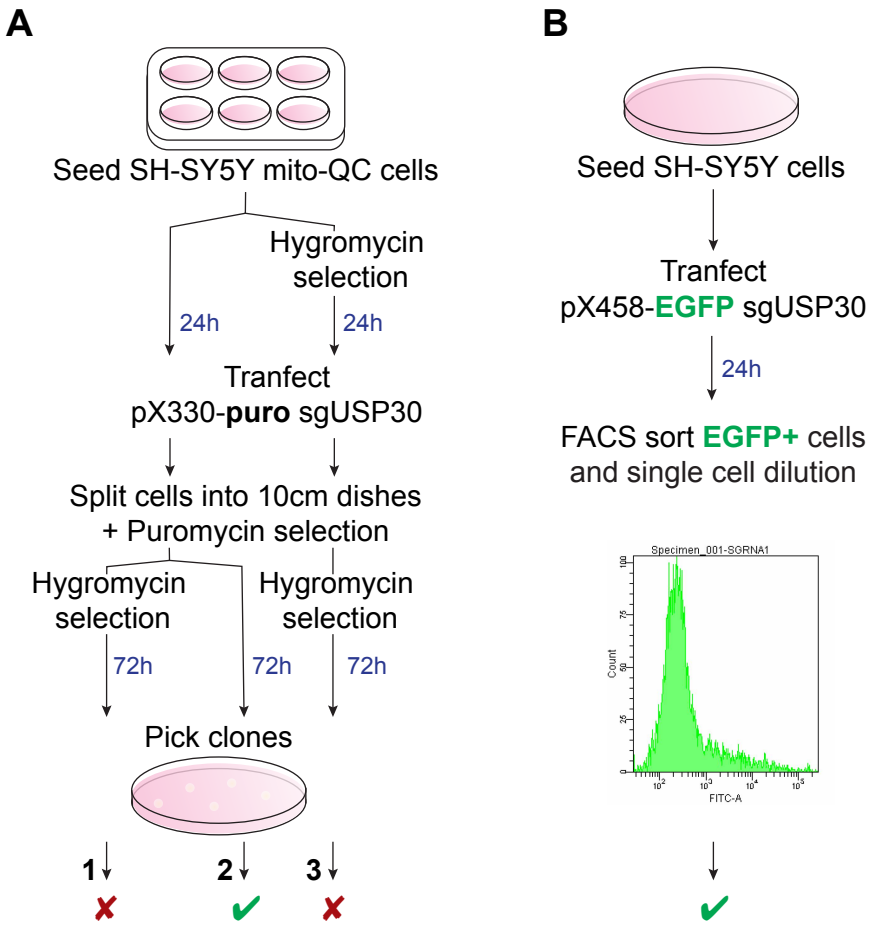

Figure 5.5: USP30 knock-out procedure in SH-SY5Y mito-QC and SH-SY5Y cells.

A) SH-SY5Y mito-QC cells were seeded in 6-well plates then transfected with the pX330-puro sgUSP30#1 and #2 plasmids for 24h. The transfected cells were then split into 10cm dishes and positively selected using a range of puromycin concentrations (from 0.5 µg.ml^{-1} to 1.5 µg.ml^{-1}) for 72h. **B)** SH-SY5Y cells were seeded into 10cm dishes and then transfected with the pX458 sgUSP30#1 and #2 for 24h. The successfully transfected cells expressed EGFP and were selected by FACS. This EGFP+ population was single cell diluted into 96 well plates.The marks and crosses indicate whether the process led to the generation of viable knockout clones.

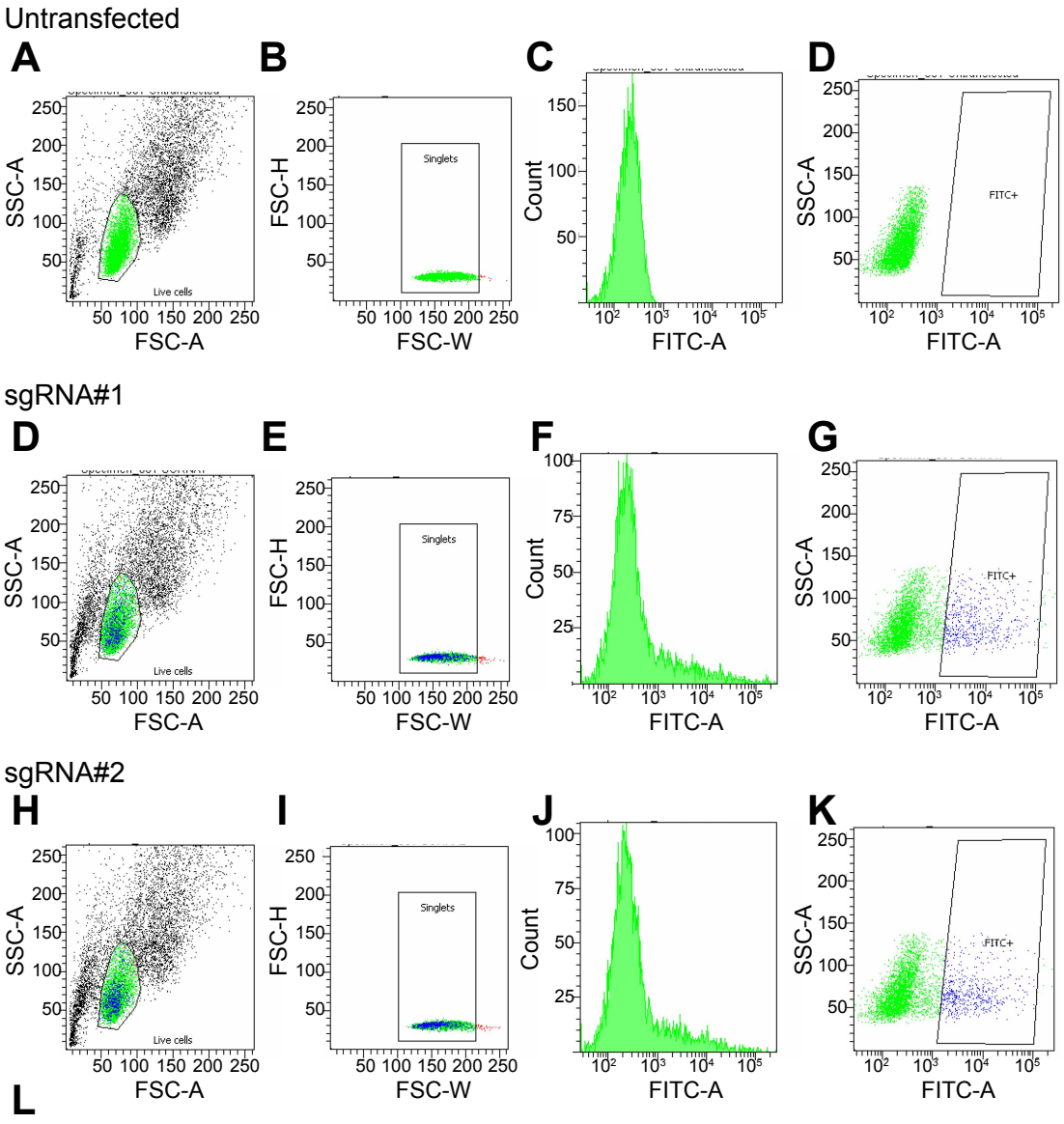

Population:	No. cells UNT	sgRNA#1	sgRNA#2	%Selected cells UNT	sgRNA#1	sgRNA#2
Total cells	10,000	10,000	10,000			
Live cells	4,766	4,349	4,448	47.7	43.5	44.5
Singlets	4,749	4,302	4,409	99.6	98.9	99.1
FITC+	0	554	550	0.0	12.9	12.5

Figure 5.6: Sorting of CRISPR transfected SH-SY5Y cells by flow cytometry.

SH-SY5Y cells untransfected (UNT) or transfected with either pX458-sgUSP30#1 (sgRNA#1) or pX458-sgUSP30#2 (sgRNA#2) were sorted by flow cytometry. Untransfected SH-SY5Y cells were used as a negative control. Only living, single and GFP+ cells were selected for further single cell dilution. **A, D, H)** The live cells were selected by granulometry, using the Side Scatter values - Area (SSC-A) and by size, employing the Forward Scatter values - Area (FSC-A). **B, E, I)** Further on, singlets were selected depending on their width and height: FSC-W (width) and FSC-H (height). **C-D, F-G, J-K)** Finally, GFP+ cells (annotated as FITC-A) were sorted using a 488nm laser. **L)** The percentage of live cells, singlets and GFP+ (FITC+) are represented in the above table.

5.2.1.4 Western blot screen of USP30 knockout clones

All selected clones were expanded into six well plates and lysed for a western blot screen. No SH-SY5Y mito-QC clone survived from condition 1 (transfection then combined treatment with puromycin and hygromycin). Colonies from condition 3 (pre-treatment with hygromycin and transfection then puromycin + hygromycin treatment), only grew in low puromycin concentrations (0.5-0.75µg.ml^{-1}) and none of these had lost USP30 expression (**Figure 5.7D-F**).

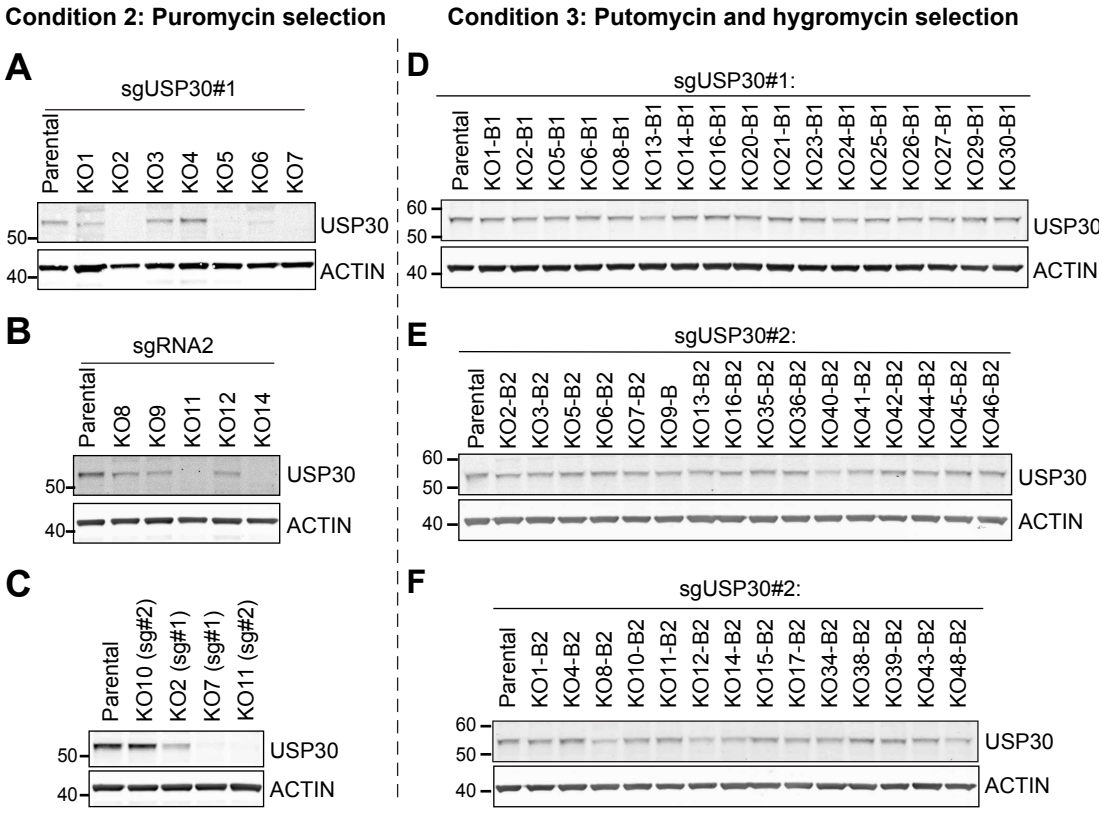

Figure 5.7: Western blot screen for SH-SY5Y mito-QC USP30 knockout cells.

SH-SY5Y mito-QC cells were transfected with two sgRNA targeting USP30: sgUSP30#1 (sg#1) and sgUSP30#2 (sg#2). A-C) Condition 2: Following transfection, SH-SY5Y mito-QC cells were maintained under puromycin selection (0.5-1µg.ml^{-1}), for 72h, to select for positively transfected cells. C) Three passages later, fresh lysates of KO2, KO7, KO10 and KO11 were immunoblotted against USP30. D-F) Condition 3: SH-SY5Y mito-QC cells were maintained in hygromycin (500µg.ml^{-1}) for 24h prior transfection. Following transfection, the cells were selected with puromycin (0.5-0.75µg.ml^{-1}) and hygromycin (500µg.ml^{-1}) for 72h.

A total of 13 SH-SY5Y mito-QC clones survived the selection process of condition 2 (Puromycin only selection) (**Figure 5.7A-C**). In the first round of immunoblotting, 5 clones appeared to have lost USP30: Clone#2, 5 and 7 (sgUSP30#1) and Clone#11 and 14 (sgUSP30#2) (**Figure 5.7A-B**). After three passages, only Clone#7 (KO7) and Clone#11 (KO11) remained free of USP30 signal (**Figure 5.7C**).

SH-SY5Y cells transfected with pX458-sgUSP30 plasmids grew very slowly and poorly recovered from the FACS sorting. I previously observed that SH-SY5Y cells tend to grow slowly when seeded at a low confluency. This is possibly due to a lack of some growth factors or metabolites secreted by the nearby cells. To counter this issue, I decided to use a 1:4 mix of condition media in full media. However, even then, out of the four 96 well plates only 9 clones survived and proliferated. Immunoblotting showed that Clone-C and D (KOC and KOD, sgUSP30#1) were depleted of USP30 **(Figure 5.8).**

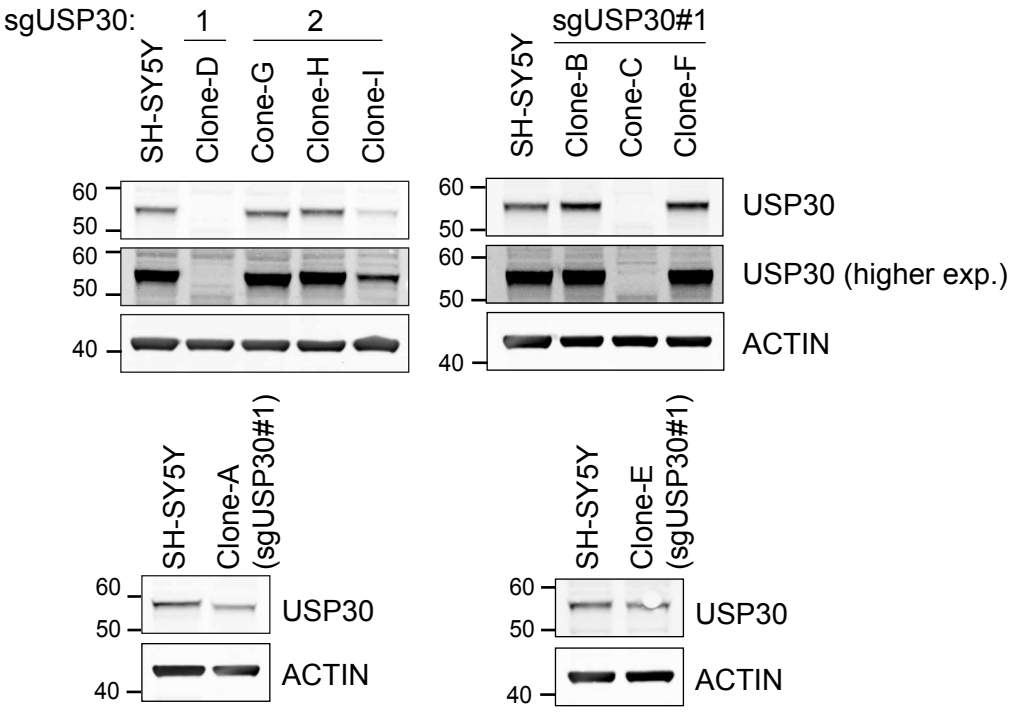

Figure 5.8: Western blotting screen for USP30 knocked-out SH-SY5Y clones.

SH-SY5Y cells were transfected with two sgRNA targeting USP30 (sgUSP30#1 and #2). Six sgUSP30#1 and three sgUSP30#2 transfected clones were expanded and screened by western blotting. Their lysates were probed for USP30.

5.2.1.5 Sequencing of USP30 knockout clones

I next undertook genomic sequencing to see what mutations were suffered by KOC, KOD, KO7 and KO11.

I extracted genomic DNA from each clone and amplified exon 3 by PCR using the following sets of primers: 2225/2226 (KO11), 2227/2228 (KO11) & 2229/2230 (KO7, KOC and KOD). I inserted the PCR products into pCR4-TOPO plasmids and transformed them into TOP10 bacteria. I picked 6-10 colonies per clone and sets of primer. I extracted the plasmid DNA and checked whether it contained an insert by a diagnostic restriction digest with EcoRI (two sites for this enzyme flank the insertion site). All plasmids positive for this exon 3 insert were sent for Sanger sequencing at the Dundee's DNA Sequencing and Services Unit.

The alignment of the sequencing results with the USP30 exon 3 sequence highlights the Indels produced by the NHEJ repair machinery, allowing me to predict the resulting frameshifts and early stop codons (**Figure 5.9**). All sequences had Indels in the exon 3 sequence coding for a section of the USP domain and would result in frameshifts and premature stop codons. Such truncations in a folded domain region of a protein have a high likelihood to give rise to non-functional and misfolded proteins that are degraded by the proteasome (Shi et al., 2015), (**Figure 5.10**).

The USP30 gene is located on chromosome 12 at location 12q24.11; this region shows no chromosomal abnormalities and is present on only two alleles in SH-SY5Y cells (Spengler et al., 2002; Yusuf et al., 2013). KOC, KOD and KO11 have distinct mutations on each allele whilst I only detected a single edition in KO7 (**Figure 5.10B**).

A Alignment of Sequence_1: [PCR_UP_product_exon3.xdna] with Sequence_2: [11.1 C-M13 Fwd-130917-07-39.seq.xdna] :

```
Seq_1   1     ------------------------------GTGCCTGGCCTTGTTAATTTAGGGAACACC  30
                                            ||||||||||||||||||||||||||||||
Seq_2   449   AGTCCTGCAGGTTTAAACGAATTCGCCCTTGTGCCTGGCCTTGTTAATTTAGGGAACACC  390

Seq_1   31    TGCTTCATGAACTCCCTGCTACAAGGCCTGTCTGCCTGTCCTGCTTTCATCAGGTGGCTG  90
              ||||||||||||||||||||||||||||||||        ||||||||||||||||||||
Seq_2   389   TGCTTCATGAACTCCCTGCTACAAGGCCTGTC--------CTGCTTTCATCAGGTGGCTG  338

Seq_1   91    GAAGAGTTCACCTCCCAGTACTCCAGGGATCAGAAGGAGCCCCCCTCACACCAGTATTTA  150
              ||||||||||||||||||||||||||||||||||||||||||||||||||||||||||||
Seq_2   337   GAAGAGTTCACCTCCCAGTACTCCAGGGATCAGAAGGAGCCCCCCTCACACCAGTATTTA  278

Seq_1   151   TCCTTAACACTCTTGCACCTTCTGAAAGGTATCTAGATGGGAATTTCAAGGGAATTATGT  210
              ||||||||||||||||||||||||||||||||||||||||||||||||||||||||||||
Seq_2   277   TCCTTAACACTCTTGCACCTTCTGAAAGGTATCTAGATGGGAATTTCAAGGGAATTATGT  218

Seq_1   211   ACCTTTTCAAAGAAGTCCAGATGACAGAGACTCTTATAACAAAGAGTTAATACCTTATTG  270
              ||||||||||||||||||||||||||||||||||||||||||||||||||||||||||||
Seq_2   217   ACCTTTTCAAAGAAGTCCAGATGACAGAGACTCTTATAACAAAGAGTTAATACCTTATTG  158

Seq_1   271   TAGGAAAAGATCATACAGATCATTATGAATAAACAACACCAAGAGCCCAATAGATACAAA  330
              ||||||||||||||||||||||||||||||||||||||||||||||||||||||||||||
Seq_2   157   TAGGAAAAGATCATACAGATCATTATGAATAAACAACACCAAGAGCCCAATAGATACAAA  98

Seq_1   331   CAAGTATTTTTTAAAAATCAAAGATGGAGGCCGGGTGCAGTGGCTCATGCCTG-------  383
              ||||||||||||||||||||||||||||||||||||||||||||||||||||||||
Seq_2   97    CAAGTATTTTTTAAAAATCAAAGATGGAGGCCGGGTGCAGTGGCTCATGCCTGAAGGGCG  38
```

B

Mutation: 8nt deletion, position 262-269aa

Resulting protein translation:

MLSSRAEAAMTAADRAIQRFLRTGAAVRYKVMKNWGVIGGIAAALAAGIYVIWGPITERKKRRKGLVPGLVNLGNTC
FMNSLLQGLSCFHQVAGRVHLPVLQGSEGAPLTPVFILNTLAPSESLVLPRSY*

Wild type protein sequence:

MLSSRAEAAMTAADRAIQRFLRTGAAVRYKVMKNWGVIGGIAAALAAGIYVIWGPITERKKRRKGLVPGLVNLGNTC
FMNSLLQGLSACPAFIRWLEEFTSQYSRDQKEPPSHQYLSLTLLHLLKALSCQEVTDDEVLDASCLLDVLRMYRWQI
SSFEEQDAHELFHVITSSLEDERDRQPRVTHLFDVHSLEQQSEITPKQITCRTRGSPHPTSNHWKSQHPFHGRLTSN
MVCKHCEHQSPVRFDTFDSLSLSIPAATWGHPLTLDHCLHHFISSESVRDVVCDNCTKIEAKGTLNGEKVEHQRTTF
VKQLKLGKLPQCLCIHLQRLSWSSHGTPLKRHEHVQFNEFLMMDIYKYHLLGHKPSQHNPKLNKNPGPTLELQDGPG
APTPVLNQPGAPKTQIFMNGACSPSLLPTLSAPMPFPLPVVPDYSSSTYLFRLMAVVVHHGDMHSGHFVTYRRSPPS
ARNPLSTSNQWLWVSDDTVRKASLQEVLSSSAYLLFYERVLSRMQHQSQECKSEE*

Figure 5.9: Alignment a KO11 exon 3 variant with USP30's wildtype exon 3.

USP30 exon 3 of SH-SY5Y and SH-SY5Y mito-QC knockout cells (here KO11) were sequenced and the results aligned with their wild type sequence. **A)** KO11 nucleotide sequence (Seq_2) aligned with wildtype USP30 exon 3 (Seq_1) using SerialCloner. The position of the catalytic cysteine C77 (orange), sgUSP30#1 (blue) and sgUSP30#2 (green) are annotated on the figure. **B)** Description of the deletion observed in A and prediction of the resulting mutated protein sequence compared with wildtype USP30 amino acid sequence. The USP domain is highlighted in yellow and the catalytic triad (C77, H452, S477) is coloured in orange. In dark red are annotated the predicted amino acids produced by the frameshift. The stars (*) represent stop codons.

A

```
Reference 1     GCCTGTCCTGCTTTCATCAGGTGGCTGGAAGAGTTCACCTCCCAGTACTCCAGGGATCAG TSS +261
KOC-allele 1    GCCTGTCCTGCTTTCATCAGGTGGCTGGAAGAGTTCACCTCCCAGTACTTCCAGGGATCAG    +1bp
KOC-allele 2    GCCTGTCCTGCTTTCATCAGGTGGCTGGAAGAGTTCACCTCCCAGTACCTCCAGGGATCAG    +1bp

Reference 1     GCCTGTCCTGCTTTCATCAGGTGGCTGGAAGAGTTCACCTCCCAGTACTCCAGGGATCAG TSS +261
KOD-allele 1    GCCTGTCCTGCTTTCATCAGGTGGCTGGAAGAGTTCACCTCCCAGTAC-------ATCAG     -7nt
KOD-allele 2    GCCTGTCCTGCTTTCATCAGGTGGCTGGAAGAGTTCACCTCCCAGT----------G    -13nt

Reference 1     GCCTGTCCTGCTTTCATCAGGTGGCTGGAAGAGTTCACCTCCCAGTACTCCAGGGATCAG TSS +261
KO7-alleles     GCCTGTCCTGCTTTCATCAGGTGGCTGGAAGAGTTCACCTCCCAGTACGATCCAGGGATCAG   +2bp

Reference 2     TGCTTCATGAACTCCCTGCTACAAGGCCTGTCTGCCTGTCCTGCTTTCATCAGGTGGCTG TSS +228
KO11-allele 1 TGCTTCATGAACTCCCTGCTACAAGGCCTGTC--------CTGCTTTCATCAGGTGGCTG     -8bp
KO11-allele 2 TGCTTCATGAACTCCCTGCTACAAGGCCTGTCTTGCCTGTCCTGCTTTCATCAGGTGGCTG    +1bp
```

B

Name	sgRNA	Mutation	Predicted protein	Frequency
KOC	sgRNA#1 (pX458)	T insertion after 310	STOP at 400 14.4 kDa protein	5/10
		C insertion after 309	STOP at 400 14.4 kDa protein	5/15
KOD	sgRNA#1 (pX458)	Deletion after 309 (7nt)	STOP at 346 12.6 kDa protein	7/10
		Deletion after 307 (13nt)	STOP at 307 11.1kDa protein	3/10
KO7	sgRNA#1 (pX330-puro)	Insertion after 309 (2nt)	STOP at 355 12.9 kDa protein	13/13
KO11	sgRNA#2 (pX330-puro)	Deletion after 260 (8nt)	STOP at 403 13.9 kDa protein	4/5
		T insertion after 261	STOP at 403 14kDa kDa protein	1/5

Figure 5.10: Details of the mutations suffered by SH-SY5Y and SH-SY5Y mito-QC USP30 knockout clones.

A) USP30 was deleted in SH-SY5Y mito-QC and SH-SY5Y cells using two sgRNAs, sgRNA#1 (blue & underlined) and sgRNA#2 (orange & underlined). The genomic DNA of USP30 knockout clones was extracted and the edited region was amplified by PCR. The PCR product was ligated into a plasmid vector, transformed into competent cells and multiple bacterial colonies were selected and analysed by sequencing. The mutation suffered per allele and per clone is highlighted in bold red. The catalytic cysteine C77 is highlighted in green. TSS: Transcription start site. **B)** The table summarises the sequencing results obtained from SH-SY5Y (KOC and KOD) and SH-SY5Y mito-QC (KO7 and KO11) USP30 KO clones. The editing observed for each clone is reported in the mutation column and the resulting expected protein is described in the protein section. Plasmids extracted from between 5 and 13 colonies of competent cells were sequenced per knockout clone. The frequency of occurrence for each mutation is reported in the Frequency column.

5.2.1.6 Loss of the mito-QC construct in KO7 and KO11 cells

5.2.1.6.1 Fluorescence and confocal microscopy characterisation of KO7 and KO11.

In parallel of the sequencing process, I assessed the mito-QC USP30 KO clones by live cell epifluorescence and confocal microscopy and compared them with the parental cell line **(Figure 5.11).** All cells were morphologically similar to the parental cells, However, only 10-20% of KO7 and KO11 cells were expressing mito-QC. In an attempt to enrich the small percentage of mitoQC expressing USP30 KO cells, I treated the clones with 500µg.ml^{-1} hygromycin for 7 days, then lysed and immunoblotted the selected cell against USP30 (**Figure 5.12**). All hygromycin selected cells were expressing USP30. Most likely, KO7 and KO11 were mixed populations containing both USP30 KO cells that are mitoQC negative as well as a small percentage of wildtype cells expressing mito-QC.

I decided to single cell dilute the original KO11 and KO7 “clones” to separate the USP30 wildtype from USP30 knockout cells.

However, post-single cell dilution, the cells didn’t divide and ended up dying. As I had previously observed with single the cell dilution by flow cytometry, SH-SY5Y cells are very sensitive to cell confluency and fail to expand when grown in isolation.

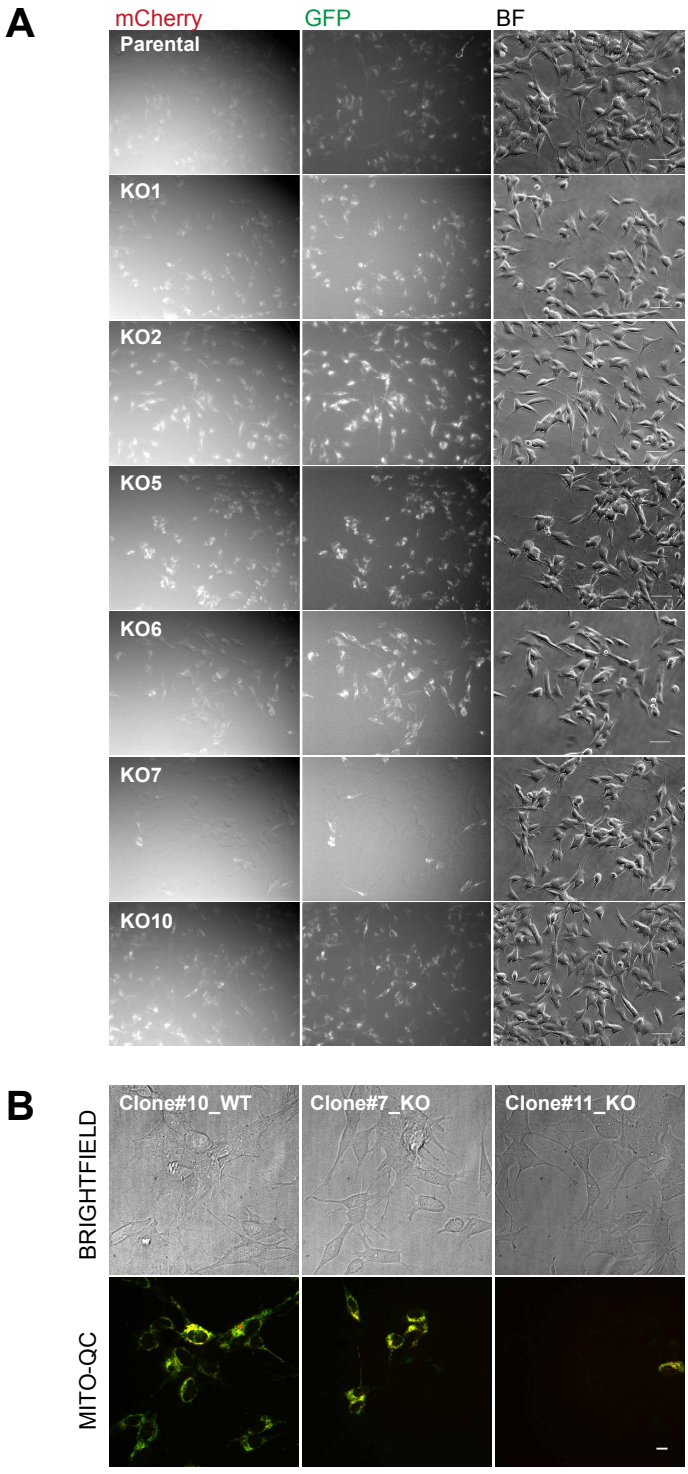

Figure 5.11: USP30 knockout clones 7 and 11 (KO7, KO11) only partially express mito-QC.

A) Following USP30-targeted sgRNA transfection, six clones were imaged by fluorescence microscopy on a Nikon Ti-Eclipse microscope and compared with the parental SH-SY5Y mito-QC cell line. mCherryFIS1 Ex/Em: 561/610; GFP Ex/Em: 488/507; BF: brightfield. 20X Objective lens. Scale bar: 50µm. **B)** Clone#10 (WT1), Clone#7 (KO7) and Clone#11 (KO11), were grown on IDIBI dished and imaged using a 3i spinning disk confocal. TOP panel: Brightfield images of control cells WT1 and USP30 knockout clones KO7, KO11 cells. BOTTOM panel: Corresponding merge images of GFP (488nm) and mCherry (561nm). Objective lens: 40X. Scale bar: 10µm.

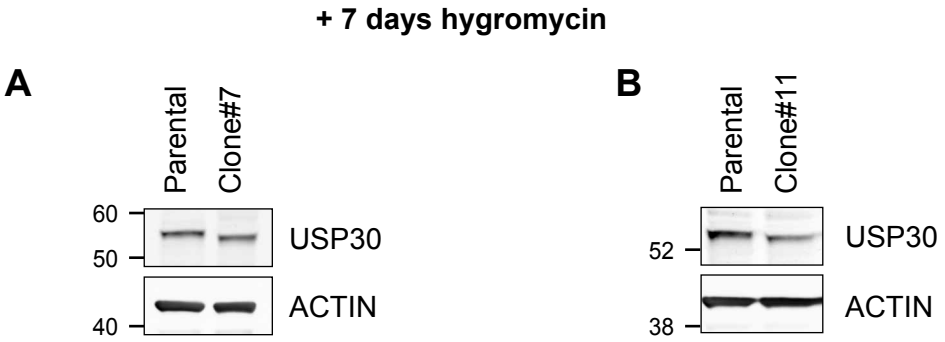

Figure 5.12: Hygromycin selection of mito-QC expressing KO7 and KO11 cells.

A) "KO7" and **B)** "KO11" mixed populations were treated with 500µg.ml^{-1} Hygromycin for 7 days to select for mito-QC expressing cells. The resulting pools were lysed and then analysed by western blotting.

5.2.1.6.2 Negative FACS sorting of mito-QC negative cells in KO7 and KO11 mixed clones

As a last resort to obtain a clonal population of USP30 KO cells, I decided to use flow cytometry to negatively sort the mito-QC positive cells (FACS sorting performed by Christopher Law). We used a mix of wildtype SH-SY5Y mito-QC and SH-SY5Y cells to discriminate between the background autofluorescence of SH-SY5Y cells and Cherry+ signal using a PE-TxRed specific laser (Ex/Em:561/610-620 nm) on the FACS AriaIII instrument (**Figure 5.13**). Side scatter and forward scatter measurements (SSC and FSC) permitted to select live and singlet cells (**Figure 5.13 A-B, D-E, H-I**).

The mCherry-positive cells present in KO7 and KO11 populations were discarded and the mCherry-negative cells were maintained as a pool, expanded and screened by western blotting (**Figure 5.13C, F-G, J-L**). The FACS sorted KO7 cells were still expressing low levels of USP30 (**Figure 5.13K**). However, KO11 appeared to be cleared from USP30 expressing cells (**Figure 5.13G**).

For most of the following experiments I have therefore mainly been using KO11, KOC and KOD, which derive from two different parent lines, but neither of which express mito-QC.

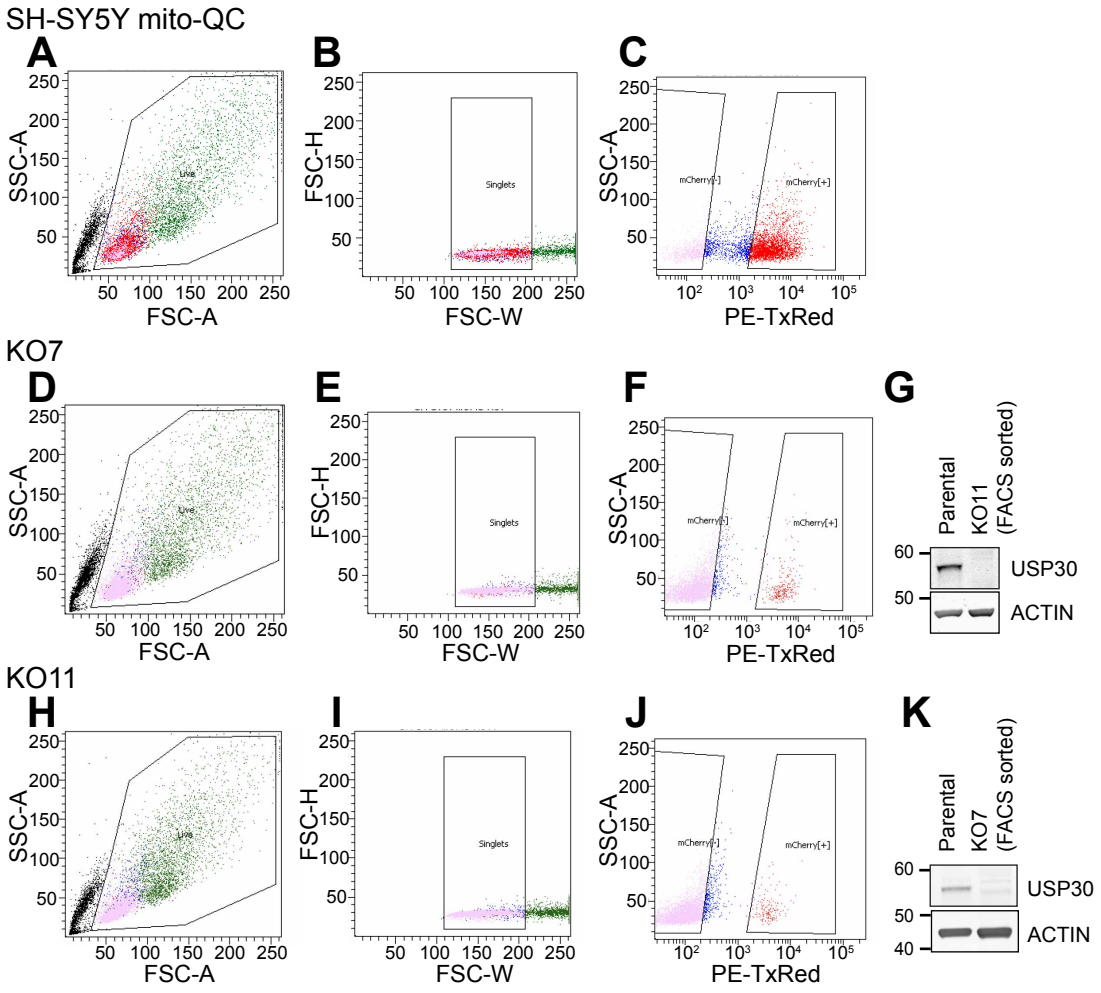

L

Population:	No. cells PAR	KO7	KO11	%Selected cells PAR	KO7	KO11
Total cells	10,000	10,000	10,000			
Live cells	7,154	6,868	8,003	71.5	68.7	80.0
Singlets	4,510	4,349	5,307	63.0	63.3	66.3
mCherry+	2,974	282	165	65.9	6.5	3.1
mCherry-	685	3,824	4,776	15.2	87.9	90.0

Figure 5.13: Negative FACS sorting of mito-QC positive cell in KO7 in KO11 mixed populations.

SH-SY5Y cells stably expressing mito-QC from KO7 and KO11 cells were sorted by flow cytometry. **A-C)** FACS sorting gates were previously set using the parental SH-SY5Y MGFIS cell line. **A, D, H)** Live cells were selected by granulometry, using the Side Scatter values - Area (SSC-A) and by size, employing the Forward Scatter values - Area (FSC-A). **B, E, I)** Singlets were selected depending on their width and height: FSC-W (width) and FSC-H (height). **C, F, J)** Finally, gates were set to discriminate between mito-QC-positive (mCherry[+]) and mito-QC-negative (mCherry[-]) cells using a PE-TxRed laser (Ex:561nm). **G, K)** Following FACS sorting, **G)** KO7 and **K)** KO11 mCherry- cells were lysed and analysed by western blotting. The lysates were probed against USP30. **L)** The percentage of live cells, singlets, mCherry-positive and mCherry-positive is shown in the above table.

5.2.2 Identifying USP30 substrates and function

5.2.2.1 Mitochondria fission and fusion dynamics

Hirose and Nakamura were the first to identify USP30 as a mitochondrial DUB and proposed that it functions in mitochondrial dynamics (Nakamura and Hirose, 2008). They reported that knocking-down USP30 promotes the fusion of the mitochondrial network in HeLa cells. Hirose and Nakamura were however not able to explain the mechanism underlying the USP30-induced elongation of mitochondria as they found no changes in fusion proteins (MFNs, OPA1) or fission proteins (FIS1, DNM1L). Later, Yue and colleagues made use of a non-selective inhibitor, S3, that induces mitochondrial fission, enhances non-degradative ubiquitylation of MFNs and could bind catalytically active USP30. From these observations, they suggested that USP30 deubiquitylates the fission factors MFN1 and MFN2 to promote fission, without affecting their stability (Yue et al., 2014).

Neither of the two studies have studied the effect of USP30 deletion on the mitochondrial network. To assess this, I fixed and stained SH-SY5Y and KO11 cells against the outer mitochondrial protein TOMM20 (**Figure 5.14**). I measured the number of fragmented mitochondria, the number of branched mitochondria (networks), and the number and length of branches for each network using MiNA, a FIJI plugin. USP30 knockout did not increase the number of networks, nor the number of branches, nor did it affect the branches' length (**Figure 5.14D-F**). In the contrary, if anything I noted a trend towards an increase of the number of fragmented mitochondria (dots and unconnected rods) and towards a reduction of the mitochondrial mass (Mitochondria footprint) (**Figure 5.14B-C**). In parallel, I determined by immunofluorescence whether USP30 knockout could result in a decrease in the peroxisome pool by raising basal pexophagy (**Figure 5.15**). Using the Fiji plug-in 'Analyse Particle', I found that both KO11 and SH-SY5Y cells had on average 110 peroxisomes per cell in one confocal slice (0.34 µM). Similarly, my colleague Elena Marcassa found that neither the mitochondrial nor the peroxisomal networks of RPE1 cells were affected by USP30 knockout (Marcassa et al., 2018).

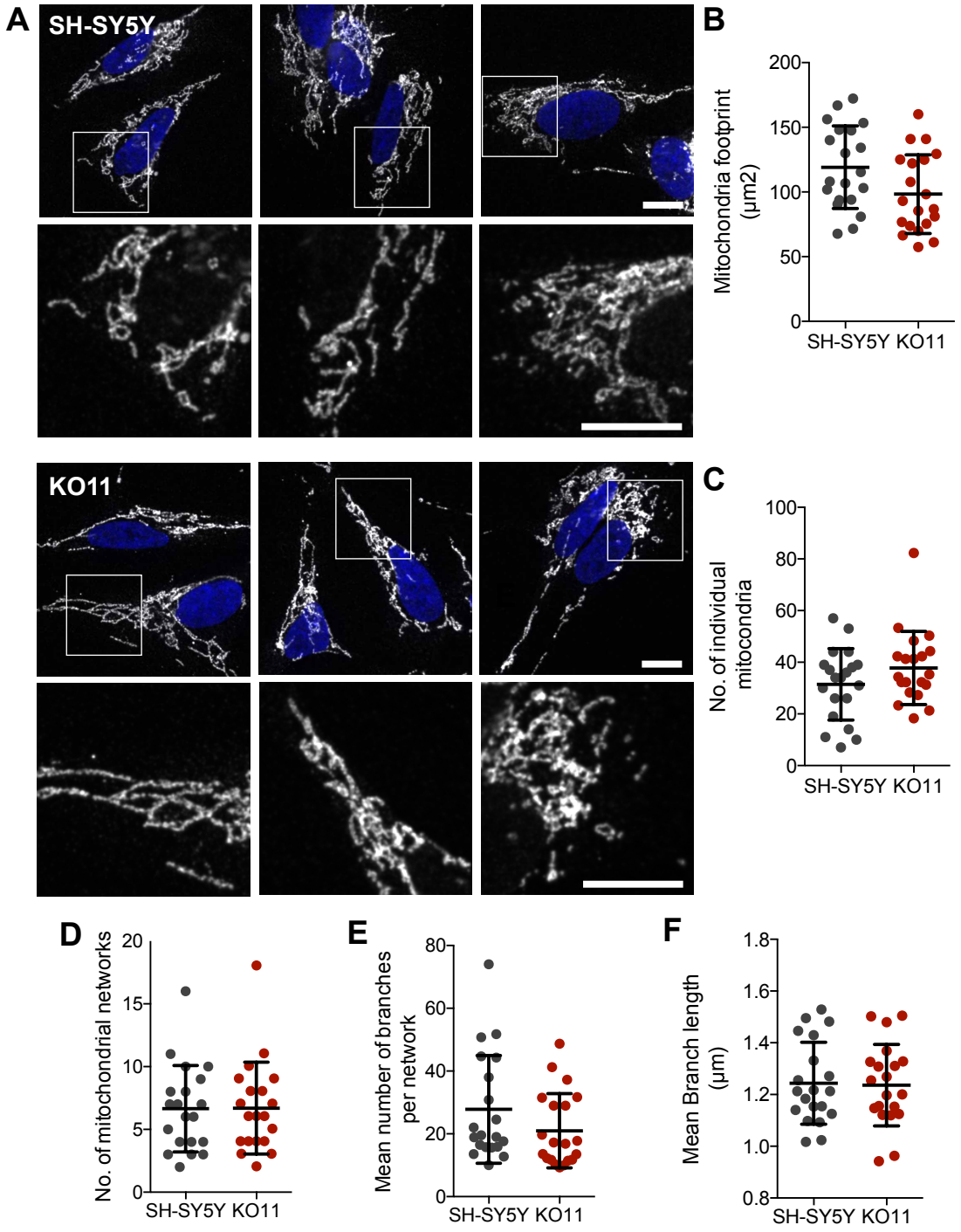

Figure 5.14: The mitochondrial network is unaffected by USP30 depletion in SH-SY5Y cells.

A) SH-SY5Y and KO11 cells were fixed and stained by immunofluorescence for the mitochondrial protein TOMM20. Images were taken using a 3i spinning disk confocal. Objective lens: 63X. Scale bar: 10µm. **B, C, D, E and F)** Images were analysed using the MiNA plug-in on FIJI; 20 cells were quantified per cell line. **B)** Mitochondrial footprint: Total area of the cell occupied by the TOMM20 signal. **C)** Number of unbranched mitochondria (punctate and rods) per cell. **D)** Number of branched mitochondria (networks) per cell. **E)** Mean number of branches per network and per cell. **F)** Mean length of the branches. Error bars: mean ± SD. Data from a single experiment.

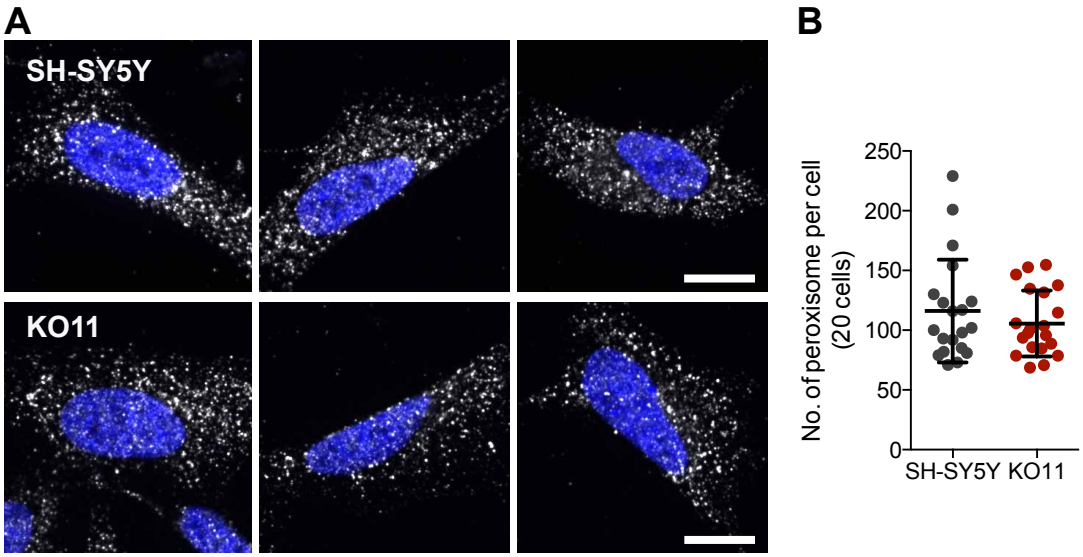

Figure 5.15: The peroxisomal network is not affected by USP30 depletion.

A) SH-SY5Y cells and KO11 cells were fixed and stained by immunofluorescence for PMP70, a peroxisomal proteins. The images were taken with 3i a spinning disk confocal. Objective lens: 63X. Scale bar: 10µm. **B)** The images were analysed using Analyse particle, a FIJI plugin. The graph represents the number of peroxisomes per cell (from a single confocal plane) and per cell line. Each dot represents a single cell. Error bars: mean ± SD. Data from a single experiment.

5.2.2.2 Mitochondrial metabolism

I then wondered if USP30 could affect the mitochondrial metabolism and energy production. I decided to measure ATP synthesis in oxidative or glycolytic conditions. I employed a chemiluminescence assay, the CellTitre-Glo assay, in which luciferase's luminescence is directly proportional to the ATP concentration (**Figure 5.16**). To block oxidative phosphorylation (OXPHOS), I treated the cells with an inhibitor of Complex V of the respiratory chain, Oligomycin A, for 30 minutes at 10µM. Both the parental lines, SH-SY5Y and SH-SY5Y mito-QC, and the USP30 knockout lines, KOC, KOD and KO11, could efficiently compensate for inhibition of OXPHOS. The cells were producing 96% ± 0.02 of their ATP production capacity. To test for the cells' dependency on glycolysis for ATP production, I supplemented the media with 50mM 2-Deoxyglucose (2-DG). 2-DG is a glucose molecule which lacks the 2-hydroxyl group and acts as a competitive inhibitor of glycolysis via Hexokinase 2. Indeed, the resulting 2-deoxyglucose-6-phosphate cannot be utilized by phosphoglucose isomerase (Wick et al., 1957). With 2-DG, the ATP production of SH-SY5Y and SH-SY5Y mito-QC cells was reduced by 50%, their OXPHOS

machinery was not sufficient to fully compensate for glycolysis inhibition. In the knockout cells the results were less clear. KOC cells were more glycolytic, with 2-DG their ATP synthesis dropped by 73%; KOD cells reacted just as the parental lines, their ATP production was decreased to 50%; KO11 cells were less sensitive to glycolysis inhibition than the parental lines, OXPHOS could compensate for 67% of ATP generation in those cells.

The differences observed are likely to be due to clonal variation rather than a direct effect of USP30 knockout. Andreas Kallinos' findings in RPE1 and HCT116 cells support this hypothesis. In HCT116, the loss of USP30 does not affect ATP production and in RPE1 cells he observed a variable response that indicates clonal variation amongst wildtype and USP30 knockout cells.

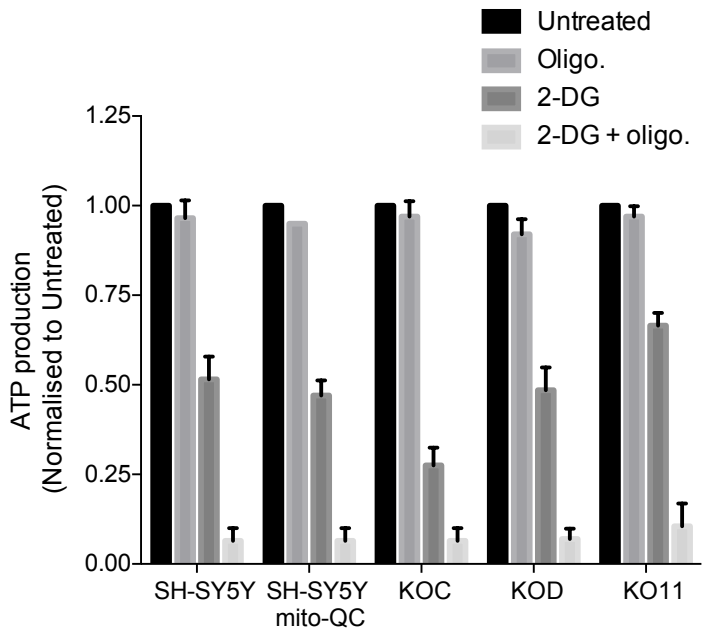

Figure 5.16: USP30 knockout and wildtype SH-SY5Y cells are dependent on their glycolytic metabolism to produce ATP.

ATP produced by the parental cell lines (SH-SY5Y and SH-SY5Y mito-QC cells) and SH-SY5Y USP30 KO cells (KOC, KOD and KO11) was assessed using the CellTitre-Glo assay. Cells were treated with Oligomycin (Oligo., 10μM), 2-Deoxyglucose (2-DG, 50mM) or a combination of both for 30 min then lysed. This assay employs luciferase, an enzyme which produces luminescence directly proportional to the ATP concentration. The graph represents the chemiluminescence measurements normalised to the untreated conditions. Results from 2 experiments. Error bars: mean ± SD.

5.2.2.3 Mitophagy: TOMM20- and pS65-Ubiquitylation

In Chapter IV, I described that USP30 knockdown increases AO-induced mitophagy. In this chapter, I will be assessing USP30 substrates involved in mitophagy. I started by measuring the levels of expression of the major mitophagy regulators, PINK1 and Parkin, in SH-SY5Y Mito-QC cells transfected with sgUSP30 (prior to the FACS sorting of KO7 and KO11) (**Figure 5.17**). I found that neither PINK1 accumulation nor Parkin general expression levels were affected by USP30 deletion in KO7 and KO11 clones in response to depolarisation. Similarly, I did not observe a variation in PINK1 accumulation in the SH-SY5Y knockout KOD cell line (**Figure 5.18E**). In SH-SY5Y KOC, PINK1's accumulation was slightly reduced at the 8h time point compared to WT SH-SY5Y cells (~25% less). Unlike KOD, KOC also appeared to have twice more ubiquitylated FIS1 species than the control cells (**Figure 5.18D-E**). However, the only striking and consistent phenomenon occurring in USP30 KO clones was the appearance of TOMM20 ubiquitylated species upon AO stimulation (4h and 8h AO) (**Figure 5.18C**).

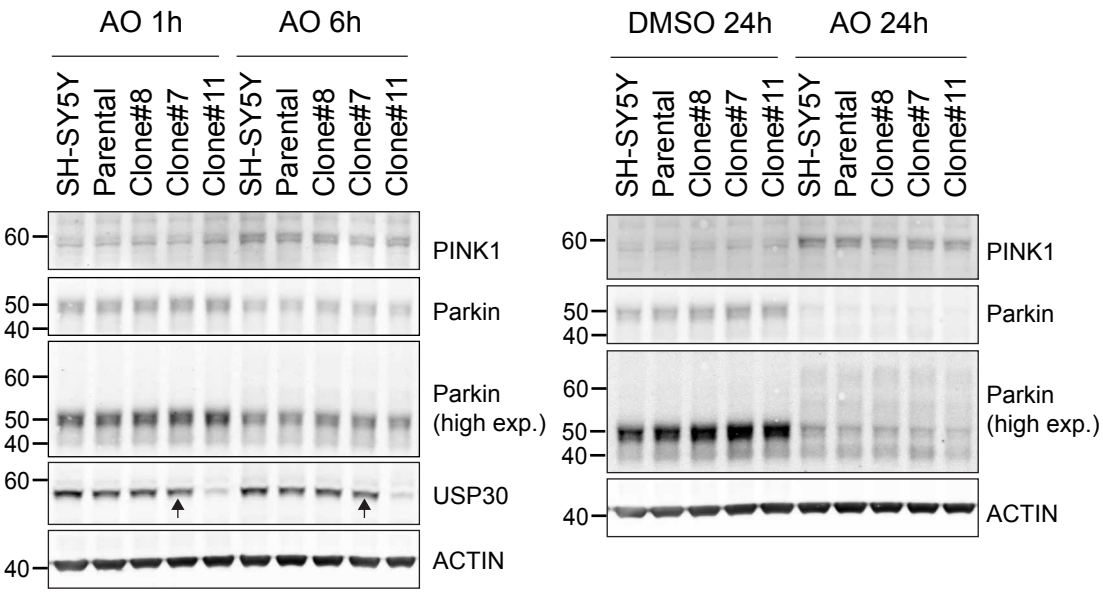

Figure 5.17: Antimycin and Oligomycin time course in SH-SY5Y USP30 wildtype and knockout cells.

SH-SY5Y, parental SH-SY5Y mito-QC, clone#8 (WT8), clone#7 ("KO7"), Clone#11 ("KO11") were treated with Antimycin A and Oligomycin A (AO, 1µM each) for 1, 6 and 24h to trigger mitophagy. The cells were then lysed in NP40 buffer and immunoblotted. The lysates were probed for proteins regulating mitophagy.

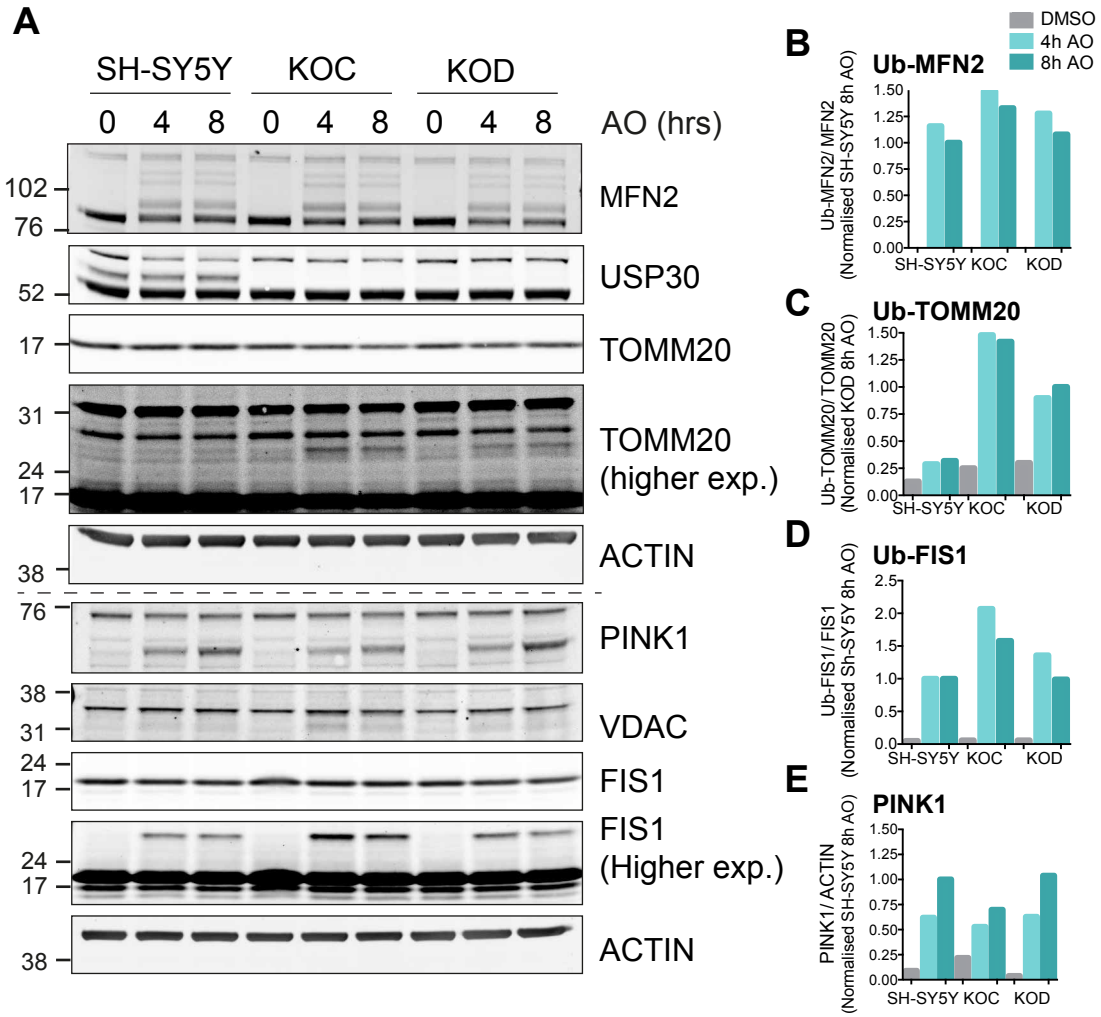

Figure 5.18: Antimycin and Oligomycin time course in SH-SY5Y USP30 wildtype and knockout cells.

SH-SY5Y, KOC and KOD were treated with Antimycin A and Oligomycin A (AO, 1µM each) for 4 and 8h to depolarise mitochondria. **A)** The cells were then lysed in NP40 buffer and immunoblotted. The lysates were probed for proteins involved in mitophagy. Quantification of **B)** Ub-MFN2, **C)** Ub-TOMM20, **D)** Ub-FIS1 over their non-ubiquitylated form and normalised to SH-SY5Y 8h AO or **C)** to KOD 8h AO. **E)** Bar charts representing total PINK1 normalised over Actin then to SH-SY5Y 8h AO. Data from a single experiment.

In mitochondria enriched samples, TOMM20 ubiquitylation is detected in all KO clones (KOC, KOD and KO11) following 1h AO treatment (**Figure 5.19, 5.20.1**). Those samples also suggest that USP30 knockout cells have slightly higher detectable levels of TOMM20 ubiquitylation without depolarisation (**Figure 5.19A-B, 5.20.1A-B**).

Interestingly, the ubiquitylation of TOMM20 forms close doublets (indicated by red arrows). The upper band of the doublet could correspond to modified ubiquitin species, such as phosphorylated ubiquitin. When further depolarising mitochondria for 4h, the TOMM20-ubiquitylation doublet is enhanced 3-fold and a new ubiquitin band appears in the KO samples ~14kDa above TOMM20 (**Figure 5.21**). In the experiment performed in whole cell lysate, I did not measure a further increase of ubiquitylation upon 8h depolarisation, however this was not assessed in the mitochondria enriched fractions (**Figure 5.18**).

Again, those changes in ubiquitylation pattern were not accompanied by a greater accumulation of PINK1 on mitochondria nor by a differential recruitment of Parkin to mitochondrial fraction (**5.19A, 5.20.1C-D, 5.21E**). Interestingly, although PINK1 is unaffected, the levels of phospho-Ser65 Ubiquitin (pS65-Ub) are increased in the USP30 knockout fractions (**Figure 5.20.2 and 5.21**). To determine the molecular weight range of the proteins differently phospho-ubiquitylated in response to USP30 knockout, I generated line graphs using Fiji in two separate experiments. These line graphs represent the intensity of pS65-Ub along the smear (From the top of the band ~ 300kDa to the bottom at ~0kDa) (**Figure 5.20.2D-G**).

The maximum intensity peaks of those graphs were at ~300kDa and masked any variation of pS65-Ub at lower molecular weight (**Figure 5.20.2B**). I noticed that pS65-Ub was clearly stronger in KOD and KO11 below 76kDa. I therefore generated line graphs in that segment of the blot (**Figure 5.20.2E, G**). Those graphs revealed that the levels of pS65-Ub-proteins ranging between 76 and 38kDa were specifically increased in KOD and KO11 after 1h AO. The overall pS65-Ub intensity signal in the 0-76kDa range was increased by ~50% in the knockout lines (**Figure 5.20.2C)**. After 4h AO, smaller proteins (<38kDa) were differentially pS65-Ubiquitylated in KOD and KO11 (**Figure 5.21H, K**). Proteins such as TOMM20 and FIS1 would fall in that second category.

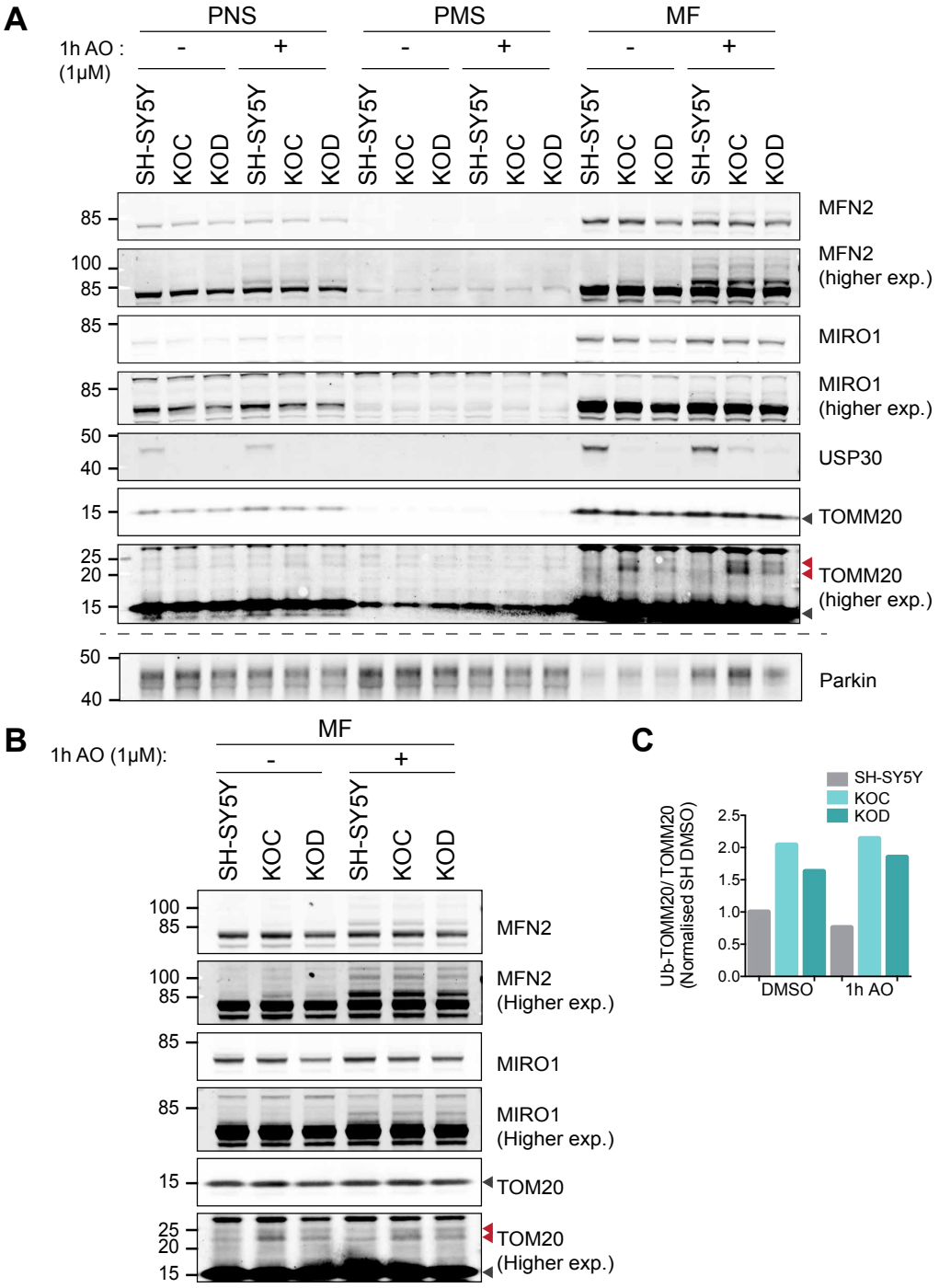

Figure 5.19: Mitochondria fraction: USP30 depletion increases TOMM20 ubiquitylation.

SH-SY5Y, KOC and KOD cells were treated with 1μM Antimycin A and Oligomycin A (AO) for 1h. The cells were then homogenised in HIM buffer. The nuclei were span down at 600g to collect the Post Nuclear Supernatant (PNS). The PNS was span a second time at 7,000g. The resulting pellet was labelled as Mitochondrial Fraction (MF) and the supernatant as Post Mitochondrial Supernatant (PMS). **A)** All fractions were ran on a 20 well gel for western blotting. **B)** The mitochondrial fraction was resolved on a 10-well gel. The lysates were probed for mitophagy substrates and regulators. The black arrows indicate the unmodified TOMM20 band; the red arrows point towards ubiquitylated-TOMM20. **C)** Quantification of (B) mitochondrial Ub-TOMM20 ratioed over non-ubiquitylated TOMM20 and normalised to SH DMSO.

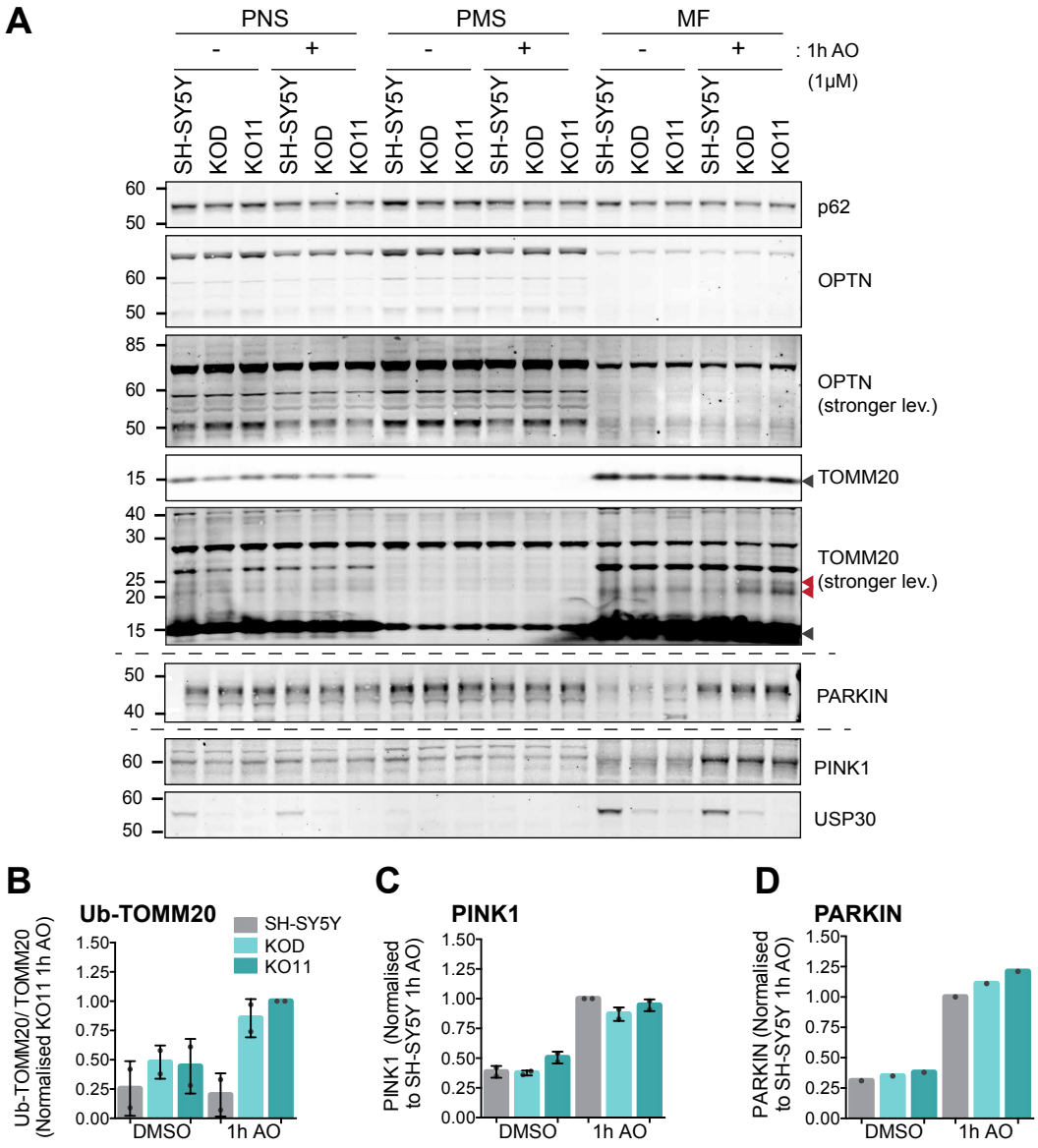

Figure 5.20.1: USP30 depletion increases TOMM20 ubiquitylation and phospho-ubiquitylation of medium-sized proteins.

SH-SY5Y, KOD and KO11 cells were treated with 1μM Antimycin A and Oligomycin A (AO) for 1h. The cells were then homogenised in HIM buffer. The nuclei were span down at 600g to collect the Post Nuclear Supernatant (PNS). The PNS was span a second time at 7,000g. The resulting pellet was labelled as Mitochondrial Fraction (MF) and the supernatant as Post Mitochondrial Supernatant (PMS). **A)** All fractions were immunoblotted against proteins involved in mitophagy. The black arrows indicate the unmodified TOMM20 band; the red arrows point towards ubiquitylated-TOMM20. **B)** Quantification of mitochondrial Ub-TOMM20 ratioed over non-ubiquitylated TOMM20 and normalised to KO11 1h AO. Bar charts representing total **C)** PINK1 or **D)** Parkin localised at the mitochondrial fraction and normalised to SH-SY5Y 1h AO. n=2.

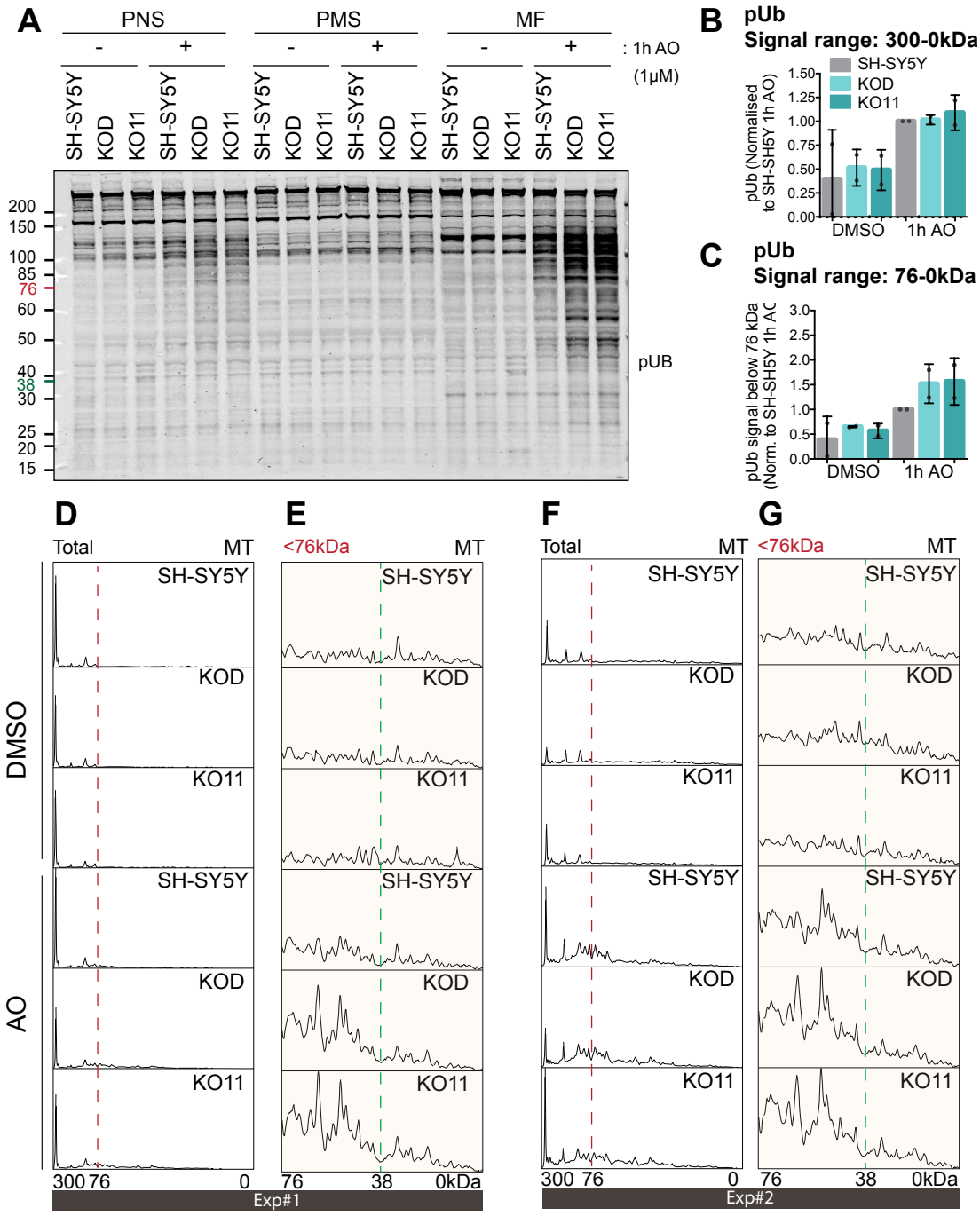

Figure 5.20.2: USP30 depletion increases TOMM20 ubiquitylation and phospho-ubiquitylation of medium-sized proteins.

SH-SY5Y, KOD and KO11 cells were treated with 1µM Antimycin A and Oligomycin A (AO) for 1h. The cells were then homogenised in HIM buffer. The nuclei were span down at 600g to collect the Post Nuclear Supernatant (PNS). The PNS was span a second time at 7,000g. The resulting pellet was labelled as Mitochondrial Fraction (MF) and the supernatant as Post Mitochondrial Supernatant (PMS). **A)** All fractions were immunoblotted against pUb. **B)** Quantification of total mitochondrial pUb normalised to SH-SY5Y 1h AO. **C)** Bar chart representing the pUb signal measured below 76kDa and normalised to SH-SY5Y 1h AO. **D and F)** Line graph of the pUb signal measured in the mitochondrial fraction of two separate experiments. **E and G)** Line graph of pUb signal found below 76kDa. The 76kDa and 38kDa limits are respectively represented as a red and green dashed line. N=2.

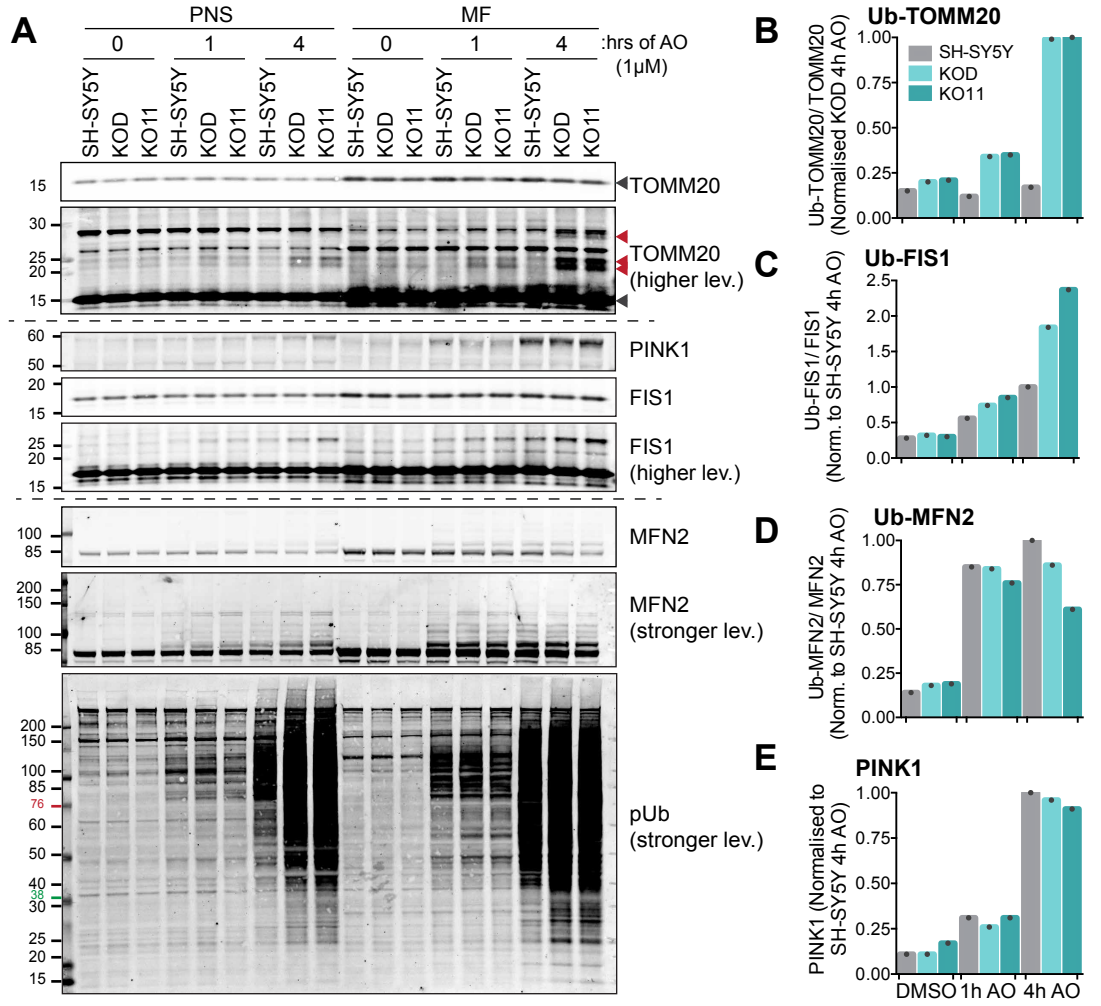
A
PNS
MF
0
1
4
:hrs of AO (1μM)
SH-SY5Y
KOD
KO11
TOMM20
TOMM20 (higher lev.)
PINK1
FIS1
FIS1 (higher lev.)
MFN2
MFN2 (stronger lev.)
pUb (stronger lev.)
B
Ub-TOMM20
Ub-TOMM20/ TOMM20 (Normalised KOD 4h AO)
C
Ub-FIS1
Ub-FIS1/ FIS1 (Norm. to SH-SY5Y 4h AO)
D
Ub-MFN2
Ub-MFN2/ MFN2 (Norm. to SH-SY5Y 4h AO)
E
PINK1
PINK1 (Normalised to SH-SY5Y 4h AO)
DMSO 1h AO 4h AO

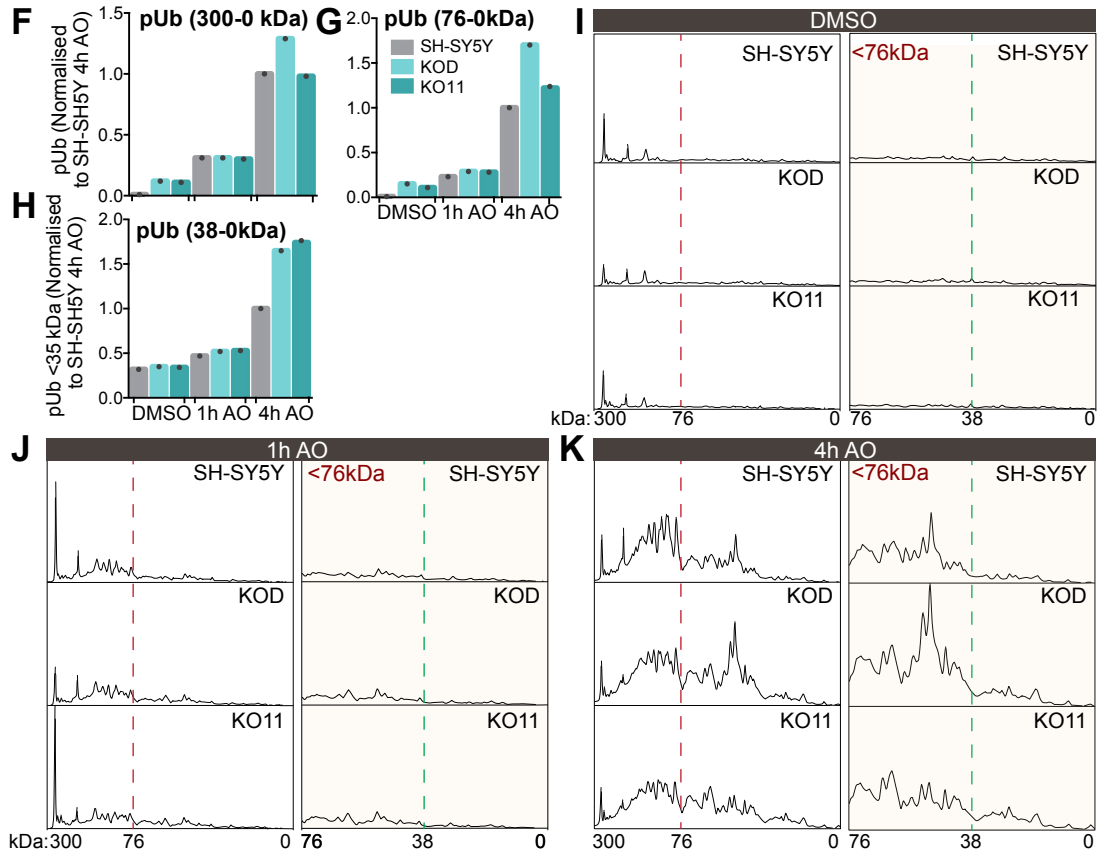
F
pUb (300-0 kDa)
pUb (Normalised to SH-SH5Y 4h AO)
G
pUb (76-0kDa)
SH-SY5Y
KOD
KO11
DMSO 1h AO 4h AO
H
pUb (38-0kDa)
pUb <35 kDa (Normalised to SH-SH5Y 4h AO)
I
DMSO
<76kDa
kDa: 300 76 0 76 38 0
J
1h AO
K
4h AO

Figure 5.21: Mitochondria fraction: USP30 depletion increases phospho-ubiquitylation of low molecular weight proteins.

SH-SY5Y, KOD and KO11 cells were treated with 1μM Antimycin A and 1μM Oligomycin A (AO) for both 1h and 4h. The cells were then homogenised in HIM buffer. The Post Nuclear Supernatant (PNS), Post Mitochondrial Supernatant (PMS) and Mitochondrial Fraction (MF) were obtained by differential centrifugation. **A)** The fractions were immunoblotted against proteins involved in mitophagy. The black arrows indicate the unmodified TOMM20 band; the red arrows point towards ubiquitylated-TOMM20. **B, C and D)** Ubiquitylated-TOMM20, -FIS1 and -MFN2 from the MF were quantified using ImageStudio, ratioed to their unmodified form and normalised to SH-SY5Y 4h AO or to **B)** KO11 4h AO. **E)** The intensity of the PINK1 band from the MF was also measured and normalised to SH-SY5Y 4h AO. **F)** Total phospho-ubiquitin signal, phospho-ubiquitin signal running **G)** below 76kDa or **H)** below 35kDa was detected and normalised to SH-SY5Y 4h AO. I, J and K) Line graph of the entire mitochondrial pUb smear and, in orange, line graph of the pUb bands running below 76kDa. The 76kDa and 38kDa limits are respectively represented as a red and green dashed line.

I then assessed, by immunofluorescence, whether I could observe enhanced pS65-Ub accumulation at mitochondria in USP30 KO cells. I depolarised SH-SY5Y and KOD cells with AO for 4h, fixed and stained them for TOMM20 and pS65-Ub (**Figure 5.22A**). Without AO, the antibody signal of pS65-Ub is low and rather ubiquitous, with the exception of a strong centrosomal-like staining. My colleague Andreas demonstrated that the centrosomal staining was retained even after PINK1 knockdown and was thus non-specific, caused by unknown cross-reactivity.

Following AO-treatment, I observed puncta of pS65-Ub that partially colocalised with TOMM20, which identifies the now fragmented mitochondrial network (**Figure 5.22A**). I manually counted the number of cells with pS65-Ub concentrated on mitochondrial membranes and found that there was higher percentage of KOD and KO11 cells with mitochondrial pS65-Ub (~15%) than SH-SY5Y cells (~3%) (**Figure 5.22B-C**). Ideally, these conditions would have been compared with PINK1 knockdown to validate the specificity of the mitochondrial pS65-Ub staining.

This variation of pS65-Ub could be the result of a global increase in ubiquitin. To verify this, I probed mitochondrial fractions with the VU-1 antibody (LifeSensors), which recognises free ubiquitin and poly-ubiquitin of all chain types, including K6-chains which are the proposed substrate of USP30 (Gersch et al., 2017; Gilda et al., 2015).

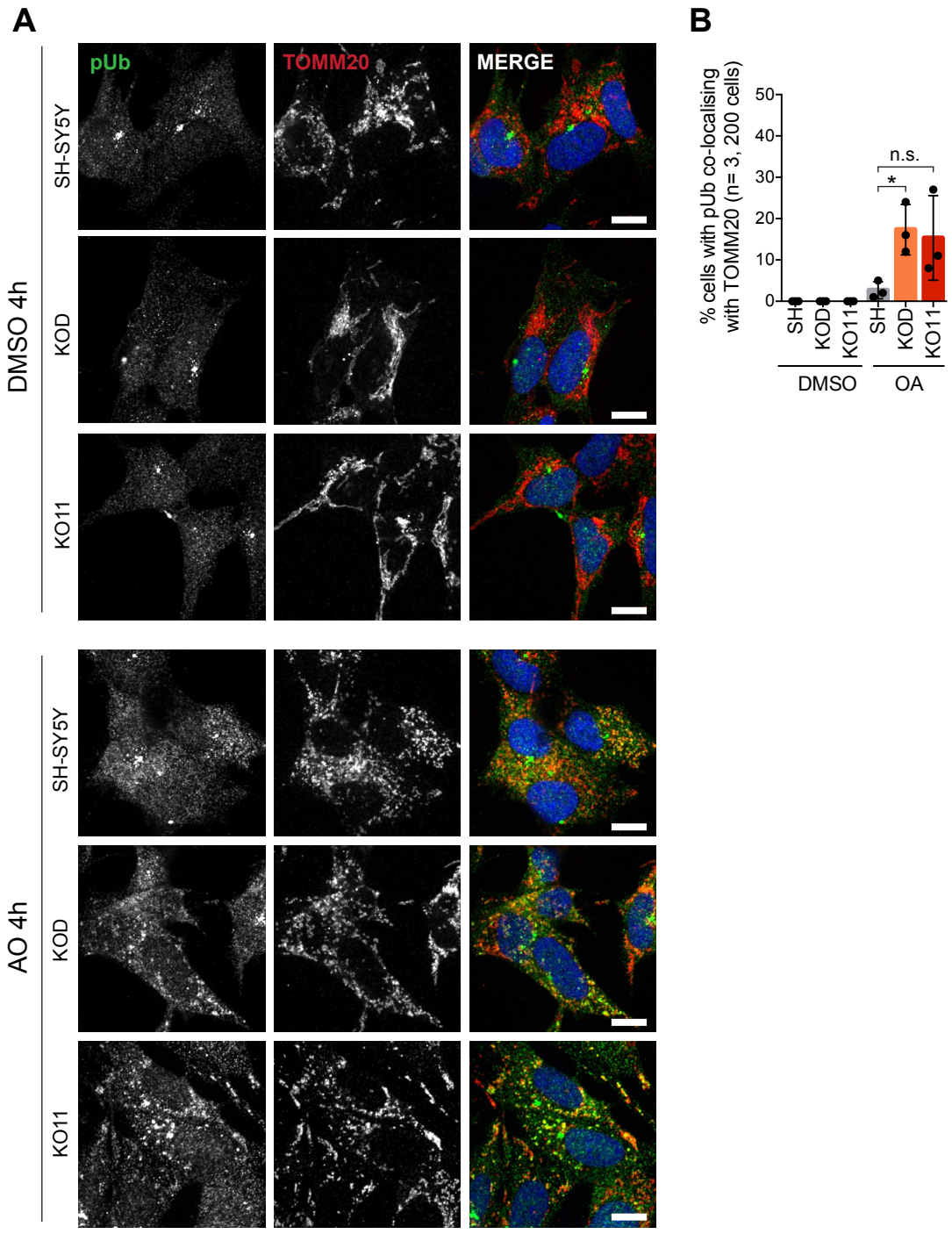
A
pUb
TOMM20
MERGE
DMSO 4h
AO 4h
SH-SY5Y
KOD
KO11
B
% cells with pUb co-localising with TOMM20 (n= 3, 200 cells)
50
40
30
20
10
0
n.s.
*
SH
KOD
KO11
SH
KOD
KO11
DMSO
OA

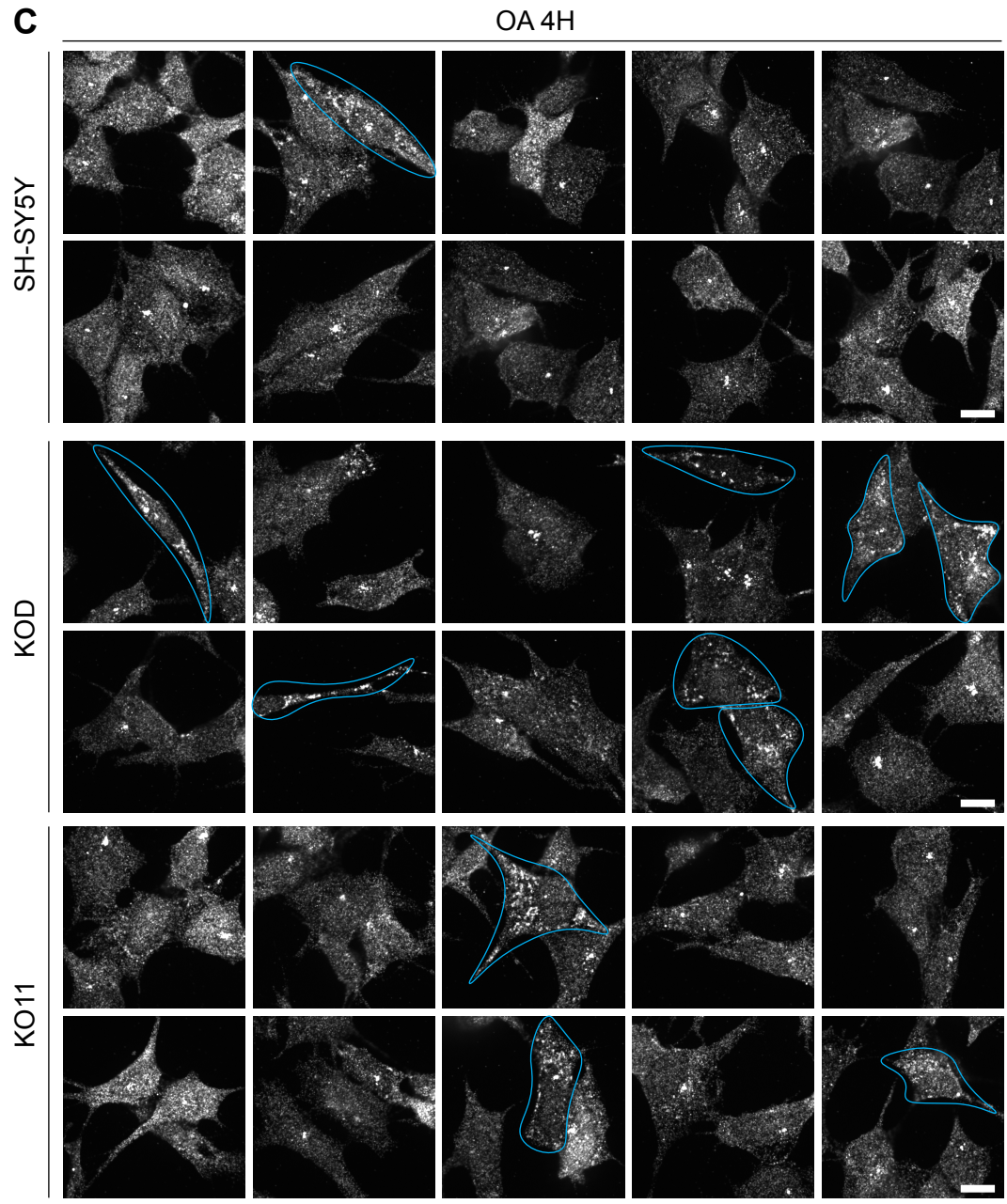

Figure 5.22: USP30 knockout increases pUb accumulation on mitochondria following depolarisation.

SH-SY5Y, KOD and KO11 cells were treated with 1μM Antimycin and 10μM Oligomycin (AO) for 4h. The cells where then fixed with PFA and co-stained with anti-pUb and anti-TOMM20 antibodies. The coverslips were mounted using mowiol mixed with DAPI. **A)** Images were taken with a spinning disk confocal microscope. Scale bar: 10μM. **B)** The number of cells with pUb aggregates overlapping with TOMM20 were manually counted and plotted over the total number of cells. Analysis: one-way ANOVA with Tukey's multiple comparison test. *: $p < 0.05$. Results from 3 experiments; 200 cells were quantified in total. Error bars: mean ± SD. **C)** Representative images depicting pUb re-localisation following AO treatment. The cells with pUb aggregates localising to mitochondria (TOMM20) are outlined in blue.

In AO treated cells, total ubiquitin is increased by 25%, irrespective of the USP30 status, in the high molecular weight range (>76kDa) (**Figure 5.23D**). MIRO1 (72kDa), MFN1 (84kDa) or MFN2 (86kDa) are ubiquitylated early on during mitophagy, although lower molecular weight proteins that are modified with long ubiquitin chains may also contribute to this ubiquitin smear (**Figure 5.18-5.19, 5.21-5.23**).

As USP30 preferentially deubiquitylates K6-chains, I also made use of a highly specific K6-affimer. (**Figure 5.23E**) (Gersch et al., 2017; Michel et al., 2017). Affimers are small (12kDa) engineered binding proteins used as alternatives to antibodies. They are derived from sequences of cystatins and consist of an α-helix and four antiparallel β-sheets. Two surface loops linking the β-sheets can be randomised and produce affimer libraries with substrate specificity (Tiede et al., 2014, 2017). I made use of a K6-affimer linked to a GFP tag and thus detected it with a GFP antibody (**Figure 5.23E**).

As I used the parental SH-SY5Y mito-QC line as a control, the GFP antibody also detected the mito-QC probe. This reporter contains mCherry (26.7 kDa), EGFP (26.9 kDa) and $FIS1_{101-152}$ (5.26 kDa) and therefore the full-length construct runs approximatively at 60kDa. Multiple lower molecular weight fragments of the probe were also apparent and made it difficult to interpret the signal above 76 kDa (**Figure 5.23A, E**). There is also an apparent mono-Ub form of the mito-QC probe that is enhanced with AO-mediated depolarisation (red arrow). FIS1 is known to be ubiquitylated by Parkin at K25 but also at K108, amongst other lysines, during mitophagy (Ordureau et al., 2020; Rose et al., 2016). It is possible that the $FIS1_{101-152}$ fragment of mito-QC gets ubiquitylated.

Just as for total ubiquitin, AO elevated by 20% the amount K6-chains in the high molecular weight range of mitochondrial fractions (**Figure 5.23E**). Interestingly, USP30 knockout did not promote an increase of those high molecular weight range K6-chains. This could indicate that USP30 has only selective substrates, such as TOMM20, rather than globally deubiquitylating mitochondria. USP30's substrates could also be modified by other chain types or monoubiquitin. Another hypothesis would be that another deubiquitylase is compensating for the loss of USP30.

Those results would be in agreement with the model we have presented in Chapter IV, in which USP30 acts upstream of PINK1 to limit the availability of ubiquitylated-proteins for further phosphorylation (**Figure 4.16**).

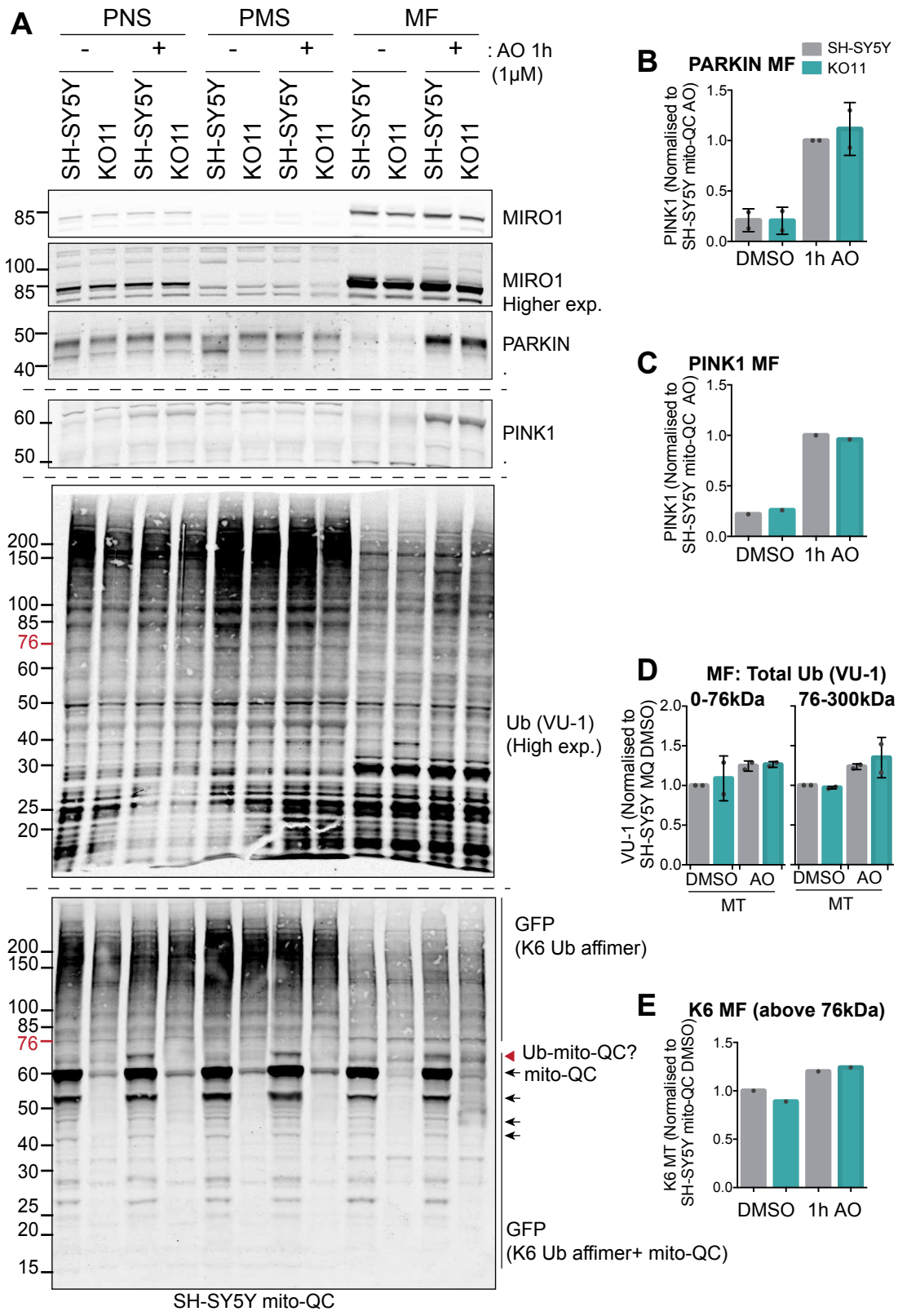

Figure 5.23: Mitochondria fraction: USP30 depletion does not affect the unmodified mitochondrial ubiquitin pool.

SH-SY5Y mito-QC (annotated as SH-SY5Y) and KO11 cells were treated with 1μM Antimycin A and 1μM Oligomycin A (AO) for 1h. The cells were then homogenised in HIM buffer. The Post Nuclear Supernatant (PNS), Post Mitochondrial Supernatant (PMS) and Mitochondrial Fraction (MF) were obtained by differential centrifugation. **A)** The fractions were immunoblotted against proteins involved in mitophagy, ubiquitin and K6-ubiquitin chains. The general ubiquitin antibody VU-1 recognises free ubiquitin, K48-, K63-, K11- and linear- ubiquitin chains. The K6 affimer (Anti di-Ubiquitin K6 Affimer (K6-29) - 7X His and GFP tags) was detected using a GFP antibody. The GFP antibody also recognises the mito-QC probe, which runs at 58.9kDa; the arrows indicate mito-QC and possible cleaved forms of the probe. **B and C)** Mitochondrial PINK1 and Parkin were quantified using ImageStudio and normalised to SH-SY5Y mito-QC 1h AO. **D)** Quantification of total Ub (VU-1) bands running between 0-76kDa or 76-300kDa normalised to SH-SY5Y mito-QC DMSO. **E)** Mitochondrial K6 chains were measured above 76kDa and normalised to SH-SY5Y mito-QC DMSO. Data from a single or two (VU-1 and Parkin blots) experiments. Error bars: mean ± SD.

5.2.3 Identifying new E3 ligases opposing USP30 in mitophagy

We have been hypothesising that USP30 deubiquitylates mitochondrial proteins upstream of PINK1 and PRKN. This model implies that there are priming E3(s) ligase(s) at mitochondria which decorate the OMM with ubiquitin upstream of PARKN (**Figure 5.24**). MARCH5, MUL1, RNF185 could be potential candidates as they are E3 ligases possessing transmembrane domains which anchor them to the OMM (**Figure 5.25**). Moreover, those E3 ligases have also been reported to regulate canonical or non-canonical pathways of mitophagy as well as other mitochondrial quality control pathways, mitochondria dynamics and innate immunity (**Table 5.1 and 5.2**) (Chen et al., 2017; Koyano et al., 2019a; Li et al., 2015; Puri et al., 2019a, 2019b; Rojansky et al., 2016; Tang et al., 2011; Yun et al., 2014), Cytoplasmic and ER E3 ligases, such as FBXO7, ARIH1, HUWE1, AMFR, SMURF1, SIAH1 and TRAF2 have also been reported to regulate mitophagy (**Figure 5.25, Table 5.1**) (Burchell et al., 2013; Di Rita et al., 2018; Fu et al., 2013; Joshi et al., 2018; Leboucher et al., 2012; Orvedahl et al., 2011; Strappazzon et al., 2019; Szargel et al., 2016; Villa et al., 2017; Yang et al., 2015).

I decided to focus on MARCH5, HUWE1, FBXO7 and MUL1 and chose to look at ubiquitylation of TOMM20 and pS65-Ub as a read-out. According to our model, depleting the priming E3 ligase(s) should reduce the availability of putative trigger ubiquitin sites, such as TOMM20 ubiquitylation, for the PINK1-Parkin feedforward loop and therefore diminish the initial phospho-ubiquitin

signal, the further ubiquitylation amplification and the number of mitophagy events.

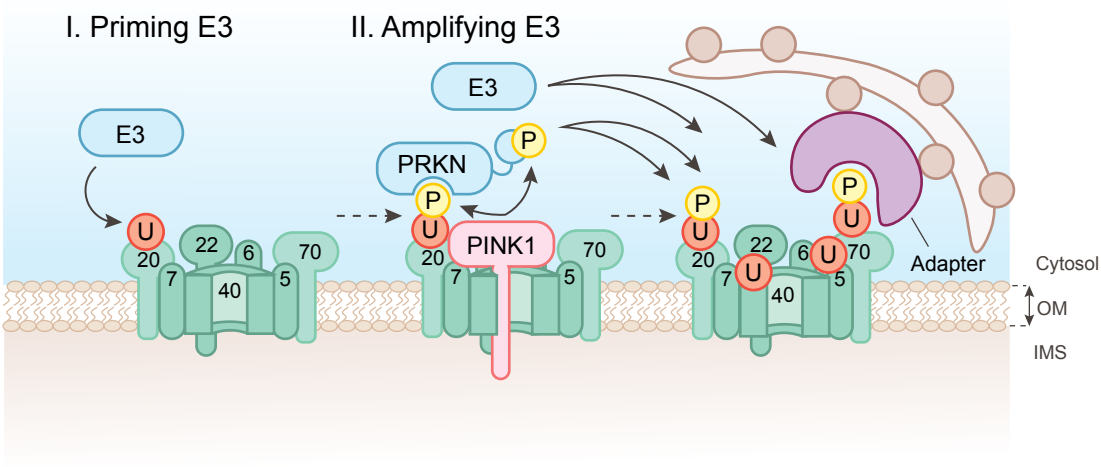

Figure 5.24: Model detailing the respective function of priming and amplifying E3 ligases during mitophagy.

Unidentified E3 priming ligases ubiquitylate putative trigger OMM proteins (namely proteins of the TOMM complex) at PINK1's reach. PINK1 can then phosphorylate those seed ubiquitin moieties and initiate the feedforward process by recruiting amplifying E3 ligases such as Parkin. The amplifying E3 enhance the ubiquitin signal and autophagy adaptors (NDP52, OPTN, TAX1BP1, p62) bring the autophagosomes to the ubiquitylated mitochondria.

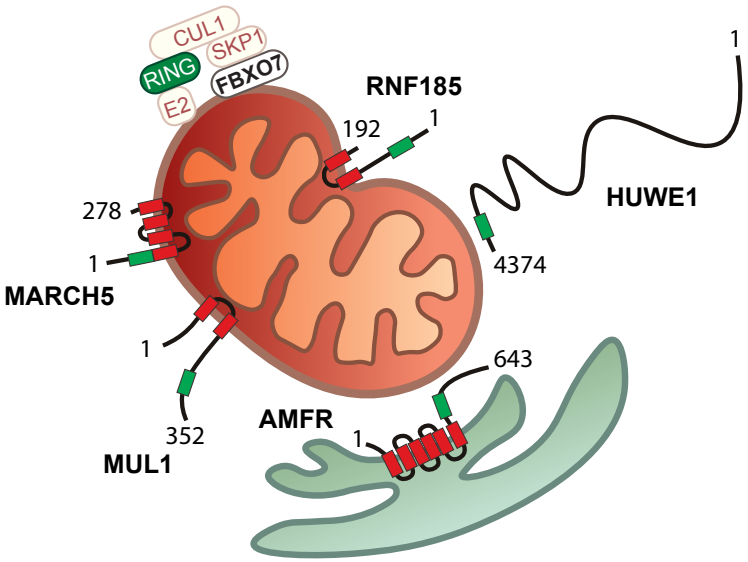

Figure 5.25: Example of alternative ubiquitin E3 ligases.

Here are represented ubiquitin E3 ligases with a reported role on mitochondria and/or in mitophagy. HECT (HUWE1) and RING domains (all others) are shown in green, transmembrane domains in red and the endoplasmic reticulum (ER) in green.

Table 5.1 : A not exhaustive alphabetical list of E3 ligases, other than Parkin, associated with mitophagy.

(In brackets are shown those E3 ligases with a less robust literature linking their function to mitophagy). mt: Mitochondria; Ub: ubiquitin; ER: endoplasmic reticulum.

	Classification	Common aliases	Cellular localisation	Mitophagy pathway	Reference
ARIH1	RBR	HHAR1	Cytoplasm, nucleus	Parkin-independent, PINK1-dependent	(Villa et al., 2017)
FBXO7	SCF	PARK15	Cytoplasm, Mitochondria	Promotes Parkin recruitment	(Burchell et al., 2013)
HUWE1	HECT	MULE, LASU1	Cytoplasm, Nucleus	AMBRA1-dependent, May regulate PINK1 via Myc	(Dadson et al., 2017; Di Rita et al., 2018; Strappazzon et al., 2019)
MARCH5	RING	MITOL, MARCHV	Mitochondria	Hypoxia induced (FUNDC1), Parkin recruitment (“seed Ub”)	(Chen et al., 2017; Koyano et al., 2019a)
MUL1	RING	MAPL, MULAN, GIDE, HADES	Mitochondria, Peroxisomes	ULK1 dependent and Selenite induced; Gemcitabine-induced via PINK1 stabilisation and Parkin independent; inhibits Parkin dep. (MFN2) in neurons; paternal mt with Parkin	(Igarashi et al., 2020; Li et al., 2015; Puri et al., 2019b; Rojansky et al., 2016; Yun et al., 2014)
(AMFR)	RING	Gp78, RNF45	ER	Parkin-independent, PINK1 dependent (MFN1)	(Fu et al., 2013), preprint: (Joshi et al., 2018)
(RNF185)	RING	-	Mitochondria?, ER?	BNIP1 dependent	(Tang et al., 2011)
(SMURF1)	HECT	-	Plasma membrane, cytoplasm	Parkin-dependent (Independent of SMURF1 E3 ligase activity)	(Orvedahl et al., 2011)
(SIAH1)	RING	HUMSIAH1	Cytoplasm, nucleus	PINK1/synphilin-1/SIAH pathway, Parkin-independent	(Szargel et al., 2016)
(TRAF2)	RING	TRAP3	Cytoplasm	Parkin mitophagy in cardiomyocytes	(Yang et al., 2015)

Table 5.2: Mitochondria localised E3 ligases and associated functions (other than mitophagy).

mt: mitochondria; Ub: ubiquitin; TM: transmembrane domain; MDV: Mitochondrial-derived vesicles; ER: endoplasmic reticulum.

	Classification	Common aliases	Cellular localisation	Mitochondria pathway	Reference
MARCH5	RING	MITOL, MARCHV	Mitochondria, peroxisome? 4 TM	mt dynamics (DNM1L), ER-mt tethering (MFN2-Ub), mt-peroxisome translocation, MAVS degradation	(Karbowski et al., 2007; Koyano et al., 2019b; Nakamura et al., 2006; Park et al., 2020; Sugiura et al., 2013; Takeda et al., 2019; Yonashiro et al., 2006; Yoo et al., 2015)
MUL1	RING	MAPL, MULAN, GIDE, HADES	Mitochondria, Peroxisomes, 2 TM	MDV, RIG1-MAVS immunity, MFN2-Ub and DNM1L -SUMO mediated fission and ER-mt tethering	(Braschi et al., 2009, 2010; Doiron et al., 2017; Li et al., 2008; Neuspiel et al., 2008; Prudent et al., 2015; Puri et al., 2019b)
FBXO7	SCF	PARK15	Cytoplasm, Mitochondria	TOMM20 is a substrate of FBXO7	(Teixeira et al., 2016)
RNF185	RING	-	Mitochondria?, ER?, 2 TM	Innate immunity (ubiquitylates cGAS, cGAS-STING pathway)	(El Khouri et al., 2013; Tang et al., 2011; Wang et al., 2017a)

I employed SH-SY5Y and KOD cells and transfected them with E3 ligase-targeting siRNA oligos for 96h. I then treated the cells for 4h with AO (1μM each) to trigger the generation of pS65-Ub and Ub-TOMM20. (**Figure 5.26-5.29**)

I first knocked-down the canonical mitophagy E3, Parkin, and the kinase PINK1 as a positive control (**Figure 5.26**). AO-mediated depolarisation induced the ubiquitylation of MFN2 and FIS1 and raised pS65-Ub levels in both SH-SY5Y and KOD cells **(Figure 5.26A**). Ub-TOMM20 was only increased in KOD cells following AO treatment (**Figure 5.26C**). PINK1 and Parkin knockdown drastically reduced the levels of pS65-Ub and ubiquitylation of MFN2, FIS1 and TOMM20 (**Figure 5.26B-E**). As expected, PINK1 and Parkin are the core regulators of AO-induced ubiquitylation of OMM proteins. Interestingly, Parkin knockdown did not completely abolish pS65-Ub, with ~35% of residual pS65-Ub signal remaining in Parkin depleted cells whereas PINK1 knockdown suppressed all but ~13% of the pS65-Ub signal (**Figure 5.26B**). This provides first evidence for the existence of a priming E3 ligase or an alternative amplifying E3 ligase to Parkin involved in PINK1-dependant mitophagy.
Likewise, ubiquitylation of FIS1, MFN2 and TOMM20 is more sensitive to PINK1 than to Parkin knockdown (**Figure 5.26C-E**).

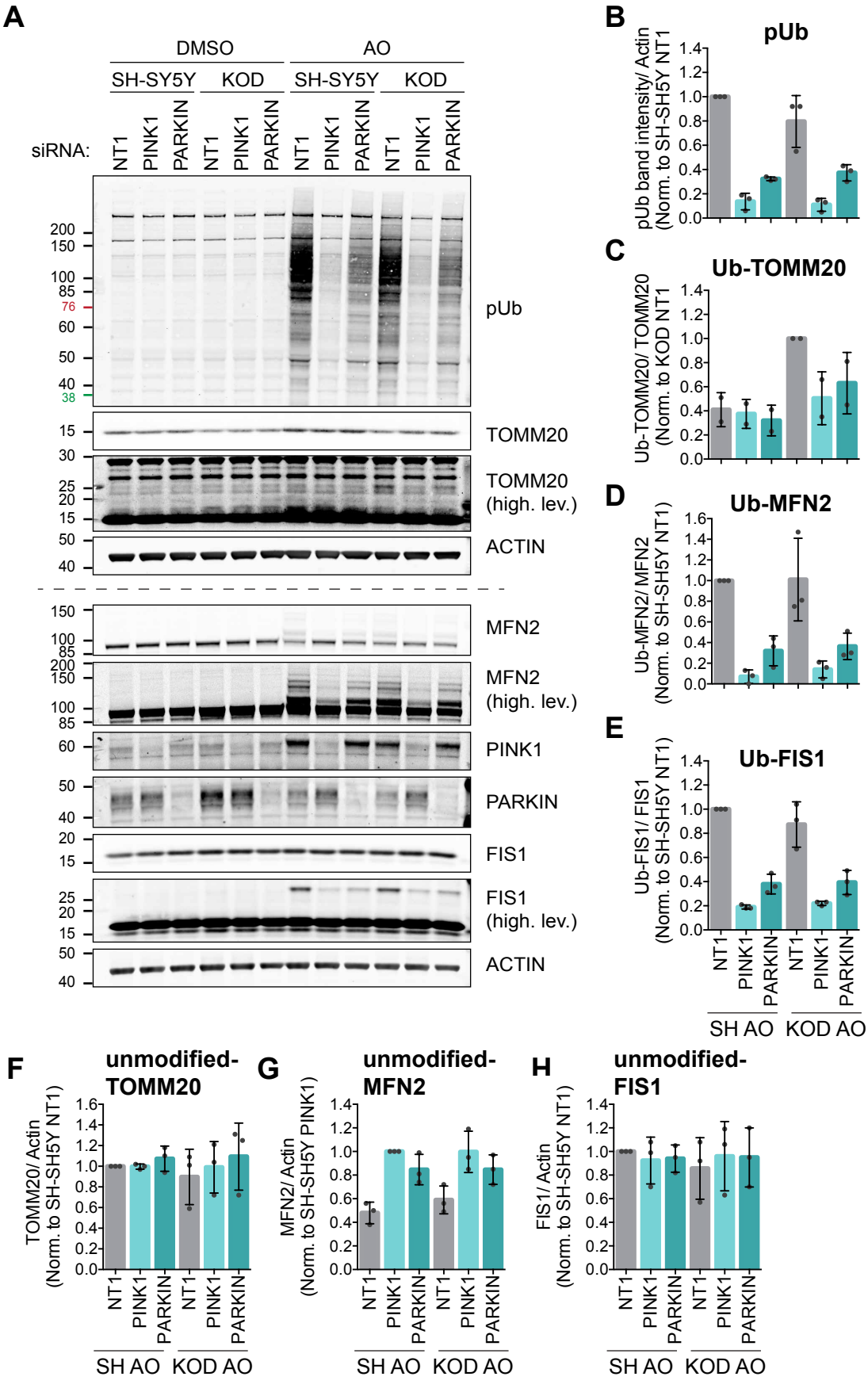
A
DMSO
AO
SH-SY5Y
KOD
siRNA:
NT1
PINK1
PARKIN
pUb
TOMM20
TOMM20 (high. lev.)
ACTIN
MFN2
MFN2 (high. lev.)
PINK1
PARKIN
FIS1
FIS1 (high. lev.)
ACTIN
B
pUb
pUb band intensity/ Actin (Norm. to SH-SH5Y NT1
C
Ub-TOMM20
Ub-TOMM20/ TOMM20 (Norm. to KOD NT1
D
Ub-MFN2
Ub-MFN2/ MFN2 (Norm. to SH-SH5Y NT1)
E
Ub-FIS1
Ub-FIS1/ FIS1 (Norm. to SH-SH5Y NT1)
SH AO
KOD AO
F
unmodified-TOMM20
TOMM20/ Actin (Norm. to SH-SH5Y NT1)
G
unmodified-MFN2
MFN2/ Actin (Norm. to SH-SH5Y PINK1)
H
unmodified-FIS1
FIS1/ Actin (Norm. to SH-SH5Y NT1)

Figure 5.26: PINK1 and Parkin regulate the ubiquitylation of TOMM20 and other outer-mitochondrial proteins.

SH-SY5Y (SH) cells and SH-SY5Y USP30-knockout cells (KOD) were transfected for 96h with 40nM of non-targeting siRNA oligo (NT1) or PINK1- and Parkin-targeting siRNA oligos. The cells were treated for 4h with 1μM of Antimycin and Oligomycin (AO) then lysed in NP40 lysis buffer containing phosStop. **A)** The lysates were immunoblotted against mitochondrial proteins. Quantification of **B)** pUb, **F)** TOMM20, **G)** MFN2 and **H)** FIS1 normalised over Actin then to SH-SY5Y AO NT1 or **G)** to SH-SY5Y AO PINK1. Bar charts representing **C)** Ub-TOMM20, **D)** Ub-MFN2, **E)** Ub-FIS1 over their non-ubiquitylated form and normalised to SH-SY5Y AO NT1 or **C)** to KOD OA NT1. Results from 3 experiments. Error bars: mean ± SD.

HUWE1

HUWE1 is one of the E3 ligases which has been reported to regulate mitophagy and that could act as a priming E3 ligase **(Table 5.1).** HUWE1 was found to be recruited from the cytosol to mitochondria upon AO treatment in HeLa cells (Di Rita et al., 2018; Strappazzon et al., 2019). Once at mitochondria, HUWE1 binds to both the LIR containing protein AMBRA1 and to MFN2, stimulates AMBRA1 phosphorylation by IKKα and MFN2 ubiquitylation, which promotes AMBRA1-mediated mitophagy in the absence of Parkin (Di Rita et al., 2018). Another study described that following cellular stress caused by Doxorubicin, HUWE1 was recruited to mitochondria and mediated MFN2 ubiquitylation leading further to mitochondrial fragmentation (Leboucher et al., 2012).

I used siRNA to knock-down HUWE1 in WT and USP30 KO SH-SY5Y cells to test whether HUWE1 opposes USP30 during mitophagy (**Figure 5.27, 5.28, 5.29**). Surprisingly, HUWE1 knockdown did not affect the levels of MFN2 ubiquitylation. On average HUWE1 KD had little to no effect on pUb, I only measured a negligible decrease of pUb in WT cells (~10%), (**Figure 5.27B, D, 5.28 and 5.29**).

However, depleting HUWE1 decreased TOMM20 mono-ubiquitylation by approximately 25% in KOD cells, whilst FIS1 ubiquitylation was unaffected in either cell line (**Figure 5.27C, E, 5.28, 5.29).** This suggests that HUWE1 may contribute to the ubiquitylation of TOMM20 in response to AO and thus opposes USP30 during mitophagy.

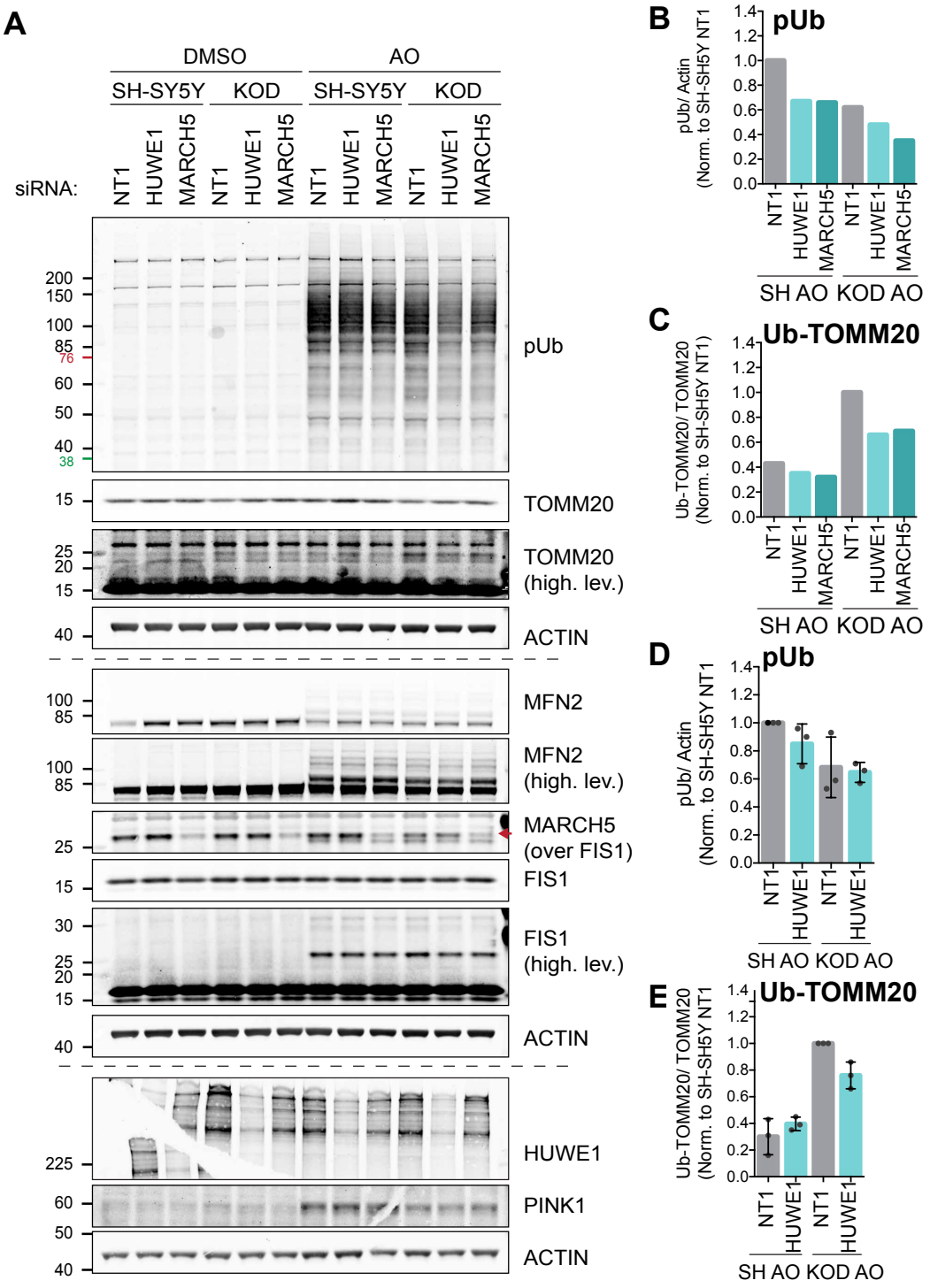

Figure 5.27: HUWE1 and MARCH5 oppose USP30-mediated deubiquitylation of TOMM20.

SH-SY5Y (SH) cells and SH-SY5Y USP30-knockout cells (KOD) were transfected for 96h with 40nM of non-targeting siRNA oligo (NT1) or HUWE1- and MARCH5-targeting siRNA oligos. The cells were treated for 4h with 1µM of Antimycin and Oligomycin (AO) then lysed in NP40 lysis buffer containing phosStop. **A)** The lysates were immunoblotted against mitochondrial proteins**. B)** Quantification of pUb was normalised over Actin and further to SH-SY5Y AO NT1. **C)** Bar chart representing Ub-TOMM20 over non-ubiquitylated TOMM20 and normalised to KOD OA NT1. **D-E)** Average quantitation of **D)** pUb and **E)** Ub-TOMM20 from experiments shown in Figure 5.27, 5.28 and 5.29. Error bars: mean ± SD.

HUWE1 is a well-known regulator of the transcription factor and proto-oncogene c-Myc (Adhikary et al., 2005; Zhao et al., 2008). Dadson and colleagues suggested that deletion of HUWE1 in mouse heart correlated with reduced PINK1 expression possibly through stabilisation c-Myc (Dadson et al., 2017). Interestingly, in SH-SY5Y cells, HUWE1 KD did not affect PINK1 stability (**Figure 5.27-5.29**). However, This neuroblastoma line has a c-Myc amplification that might make it less sensitive to HUWE1 to that regard (Zimmerman et al., 2018).

MARCH5

MARCH5 has four predicted carboxyl terminal transmembrane spanning domains, is localised on mitochondria and was first studied for its role in mitochondrial dynamics (Karbowski et al., 2007; Nakamura et al., 2006; Yonashiro et al., 2006). More recently, Quan Chen's group reported that MARCH5 is involved in fine tuning of hypoxia-induced mitophagy by mediating the ubiquitylation and proteasomal degradation of FUNDC1, a receptor of hypoxia-induced mitophagy in HeLa cells (Chen et al., 2017) **(Table 5.1)**.

I found that knocking down MARCH5 decreased the overall levels of pS65-Ub by ~35% in both USP30 WT and USP30 KO SH-SY5Y cells treated with AO **(Figure 5.27A-B)**. MARCH5 depletion also appeared to result in 30% less TOMM20's ubiquitylation in KOD cells **(Figure 5.27C-D**). Although this experiment seems to indicate that MARCH5 is involved in AO-induced mitophagy, it would need to be repeated to be conclusive.

MUL1

MUL1 had already been linked to several mitophagy pathways such as selenite-induced and gemcitabine-induced mitophagy or the elimination of paternal mitochondria in mouse embryo (Igarashi et al., 2020; Li et al., 2015; Rojansky et al., 2016). It is also present at mitochondrial-associated vesicles, regulates innate immunity at mitochondria (MAVS pathways) and controls mitochondrial fusion and fission dynamics (Braschi et al., 2009, 2010; Doiron et al., 2017; Li et al., 2008; Neuspiel et al., 2008), (**Table 5.1 and 5.2**).

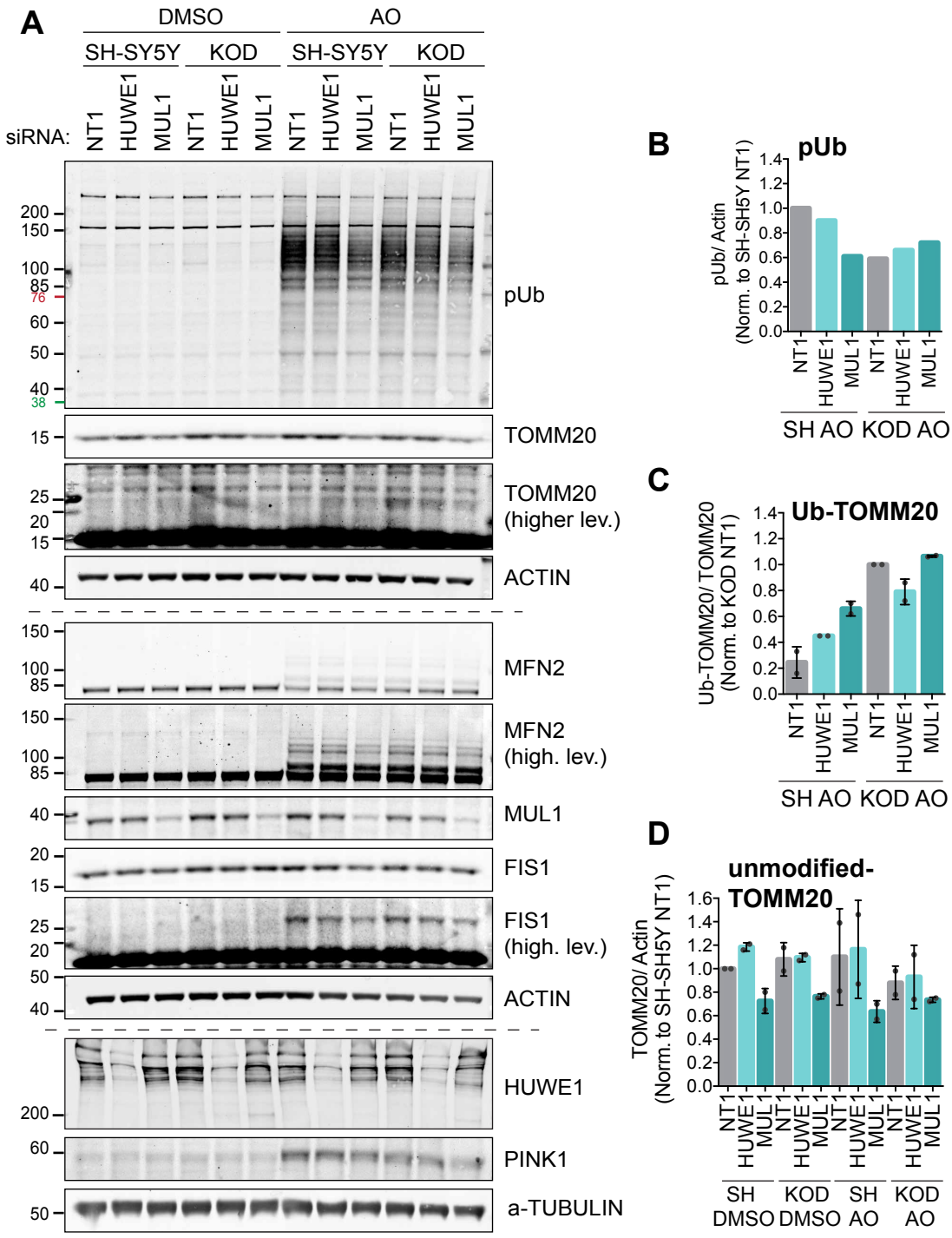
A
DMSO
AO
SH-SY5Y
KOD
siRNA:
NT1
HUWE1
MUL1
pUb
TOMM20
TOMM20 (higher lev.)
ACTIN
MFN2
MFN2 (high. lev.)
MUL1
FIS1
FIS1 (high. lev.)
HUWE1
PINK1
a-TUBULIN
B
pUb
pUb/ Actin (Norm. to SH-SH5Y NT1)
SH AO KOD AO
C
Ub-TOMM20
Ub-TOMM20/ TOMM20 (Norm. to KOD NT1)
SH AO KOD AO
D
unmodified-TOMM20
TOMM20/ Actin (Norm. to SH-SH5Y NT1)
SH DMSO
KOD DMSO
SH AO
KOD AO

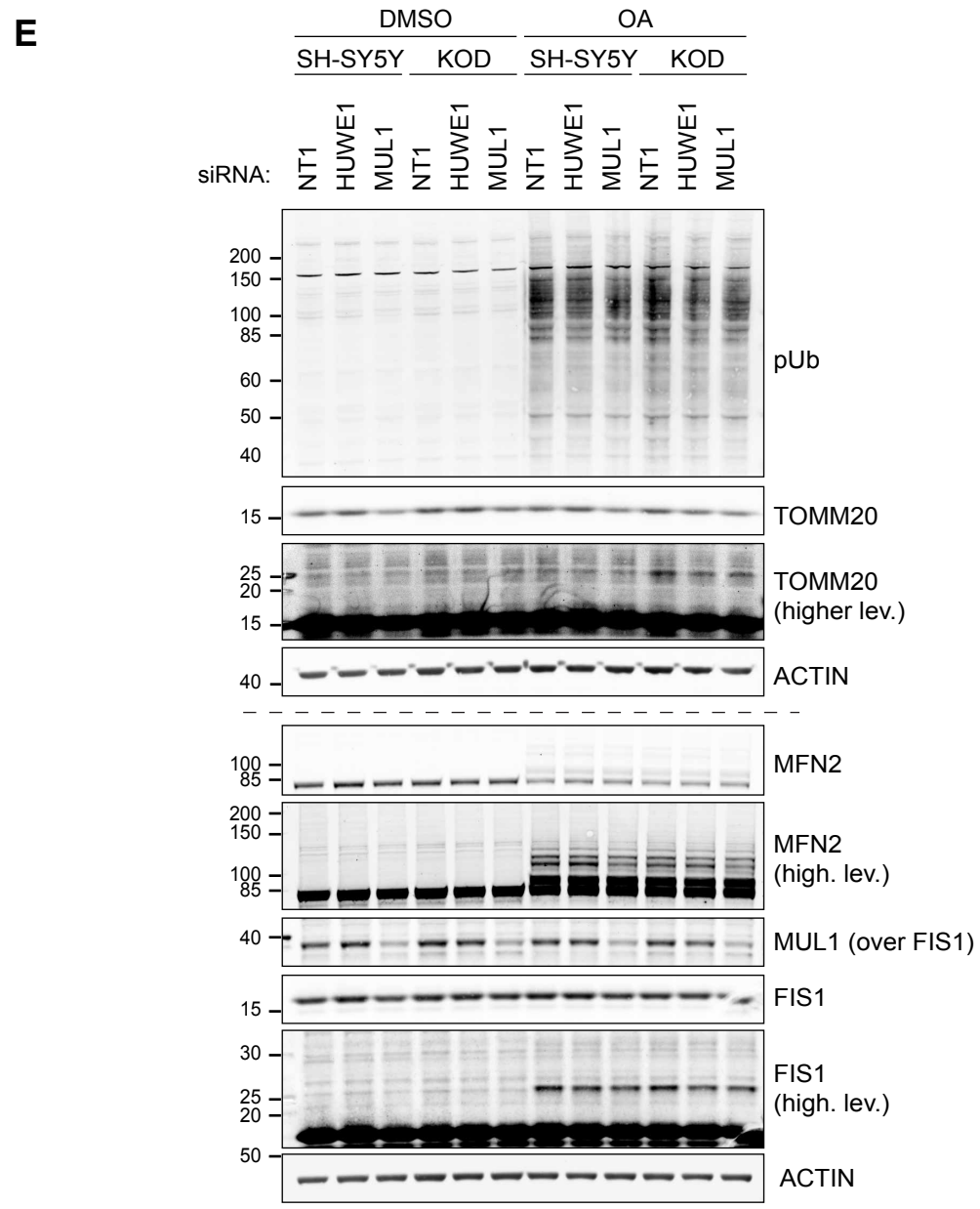

Figure 5.28: MUL1 counteracts the loss of TOMM20 in SH-SY5Y cells.

SH-SY5Y (SH) cells and SH-SY5Y USP30-knockout cells (KOD) were transfected for 96h with 40nM of non-targeting siRNA oligo (NT1) or HUWE1- and MUL1-targeting siRNA oligos. The cells were treated for 4h with 1µM of Antimycin and Oligomycin (AO) then lysed in NP40 lysis buffer containing phosStop. **A and E)** The lysates were immunoblotted against mitochondrial proteins. Quantification of **B)** pUb and **D)** TOMM20 normalised over Actin and further to **B)** SH-SY5Y AO NT1 or **D)** SH-SY5Y DMSO NT1. **C)** Bar chart representing Ub-TOMM20 over non-ubiquitylated TOMM20 and normalised to KOD OA NT1. Average of (A) and (E). pUb was only quantified for (A) ((E): distorted lanes due to DNA). Error bars: mean ± SD.

I observed that MUL1 depletion correlated with reduced TOMM20 expression (29% reduction) independently on depolarisation (**Figure 5.28D**). However, when reported to the levels of unmodified TOMM20, the ubiquitylation of TOMM20 itself did not seem affected by the MUL1 loss (**Figure 5.28C**). pS65-Ub was also decreased by ~20% following MUL1 knockdown in WT SH-SY5Y cells (**Figure 5.28B**). It was less clear in KOD cells whether siMUL1 had reduced the levels of pS65-Ub as the lane was underloaded. The normalisation to actin suggested that it did not (**Figure 5.28A-B**).
From these western blot analyses, it seems that MUL1 stabilises TOMM20.

FBXO7

Mutations in the gene coding for FBXO7 have been found associated with early-onset forms of PD (Di Fonzo et al., 2009; Paisán-Ruiz et al., 2010; Shojaee et al., 2008). It is a member of the SKIP1-CUL1-F-box E3 ligase complex and was reported to regulate CCCP-induced mitophagy in mammalian cells over-expressing Parkin (Burchell et al., 2013). Burchell and colleagues showed that FBXO7 interacts with Parkin and PINK1 and that the knockdown of FBXO7 decreased Parkin's translocation to mitochondria as well as mitochondria degradation, following CCCP treatment. Moreover, they reported that *Fbxo7* overexpression rescues motor function in *Parkin* mutant *Drosophila* (*Park*^{25}). Heike Laman and David Komander's group jointly revealed, using protein arrays and in vitro ubiquitylation reactions, that TOMM20 is a substrate of FBXO7 (Teixeira et al., 2016).

I found that knocking down FBXO7 neither affected the levels of pS65-Ub nor did it impact the degree of ubiquitylation of OMM proteins (MFN2, FIS1 and TOMM20), nor the stability of TOMM20 (**Figure 5.29A-E**).
Knocking down FBXO7 did not enhance (neither decrease) the percentage of cells undergoing mitophagy in AO treated cells. Nor did it affect the enhanced mitophagy seen in USP30 deleted cells, suggesting that FBXO7 is not the priming E3 (**Figure 5.30**). I studied a duplicate of this experiment by western blotting and measured no changes in the ubiquitylation status of OMM proteins (Ub-FIS1 or Ub-MFN2) (**Figure 5.30B**).

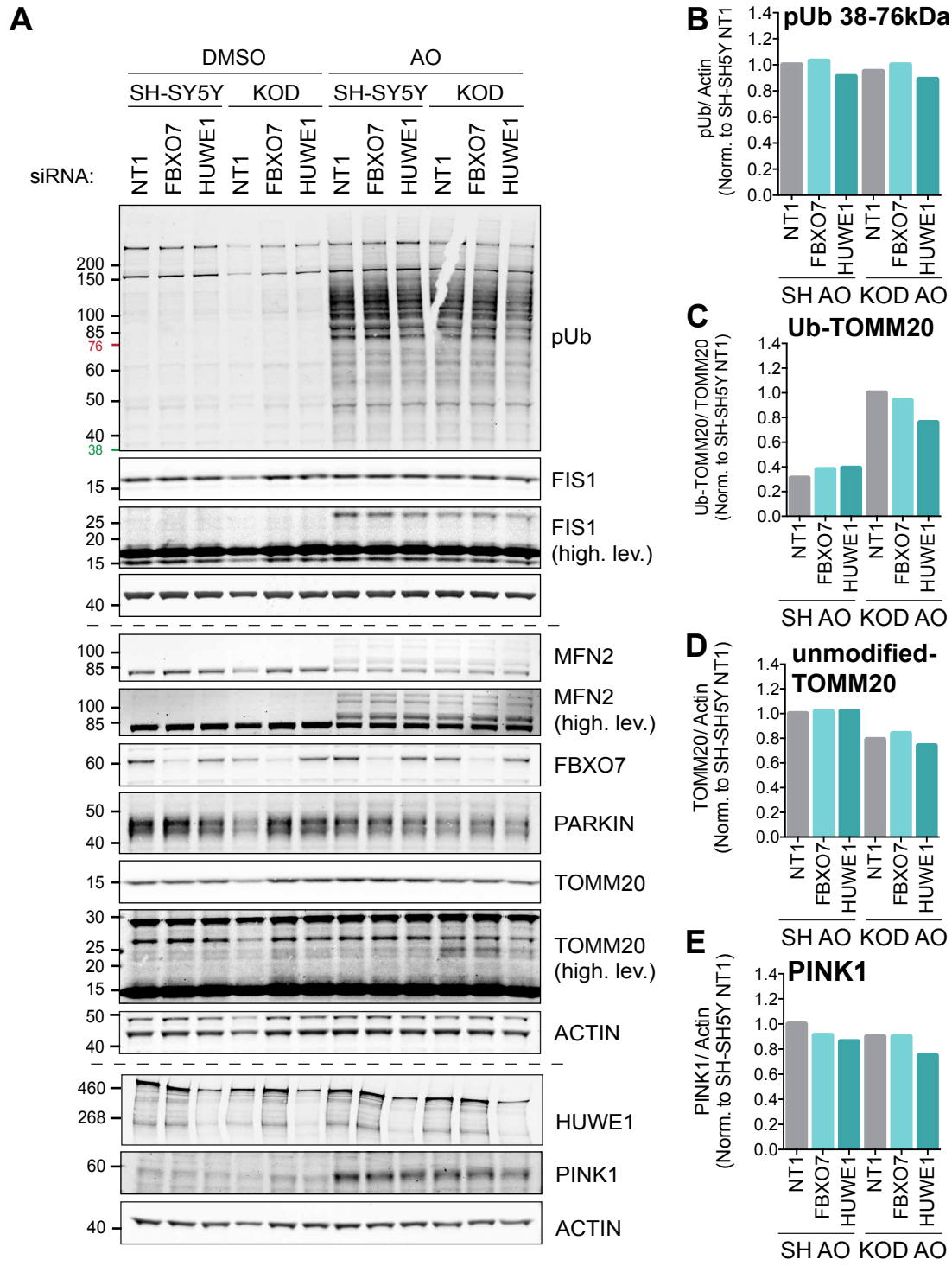

Figure 5.29: FBXO7 depletion does not affect the ubiquitylation of outer mitochondrial membrane proteins.

SH-SY5Y (SH) cells and SH-SY5Y USP30-knockout cells (KOD) were transfected for 96h with 40nM of non-targeting siRNA oligo (NT1) or HUWE1- and FBXO7-targeting siRNA oligos. The cells were treated for 4h with 1µM of Antimycin and Oligomycin (AO) then lysed in NP40 lysis buffer containing phosStop. **A)** The lysates were immunoblotted against mitochondrial proteins. Quantification of **B)** pUb, **D)** TOMM20 and **E)** PINK1 normalised over Actin and further to SH-SY5Y AO NT1. **C)** Bar chart representing Ub-TOMM20 over non-ubiquitylated TOMM20 and normalised to KOD OA NT1. Data from a single experiment.

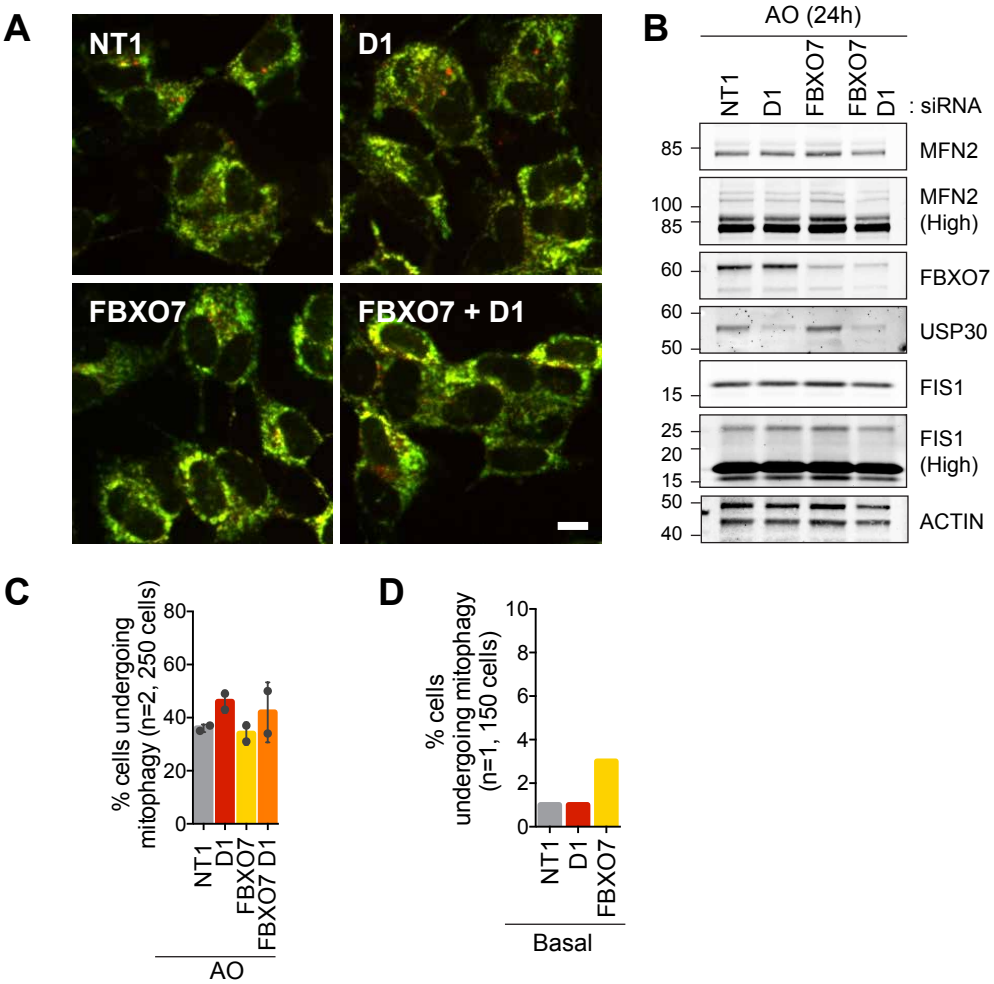

Figure 5.30: FBXO7 depletion does not affect AO-induced mitophagy in SH-SY5Y mito-QC cells.

A) SH-SY5Y mito-QC cells were transfected for 72h with 40nM siRNA targeting USP30 (D1), FBXO7 or non-targeting siRNA (NT1). The cells were then depolarised for 24h with 1M Antimycin A and 10μM Oligomycin A (AO). The cells were imaged on a spinning disk confocal microscope using a 40X objective lens. Scale bar: 10μm. **B)** Representative western blot figure showing the knockdown efficiency of FBXO7 and USP30. **C)** Cells with more than 3 mitolysosomes were considered are undergoing mitophagy. The cells were manually counted. **D)** A separate experiment was performed without AO treatment. Error bars: mean ± SD.

Cullin Ring Ligases CRLs

ARIH1 is a cytosolic RING-between-RING (RBR) E3 ligase, like Parkin, which was found to be recruited to mitochondria and to promote PINK1-dependent mitophagy in depolarised cells lacking Parkin (Villa et al., 2017). This E3 ligase shares the same E2 ligase as Parkin, UBCH7, and works in cooperation with Cullin-RING ligases (CRLs) (Wenzel et al., 2011). ARIH1 acts as a priming E3 ligase, adding monoubiquitin on specific CLR substrates for subsequent ubiquitin chain elongation by CLRs (Scott et al., 2016). I thus thought that it would be interesting to assess whether inhibiting CLRs function would affect mitophagy.

These multi-subunit E3 ubiquitin ligases are activated through neddylation of their Cullin subunit (Lydeard et al., 2013). I used MLN492, an inhibitor of the Nedd8 E1 activating enzyme (NAE) to indirectly inhibit CRLs.

I characterised the effect of CRLs inhibition by western blotting **(Figure 5.31).** I found that treating SH-SY5Y cells with 1μM MLN492 for 30min was sufficient to fully de-neddylate cullins (**Figure 5.31A**). I then assessed the involvement of CLRs in AO-induced mitophagy. I found that inhibiting CLRs using MLN492 did not reduce AO-induced ubiquitylation of OMM proteins: Ub-MFN2, Ub-MFN1, Ub-MIRO1, Ub-FIS1, Ub-VDAC and Parkin auto-Ub remained stable (**Figure 5.31B-C**). However, in a parallel imaging experiment of SHSY5Y mito-QC cells, I observed that inhibition of Cullins (with 1 μM MLN492 for 24h) induced a potent activation of basal mitophagy (55.3 ± 6.1% of cells undergoing mitophagy compared to 2.3 ± 2.3% in DMSO treated cells) which was in fact significantly higher than AO-induced mitophagy (34.0 ± 6.2%). Co-treating the cells with AO and MLN492, did not further enhance mitophagy significantly (68.7±14.5 %) (**Figure 5.31D-E**).

Surprisingly, I observed that inhibition of CRL is sufficient to trigger potent mitophagy. A preliminary experiment suggests that it is not dependent on FBXO7 inhibition (3% of cells undergoing mitophagy in FBXO7 knockdown cells compared to 1% of control cells) (**Figure 5.30D**). MLN492-induced mitophagy was not accompanied by the ubiquitylation of common mitophagy substrates such as MFN2, MFN1, MIRO1 or FIS1 which could indicate that it is not dependent on ubiquitylation. It would be important to assess whether this mitophagy peak reflects a global induction of autophagy.

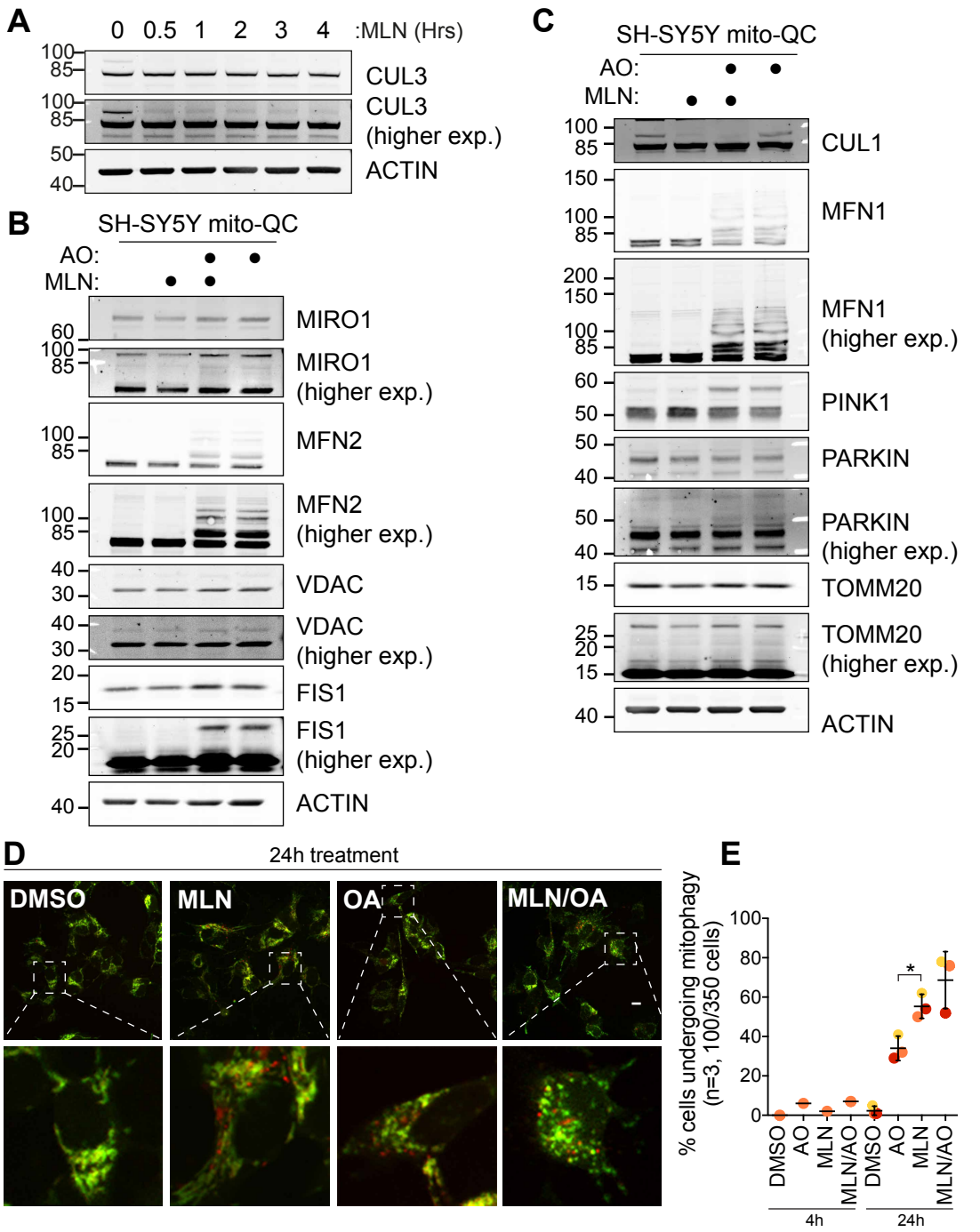

Figure 5.31: FBXO7 depletion does not affect AO-induced mitophagy in SH-SY5Y mito-QC cells.

A) SH-SY5Y cells were treated with 1μM MLN4924 up to 4h and lysed in NP40 buffer. The lysates were probed for cullin 3 (CUL3), a component of Cullin-RING E3 ubiquitin ligases complexes and substrate of neddylation. **B and C)** SH-SY5Y mito-QC cells were pre-treated with 1μM MLN4924 for 30min then treated for 4h with 1μM Antimycin A, 10μM Oligomycin A (AO) with/without 1μM MLN (1μM). The cells were lysed and immunoblotted against common mitophagy players. **D)** SH-SY5Y Mito-QC were treated as in B, C) and imaged live on a spinning disk confocal using a 40X objective lens. Scale bar 10μM. n=2 (Exp#1 and 3: 24h treatment only, Exp#2: 4h vs 24h treatment). **E)** The number of cells undergoing mitophagy (> 3 mitolysosomes) was counted manually and reported on this graph. Analysis: One-way ANOVA with Tukey's multiple comparison test. *: $p < 0.05$

5.3 Characterisation of USP30 inhibitors

As reported in the Introduction chapter, a subset of hereditary and early-onset forms of PD are caused by loss of function mutations targeting PINK1 and Parkin (Corti et al., 2011; Deas et al., 2009; Kitada et al., 1998; Valente et al., 2004). Parkin inactivation was also reported in sporadic PD and correlates with Parkin post translational modification resulting from dopaminergic, oxidative and nitrosative stress (Dawson and Dawson, 2014; LaVoie et al., 2005, 2007; Wong et al., 2007). A widespread hypothesis is that defects in mitophagy underly neurodegeneration in PD. Hence, efforts have been put into finding means of activating mitophagy as a therapeutic approach. This includes the development of PINK1 and Parkin activators as well as USP30 inhibitors (Miller and Muqit, 2019).

We have previously shown, with others, that USP30 depletion increases both induced and basal mitophagy in human cell lines (Chapter III and IV), (Bingol et al., 2014; Cunningham et al., 2015; Liang et al., 2015; Wang et al., 2015; Marcassa et al., 2018).

The Bingol lab has further shown that *Usp30* knockdown was able to rescue PD-pathogenic phenotypes in PINK1 and Parkin mutant *Drosophila* (Bingol et al., 2014). These observations suggest that inhibiting USP30 could rescue pathogenic defects caused by the slow accumulation of damaged mitochondria in humans affected by PD.

I have had the chance and the opportunity to participate in the characterision of a first generation of highly selective USP30 inhibitor (Rusilowicz-Jones et al., 2020). USP30 is a good target for the development of inhibitors as CRISPR essentiality screens show that its depletion is well tolerated across a broad range of cell lines (Lenoir et al., 2018; Meyers et al., 2017). As USPs are cysteine proteases, multiple groups have aimed at targeting the reactive cysteine to produce potent inhibitors, as exemplified by USP7 inhibitors (Pozhidaeva et al., 2017; Reverdy et al., 2012; Turnbull et al., 2017). Cyanopyrrolidines have been reported to inhibit cysteine proteases, notably cathepsin C and DUBs such as UCHL1, USP7 and USP30 (Bashore et al.,

2020; Krabill et al., 2020; Lainé et al., 2011), (Patents: WO2014041111A1, WO2016156816, WO2018060742A1, EP3433246A1).
We introduce here two new USP30 N-cyano pyrrolidines compounds inhibitors.

5.3.1 First generation inhibitor

We have been working in collaboration with FORMA Therapeutics/Celgene to characterise new USP30 inhibitors. The first experiments I have performed used a first-generation version of the FT385 inhibitor (hereafter referred to as USP30i) (Rusilowicz-Jones et al., 2020). Together with Aitor Martinez-Zarate, I assessed the effect of USP30i mediated inhibition of USP30 in cells with endogenous or over-expressed Parkin.

5.3.1.1 USP30i in cells over-expressing Parkin

Using YFP-Parkin overexpressing hTERT-RPE1 cells, I tested whether USP30i would phenocopy USP30 knockdown and prevent the deubiquitylation of USP30 substrates such as TOMM20. I treated the cells with increasing USP30i concentration (0.5-5μM) for 4h with or without AO-mediated depolarisation (**Figure 5.32**). In the absence of a depolarising trigger, TOMM20 ubiquitylation was not affected by USP30i. Treating the cells for 4h with AO clearly induced the ubiquitylation of TOMM20 and this was further increased by up to 1.6-fold when USP30i was included (**Figure 5.32B**).

It has previously been reported that knocking-down or inhibiting USP30 promotes fusion of the mitochondrial network in HeLa and mouse embryonic fibroblasts (MEF) cells, respectively (Nakamura and Hirose, 2008; Yue et al., 2014). Yue and colleagues had further shown that USP30 inhibition using the non-selective small inhibitor 15-oxospiramilactone, had the ability to revert the mitochondrial fragmentation in MFN1 or MFN2 KO MEF cells (Yue et al., 2014). In contrast, I did not observe a mitochondria hyperfused phenotype in hTERT-RPE1-YFP-Parkin cells (TOMM20 staining) following USP30i-meditated inhibition of USP30 (**Figure 5.33**).

I next moved onto cells that do not express Parkin or express endogenous Parkin and visualised mitophagy live in these cells. The mitochondrial network of those cells was unchanged with USP30i treatment.

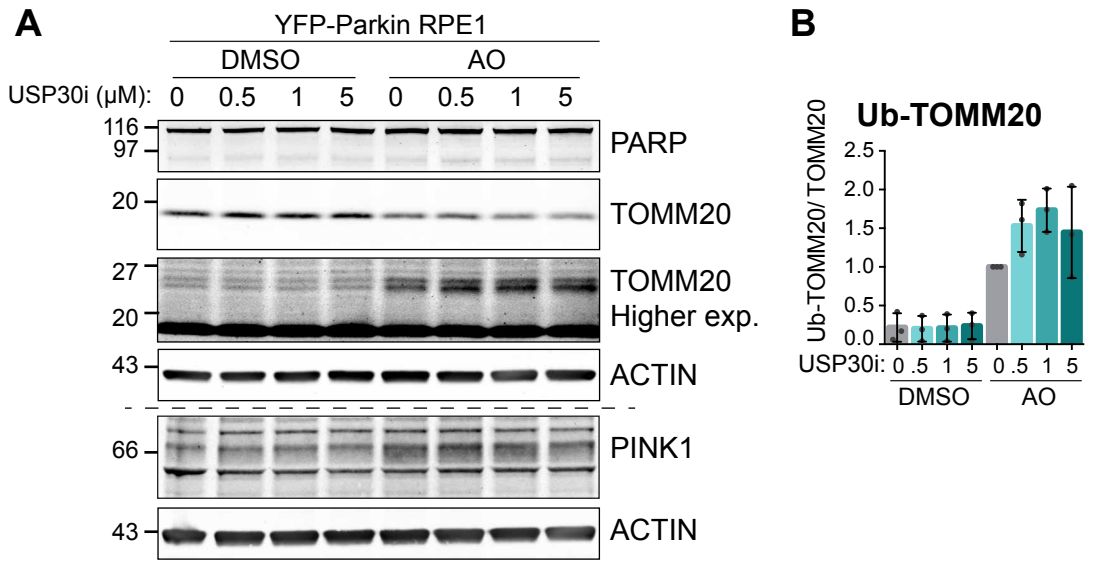

Figure 5.32: USP30 inhibition by USP30i induces ubiquitylation of TOMM20 in hTERT-RPE1-YFP-Parkin RPE1 cells.

A) hTERT-RPE1-YFP-Parkin cells were depolarised with 1μM Antimycin A and 1μM Oligomycin A (AO) and co-treated with a range of concentrations of USP30i (0-5μM) for 4h. The cells were then lysed in RIPA buffer and immunoblotted. **B)** Graph representing ubiquitylated TOMM20 ratioed to unmodified-TOMM20 and normalised to the 4h AO condition. Data shown are the average of three independent experiments, error bars show standard deviation.

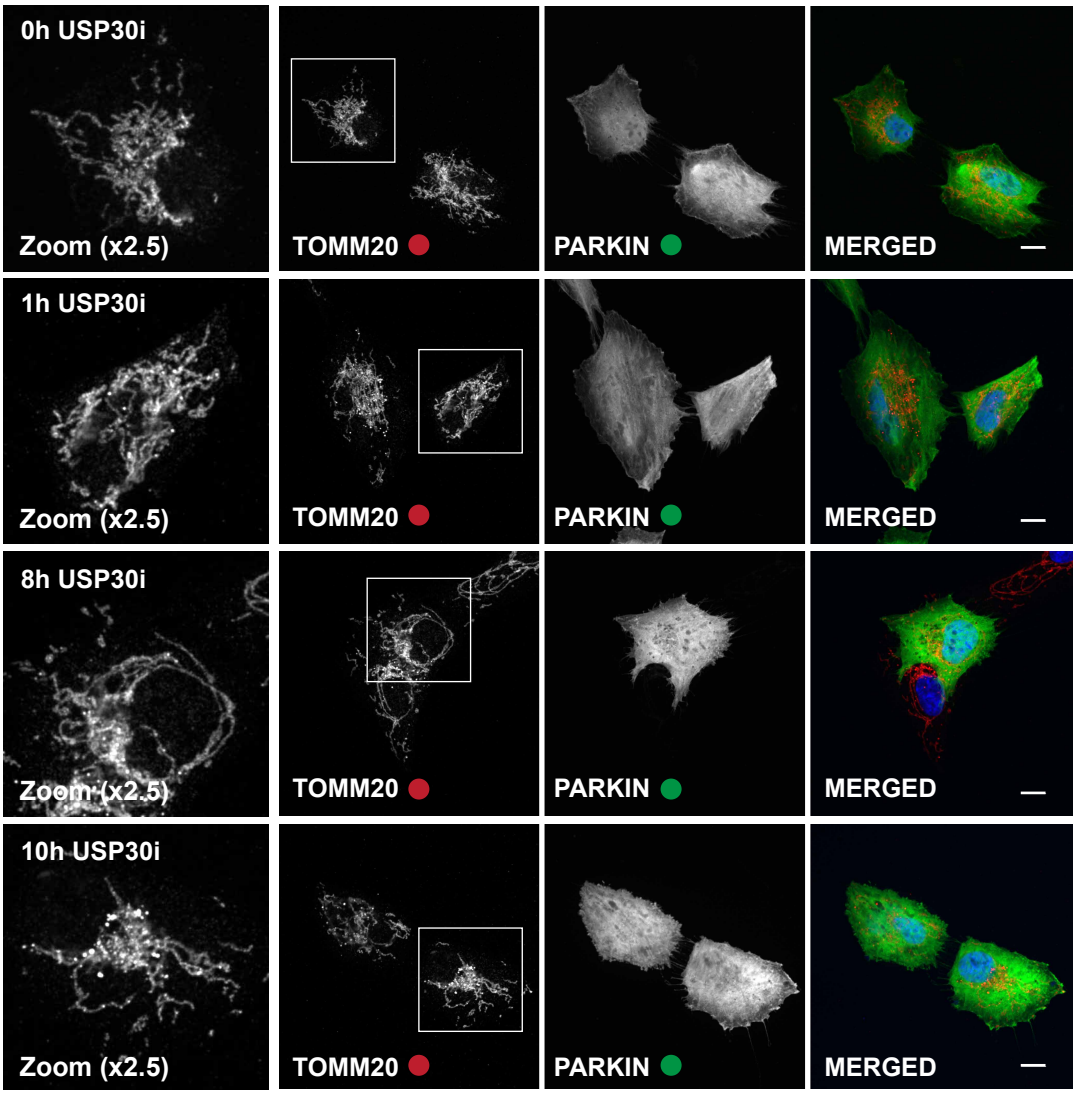

Figure 5.33: USP30i does not affect the mitochondrial network of hTERT-RPE1-YFP-Parkin cells.

hTERT-RPE1-YFP-Parkin cells treated with 5μM USP30i for 1, 8 and 10h. The cells where then fixed with PFA and stained with an anti-TOMM20 antibody. The coverslips were mounted using mowiol mixed with DAPI. The cells were imaged live on a 3i spinning disk confocal equipped of an sCMOS camera and using a 63X objective lens. Scale bar: 10μm. Data from a single experiment.

5.3.1.2 USP30i in cells with endogenous Parkin expression

I employed the mito-QC probe to measure mitophagy in U2OS cells, kindly provided by Ian Ganley (MRC-PPU, Dundee), following USP30 inhibition.
Using these same cells, my colleague Elena Marcassa had previously shown that basal mitophagy is enhanced following 72 h of knockdown (Marcassa et al., 2018). In order to mirror those conditions, I first treated those cells for 72h with USP30i (0.5-10μM) (**Figure 5.34**). Treatment with 5μM and 10μM USP30i increased the number of mitolysosomes, by 1.6 and 1.7-fold respectively, and increased the mitolysosomes area by 1.5 and 2.6 times (**Figure 5.34B, C and D**).
This enhancement of basal mitophagy events upon USP30 inhibition was also apparent for a shorter exposure time (24h). The number of mitolysosomes was multiplied 1.4-fold and their area was doubled with 5μM USP30i (**Figure 5.35A-D)**. I thus concluded that in U20S cells, USP30i phenocopies USP30 KD by triggering mitophagy. The mitolysosome swelling was however only observed with the inhibitor and should be assessed with other inhibitors to verify the specificity of that response. Mitolysosome swelling could indicate that the autophagosomes have incorporated multiple mitochondrial fragments or larger fragments.

I then observed the impact of USP30 inhibition in SH-SY5Y cells stably expressing the mito-QC probe (**Figure 5.35E-H**). I found that at concentrations above 2.5μM, USP30i induced cell death in SH-SY5Y mito-QC cells (data not shown). SH-SY5Y mito-QC cells treated with the vehicle (DMSO) alone showed very few mitolysosomes, only 0.69 per cell on average with ~ 65% of cells having no mitolysosomes. In SH-SY5Y mito-QC cells treated for 24h with USP30i, I measured a trend towards an increase of both the number of mitolysosomes per cell and of the mitolysosome area (**Figure 5.35F-H**). On average, the number of mitolysosomes was multiplied by 5.8±5.5 (1μM USP30i) and by 5.1 ±5.1 (2.5 μM USP30i). However, only few cells were showing signs of mitophagy (45% and 40% of cells still had no mitolysosomes with 1 and 2.5μM USP30i respectively). Thus, in SH-SY5Y cells, USP30i also recapitulates the effects of USP30 knockdown in that it enhances basal mitophagy.

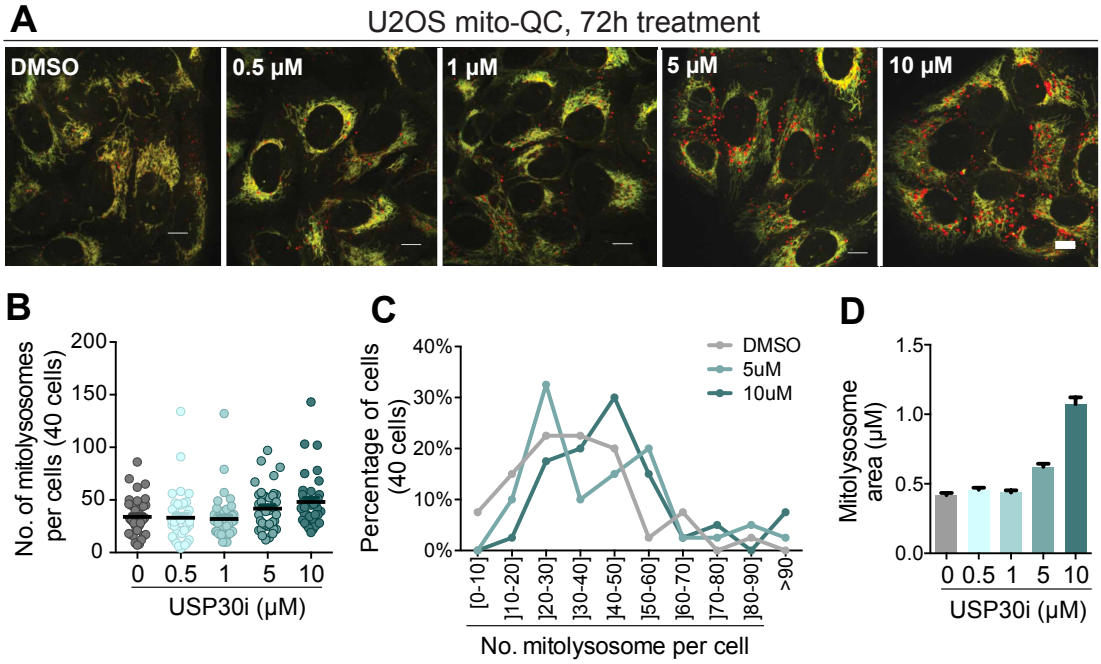

Figure 5.34: USP30 inhibition induces mitophagy in U2OS mito-QC cells.

A) U2OS mito-QC cells were treated with the USP30i inhibitor for 72h at indicated concentrations. The cells were imaged live on a spinning disk confocal microscope using a 63X objective lens. Scale bar: 10µm. **B)** The number of dots per cell was quantified using Analyse particle on Fiji. **C)** Graph categorising the cells by no. of mitolysosomes. **D)** Mean mitolysosome area per condition. Error bars: mean ± SD. Data from a single experiment.

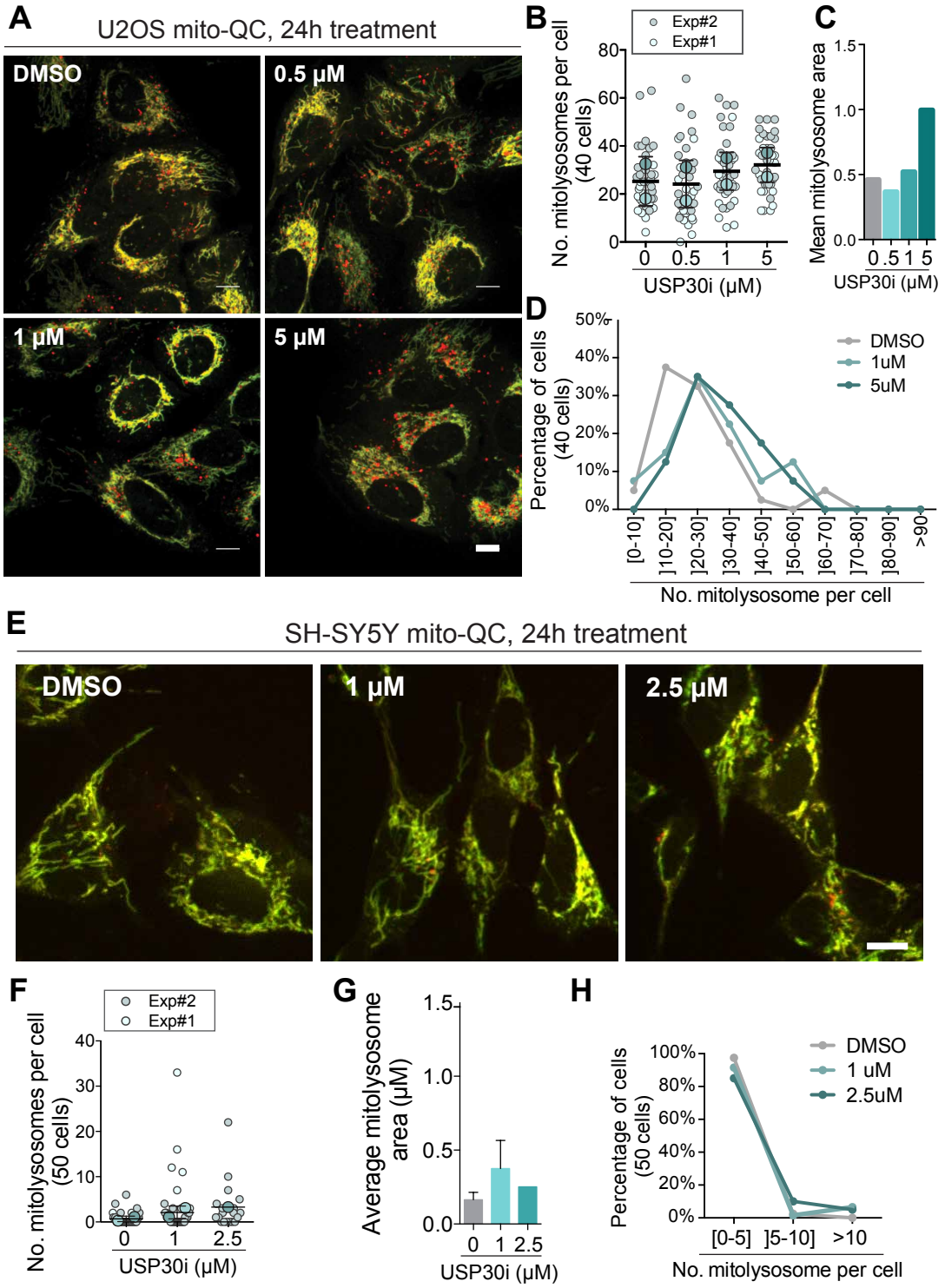

Figure 5.35: USP30 inhibition by USP30i induces mitophagy in U2OS mito-QC cells.

A) U2OS mito-QC cells or E) SH-SY5Y mito-QC cells were treated with USP30i for 24h at the indicated concentrations. The cells were imaged live on a spinning disk confocal using a 63X objective lens. Scale bar: 10µm. **B and F)** The number of mitolysosomes per cell was quantified using Analyse particle on Fiji. **C and G)** The average mitolysosome area was assessed with Analyse particle. (In (C) The mitolysosome area was analysed for Exp#1 only). **D and H)** Graph categorising the cells by no. of mitolysosomes; the values are normalised to the total number of cells. Error bars: mean ± SD.

SH-SY5Y cells can be differentiated into neuron-like cells with retinoic acid (RA) and 12-O-tetradecanoly-phorbol-13-acetate (TPA) dopaminergic-like neurons (Kovalevich and Langford, 2013; Presgraves et al., 2004). I thus assessed whether I could monitor mitophagy in differentiated cells.

Following sequential 72h treatments with RA then TPA, I obtained a mixed population of undifferentiated (~90%) and differentiated (~10%) SH-SY5Y mito-QC cells with prominent neurite like extensions (**Figure 5.36**). I treated those cells with DMSO or 2.5μM USP30i for 48h and imaged 5 cells with a typical neuron-like appearance per condition for 5min. Overall, the differentiated cells had a dense mitochondrial network in the perinuclear area with elongated filamentous mitochondria extending into the neurites. The mitolysosomes were typically located in the perinuclear area. Although the efficiency of differentiation was too low to gain definitive answers, based on this small sample, I had the impression that USP30i treated cells had a more fused mitochondrial network and more mitolysosomes.

In an attempt to improve the efficiency of differentiation, I adopted an alternative protocol optimised by Heather Mortiboys (SITraN, Sheffield). SH-SY5Y cells are grown in neurobasal medium mixed with N2 supplement and treated for 7 days with 10μM RA. I tested this protocol in SH-SY5Y, SH-SY5Y mito-QC, KOC, KOD and KO11 cells and found that only the KO11 line survived the procedure (**Figure 5.37**). The KO11 cells appeared differentiated with elongated cellbodies and extended neurites.

One possible cause for cell death (RA protocol) and low differentiation rate (RA + TPA) is the passage number of the cells I used. I inherited of late passage SH-SY5Y cells (p20 and p25) and stable SH-SY5Y mito-QC cells that are most likely older than p15. ECACC report that SH-SY5Y cells start to lose their neuronal characteristics and potential to differentiate with passages; they recommend maintaining SH-SY5Y cells below passage number 20. Others suggest maintaining SH-SY5Y cells below passage 15 when wanting to differentiate them. "Older" cell populations will be enriched in a subset of epithelial-like SH-SY5Y cells that cannot differentiate into neurons and which undergo cell death during the differentiation process (Shipley et al., 2016).

I did not further pursue the experiments with USP30i as we received in the meantime a more potent and specific USP30 inhibitor (FT385).

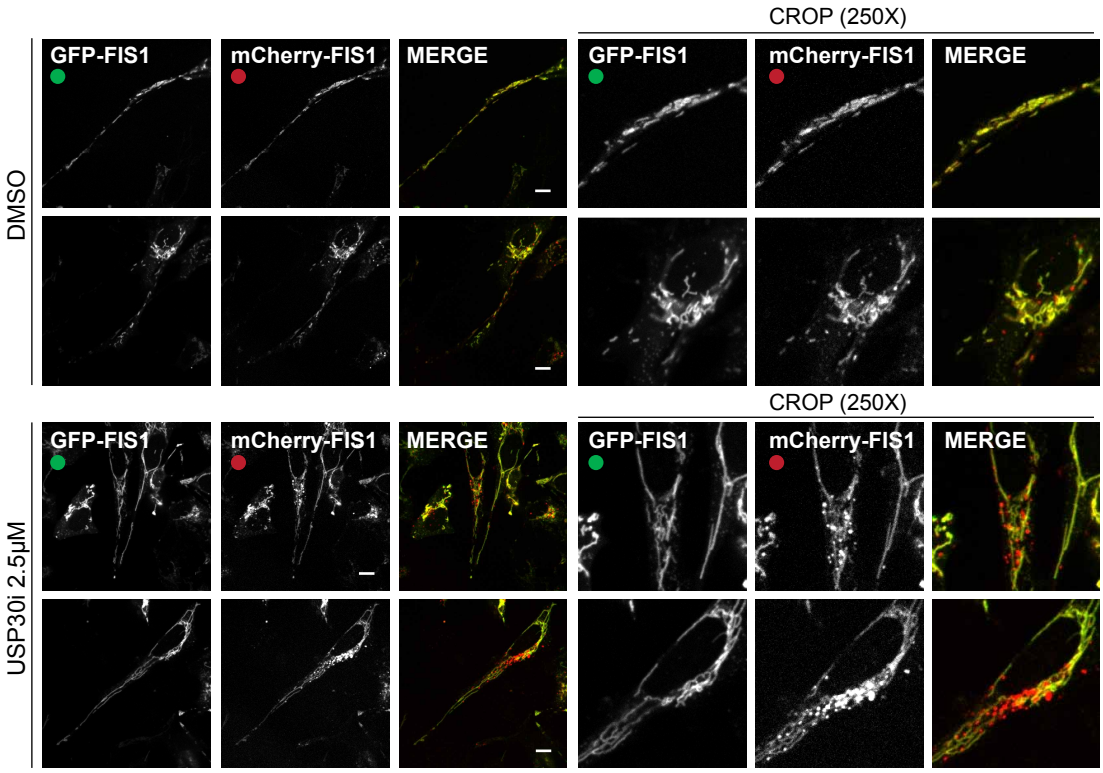

Figure 5.36: Differentiation of SH-SY5Y mito-QC cells into dopaminergic-like neurons using RA and TPA.

SH-SY5Y mito-QC cells were treated sequentially with 10µM retinoic acid (RA) for 72h and 12-O-tetradecanoyl-phorbol-13-acetate (TPA) for 72h. Subsequently the cells were incubated with 2.5µM USP30i for 48h and then imaged using a 3i spinning disk confocal equipped of an EMCCD camera and using a 63X objective lens. Scale bar: 10µm. Data from a single experiment.

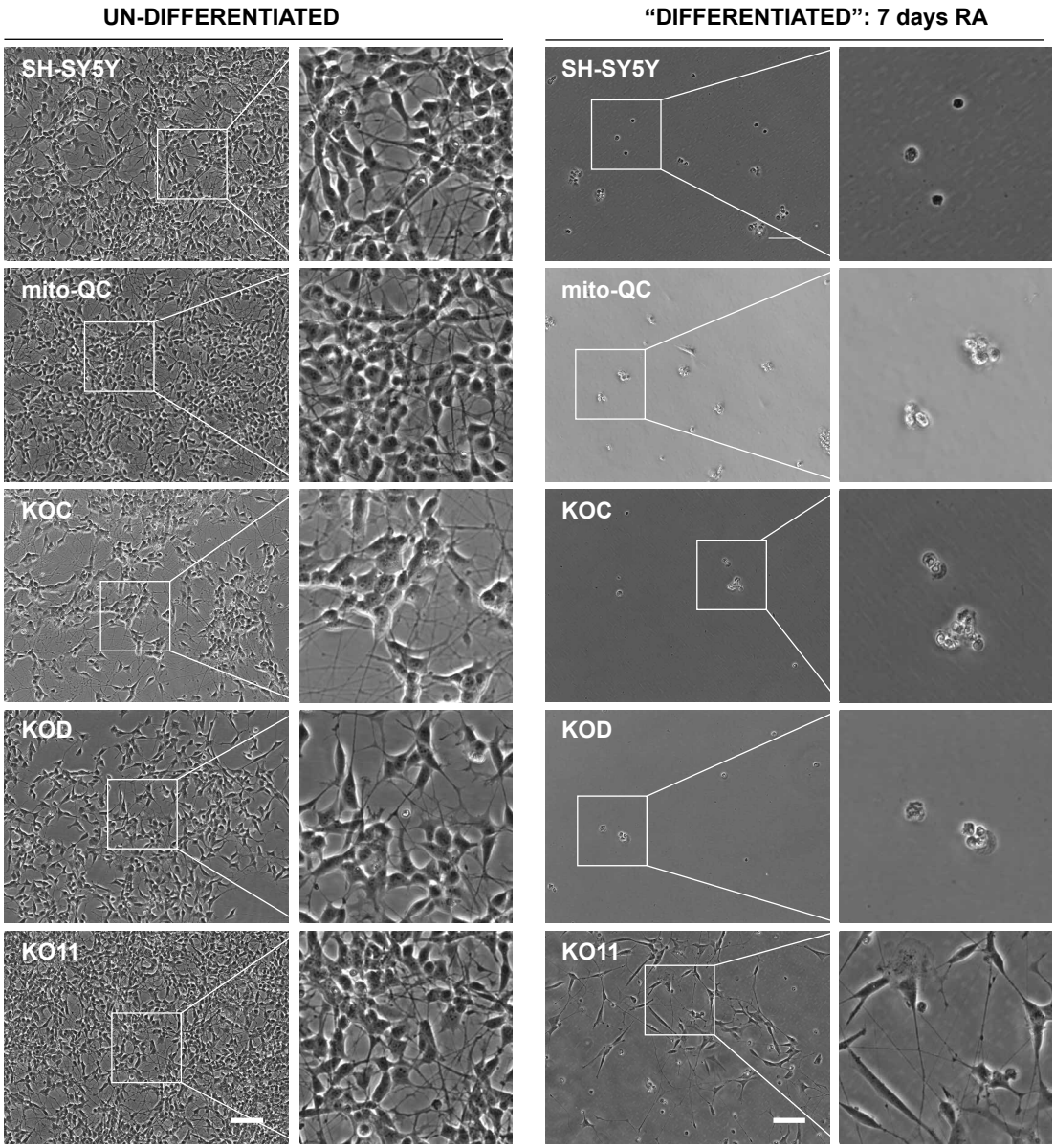

Figure 5.37: Differentiation of SH-SY5Y cells into dopaminergic-like neurons using RA and neurobasal medium.

SH-SY5Y, SH-SY5Y mito-QC, KOC, KOD and KO11 cells were incubated with 10μM retinoic acid (RA) for 7 days in neurobasal medium and subsequently imaged using a NIKON epifluorescence microscope with a 10X objective lens. Scale bar: 100μm. Representative images from two experiments.

5.3.2 Second generation inhibitor: FT385

We received another inhibitor, FT385, which arose from further development of the first-generation inhibitor (USP30i) and based on the same scaffold. Both inhibitors are N-cyano pyrrolidine compounds. The characterisation of the FT385 USP30 inhibitor is published in Rusilowicz et al. (Rusilowicz-Jones et al., 2020). The Chemical and biochemical characterisation of the inhibitor was performed at FORMA Therapeutics (Watertown, MA, USA) and by collaborators in Oxford (Target Discovery Institute, University of Oxford).

The half maximal inhibitory concentration of FT385 (IC_{50}) for USP30 was ~1nM compared to ~90nM for USP30i using ubiquitin-rhodamine as a fluorogenic substrate.

The specificity of FT385 towards USP30 was further assessed by screening *in vitro* its inhibitory activity across a large panel of DUBs and using ubiquitin-rhodamine 110 as a substrate (DUB profiler screen, Ubiquigent, Dundee, UK), (Rusilowicz-Jones et al., 2020). At 2nM FT385 specifically inhibited USP30's activity (activity decreased by 58%) without affecting any other DUBs in the panel. At 20nM, FT385 fully inhibited USP30's activity (activity decreased by 97%) and partially inhibited USP6 (42% decrease in activity). Strikingly, even at the highest concentration measured (200 nM), FT385 did not affect any of 42 other DUBs tested.

USP6 is localised at the plasma membrane has been studied in the context of trafficking and tumorigenesis (Martinu et al., 2004; Urbé et al., 2012; Funakoshi et al., 2014). It is however restricted to very few tissues, including testis and skeletal muscles (The Human Protein Atlas v19.3), (CCLE, Broad Institute),(Barretina et al., 2012; Uhlén et al., 2015). We did not detect USP6 in any of our proteomic studies, neither was it identified by our colleagues in Oxford in their analysis of a variety of cells lines nor was it detected in recent high coverage DUB screens employing ubiquitin Activity based probes (ABP) assays, (Hewings et al., 2018; Pinto-Fernández et al., 2019).

FT385 is thus a highly selective and potent inhibitor of USP30. The chemical characterisation of this compound further reveals that it binds covalently to USP30 (Rusilowicz-Jones et al., 2020).

5.3.2.1 FT385 efficiently binds to USP30

Assisted by my colleague Emma Rusilowicz-Jones, I tested the specificity of FT385 and assessed the optimal concentration necessary to inhibit USP30 using an ABP assay (**Figure 5.38**). These assays are used to study enzymatic activity. The probes covalently bind to active site residues of the enzyme (Niphakis and Cravatt, 2014; Sanman and Bogyo, 2014). The ABP usually consists of a reactive group (also known as warhead) that reacts with the active site, a recognition element that is responsible of target selectivity and a reporter tag (ex: HA) (Hewings et al., 2017). ABPs developed against DUBs of the cysteine protease family target the catalytic cysteine nucleophile using an electrophilic reactive group. Common reactive groups used against cysteine protease DUBs include vinyl sulfones (VS), vinyl methyl ester (VME) and propargyl amide (PA), (Hewings et al., 2017).

The Ubiquitin-propargylamide (Ub-PA) activity probe is a so-called suicide substrate composed of full-length ubiquitin, which serves as the recognition element, and a PA reactive group that replaces the C-terminal GlyGly of ubiquitin. I used the competition between FT385 and Ub-PA for USP30's catalytic cysteine to determine target engagement and assess the optimal FT385 concentrations to use for experiments in SH-SY5Y cells.

I treated SH-SY5Y cells for 4h with FT385 at concentrations ranging from 5 to 625nM and with 500nM of an unrelated compound as a control (CTRL). I then homogenised the cells, incubated the PNS with the Ub-PA probe for 15min and analysed the samples by western blotting using a USP30 antibody (**Figure 5.38**). Two USP30-antibody reactive bands can be detected in this experiment: Ub-PA bound USP30 (65 kDa) and Ub-PA unbound USP30 (56kDa). As a covalent USP30 inhibitor is expected to prevent the binding of the probe, the Ub-PA unbound band indirectly reflects the proportion of USP30 bound to FT385.

When the cells were treated with DMSO, 85% of USP30 in the PNS was able to bind to the Ub-PA probe. For cells treated with 625μM FT385, this Ub-PA bound portion decreased to 24%. I found that 125nM FT385 was an optimal concentration to efficiently inhibit USP30 in SH-SY5Y cells: only 33% of USP30 was bound to Ub-PA, indicating that there was approximatively 67% of USP30 inhibited by FT385.

Based on the Ub-PA and the Ubiquigent DUB profiler assay, I decided to adopt FT385 concentrations ranging between 100 and 200nM, as those concentrations were sufficient to observe target engagement without compromising inhibitor selectivity.

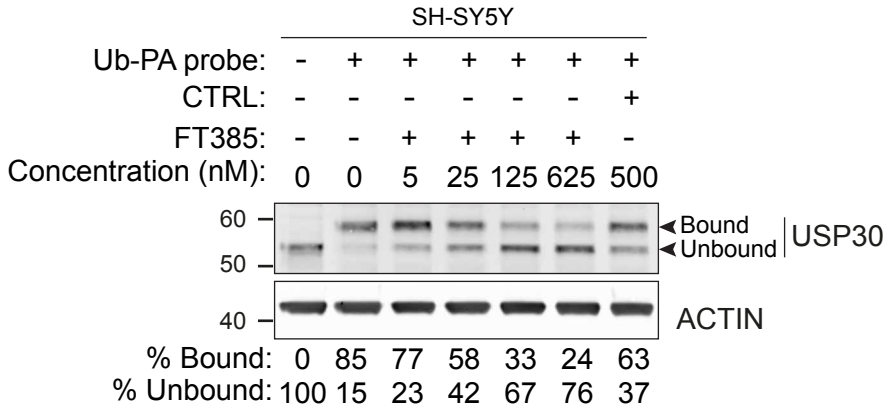

Figure 5.38: FT385 efficiently binds to USP30

Ubiquitin-propargylamide (Ub-PA) probe engagement assay. SH-SY5Y cells were treated for 4h with 0-625nM of the USP30 inhibitor FT385 or with 500nM of an unrelated control compound (CTRL). The cells were then homogenised in HIM buffer mixed with TCEP and the nuclei pelleted at 600g to collect the Post Nuclear Supernatant (PNS). The PNS was incubated with the Ub-PA activity probe at a 1:100 w/w probe to protein ratio for 15min and 37°C. The homogenates were then immunoblotted for USP30 and Actin. The percentage of bound and unbound USP30 over total USP30 was quantified using ImageStudio.

5.3.2.2 FT385 promotes TOMM20 ubiquitylation and pS65 Ubiquitylation

The USP30 substrates that I was able to detect directly by western blotting in USP30 KO cells were TOMM20 and pS65-Ub (**Figure 5.18-22**). I therefore decided to monitor the effect of FT385 on these proteins in the absence and presence of AO over a 24 h timecourse. I treated SH-SY5Y mito-QC cells with a combination of FT385 (100nM) and AO (1µM, each), and compared these directly to AO treated USP30 KO cells (KO11) (**Figure 5.39**). In agreement with the data shown in section 2.2.3 (Chapter V), I observed the accumulation of TOMM20-ubiquitylated species in response to AO specifically in USP30 KO cells (2.5- and 3.5-fold increase at 4h and 8h AO respectively compared to DMSO).
Although more subtle than USP30 deletion, inhibiting USP30 also enhanced the ubiquitylation of TOMM20 in SH-SY5Y cells (up to 2.1-fold increase at 8h) (**Figure 5.39B-C).** Unlike for TOMM20, the AO-induced ubiquitylation of MIRO1 and Parkin appeared unaffected by either USP30 KO or USP30 inhibition (**Figure 5.39B, D**).

Although those results seemed encouraging, the TOMM20 ubiquitylating pattern was hard to see in whole cell lysates. I thus decided to confirm those observations in mitochondrial enriched fractions.

I first treated SH-SY5Y cells for 24h with 100nM FT385 and looked at early ubiquitylation events (**Figure 5.40**). Following 1h depolarisation, I observed a consistent ubiquitylation of MFN2 across WT, FT385-treated WT and KO11 cells. However, only KO11 cells showed increased Ub-TOMM20.
I then wondered if a longer FT385 treatment would promote TOMM20 ubiquitylation. I treated SH-SY5Y cells for 72h with FT385 and 1h with AO (**Figure 5.41**). Increased FT385 treatment length did not raise TOMM20 ubiquitylation.

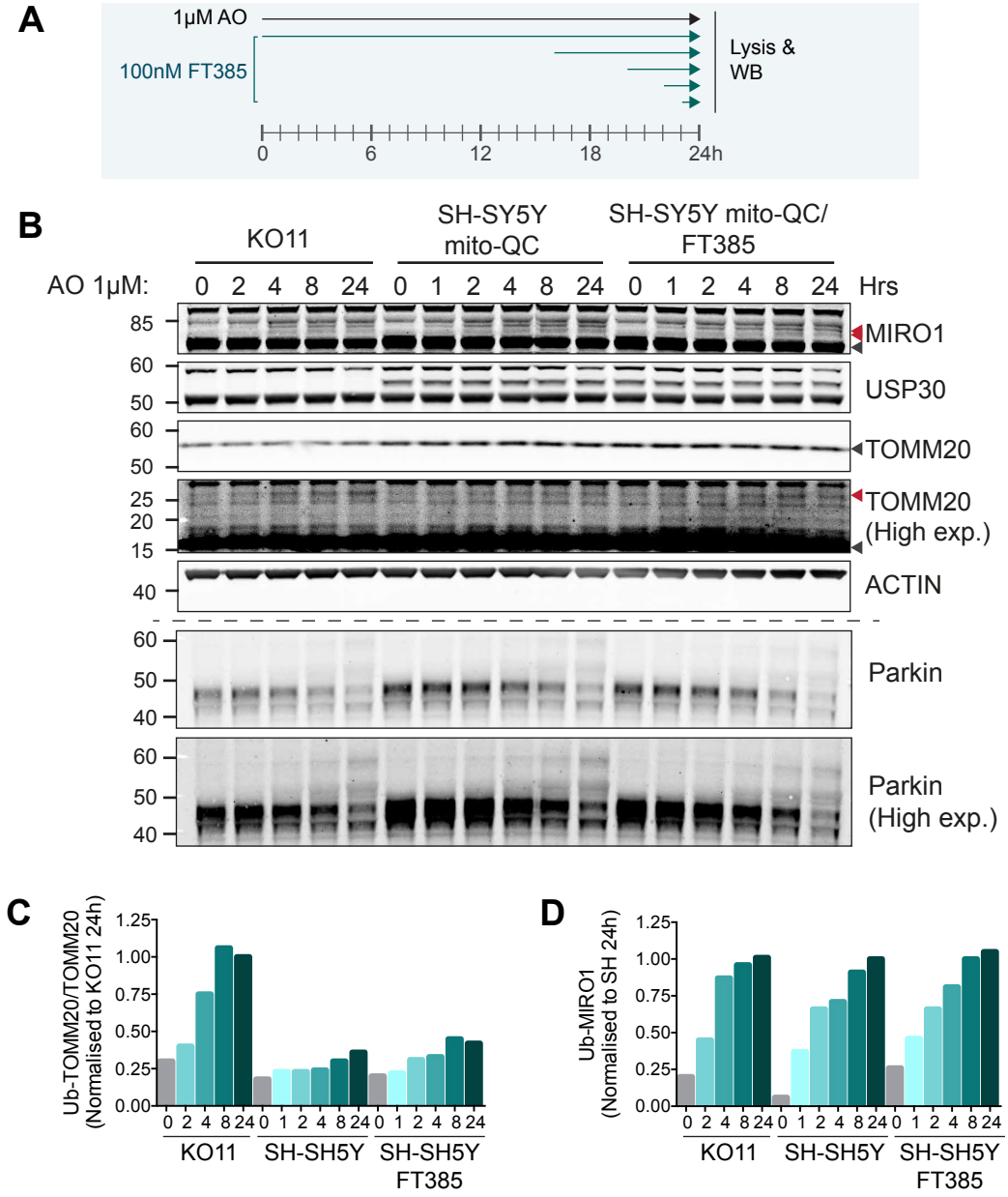

Figure 5.39: AO and FT385 time course in SH-SY5Y mito-QC and KO11.

SH-SY5Y mito-QC and KO11 cells were treated for 1-24h with Antimycin A and Oligomycin A (1μM each); a set of SH-SY5Y mito-QC cells was co-treated with 100nM FT385 (USP30i) for 24h. The cells were lysed in NP40. **A)** Schematic representation of the treatment. **B)** The lysates were immunoblotted and probed against mitophagy proteins. The black arrows indicate the unmodified protein bands; the red arrows point towards ubiquitylated-proteins. Graphs representing **C)** Ub-TOMM20 and **D)** Ub-MIRO1 ratioed to unmodified TOMM20 or MIRO1 respectively and normalised to **C)** 24h AO KO11 or **D)** 24h AO SH-SY5Y mito-QC. Data from a single experiment.

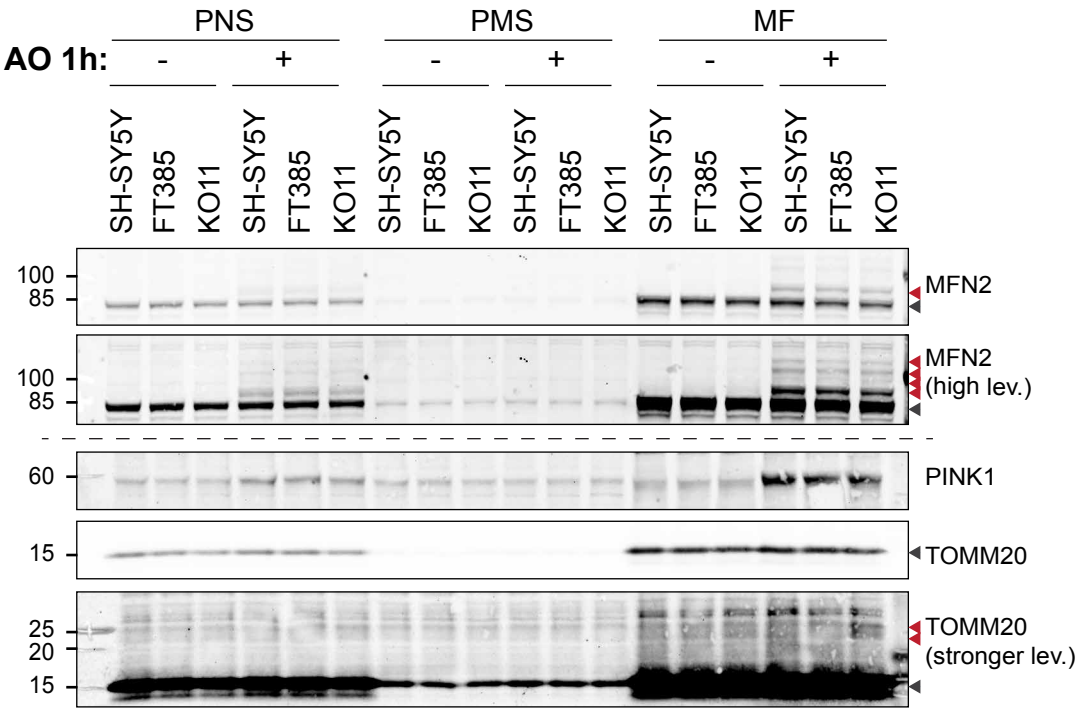

Figure 5.40: Assessing TOMM20-ubiquitylation upon 1h AO and 24h USP30 inhibition with 100nM FT385 or USP30 KO.

SH-SY5Y mito-QC and KO11 cells were treated with Antimycin A and Oligomycin A (AO, 1μM each) for 1h; a set of SH-SY5Y mito-QC cells was pre-treated with 100nM FT385 for 24h. The cells were then homogenised in HIM buffer. The Post Nuclear Supernatant (PNS), Post Mitochondrial Supernatant (PMS) and Mitochondrial Fraction (MF) were obtained by differential centrifugation. The fractions were immunoblotted against proteins involved in mitophagy. The black arrows indicate unmodified-proteins; the red arrows point towards ubiquitylated-proteins.

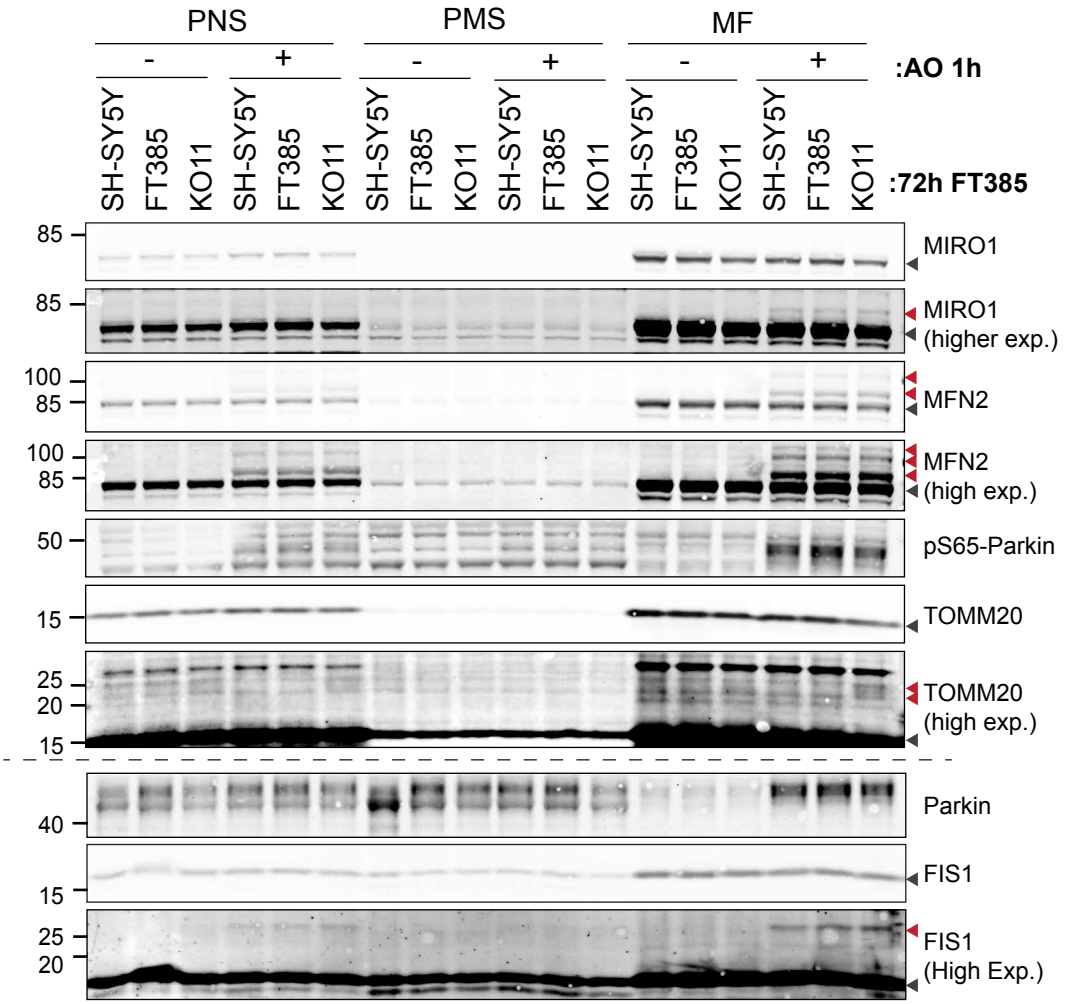

Figure 5.41: Assessing TOMM20-ubiquitylation upon 1h AO and 72h USP30 inhibition with 100nM FT385 or USP30 KO.

SH-SY5Y mito-QC and KO11 cells were treated with Antimycin A and Oligomycin A (AO, 1μM each) for 1h; a set of SH-SY5Y mito-QC cells was pre-treated with 100nM FT385 for 72h. The cells were then homogenised in HIM buffer. The Post Nuclear Supernatant (PNS), Post Mitochondrial Supernatant (PMS) and Mitochondrial Fraction (MF) were obtained by differential centrifugation. The fractions were immunoblotted against proteins involved in mitophagy. The black arrows indicate unmodified-proteins; the red arrows point towards ubiquitylated-proteins.

I next increased the depolarisation length to 4h. Cells were treated for 24h with 100nM FT385 and 4h AO (**Figure 5.42**). Once again, this treatment combination did not lead to TOMM20-ubiquitylation. Interestingly, I had made use of late passage KOD cells which had accumulated wildtype USP30 expressing cells (50% of residual USP30) and I could still detect TOMM20 ubiquitylation. Remarkably, with 4h AO I could also detect TOMM22 ubiquitylation in KOD and KO11 cells only. FIS1's ubiquitylation was also enhanced in KOD and KO11 – similar to my previous observations in Figure 5.28. These blots indicate that FIS1 and TOMM22 are substrates of USP30.

Finally, I treated SH-SY5Y cells for 24h with both 100nM FT385 and the depolarisation cocktail, AO (**Figure 5.43**). Under those conditions, I did observe a TOMM20 ubiquitylation band in the FT385 treated cells. I failed to reproduce this observation with a second batch of the inhibitor. However subsequent experiments by my colleague Andreas Kallinos using this time 200nM of FT385 for 24h with 4h AO consistently enhanced Ub-TOMM20 in SH-SY5Y cells (Rusilowicz-Jones et al., 2020).
Supporting these observations, Emma Rusilowicz-Jones reported that 200nM FT385 enhanced AO-induced ubiquitylation of TOMM20 in hTERT-RPE1-YFP-Parkin cells (Rusilowicz-Jones et al., 2020).

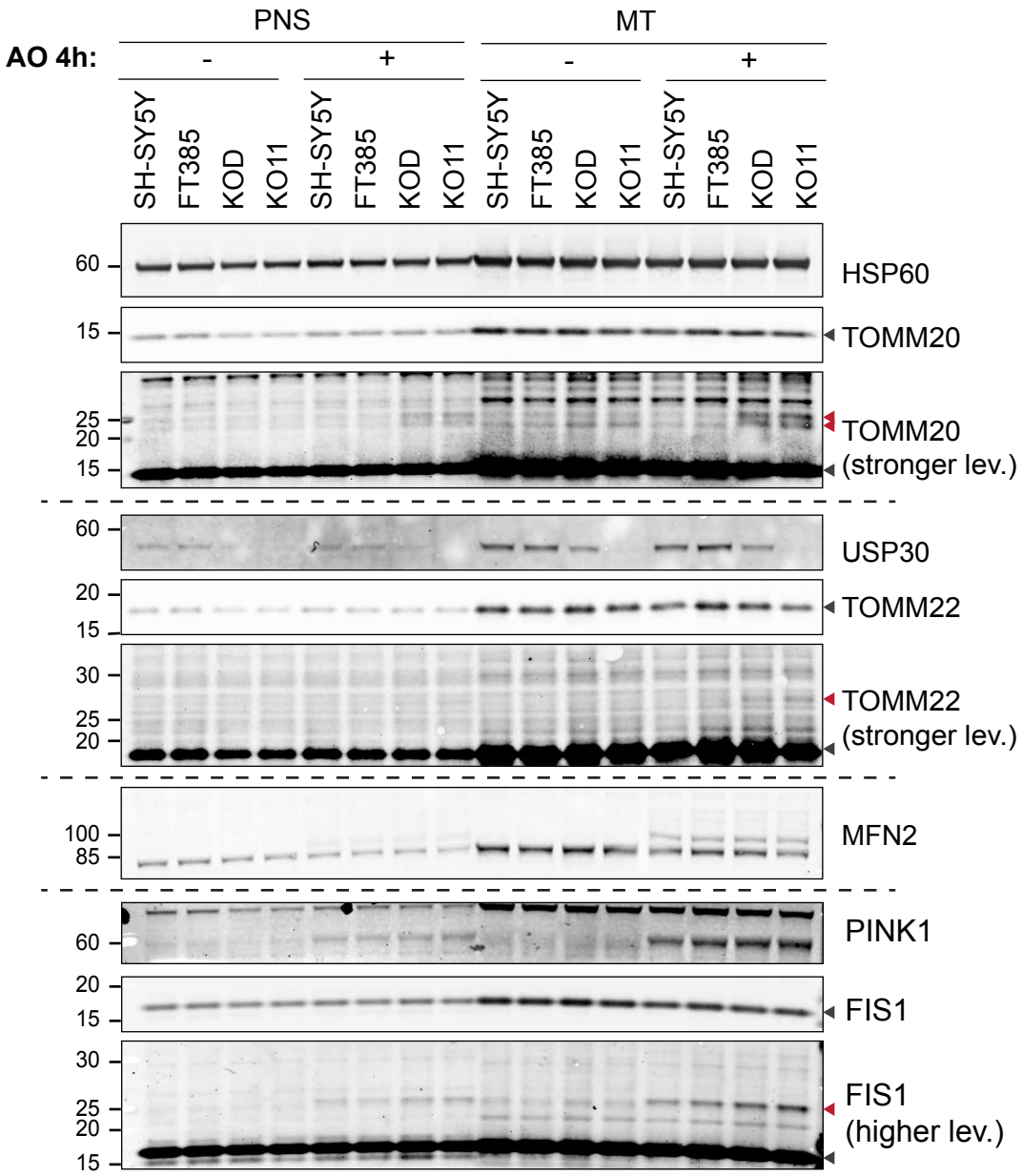

Figure 5.42: Assessing TOMM20-ubiquitylation upon 4h AO and 24hh USP30 inhibition with 100nM FT385 or USP30 KO.

SH-SY5Y, KOD and KO11 cells were treated with Antimycin A and Oligomycin A (AO, 1µM each) for 4h; a set of SH-SY5Y cells was pre-treated with 100nM FT385 for 24h. The cells were then homogenised in HIM buffer. The Post Nuclear Supernatant (PNS), Post Mitochondrial Supernatant (PMS) and Mitochondrial Fraction (MF) were obtained by differential centrifugation. The fractions were immunoblotted against proteins involved in mitophagy. The black arrows indicate unmodified-proteins; the red arrows point towards ubiquitylated-proteins.

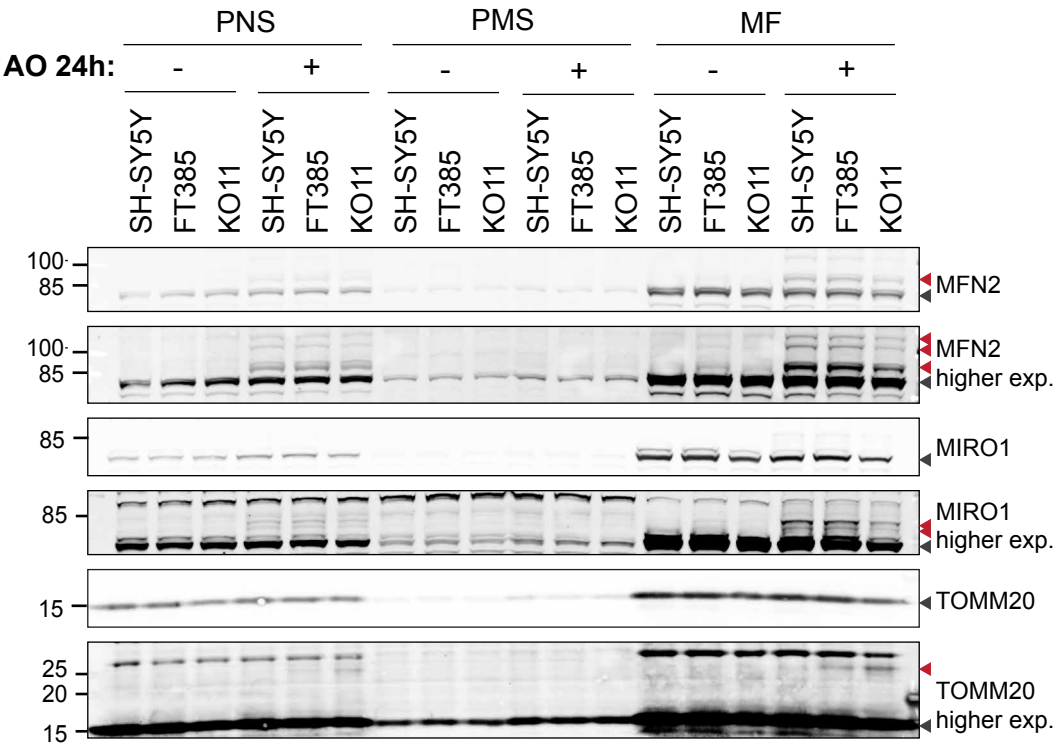

Figure 5.43: 24h FT385 increases TOMM20 ubiquitylation with 24h AO; reproducing the effect of USP30 knockout in SH-SY5Y cells.

SH-SY5Y mito-QC and KO11 cells were treated with Antimycin A and Oligomycin A (AO, 1μM each) for 24h; a set of SH-SY5Y mito-QC cells was co-treated with 100nM FT385 for 24h. The cells were then homogenised in HIM buffer. The Post Nuclear Supernatant (PNS), Post Mitochondrial Supernatant (PMS) and Mitochondrial Fraction (MF) were obtained by differential centrifugation. The fractions were immunoblotted against proteins involved in mitophagy. The black arrows indicate unmodified-proteins; the red arrows point towards ubiquitylated-proteins.

5.3.2.3 FT385 enhances pS65-ubiquitin deposition at mitochondria

I next went on to analyse the effect of USP30 inhibition on the rate of pS65-ubiquitylation by western blotting (**Figure 5.44**). To do so I re-probed the samples from Figure 5.40, 5.42 and 5.43 with a pS65-Ub specific antibody. pS65-Ub was predominantly seen on mitochondria which is consistent with PINK1 accumulating on the mitochondria fraction in Figure 5.42.

To specifically determine at what molecular weight the pS65-Ub smear fluctuates, I used line graphs, which quantify the pS65-Ub band intensity across the whole smear.

Mitochondrial depolarisation (1h AO) induced a strong accumulation of pS65-Ub in the mitochondrial fractions (**Figure 5.44 A-B, G**). Most pS65-Ub-modified proteins run in the higher molecular weight range (76-150kDa) and were not affected by USP30 inhibition or deletion. There was however a slight increase of pS65-Ub in the KO11 line graph below 76kDa. With 4h AO, the integrated intensity of the pS65-Ub signal was increased in KOD and KO11 cell lines (**Figure 5.44C-D, H**). Unlike USP30 KO, FT385 only slightly increased the number of pS65-Ub proteins compared to control cells. However, when treating SH-SY5Y cells for 24h with AO and FT385, the amount of pS65-Ub-proteins was clearly increased (**Figure 5.44E-F, I**).

As seen for TOMM20 ubiquitylation, USP30 inhibition with 100nM FT385 had a more subtle effect on pS65-Ub than knocking-out USP30.

In the USP30KO cells, I was able to detect increased TOMM20 ubiquitylation and pSer65-Ub already at 1h AO and 4h respectively. In contrast, with 100nM of the inhibitor it was only with 24h AO and FT385 that I measured an enhancement of both TOMM20 ubiquitylation and pSer65-Ub compared to control cells. This inhibitor concentration might have been slightly suboptimal as Andreas has reported that 200nM FT385 completly reproduced the effect of USP30 KO on TOMM20 ubiquitylation and pS65-Ub accumulation (Rusilowicz-Jones et al., 2020).

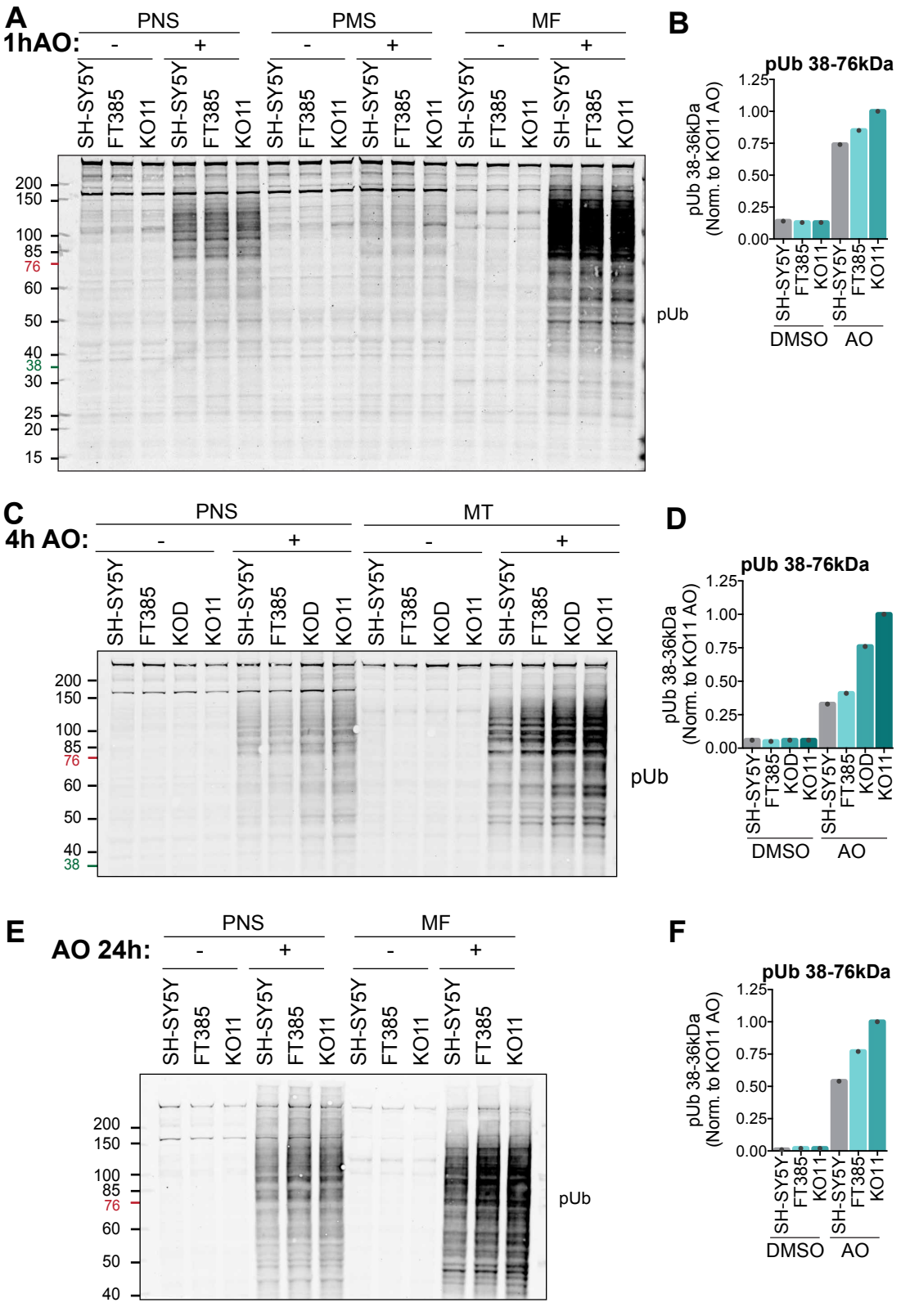
A
1hAO:
PNS
PMS
MF
SH-SY5Y
FT385
KO11
pUb
B
pUb 38-76kDa
pUb 38-36kDa (Norm. to KO11 AO)
DMSO
AO
C
4h AO:
PNS
MT
KOD
D
E
AO 24h:
F

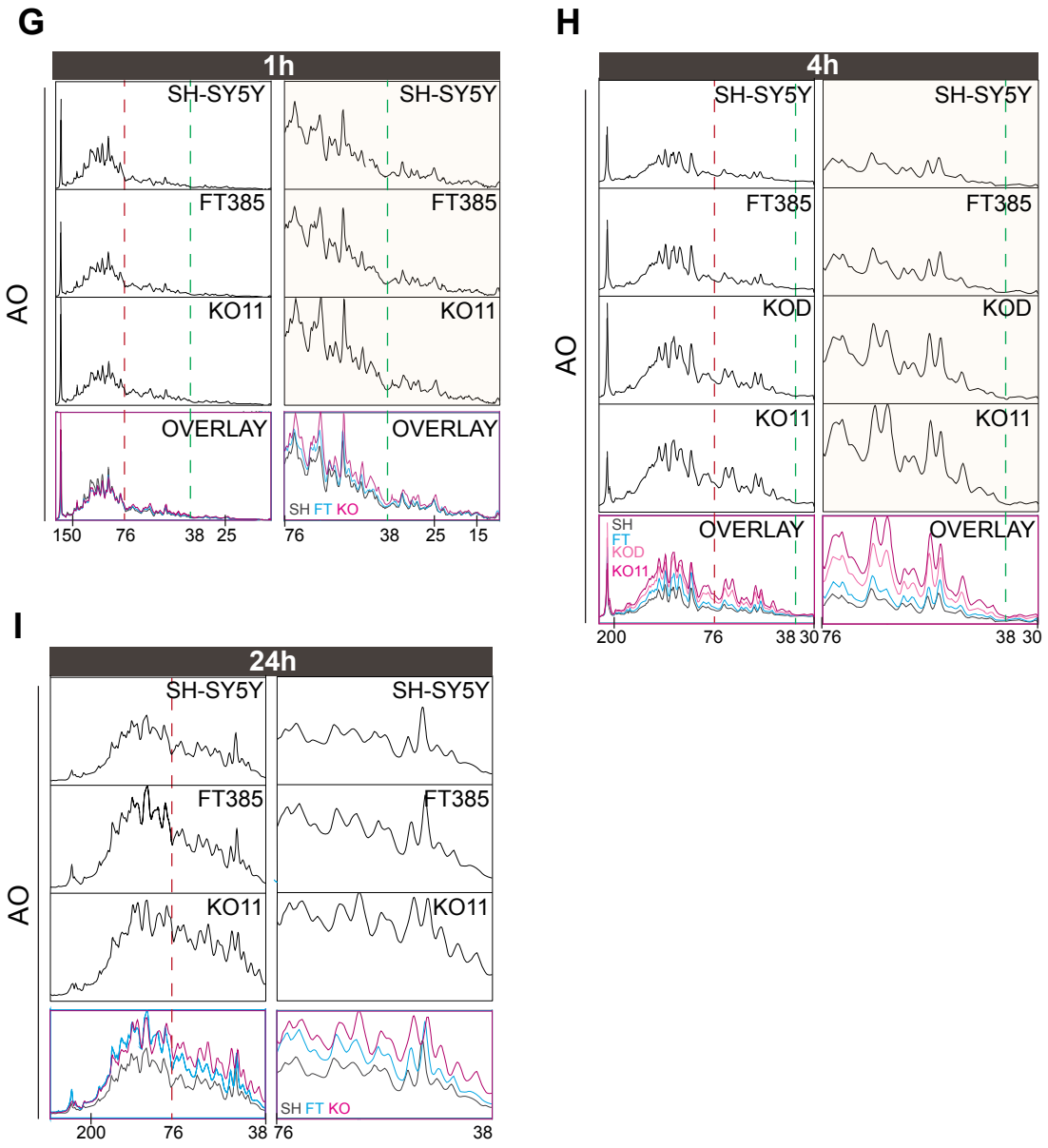

Figure 5.44: FT385 increases AO-mediated pS65-Ub of mitochondrial proteins.

SH-SY5Y, KOD and KO11 cells were treated with Antimycin A and Oligomycin A (AO, 1µM each) for **A)** 1h, **C)** 4h or **E)** 24h; a set of SH-SY5Y cells was **A and C)** pre-treated with or **E)** co-treated with 100nM FT385 for 24h. The cells were then homogenised in HIM buffer. The Post Nuclear Supernatant (PNS), Post Mitochondrial Supernatant (PMS) and Mitochondrial Fraction (MF) were obtained by differential centrifugation. **A, C and E)** The fractions were immunoblotted against pS65-Ub. **B, D and F)** Mitochondrial pS65-Ub bands were quantified and normalised to KO11 AO. **G, H, I)** Line graphs of the mitochondrial pUb signal and, in orange, line graph of the pUb bands running below 76kDa. The 76kDa and 35kDa limits are respectively represented as a red and green dashed line. **A, B, G)** Same lysates as in Figure 5.40; **C, D, H)** Same lysates as in Figure 5.42; **E, F, I)** Same lysates as in figure 5.43.

5.3.2.4 FT385 enhances basal mitophagy

Finally, I decided to verify if FT385 promoted mitolysosome formation in SH-SY5Y cells. Indeed, in section 3.1.2 (Chapter V), I showed that treating U2OS mito-QC cells with 5μM of the USP30 inhibitor USP30i was sufficient to induce mitophagy and promote the swelling of mitolysosomes (**Figure 5.34 and 5.35A-D**). Alas, such concentrations were toxic for SH-SY5Y cells and treating SH-SY5Y mito-QC with lower doses of USP30i (2.5μM) only provoked a subtle and insignificant increase in the number of mitolysomes (**Figure 5.35E-H**). I wondered if a more potent and specific inhibitor such as FT385 which can be used at submicromolar doses could induce mitophagy in SH-SY5Y cells without triggering cell death. I used SH-SY5Y mito-QC cells and treated them for 24h with DMSO, FT385 (100nM) with or without Antimycin (1μM) and Oligomycin (Low: 1μM or High: 10μM) (**Figure 5.45**).

AO-"Low" (AO-L, 1μM each) can trigger the ubiquitylation of OMM proteins but isn't sufficient to visibly enhance basal mitophagy within 24h in SH-SY5Y cells. I thus tested whether FT385 could enhance basal mitophagy by itself or enhance basal mitophagy in "pre-stressed" cells (AO-Low) or enhance AO-induced mitophagy ("AO-High", 1μM and 10μM respectively).

On its own, FT385 neither promoted mitolysosome formation nor did it raise the area of mitolysosomes (**Figure 5.45 B-E**). AO-"Low" (AO-L, 1μM each) was insufficient to facilitate mitophagy and co-treating with FT385 had no effect. Only AO-"High" (AO-H, 1μM and 10μM respectively) triggered mitochondria engulfment into mitolysosomes (**5.45B, 5.46B**). Combining AO-"high" and FT385 treatments did not further increase mitolysosome formation nor did it affect mitolysosome area (**Figure 5.45B-C**, **5.46A-E**). I finally compared USP30 inhibition and USP30 knockdown and confirmed that unlike knocking-down USP30, inhibiting USP30 for 24h with 100nM FT385 did not accelerate AO-induced mitophagy (**Figure 5.47 and 4.14**).

The western blotting experiments seemed to indicate that 100nM is a suboptimal concentration of FT385 to induce TOMM20 ubiquitylation and pS65-Ub, as it delayed the occurrence and the strength of those events compared to USP30 KO.

To observe mitophagy events downstream of USP30 inhibition it seemed necessary to either extend or increase the concentration of the FT385

treatment in SH-SY5Y mito-QC. Francesco Barone and Katy McCarron, PhD students in the Clague-Urbé lab, decided to test this hypothesis and measured mitophagy in SH-SY5Y mito-QC cells treated with 200nM and 500nM FT385 for 96h (Rusilowicz-Jones et al., 2020). They further adopted a semi-automated method to quantify mitophagy which has been recently been introduced by the Ganley lab (Montava-Garriga et al., 2020). Using these parameters, they found that USP30 inhibition with FT385 alone significantly enhanced basal mitophagy. The number of mitolysosomes per cells was increased by 1.7- and 2-fold when cells were treated for 96h with 200 and 500nM FT385 respectively.

We have thus shown that USP30 inhibition enhances depolarisation induced-TOMM20 ubiquitylation and pS65 ubiquitylation and increases basal mitophagy in SH-SY5Y cells. Thus, this new compound recapitulates the observation we have made with knockdown and knockout mediated depletion of USP30.

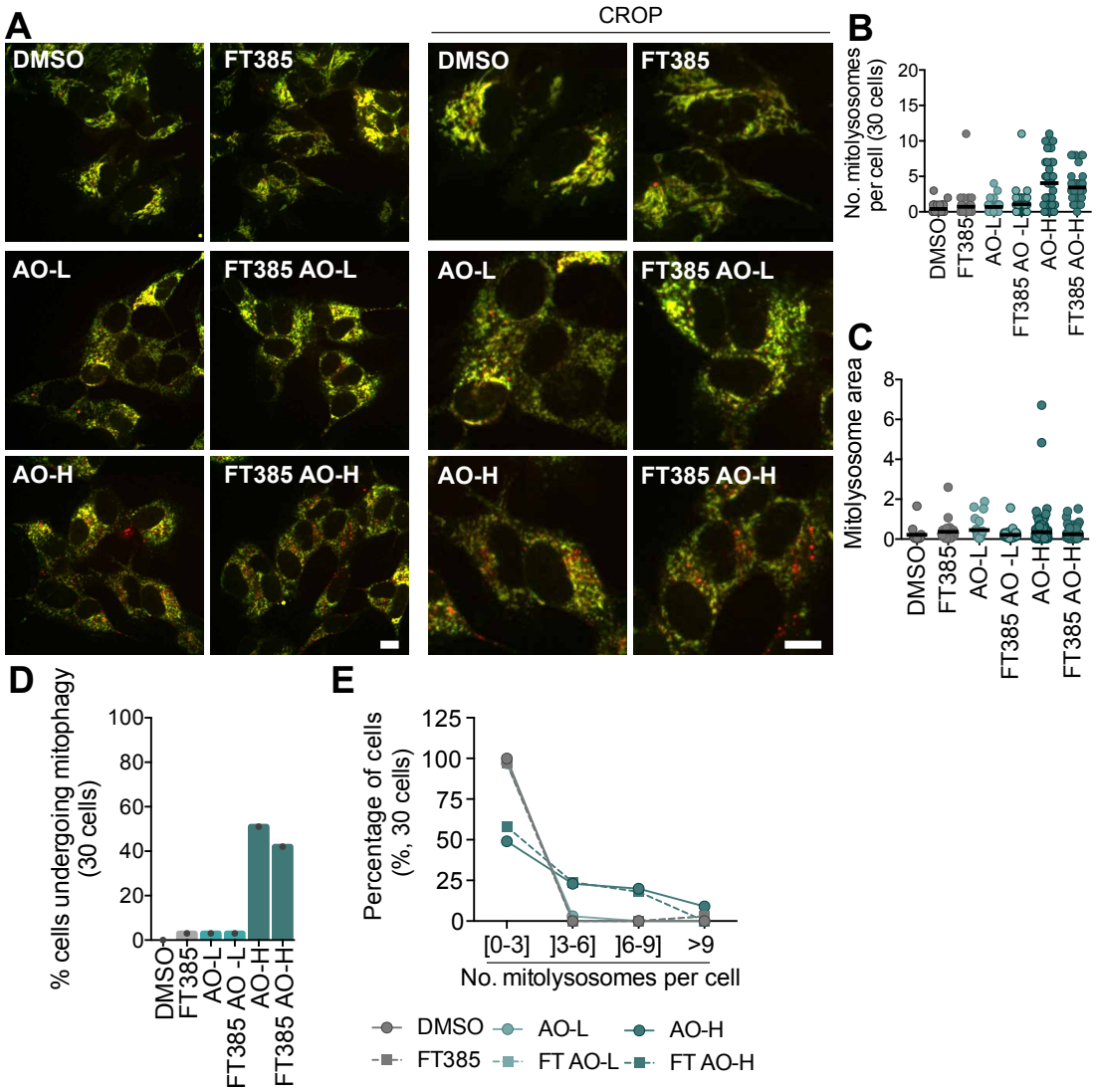

Figure 5.45: USP30 inhibition using 100nM FT385 is not sufficient to enhance mitophagy in SH-SY5Y mito-QC cells.

A) SH-SY5Y mito-QC cells were treated with DMSO, Antimycin A and "low" Oligomycin A (1µM each, AO-L), Antimycin A and "high" Oligomycin A (1µM and 10µM respectively, AO-H) for 24h. A set of cells were co-treated with 100nM FT385 for 24h. The cells were then imaged live on a spinning disk confocal using an EMCCD camera and a 63X objective lens. Scale bar: 10µm. **B)** The number of mitolysosomes and **C)** the mitolysosome area were quantified using Analyse Particles on Fiji. **D)** Cells having more than 3 mitolysosomes were considered as undergoing mitophagy. **E)** The cells were categorised depending on the number of mitolysosomes they contained. The graph represents the percentage of cells per category. Dashed lines represent AO conditions. Data from a single experiment.

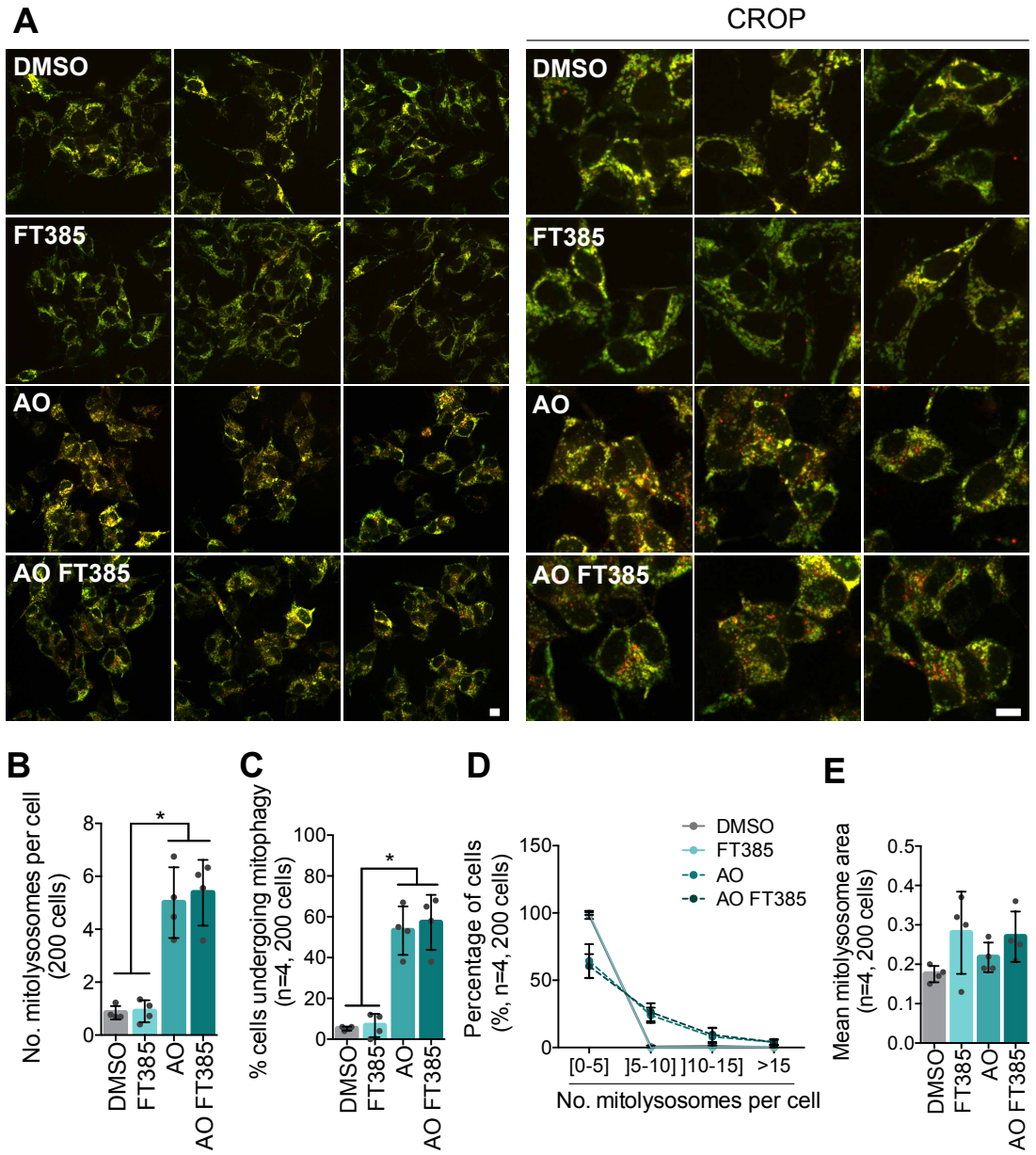

Figure 5.46: USP30 inhibition using 100nM FT385 is not sufficient to enhance mitophagy in SH-SY5Y mito-QC cells.

A) SH-SY5Y mito-QC cells were treated with DMSO, FT385 (100nM) and/or Antimycin A and Oligomycin A (1µM and 10µM respectively, AO) for 24h. A set of cells were co-treated with 100nM FT385 for 24h. The cells were then imaged live on a spinning disk confocal using an sCMOS camera and a 40X objective lens. Scale bar: 10µm. **B)** The number of mitolysosomes and **E)** the mitolysosome area were quantified using Analyse Particles on Fiji. **C)** Cells having more than 3 mitolysosomes were considered as undergoing mitophagy. **D)** The cells were categorised depending on the number of mitolysosomes they contained. The graph represents the percentage of cells per category. Dashed lines represent AO conditions. Analysis: one-way ANOVA with Tukey's multiple comparison test. *: $p < 0.05$. Results from 4 experiments; 50 cells were quantified per experiment. Error bars: mean ± SD.

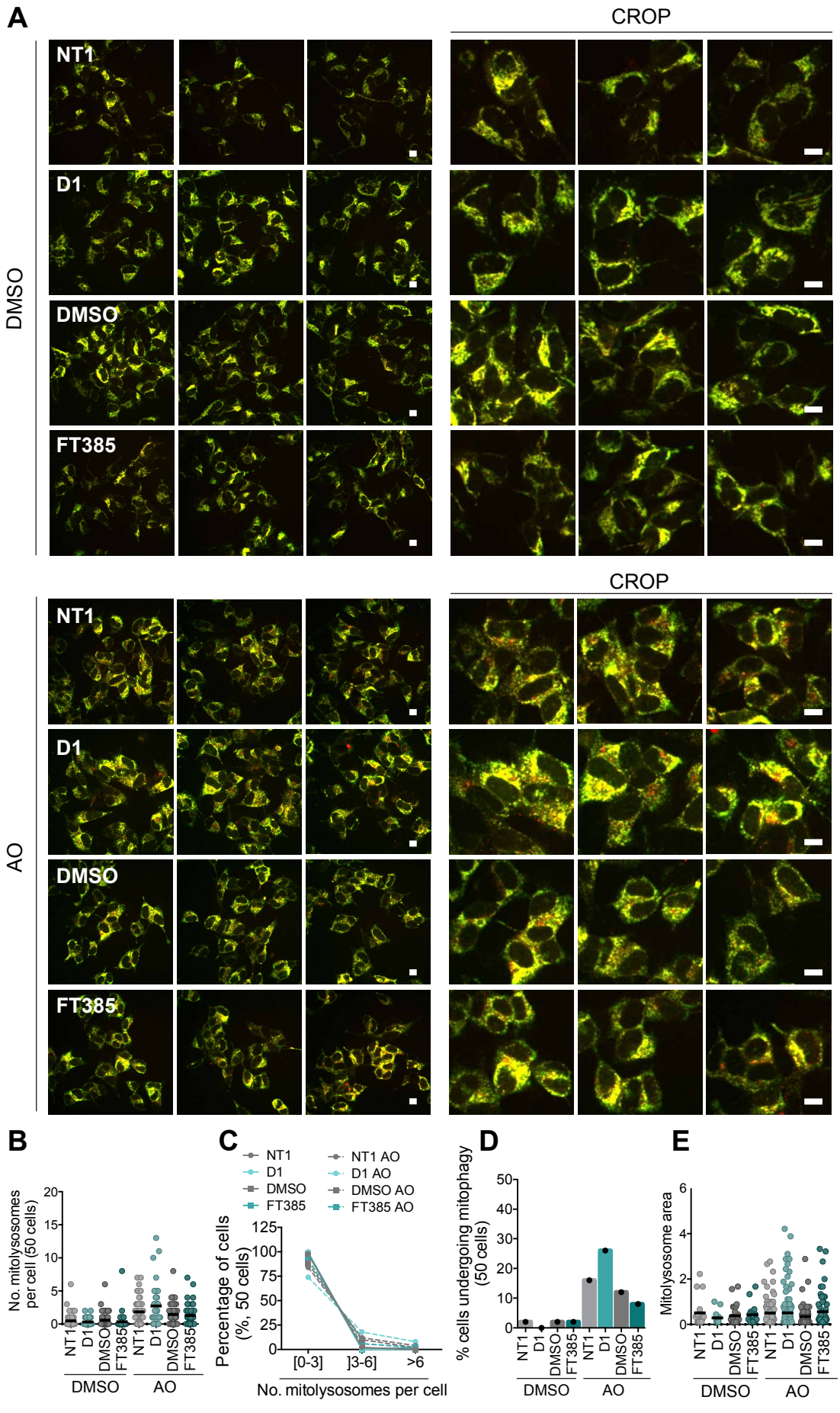
A
CROP
NT1
D1
DMSO
FT385
DMSO
CROP
NT1
D1
DMSO
FT385
AO
B
No. mitolysosomes per cell (50 cells)
NT1
D1
DMSO
FT385
DMSO
AO
C
NT1
D1
DMSO
FT385
NT1 AO
D1 AO
DMSO AO
FT385 AO
Percentage of cells (%, 50 cells)
[0-3]
]3-6]
>6
No. mitolysosomes per cell
D
% cells undergoing mitophagy (50 cells)
DMSO
AO
E
Mitolysosome area
DMSO
AO

Figure 5.47: USP30 knockdown but not inhibition with 100nM FT385 amplifies AO-induced mitophagy in SH-SY5Y mito-QC cells.

A) SH-SY5Y mito-QC cells were transfected for 72h with USP30-targeted (D1) or non-targeting (NT1) siRNA oligos. The cells were then treated for 24h with Antimycin A and Oligomycin A (1 and 10μM respectively); a set of untransfected SH-SY5Y mito-QC cells were co-treated with DMSO or 100nM FT385 for 24h. The cells were then imaged live on a 3i spinning disk confocal using an EMCCD camera and a 40X objective lens. Scale bar: 10μm. **B)** The number of mitolysosomes and **E)** the mitolysosome area were quantified using Analyse Particles on Fiji. **C)** The cells were categorised depending on the number of mitolysosomes they contained. The graph represents the percentage of cells per category. Dashed lines represent AO-treated conditions. **D)** Cells having more than 3 mitolysosomes were considered as undergoing mitophagy. Error bars: mean ± SD. Data from a single experiment.

5.4 Identifying USP30 substrates using SILAC based proteomics

To have a more global view on USP30 substrates and in hope of finding biomarkers for testing the efficacy of compounds against USP30 in pre-clinical models, I carried out Mass Spectrometry experiments on SH-SY5Y cells, with the help of Emma Rusilowicz-Jones. I used triple SILAC labelling in order to simultaneously analyse WT, USP30 KO cells and USP30 inhibitor treated cells. I analysed these cells' proteomes as well as their ubiquitylomes. Trypsin digestion of ubiquitylated proteins leaves a GlyGly residual peptide still covalently attached to the modified lysine (KGG). This remnant induces a characteristic 114.1 Da mass shift that is detected by mass spectrometry (Peng et al., 2003). The samples used for ubiquitylomics were further enriched for ubiquitylated peptides by immunoprecipitation using a KGG specific antibody. This technique has already successfully been used to identify Parkin substrates (Sarraf et al., 2013; Rose et al., 2016).

Deleting or inhibiting USP30 was expected to result in an increase of USP30 substrate ubiquitylation or to promote the degradation of USP30 substrate that are modified with degradative ubiquitin labels.

5.4.1 Depolarisation treatment optimisation

I labelled SH-SY5Y cells with “Light” Amino acids (Arg0, Lys0, Pro0; hereafter referred to as SHSY5Y-L), KO11 cells with “Medium” Amino acids (Arg6, Lys4, Pro0; hereafter referred to as KO11-M) and SH-SY5Y and KOD cells with “Heavy” Amino acids (Arg10, Lys8, Pro0; hereafter referred to as SH-SY5Y-H and KOD-H). The cells were labelled until over 99% of proteins had incorporated the labels (see method sections 1.4.2 and 1.4.3 (Chapter I)). Prior to mass spectrometry experiments, we determined the optimal Oligomycin and Antimycin concentrations required to induce ubiquitylation and degradation of mitochondrial proteins in the SILAC labelled SH-SY5Y, KOD and KO11 cells (**Figure 5.48**).

One major difference between our standard media used in all previous experiments and the SILAC media used for the proteomics experiments is the serum, which in the case of the SILAC media has to be dialysed to remove all amino acids. In addition, the medium is also filtered which in principle could remove additional constituents that in standard medium contribute may "adsorb and quench" some of the depolarising drugs used to induce mitophagy (Soutar et al., 2019). Moreover, from our experience, SILAC labelled SH-SY5Y cells grow slower and might be more sensitive to AO. Therefore, we first determined the optimal AO concentration to use for SILAC based proteomic experiments.

I treated SH-SY5Y-L, KO11-M and KOD-H for 4h with Antimycin (0.1 or 1μM) and Oligomycin (0.1 or 1μM) (**Figure 5.48**). The cells appeared healthy in all conditions. Across the board, the combination of 1μM Antimycin and 1μM Oligomycin promoted the strongest pS65-Ub smear and Ub-FIS1 band in all cell lines; lower AO concentrations (0.1μM each) were sufficient to optimally ubiquitylate MFN2. I made use of 1μM of Antimycin and Oligomycin in the Mass spectrometry experiments to detect the broadest variety of USP30 substrates.

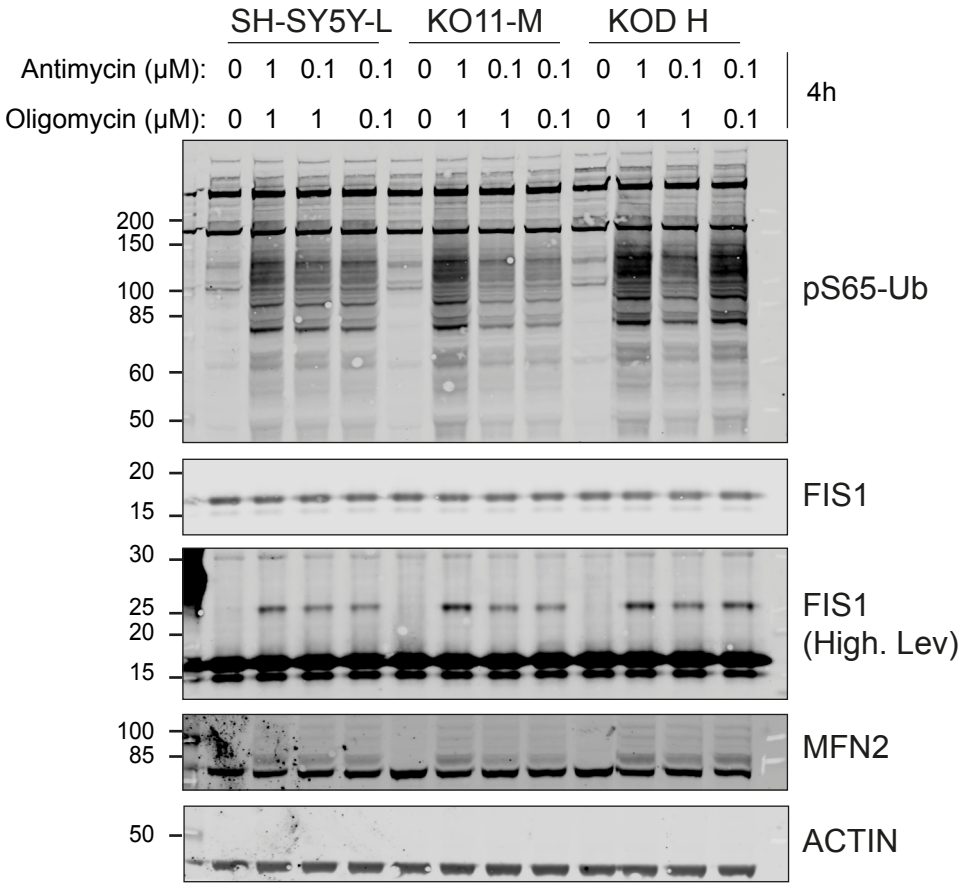

Figure 5.48: AO-treatment optimisation for SILAC based quantitative mass spectrometry.

SH-SY5Y, KOD and KO11 cells were labelled using SILAC amino acids (L = light, M = medium and H = heavy). The cells were then treated for 4h with Antimycin A and Oligomycin A at the indicated concentrations and lysed in NP40. The samples were finally probed for pS65-Ub and mitochondrial proteins (MFN2, FIS1).

5.4.2 Proteome and ubiquitylome experiment description

5.4.2.1 Proteome and ubiquitylome analysis of USP30 KO versus USP30 inhibition following 24h depolarisation

In the first set of mass spectrometry experiments SH-SY5Y-H cells were treated with 200nM FT385 and both SH-SY5Y-L and KO11-M with DMSO for 24h. These cells were either co-treated with AO (1µM each) or DMSO (**Figure 5.49**). The samples were processed for proteomic and ubiquitylomic analysis by Emma Rusilowicz with the help of Adan Pinto in the lab of Benedikt Kessler (Oxford, UK). We analysed the proteomics data files obtained from the mass spectrometer using MaxQuant (version 1.6.7.0), (Tyanova et al., 2016b). We identified 6,423 peptides and 9,536 KGG-modified peptides from 2,915 proteins. Statistical analysis was performed using Perseus to determine the outliers (Significance B, $p < 0.05$), (**Appendix 1 and 2**), (Tyanova et al., 2016a).

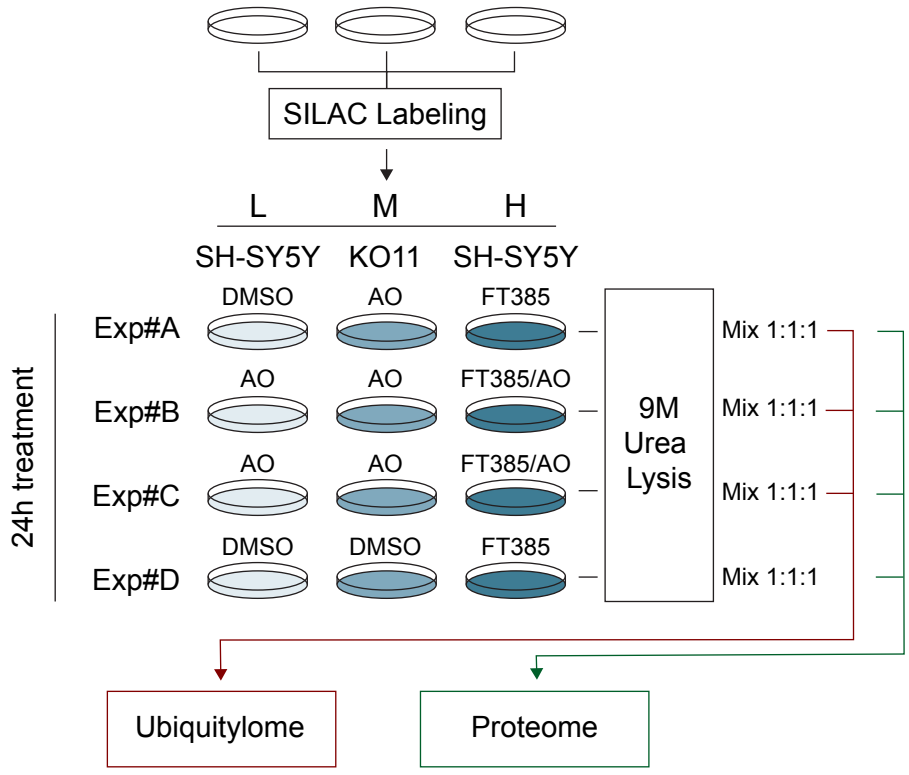

Figure 5.49: Schematic flow chart of SILAC based quantitative mass spectrometry performed on USP30 KO and USP30 inhibited SH-SY5Y cells.

SH-SY5Y and KO11 cells were labelled using SILAC amino acids as shown (L = light, M = medium and H = heavy). The cells were then treated for 24h with DMSO or Antimycin A and Oligomycin A (AO; 1µM each) and/or 200nM FT385 as indicated. The cells were lysed and processed either for ubiquitylomic or proteomic analysis.

5.4.2.2 Proteome and ubiquitylome analysis of USP30 mitochondrial substrates following 4h depolarisation.

We next performed a second series of mass spectrometry experiments in which we compared KO11 with KOD cells, that had been made with two independent sgRNA, to control for clonal variability (**Figure 5.50**). These experiments were performed in collaboration with Matthias Trost's group (Newcastle, UK). In whose lab the samples were run on an Orbitrap Fusion Lumos.

In our previous experiments we had depolarised cells for 24h as our focus was on detecting proteins that may be lost due to enhanced degradation in the absence of USP30 activity and which may serve as future biomarkers to help validate USP30 inhibitors in a translational setting. Here we wished to focus on the more immediate effects of USP30 loss on protein ubiquitylation whether this is linked to protein degradation or not.

We thus only treated the cells for 4h with Antimycin A and Oligomycin A. This time point had previously been established as optimal to observe the ubiquitylation of FIS1, TOMM20 and other suspected USP30 substrates (**Figure 5.21**). Finally, as USP30 is an OMM protein, for the ubiquitylome analysis only we fractionated our samples to obtain mitochondria enriched samples in the hope of enriching our dataset with mitochondrial USP30 substrates. We identified 7,372 peptides in the total proteome and 940 KGG-modified peptides from 541 proteins in the mitochondria enriched fractions (**Appendix 3 and 4**).

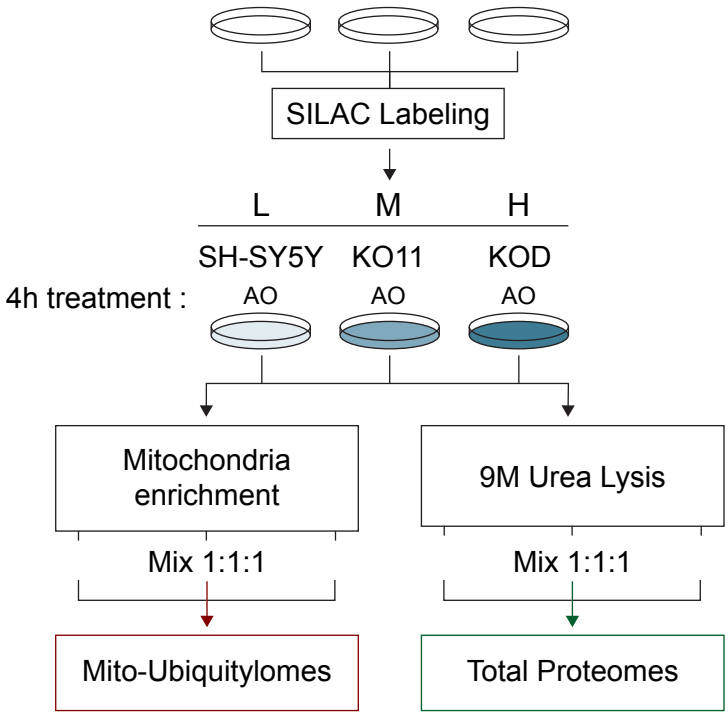

Figure 5.50: Schematic flow chart of SILAC based quantitative mass spectrometry performed on two USP30 KO clones.

SH-SY5Y, KO11 and KOD cells were labelled using SILAC amino acids as shown (L = light, M = medium and H = heavy) and then treated for 4h with Antimycin A and Oligomycin A (AO; 1µM each). The cells were either lysed for total proteome analysis or further processed by subcellular fractionation to obtain mitochondrial fractions for ubiquitylome analysis.

5.4.3 Proteome analysis

5.4.3.1 In the absence of depolarisation agents

I started by observing the changes in the global proteome occurring after inhibiting USP30 for 24h without depolarisation agents, for which we had two replicate experiments (**Figure 5.51**).

TOMM7, a component of the TOM complex, was the only significantly downregulated protein in both FT385 replicates and TOMM7 levels were similarly decreased in KO11 cells **(Figure 5.52A)**.

Aside from reducing TOM7 availability, blocking USP30's deubiquitylating activity mainly affected three pathways: there was a significant upregulation of a) proteins promoting cell cycle progression (significantly upregulated: CKS1B, CDK1, GSG2; high fold change but not significant: in CKS2, NUF2), b) proteins involved in DNA replication or mRNA translation (significantly upregulated: DUT, LIG1, RBM3, C14orf142; high fold change but not

significant: POLE), c) proteins involved in neuronal differentiation or function (significantly upregulated: NRP1), including neuroendocrine secretory granule proteins (significantly upregulated: CHGB, CYB561) and down regulation of a histone demethylase which participates in the transcriptional repression of neuronal genes (KDM5C).

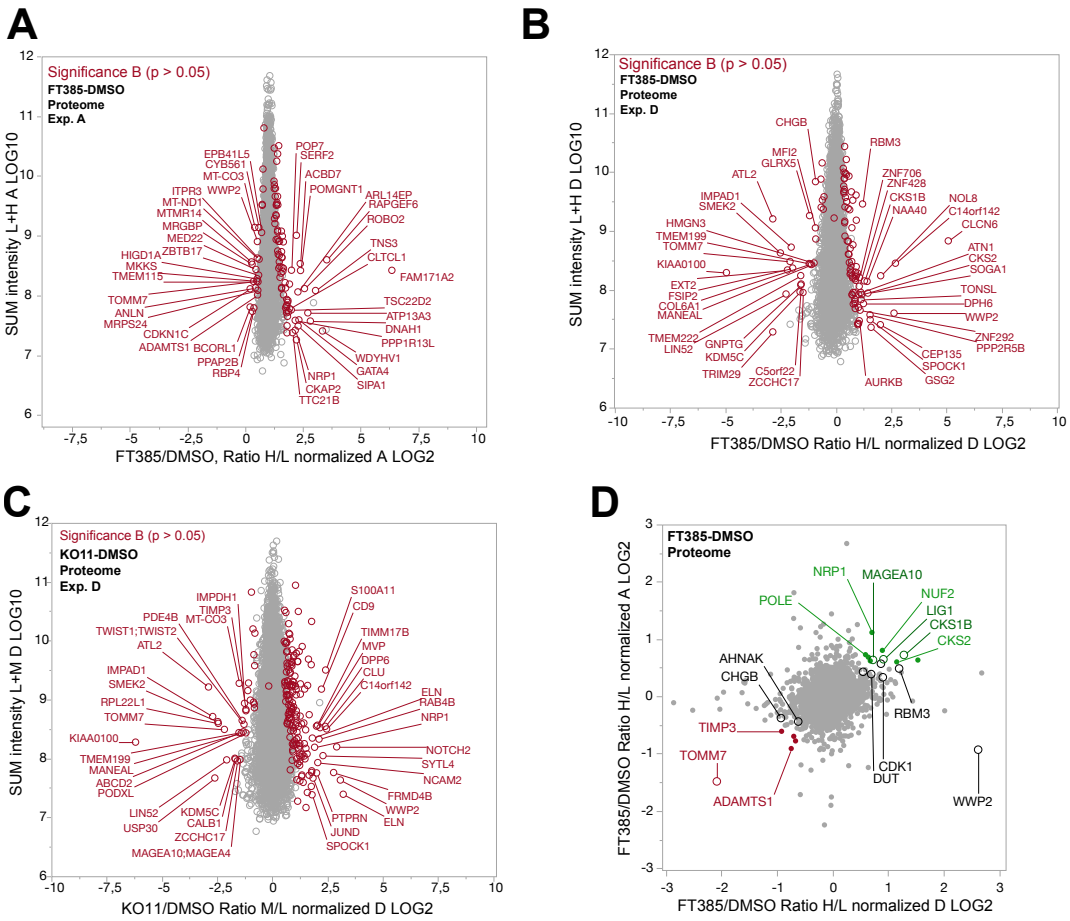

Figure 5.51: Scatter plots from the proteome analysis of USP30 KO or inhibited samples in the absence of depolarisation agents.

A-C) Scatter plots depicting the protein intensity (Log10; y-axis) over the fold change in the proteome of DMSO treated cells ± FT385 or USP30 KO (KO11) (Log2; x-axis). Proteins in red have a significance B score of p<0.05, proteins in grey have a significance B score of p>0.05. **D)** Scatter plots depicting fold change in the proteome of DMSO treated cells ± FT385 of experiment A (Log2; y-axis) over experiment D (Log2; x-axis). Proteins with a Log2 ratio <-0.585 are shown in red and proteins with a Log2 ratio >0.585 are shown in green. Proteins with hollow circles have a significance B score of p<0.05, proteins with a solid circle have a significance B score of p>0.05.

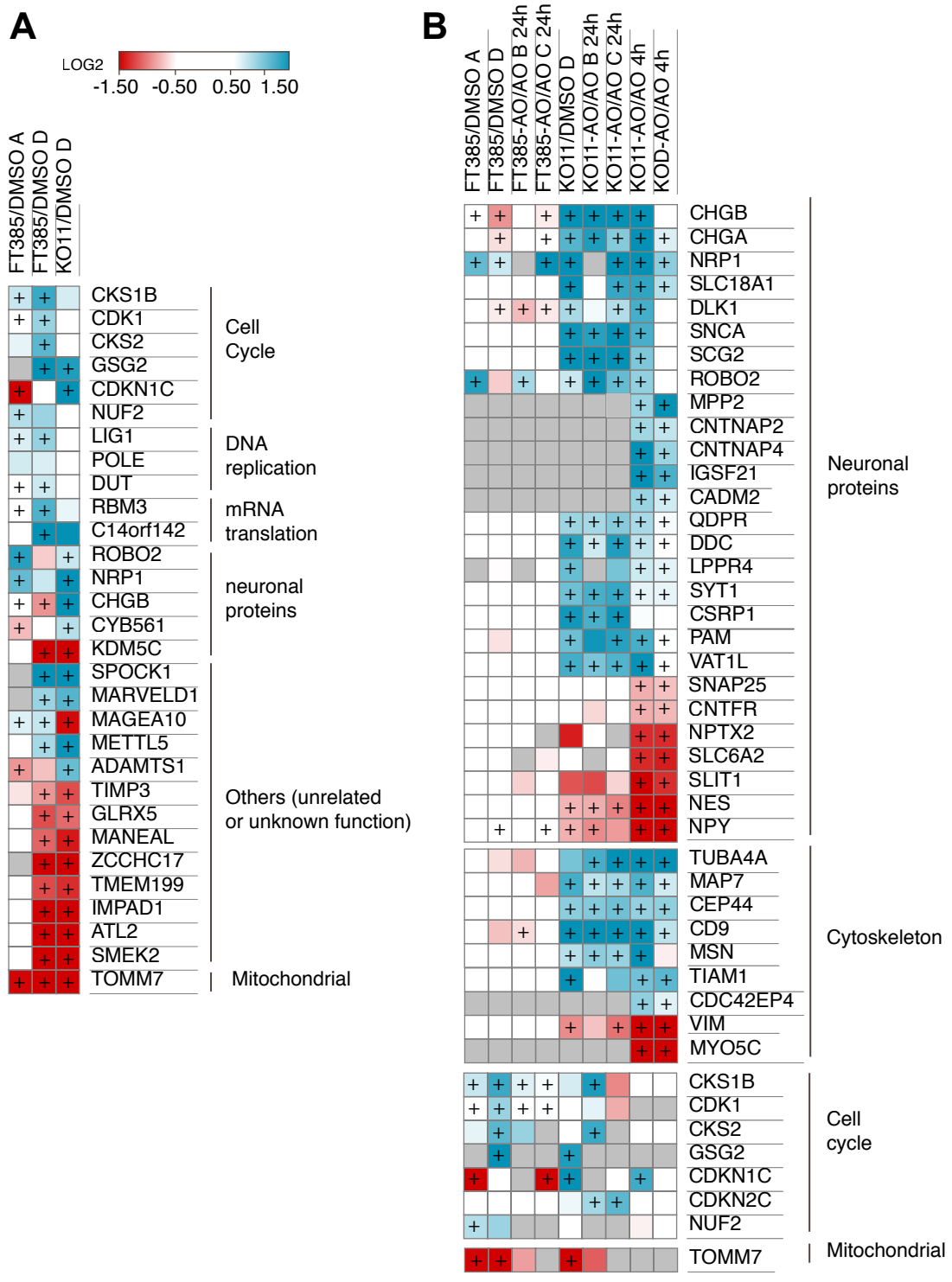

Figure 5.52: Heatmaps of proteins affected by USP30 KO and USP30 inhibition independently of depolarisation.

A) Heatmap depicting the fold change in the proteome of DMSO treated cells ± FT385 or ± USP30 KO. **B)** Heatmap depicting a consistent fold change in the proteome of USP30 KO or USP30 inhibitor treated cells independently of depolarisation. All three sets of proteome analyses are included (DMSO, 24h and 4h). Proteins with a Log2 ratio <-0.585 are in shades of red and proteins with a Log2 ratio >0.585 are in shades of blue. Proteins with a plus sign have a significance B score of $p<0.05$. Proteins are grouped by function or localisation.

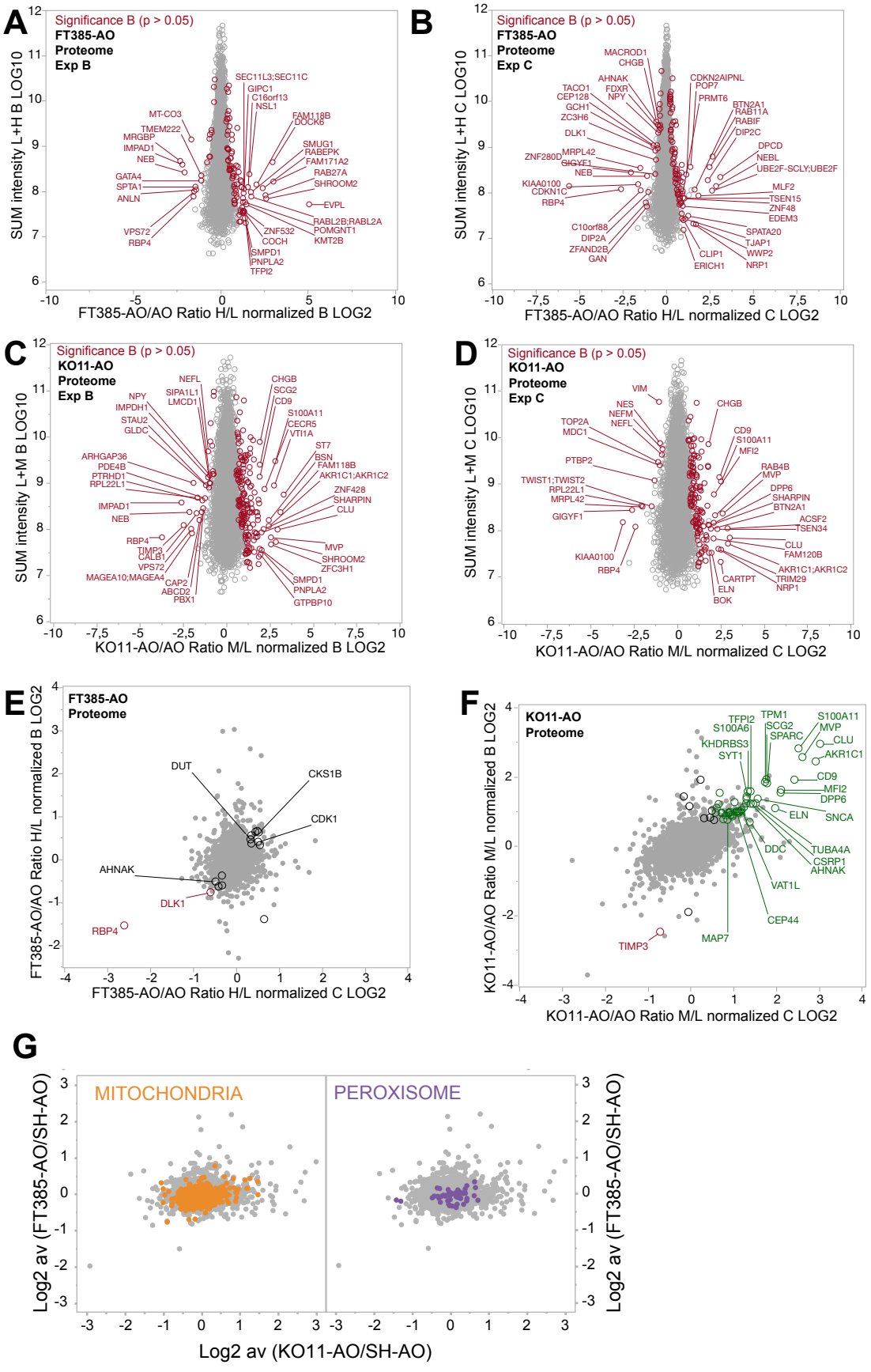
A
Significance B (p > 0.05)
FT385-AO
Proteome
Exp B
SUM intensity L+H B LOG10
FT385-AO/AO Ratio H/L normalized B LOG2
B
Significance B (p > 0.05)
FT385-AO
Proteome
Exp C
SUM intensity L+H C LOG10
FT385-AO/AO Ratio H/L normalized C LOG2
C
Significance B (p > 0.05)
KO11-AO
Proteome
Exp B
SUM intensity L+M B LOG10
KO11-AO/AO Ratio M/L normalized B LOG2
D
Significance B (p > 0.05)
KO11-AO
Proteome
Exp C
SUM intensity L+M C LOG10
KO11-AO/AO Ratio M/L normalized C LOG2
E
FT385-AO
Proteome
FT385-AO/AO Ratio H/L normalized B LOG2
FT385-AO/AO Ratio H/L normalized C LOG2
DUT
CKS1B
CDK1
AHNAK
DLK1
RBP4
F
KO11-AO
Proteome
KO11-AO/AO Ratio M/L normalized B LOG2
KO11-AO/AO Ratio M/L normalized C LOG2
G
MITOCHONDRIA
PEROXISOME
Log2 av (FT385-AO/SH-AO)
Log2 av (KO11-AO/SH-AO)

Figure 5.53: Scatter plots from the proteome analysis of USP30 KO or inhibited samples treated with AO for 24h.

A-D) Scatter plots depicting the protein intensity (Log10; y-axis) over the fold change in the proteome of AO treated cells ± FT385 or USP30 KO (KO11) (Log2; x-axis). Proteins in red have a significance B score of $p<0.05$, proteins in grey have a significance B score of $p>0.05$. **E-F)** Scatter plots depicting fold change in the proteome of AO treated cells ± **E)** FT385 or **F)** USP30 KO of experiment B (Log2; y-axis) over experiment C (Log2; x-axis). Proteins with a Log2 ratio <-0.585 are in red and proteins with a Log2 ratio >0.585 are in green. Proteins with hollow circles have a significance B score of $p<0.05$, proteins with a solid circle have a significance B score of $p>0.05$. **G)** Scatter plots depicting the average fold change (Experiment B and C) in the proteome of AO treated cells ± FT385 (Log2; y-axis) over AO treated cells ± KO11 (Log2; x-axis). Mitochondrial and peroxisomal proteins are shown in orange and purple respectively.

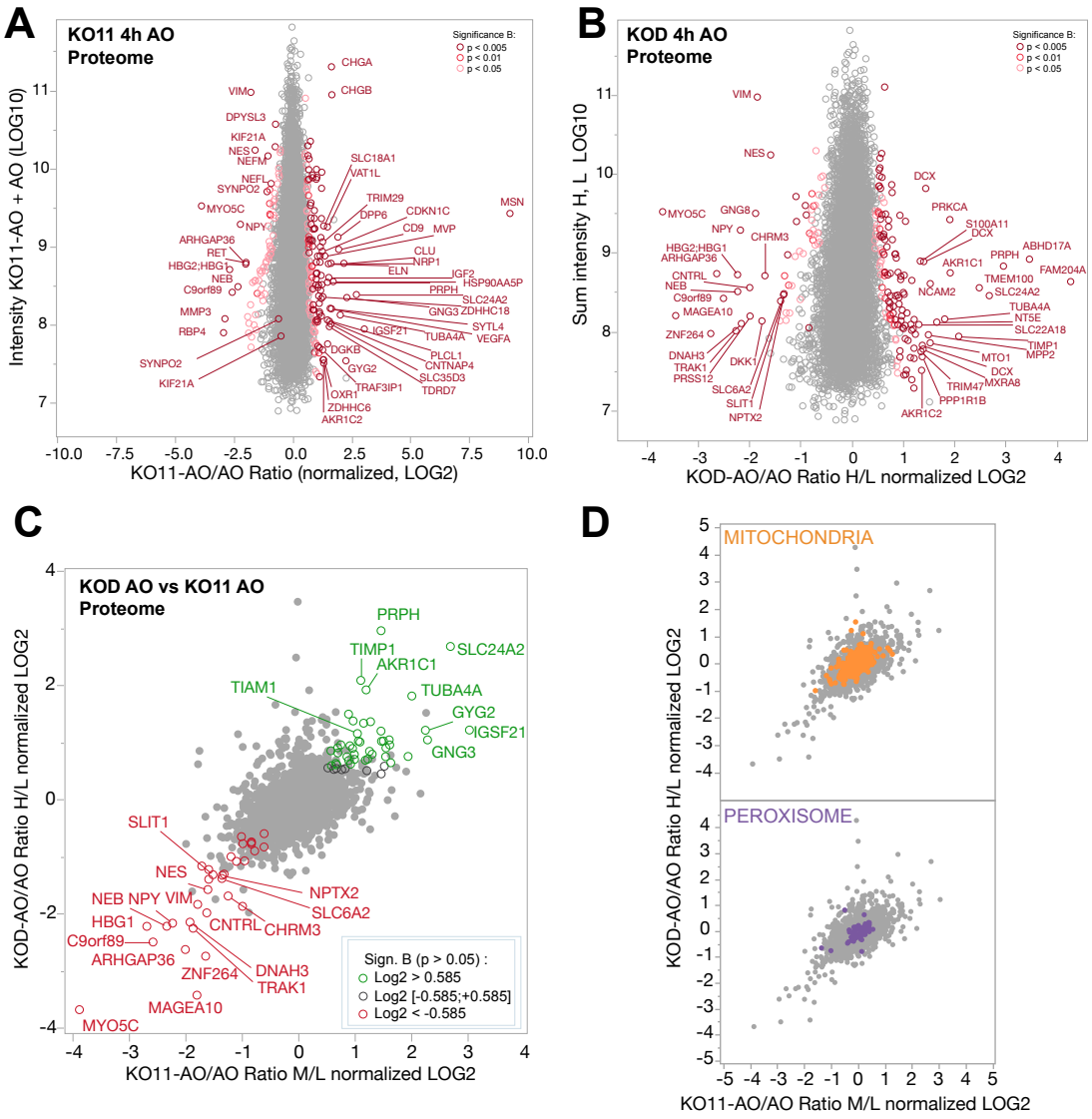

Figure 5.54: Scatter plots from the proteome analysis of USP30 KO samples treated with AO for 4h.

A-B) Scatter plots depicting the protein intensity (Log10; y-axis) over the fold change in the proteome of AO treated cells ± USP30 KO (KO11 or KO11) (Log2; x-axis). Proteins in dark red, red and pink have a significance B score of p<0.005, p<0.01 and p<0.05, respectively. Proteins in grey have a significance B score of p>0.05. **C)** Scatter plot depicting fold changes in the proteome of 4h AO treated cells ± USP30 KO with KOD (Log2; y-axis) over KO11 (Log2; x-axis). Proteins with a Log2 ratio <-0.585 are in red and proteins with a Log2 ratio >0.585 are in green. Proteins with hollow circles have a significance B score of p<0.05, proteins with a solid circle have a significance B score of p>0.05. **D)** Scatter plot in (C) with mitochondrial and peroxisomal proteins shown in orange and purple respectively.

5.4.3.2 Cross comparison of proteome datasets

5.4.3.2.1 Mitochondrial and peroxisomal proteomes

In SH-SY5Y cells treated with AO (4h and 24h), I did not measure any global changes in the mitochondrial and peroxisomal mass upon deletion or inhibition of USP30 (**Figure 5.53G, 5.54D**).

5.4.3.2.2 Proteins involved in neuronal structure and function

A cross comparison of proteome datasets revealed consistent changes in neuronal proteins (**Figure 5.52B, 5.53, 5.54**). I observed changes in neuronal components (CNTNAP2, LPPR4, NES, NRP1), synapse constituents (CNTNAP4, CAMD2, MPP2, SYT1, SNAP25, NPTX2), elements of synaptic vesicles and neurotransmitter release (CHGA, CHGB SNAP25, SLC6A2, NPY, CNTNAP4, SLC18A1, SNCA, SCG2), in dopamine production (DDC, QDPR, PAM), and in neuronal differentiation and survival proteins (CNTFR, SLIT1, CSRP1).

In addition to this striking increase in individual neuronal marker proteins, multiple components of signalling pathways that play a key role in neuronal differentiation, such as the SLIT/ ROBO pathway, were also affected (**Figure 5.52B, 5.53, 5.54**). The protein abundance of the slit guidance ligand 1 (SLIT1) was significantly reduced in both USP30 KO lines and one of the SLIT receptors, ROBO2, was conversely significantly more abundant in KO11 and FT385 treated cells.

5.4.3.2.3 Cytoskeleton

Multiple cytoskeleton proteins were upregulated across USP30 KO proteomes. This include microtubule proteins (TUBA4A, MAP7, CEP44), and other cytoskeleton interacting proteins (MSN, CD9, TIAM1, CDC42EP4). Conversely, the myosin MYO5C and the intermediate filaments VIM were significantly downregulated (**Figure 5.52B, 5.53, 5.54**).

Vimentin (VIM) is highly abundant in mesenchymal cells and involved in epithelial to mesenchymal transition (EMT) and thus is a common marker of EMT (Liu et al., 2015). Conversely a loss of vimentin, seen here in the USP30 KO cells, may be indicative of the opposite process, mesenchymal to epithelial transition (MET). During EMT, epithelial cells lose their cell adhesion

properties and gain the ability to migrate and invade. This process is particularly important during metastasis. Cell scattering assays mimic the cancer cell dispersal occurring during EMT and metastasis. Interestingly, Ricky Buus, a former lab member, had picked up USP30 in a siRNA-based DUB screen as necessary for HGF-mediated A549 cell scattering. Similarly, USP30 depletion prevented HGF-Dependent wound healing in A549 cells, another process commonly upregulated in response to EMT (Buus et al., 2009). Furthermore, our lab has previously discovered that knocking down USP30 also interferes with anchorage independent cell growth, another hallmark of cancer cells (unpublished data; personal communication, Monika Faronato, Sylvie Urbé and Michael Clague). Collectively these result points towards a role of USP30 in EMT and metastasis.

5.4.3.2.4 Proteins reacting in opposite fashion to USP30 inhibition and to USP30 deletion.

Some proteins reacted in an opposite fashion in response to treatment with the FT385 USP30 inhibitor compared to USP30 deletion. As an example, MAGEA10, which is a protein of unknown function, was one of the most highly upregulated proteins after 24h FT385 treatment in DMSO treated cells but conversely was significantly decreased in KO11 cells (**Figure 5.51, 5.52, 5.53, 5.54**). I could confirm the decrease in the KO cells by western blotting, while I did not detect an obvious change in WT and FT385 treated cells (**Figure 5.55A-B**).

This discrepancy between inhibition and deletion of USP30 could be explained by the fact that the catalytically inhibited deubiquitylase still retains the ability to interact with other proteins. The half-life of a protein can be extended when it is part of a complex due to its scaffolding function (McShane et al., 2016). USP30 and MAGEA10 could be part of a complex. In USP30 knockout cells, singled out MAGEA10 may therefore get degraded quicker.

Proteins specifically upregulated or downregulated by FT385 and unaffected by USP30 knockout cells, are likely off-targets effects of the inhibitor.

5.4.3.2.5 Contaminants

The presence of certain proteins in mass spectrometry datasets needs to be interpreted with caution. Some constituents of fetal bovine serum (FBS), such as albumin or secreted protein, will be detected by the mass spectrometer. These proteins won't be labelled, and therefore will be associated with decreased ratios in "medium-" and "heavy-" labelled conditions. Some of those proteins have conserved sequences between human and bovine and will thus be detected as "hits". Retinol binding protein 4 (RBP4) is a protein consistently destabilised by USP30 inhibition and USP30 knockout across proteomes and therefore appears as a major USP30 substrate (**Figure 5.51, 5.53**). However, RBP4 is a protein found in serum and which is secreted by the liver, adipose tissues and macrophages to permit the circulation of retinol (Atawia et al., 2019). Aligning the amino-acid sequence of bovine and human RBP4, I found that 96% of the protein sequence was conserved between both species (**Figure 5.56**). Moreover, the amino acid sequences of most peptides detected in both proteome analyses are conserved across both species. One peptide does align with the human protein selectively but has only been detected once. RBP4 is still most likely a contaminant and not a genuine USP30 substrate.

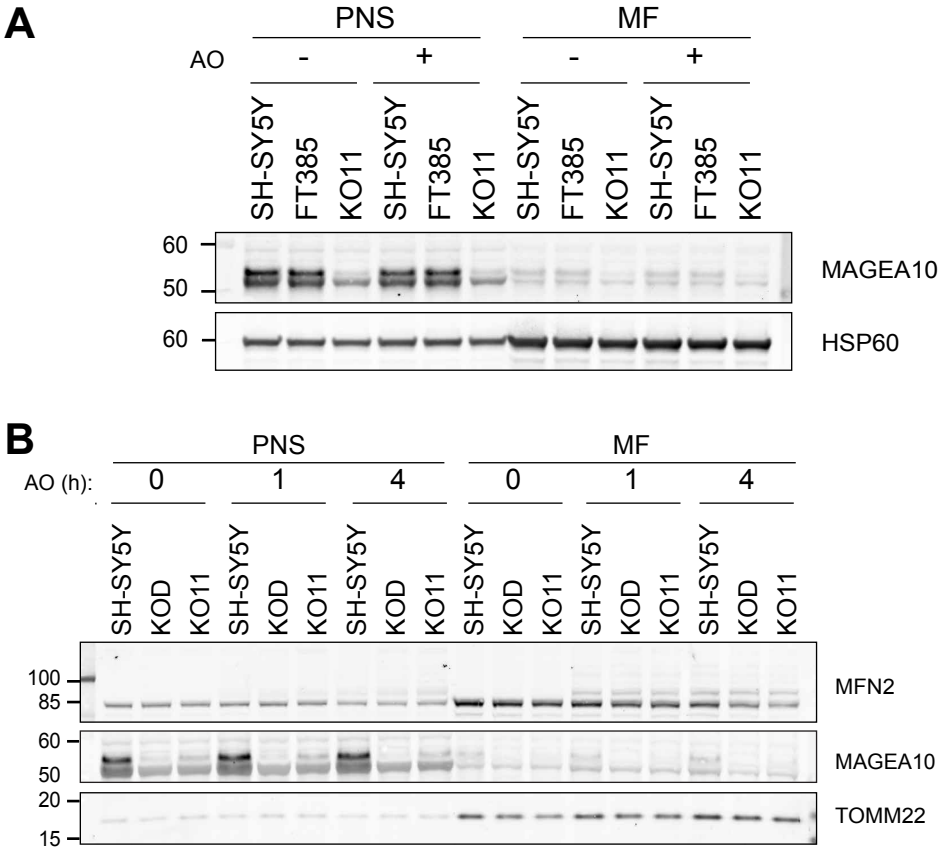

Figure 5.55: Western blot analysis of MAGEA10 protein levels in USP30 inhibited and KO cells.

A-B) SH-SY5Y, KOD and KO11 cells were treated with Antimycin A and Oligomycin A (AO, 1µM each) for A) 24h or B) 1 and 4h, and A) a set of SH-SY5Y cells was co-treated with 100nM FT385 for 24h. The cells were then homogenised in HIM buffer. The Post Nuclear Supernatant (PNS), Post Mitochondrial Supernatant (PMS) and Mitochondrial Fraction (MF) were obtained by differential centrifugation. **A-B)** The fractions were immunoblotted against MAGEA10 and mitochondrial proteins.

A

#1

```
>sp|P02753|RET4_HUMAN Retinol-binding protein 4 OS=Homo sapiens
OX=9606 GN=RBP4 PE=1 SV=3
MKWVWALLLLAALGSGRAERDCRVSSFRVKENFDKARFSGTWYAMAKKDPEGLFLQDNIV
AEFSVDETGQMSATAKGRVRLLNNWDVCADMVGTFTDTEDPAKFKMKYWGVASFLQKGND
DHWIVDTDYDTYAVQYSCRLLNLDGTCADSYSFVFSRDPNGLPPEAQKIVRQRQEELCLA
RQYRLIVHNGYCDGRSERNLL
```

#2

```
>tr|Q32L14|Q32L14_BOVIN Retinol-binding protein OS=Bos taurus
OX=9913 GN=RBP4 PE=2 SV=1
MEWVWALVLLAALGSARAERDCRVSSFRVKENFDKARFAGTWYAMAKKDPEGLFLQDNIV
AEFSVDENGHMCATAKGRVRLLNNWDVCADMVGTFTDTEDPAKFKMKYWGVASFLQKGND
DHWIIDTDYETFAVQYSCRLLNLDGTCADSYSFVFARDPSGFSPEVQKIVRQRQDELCLA
RQYRLIPHNGYCDGKSERNIL
```

B

```
Alignment of Sequence_1:  [HUMAN RBP4, Protein Sequence #1] with  Sequence_2:
[BOVINE RBP4 Protein Sequence Window #2]

Similarity : 193/201 (96.02 %)

Seq_1  1     MKWVWALLLLAALGSGRAERDCRVSSFRVKENFDKARFSGTWYAMAKKDPEGLFLQDNIV  60
             | |||||:||||||| |||||||||||||||||||| ||||||||||||||||||||
Seq_2  1     MEWVWALVLLAALGSARAERDCRVSSFRVKENFDKARFAGTWYAMAKKDPEGLFLQDNIV  60


Seq_1  61    AEFSVDETGQMSATAKGRVRLLNNWDVCADMVGTFTDTEDPAKFKMKYWGVASFLQKGND  120
             |||||||:|:|:||||||||||||||||||||||||||||||||||||||||||||||||
Seq_2  61    AEFSVDENGHMCATAKGRVRLLNNWDVCADMVGTFTDTEDPAKFKMKYWGVASFLQKGND  120


Seq_1  121   DHWIVDTDYDTYAVQYSCRLLNLDGTCADSYSFVFSRDPNGLPPEAQKIVRQRQEELCLA  180
             |||| |||| | |||||||||||||||||||||| |||:|::||:|||||||:|||||
Seq_2  121   DHWIIDTDYETFAVQYSCRLLNLDGTCADSYSFVFARDPSGFSPEVQKIVRQRQDELCLA  180


Seq_1  181   RQYRLIVHNGYCDGRSERNLL  201
             |||||| |||||||:||||:|
Seq_2  181   RQYRLIPHNGYCDGKSERNIL  201
```

C

```
RBP4 peptides detected:
LLNNWDVCADMVGTFTDTEDPAKFK; QRQEELCLAR; VKENFDK; VKENFDKAR
```

Figure 5.56: Human and bovine RBP4 protein alignment.

A) Amino-acid sequences of human and bovine RBP4. **B)** The amino acid sequences of human and bovine RBP4 were aligned using Serial Cloner (v2.6.1). The RBP4 peptides sequences detected in the mass spectrometry analysis are highlighted in yellow. **C)** Amino acid sequences of the three RBP4 peptides which were detected in the proteome analysis.

5.4.4 Ubiquitylome analysis

I then measured the effect of USP30 KO or inhibition on protein ubiquitylation in SH-SY5Y cells (**Figure 5.57, 5.58**). A change in the ratio of ubiquitylated peptides between WT and USP30 KO or USP30 inhibited cells can either genuinely result from a change in the ubiquitylation status or simply reflect changes in protein abundance. I therefore analysed the proteomes and ubiquitylomes side by side to determine *bona fide* USP30 substrates for which we would expect to see either an increase in ubiquitylated species with no changes at the proteome level or a decrease in both proteome and ubiquitylome datasets. SYT1 K105 was an example of a ubiquitylated peptides enriched in all KO11 and FT385 datasets that was also significantly increased in the proteome.

5.4.4.1 Total ubiquitylome (24h AO)

In SH-SY5Y cells treated with AO for 24h, the deletion or inhibition of USP30 primarily enhanced the ubiquitylation of the Voltage-Dependent Anion Channel (VDAC) subunits (VDAC1, VDAC2 and VDAC3) located at the OMM, whilst the few TOMM subunit ubiquitylation events detected in this dataset were unaffected by USP30 loss (Lysines detected: TOMM70 (K168, K170, K178); TOMM40 (K175), TOMM22 (K141)). (**Figure 5.57**). GAPDH, another predicted mitochondria-localising protein, was ubiquitylated at K196 in the absence of USP30 activity.

USP30 deletion or inhibition also enhanced the ubiquitylation of ribosomal proteins (RPS20, RLP19, HNRNPDL), histones (H3F3B and HIST1H2BD), amino acid transporters (SLC1A5, SLC29A1, SLC7A5), neuronal proteins (KIDINS220, NOVA2, SYNGR2, TMEM230, TMEM230) and proteins involved in the endosomal pathway (VPS45, VAMP2, LAMTOR1).

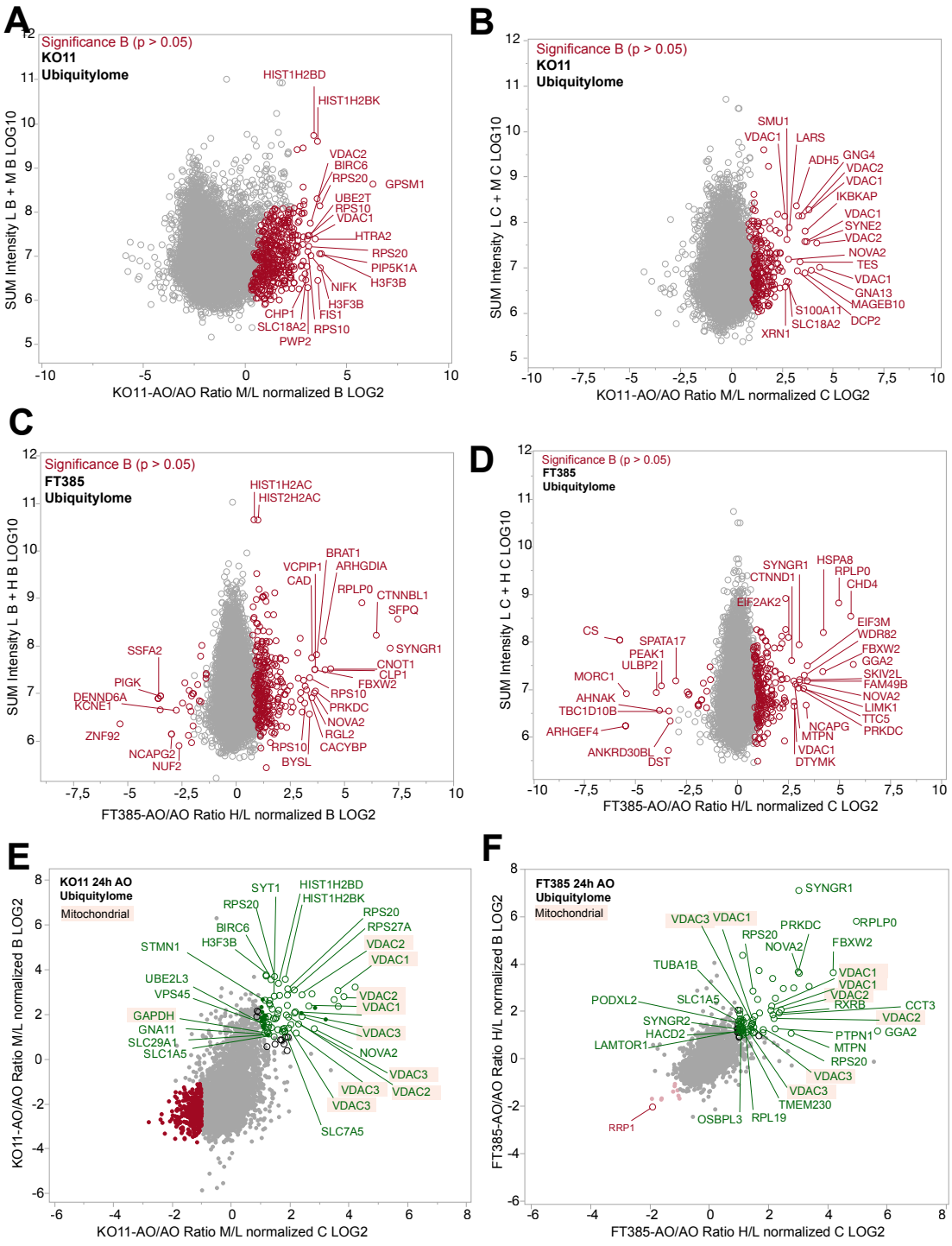
A
Significance B (p > 0.05)
KO11
Ubiquitylome
SUM Intensity L B + M B LOG10
KO11-AO/AO Ratio M/L normalized B LOG2
HIST1H2BD
HIST1H2BK
VDAC2
BIRC6
RPS20
GPSM1
UBE2T
RPS10
VDAC1
HTRA2
RPS20
PIP5K1A
H3F3B
NIFK
H3F3B
CHP1
FIS1
SLC18A2
RPS10
PWP2
B
Significance B (p > 0.05)
KO11
Ubiquitylome
SUM Intensity L C + M C LOG10
KO11-AO/AO Ratio M/L normalized C LOG2
SMU1
VDAC1
LARS
ADH5
GNG4
VDAC2
VDAC1
IKBKAP
VDAC1
SYNE2
VDAC2
NOVA2
TES
VDAC1
GNA13
MAGEB10
S100A11
SLC18A2
DCP2
XRN1
C
Significance B (p > 0.05)
FT385
Ubiquitylome
SUM Intensity L B + H B LOG10
FT385-AO/AO Ratio H/L normalized B LOG2
HIST1H2AC
HIST2H2AC
BRAT1
VCPIP1
ARHGDIA
CAD
RPLP0
CTNNBL1
SFPQ
SYNGR1
SSFA2
CNOT1
CLP1
PIGK
FBXW2
DENND6A
KCNE1
RPS10
PRKDC
NOVA2
ZNF92
RGL2
CACYBP
NCAPG2
RPS10
NUF2
BYSL
D
Significance B (p > 0.05)
FT385
Ubiquitylome
SUM Intensity L C + H C LOG10
FT385-AO/AO Ratio H/L normalized C LOG2
SYNGR1
HSPA8
CTNND1
RPLP0
CHD4
EIF2AK2
EIF3M
CS
WDR82
SPATA17
FBXW2
PEAK1
GGA2
ULBP2
SKIV2L
MORC1
FAM49B
NOVA2
AHNAK
LIMK1
TBC1D10B
TTC5
NCAPG
PRKDC
ARHGEF4
MTPN
VDAC1
ANKRD30BL
DTYMK
DST
E
KO11 24h AO
Ubiquitylome
Mitochondrial
KO11-AO/AO Ratio M/L normalized B LOG2
KO11-AO/AO Ratio M/L normalized C LOG2
SYT1
HIST1H2BD
RPS20
HIST1H2BK
BIRC6
RPS20
RPS27A
H3F3B
STMN1
VDAC2
VDAC1
UBE2L3
VPS45
VDAC2
VDAC1
GAPDH
GNA11
VDAC3
SLC29A1
SLC1A5
NOVA2
VDAC3
VDAC3
VDAC2
VDAC3
SLC7A5
F
FT385 24h AO
Ubiquitylome
Mitochondrial
FT385-AO/AO Ratio H/L normalized B LOG2
FT385-AO/AO Ratio H/L normalized C LOG2
SYNGR1
VDAC3
VDAC1
RPLP0
PRKDC
RPS20
FBXW2
NOVA2
TUBA1B
VDAC1
VDAC1
PODXL2
SLC1A5
VDAC2
RXRB
CCT3
SYNGR2
VDAC2
HACD2
PTPN1
GGA2
LAMTOR1
MTPN
RPS20
VDAC3
VDAC3
TMEM230
RRP1
OSBPL3
RPL19

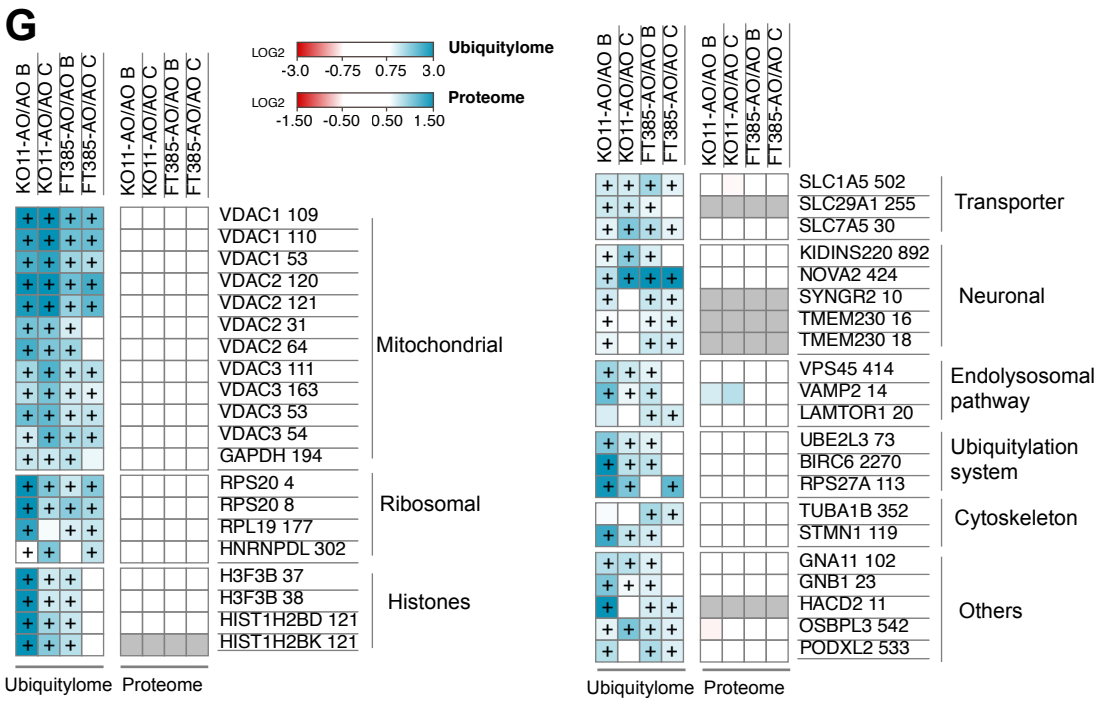

Figure 5.57: Scatter plots from the ubiquitylome analysis of USP30 KO and USP30 inhibited samples treated with AO for 24h.

A-D) Scatter plots depicting the peptide intensity (Log10; y-axis) over the fold change in the ubiquitylome of AO treated cells ± FT385 or ± USP30 KO (KO11) (Log2; x-axis). Proteins in red have a significance B score of p<0.05, respectively. Proteins in grey have a significance B score of p>0.05. **E-F)** Scatter plots depicting fold change in the ubiquitylome of 24h AO treated cells ± **E)** USP30 KO or **F)** FT385 of experiment B (Log2; y-axis) over experiment C (Log2; x-axis). Proteins with a Log2 ratio <-1 are in red and proteins with a Log2 ratio >1 are in green. Proteins with hollow circles have a significance B score of p<0.05, proteins with a solid circle have a significance B score of p>0.05. **G)** Heatmap depicting the fold change in the ubiquitylome and proteome of USP30 KO (KO11) and USP30 inhibited cells treated with 24h AO. Ubiquitylome: peptides with a Log2 ratio <-0.75 are in shades of red and proteins with a Log2 ratio >0.75 are in shades of blue. Proteome: Proteins with a Log2 ratio <-0.585 are in shades of red and proteins with a Log2 ratio >0.585 are in shades of blue. Peptides with a plus sign have a significance B score of p<0.05. Proteins are grouped by function or localisation.

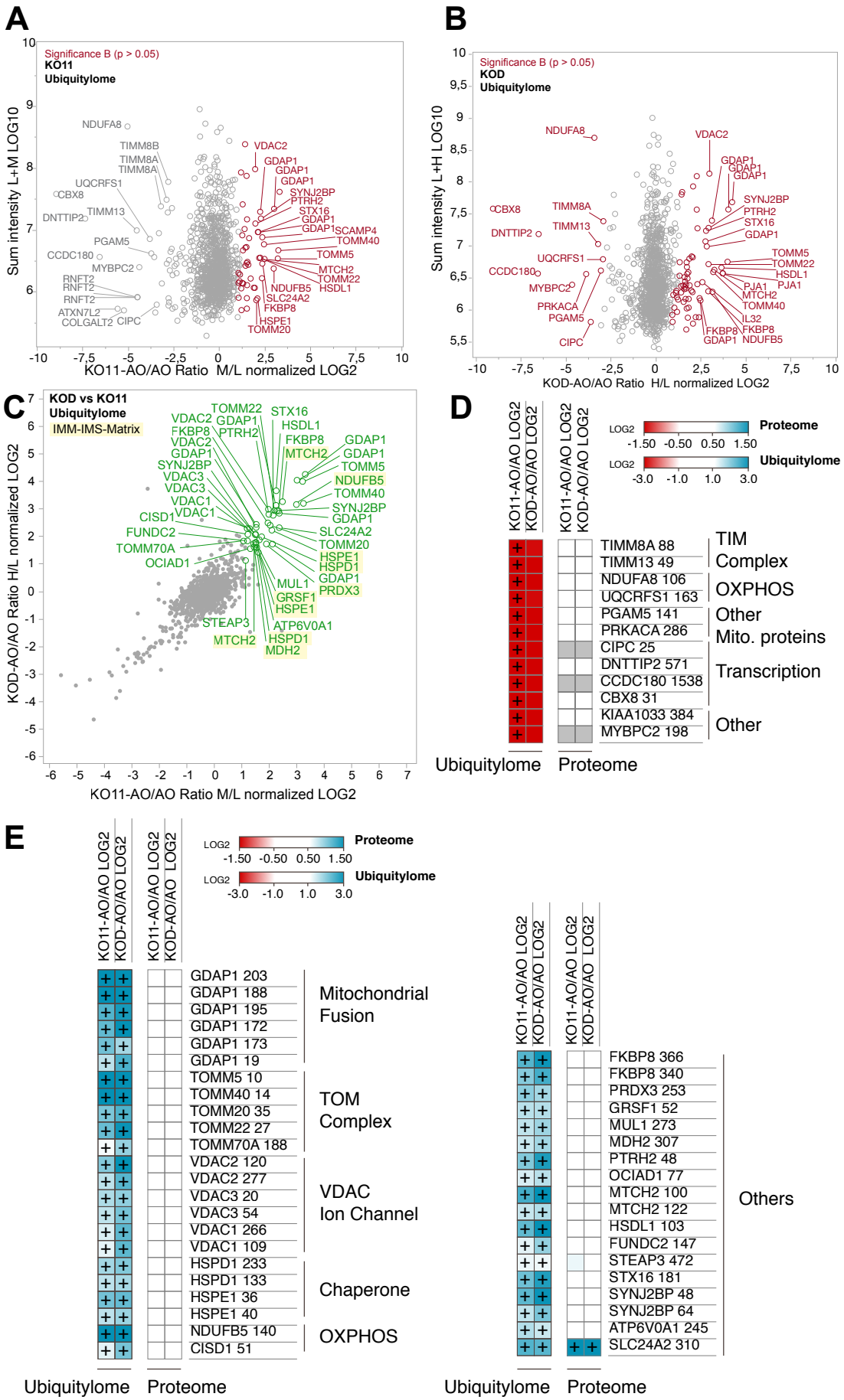
A
Significance B (p > 0.05)
KO11
Ubiquitylome
Sum intensity L+M LOG10
KO11-AO/AO Ratio M/L normalized LOG2
B
Significance B (p > 0.05)
KOD
Ubiquitylome
Sum intensity L+H LOG10
KOD-AO/AO Ratio H/L normalized LOG2
C
KOD vs KO11
Ubiquitylome
IMM-IMS-Matrix
KOD-AO/AO Ratio H/L normalized LOG2
KO11-AO/AO Ratio M/L normalized LOG2
D
KO11-AO/AO LOG2
KOD-AO/AO LOG2
Proteome
Ubiquitylome
TIMM8A 88
TIMM13 49
NDUFA8 106
UQCRFS1 163
PGAM5 141
PRKACA 286
CIPC 25
DNTTIP2 571
CCDC180 1538
CBX8 31
KIAA1033 384
MYBPC2 198
TIM Complex
OXPHOS
Other Mito. proteins
Transcription
Other
Ubiquitylome
Proteome
E
GDAP1 203
GDAP1 188
GDAP1 195
GDAP1 172
GDAP1 173
GDAP1 19
TOMM5 10
TOMM40 14
TOMM20 35
TOMM22 27
TOMM70A 188
VDAC2 120
VDAC2 277
VDAC3 20
VDAC3 54
VDAC1 266
VDAC1 109
HSPD1 233
HSPD1 133
HSPE1 36
HSPE1 40
NDUFB5 140
CISD1 51
Mitochondrial Fusion
TOM Complex
VDAC Ion Channel
Chaperone
OXPHOS
FKBP8 366
FKBP8 340
PRDX3 253
GRSF1 52
MUL1 273
MDH2 307
PTRH2 48
OCIAD1 77
MTCH2 100
MTCH2 122
HSDL1 103
FUNDC2 147
STEAP3 472
STX16 181
SYNJ2BP 48
SYNJ2BP 64
ATP6V0A1 245
SLC24A2 310
Others
Ubiquitylome
Proteome

Figure 5.58: Scatter plots and heatmaps from the ubiquitylome analysis of USP30 KO samples treated with AO for 4h.

A-B) Scatter plots depicting the peptide intensity (Log10; y-axis) over the fold change in the ubiquitylome of AO treated cells ± USP30 KO (KO11 or KOD) (Log2; x-axis). Proteins in red have a significance B score of $p<0.05$, respectively. Proteins in grey have a significance B score of $p>0.05$. **C)** Scatter plot depicting fold changes in the ubiquitylome of 4h AO treated cells KOD (Log2; y-axis) over KO11 cells (Log2; x-axis). Proteins with a Log2 ratio <-1 are in red and proteins with a Log2 ratio >1 are in green. Proteins with hollow circles have a significance B score of $p<0.05$, proteins with a solid circle have a significance B score of $p>0.05$. **D-E)** Heatmap depicting the fold change in the ubiquitylome and proteome of 4h AO treated KOD and KO11 cells. **D)** Decreased and **E)** increased fold change. Proteome: Proteins with a Log2 ratio <-0.585 are in shades of red and proteins with a Log2 ratio >0.585 are in shades of blue. Ubiquitylome: peptides with a Log2 ratio <-1 are in shades of red and proteins with a Log2 ratio >1 are in shades of blue. Peptides with a plus sign have a significance B score of $p<0.05$. Proteins are grouped by function or localisation.

5.4.4.2 Mito-ubiquitylome (4h AO)

The mito-ubiquitylome revealed additional mitochondria localised substrates of USP30 (**Figure 5.58**). Many of those proteins are localised at the OMM such as GDAP1, which has six lysines significantly more ubiquitylated upon USP30 loss and inhibition (K19, K172, K173, K188, K195 and K203) and members of the TOM complex. USP30's deubiquitylating activity towards the TOM complex was not restricted to TOMM20. Most of the TOM core complex components except for TOMM6, which has no lysines, and TOMM7 were significantly more ubiquitylated.

Intriguingly, although USP30 localises at the OMM, USP30 deletion in both clones led to a significant increase in the ubiquitylation of IMM and matrix proteins. These include chaperone proteins (HSPD1, HSPE1), OXPHOS proteins (NDUFB5), Krebs cycle enzymes (MDH2), peroxidases (PRDX3), proteins regulating mitochondrial mRNA translation (GRSF1) and mitochondrial carriers (MTCH2). In contrast some other, IMM and matrix proteins, TIMM complex and OXPHOS components, had lysines which were >8-fold less ubiquitylated in KO11 (significant) and KOD (not significant).

5.4.4.3 Cross-comparison of ubiquitylome

The VDAC proteins were a consistent hit across depolarised KOD, KO11 and FT385 cells (**Figure 5.59 and 5.60**). USP30 appears to specifically deubiquitylate K20, K53, K109, K266 in VDAC1, K120 in VDAC2 and both K20 and K54 in VDAC3. On average USP30 deletion or inhibition induced a 1.5 to 7-fold increase in these ubiquitylated lysines across the board. The OMM protein, synaptojanin 2-binding protein (SYNJ2BP), was another hit with K48 and K64 ubiquitylation being increase by 4-fold on average. The other four hits were the pro-fission protein GDAP1 (K203, ~4-fold increase), the OMM protein PTRH2 (K48, ~2.6-fold increase), the monoamine neurotransmitter transporter SLC18A2 (K491, ~2.5-fold increase) and the peroxisomal protein ABCD3 (also known as PMP70, ~1.7-fold increase).

5.4.4.4 Substrates in common with Parkin

USP30 KO in both clones and FT385 enhanced the ubiquitylation of multiple OMM proteins, all of which have been reported as substrates of the E3 ligase Parkin (VDAC1/2/3, TOMM5/20/22/40/70, GDAP1, …) (**Figure 5.60**) (Heo et al., 2019; Ordureau et al., 2018; Rose et al., 2016; Sarraf et al., 2013). Our lab had previously reported in *Drosophila*, that *porin* (VDAC1, 2 and 3 in mammals) was amongst the most ubiquitylated proteins in *Drosophila* neurons overexpressing *Parkin*, second to *MitoNEET* (the *Drosophila* homolog of human CISD1 and CISD2), (Martinez et al., 2017). In a small proteomic study performed in HeLa depolarised with CCCP by Richard Youle's lab, GDAP1 emerged as the second most destabilised protein following Parkin overexpression (Narendra et al., 2012).

Comparing the ubiquitylation sites affected by USP30 in our mass spectrometry experiments (of hit proteins) with those reported to be substrates of Parkin, indicated that roughly 2/3 of those sites are substrates of both USP30 and Parkin (**Figure 5.60**), (Sarraf et al., 2013; Bingol et al., 2014; Ordureau et al., 2018, 2020). This confirms that USP30 is the bona fide deubiquitylating enzyme which opposes Parkin in the canonical PINK1-Parkin pathways of mitophagy. USP30 did, however, have specific ubiquitylations sites on VDAC2 (K121, K277), VDAC3 (K111), TOMM5 (K10), TOMM22

(K27), TOMM40 (K14), TOMM70 (K188), SYNJ2BP (K48) and ABCD3 (K260) that are not ubiquitylated by parkin.

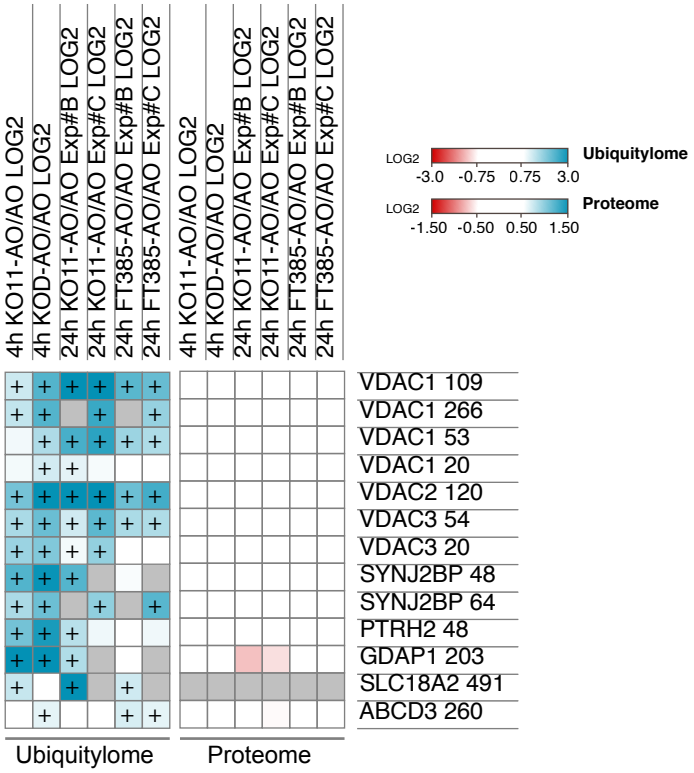

Figure 5.59: Heatmaps of ubiquitylation sites consistently affected by USP30 KO and USP30 inhibition across experiments.

Heatmap depicting the fold change in the ubiquitylome and proteome of USP30 KO (KO11 and KOD) and USP30 inhibited cells across all datasets. Ubiquitylome: peptides with a Log2 ratio <-0.75 are in shades of red and proteins with a Log2 ratio >0.75 are in shades of blue. Proteome: Proteins with a Log2 ratio <-0.585 are in shades of red and proteins with a Log2 ratio >0.585 are in shades of blue. Peptides with a plus sign have a significance B score of $p<0.05$.

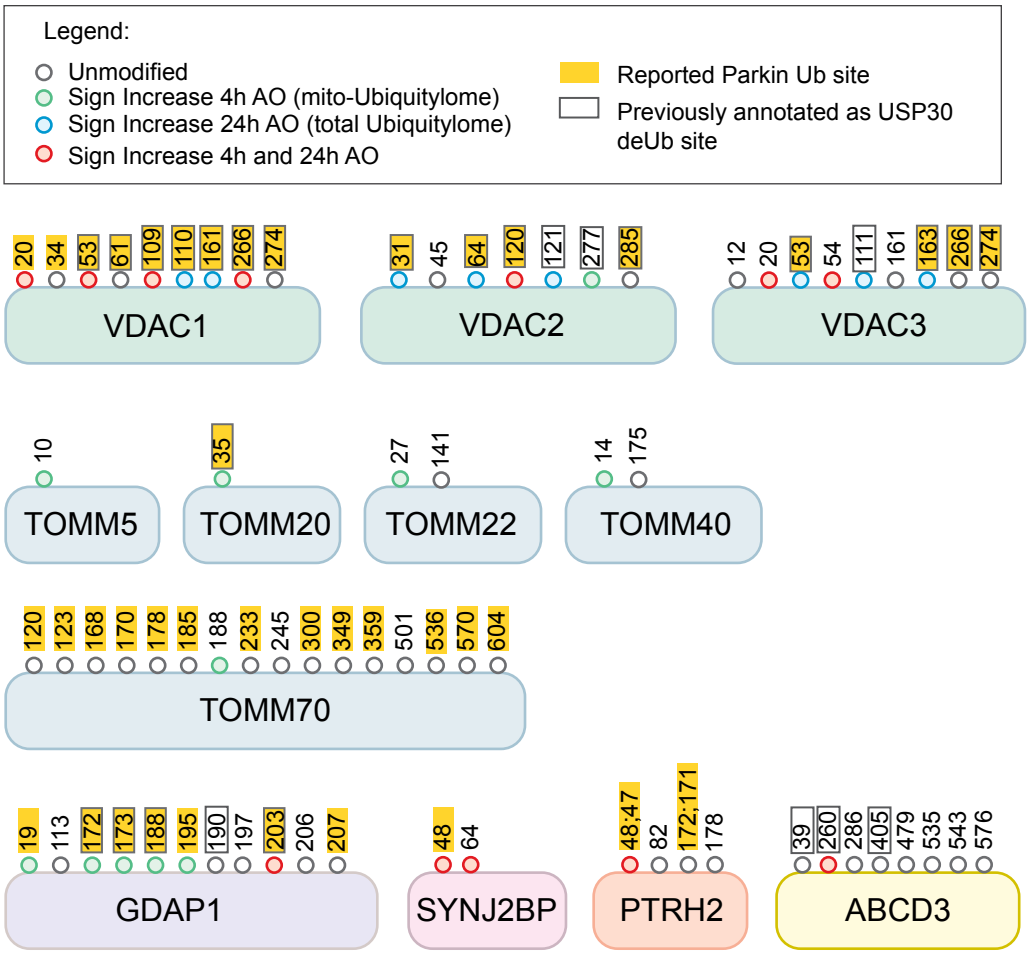

Figure 5.60: Schematic representation of USP30's deubiquitylation sites.

Schematics depicting VDACs, TOMMs , GDAP1, SYNJ2BP, PTRH2 and ABCD3's ubiquitylated peptides detected in the ubiquitylome (24h AO) and mito-ubiquitylome (4h AO) experiments. Peptides are described as significantly increased if they have a significance B score of $p<0.05$. The peptides which have been characterised as USP30 and/or Parkin substrates in other mass spectrometry analysis are outlines in black and/or highlighted in yellow, respectively. (Data compared with Sarraf et al., 2011; Rose et al., 2012; Ordureau et al., 2018; Ordureau et al., 2020; Phu et al., 2020).

5.5 Discussion

In this Chapter, I have introduced USP30 KO SH-SY5Y cell lines, characterised novel USP30 targeted inhibitors and further studied and discussed novel pathways regulated by USP30.

5.5.1 TOMM20-ubiquitylation and pS65-ubiquitin deposition at mitochondria

I successfully generated USP30 KO SH-SY5Y lines with two distinct sgRNA (KOD with sgRNA#1 and KO11 with sgRNA#2). By western blotting and subcellular fractionation, I showed that USP30 deletion enhanced both basal and AO-induced ubiquitylation of TOMM20 in SH-SY5Y cells expressing Parkin endogenously. This was in agreement with Amos's findings which describe that USP30 knockdown enhances the ubiquitylation of TOMM20 in response to CCCP in hTERT-RPE1-YFP-Parkin cells (Liang et al., 2015). Our ubiquitylomic experiment performed on mitochondrial fractions revealed that USP30 deletion significantly upregulated TOMM20's ubiquitylation at K35 by over 4-fold. TOMM20 was unique in the sense that it was the only Parkin substrate for which I saw consistently a clear increase in ubiquitylation with USP30 deletion in western blot assays.

Using a combination of microscopy and western blotting, I showed that pSer65-ubiquitin accumulates substantially on mitochondria of USP30 KO cell lines upon AO depolarisation (Rusilowicz-Jones et al., 2020). While writing our manuscript, Ordureau and colleagues also reported what they referred to as a modest acceleration of pS65-Ub accumulation in USP30$^{-/-}$ iNeurons but only when using a low concentration of AO (0.5μM each against 1μM each in our western blot experiments). Their initial experiments employed much higher concentrations of AO (10μM Antimycin + 5μM Oligomycin), which masked any effect of USP30 deletion on the levels of pSer65-Ub (Ordureau et al., 2020). Interestingly, this increase in pS65-Ub does not correlate with enhanced Parkin or PINK1 levels and furthermore phosphorylated ubiquitin is a poor substrate for USP30 (Wauer et al., 2015a; Gersch et al., 2017). We thus believe that USP30 acts upstream of PINK1 to fine tune mitophagy.

5.5.2 E3 ligases opposing USP30

I have searched for new E3 ligases that could oppose USP30 and prime mitochondria with ubiquitin prior to Parkin recruitment during AO-induced mitophagy. My preliminary results suggested that both HUWE1 and MARCH5 ubiquitylate TOMM20 and are involved in ubiquitylation prior to PINK1 phosphorylation (decreased pS65-Ub and Ub-TOMM20 with HUWE1 and MARCH5 knockdown).

Consistent with these observations, the cytosolic E3 ubiquitin ligase HUWE1, was reported to be involved in AMBRA1-mediated mitophagy (Di Rita et al., 2018; Strappazzon et al., 2019). The Cecconi group have shown that targeting AMBRA1 to mitochondria (AMBRA1^{Acta} overexpression) induced mitophagy in HeLa cells (Strappazzon et al., 2015). In their 2018 paper, they described that HUWE1 binds to both the mitophagy receptor AMBRA1 and to MFN2, promotes the activation of AMBRA1 (positive regulation of AMBRA1-S1014 phosphorylation), and further enables the ubiquitylation and degradation of mitochondria in cells overexpressing AMBRA1^{Acta} and lacking Parkin (Di Rita et al., 2018).

Interestingly, both HUWE1 and USP30 are key modulators of cellular K6-linked ubiquitin chains and could therefore oppose each other in the regulation of mitochondrial ubiquitylation (Cunningham et al., 2015; Gersch et al., 2017; Michel et al., 2017). Remarkably, Elena Marcassa has observed in U2OS mito-QC cells that enhancement of basal mitophagy by USP30 depletion is abolished by HUWE1 knockdown (unpublished data- Elena Marcassa).

On the other hand, Koyano and colleagues have suggested that MARCH5 (also known as MITOL) adds the “seed” ubiquitin onto mitophagy substrates prior to Parkin recruitment. They described that MARCH5 knockdown and knockout delayed the recruitment of Parkin to mitochondria and reduced the ubiquitylation of mitochondrial proteins, such as TOMM20 and CISD1 in Parkin overexpressing cells following CCCP treatment (Koyano et al., 2019a).

A recent study by the Bingol lab disclosed that USP30 and MARCH5 fine tune protein import at the TOM complex (Phu et al., 2020). This finding stemmed from the observation that many of USP30 substrates they found by mass

spectrometry were IMM or matrix proteins in USP30 inhibited or USP30 KO HEK293 cells (Phu et al., 2020).

In agreement with this, our ubiquitylomics studies also described that matrix and IMS proteins such as MDH2, MTCH2, GRSF1, HSPD1, HSPE1, NDUFB5 or PRDX3 are more ubiquitylated in USP30 KO cells (Rusilowicz-Jones et al., 2020). Similarly, ubiquitylomics performed in USP30 KO iNeurons show increased ubiquitylation of proteins targeted to the mitochondrial matrix such as Citrate Synthase or subunits of Complex I, IV and V, using USP30 KO iNeurons (Ordureau et al., 2020).

Phu and colleagues employed a mitochondrial 'import assay" based on a split GFP system, the MTS-Scarlett-GFP(1-10) split probe with DOX induced GFP(11) fused to any import substrate, to assess USP30's involvement in protein import. Using USP30 KO HEK293 and siRNA targeting MARCH5, they showed that MARCH5 ubiquitylates proteins getting imported to send them for proteasomal degradation whilst USP30 deubiquitylates them to permit their import (Phu et al., 2020). Likewise, Wade Harper's group observed an increase in the ubiquitylation of IMM and matrix protein (citrate synthase and subunits of CI, CIV and CV of the electron transport chain) in USP30 KO iNeurons. However, they found that neither knocking out MUL1 nor MARCH5 in USP30 KO iNeurons suppressed the ubiquitylation of citrate synthase (Ordureau et al., 2020).

Interestingly I have also found that HSPE1 and HSP60, chaperones involved in protein import and protein folding, were also more ubiquitylated USP30 KO cells. However, those proteins were also found to be ubiquitylated by Parkin. HSPE1 and HSP60 ubiquitylation thus maybe relates more to mitophagy induction rather than protein import (Rose et al., 2016).

5.5.3 FT385 is a highly specific and potent USP30 inhibitor

I have introduced two novel cyano-pyrrolidines inhibitor targeting USP30: USP30i and FT385.

The USP30i compound inhibitor was able to augment basal mitophagy by 1.6 and 1.7-fold and increased the mitolysosomes area in U2OS cells (5-10μM). However, in SH-SY5Y cells at 5μM, USP30i induced cell death and lower

USP30i doses showed only subtle effects (small trend towards an increase of mitolysosomes and mitolysosome area).

The FT385 compound emerged as a highly specific and potent USP30 inhibitor (USP30 IC_{50}: 1 nM against 90nM for USP30i) (Rusilowicz-Jones et al., 2020). By western blot analysis, FT385 phenocopied USP30 knockdown and knockout in SH-SY5Y cells, increasing AO-induced TOMM20 ubiquitylation and pS65-Ub accumulation at mitochondria. Further characterisation by Emma Rusilowicz-Jones in hTERT-RPE1-YFP-Parkin cells, revealed that FT385-mediated inhibition of USP30 increases AO-induced TOMM20-ubiquitylation to the same extent as USP30 deletion. Treating USP30 KO cells with FT385 did not further augment TOMM20 ubiquitylation, indicating that it is an on-target effect of FT385 (Rusilowicz-Jones et al., 2020). Remarkably FT385 also phenocopied USP30 KO by ubiquitylomics, proving for the first time that these ubiquitylation events are regulated by USP30's catalytic activity. FT385 confirmed that VDAC1, 2 and 3 are genuine substrates of USP30 and led me to identify SYNJ2BP as a novel USP30 substrate.

Treating SH-SY5Y cells for 24h with 100nM FT385 was insufficient to either enhance AO-induced mitophagy or augment basal mitophagy. However, Katy McCarron and Francesco Barone showed that treating these cells with 200nM FT385 for 96h significantly enhanced basal mitophagy by 1.7-fold (Rusilowicz-Jones et al., 2020). Through the pharmacological inhibition of USP30, with USP30i and FT385, we have thus confirmed that USP30 regulates basal mitophagy.

Other USP30 inhibitors have been published but were less potent with >60-fold higher USP30 IC_{50} and/or used in mammalian cells at micromolar doses (2-5μM vs 100-200nM with FT385). These inhibitors were also not as selective or not tested for specificity (Yue et al., 2014; Kluge et al., 2018; Stockley et al., 2018; Phu et al., 2020).

Congruent with our data, another USP30 inhibitor, MF-094 (USP30 IC_{50}: 120nM), was shown to enhance the decay of BrdU labelled mtDNA in postmitotic C2C12 mice myotubes cells which indirectly suggests an increase in mitochondrial degradation (Kluge et al., 2018).

I did not observe any distinct fusion of the mitochondrial network with FT385 in SH-SY5Y cells unlike that reported by Yue and colleagues with the 15-oxospiramilactone USP30 inhibitor in MEF cells, (Yue et al., 2014). Neither FT385 treated, nor USP30 knocked-down nor KO SH-SY5Y cells had mitochondria which were more elongated than wildtype cells. Similar observations were made by Andreas, Elena, Aitor and Emma which had respectively generated USP30 knockout lines in HCT116, RPE1 and U2OS cells.

While our manuscript was in preparation, Bingol's group published a complementary study describing the effect of USP30 inhibition on HEK293 cells by mass spectrometry (Phu et al., 2020). They focussed their study on constitutive conditions (no depolarisation) and made use of a much higher inhibitor concentration (5μM). They obtained a 2-fold deeper total ubiquitylome coverage than ours, which contained a much higher number of hit proteins belonging to the IMM and mitochondrial matrix. Their publication was thus focussed on the regulation of mitochondrial protein import by USP30. However, the few OMM hit proteins they found coincide with our results, with proteins such as GDAP1 and TOMM20 being more ubiquitylated with USP30 inhibition.

5.5.4 Biomarkers for USP30 deletion or inhibition

I had aimed at using the total proteomes to find supplementary biomarkers characteristic of USP30 inhibition and deletion. Despite having large proteome coverages, 6,423 peptides (24h AO total proteome) and 7,372 peptides (4h AO total proteome), I only found few proteins that similarly responded to USP30 deletion and inhibition. There were no apparent changes in the global mitochondrial or peroxisomal proteomes. This was consistent with my observations by immunofluorescence in KO11 cells where I had seen no global changes in the number of peroxisomes nor in the total mitochondrial mass. Similar observations were made by my colleague Elena Marcassa in RPE1 cells. It thus appears that in cells expressing no or endogenous Parkin, basal and induced mitophagy events occur at relatively a low rate, such that they have little impact on the total mitochondrial mass.

5.5.4.1 TOMM7

In the absence of mitochondrial depolarisation, TOMM7 was the only significantly downregulated protein in both FT385 replicates and KO11 cells. TOMM7 was similarly downregulated upon depolarisation but was not detected in all replicates.

This OMM protein is part of the TOM complex and has recently been described as a major regulator of the PINK1-Parkin pathway of mitophagy. In a CRISPR knockout screen for proteins that accelerate or decelerate mitophagy, TOMM7 KO stood out as major decelerator ranking 21st out of 1998 proteins with PINK1 KO ranking first. TOMM7 depletion restrained depolarisation-mediated degradation of OMM and IMM proteins as well as mitolysosome formation in mouse myoblasts overexpressing Parkin (Hoshino et al., 2019). Similarly, TOMM7 was highlighted as a "critical mitophagy gene" in a mitophagy flux screen using HFT cells overexpressing Parkin and mt-Keima (Heo et al., 2019). Youle and colleagues had been the first to identify TOMM7 as a regulator of Parkin translocation upstream of mitophagy in a RNAi and microscopy screen performed in HeLa cells stably expressing GFP-Parkin (Hasson et al., 2013). They then showed that upon depolarisation, TOMM7 tethers PINK1 to the OMM to promote its stabilisation and initiates mitophagy (Hasson et al., 2013; Sekine et al., 2019).

Loss of TOMM7 in the USP30 KO cells would then be predicted to lead to reduced PINK1 stabilisation and reduced mitophagy, which is opposite to my findings. I also did not observe a decrease in PINK1 stabilisation in any of my previous western blot experiments.

Our analysis only relies on three TOMM7 peptides, which is not surprising as TOMM7 is a small protein (6kDa). We could not further confirm this observation as we did not detect it neither in our second set of proteomic analysis (4h AO) nor by western blot analysis.

5.5.5 Pathways upregulated by USP30 deletion or inhibition

5.5.5.1 Cell cycle

In basal conditions, USP30 inhibition led to the upregulation of several cell cycle components: cyclin-dependent kinases (CDK1), positive regulators of cyclin-dependent kinases (CKS1B, CKS2), a mitosis-specific kinase of histone

3 (GSG2) and to the downregulation of a cyclin inhibitor CDKN1C (only with FT385). However, these cell cycle components did not respond to USP30 KO in a consistent manner.

These observations were of interest as Parkin is a master regulator of the cell cycle. Parkin has been reported to negatively regulate the stability of G1/S phase cyclins D and E, and this E3 ligase is also a target of the p53 tumor suppressor, which is involved in stress responses such as cell cycle arrest or apoptosis (Staropoli et al., 2003; Gong et al., 2014; Zhang et al., 2011). *Pink1* and *Parkin* are both tumour suppressors that were shown to genetically interact with the cell cycle regulatory proteins *Cdk1*, *Cdk2* and *Cdc25* in *Drosophila* and to inhibit mitosis during mitophagy (Sarraf et al., 2019). Pickrell's group propose that TBK1 mediates this mitotic arrest (Sarraf et al., 2019). Upon depolarisation, PINK1 and Parkin recruit the centrosomal kinase TBK1 to damaged mitochondria in order to promote the tethering of autophagy receptors to the autophagosome (Heo et al., 2015; Lazarou et al., 2015; Moore and Holzbaur, 2016; Richter et al., 2016). While at mitochondria, TBK1 is restricted from its function at centrosomes leading to a cell cycle arrest at the G2/M phase (Pillai et al., 2015; Sarraf et al., 2019). A mass spectrometry experiment performed in HeLa cells revealed that TBK1 was ubiquitylated by Parkin at K60 during mitochondrial depolarisation (Rose et al., 2016). In SH-SY5Y cells, I did not measure any further ubiquitylation of TBK1 in the absence or inhibition of USP30, however I did not detect the peptide containing the K60 residue.

As the upregulation of cell cycle proteins was mainly reproducible in FT385 treated cells, I concluded that it was most likely an off-target response.

5.5.5.2 Neuronal potential

Our proteomic analyses suggest that USP30 could be involved in regulating the neuronal potential of SH-SY5Y cells. I observed both the significant upregulation and downregulation of neuronal components, synapse constituents, elements of synaptic vesicles and proteins regulating neuronal migration, differentiation or survival. Remarkably, neuropilin-1 (NRP1, upregulated) involved in neuronal migration, the neurotransmitter transporter SLC18A1 (upregulated) and neuropeptide-Y (NPY, downregulated) were also

hits in two repeat proteome experiments performed by Emma Rusilowicz-Jones in AO treated (4h) -KOD and KO11 cells (Rusilowicz-Jones et al., 2020). Unfortunately, these repeat experiments had a smaller peptide coverage (~5,500 peptides each against 7,372 peptides) and did not detect the other neuronal peptides.

The protein abundance of the slit guidance ligand 1 (SLIT1) was significantly reduced in both KOD and KO11 cells and one of SLIT1's receptor, ROBO2, was conversely significantly more abundant in KO11 and FT385 treated cells. SLIT proteins are known to bind ROBO receptors and regulate various processes from axon repulsion during brain development to angiogenesis (review: (Blockus and Chédotal, 2016)). In particular, SLIT1 and SLIT2 were reported to act as chemorepellent and specifically bind to ROBO1/2 ligands during as axon guidance (reviews: (Bisiak and McCarthy, 2019; Tong et al., 2019; Blockus and Chédotal, 2016)). SH-SY5Y cells are derived from neuroblastoma cells and have typically two morphologies: neuroblast-like and epithelial-like. Neuroblast-type SH-SY5Y have maintained neuronal functions such as tyrosine hydroxylase and dopamine-β-hydroxylase activity (Kovalevich and Langford, 2013).

As described earlier, SH-SY5Y cells can also be differentiated into neuron-like cells. Differentiated SH-SY5Y cells typically express mature neuronal markers (synaptophysin (SYP), RBFOX3, DLG1, ENO2), differentiation promoting genes (NEUROD1, NEUROD6), TH, dopamine transporter (SLC6A3), dopamine receptors (DRD2, DRD3) and vesicular monoamine transporters (VMATs: SLC18A1 and SLC18A2) (Cheung et al., 2009; Constantinescu et al., 2007; Kovalevich and Langford, 2013; Lopes et al., 2010). In my proteome analyses, SLC18A1 was upregulated across all conditions, SYP was upregulated in two KO11 samples (KO11 DMSO and KO11 4h AO), ENO2 was upregulated in only one KO11 sample (24h AO), DLG1 was unchanged and none of the other markers were detected.

Visually, SH-SY5Y cells treated with FT385 for 24h or USP30 KO did not present obvious neuronal phenotypical characteristics (elongation, neurite protrusion).

From these proteomic data, it appears that USP30 deletion and inhibition elevates this neuronal potential, indicating that USP30 might play a negative regulatory role in neuronal development or differentiation.

5.5.6 Characterising USP30's favoured deubiquitylation sites

5.5.6.1 Peroxisomal proteins

We have shown that USP30 localises at peroxisomes and decelerates basal pexophagy in mammalian cells (Marcassa et al., 2018). This is in agreement with studies from the Kim lab, which describe, using immunoprecipitation assays, that USP30 opposes starvation induced pexophagy by opposing PEX2-mediated ubiquitylation of PEX5 and PMP70 in HEK293 cells overexpressing HA-ubiquitin; whilst we had previously failed to see any clear changes in our RPE1 KO cells (Marcassa et al., 2018; Riccio et al., 2019; Sargent et al., 2016). By mass spectrometry analysis, I found that PMP70 (or ABCD3) is ubiquitylated at K260 upon inhibition or deletion of USP30 in SH-SY5Y cells but failed to pick up any changes in PEX5 ubiquitylation.

Kim's group have further demonstrated that following amino acid starvation, the peroxisome E3 ligase PEX2 ubiquitylates PEX5 and PMP70 to recruit the adaptor protein NBR1 for the engulfment of peroxisomes into autophagosomal membranes (Riccio et al., 2019; Sargent et al., 2016). Contrasting with our observation in SH-SY5Y cells, Kim and colleagues measured a global reduction in PEX14 expression and a decrease of ABCD3 positive peroxisomes when knocking down USP30 in HeLa cells (Riccio et al., 2019). In our proteomic analysis, PEX14 and ABCD3 protein levels remained stable upon USP30 inhibition or depletion. Overall, we did not measure any global shift in peroxisomal proteins number. It is important to note that I did not use the SKL-Keima construct to directly assess whether USP30 deletion increases pexophagy in SH-SY5Y cells.

5.5.6.2 Common substrates with Parkin

When performing ubiquitylomic analysis on mitochondria enriched fractions of depolarised USP30 KO SH-SY5Y cells, I found that USP30 deubiquitylated many residues on OMM proteins. Most of these proteins were also substrates of Parkin such as GDAP1 or members of the TOM and VDAC complexes

(Rusilowicz-Jones et al., 2020). This was in agreement with proteomic studies performed in cells overexpressing Parkin which were either co-expressing USP30 or depleting it (Bingol et al., 2014; Cunningham et al., 2015).

However, when specifically assessing the residues modified by USP30 and Parkin respectively, I noticed that these enzyme's ubiquitylating and deubiquitylating activities do not fully overlap. About 1/3 of USP30 target lysine residues in top hit proteins (VDACs, TOMMs, GDAP1, SYNJ2BP, PTRH2 and ABCD3) have not been reported to be ubiquitylated by Parkin (Sarraf et al., 2013; Rose et al., 2016; Ordureau et al., 2018, 2020). Congruently, many Parkin ubiquitylation sites were unaffected by USP30 deletion or inhibition: I measured thirteen TOMM70 ubiquitylated residues, which are Parkin substrates, that did not change with the loss of USP30.

While we were writing the manuscript for our paper, the Harper lab published a series of mass spectrometry experiments including a ubiquitylome analysis performed in mitochondrial fractions of USP30 KO iNeurons. They concluded that USP30 deubiquitylates a pool of Parkin substrates but that the majority of Parkin ubiquitylation sites are unaffected in USP30$^{-/-}$ iNeurons. Their new conclusion is in agreement with our own hypothesis wherein we propose that USP30 sets the threshold for Parkin activation by suppressing the initial ubiquitin-phosphorylation burst by PINK1 rather than directly opposing Parkin ubiquitylation (Ordureau et al., 2020).

5.5.6.3 Ribosome-associated Quality Control

In the total ubiquitylome dataset but not in the mito-ubiquitylome, the ribosomal protein RPS20 was a strong hit: its K4 and K8 residues were five times more ubiquitylated with USP30 deletion and inhibition. Interestingly, those sites have been reported to be ubiquitylated by ZNF598 in the context of Ribosome-associated Quality Control (RQC) (Sundaramoorthy et al., 2017), (see short review: (Ikeuchi et al., 2019)). The E3 ubiquitin ligase ZNF598 and the 40S ribosomal protein RACK1 mediated ubiquitylation of 40S ribosome proteins, such as RPS20, to alleviate ribosome stalling through the dissociation and recycling of the ribosomal subunits. USP30 could therefore oppose ZNF598 and fine tunes RQC. The K4- and K8-ubiquitylation of RPS20 was unchanged in the mito-ubiquitylome. This could either suggest that USP30 loss of function

induces stalling of primarily cytosolic or ER associated ribosomes or that prolonged mitochondria depolarisation indirectly promotes ribosomal stalling revealing the involvement of USP30 in this process.

Other DUBs have recently been linked to RQC. Eric Bennett's team performed a DUB screen using an RQC-fluorescence probe (GFP-poly(A)-CherryFP) to search for DUBs limiting RQC activation. They found that OTUD3 and USP21 efficiently opposed ZNF598 ubiquitylation of RPS10 and RPS20 (Garshott et al., 2020). Using a specific USP9X inhibitor, my colleague Anne Clancy found that USP9X instead positively regulates RQC by stabilising the E3 ligase ZNF598 (Clancy et al., 2020).

Another link between USP30 and RQC was found in the ubiquitylome analysis performed in mitochondria enriched samples following 4h depolarisation. The mitochondrial peptidyl-tRNA hydrolase PTRH2 was highly ubiquitylated in the absence of USP30. This was confirmed in two replicate experiments performed by Emma where PTRH2's K48 residues was ubiquitylated four times more with USP30 deletion (Rusilowicz-Jones et al., 2020). *In vitro* studies report that PTRH2 has a hydrolase activity suggesting it functions in tRNA recycling and translation regulation (Pereda et al., 2004). Cytosolic PTRH1 was shown to release nascent chains from stalled ribosomes during RQC. *In vitro*, mitochondrial PTRH2 has also the ability to release those nascent chains from 60S ribosome-nascent chain complex and 80S stalled ribosomes (Kuroha et al., 2018).

As USP30 is a mitochondrial anchored protein it potentially could regulate mRNA translation and protein synthesis at mitochondria, and more specifically, at the TOM complex (Nakamura and Hirose, 2008; Marcassa et al., 2018). Indeed, western blotting data points towards TOMM20 as one of the key substrates of USP30. On top of this, our lab has previously shown that USP30 associates with both TOMM20 and TOMM22 independently of its catalytic activity (Liang et al., 2015). The mass spectrometry analysis now has added additional TOM components to the list of USP30 substrates, which I have not probed for before (TOMM5, TOMM40 and TOMM70). Both TOMM20 and TOMM22 serve as cytosolic receptors in the presequence import pathway; they bind to the precursor proteins via hydrophobic interactions and promote their translocation into the TOMM40 barrel (Araiso et al., 2019; Tucker and

Park, 2019). Mitochondrial protein synthesis is most likely occurring in the vicinity of the TOM complex and USP30. Consolidating this hypothesis, a cryo-EM study revealed that the TOM complex directly interacts with ribosomes (Gold et al., 2017).

To further delve into USP30 function and its application in *in vivo* models I will characterise two novel *Drosophila* models in Chapter VI: the mt-Keima and the *Usp30* knockout fly models.

Chapter 6: The mt-keima *Drosophila*: an innovative tool to study mitophagy in vivo

6.1 Introduction

There is considerable interest in understanding the process of mitophagy in vivo. Thanks to mitophagy probes, such as the mt-QC or mito-Keima reporters, it is now possible to study mitophagy not only in live cells but also in whole organisms. Both the Finkel and Ganley labs have engineered mouse models of mitophagy, the mt-Keima and the mito-QC mice respectively (Sun et al., 2015; McWilliams et al., 2016). Here I present the mt-Keima fly, a novel model for the study of mitophagy. In this Chapter I will detail how this fly model has been generated initially by Aitor Martinez, then follow with its characterisation and finally, I will reveal a new model we have produced: the *Usp30* knockout fly, which when crossed with the mt-Keima fly can provide indications on the function of *Usp30* within the brain.

6.2 Generation of mt-Keima *Drosophila* models

6.2.1 The mt-Keima fluorophore

As explained in Chapter III, Keima is a pH-dependent dual-excitation fluorophore: its excitation peak shifts from 440nm to 586nm with increasing acidity (**Figure 6.1**), (Katayama et al., 2011). It was engineered by the Miyawaki lab, first as a homotrimeric complex (tKeima) then mutated into dimeric (dKeima) or monomeric (mKeima) forms (Kogure et al., 2006). These 3 variants have the same excitation peaks and but have slightly different emission spectra: tKeima and dKeima peak at 616 whereas mKeima peaks at 620nm (Kogure et al., 2006). dKeima has the particularity of being 2-fold brighter than mKeima and tKeima; mKeima has the advantage of responding more strongly to pH than dKeima: at pH4 mKeima's 586/440 ratio is 2-fold higher than dKeima's (Katayama et al., 2011; Kogure et al., 2006). Thus, Miyawaki's group made use of mKeima to produce a mitophagy probe: they fused mKeima with a tandem COXVIII-mitochondrial targeting sequence (MTS), which targets it to the mitochondrial matrix (Katayama et al., 2011).

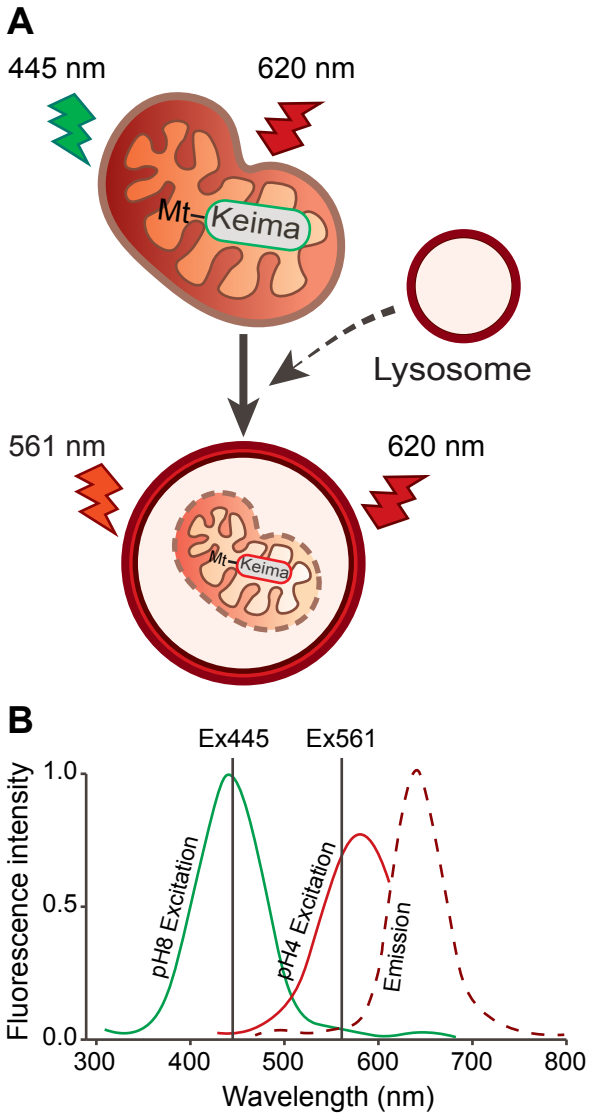

Figure 6.1: Schematic representation of the mt-Keima mitophagy reporter.

A) Keima is a pH-ratiometric fluorophore and is tagged onto the mitochondrial matrix targeting sequence of COX VIII. When expressed in cells, the mt-Keima probe is targeted to the mitochondrial matrix and has a dual excitation that is pH dependent. At pH4, mt-Keima is preferentially excited at 561 nm whereas at neutral pH it is more excitable at 445 nm. This enables an easy discrimination between healthy mitochondria and mitolysosomes. **B)** Graph representing mt-Keima's excitation and emission spectra at pH8 (mitochondrial pH, in green) and pH4 (lysosomal pH, in red). Dashed line represents emission wavelength. At pH8 mt-Keima excitation's peaks at 440nm; at pH4 it peaks at 586nm. Mt-Keima's emission spectra is constant and peaks at 620nm. Imaging setup: Mt-Keima is sequentially imaged using a 3i spinning disk confocal microscope (Ex445/Em620 then Ex561/Em620). The excitation settings are annotated on the graph. This graph is adapted from Sun et al., 2017 (Figure 1).

Interestingly, mt-mKeima (hereafter referred to as mt-Keima) is acid stable which makes it resistant to lysosomal degradation. The probe therefore permits to follow the targeting of mitochondria to lysosomal compartments.

Similarly, Aitor Martinez-Zarate, a former post-doctoral researcher in my host lab, generated a Keima reporter targeted to peroxisomes in order to monitor pexophagy. He flanked mKeima with SKL, a peroxisomal targeting sequence. Together with Aitor, I employed U2OS cells stably expressing Keima-SKL to optimise imaging settings and assess the response of Keima to cellular pH (**Figure 6.2**). One advantage of using the SKL-Keima over the mt-Keima probe for this assay is that peroxisomes maintain the same dimensions whether they undergo stress or not, unlike mitochondria which can switch from interconnected and tubular networks to a fragmented state.

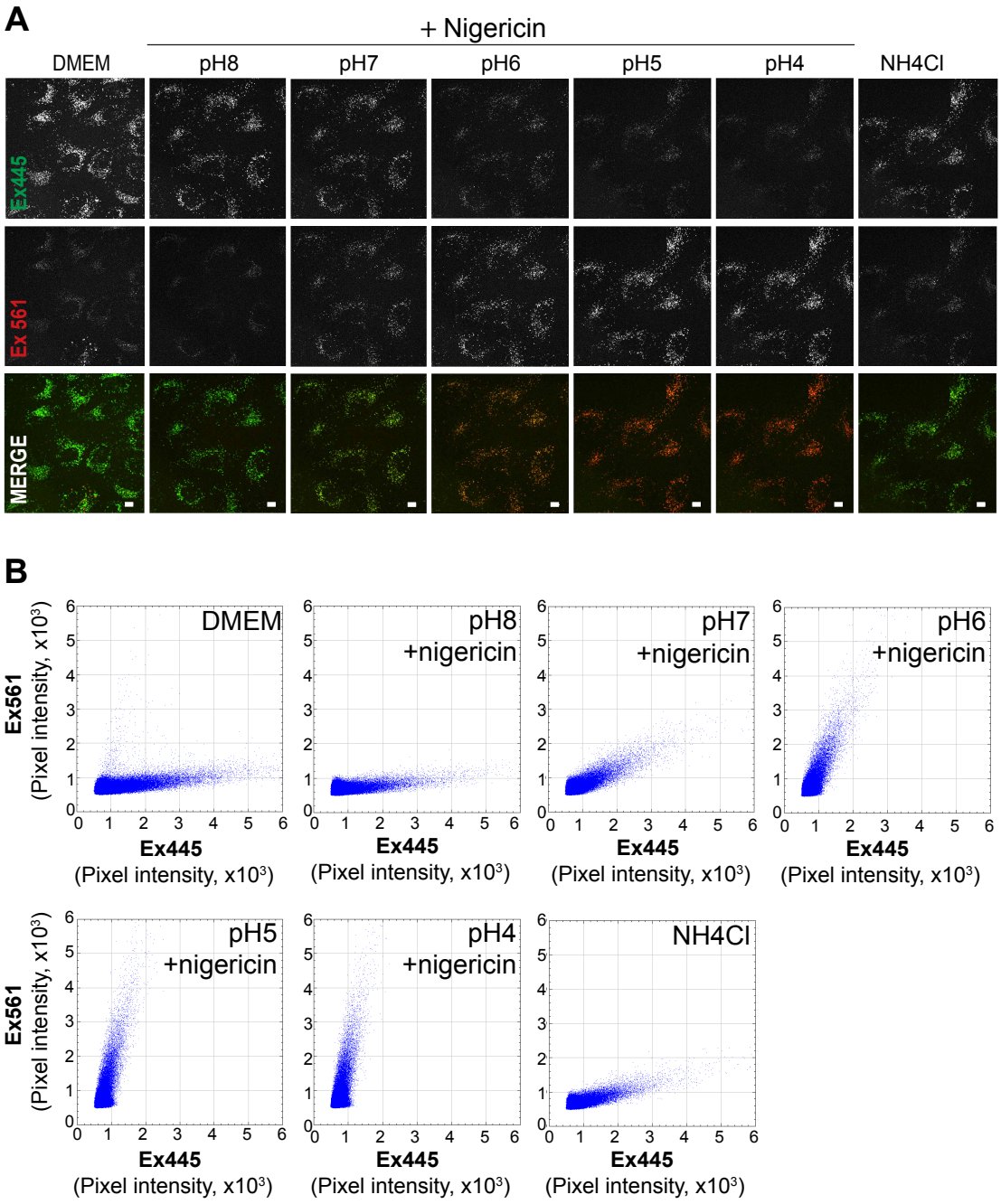

Figure 6.2: pH titration of the Keima fluorophore in U2OS-SKL-Keima cells.

A) U2OS-SKL-Keima cells were grown in DMEM and sequentially imaged on a 3i spinning disk confocal microscope equipped with an EMCCD camera and a 40X objective lens (Em445/Ex610 then Em561/Em610). The media were then exchanged for solutions (143mM KCL, 1.17mM MgCl2, 1.3mM CaCl2, 5mM Glucose) first at pH8, 7, 6, 5 then 4 and mixed with 10µM nigericin, a K+/H+ ionophore that equalises the extra- and intra-cellular pH. Finally, the cells were incubated with 50mM NH4Cl. Citric acid (20mM) was used for pH solutions ranging from pH 4-6 and HEPES (10mM) for pH 7-8 The cells were equilibrated for 5min and imaged in between each buffer exchange. Scale bar: 10µm. **B)** Plot representing the pixel intensity value in Ex561 images over Ex445 images. The plots were generated on FIJI using the "pixelAnalysis" plugin coded by Dave Mason. Representative plots from a single experiment.

We made use of nigericin, a K^+/H^+ ionophore to equilibrate the intracellular pH with the extracellular pH and exchanged the medium with buffers ranging from pH4-8. With each buffer, we sequentially imaged the cells using a spinning disk confocal microscope equipped with 445nm and 561nm lasers (Ex445/Em600 then Ex561/Em600) (**Figure 6.2A**). We false coloured the images: Ex445 in green and Ex561 in red. In the absence of nigericin and when the cells were still in DMEM, we only observed a few red-puncta which reflected basal pexophagy (**Figure 6.2A-B**). Most peroxisomes were preferentially exited at 445nm (green in our false coloured scheme), thus experienced the neutral pH of the cytosolic environment. Upon pH titration (pH8 to pH4), we observed a clear shift in Keima's excitation peak, from 445 to 561nm, correlating with media acidification.

As the the Miyawaki lab had previously described with mKeima purified recombinant proteins (Ex440 and 586), we found that the 445/561 ratio approached 1 at pH6 in U2OS cells overexpressing Keima-SKL (Katayama et al., 2011). When treating the U2OS-SKL with 50mM NH_4Cl, which neutralises lysosomes, we lost all "red puncta" (peroxisomes in acidic lysosomes). We thus confirmed that our imaging set up (Ex445/Em600 then Ex561/Em600) is suitable for ratiometric Keima imaging.

6.2.2 Characterisation of UAS-mt-Keima strains

Aitor Martinez-Zarate created a mt-Keima *Drosophila* fly model. He made use of the UAS-GAL4 system to actively direct mt-Keima's expression in chosen tissues. To do so, he inserted the mt-Keima sequence from the mammalian plasmid mt-mKeima (h)-pIND(SP1), kindly donated by Atsushi Miyawaki, into a *Drosophila* pUAST plasmid (Katayama et al., 2011). Sequencing of the thus created mt-Keima-pUAST plasmid revealed it was missing one MTS. A tandem MTS was reported to increase the import efficiency of fusion proteins to mitochondria (Galanis et al., 1991). However, using the online prediction tool MITOPROT and through preliminary transfection experiments, Aitor Martinez-Zarate assessed that a single COX VIII presequence was sufficient to target Keima to mitochondria.

The mt-Keima-pUAST plasmid was then injected in wildtype (*w1118*) *Drosophila* embryo by Bestgene Inc (California, USA). This pUAST plasmid

integrated randomly into the fly genome via its P-element, which encodes for P-transposase (Brand and Perrimon, 1993). Multiple strains were screened, and the insertions sites were analysed by Aitor Martinez-Zarate and his colleague Juanma Ramirez (UPV-EHU, Spain). They selected four UAS-mt-Keima strains: two of which carried the mt-Keima reporter on the 2nd (M3 and M7) and two on the 3rd (M2 and M4) chromosome.

I then assessed by western blot analysis the level of Keima expression of those four UAS-mt-Keima strains when crossed with either ubiquitous (*tub*-GAL4) or a neuronal (*elav*-GAL4) GAL4 driver strains (**Figure 6.3A-B**). *UAS-mt-Keima M3* and *M7* crossed with *elav*-GAL4 expressed over 2-fold more Keima than *UAS-mt-Keima M2* and *M4*. With *tub*-GAL4, all *UAS-mt-Keima* crosses expressed mt-Keima in a similar fashion.

Keima was reported to be resistant to lysosomal degradation (Katayama et al., 2011). We thus wondered if mt-Keima would accumulate over time in our *Drosophila* model. We measured the level of mt-Keima expression in old (20-25 days post hatching) versus young (0-5 days post hatching) flies and compared those flies to mito-GFP expressing ones (**Figure 6.3C**). Similar to mito-GFP, mt-Keima did not accumulate overtime; indicating that mt-Keima ultimately gets processed.

I then observed mt-Keima expression in embryonic neuronal cultures by confocal microscopy (**Figure 6.4A-C**). With a 445nm excitation, mt-Keima formed a tubular network which colocalised with the mitochondrial dye Mitotracker deep red (Ex640/Em665) (**Figure 6.4B**). Complementary to our work, our collaborators in Alex Whitworth's group reported that mt-Keima co-localised with the mitochondrial protein ATP5A in larval epidermis cells (Lee et al., 2018). With a 561nm excitation, mt-Keima fluoresced brightly at punctate structures that colocalised with the lysosomal dye Lysotraker blue (Ex405/Em422). This confirmed that despite only having one MTS, mt-Keima was targeted to *Drosophila* mitochondria and underwent a shift in its excitation peak from 445 to 561nm once in lysosomal compartments.

Using the mt-Keima mouse, which was also engineered with the mt-mKeima (h)-pIND(SP1) plasmid, the Finkel lab demonstrated that mt-Keima-mitolysosome formation is dependent on core components of the autophagy

machinery: ATG5 and ATG7, confirming that mt-Keima reports on mitophagy processes *in vivo* (Sun et al., 2015).

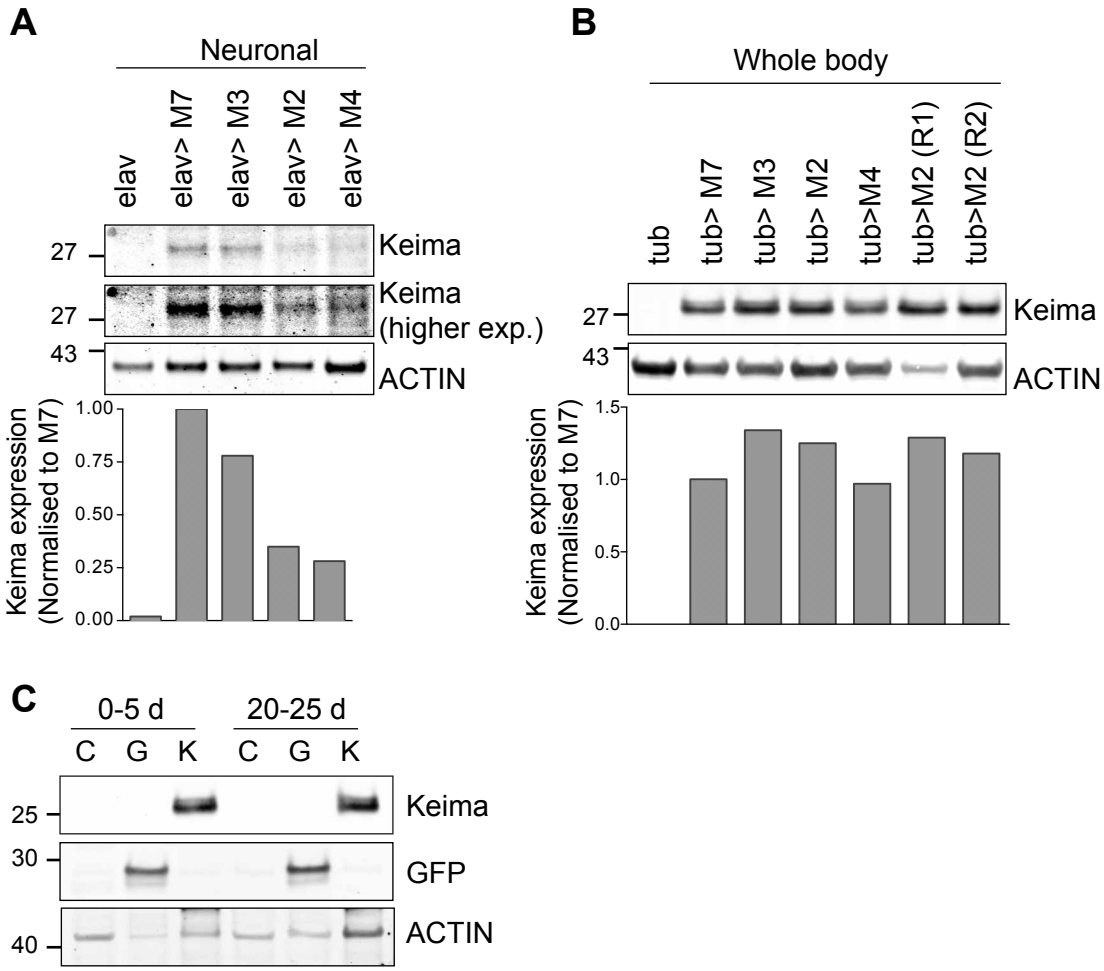

Figure 6.3: Western blot characterisation of UAS-mt-Keima fly strains.

Four strains of *UAS-mt-Keima Drosophila* (*M7, M3, M2* and *M4*) were crossed with two GAL4 driver strains having **(A)** a pan-neuronal driver (*elav*) or **(B)** a ubiquitous driver (*tub*): *UAS-mt-Keima M7/+; elav-GAL4/+* (*elav> M7*), *UAS-mt-Keima M3/+; elav-GAL4/+* (*elav> M3*), *UAS-mt-Keima M2/elav-GAL4* (*elav> M2*), *UAS-mt-Keima M4/elav-GAL4* (*elav> M4*), *UAS-mt-Keima M7/+; tub-GAL4/+* (*tub> M7*), *UAS-mt-Keima M3/+; tub-GAL4/+* (*tub> M3*), *UAS-mt-Keima M2/tub-GAL4* (*elav> M2*), *UAS-mt-Keima M4/tub-GAL4* (*tub> M4*).

The heads **(A)** or whole bodies **(B)** of the F1 progeny were snap-frozen in liquid nitrogen 0 to 4 days post-hatching, then lysed in Laemmli buffer. The corresponding lysates were probed with anti-Keima antibody. The parental GAL4 strains were used as controls: *elav* and t*ub*. In **(B)**, the lysates were compared to *mt-Keima/tub* recombinant flies (R1 and R2) lysates: *tub-GAL4, UAS-mt-Keima M2/+*. **C)** The expression levels of mt-Keima (K: *M7; tub-GAL4, UAS-mt-Keima M2/+*) and mt-GFP (G: *tub-GAL4, UAS-mt-GFP/+*) were assessed in young (0-5 days post hatching) and old (25-30 days post hatching) flies and compared to a control stain (C: *tub-GAL4/+*). The flies were snap-frozen in liquid nitrogen and lysed in Laemmli buffer.

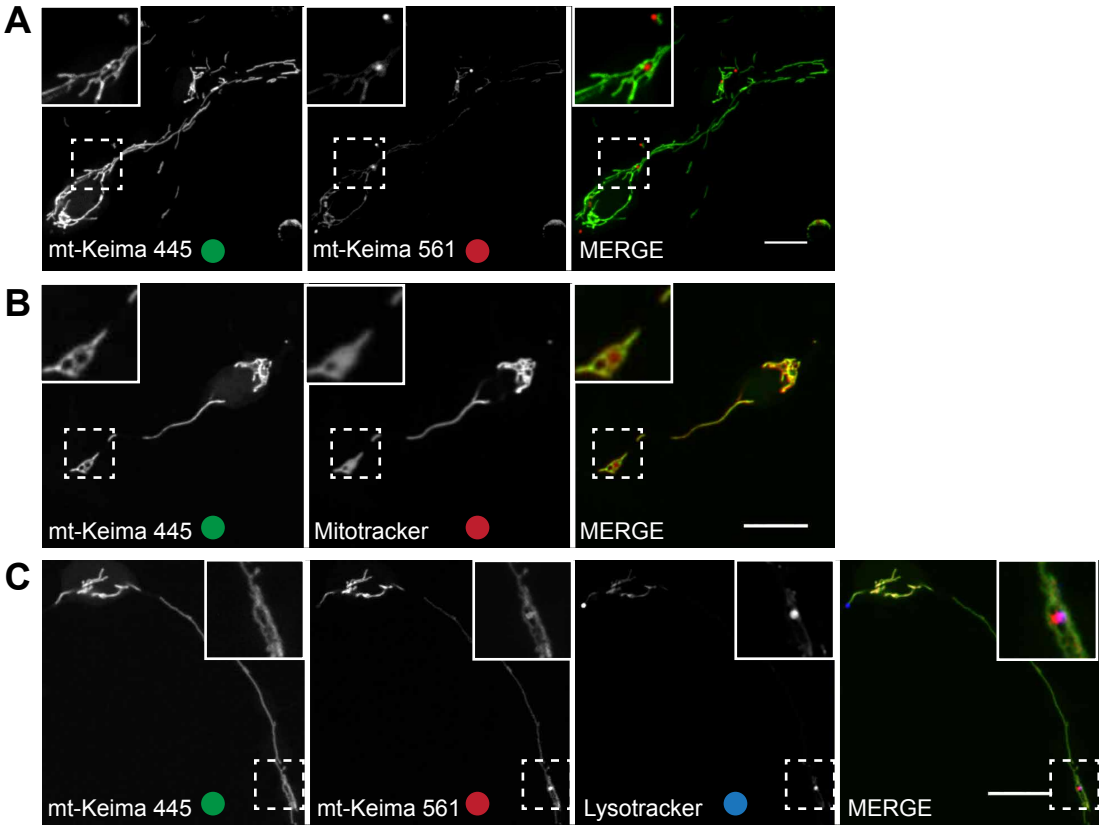

Figure 6.4: mt-Keima co-localises with mitochondria and lysosomal dyes in embryonic neuronal cultures.

Neurons dissected from stage 11 embryo (E11) of *UAS-mt-Keima M7; elav-GAL4,UAS-mtKeima M2 Drosophila* were extracted and grown on concanavalin A coated slides. They were either **(A)** untreated or incubated for 30 min with **(B)** 100nM Mitotracker Deep Red or with **(C)** 5µM Lysotracker Blue. Images were acquired sequentially using a 3i spinning disk confocal microscope with a 63x objective and an EMCCD camera. Scale bar: 10µm (higher zoom in top panels). Representative images from two experiments.

In parallel, Aitor assessed whether common mitophagy triggers could induce mitophagy in embryonic neuronal cultures expressing mt-Keima (**Appendix 5**). He treated neurons with AO (10µM each), DFP (1mM) and paraquat (100µM) for 24h. Paraquat is a mitochondrial toxin that promotes motor impairments, reduced lifespan and mitophagy induction in *Drosophila* (Bingol et al., 2014; Moskal et al., 2020). As observed in mammalian cell models, the AO treatment resulted in a complete fragmentation of the neuronal mitochondrial network. Importantly, each compound promoted mitophagy in the mt-Keima fly neurons, thus validating that the mt-Keima fly is a relevant model to study mitophagy *in vivo*.

6.3 Characterisation of basal mitophagy in live larvae and adult tissue.

Next, I analysed basal mitophagy in the mt-Keima fly. *Drosophila* larvae have the benefit of being transparent and thus enable the direct observation of tissue and organs without the need for dissection (**Figure 6.5**). I found that mitophagy was heterogenous across tissues and within organs. I observed that *Drosophila* larval body wall muscles showed low levels of mitophagy (low 561/445 ratio) whilst larval epidermal cells and anal pad cells had high numbers of mitolysosomes (**Figure 6.5B-C**).

The anal pads are two symmetrical monolayers of large cuboidal cells covered by a cuticle and surrounding the anus (Jarial, 1987). Together with the Malpighian tubules, the anal pads regulate water and ion homeostasis between the hemolymph and the surrounding medium (Andersen et al., 2017; Jarial, 1987). EM analysis of the anal pads have revealed that these cells are rich in mitochondria and lysosome-like dense bodies which would support our observations (Jarial, 1987). I found the anal pads showed a clear pattern of mitophagy: some cells were hotspot of mitophagy whilst others seemed devoid of mitolysosomes.

The gut was another organ showing a high 561/445 ratio particularly in the mid gut (**Figure 6.5B-vii,viii**) and at the anterior midgut, in structures reminiscent of the gastric caeca (small tubules, here seen behind the brain, **Figure 6.5B-iv**). Unfortunately, the gut is located at a depth in the larval tissue that makes it difficult to obtain clear images of individual intestinal cells at a high magnification (**Figure 6.5C**).

I then analysed the larval brain (**Figure 6.5B-iv,v,vi**). The larval brain is divided into three major structures comprising two brain lobes and the ventral nerve cord (VNC) (**Figure 6.5A**). In these images, only the VNC is clearly distinguishable. The neuropils, tube-like structures rich in neurites located at the centre of the VNC, appeared to undergo very low levels of mitophagy (low 561/445 ratio), (**Figure 5.5B-iv**). The 561/445 ratio seemed higher when focussing on higher planes, above the neuropiles and into the cortex, where are found the neuronal cell bodies and glial cells (**Figure 6.5B-v**).

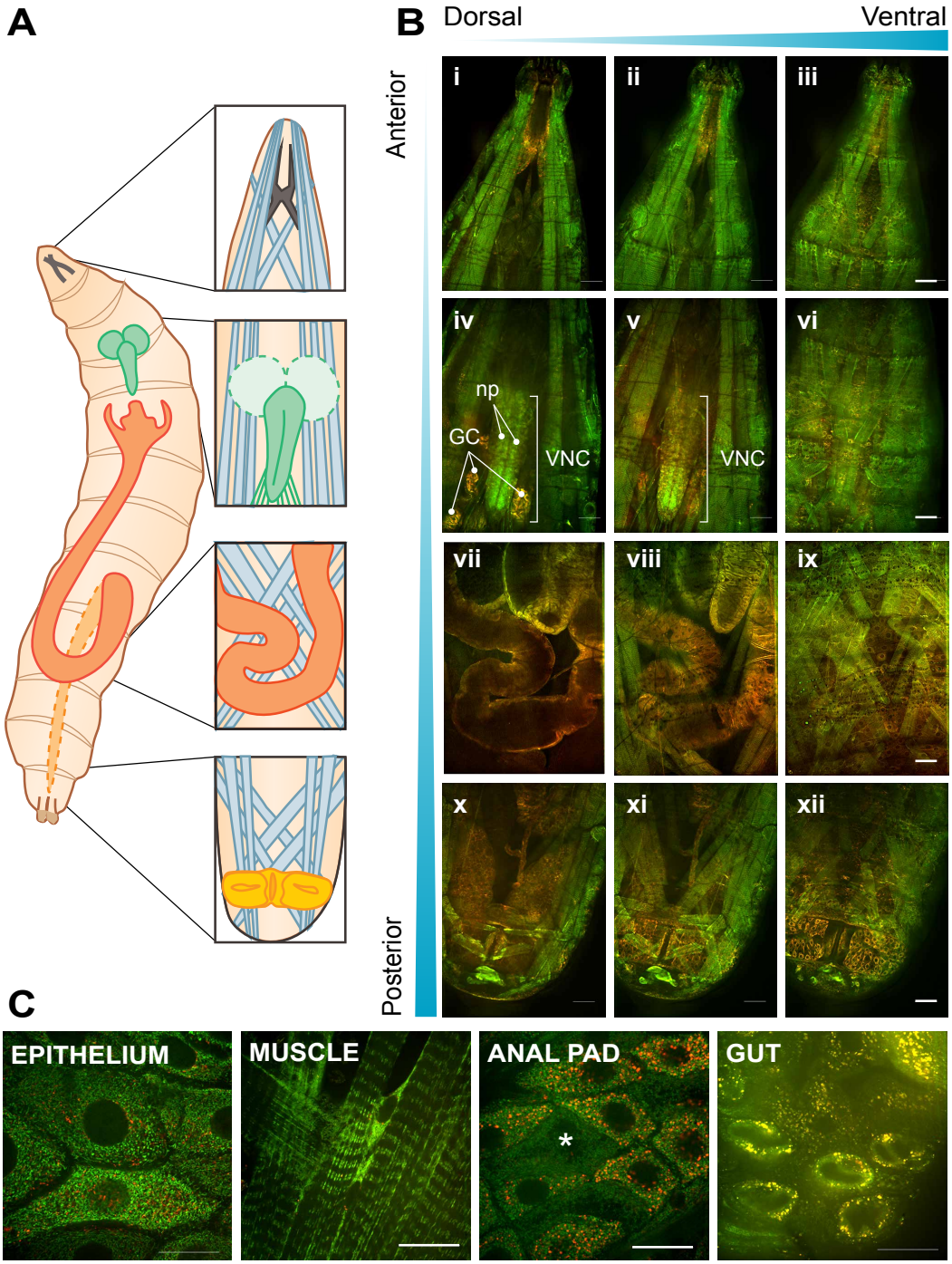

Figure 6.5: Mitophagy distribution across a mt-Keima *Drosophila* larvae.

A) Illustration depicting the structural organisation of a stage III *Drosophila melanogaster* larvae with specific organs highlighted: brain (green), guts (orange), body wall muscles (blue), anal pads (yellow). **B)** Stage III larvae expressing ubiquitously the mt-Keima probe, *UAS-mt-Keima M7; tub-GAL4, UAS-mt-Keima M2/+*, were anesthetised using chloroform and imaged sequentially on a 3i spinning disk confocal microscope. Four z-stacks were taken for each larva using a 10X objective lens and an sCMOS camera. Representative images of the four z-stacks are presented on panel B. Scale bar: 100µm. GC: Gastric caeca; VNC: Ventral nerve cord; np: Neuropils. **C)** The larvae were then imaged using the 63X objective lens. Representative image of the epithelium, muscle, anal pad and gut cells are laid out in panel C. Scale bar: 30µm. The asterisk points towards a cell showing no apparent mitophagy. Data from three experiments.

I compared mt-Keima with mito-GFP larva to assess whether the mt-Keima probe expression pattern reflects mitochondria organisation (**Figure 6.6**). Just like mt-Keima, mito-GFP is targeted to mitochondria by the presequence of COX VIII (Pilling et al., 2006). Mt-Keima's organellar and cellular organisation mirrored that of mito-GFP. Some organs such as the anal pads had a very high expression level of mito-GFP which reflects the high mitochondria density present this organ (Jarial, 1987). However, the heterogeneity in mitophagy we had observed in the anal pads of the mt-Keima larvae was not reflected in the images we obtained for this organ in the mito-GFP fly. Other tissues such as body wall muscles showed strong mito-GFP fluorescence but very little mitolysosomes, thus indicating that mitophagy was not simply a function of mitochondrial abundance in the tissue.

I then went on to characterise mitophagy in 0-5 days old adult mt-Keima flies. The adult *Drosophila* has a highly pigmented exoskeleton which prevents the direct imaging of the interior of the organism. The animals were hence anesthetised with cold, their tissues dissected and imaged live within 30 min of dissection (**Figure 6.7**). As *Drosophila* wings are transparent, they were simply plucked off the organism and then imaged by confocal microscopy (**Figure 6.7B**). Mitolysosomes accumulated at the wing veins and wing hinges. Interestingly, wings have 200-300 chemosensory and mecanosensory neurons situated at the costal, L1 and L3 veins. These neurons meet up with glial cells in the hemolymph and form nerve bundles that can easily be monitored by microscopy (Fang et al., 2013). Hence the wing is an interesting model to study neuronal or glial mitophagy. A preliminary study had employed the mito-GFP *Drosophila* model to indirectly assess mitophagy in the wing through measurements of mitochondria size and number (Cao et al., 2017). This study reported an age-dependent increase in axonal mitochondria fragmentation and suggested that mitophagy occurred rarely in axonal mitochondria. Indeed, they found that neither knocking down or mutating autophagy genes (*Atg12*, *Atg17*) or *Pink1* and *Parkin* affects axonal mitochondria (no difference in number or length) and axonal integrity. Instead, they proposed that in the wing axonal mitochondrial quality control would rather rely on fusion and fission. The UAS-mt-Keima fly could be used to confirm or refute this theory if crossed with specific neuronal GAL4 drivers.

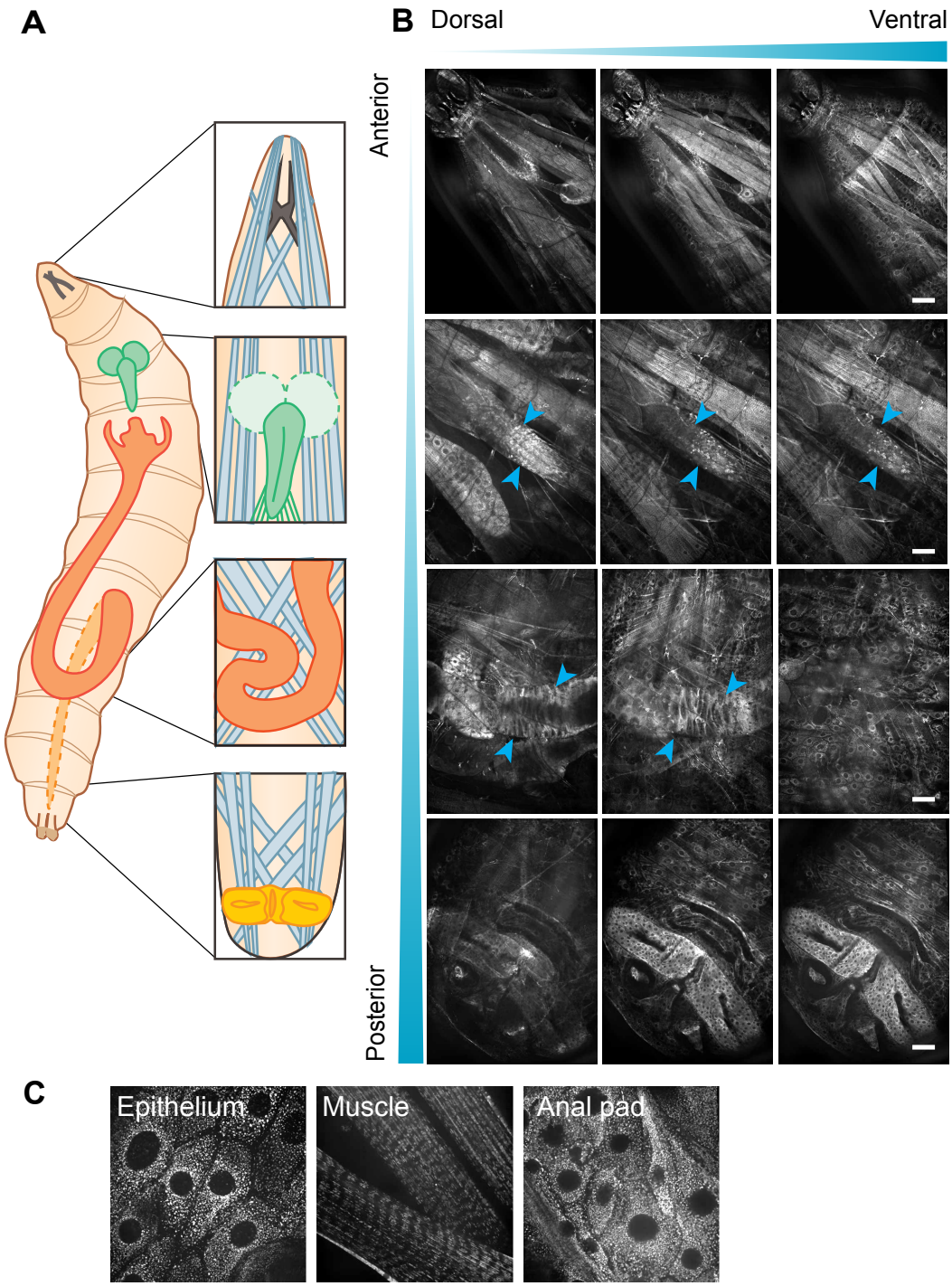

Figure 6.6: Mitochondria distribution throughout a stage III (L3) mito-GFP larvae.

A) Illustration depicting the structural organisation of a stage III *Drosophila melanogaster* larvae with specific organs highlighted: brain (green), guts (orange), body wall muscles (blue), anal pads (yellow). **B)** Stage III larvae expressing ubiquitously mito-GFP: *tub-GAL4, UAS-mito-GFP/+*, were anesthetised using chloroform and were imaged sequentially on a 3i spinning disk confocal microscope with an sCMOS camera. Four z-stacks were taken for each larva using a 10X objective lens. Representative images of the four z-stacks are presented on panel B. Scale bar: 100µm. **C)** The larvae were then imaged using the 63X objective lens. Representative image of the epithelium, muscle, anal pad and gut cells are laid out in panel C. Scale bar: 30µm. Data from two experiments.

The testis was another organ with a high mitophagy signal in *Drosophila* (**Figure 6.7C**). The high 561/445 ratio was particularly concentrated at the base of the testis where late spermatid and mature sperm are localised. Indeed, spermatogenesis is compartmentalised within the *Drosophila* testis. At the apical end (white asterisk) are found the germline stem cells that undergo asymmetric division producing goniablast and daughter stem cells. The goniablast undergo four rounds of mitosis, then towards the middle of the testis, the resulting spermatocytes undergo meiosis to form spermatids (the "onion stage" spermatids are indicated with a white arrow), which then elongate to form late spermatid and ultimately sperm cells, towards the base of the testis (orange asterisk) (Demarco et al., 2014). Whilst the complete elimination of sperm mitochondria also known as paternal mitochondria destruction (PMD) is mediated by endocytic and autophagic pathways, it occurs only after fertilisation in the zyogtic cytoplasm (Politi et al., 2014).

The high 561/445 ratio I observed at the base of the testis could however be linked to spermatid individualisation. During this process, the individualisation complex (composed of 64 investment cones rich in actin) divides the spermatids and strips off unnecessary cytoplasmic constituents: such as organelles (including excess mitochondria), membranes or mitochondrial DNA (DeLuca and O'Farrell, 2012; Fabrizio et al., 1998; Tokuyasu et al., 1972). These constituents accumulate in the spermatid syncytium (cyst) and form an enlarged structure called the cyst bulge. At the end of the individualisation process, the cyst bulges detach from the spermatids and are then called waste bags (Fabrizio et al., 1998; Tokuyasu et al., 1972), [review: (Fabian and Brill, 2012)]. It has been hypothesised that the waste bag degradation occurs through phagocytosis(Tokuyasu et al., 1972). This phenomenon could thus be detected by the mt-Keima probe.

As I had observed a strong 561/445 ratio in larval gut, I assessed whether the adult *Drosophila* gut was similarly a hotspot for mitophagy (**Figure 6.7D**). Unlike its larval counterpart, the adult *Drosophila* gut had only a moderate number of mitolysosomes.

Finally, I observed the adult brain (**Figure 6.7E**). Mitophagy appeared homogenous and low across the central brain except for the boundaries between the main brain structures. The external lobes (medulla) and the

associated intermediate segment (lobula and lobula plate) seemed to have a higher number of mitolysosomes. However, only the use of a specific GAL4 driver could give clear indications as to what compartment or subcellular cell type are undergoing mitophagy.

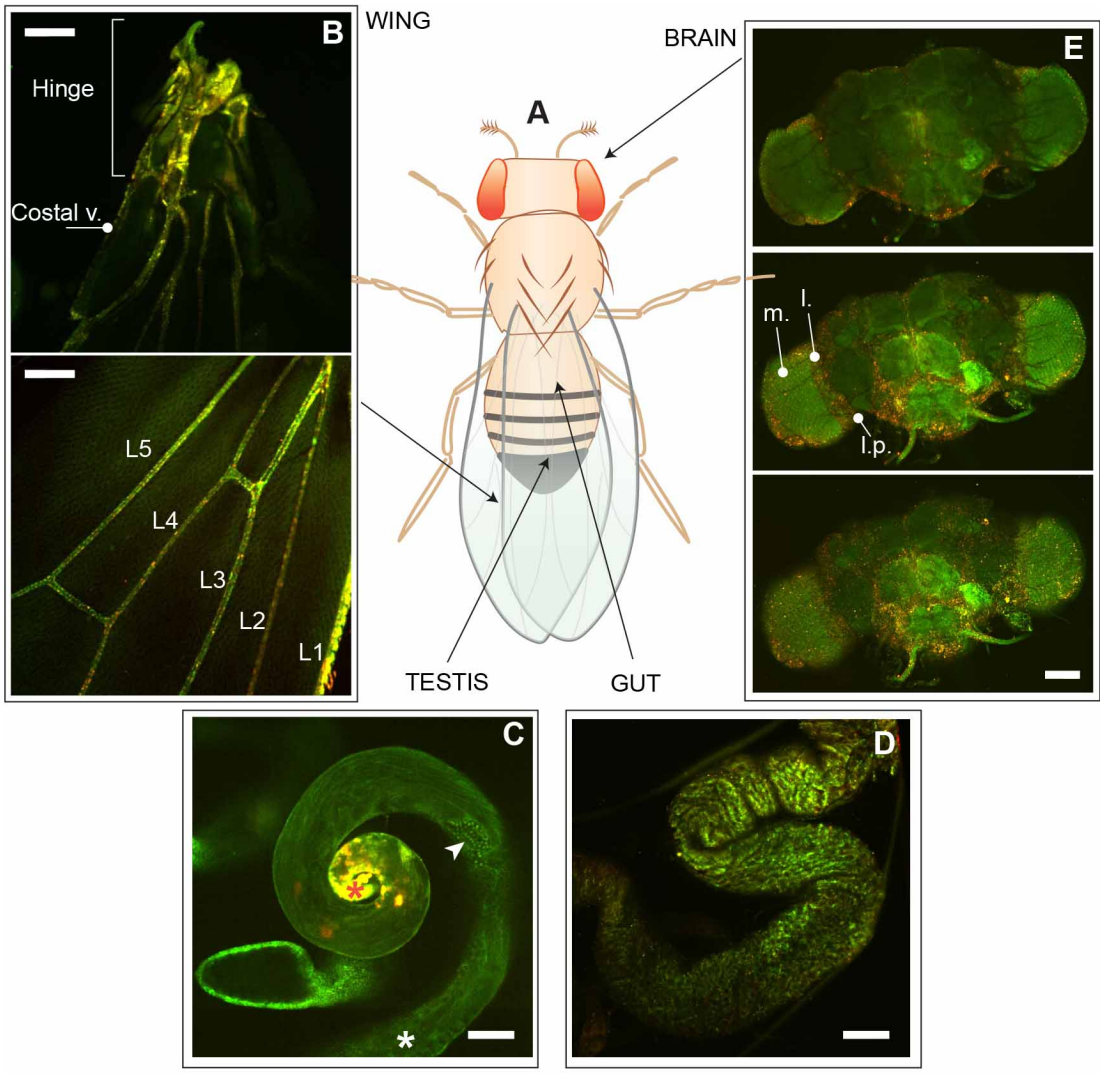

Figure 6.7: Basal mitophagy in adult mt-Keima *Drosophila*.

A) Diagram showing the anatomy of a male adult *Drosophila melanogaster*. **B-E)** Confocal images of dissected tissues from 0-5 days old mt-Keima *Drosophila* (*UAS-mt-Keima M7; tub-GAL4, UAS-mt-Keima M2/+*): **B)** base and mid-section of a wing with its costal, L1, L2, L3, L4 and L5 veins, **C)** testis, **D)** gut and **E)** brain. m.: medulla, l.: lobula, l.p.: lobula plate. In **C)** are annotated the testis apical tip (white asterisk), the "onion stage" spermatids (white arrow) and the base of the testis (orange asterisk). In **E)**, are shown 3 sections of the brain: dorsal, mid and ventral (top to bottom panel). The images were acquired sequentially using a spinning disk confocal, an sCMOS camera and a 10X objective lens. Scale bar 100µm. Data from three experiments.

I next focussed on the larval epidermal cells to assess the involvement of *Pink1* and *Parkin* in basal mitophagy. I crossed UAS siRNA strains targeting *Pink1* and *Parkin* or a wildtype fly (*w1118*) with the tubulin driven mt-Keima fly. The F1 progeny was then analysed by confocal microscopy: *UAS-mt-Keima M7/+; tub-GAL4, UAS-mt-Keima M2/+* (CTRL), *UAS-mt-Keima M7/UAS-Parkin RNAi; tub-GAL4, UAS-mt-Keima M2/+* (*Parkin* RNAi) and *UAS-mt-Keima M7/UAS- Pink1 RNAi; tub-GAL4, UAS-mt-Keima M2/+* (*Pink1* RNAi) (**Figure 6.8**). Crossing the mt-Keima fly with the UAS-RNAi lines reduced the number of mt-Keima alleles in the progeny, thus diming the signal emitted by the fluorophore whilst enhancing background signal and therefore impeding the analysis. Mitophagy was quantified following the method described by the Finkel lab: the signal intensity measured with the 561nm excitation was plotted against the emission detected using the 445nm excitation. Then the plots were divided into 4 quadrants to separate the pixels originating from mitolysosomes (b) from the rest of the pixels (a, c and d). The mitophagy index represents the "mitolysosome pixel" (b) over the sum of all pixels (**Figure 6.8B**) (Sun et al., 2015). From this experiment it appeared that neither *Pink1* nor *Parkin* knockdown lines diminished basal mitophagy and, if anything, rather increased the mitophagy index (**Figure 6.8C**). However, when looking at mitophagy per individual, it appeared that mitophagy rates also varied widely between individuals of the same genotype. This interindividual variation was also observed in a preliminary experiment in which we submitted mt-Keima larvae to normal versus hypoxic conditions (**Figure 6.9**).

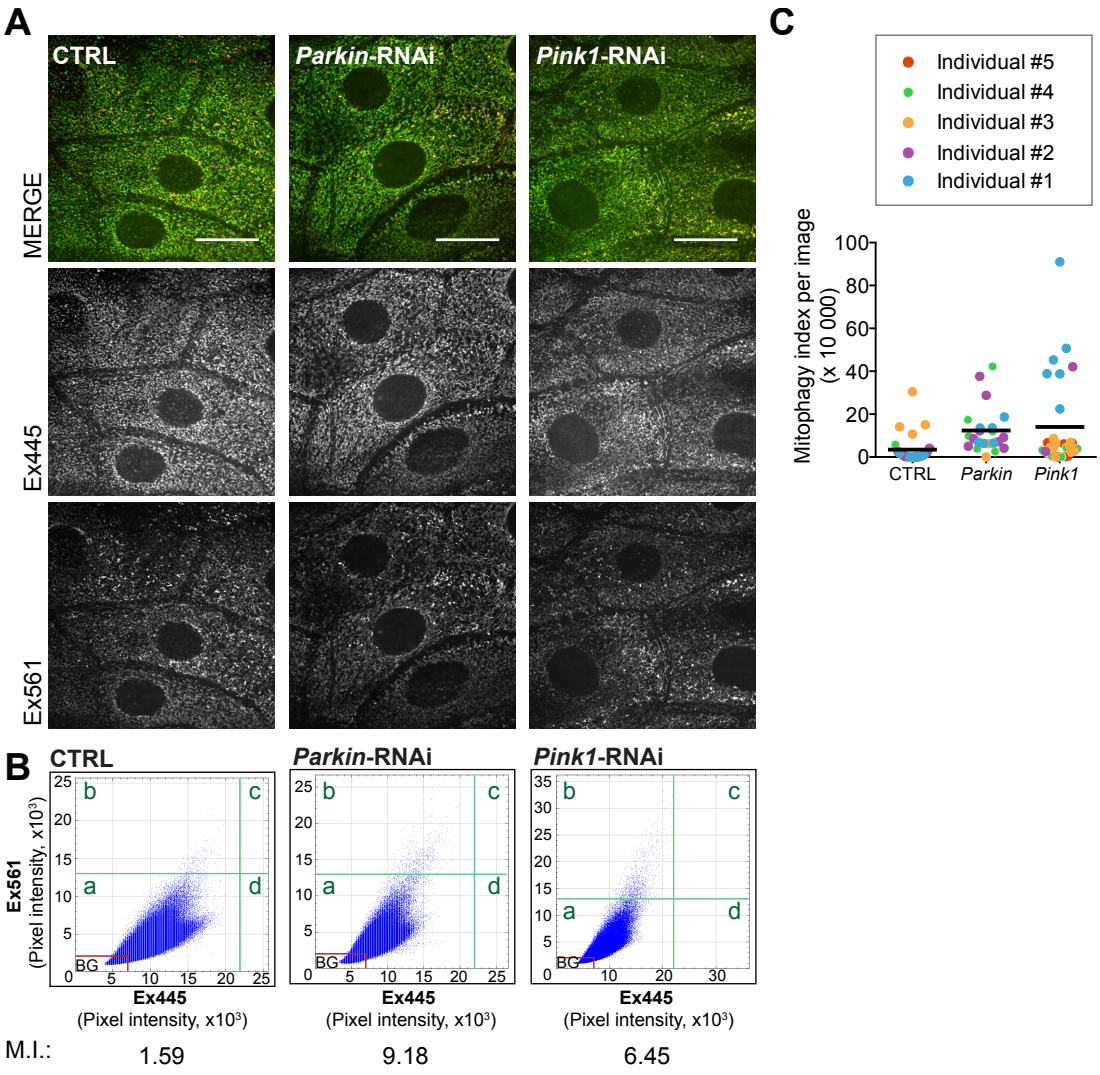

Figure 6.8: Knocking down *Pink1* and *Parkin* in mt-Keima flies.

Mt-Keima expressing flies and wildtype, UAS-*Pink1* or UAS-*Parkin* RNAi models were crossed and their F1 progeny analysed by confocal microscopy (3i spinning disk confocal microscope and sCMOS camera): *UAS-mt-Keima M7/+; tub-GAL4, UAS-mt-Keima M2/+* (CTRL), *UAS-mt-Keima M7/UAS-Parkin RNAi; tub-GAL4, UAS-mt-Keima M2/+* (*Parkin* RNAi), *UAS-mt-Keima M7/UAS- Pink1 RNAi; tub-GAL4, UAS-mt-Keima M2/+* (*Pink1* RNAi). **A)** Representative images of the epithelium of L3 larvae. 63X objective lens. Scale bar: 30µm. **B)** Plot representing the pixel intensity value in Ex561 images against Ex445 images. The plots were generated on FIJI using the "pixelAnalysis" plugin coded by Dave Mason. BG = area with no mitochondrial staining (background intensity). The plots are divided in 4 quadrants (green lines, limit set at 13,000- and 22,000- pixel intensity for Ex561 and Ex445 respectively), to separate: pixels originating from the mitochondria in acidic compartments "b" from the rest of the network "a", "c" and "d". The mitophagy index (M.I.) was calculated as follows: pixels b/ (pixels (a - BG) + b + c + d). **C)** Graph representing the mitophagy index per image and per individual. Data from obtained from one experiment, 6 images taken per individual, 5 individuals imaged per genotype.

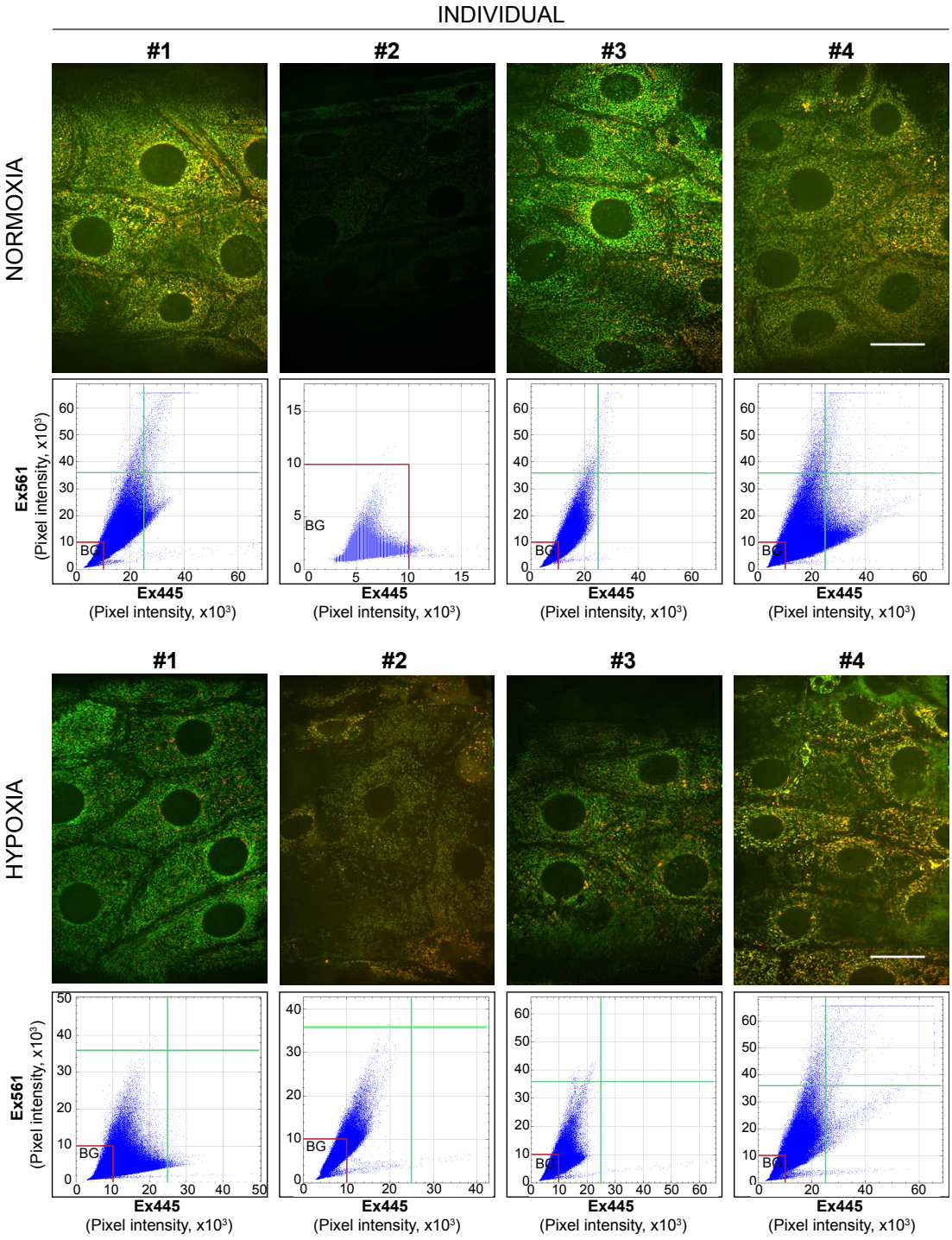

Figure 6.9: Mitophagy in mt-Keima flies in response to hypoxia.

Mt-Keima expressing stage III larvae (*UAS-mt-Keima M7; GAL4-tub, UAS-mt-Keima M2/+*) were incubated in a hypoxia (4% O2) or normoxia (21% O2) chamber for 6h then imaged sequentially on a spinning disk confocal microscope with an sCMOS camera and using a 63X objective lens. For each condition, four individuals were analysed and six images of the epidermal cells were taken per individual. Scale bar: 30µm. The mitophagy index was quantified for each image using the FIJI plugin "pixelAnalysis" coded by Dave Mason. One representative image per individual with the corresponding mitophagy index plot is shown. Data from a single experiment.

6.4 Engineering and preliminary characterisation of a USP30 knockout *Drosophila*.

To further understand the role of USP30 in vivo, I decided to engineer a *Usp30* knockout fly (**Figure 6.10**). The mutagenesis was performed by WellGenetics Inc. in wildtype flies (*w1118*) using CRISPR-Cas9 and homology-dependent repair, following the method described by Kondo and Ueda (**Figure 6.10A**),(Kondo and Ueda, 2013). They made use of a pairs of gRNAs and a donor template to delete most of *Usp30*'s (also known as *CG3016*) coding region sequence (CDS) and knock-in a selection marker (*hsp70::w*) in its place. This selection marker encodes for the orange coloured eye phenotype which facilitates genotype screening.

Except for the orange coloured eyes, the *Usp30* knockout flies did not present any particular morphological features (**Figure 6.10B**). They were the same size as their wildtype counterpart, they had normal wing posture and no visible indentations on their core and limbs. We verified that they were genuine USP30 knockout flies by RT-qPCR (**Figure 6.10C**). As most of the CDS was expected to be deleted, no mRNA encoding for *Usp30* should have been expressed. I extracted total mRNA from *Usp30* knockout flies following the protocol described by Bogart and Andrews and amplified exons of the CDS (Bogart and Andrews, 2006). No mRNA was detected in the *Usp30* knockout fly, thus validating this model.

Unlike USP30 mutations, deleting other mitophagy regulators such as *Pink1* or *Parkin* leads to strong phenotypical impairments: *Pink1* and *Parkin* null mutants have deep indentations in the thorax and downturned wings which are both caused by the degeneration of flight associated muscles (Greene et al., 2003; Clark et al., 2006; Park et al., 2006). Those features are accompanied with reduced motor functions: the null mutants are slower at climbing and unable to fly. Moreover, *Pink1* and *Parkin* null flies have a reduced lifespan and males are infertile due to spermatogenesis impairments. Although *Usp30* KO flies do not present any visible impairments we decided to assess their viability and test their motor functions (**Figure 6.10D-E**).

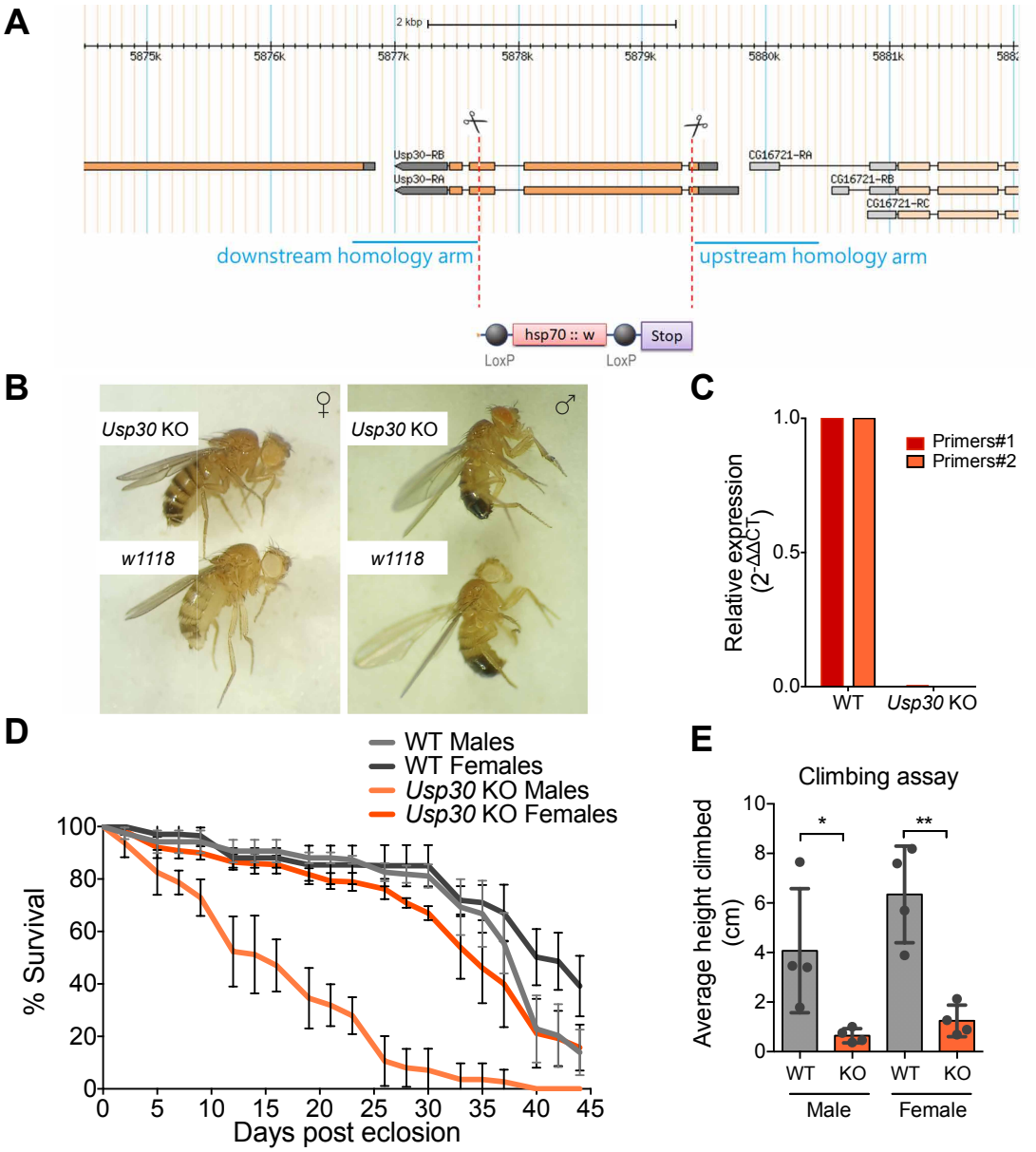

Figure 6.10: Engineering a *Usp30* knockout *Drosophila*

A) *Usp30* depletion was performed by WellGenetics Inc. in wildtype *Drosophila* (*w1118*) through CRISPR-mediated mutagenesis using two pairs of sgRNAs. Most of the coding region was deleted and replaced by an eye-marker cassette (*hsp70::w*, orange eyes), as shown on the schematic. Schematic provided by WellGenetics. **B)** Representative pictures of both male and female wildtype (*w1118*) and *Usp30* knockout flies. **C)** *Usp30* mRNA expression was assessed by RT-qPCR in both wildtype and knockout flies using two sets of primers. Relative expression = $2^{-\Delta\Delta ct}$ normalised to *αtub84b*. **D)** Graph representing the percentage of survival (ie: percentage of living flies per age category) per genotype and sex. Three experiments, 50 flies per sex and genotype each (total 150 flies). Error bars represent SD. **E)** Climbing assay: the graph represents the average height, in centimetres, climbed within 20s by 12-day-old flies classified per genotype and sex. n=4, error bars represent SD. A total of 200 flies were analysed per condition. Test: One-way anova, Tukey's multiple comparison test. pvalue: *<0.05, **<0.1.

Usp30 KO males were particularly sensitive to the loss of *Usp30* as decreased viability was observed from 5 days post eclosion onwards (**Figure 6.10D**). Following 21 days post eclosion, only 32% of *Usp30* KO male had survived against ~85% of *Usp30* KO females and WT flies. The life expectancy of most *Usp30* KO male did not exceed 35 days (4% survival) whilst at this age the pool of female KO and WT individuals had only dropped by ~40%.
Both male and female *Usp30* KO flies however presented motor defects (**Figure 6.10E**). To quantify this, I performed climbing assays (also known as negative geotaxis assays): 12 days old flies were placed in a graduated tube, the tube was briefly taped to stimulate climbing and the flies were filmed. At 20s post stimulation, the length climbed by each fly was measured (Gargano et al., 2005). I found that, on average, wildtype males and females could climb 4cm and 6cm respectively within 20s. However, this difference was not significant. *Usp30* KO flies were significantly slower than their wildtype counterpart: within 20s, males and females only climb approximatively 0.7 and 1.2cm respectively.

As USP30 inhibits mitophagy I wondered if the reduced motor functions would correlate with abnormal mitophagy rates (**Figure 6.11**). I have previously seen that the optic lobes of the adult *Drosophila* undergo high levels of mitophagy. Moreover, my colleagues Natalia Sanchez-Soriano's and Pilar Okenve-Ramos had optimised a protocol for *Drosophila* brain dissection and imaging of mt-Keima in a specific region of the optic lobes called the medulla (**Illustrated in Figure 6.11C**). I thus crossed mt-Keima and *Usp30* KO flies to obtain the following F1 progeny: *Usp30 KO; UAS-mt-Keima M7/+; tub-GAL4, UAS-mt-Keima M2/+.*
We compared mitophagy rates in young (7-9 days old) and old male (29-33 days old) of both WT and *Usp30* KO genotypes (**Figure 6.11B and D**). This preliminary experiment suggested that the mitophagy index of young *Usp30* KO flies was ~2-fold greater than young WT flies. Interestingly, in WT flies, mitophagy appeared to increase with age in the medulla. We recorded a 1.3-fold increase of the mitophagy index between these two categories. However, old *Usp30* KO flies had the lowest mitophagy rate of all categories: on average

the mitophagy index was of 6.2x10^4 (old KO) against 22.5 x10^4 (old WT), 16.8 x10^4 (young WT) and 31.3 x10^4 (young KO).

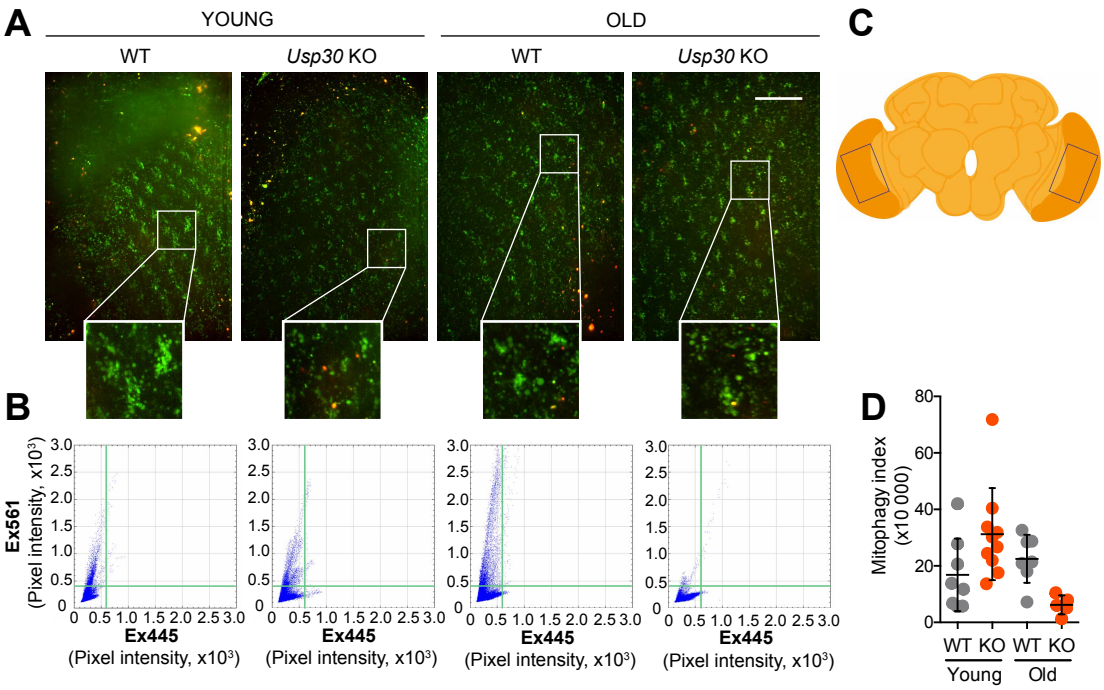

Figure 6.11: *Usp30* depletion raises mitophagy at the medulla in young flies.

A) *Usp30* knockout and *Usp30* wildtype *Drosophila* were crossed with mt-Keima reporter flies to obtain the following F1 males: *+; UAS-mt-Keima M7/+; GAL4-tub, UAS-M2/+* (WT) and *Usp30 KO; UAS-mt-Keima M7/+; GAL4-tub, UAS-M2/+* (KO). The brains of young (7-9 days old) and old (29-33 days old) WT and *Usp30* KO flies were dissected and imaged live on a spinning disk confocal using a 63X objective lens. One z-stack of images was taken per medulla. Three to five individuals were analysed per condition and both medullas were imaged when possible. A maximum projection was applied onto the z-stacks. Scale bar: 30µm. **B)** The mitophagy index was measured and plotted for each medulla using the FIJI plugin "pixelAnalysis" coded by Dave Mason. Plots shown correspond to the images in A. **C)** Schematic of the adult *Drosophila* brain. The medullas are highlighted in dark orange. The rectangles indicate the area imaged by confocal microscopy. **D)** Graph representing the mitophagy index per condition. Each dot represents one medulla. Data from one experiment.

6.5 Discussion

6.5.1 Basal mitophagy is heterogenous across organs and tissues

Using mt-Keima, I found that mitophagy was widespread in larvae and adult *Drosophila* but was also heterogenous across tissues and organs. In mt-Keima larvae for example, mitophagy was particularly low in body wall muscles and high in epidermal and anal pad cells. Using their mito-QC flies, Alex Whitworth's group confirmed that mitolysosomes were abundant in the larval epidermis (Lee et al., 2018). Following our publication, two other groups presented mt-Keima flies both derived from the mammalian mt-mKeima (h)-pIND(SP1) plasmid (Cornelissen et al., 2018b; Kim et al., 2019). Kim et al., confirmed that in mt-Keima flies, mitophagy levels are low in larval body wall muscles (Kim et al., 2019). Consistent with the observations made in larvae, the Whitworth lab further describe that mitophagy is low in pupal and adult flight muscle (Lee et al., 2018).

When I assessed mitophagy in the VNC of the larval brain it appeared that the neuropils (region enriched in neurites) had low mitophagy whilst mitophagy was more elevated in the cortex (region enriched in neuronal cell bodies and glial cells). Our colleagues in the Whitworth lab also closely assessed mitophagy in larval CNS by dissecting the VNC (here referred to as the ventral ganglion) of both mito-QC and mtKeima larvae (Lee et al., 2018). In those images, mitolysosomes were clearly distinguishable in larval CNS cell bodies.

In mice, mitophagy has likewise been described as heterogenous across organs. Unlike *Drosophila*, muscles (skeletal, tongue) of mito-QC mice have elevated mitophagy (McWilliams et al., 2016). Other organs with high energy demands such as kidneys, the heart, the brain, or the retina have been reported to have high levels of basal mitophagy in mt-Keima and mito-QC mice (Sun et al., 2015; McWilliams et al., 2016, 2018, 2019). However, this should not be taken as a rule of thumb, as other highly metabolically active organs such as the thymus or the spleen were reported to have on average lower rates of mitophagy than other organs (Sun et al., 2015; McWilliams et al., 2016).

6.5.2 Basal mitophagy is compartmentalised within tissues and organs

I discovered that mitophagy was also compartmentalised within organs and tissues. The anal pads were a striking example. These structures were composed of patches of cells with numerous mitolysosomes and cells with no detectable mitolysosomes. In the adult brain mitophagy was particularly elevated in the medulla.

These observations are in agreement with the data published by the Ganley group using the mito-QC mouse: in the adult mice, kidney mitophagy is restricted to the proximal convoluted tubules (PCT) and retinal mitophagy is enriched at the outer nuclear layer (ONL) (McWilliams et al., 2016, 2018, 2019).

6.5.3 Basal mitophagy is regulated developmentally

When I compared mitophagy in larvae and adult mt-Keima *Drosophila*, it appeared that mitophagy was regulated developmentally: the gut for example, was a hotspot of mitophagy in the larvae but had a low mitophagy index in the adult fly.

Kim and colleague's data in mt-Keima fly corroborated this hypothesis. They measured an increase in mitophagy during embryonic development. Mitophagy was especially elevated between stages E13 and E17 (Kim et al., 2019).

Similar observations have been made in mice. When focussing on the developing eye, the Ganley lab found that mitophagy hot spots varied between embryonic and adult retina. At the embryonic stage E16.5 mitophagy was restricted to the inner neuroblast layer whilst mitophagy was enriched in the retinal outer nuclear layer in adult mito-QC mouse (McWilliams et al., 2019). Likewise mitophagy varies in location and degree during mouse kidney and heart development (McWilliams et al., 2016).

6.5.4 *Pink1* and *Parkin* mildly affect basal mitophagy in *Drosophila*

I crossed *Pink1* and *Parkin* RNAi lines with the mt-Keima fly and mitophagy appeared to be mildly affected by *Pink1* or Parkin depletion in larvae epidermal cells. I was however unable to draw any real conclusions from this dataset as

there was too high interindividual differences in mt-Keima expression amongst larvae of the same genotype.

To overcome the difficulties arising from interindividual differences, Emma Rusilowicz and I started generating a new mt-Keima fly: the stripy fly (**Figure 6.12**). Wildtype flies will be transfected with a tubulin-mt-Keima vector, containing two COX VIII MTS, to constitutively express mt-Keima. Those flies will then be crossed with UAS-tagBFP, *hh*-GAL4 flies. The *hh*-GAL4 (hedgehog) driver will promotes the expression of UAS in stripes across the *Drosophila* larva. The resulting stripy fly (*tub, mt-Keima; UAS-TagBFP, hh-GAL4*) can then be crossed with any UAS strain, for example expressing RNAis, to obtain F1 progeny larvae baring both wildtype and knockdown cells within the same tissues with the latter identifiable by the BFP fluorescence.

Using the mito-QC model, which is considerably brighter than mt-Keima, our colleagues found that *Pink1* and *Parkin* deletion mutants and wild-type flies have comparable numbers of mitolysosomes in the larval epidermis cells (Lee et al., 2018). They further observed mitophagy in larval, adult brain and adult DA neurons and found that only the larval brain was sensitive to *Pink1* mutation: in the larval brain, the number of mitolysosomes is decreased by ~10% in *Pink1* ^{B9} mutants. This thus suggests that *Pink1* and *Parkin* minimally affect basal mitophagy in *Drosophila* (Lee et al., 2018).

6.5.5 *Usp30* appears to oppose basal mitophagy in the medulla of young *Drosophila*.

In a preliminary experiment, I observed that *Usp30* depletion can raise mitophagy levels in the medulla of young *Drosophila*. I found that mitophagy in young (7-9 days of age) *Usp30* KO flies was increased by 1.9-fold compared to wildtype flies. However, in old *Usp30* KO (29-33 days of age) flies mitophagy was decreased on average by 4-fold compared to their wildtype counterparts. From our survival curves, we know that only ~5% of *Usp30* KO males survived to 29-33 days of age against 75% for WT males.

In the “old” category we were thus only looking at the “fittest” *Usp30* KO flies. This could imply that low mitophagy correlated with higher probability of survival in the absence of *Usp30*. Two hypotheses could explain this

observation, either a natural selection was made towards USP30 KO flies with low endogenous mitophagy or mitophagy was inhibited by a compensatory mechanism.

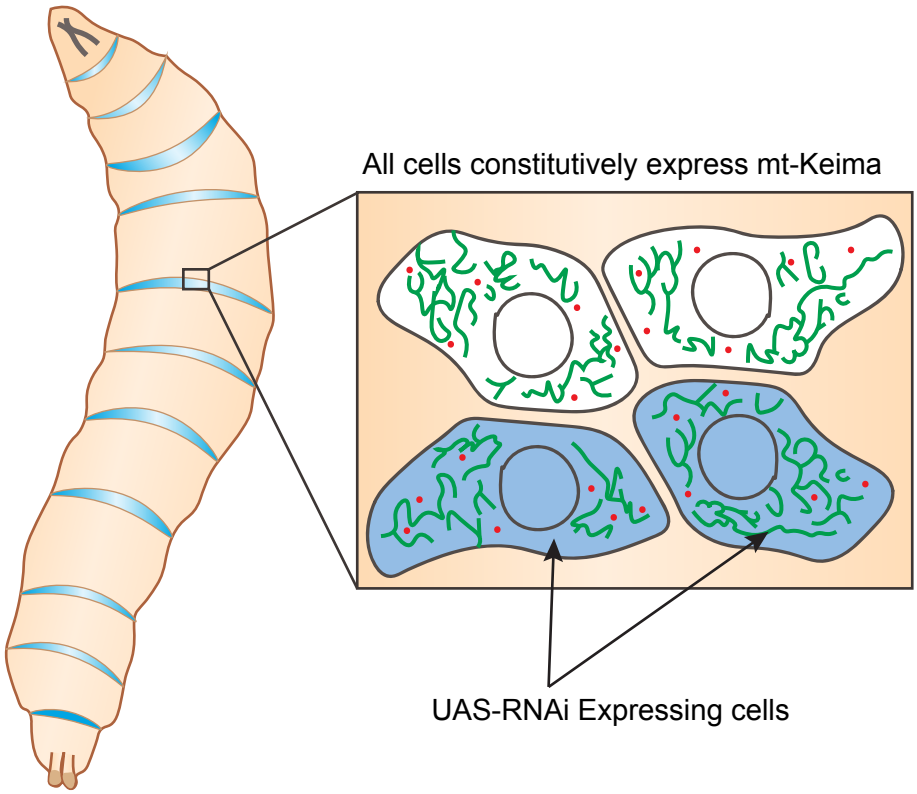

Figure 6.12: *Drosophila* model to express UAS-RNAi in stripes within tissues.

Schematic representation of a “stripy” fly. Wildtype flies will be transfected with a tubulin-mt-Keima vector to constitutively express mt-Keima. They will then be crossed with UAS-tagBFP, *hh*-GAL4 flies. *Hh*-GAL4: Hedgehog driver which promotes the expression of the UAS as stripes across the organism during larval stage. Final stripy flies genotype: *tub, mt-Keima; UAS-TagBFP, hh-GAL4*. When crossed to a UAS-RNAi strain, these flies will express the RNAi only in the *hh*-stripes and those will fluoresce in blue thanks to the UAS-TagBFP. This will enable us to directly compare mitophagy rates in WT vs knockdown cells within the same tissue and in L3 larvae.

6.5.6 Ageing and mitophagy

In the same experiment as mentioned above I noticed that mitophagy in the medulla was enhanced by 1.3-fold between young (7-9 day old) and old (29-33 days old) wildtype flies. Interestingly, the Vandenberghe lab reports that mitophagy increases with age in adult fly muscle: at 3 weeks and 4 weeks post eclosion, mitophagy is multiplied 4-fold and 8-fold respectively compared to 1-week-old mt-Keima flies. This increase in mitophagy was abolished by the overexpression of a kinase dead *Atg1* mutant, thus confirming the dependency on autophagosome (Cornelissen et al., 2018b). The degree of this increase of basal mitophagy with age seems to be tissue and cell specific. Indeed, our colleagues from the Whitworth lab have looked at mitophagy in DA neurons from the PPL1 cluster and found that it wasn't markedly increased between 2- and 30-day-old individuals: on average they detected 5 versus 6 mitolysosomes per DA cells in young and aged flies respectively (Lee et al., 2018).

Data collected in mice point in the other direction, mitophagy recorded in the dentate gyrus of the mt-Keima mice decreases by 70% with age (21/23- versus 2/3-month-old mice) (Sun et al., 2015).

Using the *Pink1*^{B9} mutant and *Parkin* RNAi flies, the Vandenberghe group confirmed that the absence of *Pink1* or *Parkin* does not reduce basal mitophagy in the flight muscles of 1-week-old fly. However, they demonstrated that *Pink1* loss of function mutation and Parkin knockdown supresses the age-dependent increase in mitophagy observed in the indirect flight muscles of 3-weeks and 4-weeks old flies (Cornelissen et al., 2018b).

The Vandenberghe lab also assessed the involvement of DUBs in age-associated mitophagy *in vivo* using their mt-Keima fly and focussed on *Usp15* and *Usp30* (Cornelissen et al., 2018b). They previously had shown using mitochondrial enrichment assays that a small pool of USP15 localised to mitochondria in HEK293 cells and had reported that USP15 opposed Parkin-mediated mitophagy HeLa cells overexpressing Parkin (Cornelissen et al., 2014). In mt-Keima flies, *Usp30* (*CG3016*) and *CG8334* RNAi rescued mitophagy deficiency caused by Parkin RNAi in 4-week-old *Drosophila* flight muscle. They report that *CG8334* is a homolog of human USP15 although

CG8334 has more homology with human USP32 (FlyBase, (Clague et al., 2013, 2019)). They further demonstrated that *CG8334* but not *Usp30* RNAi rescued mitophagy in *Pink1*^{B9} aged flies. However, neither *CG8334* nor *Usp30* RNAi further enhanced age-induced mitophagy in wildtype flies (Cornelissen et al., 2018b).

6.5.7 *Usp30* KO fly fitness

Using *Usp30* KO flies, I found that the complete deletion of *Usp30* reduced motor function (in 12-days old adult flies of both genders), decreased male life expectancy and increased male death at all stages of adulthood. A systematic DUB knockdown screen reported similar findings: *Usp30* RNAi flies died soon after eclosion and performed poorly at geotaxis assays (geotaxis assay measured over 40 days) (Tsou et al., 2012).

Counterintuitively, Baris Bingol reported that *Usp30* RNAi was able to rescue the motor functions (climbing assay) of *Pink1*^{B9} mutant and paraquat treated flies (Bingol et al., 2014). Furthermore, *Usp30* RNAi also extended the life expectancy of paraquat treated flies to 168h compared to 120h in control flies. These observations correlated with recovered dopamine production in *Pink1*^{B9} flies. *Usp30* RNAi was also able to restore mitochondrial morphology in the indirect flight muscles of *Park*^{25} flies, which were otherwise swollen with disorganised cristae. Interestingly expressing *Usp30* RNAi in solely in dopaminergic neurons (Ddc or TH GAL4 drivers) was sufficient to protect flies against paraquat.

These discrepancies could relate to the extent of the knockdown compared *Usp30* knockout. However, Baris Bingol reported that the RNAi line used in his study led to a 90% reduction in *Usp30* mRNA (*Usp30* RNAi NIG 3016R-2) against a 36% decrease seen with the RNAi line used by Sokol Todi group, with the latter being sufficient to cause climbing impairments and reduced life expectancy (*Usp30* RNAi VDRC 110616)(Bingol et al., 2014; Tsou et al., 2012).

Thus, it appears that depleting *Usp30* is overall detrimental towards *Drosophila* fitness but can alleviate PD-like symptoms in young (1-3 days old) *Pink1* and *Parkin* mutant *Drosophila*. *Usp30* deletion might unleash excessive mitophagy

in *Drosophila*. It would be interesting to knockdown *Usp30* in specific tissues to assess what causes the loss in fitness. Using inducible RNAi lines, one could also determine a what stage of development or adulthood *Usp30* is essential.

Chapter 7: Final conclusions

New cues on the mechanisms underlying Parkinson's disease have arisen in the past two decades with the identification of risk factor genes involved in hereditary and sporadic forms of PD. PARK2/PRKN (Parkin) and PARK6/PINK1 mutations are causative of early onset and recessive forms of PD whilst being core regulators of mitophagy. Defects in mitochondrial quality control are thought to underly PD pathogenesis in those patients. Mitophagy and mitochondrial impairments might not be solely restricted to individuals with PINK1 or PRKN mutations. Congruent with this hypothesis, Post-mortem analysis of the brains of patients with sporadic PD and analysis of patient derived cells report on the presence of mitochondrial impairments. These include deficiencies in the respiratory chain components, Complex I in particular, and somatic mtDNA deletions (Chen et al., 2019).

The work presented in this thesis aimed at gaining a deeper understanding of the PINK1-Parkin pathway of mitophagy and specifically focussed on USP30, the DUB known to oppose Parkin at mitochondria (Bingol et al., 2014; Cunningham et al., 2015; Liang et al., 2015).

7.1 Mitophagy is widespread, compartmentalised and developmentally regulated in *Drosophila melanogaster*.

I have characterised the mt-Keima fly which enables the study of mitophagy *in vivo*. The mt-Keima and the mito-QC fly (the latter produced in parallel by the Whitworth lab) were the first *Drosophila* models generated for in vivo imaging of mitophagy (Lee et al., 2018). Using embryonic neuronal cultures, I confirmed that mt-Keima is targeted to mitochondria and mitolysosomes, and further established that mitophagy could be induced in this model employing common mitophagy triggers.

By live microscopy, we and others have found that mitophagy is widespread but also heterogenous across *Drosophila* organs and tissues (Cornelissen et al., 2018a; Kim et al., 2019; Lee et al., 2018). I found that mitophagy is particularly high in tissues such as the larval anal pads, or larval gut cells whilst it is low in larval body wall muscles. I then observed that mitophagy is regulated

developmentally and that it increases with age in the brain of wildtype adult *Drosophila*. Both observations were confirmed by the Yun and Vandenberghe labs respectively (Cornelissen et al., 2018a; Kim et al., 2019). I obtained preliminary data suggesting that *Usp30* deletion enhances mitophagy rates in the brains of young adult *Drosophila*. These studies are currently being followed up by my colleagues Emma Rusilowicz-Jones and Francesco Barone (manuscript in preparation). Knocking-out USP30 was also found to increase mitophagy in mouse embryonic hippocampal neurons overexpressing mt-Keima (Phu et al., 2020).

7.2 USP30 regulates basal and depolarisation induced mitophagy

Using the mito-QC reporter in USP30 KO and USP30 inhibitor treated mammalian cells, I demonstrated that USP30 regulates basal and depolarisation-induced mitophagy (Marcassa et al., 2018).

In agreement with other mass spectrometry studies, I reported that USP30 deubiquitylates OMM proteins including a subset of Parkin substrates, upon depolarisation (Rusilowicz-Jones et al., 2020; Bingol et al., 2014; Cunningham et al., 2015; Ordureau et al., 2020). I further showed that USP30 limits the accumulation of phosphorylated ubiquitin moieties at the OMM, revealing that USP30 may function upstream of PINK1. Increased levels of pS65-ubiquitin were also measured in USP30 KO iNeurons by the Harper lab when using low concentrations of depolarisation agents (Ordureau et al., 2020).

Interestingly, the phosphorylation of OMM ubiquitin moieties by PINK1 might be more dynamic than expected and thus not an absolute barrier to USP30's deubiquitylase activity. Recently, two pSer65-Ub phosphatases have been identified, PTEN-L and PPEF2, and were reported to participate in mitophagy repression: they suppress PINK1-mediated phosphorylation of OMM ubiquitin, decrease Parkin recruitment to mitochondria and reduce the proteasomal degradation of OMM proteins induced by mitochondria depolarisation (Wall et al., 2019; Wang et al., 2018). These phosphatases could enable USP30 to act both upstream and downstream of PINK1.

Western blotting experiments which I performed in USP30 KO SH-SY5Y cells led me to speculate that MARCH5 and HUWE1 are priming E3 ligases which

oppose USP30 and ubiquitylate the TOM complex to initiate the PINK1/Parkin feedforward loop. Congruently, Matsuda's group has demonstrated that Parkin ubiquitylates OMM proteins more efficiently in the presence of MARCH5 in HeLa cells overexpressing Parkin (Koyano et al., 2019a).

I suggest that MARCH5, HUWE1 and USP30 set the threshold for mitophagy induction **(See model: Figure 7.1)**. However, further analysis and replicate experiments are required to confirm the "prime" E3 function of MARCH5 and HUWE1.

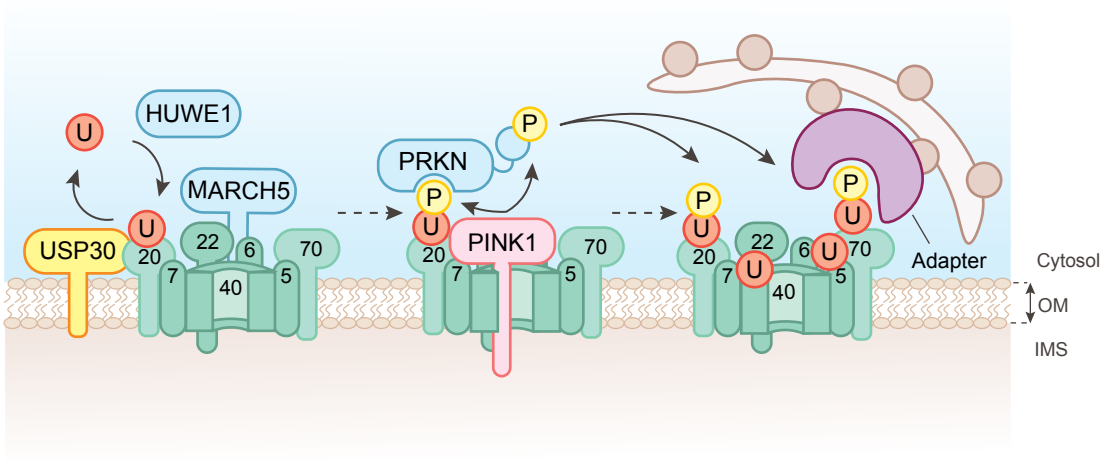

Figure 7.1: Model detailing USP30's function in mitophagy in SH-SY5Y cells.

The mitochondrial DUB USP30 localises at the TOM complex and opposes priming E3 ligases, such as cytosolic HUWE1 and mitochondrial MARCH5, from ubiquitylating proteins in the vicinity of the TOM complex. Upon depolarisation of the mitochondrial membrane, PINK1 accumulates at the TOM complex and phosphorylates both the surrounding ubiquitin and the E3 ligase Parkin at Ser65. This enables the recruitment of Parkin to mitochondria which then amplifies the ubiquitin signal. Autophagy adaptors (NDP52, OPTN, TAX1BP1, p62) bring the autophagosomes to the ubiquitylated mitochondria. By opposing TOM complex ubiquitylation, USP30 set the threshold for mitophagy induction.

7.3 USP30 regulates basal pexophagy

I found that a pool of endogenous USP30 localises at peroxisomes. Elena further demonstrated, using the SKL-Keima probe, that USP30 regulates basal pexophagy (Marcassa et al., 2018). By mass spectrometry I then discovered that the deletion of USP30 enhances PMP70 ubiquitylation at K260, suggesting that the peroxisomal protein is a substrate of USP30. The Kim lab found that USP30 opposes starvation-induced mitophagy by deubiquitylating PMP70 and PEX5, substrates of the E3 ligase PEX2 **(See model: Figure 7.2)**, (Marcassa et al., 2019).

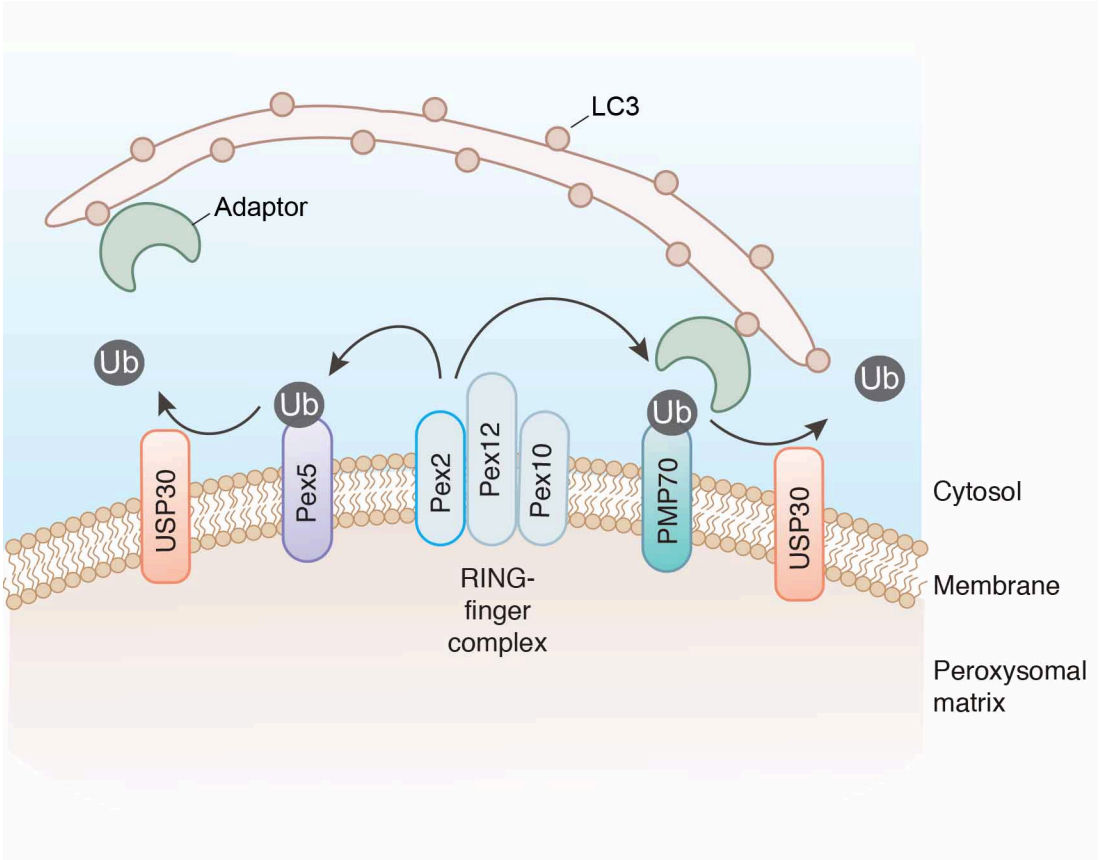

Figure 7.2: Model for USP30-regulated pexophagy.

A pool of USP30 localises at the peroxisomal membrane where it opposes PEX2-mediated ubiquitylation of Pex5 and PMP70. Pexophagy adaptor proteins (NBR1 and p62) bind ubiquitin moieties on proteins of the peroxisomal membrane and enable the engulfment of peroxisomes in autophagosomes.

7.4 A role for USP30 in fine-tuning RQC and protein import at mitochondria?

7.4.1 Ribosome Quality Control and USP30

The mass spectrometry analysis suggests that USP30 deubiquitylates the ribosomal protein RPS20 (40S subunit), and more precisely deubiquitylates its K4 and K8 ubiquitin moieties. These sites are known to be ubiquitylated by ZNF598 in order to alleviate ribosomal stalling through the dissociation and recycling of the ribosomal subunits (Sundaramoorthy et al., 2017), (see short review: (Ikeuchi et al., 2019). Furthermore, I found that the peptidyl RNA PTRH2, likely involved in releasing nascent chains from stalled ribosome, is highly ubiquitylated in the absence of USP30 (Kuroha et al., 2018). I thus proposed that USP30 might fine tunes ribosomal quality control **(See model: Figure 6.3)**.

EM studies performed in yeast have described that a pool of cytosolic ribosomes are in close contact with mitochondria (Kellems et al., 1975; Crowley and Payne, 1998). More recently it was demonstrated that RPL17A, a 60S ribosomal protein, co-precipitates with TOMM22 and TOMM40 (Gold et al., 2017). EM analysis revealed that these ribosomes are orientated such as to permit co-translational import (Gold et al., 2017).

USP30 may thus be involved in ribosome quality control during mitochondrial protein translation. Further validation of the mass spectrometry analysis would be needed draw definitive conclusions on that matter.

7.4.2 Protein import and USP30

Amos had shown that USP30 associates with both TOMM20 and TOMM22 (Liang et al., 2015). I have now seen, by proteomic analysis, that USP30 ubiquitylates nearly all TOM complex subunits (Rusilowicz-Jones et al., 2020). We deduced that USP30 primarily functions at the TOM complex. I found that a few matrix and IMS targeted proteins (GRSF1, HSPD1, HSPE1, MDH2, MTCH2, NDUFB5, PRDX3) are deubiquitylated by USP30. Both Harper's and Bingol's group published complementary mass spectrometry studies revealing that many more IMS and matrix proteins are substrates of USP30 (Phu et al., 2020; Ordureau et al., 2020). Bingol's group revealed that USP30 and MARCH5 fine tune protein import: MARCH5 ubiquitylates import intermediates

to target them for proteasomal degradation whilst USP30 permits the import of certain proteins by deubiquitylating them (Phu et al., 2020), **(See model: Figure 7.3)**.

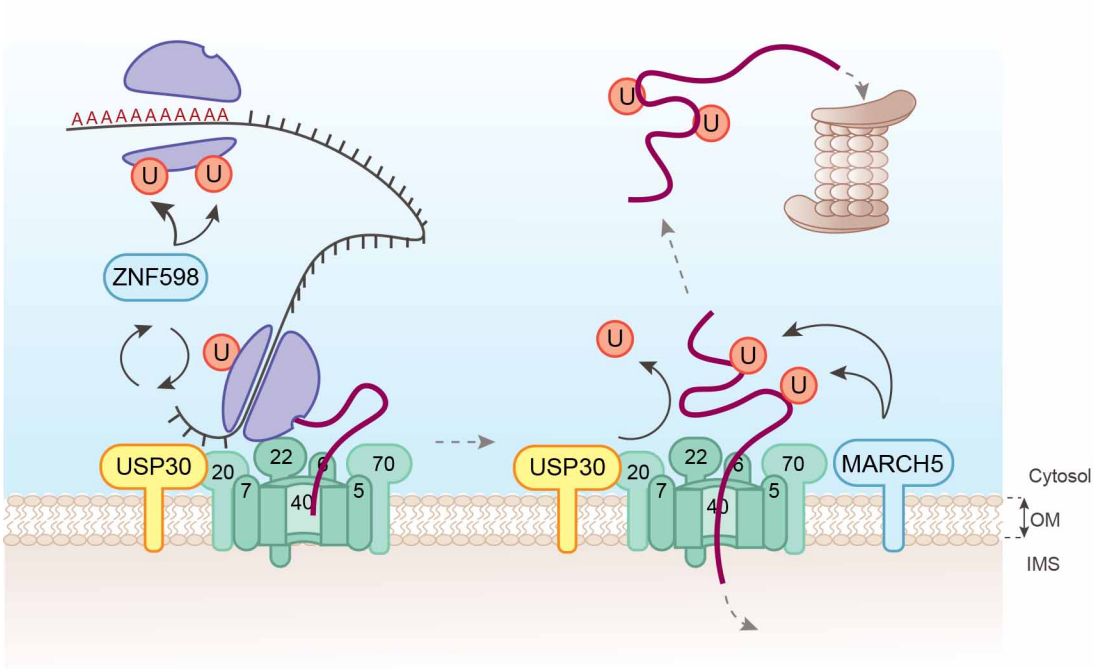

Figure 7.3: Model for USP30's role in mitochondrial protein translation and import.

The cytosolic ubiquitin E3 ligase ZNF598 ubiquitylates RPS20, a 40S ribosomal subunit, at K4 and K8 to alleviate ribosome stalling and promotes the dissociation of the ribosomal subunits. In this model, USP30 would remove K4- and K8-ubiquitin from RPS20 to prevent aberrant dissociation. The 60S ribosomal subunit binds to the TOM complex enabling co-translational import to mitochondria. MARCH5 ubiquitylates importing proteins to send them for proteasomal degradation. USP30 allows protein import by deubiquitylating them.

7.5 USP30 is an actionable target in PD

Pharmacological inhibition of USP30 is of interest in the context of PD as USP30 is the main DUB opposing PINK1 and Parkin.

Together with my colleagues, I found that deleting USP30 did not affect the viability or growth of SH-SY5Y, HCT116, RPE1 and U20S cells. CRISPR KO essentiality screens also report that overall USP30 deletion is well tolerated across cell lines, which makes USP30 an attractive drug target (Lenoir et al., 2018; Meyers et al., 2017).

I have presented a novel, highly specific and potent USP30 inhibitor (FT385) which recapitulates the effects of USP30 KD and KO in mammalian cells. I have shown that FT385 enhances the ubiquitylation of OMM proteins, including Parkin substrates, that it stimulates the PINK1-dependent phosphorylation of mitochondria and that it augments basal mitophagy in SH-SY5Y cells.

The effects of USP30 inhibition *in vivo* remains to be tested. It would be interesting generate mt-Keima flies expressing human USP30 and to measure mitophagy in those flies following a treatment with FT385. One could also assess the effect of FT385 on PINK1 and Parkin mutant flies. Promising results came from the Bingol lab, which reported that knocking down USP30 could rescue motor function, structural defects of mitochondria, and neurodegeneration in PINK1 and Parkin null mutant flies (Bingol et al., 2014). We however found that the complete deletion of USP30 is deleterious for *Drosophila* as it reduces their motor abilities and decreases male viability.

Overall, this thesis discloses new exciting roles of USP30 in the context of pexophagy, basal or induced-mitophagy, and possibly in mitochondrial co-translational import; putting a renewed emphasis on the relevance of USP30 as a therapeutic target for PD.

REFERENCES

Abdullah, C.S., Alam, S., Aishwarya, R., Miriyala, S., Bhuiyan, M.A.N., Panchatcharam, M., Pattillo, C.B., Orr, A.W., Sadoshima, J., Hill, J.A., et al. (2019). Doxorubicin-induced cardiomyopathy associated with inhibition of autophagic degradation process and defects in mitochondrial respiration. Sci Rep *9*, 1–20.

Abdul Rehman, S.A., Kristariyanto, Y.A., Choi, S.-Y., Nkosi, P.J., Weidlich, S., Labib, K., Hofmann, K., and Kulathu, Y. (2016). MINDY-1 Is a Member of an Evolutionarily Conserved and Structurally Distinct New Family of Deubiquitinating Enzymes. Molecular Cell *63*, 146–155.

Adams, M.D., Celniker, S.E., Holt, R.A., Evans, C.A., Gocayne, J.D., Amanatides, P.G., Scherer, S.E., Li, P.W., Hoskins, R.A., Galle, R.F., et al. (2000). The Genome Sequence of Drosophila melanogaster. Science *287*, 2185–2195.

Adhikary, S., Marinoni, F., Hock, A., Hulleman, E., Popov, N., Beier, R., Bernard, S., Quarto, M., Capra, M., Goettig, S., et al. (2005). The Ubiquitin Ligase HectH9 Regulates Transcriptional Activation by Myc and Is Essential for Tumor Cell Proliferation. Cell *123*, 409–421.

Aerts, L., Craessaerts, K., Strooper, B.D., and Morais, V.A. (2015). PINK1 Kinase Catalytic Activity Is Regulated by Phosphorylation on Serines 228 and 402. J. Biol. Chem. *290*, 2798–2811.

Ahmad, R., Raina, D., Meyer, C., Kharbanda, S., and Kufe, D. (2006). Triterpenoid CDDO-Me Blocks the NF-κB Pathway by Direct Inhibition of IKKβ on Cys-179. J. Biol. Chem. *281*, 35764–35769.

Akutsu, M., Dikic, I., and Bremm, A. (2016). Ubiquitin chain diversity at a glance. J Cell Sci *129*, 875–880.

Alexandre, A., and Lehninger, A.L. (1984). Bypasses of the antimycin A block of mitochondrial electron transport in relation to ubisemiquinone function. Biochimica et Biophysica Acta (BBA) - Bioenergetics *767*, 120–129.

Allen, G.F.G., Toth, R., James, J., and Ganley, I.G. (2013). Loss of iron triggers PINK1/Parkin-independent mitophagy. EMBO Rep *14*, 1127–1135.

Andersen, M.K., MacMillan, H.A., Donini, A., and Overgaard, J. (2017). Cold tolerance of Drosophila species is tightly linked to the epithelial K+ transport capacity of the Malpighian tubules and rectal pads. Journal of Experimental Biology *220*, 4261–4269.

Araiso, Y., Tsutsumi, A., Qiu, J., Imai, K., Shiota, T., Song, J., Lindau, C., Wenz, L.-S., Sakaue, H., Yunoki, K., et al. (2019). Structure of the mitochondrial import gate reveals distinct preprotein paths. Nature 1–1.

Armstrong, M.J., and Okun, M.S. (2020). Diagnosis and Treatment of Parkinson Disease: A Review. JAMA *323*, 548–560.

Ashburner, M., and Thompson, J.N.J. (1978). laboratory culture of Drosophila. Genetics and Biology of Drosophila.

Ashford, T.P., and Porter, K.R. (1962). Cytoplasmic components in hepatic cell lysosomes. J Cell Biol *12*, 198–202.

Ashrafi, G., Schlehe, J.S., LaVoie, M.J., and Schwarz, T.L. (2014). Mitophagy of damaged mitochondria occurs locally in distal neuronal axons and requires PINK1 and Parkin. J Cell Biol *206*, 655–670.

Atawia, R.T., Bunch, K.L., Toque, H.A., Caldwell, R.B., and Caldwell, R.W. (2019). Mechanisms of obesity-induced metabolic and vascular dysfunctions. Front Biosci (Landmark Ed) *24*, 890–934.

Aubry, L., and Klein, G. (2006). Purification Techniques of Subcellular Compartments for Analytical and Preparative Purposes. In Dictyostelium Discoideum Protocols, L. Eichinger, and F. Rivero, eds. (Totowa, NJ: Humana Press), pp. 171–185.

Axel, R. (2004). The Nobel Prize in Physiology or Medicine 2004.

Bainbridge, S.P., and Bownes, M. (1981). Staging the metamorphosis of Drosophila melanogaster. Development *66*, 57–80.

Baker, R.T., and Board, P.G. (1991). The human ubiquitin-52 amino acid fusion protein gene shares several structural features with mammalian ribosomal protein genes. Nucleic Acids Res *19*, 1035–1040.

Bakula, D., Müller, A.J., Zuleger, T., Takacs, Z., Franz-Wachtel, M., Thost, A.-K., Brigger, D., Tschan, M.P., Frickey, T., Robenek, H., et al. (2017). WIPI3 and WIPI4 β-propellers are scaffolds for LKB1-AMPK-TSC signalling circuits in the control of autophagy. Nature Communications *8*, 15637.

Bard, J.A.M., Goodall, E.A., Greene, E.R., Jonsson, E., Dong, K.C., and Martin, A. (2018). Structure and Function of the 26S Proteasome. Annual Review of Biochemistry *87*, 697–724.

Barretina, J., Caponigro, G., Stransky, N., Venkatesan, K., Margolin, A.A., Kim, S., Wilson, C.J., Lehár, J., Kryukov, G.V., Sonkin, D., et al. (2012). The Cancer Cell Line Encyclopedia enables predictive modeling of anticancer drug sensitivity. Nature *483*, 603–607.

Bashore, C., Jaishankar, P., Skelton, N.J., Fuhrmann, J., Hearn, B.R., Liu, P.S., Renslo, A.R., and Dueber, E.C. (2020). Cyanopyrrolidine Inhibitors of Ubiquitin Specific Protease 7 Mediate Desulfhydration of the Active-Site Cysteine. ACS Chem. Biol. *15*, 1392–1400.

Bayne, A.N., and Trempe, J.-F. (2019). Mechanisms of PINK1, ubiquitin and Parkin interactions in mitochondrial quality control and beyond. Cell. Mol. Life Sci. *76*, 4589–4611.

Bellot, G., Garcia-Medina, R., Gounon, P., Chiche, J., Roux, D., Pouysségur, J., and Mazure, N.M. (2009). Hypoxia-Induced Autophagy Is Mediated through Hypoxia-Inducible Factor Induction of BNIP3 and BNIP3L via Their BH3 Domains. Molecular and Cellular Biology *29*, 2570–2581.

Bernstein, S.H., Venkatesh, S., Li, M., Lee, J., Lu, B., Hilchey, S.P., Morse, K.M., Metcalfe, H.M., Skalska, J., Andreeff, M., et al. (2012). The mitochondrial ATP-

dependent Lon protease: a novel target in lymphoma death mediated by the synthetic triterpenoid CDDO and its derivatives. Blood *119*, 3321–3329.

Bingol, B., and Sheng, M. (2016). Mechanisms of mitophagy: PINK1, Parkin, USP30 and beyond. Free Radical Biology and Medicine *100*, 210–222.

Bingol, B., Tea, J.S., Phu, L., Reichelt, M., Bakalarski, C.E., Song, Q., Foreman, O., Kirkpatrick, D.S., and Sheng, M. (2014). The mitochondrial deubiquitinase USP30 opposes parkin-mediated mitophagy. Nature *510*, 370–375.

Bishop, P., Rocca, D., and Henley, J.M. (2016). Ubiquitin C-terminal hydrolase L1 (UCH-L1): structure, distribution and roles in brain function and dysfunction. Biochem J *473*, 2453–2462.

Bisiak, F., and McCarthy, A.A. (2019). Structure and Function of Roundabout Receptors. In Macromolecular Protein Complexes II: Structure and Function, J.R. Harris, and J. Marles-Wright, eds. (Cham: Springer International Publishing), pp. 291–319.

Bjørkøy, G., Lamark, T., Brech, A., Outzen, H., Perander, M., Øvervatn, A., Stenmark, H., and Johansen, T. (2005). p62/SQSTM1 forms protein aggregates degraded by autophagy and has a protective effect on huntingtin-induced cell death. Journal of Cell Biology *171*, 603–614.

Blauwendraat, C., Nalls, M.A., and Singleton, A.B. (2020). The genetic architecture of Parkinson's disease. The Lancet Neurology *19*, 170–178.

Blockus, H., and Chédotal, A. (2016). Slit-Robo signaling. Development *143*, 3037–3044.

Bogart, K., and Andrews, J. (2006). Extraction of Total RNA from Drosophila. CGB Tech. Report *2006*.

Bonnet, J., Romier, C., Tora, L., and Devys, D. (2008). Zinc-finger UBPs: regulators of deubiquitylation. Trends in Biochemical Sciences *33*, 369–375.

Brand, A.H., and Perrimon, N. (1993). Targeted gene expression as a means of altering cell fates and generating dominant phenotypes. Development *118*, 401–415.

Braschi, E., Zunino, R., and McBride, H.M. (2009). MAPL is a new mitochondrial SUMO E3 ligase that regulates mitochondrial fission. EMBO Rep *10*, 748–754.

Braschi, E., Goyon, V., Zunino, R., Mohanty, A., Xu, L., and McBride, H.M. (2010). Vps35 Mediates Vesicle Transport between the Mitochondria and Peroxisomes. Current Biology *20*, 1310–1315.

Budhidarmo, R., Nakatani, Y., and Day, C.L. (2012). RINGs hold the key to ubiquitin transfer. Trends in Biochemical Sciences *37*, 58–65.

Bulina, M.E., Chudakov, D.M., Britanova, O.V., Yanushevich, Y.G., Staroverov, D.B., Chepurnykh, T.V., Merzlyak, E.M., Shkrob, M.A., Lukyanov, S., and Lukyanov, K.A. (2006). A genetically encoded photosensitizer. Nat Biotechnol *24*, 95–99.

Burbulla, L.F., Fitzgerald, J.C., Stegen, K., Westermeier, J., Thost, A.-K., Kato, H., Mokranjac, D., Sauerwald, J., Martins, L.M., Woitalla, D., et al. (2014). Mitochondrial

proteolytic stress induced by loss of mortalin function is rescued by Parkin and PINK1. Cell Death Dis *5*, e1180.

Burchell, V.S., Nelson, D.E., Sanchez-Martinez, A., Delgado-Camprubi, M., Ivatt, R.M., Pogson, J.H., Randle, S.J., Wray, S., Lewis, P.A., Houlden, H., et al. (2013). The Parkinson's disease genes Fbxo7 and Parkin interact to mediate mitophagy. Nat Neurosci *16*.

Burman, J.L., Pickles, S., Wang, C., Sekine, S., Vargas, J.N.S., Zhang, Z., Youle, A.M., Nezich, C.L., Wu, X., Hammer, J.A., et al. (2017). Mitochondrial fission facilitates the selective mitophagy of protein aggregates. J Cell Biol *216*, 3231–3247.

Buus, R., Faronato, M., Hammond, D.E., Urbé, S., and Clague, M.J. (2009). Deubiquitinase Activities Required for Hepatocyte Growth Factor-Induced Scattering of Epithelial Cells. Curr Biol *19*, 1463–1466.

Campos-Ortega, J.A., and Hartenstein, V. (1997). The Embryonic Development of Drosophila melanogaster (Berlin Heidelberg: Springer-Verlag).

Cao, J., and Yan, Q. (2012). Histone Ubiquitination and Deubiquitination in Transcription, DNA Damage Response, and Cancer. Front. Oncol. *2*.

Cao, X., Wang, H., Wang, Z., Wang, Q., Zhang, S., Deng, Y., and Fang, Y. (2017). In vivo imaging reveals mitophagy independence in the maintenance of axonal mitochondria during normal aging. Aging Cell *16*, 1180–1190.

Cappadocia, L., and Lima, C.D. (2018). Ubiquitin-like Protein Conjugation: Structures, Chemistry, and Mechanism. Chem. Rev. *118*, 889–918.

Carroll, E.C., Greene, E.R., Martin, A., and Marqusee, S. (2020). Site-specific ubiquitination affects protein energetics and proteasomal degradation. Nature Chemical Biology *16*, 866–875.

Carroll, R.G., Hollville, E., and Martin, S.J. (2014). Parkin Sensitizes toward Apoptosis Induced by Mitochondrial Depolarization through Promoting Degradation of Mcl-1. Cell Reports *9*, 1538–1553.

Carvalho, A.B., Vicoso, B., Russo, C.A.M., Swenor, B., and Clark, A.G. (2015). Birth of a new gene on the Y chromosome of Drosophila melanogaster. PNAS *112*, 12450–12455.

Cavadini, S., Fischer, E.S., Bunker, R.D., Potenza, A., Lingaraju, G.M., Goldie, K.N., Mohamed, W.I., Faty, M., Petzold, G., Beckwith, R.E.J., et al. (2016). Cullin–RING ubiquitin E3 ligase regulation by the COP9 signalosome. Nature *531*, 598–603.

Caygill, E.E., and Brand, A.H. (2016). The GAL4 System: A Versatile System for the Manipulation and Analysis of Gene Expression. In Drosophila: Methods and Protocols, C. Dahmann, ed. (New York, NY: Springer), pp. 33–52.

Chan, N.C., Salazar, A.M., Pham, A.H., Sweredoski, M.J., Kolawa, N.J., Graham, R.L.J., Hess, S., and Chan, D.C. (2011). Broad activation of the ubiquitin–proteasome system by Parkin is critical for mitophagy. Hum Mol Genet *20*, 1726–1737.

Chang, D., Nalls, M.A., Hallgrímsdóttir, I.B., Hunkapiller, J., van der Brug, M., Cai, F., Kerchner, G.A., Ayalon, G., Bingol, B., Sheng, M., et al. (2017). A meta-analysis of

genome-wide association studies identifies 17 new Parkinson's disease risk loci. Nature Genetics *49*, 1511–1516.

Chen, C., Turnbull, D.M., and Reeve, A.K. (2019). Mitochondrial Dysfunction in Parkinson's Disease—Cause or Consequence? Biology *8*, 38.

Chen, Z., Liu, L., Cheng, Q., Li, Y., Wu, H., Zhang, W., Wang, Y., Sehgal, S.A., Siraj, S., Wang, X., et al. (2017). Mitochondrial E3 ligase MARCH5 regulates FUNDC1 to fine-tune hypoxic mitophagy. EMBO Rep *18*, 495–509.

Cheung, Y.-T., Lau, W.K.-W., Yu, M.-S., Lai, C.S.-W., Yeung, S.-C., So, K.-F., and Chang, R.C.-C. (2009). Effects of all-trans-retinoic acid on human SH-SY5Y neuroblastoma as in vitro model in neurotoxicity research. NeuroToxicology *30*, 127–135.

Chiu, Y.-H., Sun, Q., and Chen, Z.J. (2007). E1-L2 Activates Both Ubiquitin and FAT10. Molecular Cell *27*, 1014–1023.

Chowdhury, S., Otomo, C., Leitner, A., Ohashi, K., Aebersold, R., Lander, G.C., and Otomo, T. (2018). Insights into autophagosome biogenesis from structural and biochemical analyses of the ATG2A-WIPI4 complex. Proc Natl Acad Sci USA *115*, E9792–E9801.

Ciechanover, A. (2005). Proteolysis: from the lysosome to ubiquitin and the proteasome. Nature Reviews Molecular Cell Biology *6*, 79–87.

Ciechanover, A., Hod, Y., and Hershko, A. (1978). A heat-stable polypeptide componentof an atp-dependent proteolytic systemfrom reticdlocytes. Biochemical and biophysical research communications *81*, 6.

Ciechanover, A., Heller, H., Elias, S., Haas, A.L., and Hershko, A. (1980). ATP-dependent conjugation of reticulocyte proteins with the polypeptide required for protein degradation. Proc Natl Acad Sci U S A *77*, 1365–1368.

Ciechanover, A., Heller, H., Katz-Etzion, R., and Hershko, A. (1981). Activation of the heat-stable polypeptide of the ATP-dependent proteolytic system. Proc Natl Acad Sci U S A *78*, 761–765.

Ciechanover, A., Elias, S., Heller, H., and Hershko, A. (1982). "Covalent affinity" purification of ubiquitin-activating enzyme. J. Biol. Chem. *257*, 2537–2542.

Cipolla, C.M., and Lodhi, I.J. (2017). Peroxisomal Dysfunction in Age-Related Diseases. Trends Endocrinol Metab *28*, 297–308.

Clague, M.J., and Urbé, S. (2010). Ubiquitin: Same Molecule, Different Degradation Pathways. Cell *143*, 682–685.

Clague, M.J., Coulson, J.M., and Urbé, S. (2012). Cellular functions of the DUBs. J Cell Sci *125*, 277–286.

Clague, M.J., Barsukov, I., Coulson, J.M., Liu, H., Rigden, D.J., and Urbé, S. (2013). Deubiquitylases From Genes to Organism. Physiological Reviews *93*, 1289–1315.

Clague, M.J., Heride, C., and Urbé, S. (2015). The demographics of the ubiquitin system. Trends in Cell Biology *25*, 417–426.

Clague, M.J., Urbé, S., and Komander, D. (2019). Breaking the chains: deubiquitylating enzyme specificity begets function. Nature Reviews Molecular Cell Biology *20*, 338–352.

Clancy, A., Heride, C., Pinto-Fernández, A., Kallinos, A., Kayser-Bricker, K.J., Wang, W., Smith, V., Elcocks, H., Davis, S., Fessler, S., et al. (2020). The deubiquitylase USP9X controls ribosomal stalling. BioRxiv 2020.04.15.042291.

Clark, S.L. (1957). Cellular differentiation in the kidneys of newborn mice studied with the electron microscope. J Biophys Biochem Cytol *3*, 349–362.

Clark, I.E., Dodson, M.W., Jiang, C., Cao, J.H., Huh, J.R., Seol, J.H., Yoo, S.J., Hay, B.A., and Guo, M. (2006). Drosophila pink1 is required for mitochondrial function and interacts genetically with parkin. Nature *441*, 1162–1166.

Cong, L., Ran, F.A., Cox, D., Lin, S., Barretto, R., Habib, N., Hsu, P.D., Wu, X., Jiang, W., Marraffini, L.A., et al. (2013). Multiplex genome engineering using CRISPR/Cas systems. Science *339*, 819–823.

Constantinescu, R., Constantinescu, A.T., Reichmann, H., and Janetzky, B. (2007). Neuronal differentiation and long-term culture of the human neuroblastoma line SH-SY5Y. In Neuropsychiatric Disorders An Integrative Approach, M. Gerlach, J. Deckert, K. Double, and E. Koutsilieri, eds. (Vienna: Springer Vienna), pp. 17–28.

Cornelissen, T., Haddad, D., Wauters, F., Van Humbeeck, C., Mandemakers, W., Koentjoro, B., Sue, C., Gevaert, K., De Strooper, B., Verstreken, P., et al. (2014). The deubiquitinase USP15 antagonizes Parkin-mediated mitochondrial ubiquitination and mitophagy. Hum Mol Genet *23*, 5227–5242.

Cornelissen, T., Vilain, S., Vints, K., Gounko, N., Verstreken, P., and Vandenberghe, W. (2018a). Deficiency of parkin and PINK1 impairs age-dependent mitophagy in Drosophila. ELife *7*.

Cornelissen, T., Verstreken, P., and Vandenberghe, W. (2018b). Imaging mitophagy in the fruit fly. Autophagy *14*, 1656–1657.

Corti, O., Lesage, S., and Brice, A. (2011). What Genetics Tells us About the Causes and Mechanisms of Parkinson's Disease. Physiological Reviews *91*, 1161–1218.

Costello, J.L., Castro, I.G., Camões, F., Schrader, T.A., McNeall, D., Yang, J., Giannopoulou, E.-A., Gomes, S., Pogenberg, V., Bonekamp, N.A., et al. (2017). Predicting the targeting of tail-anchored proteins to subcellular compartments in mammalian cells. J Cell Sci *130*, 1675–1687.

Cox, J., and Mann, M. (2008). MaxQuant enables high peptide identification rates, individualized p.p.b.-range mass accuracies and proteome-wide protein quantification. Nat Biotechnol *26*, 1367–1372.

Crowley, K.S., and Payne, R.M. (1998). Ribosome Binding to Mitochondria Is Regulated by GTP and the Transit Peptide. J. Biol. Chem. *273*, 17278–17285.

Cullen, P.J., and Steinberg, F. (2018). To degrade or not to degrade: mechanisms and significance of endocytic recycling. Nature Reviews Molecular Cell Biology *19*, 679–696.

Cunningham, C.N., Baughman, J.M., Phu, L., Tea, J.S., Yu, C., Coons, M., Kirkpatrick, D.S., Bingol, B., and Corn, J.E. (2015). USP30 and parkin homeostatically regulate atypical ubiquitin chains on mitochondria. Nature Cell Biology *17*, 160–169.

Dadson, K., Hauck, L., Hao, Z., Grothe, D., Rao, V., Mak, T.W., and Billia, F. (2017). The E3 ligase Mule protects the heart against oxidative stress and mitochondrial dysfunction through Myc-dependent inactivation of Pgc-1α and Pink1. Sci Rep *7*.

Dawson, T.M., and Dawson, V.L. (2014). Parkin Plays a Role in Sporadic Parkinson's Disease. NDD *13*, 69–71.

Deas, E., Plun-Favreau, H., and Wood, N.W. (2009). PINK1 function in health and disease. EMBO Molecular Medicine *1*, 152–165.

Deas, E., Plun-Favreau, H., Gandhi, S., Desmond, H., Kjaer, S., Loh, S.H.Y., Renton, A.E.M., Harvey, R.J., Whitworth, A.J., Martins, L.M., et al. (2011). PINK1 cleavage at position A103 by the mitochondrial protease PARL. Hum Mol Genet *20*, 867–879.

DeLuca, S.Z., and O'Farrell, P.H. (2012). Barriers to Male Transmission of Mitochondrial DNA in Sperm Development. Developmental Cell *22*, 660–668.

Demarco, R.S., Eikenes, Å.H., Haglund, K., and Jones, D.L. (2014). Investigating spermatogenesis in Drosophila melanogaster. Methods *68*, 218–227.

Deosaran, E., Larsen, K.B., Hua, R., Sargent, G., Wang, Y., Kim, S., Lamark, T., Jauregui, M., Law, K., Lippincott-Schwartz, J., et al. (2013). NBR1 acts as an autophagy receptor for peroxisomes. J Cell Sci *126*, 939–952.

Despras, G., Zamaleeva, A.I., Dardevet, L., Tisseyre, C., Magalhaes, J.G., Garner, C., Waard, M.D., Amigorena, S., Feltz, A., Mallet, J.-M., et al. (2015). H-Rubies, a new family of red emitting fluorescent pH sensors for living cells. Chem. Sci. *6*, 5928–5937.

Deveau, H., Barrangou, R., Garneau, J.E., Labonté, J., Fremaux, C., Boyaval, P., Romero, D.A., Horvath, P., and Moineau, S. (2008). Phage response to CRISPR-encoded resistance in Streptococcus thermophilus. J. Bacteriol. *190*, 1390–1400.

Di Fonzo, A., Dekker, M.C.J., Montagna, P., Baruzzi, A., Yonova, E.H., Correia Guedes, L., Szczerbinska, A., Zhao, T., Dubbel-Hulsman, L.O.M., Wouters, C.H., et al. (2009). FBXO7 mutations cause autosomal recessive, early-onset parkinsonian-pyramidal syndrome. Neurology *72*, 240–245.

Di Rita, A., Peschiaroli, A., D'Acunzo, P., Strobbe, D., Hu, Z., Gruber, J., Nygaard, M., Lambrughi, M., Melino, G., Papaleo, E., et al. (2018). HUWE1 E3 ligase promotes PINK1/PARKIN-independent mitophagy by regulating AMBRA1 activation via IKKα. Nat Commun *9*.

Dikic, I., and Elazar, Z. (2018). Mechanism and medical implications of mammalian autophagy. Nature Reviews Molecular Cell Biology *19*, 349–364.

Dixit, E., Boulant, S., Zhang, Y., Lee, A.S.Y., Odendall, C., Shum, B., Hacohen, N., Chen, Z.J., Whelan, S.P., Fransen, M., et al. (2010). Peroxisomes Are Signaling Platforms for Antiviral Innate Immunity. Cell *141*, 668–681.

Doiron, K., Goyon, V., Coyaud, E., Rajapakse, S., Raught, B., and McBride, H.M. (2017). The dynamic interacting landscape of MAPL reveals essential functions for SUMOylation in innate immunity. Sci Rep *7*.

Durcan, T.M., Tang, M.Y., Pérusse, J.R., Dashti, E.A., Aguileta, M.A., McLelland, G.-L., Gros, P., Shaler, T.A., Faubert, D., Coulombe, B., et al. (2014). USP8 regulates mitophagy by removing K6-linked ubiquitin conjugates from parkin. The EMBO Journal *33*, 2473–2491.

de Duve, C. (1959). Lysosomes, a new group of cytoplasmic particles. Subcellular Particles *60*, 128–159.

de Duve, C. (1963). Structure and Functions of Lysosomes. In Funktionelle Und Morphologische Organisation Der Zelle, P. Karlson, ed. (Berlin, Heidelberg: Springer), pp. 209–218.

de Duve, C., and Wattiaux, R. (1966). Functions of Lysosomes. Annual Review of Physiology *28*, 435–492.

Eberhart, T., and Kovacs, W.J. (2018). Pexophagy in yeast and mammals: an update on mysteries. Histochem Cell Biol *150*, 473–488.

El Khouri, E., Le Pavec, G., Toledano, M.B., and Delaunay-Moisan, A. (2013). RNF185 Is a Novel E3 Ligase of Endoplasmic Reticulum-associated Degradation (ERAD) That Targets Cystic Fibrosis Transmembrane Conductance Regulator (CFTR). J Biol Chem *288*, 31177–31191.

Elmore, S.P., Qian, T., Grissom, S.F., and Lemasters, J.J. (2001). The mitochondrial permeability transition initiates autophagy in rat hepatocytes. The FASEB Journal *15*, 2286–2287.

Elmore, S.P., Nishimura, Y., Qian, T., Herman, B., and Lemasters, J.J. (2004). Discrimination of depolarized from polarized mitochondria by confocal fluorescence resonance energy transfer. Archives of Biochemistry and Biophysics *422*, 145–152.

Etlinger, J.D., and Goldberg, A.L. (1977). A soluble ATP-dependent proteolytic system responsible for the degradation of abnormal proteins in reticulocytes. Proc Natl Acad Sci U S A *74*, 54–58.

Fabian, L., and Brill, J.A. (2012). Drosophila spermiogenesis. Spermatogenesis *2*, 197–212.

Fabrizio, J.J., Hime, G., Lemmon, S.K., and Bazinet, C. (1998). Genetic dissection of sperm individualization in Drosophila melanogaster. Development *125*, 1833–1843.

Faesen, A.C., Luna-Vargas, M.P.A., Geurink, P.P., Clerici, M., Merkx, R., van Dijk, W.J., Hameed, D.S., El Oualid, F., Ovaa, H., and Sixma, T.K. (2011). The Differential Modulation of USP Activity by Internal Regulatory Domains, Interactors and Eight Ubiquitin Chain Types. Chemistry & Biology *18*, 1550–1561.

Fang, Y., Soares, L., and Bonini, N.M. (2013). Design and implementation of in vivo imaging of neural injury responses in the adult Drosophila wing. Nat Protoc *8*, 810–819.

Farré, J.-C., Mahalingam, S.S., Proietto, M., and Subramani, S. (2019). Peroxisome biogenesis, membrane contact sites, and quality control. EMBO Reports *20*, e46864.

Fiesel, F.C., James, E.D., Hudec, R., and Springer, W. (2017). Mitochondrial targeted HSP90 inhibitor Gamitrinib-TPP (G-TPP) induces PINK1/Parkin-dependent mitophagy. Oncotarget *8*, 106233–106248.

Fischer, J.A., Giniger, E., Maniatis, T., and Ptashne, M. (1988). GAL4 activates transcription in Drosophila. Nature *332*, 853–856.

Frank, M., Duvezin-Caubet, S., Koob, S., Occhipinti, A., Jagasia, R., Petcherski, A., Ruonala, M.O., Priault, M., Salin, B., and Reichert, A.S. (2012). Mitophagy is triggered by mild oxidative stress in a mitochondrial fission dependent manner. Biochimica et Biophysica Acta (BBA) - Molecular Cell Research *1823*, 2297–2310.

Fu, M., St-Pierre, P., Shankar, J., Wang, P.T.C., Joshi, B., and Nabi, I.R. (2013). Regulation of mitophagy by the Gp78 E3 ubiquitin ligase. Mol Biol Cell *24*, 1153–1162.

Fujita, N., Itoh, T., Omori, H., Fukuda, M., Noda, T., and Yoshimori, T. (2008). The Atg16L Complex Specifies the Site of LC3 Lipidation for Membrane Biogenesis in Autophagy. MBoC *19*, 2092–2100.

Funakoshi, Y., Chou, M.M., Kanaho, Y., and Donaldson, J.G. (2014). TRE17/USP6 regulates ubiquitylation and trafficking of cargo proteins that enter cells by clathrin-independent endocytosis. J Cell Sci *127*, 4750–4761.

Galanis, M., Devenish, R.J., and Nagley, P. (1991). Duplication of leader sequence for protein targeting to mitochondria leads to increased import efficiency. FEBS Letters *282*, 425–430.

Gargano, J.W., Martin, I., Bhandari, P., and Grotewiel, M.S. (2005). Rapid iterative negative geotaxis (RING): a new method for assessing age-related locomotor decline in Drosophila. Experimental Gerontology *40*, 386–395.

Garshott, D.M., Sundaramoorthy, E., Leonard, M., and Bennett, E.J. (2020). Distinct regulatory ribosomal ubiquitylation events are reversible and hierarchically organized. ELife *9*, e54023.

Gasiunas, G., Barrangou, R., Horvath, P., and Siksnys, V. (2012). Cas9–crRNA ribonucleoprotein complex mediates specific DNA cleavage for adaptive immunity in bacteria. Proceedings of the National Academy of Sciences of the United States of America *109*, E2579.

Gatica, D., Lahiri, V., and Klionsky, D.J. (2018). Cargo recognition and degradation by selective autophagy. Nature Cell Biology *20*, 233–242.

Geisler, S., Holmström, K.M., Skujat, D., Fiesel, F.C., Rothfuss, O.C., Kahle, P.J., and Springer, W. (2010). PINK1/Parkin-mediated mitophagy is dependent on VDAC1 and p62/SQSTM1. Nature Cell Biology *12*, 119–131.

Geisler, S., Jäger, L., Golombek, S., Nakanishi, E., Hans, F., Casadei, N., Terradas, A.L., Linnemann, C., and Kahle, P.J. (2019). Ubiquitin-specific protease USP36 knockdown impairs Parkin-dependent mitophagy via downregulation of Beclin-1-associated autophagy-related ATG14L. Experimental Cell Research 111641.

Georgakopoulos, N.D., Wells, G., and Campanella, M. (2017). The pharmacological regulation of cellular mitophagy. Nature Chemical Biology *13*, 136–146.

Gersch, M., Gladkova, C., Schubert, A.F., Michel, M.A., Maslen, S., and Komander, D. (2017). Mechanism and regulation of the Lys6-selective deubiquitinase USP30. Nat Struct Mol Biol *24*, 920–930.

Gibellini, L., Pinti, M., Boraldi, F., Giorgio, V., Bernardi, P., Bartolomeo, R., Nasi, M., De Biasi, S., Missiroli, S., Carnevale, G., et al. (2014). Silencing of mitochondrial Lon protease deeply impairs mitochondrial proteome and function in colon cancer cells. The FASEB Journal *28*, 5122–5135.

Gibellini, L., Pinti, M., Bartolomeo, R., De Biasi, S., Cormio, A., Musicco, C., Carnevale, G., Pecorini, S., Nasi, M., De Pol, A., et al. (2015). Inhibition of Lon protease by triterpenoids alters mitochondria and is associated to cell death in human cancer cells. Oncotarget *6*, 25466–25483.

Gilda, J.E., Ghosh, R., Cheah, J.X., West, T.M., Bodine, S.C., and Gomes, A.V. (2015). Western Blotting Inaccuracies with Unverified Antibodies: Need for a Western Blotting Minimal Reporting Standard (WBMRS). PLoS ONE *10*, e0135392.

Gladkova, C., Maslen, S.L., Skehel, J.M., and Komander, D. (2018). Mechanism of parkin activation by PINK1. Nature *559*, 410–414.

Gold, V.A., Chroscicki, P., Bragoszewski, P., and Chacinska, A. (2017). Visualization of cytosolic ribosomes on the surface of mitochondria by electron cryo-tomography. EMBO Reports *18*, 1786–1800.

Goldknopf, I.L., and Busch, H. (1977). Isopeptide linkage between nonhistone and histone 2A polypeptides of chromosomal conjugate-protein A24. Proc Natl Acad Sci U S A *74*, 864–868.

Goldstein, G., Scheid, M., Hammerling, U., Schlesinger, D.H., Niall, H.D., and Boyse, E.A. (1975). Isolation of a polypeptide that has lymphocyte-differentiating properties and is probably represented universally in living cells. Proc Natl Acad Sci U S A *72*, 11–15.

Gong, Y., Zack, T.I., Morris, L.G.T., Lin, K., Hukkelhoven, E., Raheja, R., Tan, I.-L., Turcan, S., Veeriah, S., Meng, S., et al. (2014). Pan-cancer genetic analysis identifies PARK2 as a master regulator of G1/S cyclins. Nat Genet *46*, 588–594.

Greene, J.C., Whitworth, A.J., Kuo, I., Andrews, L.A., Feany, M.B., and Pallanck, L.J. (2003). Mitochondrial pathology and apoptotic muscle degeneration in Drosophila parkin mutants. PNAS *100*, 4078–4083.

Grou, C.P., Pinto, M.P., Mendes, A.V., Domingues, P., and Azevedo, J.E. (2015). The de novo synthesis of ubiquitin: identification of deubiquitinases acting on ubiquitin precursors. Scientific Reports *5*, 12836.

Guo, W., Yan, L., Yang, L., Liu, X., E, Q., Gao, P., Ye, X., Liu, W., and Zuo, J. (2014). Targeting GRP75 Improves HSP90 Inhibitor Efficacy by Enhancing p53-Mediated Apoptosis in Hepatocellular Carcinoma. PLOS ONE *9*, e85766.

Haahr, P., Borgermann, N., Guo, X., Typas, D., Achuthankutty, D., Hoffmann, S., Shearer, R., Sixma, T.K., and Mailand, N. (2018). ZUFSP Deubiquitylates K63-Linked Polyubiquitin Chains to Promote Genome Stability. Molecular Cell *70*, 165-174.e6.

Haas, A.L., Warms, J.V., Hershko, A., and Rose, I.A. (1982). Ubiquitin-activating enzyme. Mechanism and role in protein-ubiquitin conjugation. J. Biol. Chem. *257*, 2543–2548.

Hall, J.C., Rosbash, M., and Young, M.W. (2017). The Nobel Prize in Physiology or Medicine 2017.

Hamasaki, M., Furuta, N., Matsuda, A., Nezu, A., Yamamoto, A., Fujita, N., Oomori, H., Noda, T., Haraguchi, T., Hiraoka, Y., et al. (2013). Autophagosomes form at ER–mitochondria contact sites. Nature *495*, 389–393.

Hammerling, B.C., Najor, R.H., Cortez, M.Q., Shires, S.E., Leon, L.J., Gonzalez, E.R., Boassa, D., Phan, S., Thor, A., Jimenez, R.E., et al. (2017a). A Rab5 endosomal pathway mediates Parkin-dependent mitochondrial clearance. Nature Communications *8*, 14050.

Hammerling, B.C., Shires, S.E., Leon, L.J., Cortez, M.Q., and Gustafsson, Å.B. (2017b). Isolation of Rab5-positive endosomes reveals a new mitochondrial degradation pathway utilized by BNIP3 and Parkin. Small GTPases *11*, 69–76.

Hanada, T., Noda, N.N., Satomi, Y., Ichimura, Y., Fujioka, Y., Takao, T., Inagaki, F., and Ohsumi, Y. (2007). The Atg12-Atg5 Conjugate Has a Novel E3-like Activity for Protein Lipidation in Autophagy. J. Biol. Chem. *282*, 37298–37302.

Harper, J.W., Ordureau, A., and Heo, J.-M. (2018). Building and decoding ubiquitin chains for mitophagy. Nature Reviews Molecular Cell Biology *19*, 93–108.

Hartwig, S., Knebel, B., Goeddeke, S., Koellmer, C., Jacob, S., Nitzgen, U., Passlack, W., Schiller, M., Dicken, H.-D., Haas, J., et al. (2013). So close and yet so far: mitochondria and peroxisomes are one but with specific talents. Archives of Physiology and Biochemistry *119*, 126–135.

Hasson, S.A., Kane, L.A., Yamano, K., Huang, C.-H., Sliter, D.A., Buehler, E., Wang, C., Heman-Ackah, S.M., Hessa, T., Guha, R., et al. (2013). High-content genome-wide RNAi screens identify regulators of parkin upstream of mitophagy. Nature *504*, 291–295.

He, C., and Klionsky, D.J. (2009). Regulation Mechanisms and Signaling Pathways of Autophagy. Annu. Rev. Genet. *43*, 67–93.

Heo, J.-M., Ordureau, A., Paulo, J.A., Rinehart, J., and Harper, J.W. (2015). The PINK1-PARKIN mitochondrial ubiquitylation pathway drives a program of TBK1 activation and recruitment of OPTN and NDP52 to promote mitophagy. Mol Cell *60*, 7–20.

Heo, J.-M., Ordureau, A., Swarup, S., Paulo, J.A., Shen, K., Sabatini, D.M., and Harper, J.W. (2018). RAB7A phosphorylation by TBK1 promotes mitophagy via the PINK-PARKIN pathway. Science Advances *4*, eaav0443.

Heo, J.-M., Harper, N.J., Paulo, J.A., Li, M., Xu, Q., Coughlin, M., Elledge, S.J., and Harper, J.W. (2019). Integrated proteogenetic analysis reveals the landscape of a mitochondrial-autophagosome synapse during PARK2-dependent mitophagy. Science Advances *5*, eaay4624.

Heride, C., Urbé, S., and Clague, M.J. (2014). Ubiquitin code assembly and disassembly. Current Biology *24*, R215–R220.

Hermanns, T., Pichlo, C., Woiwode, I., Klopffleisch, K., Witting, K.F., Ovaa, H., Baumann, U., and Hofmann, K. (2018). A family of unconventional deubiquitinases with modular chain specificity determinants. Nature Communications *9*, 1–13.

Hernandez, G., Thornton, C., Stotland, A., Lui, D., Sin, J., Ramil, J., Magee, N., Andres, A., Quarato, G., Carreira, R.S., et al. (2013). MitoTimer. Autophagy *9*, 1852–1861.

Hershko, A., Ciechanover, A., Heller, H., Haas, A.L., and Rose, I.A. (1980). Proposed role of ATP in protein breakdown: conjugation of protein with multiple chains of the polypeptide of ATP-dependent proteolysis. Proc Natl Acad Sci U S A *77*, 1783–1786.

Hershko, A., Heller, H., Elias, S., and Ciechanover, A. (1983). Components of ubiquitin-protein ligase system. Resolution, affinity purification, and role in protein breakdown. J. Biol. Chem. *258*, 8206–8214.

Hewings, D.S., Flygare, J.A., Bogyo, M., and Wertz, I.E. (2017). Activity-based probes for the ubiquitin conjugation–deconjugation machinery: new chemistries, new tools, and new insights. The FEBS Journal *284*, 1555–1576.

Hewings, D.S., Heideker, J., Ma, T.P., AhYoung, A.P., El Oualid, F., Amore, A., Costakes, G.T., Kirchhofer, D., Brasher, B., Pillow, T., et al. (2018). Reactive-site-centric chemoproteomics identifies a distinct class of deubiquitinase enzymes. Nature Communications *9*, 1–17.

Heytler, P.G. (1963). uncoupling of oxidative phosphorylation by carbonyl cyanide phenylhydrazones. I. Some characteristics of m-Cl-CCP action on mitochondria and chloroplasts. Biochemistry *2*, 357–361.

Heytler, P.G., and Prichard, W.W. (1962). A new class of uncoupling agents--carbonyl cyanide phenylhydrazones. Biochem. Biophys. Res. Commun. *7*, 272–275.

Hoffmann, J.A. (2011). The Nobel Prize in Physiology or Medicine 2011.

Hofmann, K., and Bucher, P. (1996). The UBA domain: a sequence motif present in multiple enzyme classes of the ubiquitination pathway. Trends in Biochemical Sciences *21*, 172–173.

Hoshino, A., Mita, Y., Okawa, Y., Ariyoshi, M., Iwai-Kanai, E., Ueyama, T., Ikeda, K., Ogata, T., and Matoba, S. (2013). Cytosolic p53 inhibits Parkin-mediated mitophagy and promotes mitochondrial dysfunction in the mouse heart. Nature Communications *4*, 1–12.

Hoshino, A., Wang, W., Wada, S., McDermott-Roe, C., Evans, C.S., Gosis, B., Morley, M.P., Rathi, K.S., Li, J., Li, K., et al. (2019). The ADP/ATP translocase drives mitophagy independent of nucleotide exchange. Nature 1–5.

Hunt, L.T., and Dayhoff, M.O. (1977). Amino-terminal sequence identity of ubiquitin and the nonhistone component of nuclear protein A24. Biochemical and Biophysical Research Communications *74*, 650–655.

Husnjak, K., and Dikic, I. (2012). Ubiquitin-Binding Proteins: Decoders of Ubiquitin-Mediated Cellular Functions. Annu. Rev. Biochem. *81*, 291–322.

Igarashi, R., Yamashita, S., Yamashita, T., Inoue, K., Fukuda, T., Fukuchi, T., and Kanki, T. (2020). Gemcitabine induces Parkin-independent mitophagy through

mitochondrial-resident E3 ligase MUL1-mediated stabilization of PINK1. Scientific Reports *10*, 1–11.

Ikeuchi, K., Izawa, T., and Inada, T. (2019). Recent Progress on the Molecular Mechanism of Quality Controls Induced by Ribosome Stalling. Front. Genet. *9*.

Ishihara, N., Fujita, Y., Oka, T., and Mihara, K. (2006). Regulation of mitochondrial morphology through proteolytic cleavage of OPA1. The EMBO Journal *25*, 2966–2977.

Ishino, Y., Shinagawa, H., Makino, K., Amemura, M., and Nakata, A. (1987). Nucleotide sequence of the iap gene, responsible for alkaline phosphatase isozyme conversion in Escherichia coli, and identification of the gene product. J. Bacteriol. *169*, 5429–5433.

Islinger, M., Voelkl, A., Fahimi, H.D., and Schrader, M. (2018). The peroxisome: an update on mysteries 2.0. Histochem Cell Biol *150*, 443–471.

Itzhak, D.N., Tyanova, S., Cox, J., and Borner, G.H. (2016). Global, quantitative and dynamic mapping of protein subcellular localization. ELife *5*, e16950.

Ivanes, F., Faccenda, D., Gatliff, J., Ahmed, A.A., Cocco, S., Cheng, C.H.K., Allan, E., Russell, C., Duchen, M.R., and Campanella, M. (2014). The compound BTB06584 is an IF1-dependent selective inhibitor of the mitochondrial F1Fo-ATPase. Br J Pharmacol *171*, 4193–4206.

Iwashita, H., Torii, S., Nagahora, N., Ishiyama, M., Shioji, K., Sasamoto, K., Shimizu, S., and Okuma, K. (2017). Live Cell Imaging of Mitochondrial Autophagy with a Novel Fluorescent Small Molecule. ACS Chem. Biol. *12*, 2546–2551.

Jarial, M.S. (1987). Ultrastructure of the anal organ of Drosophila larva with reference to ion transport. Tissue and Cell *19*, 559–575.

Jimenez-Orgaz, A., Kvainickas, A., Nägele, H., Denner, J., Eimer, S., Dengjel, J., and Steinberg, F. (2018). Control of RAB7 activity and localization through the retromer-TBC1D5 complex enables RAB7-dependent mitophagy. The EMBO Journal *37*, 235–254.

Jin, S.M., and Youle, R.J. (2013). The accumulation of misfolded proteins in the mitochondrial matrix is sensed by PINK1 to induce PARK2/Parkin-mediated mitophagy of polarized mitochondria. Autophagy *9*, 1750–1757.

Jin, J., Li, X., Gygi, S.P., and Harper, J.W. (2007). Dual E1 activation systems for ubiquitin differentially regulate E2 enzyme charging. Nature *447*, 1135–1138.

Jin, S.M., Lazarou, M., Wang, C., Kane, L.A., Narendra, D.P., and Youle, R.J. (2010). Mitochondrial membrane potential regulates PINK1 import and proteolytic destabilization by PARL. J Cell Biol *191*, 933–942.

Jinek, M., Chylinski, K., Fonfara, I., Hauer, M., Doudna, J.A., and Charpentier, E. (2012). A programmable dual-RNA-guided DNA endonuclease in adaptive bacterial immunity. Science *337*, 816–821.

Joshi, B., Mohammadzadeh, Y., Gao, G., and Nabi, I.R. (2018). Gp78 E3 ubiquitin ligase mediates both basal and damage-induced mitophagy. BioRxiv 407593.

Kaiser, S.E., Riley, B.E., Shaler, T.A., Trevino, R.S., Becker, C.H., Schulman, H., and Kopito, R.R. (2011). Protein standard absolute quantification (PSAQ) method for the measurement of cellular ubiquitin pools. Nature Methods *8*, 691–696.

Kakidani, H., and Ptashne, M. (1988). GAL4 activates gene expression in mammalian cells. Cell *52*, 161–167.

Kane, L.A., Lazarou, M., Fogel, A.I., Li, Y., Yamano, K., Sarraf, S.A., Banerjee, S., and Youle, R.J. (2014). PINK1 phosphorylates ubiquitin to activate Parkin E3 ubiquitin ligase activity. J Cell Biol *205*, 143–153.

Karbowski, M., Neutzner, A., and Youle, R.J. (2007). The mitochondrial E3 ubiquitin ligase MARCH5 is required for Drp1 dependent mitochondrial division. J Cell Biol *178*, 71–84.

Kasianowicz, J., Benz, R., and McLaughlin, S. (1984). The kinetic mechanism by which CCCP (carbonyl cyanide m-chlorophenylhydrazone) transports protons across membranes. J. Membr. Biol. *82*, 179–190.

Katayama, H., Kogure, T., Mizushima, N., Yoshimori, T., and Miyawaki, A. (2011). A Sensitive and Quantitative Technique for Detecting Autophagic Events Based on Lysosomal Delivery. Chemistry & Biology *18*, 1042–1052.

Kazlauskaite, A., Kondapalli, C., Gourlay, R., Campbell, D.G., Ritorto, M.S., Hofmann, K., Alessi, D.R., Knebel, A., Trost, M., and Muqit, M.M.K. (2014). Parkin is activated by PINK1-dependent phosphorylation of ubiquitin at Ser65. Biochem J *460*, 127–139.

Kellems, R.E., Allison, V.F., and Butow, R.A. (1975). Cytoplasmic type 80S ribosomes associated with yeast mitochondria. IV. Attachment of ribosomes to the outer membrane of isolated mitochondria. J Cell Biol *65*, 1–14.

Kim, Y.Y., Um, J.-H., Yoon, J.-H., Kim, H., Lee, D.-Y., Lee, Y.J., Jee, H.J., Kim, Y.M., Jang, J.S., Jang, Y.-G., et al. (2019). Assessment of mitophagy in mt-Keima Drosophila revealed an essential role of the PINK1-Parkin pathway in mitophagy induction in vivo. The FASEB Journal *33*, 9742–9751.

Kimura, S., Noda, T., and Yoshimori, T. (2007). Dissection of the Autophagosome Maturation Process by a Novel Reporter Protein, Tandem Fluorescent-Tagged LC3. Autophagy *3*, 452–460.

Kinner, A., and Kölling, R. (2003). The yeast deubiquitinating enzyme Ubp16 is anchored to the outer mitochondrial membrane. FEBS Letters *549*, 135–140.

Kirkin, V., and Rogov, V.V. (2019). A Diversity of Selective Autophagy Receptors Determines the Specificity of the Autophagy Pathway. Molecular Cell *76*, 268–285.

Kitada, T., Asakawa, S., Hattori, N., Matsumine, H., Yamamura, Y., Minoshima, S., Yokochi, M., Mizuno, Y., and Shimizu, N. (1998). Mutations in the parkin gene cause autosomal recessive juvenile parkinsonism. Nature *392*, 605–608.

Kluge, A.F., Lagu, B.R., Maiti, P., Jaleel, M., Webb, M., Malhotra, J., Mallat, A., Srinivas, P.A., and Thompson, J.E. (2018). Novel highly selective inhibitors of ubiquitin specific protease 30 (USP30) accelerate mitophagy. Bioorganic & Medicinal Chemistry Letters *28*, 2655–2659.

Kobayashi, S., Volden, P., Timm, D., Mao, K., Xu, X., and Liang, Q. (2010). Transcription Factor GATA4 Inhibits Doxorubicin-induced Autophagy and Cardiomyocyte Death. J Biol Chem *285*, 793–804.

Koch, A., Yoon, Y., Bonekamp, N.A., McNiven, M.A., and Schrader, M. (2005). A Role for Fis1 in Both Mitochondrial and Peroxisomal Fission in Mammalian Cells. Mol Biol Cell *16*, 5077–5086.

Kogure, T., Karasawa, S., Araki, T., Saito, K., Kinjo, M., and Miyawaki, A. (2006). A fluorescent variant of a protein from the stony coral Montipora facilitates dual-color single-laser fluorescence cross-correlation spectroscopy. Nature Biotechnology *24*, 577–581.

Komander, D., and Rape, M. (2012). The Ubiquitin Code. Annu. Rev. Biochem. *81*, 203–229.

Komander, D., Clague, M.J., and Urbé, S. (2009). Breaking the chains: structure and function of the deubiquitinases. Nature Reviews Molecular Cell Biology *10*, 550–563.

Kondo, S., and Ueda, R. (2013). Highly Improved Gene Targeting by Germline-Specific Cas9 Expression in Drosophila. Genetics *195*, 715–721.

Kovalevich, J., and Langford, D. (2013). Considerations for the use of SH-SY5Y neuroblastoma cells in neurobiology. Methods Mol. Biol. *1078*, 9–21.

Koyano, F., Okatsu, K., Kosako, H., Tamura, Y., Go, E., Kimura, M., Kimura, Y., Tsuchiya, H., Yoshihara, H., Hirokawa, T., et al. (2014). Ubiquitin is phosphorylated by PINK1 to activate parkin. Nature *510*, 162–166.

Koyano, F., Yamano, K., Kosako, H., Tanaka, K., and Matsuda, N. (2019a). Parkin recruitment to impaired mitochondria for nonselective ubiquitylation is facilitated by MITOL. J Biol Chem *294*, 10300–10314.

Koyano, F., Yamano, K., Kosako, H., Kimura, Y., Kimura, M., Fujiki, Y., Tanaka, K., and Matsuda, N. (2019b). Parkin-mediated ubiquitylation redistributes MITOL/March5 from mitochondria to peroxisomes. EMBO Reports *0*, e47728.

Krabill, A.D., Chen, H., Hussain, S., Feng, C., Abdullah, A., Das, C., Aryal, U.K., Post, C.B., Wendt, M.K., Galardy, P.J., et al. (2020). Ubiquitin C-Terminal Hydrolase L1: Biochemical and Cellular Characterization of a Covalent Cyanopyrrolidine-Based Inhibitor. ChemBioChem *21*, 712–722.

Kristariyanto, Y.A., Abdul Rehman, S.A., Weidlich, S., Knebel, A., and Kulathu, Y. (2017). A single MIU motif of MINDY-1 recognizes K48-linked polyubiquitin chains. EMBO Reports *18*, 392–402.

Ksenzenko, M., Konstantinov, A.A., Khomutov, G.B., Tikhonov, A.N., and Ruuge, E.K. (1983). Effect of electron transfer inhibitors on superoxide generation in the cytochrome bc 1 site of the mitochondrial respiratory chain. FEBS Letters *155*, 19–24.

Kulak, N.A., Pichler, G., Paron, I., Nagaraj, N., and Mann, M. (2014). Minimal, encapsulated proteomic-sample processing applied to copy-number estimation in eukaryotic cells. Nature Methods *11*, 319–324.

Kumar, A., Aguirre, J.D., Condos, T.E., Martinez-Torres, R.J., Chaugule, V.K., Toth, R., Sundaramoorthy, R., Mercier, P., Knebel, A., Spratt, D.E., et al. (2015). Disruption of the autoinhibited state primes the E3 ligase parkin for activation and catalysis. The EMBO Journal *34*, 2506–2521.

Kuroha, K., Zinoviev, A., Hellen, C.U.T., and Pestova, T.V. (2018). Release of Ubiquitinated and Non-ubiquitinated Nascent Chains from Stalled Mammalian Ribosomal Complexes by ANKZF1 and Ptrh1. Molecular Cell *72*, 286-302.e8.

Kwasna, D., Abdul Rehman, S.A., Natarajan, J., Matthews, S., Madden, R., De Cesare, V., Weidlich, S., Virdee, S., Ahel, I., Gibbs-Seymour, I., et al. (2018). Discovery and Characterization of ZUFSP/ZUP1, a Distinct Deubiquitinase Class Important for Genome Stability. Mol Cell *70*, 150-164.e6.

Lainé, D., Palovich, M., McCleland, B., Petitjean, E., Delhom, I., Xie, H., Deng, J., Lin, G., Davis, R., Jolit, A., et al. (2011). Discovery of Novel Cyanamide-Based Inhibitors of Cathepsin C. ACS Med. Chem. Lett. *2*, 142–147.

Laker, R.C., Xu, P., Ryall, K.A., Sujkowski, A., Kenwood, B.M., Chain, K.H., Zhang, M., Royal, M.A., Hoehn, K.L., Driscoll, M., et al. (2014). A Novel MitoTimer Reporter Gene for Mitochondrial Content, Structure, Stress, and Damage in Vivo. J Biol Chem *289*, 12005–12015.

Laker, R.C., Drake, J.C., Wilson, R.J., Lira, V.A., Lewellen, B.M., Ryall, K.A., Fisher, C.C., Zhang, M., Saucerman, J.J., Goodyear, L.J., et al. (2017). Ampk phosphorylation of Ulk1 is required for targeting of mitochondria to lysosomes in exercise-induced mitophagy. Nat Commun *8*.

Lane, J.D., and Nakatogawa, H. (2013). Two ubiquitin-like conjugation systems that mediate membrane formation during autophagy. Essays Biochem *55*, 39–50.

Lane, C.A., Hardy, J., and Schott, J.M. (2018). Alzheimer's disease. European Journal of Neurology *25*, 59–70.

LaVoie, M.J., Ostaszewski, B.L., Weihofen, A., Schlossmacher, M.G., and Selkoe, D.J. (2005). Dopamine covalently modifies and functionally inactivates parkin. Nature Medicine *11*, 1214–1221.

LaVoie, M.J., Cortese, G.P., Ostaszewski, B.L., and Schlossmacher, M.G. (2007). The effects of oxidative stress on parkin and other E3 ligases. Journal of Neurochemistry *103*, 2354–2368.

Law, K.B., Bronte-Tinkew, D., Di Pietro, E., Snowden, A., Jones, R.O., Moser, A., Brumell, J.H., Braverman, N., and Kim, P.K. (2017). The peroxisomal AAA ATPase complex prevents pexophagy and development of peroxisome biogenesis disorders. Autophagy *13*, 868–884.

Lazarou, M., Sliter, D.A., Kane, L.A., Sarraf, S.A., Wang, C., Burman, J.L., Sideris, D.P., Fogel, A.I., and Youle, R.J. (2015). The ubiquitin kinase PINK1 recruits autophagy receptors to induce mitophagy. Nature *524*, 309–314.

Leboucher, G.P., Tsai, Y.C., Yang, M., Shaw, K.C., Zhou, M., Veenstra, T.D., Glickman, M.H., and Weissman, A.M. (2012). Stress-Induced Phosphorylation and Proteasomal Degradation of Mitofusin 2 Facilitates Mitochondrial Fragmentation and Apoptosis. Mol Cell *47*, 547–557.

Lee, B.-H., Lu, Y., Prado, M.A., Shi, Y., Tian, G., Sun, S., Elsasser, S., Gygi, S.P., King, R.W., and Finley, D. (2016). USP14 deubiquitinates proteasome-bound substrates that are ubiquitinated at multiple sites. Nature *532*, 398–401.

Lee, J.J., Sanchez-Martinez, A., Zarate, A.M., Benincá, C., Mayor, U., Clague, M.J., and Whitworth, A.J. (2018). Basal mitophagy is widespread in Drosophila but minimally affected by loss of Pink1 or parkin. J Cell Biol *217*, 1613–1622.

Lemaitre, B., Nicolas, E., Michaut, L., Reichhart, J.-M., and Hoffmann, J.A. (1996). The Dorsoventral Regulatory Gene Cassette spätzle/Toll/cactus Controls the Potent Antifungal Response in Drosophila Adults. Cell *86*, 973–983.

Lemasters, J.J., Nieminen, A.L., Qian, T., Trost, L.C., Elmore, S.P., Nishimura, Y., Crowe, R.A., Cascio, W.E., Bradham, C.A., Brenner, D.A., et al. (1998). The mitochondrial permeability transition in cell death: a common mechanism in necrosis, apoptosis and autophagy. Biochim. Biophys. Acta *1366*, 177–196.

Lenoir, W.F., Lim, T.L., and Hart, T. (2018). PICKLES: the database of pooled in-vitro CRISPR knockout library essentiality screens. Nucleic Acids Res *46*, D776–D780.

Lewis, E.B. (1978). A gene complex controlling segmentation in Drosophila. Nature *276*, 565–570.

Lewis, E.B., Nüsslein-Volhard, C., and Wieschaus, E.F. (1995). The Nobel Prize in Physiology or Medicine 1995.

Leznicki, P., Natarajan, J., Bader, G., Spevak, W., Schlattl, A., Rehman, S.A.A., Pathak, D., Weidlich, S., Zoephel, A., Bordone, M.C., et al. (2018). Expansion of DUB functionality generated by alternative isoforms – USP35, a case study. J Cell Sci *131*.

Li, J., Qi, W., Chen, G., Feng, D., Liu, J., Ma, B., Zhou, C., Mu, C., Zhang, W., Chen, Q., et al. (2015). Mitochondrial outer-membrane E3 ligase MUL1 ubiquitinates ULK1 and regulates selenite-induced mitophagy. Autophagy *11*, 1216–1229.

Li, W., Bengtson, M.H., Ulbrich, A., Matsuda, A., Reddy, V.A., Orth, A., Chanda, S.K., Batalov, S., and Joazeiro, C.A.P. (2008). Genome-Wide and Functional Annotation of Human E3 Ubiquitin Ligases Identifies MULAN, a Mitochondrial E3 that Regulates the Organelle's Dynamics and Signaling. PLoS One *3*.

Liang, J.-R., Martinez, A., Lane, J.D., Mayor, U., Clague, M.J., and Urbé, S. (2015). USP30 deubiquitylates mitochondrial Parkin substrates and restricts apoptotic cell death. EMBO Rep *16*, 618–627.

Liberman, E.A., Topaly, V.P., Tsofina, L.M., Jasaitis, A.A., and Skulachev, V.P. (1969). Mechanism of Coupling of Oxidative Phosphorylation and the Membrane Potential of Mitochondria. Nature *222*, 1076–1078.

Lin, W., and Kang, U.J. (2008). Characterization of PINK1 processing, stability, and subcellular localization. J Neurochem *106*, 464–474.

Liu, C.-Y., Lin, H.-H., Tang, M.-J., and Wang, Y.-K. (2015). Vimentin contributes to epithelial-mesenchymal transition cancer cell mechanics by mediating cytoskeletal organization and focal adhesion maturation. Oncotarget *6*, 15966–15983.

Liu, L., Feng, D., Chen, G., Chen, M., Zheng, Q., Song, P., Ma, Q., Zhu, C., Wang, R., Qi, W., et al. (2012). Mitochondrial outer-membrane protein FUNDC1 mediates hypoxia-induced mitophagy in mammalian cells. Nature Cell Biology *14*, 177–185.

Liu, Y., Yagita, Y., and Fujiki, Y. (2016). Assembly of Peroxisomal Membrane Proteins via the Direct Pex19p-Pex3p Pathway. Traffic *17*, 433–455.

Llopis, J., McCaffery, J.M., Miyawaki, A., Farquhar, M.G., and Tsien, R.Y. (1998). Measurement of cytosolic, mitochondrial, and Golgi pH in single living cells with green fluorescent proteins. Proc Natl Acad Sci U S A *95*, 6803–6808.

Lopes, F.M., Schröder, R., Júnior, M.L.C. da F., Zanotto-Filho, A., Müller, C.B., Pires, A.S., Meurer, R.T., Colpo, G.D., Gelain, D.P., Kapczinski, F., et al. (2010). Comparison between proliferative and neuron-like SH-SY5Y cells as an in vitro model for Parkinson disease studies. Brain Research *1337*, 85–94.

Lu, Y., Lee, B., King, R.W., Finley, D., and Kirschner, M.W. (2015). Substrate degradation by the proteasome: A single-molecule kinetic analysis. Science *348*.

Lydeard, J.R., Schulman, B.A., and Harper, J.W. (2013). Building and remodelling Cullin–RING E3 ubiquitin ligases. EMBO Rep *14*, 1050–1061.

MacVicar, T.D.B., and Lane, J.D. (2014). Impaired OMA1-dependent cleavage of OPA1 and reduced DRP1 fission activity combine to prevent mitophagy in cells that are dependent on oxidative phosphorylation. J Cell Sci *127*, 2313–2325.

Malakhov, M.P., Malakhova, O.A., Kim, K.I., Ritchie, K.J., and Zhang, D.-E. (2002). UBP43 (USP18) Specifically Removes ISG15 from Conjugated Proteins. J. Biol. Chem. *277*, 9976–9981.

Marcassa, E., Kallinos, A., Jardine, J., Rusilowicz-Jones, E.V., Martinez, A., Kuehl, S., Islinger, M., Clague, M.J., and Urbé, S. (2018). Dual role of USP30 in controlling basal pexophagy and mitophagy. EMBO Rep. *19*.

Marcassa, E., Kallinos, A., Jardine, J., Rusilowicz-Jones, E.V., Clague, M.J., and Urbé, S. (2019). New aspects of USP30 biology in the regulation of pexophagy. Autophagy *15*, 1634–1637.

Markow, T.A. (2015). The secret lives of Drosophila flies. ELife *4*, e06793.

Martinez, A., Lectez, B., Ramirez, J., Popp, O., Sutherland, J.D., Urbé, S., Dittmar, G., Clague, M.J., and Mayor, U. (2017). Quantitative proteomic analysis of Parkin substrates in Drosophila neurons. Molecular Neurodegeneration *12*, 29.

Martinu, L., Masuda-Robens, J.M., Robertson, S.E., Santy, L.C., Casanova, J.E., and Chou, M.M. (2004). The TBC (Tre-2/Bub2/Cdc16) domain protein TRE17 regulates plasma membrane-endosomal trafficking through activation of Arf6. Mol. Cell. Biol. *24*, 9752–9762.

Mateja, A., Paduch, M., Chang, H.-Y., Szydlowska, A., Kossiakoff, A.A., Hegde, R.S., and Keenan, R.J. (2015). Structure of the Get3 targeting factor in complex with its membrane protein cargo. Science *347*, 1152–1155.

Matsuda, N., Sato, S., Shiba, K., Okatsu, K., Saisho, K., Gautier, C.A., Sou, Y., Saiki, S., Kawajiri, S., Sato, F., et al. (2010). PINK1 stabilized by mitochondrial

depolarization recruits Parkin to damaged mitochondria and activates latent Parkin for mitophagy. J Cell Biol *189*, 211–221.

McBride, H., and Soubannier, V. (2010). Mitochondrial Function: OMA1 and OPA1, the Grandmasters of Mitochondrial Health. Current Biology *20*, R274–R276.

McCullough, J., Clague, M.J., and Urbé, S. (2004). AMSH is an endosome-associated ubiquitin isopeptidase. J Cell Biol *166*, 487–492.

McLelland, G.-L., Soubannier, V., Chen, C.X., McBride, H.M., and Fon, E.A. (2014). Parkin and PINK1 function in a vesicular trafficking pathway regulating mitochondrial quality control. EMBO J *33*, 282–295.

McLelland, G.-L., Lee, S.A., McBride, H.M., and Fon, E.A. (2016). Syntaxin-17 delivers PINK1/parkin-dependent mitochondrial vesicles to the endolysosomal systemMitochondrial vesicles fuse with endolysosomes. J Cell Biol *214*, 275–291.

McShane, E., Sin, C., Zauber, H., Wells, J.N., Donnelly, N., Wang, X., Hou, J., Chen, W., Storchova, Z., Marsh, J.A., et al. (2016). Kinetic Analysis of Protein Stability Reveals Age-Dependent Degradation. Cell *167*, 803-815.e21.

McWilliams, T.G., Prescott, A.R., Allen, G.F.G., Tamjar, J., Munson, M.J., Thomson, C., Muqit, M.M.K., and Ganley, I.G. (2016). mito-QC illuminates mitophagy and mitochondrial architecture in vivo. J Cell Biol *214*, 333–345.

McWilliams, T.G., Prescott, A.R., Montava-Garriga, L., Ball, G., Singh, F., Barini, E., Muqit, M.M.K., Brooks, S.P., and Ganley, I.G. (2018). Basal Mitophagy Occurs Independently of PINK1 in Mouse Tissues of High Metabolic Demand. Cell Metabolism *27*, 439-449.e5.

McWilliams, T.G., Prescott, A.R., Villarejo-Zori, B., Ball, G., Boya, P., and Ganley, I.G. (2019). A comparative map of macroautophagy and mitophagy in the vertebrate eye. Autophagy *15*, 1296–1308.

Mercer, T.J., Gubas, A., and Tooze, S.A. (2018). A molecular perspective of mammalian autophagosome biogenesis. J. Biol. Chem. *293*, 5386–5395.

Metzger, M.B., Pruneda, J.N., Klevit, R.E., and Weissman, A.M. (2014). RING-type E3 ligases: Master manipulators of E2 ubiquitin-conjugating enzymes and ubiquitination. Biochimica et Biophysica Acta (BBA) - Molecular Cell Research *1843*, 47–60.

Mevissen, T.E.T., and Komander, D. (2017). Mechanisms of Deubiquitinase Specificity and Regulation. Annu. Rev. Biochem. *86*, 159–192.

Mevissen, T.E.T., Hospenthal, M.K., Geurink, P.P., Elliott, P.R., Akutsu, M., Arnaudo, N., Ekkebus, R., Kulathu, Y., Wauer, T., El Oualid, F., et al. (2013). OTU Deubiquitinases Reveal Mechanisms of Linkage Specificity and Enable Ubiquitin Chain Restriction Analysis. Cell *154*, 169–184.

Meyer, H.-J., and Rape, M. (2014). Enhanced Protein Degradation by Branched Ubiquitin Chains. Cell *157*, 910–921.

Meyers, R.M., Bryan, J.G., McFarland, J.M., Weir, B.A., Sizemore, A.E., Xu, H., Dharia, N.V., Montgomery, P.G., Cowley, G.S., Pantel, S., et al. (2017).

Computational correction of copy number effect improves specificity of CRISPR–Cas9 essentiality screens in cancer cells. Nature Genetics *49*, 1779–1784.

Michael, N., Vincent, P., Dena, H., Manu, S., Una-Marie, U.-M., Mohamad, M., Javier, S.-S., Claudia, S., Suzanne, L., Sigurlaug, S., et al. (2011). Imputation of sequence variants for identification of genetic risks for Parkinson's disease: a meta-analysis of genome-wide association studies. The Lancet *377*, 641–649.

Michel, M.A., Swatek, K.N., Hospenthal, M.K., and Komander, D. (2017). Ubiquitin Linkage-Specific Affimers Reveal Insights into K6-Linked Ubiquitin Signaling. Mol Cell *68*, 233-246.e5.

Miller, S., and Muqit, M.M.K. (2019). Therapeutic approaches to enhance PINK1/Parkin mediated mitophagy for the treatment of Parkinson's disease. Neuroscience Letters *705*, 7–13.

Mohanty, A., and McBride, H.M. (2013). Emerging roles of mitochondria in the evolution, biogenesis, and function of peroxisomes. Front Physiol *4*.

Mojica, F.J.M., Juez, G., and Rodriguez-Valera, F. (1993). Transcription at different salinities of Haloferax mediterranei sequences adjacent to partially modified PstI sites. Molecular Microbiology *9*, 613–621.

Mojica, F.J.M., Díez-Villaseñor, C., García-Martínez, J., and Soria, E. (2005). Intervening sequences of regularly spaced prokaryotic repeats derive from foreign genetic elements. J. Mol. Evol. *60*, 174–182.

Montava-Garriga, L., Singh, F., Ball, G., and Ganley, I.G. (2020). Semi-automated quantitation of mitophagy in cells and tissues. Mechanisms of Ageing and Development *185*, 111196.

Moore, A.S., and Holzbaur, E.L.F. (2016). Dynamic recruitment and activation of ALS-associated TBK1 with its target optineurin are required for efficient mitophagy. Proc Natl Acad Sci U S A *113*, E3349–E3358.

Morgan, T.H. (1933). The Nobel Prize in Physiology or Medicine 1933.

Morgan, T.H., Sturtevant, A.H., Muller, H.J., and Bridges, C.B. (1915). The Mechanism of Mendelian heredity, by T. H. Morgan, A. H. Sturtevant, H. J. Muller [and] C. B. Bridges. (New York : H. Holt and company,).

Moskal, N., Riccio, V., Bashkurov, M., Taddese, R., Datti, A., Lewis, P.N., and McQuibban, G.A. (2020). ROCK inhibitors upregulate the neuroprotective Parkin-mediated mitophagy pathway. Nat Commun *11*, 1–14.

Muller, H. (1946). The Nobel Prize in Physiology or Medicine 1946.

Muller, H.J. (1927). Artificial Transmutation of the Gene. Science *66*, 84–87.

Nagaraj, N., Wisniewski, J.R., Geiger, T., Cox, J., Kircher, M., Kelso, J., Pääbo, S., and Mann, M. (2011). Deep proteome and transcriptome mapping of a human cancer cell line. Mol Syst Biol *7*, 548.

Nakamura, N., and Hirose, S. (2008). Regulation of Mitochondrial Morphology by USP30, a Deubiquitinating Enzyme Present in the Mitochondrial Outer Membrane. Mol Biol Cell *19*, 1903–1911.

Nakamura, N., Kimura, Y., Tokuda, M., Honda, S., and Hirose, S. (2006). MARCH-V is a novel mitofusin 2- and Drp1-binding protein able to change mitochondrial morphology. EMBO Rep *7*, 1019–1022.

Nakatogawa, H. (2020). Mechanisms governing autophagosome biogenesis. Nature Reviews Molecular Cell Biology *21*, 439–458.

Nalls, M.A., Pankratz, N., Lill, C.M., Do, C.B., Hernandez, D.G., Saad, M., DeStefano, A.L., Kara, E., Bras, J., Sharma, M., et al. (2014). Large-scale meta-analysis of genome-wide association data identifies six new risk loci for Parkinson's disease. Nat Genet *46*, 989–993.

Narendra, D., Tanaka, A., Suen, D.-F., and Youle, R.J. (2008). Parkin is recruited selectively to impaired mitochondria and promotes their autophagy. J Cell Biol *183*, 795–803.

Narendra, D., Walker, J.E., and Youle, R. (2012). Mitochondrial Quality Control Mediated by PINK1 and Parkin: Links to Parkinsonism. Cold Spring Harb Perspect Biol *4*.

Narendra, D.P., Jin, S.M., Tanaka, A., Suen, D.-F., Gautier, C.A., Shen, J., Cookson, M.R., and Youle, R.J. (2010a). PINK1 Is Selectively Stabilized on Impaired Mitochondria to Activate Parkin. PLOS Biology *8*, e1000298.

Narendra, D.P., Kane, L.A., Hauser, D.N., Fearnley, I.M., and Youle, R.J. (2010b). p62/SQSTM1 is required for Parkin-induced mitochondrial clustering but not mitophagy; VDAC1 is dispensable for both. Autophagy *6*, 1090–1106.

Neuspiel, M., Schauss, A.C., Braschi, E., Zunino, R., Rippstein, P., Rachubinski, R.A., Andrade-Navarro, M.A., and McBride, H.M. (2008). Cargo-Selected Transport from the Mitochondria to Peroxisomes Is Mediated by Vesicular Carriers. Current Biology *18*, 102–108.

Niphakis, M.J., and Cravatt, B.F. (2014). Enzyme Inhibitor Discovery by Activity-Based Protein Profiling. Annu. Rev. Biochem. *83*, 341–377.

Nishimura, T., Tamura, N., Kono, N., Shimanaka, Y., Arai, H., Yamamoto, H., and Mizushima, N. (2017). Autophagosome formation is initiated at phosphatidylinositol synthase-enriched ER subdomains. The EMBO Journal *36*, 1719–1735.

Niu, K., Fang, H., Chen, Z., Zhu, Y., Tan, Q., Wei, D., Li, Y., Balajee, A.S., and Zhao, Y. (2019). USP33 deubiquitinates PRKN/parkin and antagonizes its role in mitophagy. Autophagy 1–11.

Norris, A., and Grant, B.D. (2020). Endosomal microdomains: Formation and function. Current Opinion in Cell Biology *65*, 86–95.

Novikoff, A.B., and Essner, E. (1962). CYTOLYSOMES AND MITOCHONDRIAL DEGENERATION. J Cell Biol *15*, 140–146.

Nüsslein-Volhard, C., and Wieschaus, E. (1980). Mutations affecting segment number and polarity in Drosophila. Nature *287*, 795–801.

Ohsumi, Y. (2014). Historical landmarks of autophagy research. Cell Research *24*, 9–23.

Okatsu, K., Saisho, K., Shimanuki, M., Nakada, K., Shitara, H., Sou, Y.-S., Kimura, M., Sato, S., Hattori, N., Komatsu, M., et al. (2010). p62/SQSTM1 cooperates with Parkin for perinuclear clustering of depolarized mitochondria. Genes Cells *15*, 887–900.

Okatsu, K., Oka, T., Iguchi, M., Imamura, K., Kosako, H., Tani, N., Kimura, M., Go, E., Koyano, F., Funayama, M., et al. (2012). PINK1 autophosphorylation upon membrane potential dissipation is essential for Parkin recruitment to damaged mitochondria. Nat Commun *3*, 1016.

Okatsu, K., Uno, M., Koyano, F., Go, E., Kimura, M., Oka, T., Tanaka, K., and Matsuda, N. (2013). A Dimeric PINK1-containing Complex on Depolarized Mitochondria Stimulates Parkin Recruitment. J. Biol. Chem. *288*, 36372–36384.

Okatsu, K., Kimura, M., Oka, T., Tanaka, K., and Matsuda, N. (2015a). Unconventional PINK1 localization to the outer membrane of depolarized mitochondria drives Parkin recruitment. J Cell Sci *128*, 964–978.

Okatsu, K., Koyano, F., Kimura, M., Kosako, H., Saeki, Y., Tanaka, K., and Matsuda, N. (2015b). Phosphorylated ubiquitin chain is the genuine Parkin receptorPhosphorylated ubiquitin chain is a Parkin receptor. J Cell Biol *209*, 111–128.

Ordureau, A., Sarraf, S.A., Duda, D.M., Heo, J.-M., Jedrychowski, M.P., Sviderskiy, V.O., Olszewski, J.L., Koerber, J.T., Xie, T., Beausoleil, S.A., et al. (2014). Quantitative proteomics reveal a feedforward mechanism for mitochondrial PARKIN translocation and ubiquitin chain synthesis. Mol. Cell *56*, 360–375.

Ordureau, A., Paulo, J.A., Zhang, W., Ahfeldt, T., Zhang, J., Cohn, E.F., Hou, Z., Heo, J.-M., Rubin, L.L., Sidhu, S.S., et al. (2018). Dynamics of PARKIN-Dependent Mitochondrial Ubiquitylation in Induced Neurons and Model Systems Revealed by Digital Snapshot Proteomics. Molecular Cell *70*, 211-227.e8.

Ordureau, A., Paulo, J.A., Zhang, J., An, H., Swatek, K.N., Cannon, J.R., Wan, Q., Komander, D., and Harper, J.W. (2020). Global Landscape and Dynamics of Parkin and USP30-Dependent Ubiquitylomes in iNeurons during Mitophagic Signaling. Molecular Cell *77*, 1124-1142.e10.

Orvedahl, A., Sumpter, R., Xiao, G., Ng, A., Zou, Z., Tang, Y., Narimatsu, M., Gilpin, C., Sun, Q., Roth, M., et al. (2011). Image-Based Genome-Wide siRNA Screen Identifies Selective Autophagy Factors. Nature *480*, 113–117.

Padman, B.S., Bach, M., Lucarelli, G., Prescott, M., and Ramm, G. (2013). The protonophore CCCP interferes with lysosomal degradation of autophagic cargo in yeast and mammalian cells. Autophagy *9*, 1862–1875.

Paisán-Ruiz, C., Guevara, R., Federoff, M., Hanagasi, H., Sina, F., Elahi, E., Schneider, S.A., Schwingenschuh, P., Bajaj, N., Emre, M., et al. (2010). Early-onset L-dopa-responsive parkinsonism with pyramidal signs due to ATP13A2, PLA2G6, FBXO7 and spatacsin mutations. Movement Disorders *25*, 1791–1800.

Pankiv, S., Clausen, T.H., Lamark, T., Brech, A., Bruun, J.-A., Outzen, H., Øvervatn, A., Bjørkøy, G., and Johansen, T. (2007). p62/SQSTM1 Binds Directly to Atg8/LC3 to Facilitate Degradation of Ubiquitinated Protein Aggregates by Autophagy. J. Biol. Chem. *282*, 24131–24145.

Park, J., Lee, S.B., Lee, S., Kim, Y., Song, S., Kim, S., Bae, E., Kim, J., Shong, M., Kim, J.-M., et al. (2006). Mitochondrial dysfunction in Drosophila PINK1 mutants is complemented by parkin. Nature *441*, 1157–1161.

Park, Y.-J., Oanh, N.T.K., Heo, J., Kim, S.-G., Lee, H.-S., Lee, H., Lee, J.-H., Kang, H.C., Lim, W., Yoo, Y.-S., et al. (2020). Dual targeting of RIG-I and MAVS by MARCH5 mitochondria ubiquitin ligase in innate immunity. Cellular Signalling *67*, 109520.

Parkinson, J. (2002). An Essay on the Shaking Palsy. JNP *14*, 223–236.

Pelzer, C., Kassner, I., Matentzoglu, K., Singh, R.K., Wollscheid, H.-P., Scheffner, M., Schmidtke, G., and Groettrup, M. (2007). UBE1L2, a Novel E1 Enzyme Specific for Ubiquitin. J. Biol. Chem. *282*, 23010–23014.

Peng, J., Schwartz, D., Elias, J.E., Thoreen, C.C., Cheng, D., Marsischky, G., Roelofs, J., Finley, D., and Gygi, S.P. (2003). A proteomics approach to understanding protein ubiquitination. Nature Biotechnology *21*, 921–926.

Pereda, J.M. de, Waas, W.F., Jan, Y., Ruoslahti, E., Schimmel, P., and Pascual, J. (2004). Crystal Structure of a Human Peptidyl-tRNA Hydrolase Reveals a New Fold and Suggests Basis for a Bifunctional Activity. J. Biol. Chem. *279*, 8111–8115.

Phu, L., Rose, C.M., Tea, J.S., Wall, C.E., Verschueren, E., Cheung, T.K., Kirkpatrick, D.S., and Bingol, B. (2020). Dynamic Regulation of Mitochondrial Import by the Ubiquitin System. Molecular Cell *77*, 1107-1123.e10.

Pickles, S., Vigié, P., and Youle, R.J. (2018). Mitophagy and Quality Control Mechanisms in Mitochondrial Maintenance. Current Biology *28*, R170–R185.

Pillai, S., Nguyen, J., Johnson, J., Haura, E., Coppola, D., and Chellappan, S. (2015). Tank binding kinase 1 is a centrosome-associated kinase necessary for microtubule dynamics and mitosis. Nat Commun *6*.

Pilling, A.D., Horiuchi, D., Lively, C.M., and Saxton, W.M. (2006). Kinesin-1 and Dynein Are the Primary Motors for Fast Transport of Mitochondria in Drosophila Motor Axons. Mol Biol Cell *17*, 2057–2068.

Pimenta de Castro, I., Costa, A.C., Lam, D., Tufi, R., Fedele, V., Moisoi, N., Dinsdale, D., Deas, E., Loh, S.H.Y., and Martins, L.M. (2012). Genetic analysis of mitochondrial protein misfolding in Drosophila melanogaster. Cell Death & Differentiation *19*, 1308–1316.

Pinti, M., Gibellini, L., Nasi, M., De Biasi, S., Bortolotti, C.A., Iannone, A., and Cossarizza, A. (2016). Emerging role of Lon protease as a master regulator of mitochondrial functions. Biochimica et Biophysica Acta (BBA) - Bioenergetics *1857*, 1300–1306.

Pinto-Fernández, A., Davis, S., Schofield, A.B., Scott, H.C., Zhang, P., Salah, E., Mathea, S., Charles, P.D., Damianou, A., Bond, G., et al. (2019). Comprehensive Landscape of Active Deubiquitinating Enzymes Profiled by Advanced Chemoproteomics. Front. Chem. *7*.

Poewe, W., Seppi, K., Tanner, C.M., Halliday, G.M., Brundin, P., Volkmann, J., Schrag, A.-E., and Lang, A.E. (2017). Parkinson disease. Nature Reviews Disease Primers *3*, 17013.

Politi, Y., Gal, L., Kalifa, Y., Ravid, L., Elazar, Z., and Arama, E. (2014). Paternal Mitochondrial Destruction after Fertilization Is Mediated by a Common Endocytic and Autophagic Pathway in Drosophila. Developmental Cell *29*, 305–320.

Polson, H.E.J., Lartigue, J. de, Rigden, D.J., Reedijk, M., Urbé, S., Clague, M.J., and Tooze, S.A. (2010). Mammalian Atg18 (WIPI2) localizes to omegasome-anchored phagophores and positively regulates LC3 lipidation. Autophagy *6*, 506–522.

Polymeropoulos, M.H., Lavedan, C., Leroy, E., Ide, S.E., Dehejia, A., Dutra, A., Pike, B., Root, H., Rubenstein, J., Boyer, R., et al. (1997). Mutation in the α-Synuclein Gene Identified in Families with Parkinson's Disease. Science *276*, 2045–2047.

Poole, A.C., Thomas, R.E., Yu, S., Vincow, E.S., and Pallanck, L. (2010). The Mitochondrial Fusion-Promoting Factor Mitofusin Is a Substrate of the PINK1/Parkin Pathway. PLOS ONE *5*, e10054.

de Poot, S.A.H., Tian, G., and Finley, D. (2017). Meddling with Fate: The Proteasomal Deubiquitinating Enzymes. Journal of Molecular Biology *429*, 3525–3545.

Pourcel, C., Salvignol, G., and Vergnaud, G. (2005). CRISPR elements in Yersinia pestis acquire new repeats by preferential uptake of bacteriophage DNA, and provide additional tools for evolutionary studies. Microbiology (Reading, Engl.) *151*, 653–663.

Pozhidaeva, A., Valles, G., Wang, F., Wu, J., Sterner, D.E., Nguyen, P., Weinstock, J., Kumar, K.G.S., Kanyo, J., Wright, D., et al. (2017). USP7-Specific Inhibitors Target and Modify the Enzyme's Active Site via Distinct Chemical Mechanisms. Cell Chemical Biology *24*, 1501-1512.e5.

Presgraves, S.P., Ahmed, T., Borwege, S., and Joyce, J.N. (2004). Terminally differentiated SH-SY5Y cells provide a model system for studying neuroprotective effects of dopamine agonists. Neurotox Res *5*, 579–598.

Prudent, J., Zunino, R., Sugiura, A., Mattie, S., Shore, G.C., and McBride, H.M. (2015). MAPL SUMOylation of Drp1 Stabilizes an ER/Mitochondrial Platform Required for Cell Death. Molecular Cell *59*, 941–955.

Puri, R., Cheng, X.-T., Lin, M.-Y., Huang, N., and Sheng, Z.-H. (2019a). Defending Stressed Mitochondria: Uncovering the Role of MUL1 in Suppressing Neuronal Mitophagy. Autophagy 15548627.2019.1687216.

Puri, R., Cheng, X.-T., Lin, M.-Y., Huang, N., and Sheng, Z.-H. (2019b). Mul1 restrains Parkin-mediated mitophagy in mature neurons by maintaining ER-mitochondrial contacts. Nat Commun *10*.

Rabinovitz, M., and Fisher, J.M. (1964). Characteristics of the inhibition of hemoglobin synthesis in rabbit reticulocytes by threo-α-amino-β-chlorobutyric acid. Biochimica et Biophysica Acta (BBA) - Specialized Section on Nucleic Acids and Related Subjects *91*, 313–322.

Ran, F.A., Hsu, P.D., Wright, J., Agarwala, V., Scott, D.A., and Zhang, F. (2013). Genome engineering using the CRISPR-Cas9 system. Nature Protocols *8*, 2281–2308.

Rasool, S., Soya, N., Truong, L., Croteau, N., Lukacs, G.L., and Trempe, J.-F. (2018). PINK1 autophosphorylation is required for ubiquitin recognition. EMBO Reports *19*, e44981.

Rath, D., Amlinger, L., Rath, A., and Lundgren, M. (2015). The CRISPR-Cas immune system: Biology, mechanisms and applications. Biochimie *117*, 119–128.

Reiter, L.T., Potocki, L., Chien, S., Gribskov, M., and Bier, E. (2001). A Systematic Analysis of Human Disease-Associated Gene Sequences In Drosophila melanogaster. Genome Res. *11*, 1114–1125.

Reverdy, C., Conrath, S., Lopez, R., Planquette, C., Atmanene, C., Collura, V., Harpon, J., Battaglia, V., Vivat, V., Sippl, W., et al. (2012). Discovery of Specific Inhibitors of Human USP7/HAUSP Deubiquitinating Enzyme. Chemistry & Biology *19*, 467–477.

Reyes-Turcu, F.E., Horton, J.R., Mullally, J.E., Heroux, A., Cheng, X., and Wilkinson, K.D. (2006). The Ubiquitin Binding Domain ZnF UBP Recognizes the C-Terminal Diglycine Motif of Unanchored Ubiquitin. Cell *124*, 1197–1208.

Reyes-Turcu, F.E., Shanks, J.R., Komander, D., and Wilkinson, K.D. (2008). Recognition of Polyubiquitin Isoforms by the Multiple Ubiquitin Binding Modules of Isopeptidase T. J. Biol. Chem. *283*, 19581–19592.

Riccio, V., Demers, N., Hua, R., Vissa, M., Cheng, D.T., Strilchuk, A.W., Wang, Y., McQuibban, G.A., and Kim, P.K. (2019). Deubiquitinating enzyme USP30 maintains basal peroxisome abundance by regulating pexophagy. J Cell Biol *218*, 798–807.

Richter, B., Sliter, D.A., Herhaus, L., Stolz, A., Wang, C., Beli, P., Zaffagnini, G., Wild, P., Martens, S., Wagner, S.A., et al. (2016). Phosphorylation of OPTN by TBK1 enhances its binding to Ub chains and promotes selective autophagy of damaged mitochondria. Proc Natl Acad Sci U S A *113*, 4039–4044.

Roberts, C.G., and Pruneda, J.N. (2020). Unraveling proteasome engagement. Nature Chemical Biology *16*, 813–815.

Roberts, R.F., Tang, M.Y., Fon, E.A., and Durcan, T.M. (2016). Defending the mitochondria: The pathways of mitophagy and mitochondrial-derived vesicles. The International Journal of Biochemistry & Cell Biology *79*, 427–436.

Rodriguez-Enriquez, S., He, L., and Lemasters, J.J. (2004). Role of mitochondrial permeability transition pores in mitochondrial autophagy. The International Journal of Biochemistry & Cell Biology *36*, 2463–2472.

Rojansky, R., Cha, M.-Y., and Chan, D.C. (2016). Elimination of paternal mitochondria in mouse embryos occurs through autophagic degradation dependent on PARKIN and MUL1. ELife *5*.

Rosado, C., Mijaljica, D., Hatzinisiriou, I., Prescott, M., and Devenish, R.J. (2008). Rosella: A fluorescent pH-biosensor for reporting vacuolar turnover of cytosol and organelles in yeast. Autophagy *4*, 205–213.

Rose, C.M., Isasa, M., Ordureau, A., Prado, M.A., Beausoleil, S.A., Jedrychowski, M.P., Finley, D.J., Harper, J.W., and Gygi, S.P. (2016). Highly Multiplexed Quantitative Mass Spectrometry Analysis of Ubiquitylomes. Cell Syst *3*, 395-403.e4.

Rotin, D., and Kumar, S. (2009). Physiological functions of the HECT family of ubiquitin ligases. Nature Reviews Molecular Cell Biology *10*, 398–409.

Rousseau, A., and Bertolotti, A. (2018). Regulation of proteasome assembly and activity in health and disease. Nature Reviews Molecular Cell Biology *19*, 697–712.

Rusilowicz-Jones, E.V., Jardine, J., Kallinos, A., Pinto-Fernandez, A., Guenther, F., Giurrandino, M., Barone, F.G., McCarron, K., Burke, C.J., Murad, A., et al. (2020). USP30 sets a trigger threshold for PINK1-PARKIN amplification of mitochondrial ubiquitylation. Life Sci Alliance *3*.

Saito, T., Nah, J., Oka, S., Mukai, R., Monden, Y., Maejima, Y., Ikeda, Y., Sciarretta, S., Liu, T., Li, H., et al. (2019). An alternative mitophagy pathway mediated by Rab9 protects the heart against ischemia. J Clin Invest *129*, 802–819.

Sanman, L.E., and Bogyo, M. (2014). Activity-Based Profiling of Proteases. Annu. Rev. Biochem. *83*, 249–273.

Sargent, G., van Zutphen, T., Shatseva, T., Zhang, L., Di Giovanni, V., Bandsma, R., and Kim, P.K. (2016). PEX2 is the E3 ubiquitin ligase required for pexophagy during starvation. J Cell Biol *214*, 677–690.

Sarraf, S.A., Raman, M., Guarani-Pereira, V., Sowa, M.E., Huttlin, E.L., Gygi, S.P., and Harper, J.W. (2013). Landscape of the PARKIN-dependent ubiquitylome in response to mitochondrial depolarization. Nature *496*, 372–376.

Sarraf, S.A., Sideris, D.P., Giagtzoglou, N., Ni, L., Kankel, M.W., Sen, A., Bochicchio, L.E., Huang, C.-H., Nussenzweig, S.C., Worley, S.H., et al. (2019). PINK1/Parkin Influences Cell Cycle by Sequestering TBK1 at Damaged Mitochondria, Inhibiting Mitosis. Cell Rep *29*, 225-235.e5.

Sauvé, V., Sung, G., Soya, N., Kozlov, G., Blaimschein, N., Miotto, L.S., Trempe, J.-F., Lukacs, G.L., and Gehring, K. (2018). Mechanism of parkin activation by phosphorylation. Nat Struct Mol Biol *25*, 623–630.

Schrader, M., Costello, J., Godinho, L.F., and Islinger, M. (2015). Peroxisome-mitochondria interplay and disease. Journal of Inherited Metabolic Disease *38*, 681–702.

Schuldiner, M., Metz, J., Schmid, V., Denic, V., Rakwalska, M., Schmitt, H.D., Schwappach, B., and Weissman, J.S. (2008). The GET Complex Mediates Insertion of Tail-Anchored Proteins into the ER Membrane. Cell *134*, 634–645.

Schulman, B.A., and Harper, W.J. (2009). Ubiquitin-like protein activation by E1 enzymes: the apex for downstream signalling pathways. Nature Reviews Molecular Cell Biology *10*, 319–331.

Schulz, S., Chachami, G., Kozaczkiewicz, L., Winter, U., Stankovic-Valentin, N., Haas, P., Hofmann, K., Urlaub, H., Ovaa, H., Wittbrodt, J., et al. (2012). Ubiquitin-specific protease-like 1 (USPL1) is a SUMO isopeptidase with essential, non-catalytic functions. EMBO Reports *13*, 930–938.

Schwanhäusser, B., Busse, D., Li, N., Dittmar, G., Schuchhardt, J., Wolf, J., Chen, W., and Selbach, M. (2011). Global quantification of mammalian gene expression control. Nature *473*, 337–342.

Schweitzer, A., Aufderheide, A., Rudack, T., Beck, F., Pfeifer, G., Plitzko, J.M., Sakata, E., Schulten, K., Förster, F., and Baumeister, W. (2016). Structure of the

human 26S proteasome at a resolution of 3.9 Å. Proc Natl Acad Sci U S A *113*, 7816–7821.

Scott, D.C., Rhee, D.Y., Duda, D.M., Kelsall, I.R., Olszewski, J.L., Paulo, J.A., Jong, A. de, Ovaa, H., Alpi, A.F., Harper, J.W., et al. (2016). Two Distinct Types of E3 Ligases Work in Unison to Regulate Substrate Ubiquitylation. Cell *166*, 1198-1214.e24.

Scully, R., Panday, A., Elango, R., and Willis, N.A. (2019). DNA double-strand break repair-pathway choice in somatic mammalian cells. Nature Reviews Molecular Cell Biology *20*, 698–714.

Sekine, S., Wang, C., Sideris, D.P., Bunker, E., Zhang, Z., and Youle, R.J. (2019). Reciprocal Roles of Tom7 and OMA1 during Mitochondrial Import and Activation of PINK1. Molecular Cell *73*, 1028-1043.e5.

Shi, J., Wang, E., Milazzo, J.P., Wang, Z., Kinney, J.B., and Vakoc, C.R. (2015). Discovery of cancer drug targets by CRISPR-Cas9 screening of protein domains. Nature Biotechnology *33*, 661–667.

Shipley, M.M., Mangold, C.A., and Szpara, M.L. (2016). Differentiation of the SH-SY5Y Human Neuroblastoma Cell Line. J Vis Exp.

Shojaee, S., Sina, F., Banihosseini, S.S., Kazemi, M.H., Kalhor, R., Shahidi, G.-A., Fakhrai-Rad, H., Ronaghi, M., and Elahi, E. (2008). Genome-wide Linkage Analysis of a Parkinsonian-Pyramidal Syndrome Pedigree by 500 K SNP Arrays. The American Journal of Human Genetics *82*, 1375–1384.

Siegelin, M.D., Dohi, T., Raskett, C.M., Orlowski, G.M., Powers, C.M., Gilbert, C.A., Ross, A.H., Plescia, J., and Altieri, D.C. (2011). Exploiting the mitochondrial unfolded protein response for cancer therapy in mice and human cells. J Clin Invest *121*, 1349–1360.

Simón-Sánchez, J., Schulte, C., Bras, J.M., Sharma, M., Gibbs, J.R., Berg, D., Paisan-Ruiz, C., Lichtner, P., Scholz, S.W., Hernandez, D.G., et al. (2009). Genome-wide association study reveals genetic risk underlying Parkinson's disease. Nature Genetics *41*, 1308–1312.

Sims, J.J., and Cohen, R.E. (2009). Linkage-Specific Avidity Defines the Lysine 63-Linked Polyubiquitin-Binding Preference of Rap80. Molecular Cell *33*, 775–783.

Skowyra, D., Craig, K.L., Tyers, M., Elledge, S.J., and Harper, J.W. (1997). F-Box Proteins Are Receptors that Recruit Phosphorylated Substrates to the SCF Ubiquitin-Ligase Complex. Cell *91*, 209–219.

Smit, J.J., and Sixma, T.K. (2014). RBR E3-ligases at work. EMBO Reports *15*, 142–154.

Smith, J.J., and Aitchison, J.D. (2013). Peroxisomes take shape. Nature Reviews Molecular Cell Biology *14*, 803–817.

Sokolowski, M.B., Kent, C., and Wong, J. (1984). Drosophila larval foraging behaviour: Developmental stages. Animal Behaviour *32*, 645–651.

Soubannier, V., Rippstein, P., Kaufman, B.A., Shoubridge, E.A., and McBride, H.M. (2012a). Reconstitution of mitochondria derived vesicle formation demonstrates selective enrichment of oxidized cargo. PLoS ONE *7*, e52830.

Soubannier, V., McLelland, G.-L., Zunino, R., Braschi, E., Rippstein, P., Fon, E.A., and McBride, H.M. (2012b). A Vesicular Transport Pathway Shuttles Cargo from Mitochondria to Lysosomes. Current Biology *22*, 135–141.

Soutar, M.P.M., Kempthorne, L., Annuario, E., Luft, C., Wray, S., Ketteler, R., Ludtmann, M.H.R., and Plun-Favreau, H. (2019). FBS/BSA media concentration determines CCCP's ability to depolarize mitochondria and activate PINK1-PRKN mitophagy. Autophagy *15*, 2002–2011.

Spengler, B.A., Biedler, J.L., and Ross, R.A. (2002). A corrected karyotype for the SH-SY5Y human neuroblastoma cell line. Cancer Genetics and Cytogenetics *138*, 177–178.

Starkov, A.A., and Fiskum, G. (2001). Myxothiazol Induces H2O2 Production from Mitochondrial Respiratory Chain. Biochemical and Biophysical Research Communications *281*, 645–650.

Staropoli, J.F., McDermott, C., Martinat, C., Schulman, B., Demireva, E., and Abeliovich, A. (2003). Parkin Is a Component of an SCF-like Ubiquitin Ligase Complex and Protects Postmitotic Neurons from Kainate Excitotoxicity. Neuron *37*, 735–749.

Stockley, M.L., Kemp, M.I., and Madin, A. (2018). Cyanopyrrolidine derivatives with activity as inhibitors of usp30.

Stotland, A., and Gottlieb, R.A. (2016). α-MHC MitoTimer mouse: In vivo mitochondrial turnover model reveals remarkable mitochondrial heterogeneity in the heart. J Mol Cell Cardiol *90*, 53–58.

Strappazzon, F., Nazio, F., Corrado, M., Cianfanelli, V., Romagnoli, A., Fimia, G.M., Campello, S., Nardacci, R., Piacentini, M., Campanella, M., et al. (2015). AMBRA1 is able to induce mitophagy via LC3 binding, regardless of PARKIN and p62/SQSTM1. Cell Death & Differentiation *22*, 419–432.

Strappazzon, F., Di Rita, A., Peschiaroli, A., Leoncini, P.P., Locatelli, F., Melino, G., and Cecconi, F. (2019). HUWE1 controls MCL1 stability to unleash AMBRA1-induced mitophagy. Cell Death Differ.

Sugiura, A., Nagashima, S., Tokuyama, T., Amo, T., Matsuki, Y., Ishido, S., Kudo, Y., McBride, H.M., Fukuda, T., Matsushita, N., et al. (2013). MITOL Regulates Endoplasmic Reticulum-Mitochondria Contacts via Mitofusin2. Molecular Cell *51*, 20–34.

Sugiura, A., McLelland, G.-L., Fon, E.A., and McBride, H.M. (2014). A new pathway for mitochondrial quality control: mitochondrial-derived vesicles. EMBO J *33*, 2142–2156.

Sugiura, A., Mattie, S., Prudent, J., and McBride, H.M. (2017). Newly born peroxisomes are a hybrid of mitochondrial and ER-derived pre-peroxisomes. Nature *542*, 251–254.

Sun, N., Yun, J., Liu, J., Malide, D., Liu, C., Rovira, I.I., Holmström, K.M., Fergusson, M.M., Yoo, Y.H., Combs, C.A., et al. (2015). Measuring In Vivo Mitophagy. Mol. Cell *60*, 685–696.

Sundaramoorthy, E., Leonard, M., Mak, R., Liao, J., Fulzele, A., and Bennett, E.J. (2017). ZNF598 and RACK1 Regulate Mammalian Ribosome-Associated Quality Control Function by Mediating Regulatory 40S Ribosomal Ubiquitylation. Mol. Cell *65*, 751-760.e4.

Swatek, K.N., and Komander, D. (2016). Ubiquitin modifications. Cell Research *26*, 399–422.

Swerdlow, P.S., Finley, D., and Varshavsky, A. (1986). Enhancement of immunoblot sensitivity by heating of hydrated filters. Analytical Biochemistry *156*, 147–153.

Szargel, R., Shani, V., Abd Elghani, F., Mekies, L.N., Liani, E., Rott, R., and Engelender, S. (2016). The PINK1, synphilin-1 and SIAH-1 complex constitutes a novel mitophagy pathway. Hum Mol Genet *25*, 3476–3490.

Takeda, K., Nagashima, S., Shiiba, I., Uda, A., Tokuyama, T., Ito, N., Fukuda, T., Matsushita, N., Ishido, S., Iwawaki, T., et al. (2019). MITOL prevents ER stress-induced apoptosis by IRE1α ubiquitylation at ER–mitochondria contact sites. EMBO J *38*.

Tang, F., Wang, B., Li, N., Wu, Y., Jia, J., Suo, T., Chen, Q., Liu, Y.-J., and Tang, J. (2011). RNF185, a Novel Mitochondrial Ubiquitin E3 Ligase, Regulates Autophagy through Interaction with BNIP1. PLOS ONE *6*, e24367.

Teixeira, F.R., Randle, S.J., Patel, S.P., Mevissen, T.E.T., Zenkeviciute, G., Koide, T., Komander, D., and Laman, H. (2016). Gsk3β and Tomm20 are substrates of the SCFFbxo7/PARK15 ubiquitin ligase associated with Parkinson's disease. Biochem J *473*, 3563–3580.

Terskikh, A., Fradkov, A., Ermakova, G., Zaraisky, A., Tan, P., Kajava, A.V., Zhao, X., Lukyanov, S., Matz, M., Kim, S., et al. (2000). "Fluorescent Timer": Protein That Changes Color with Time. Science *290*, 1585–1588.

Thorne, C., Eccles, R.L., Coulson, J.M., Urbé, S., and Clague, M.J. (2011). Isoform-Specific Localization of the Deubiquitinase USP33 to the Golgi Apparatus. Traffic *12*, 1563–1574.

Tiede, C., Tang, A.A.S., Deacon, S.E., Mandal, U., Nettleship, J.E., Owen, R.L., George, S.E., Harrison, D.J., Owens, R.J., Tomlinson, D.C., et al. (2014). Adhiron: a stable and versatile peptide display scaffold for molecular recognition applications. Protein Eng Des Sel *27*, 145–155.

Tiede, C., Bedford, R., Heseltine, S.J., Smith, G., Wijetunga, I., Ross, R., AlQallaf, D., Roberts, A.P., Balls, A., Curd, A., et al. (2017). Affimer proteins are versatile and renewable affinity reagents. ELife *6*, e24903.

Tokuyasu, K.T., Peacock, W.J., and Hardy, R.W. (1972). Dynamics of spermiogenesis in Drosophila melanogaster. Z. Zellforsch. *124*, 479–506.

Tong, M., Jun, T., Nie, Y., Hao, J., and Fan, D. (2019). The Role of the Slit/Robo Signaling Pathway. J Cancer *10*, 2694–2705.

Trompier, D., Vejux, A., Zarrouk, A., Gondcaille, C., Geillon, F., Nury, T., Savary, S., and Lizard, G. (2014). Brain peroxisomes. Biochimie *98*, 102–110.

Tsou, W.-L., Sheedlo, M.J., Morrow, M.E., Blount, J.R., McGregor, K.M., Das, C., and Todi, S.V. (2012). Systematic Analysis of the Physiological Importance of Deubiquitinating Enzymes. PLoS One *7*.

Tsukada, M., and Ohsumi, Y. (1993). Isolation and characterization of autophagy-defective mutants of Saccharomyces cerevisiae. FEBS Letters *333*, 169–174.

Tucker, K., and Park, E. (2019). Cryo-EM structure of the mitochondrial protein-import channel TOM complex at near-atomic resolution. Nature Structural & Molecular Biology 1–9.

Turnbull, A.P., Ioannidis, S., Krajewski, W.W., Pinto-Fernandez, A., Heride, C., Martin, A.C.L., Tonkin, L.M., Townsend, E.C., Buker, S.M., Lancia, D.R., et al. (2017). Molecular basis of USP7 inhibition by selective small-molecule inhibitors. Nature *550*, 481–486.

Twig, G., Elorza, A., Molina, A.J.A., Mohamed, H., Wikstrom, J.D., Walzer, G., Stiles, L., Haigh, S.E., Katz, S., Las, G., et al. (2008). Fission and selective fusion govern mitochondrial segregation and elimination by autophagy. The EMBO Journal *27*, 433–446.

Tyanova, S., Temu, T., Sinitcyn, P., Carlson, A., Hein, M.Y., Geiger, T., Mann, M., and Cox, J. (2016a). The Perseus computational platform for comprehensive analysis of (prote)omics data. Nature Methods *13*, 731–740.

Tyanova, S., Temu, T., and Cox, J. (2016b). The MaxQuant computational platform for mass spectrometry-based shotgun proteomics. Nature Protocols *11*, 2301–2319.

Tyler, M.S. (2000). Developmental biology: a guide for experimental study (Sunderland, Mass: Sinauer Associates).

Tysnes, O.-B., and Storstein, A. (2017). Epidemiology of Parkinson's disease. J Neural Transm *124*, 901–905.

Uhlén, M., Fagerberg, L., Hallström, B.M., Lindskog, C., Oksvold, P., Mardinoglu, A., Sivertsson, Å., Kampf, C., Sjöstedt, E., Asplund, A., et al. (2015). Tissue-based map of the human proteome. Science *347*.

Urbé, S., Liu, H., Hayes, S.D., Heride, C., Rigden, D.J., and Clague, M.J. (2012). Systematic survey of deubiquitinase localization identifies USP21 as a regulator of centrosome- and microtubule-associated functions. Mol Biol Cell *23*, 1095–1103.

Valente, E.M., Abou-Sleiman, P.M., Caputo, V., Muqit, M.M.K., Harvey, K., Gispert, S., Ali, Z., Turco, D.D., Bentivoglio, A.R., Healy, D.G., et al. (2004). Hereditary Early-Onset Parkinson's Disease Caused by Mutations in PINK1. Science *304*, 1158–1160.

Vargas, J.N.S., Wang, C., Bunker, E., Hao, L., Maric, D., Schiavo, G., Randow, F., and Youle, R.J. (2019). Spatiotemporal Control of ULK1 Activation by NDP52 and TBK1 during Selective Autophagy. Molecular Cell *74*, 347-362.e6.

Veeriah, S., Taylor, B.S., Meng, S., Fang, F., Yilmaz, E., Vivanco, I., Janakiraman, M., Schultz, N., Hanrahan, A.J., Pao, W., et al. (2010a). Somatic mutations of the

Parkinson's disease-associated gene PARK2 in glioblastoma and other human malignancies. Nat. Genet. *42*, 77–82.

Veeriah, S., Morris, L., Solit, D., and Chan, T.A. (2010b). The familial Parkinson disease gene PARK2 is a multisite tumor suppressor on chromosome 6q25.2-27 that regulates cyclin E. Cell Cycle *9*, 1451–1452.

Velazquez, A.F.C., and Jackson, W.T. (2018). So Many Roads: the Multifaceted Regulation of Autophagy Induction. Molecular and Cellular Biology *38*.

Vijay-Kumar, S., Bugg, C.E., and Cook, W.J. (1987). Structure of ubiquitin refined at 1.8Åresolution. Journal of Molecular Biology *194*, 531–544.

Villa, E., Proïcs, E., Rubio-Patiño, C., Obba, S., Zunino, B., Bossowski, J.P., Rozier, R.M., Chiche, J., Mondragón, L., Riley, J.S., et al. (2017). Parkin-Independent Mitophagy Controls Chemotherapeutic Response in Cancer Cells. Cell Reports *20*, 2846–2859.

Vives-Bauza, C., Zhou, C., Huang, Y., Cui, M., Vries, R.L.A. de, Kim, J., May, J., Tocilescu, M.A., Liu, W., Ko, H.S., et al. (2010). PINK1-dependent recruitment of Parkin to mitochondria in mitophagy. PNAS *107*, 378–383.

Vosshall, L.B., Amrein, H., Morozov, P.S., Rzhetsky, A., and Axel, R. (1999). A Spatial Map of Olfactory Receptor Expression in the Drosophila Antenna. Cell *96*, 725–736.

Walden, M., Masandi, S.K., Pawłowski, K., and Zeqiraj, E. (2018). Pseudo-DUBs as allosteric activators and molecular scaffolds of protein complexes. Biochem Soc Trans *46*, 453–466.

Wall, C.E., Rose, C.M., Adrian, M., Zeng, Y.J., Kirkpatrick, D.S., and Bingol, B. (2019). PPEF2 Opposes PINK1-Mediated Mitochondrial Quality Control by Dephosphorylating Ubiquitin. Cell Reports *29*, 3280-3292.e7.

Wanders, R.J.A. (2013). Peroxisomes in Human Health and Disease: Metabolic Pathways, Metabolite Transport, Interplay with Other Organelles and Signal Transduction. In Peroxisomes and Their Key Role in Cellular Signaling and Metabolism, L.A. del Río, ed. (Dordrecht: Springer Netherlands), pp. 23–44.

Wanders, R.J.A., and Waterham, H.R. (2006). Biochemistry of Mammalian Peroxisomes Revisited. Annu. Rev. Biochem. *75*, 295–332.

Wang, L., Cho, Y.-L., Tang, Y., Wang, J., Park, J.-E., Wu, Y., Wang, C., Tong, Y., Chawla, R., Zhang, J., et al. (2018). PTEN-L is a novel protein phosphatase for ubiquitin dephosphorylation to inhibit PINK1–Parkin-mediated mitophagy. Cell Research *28*, 787–802.

Wang, Q., Huang, L., Hong, Z., Lv, Z., Mao, Z., Tang, Y., Kong, X., Li, S., Cui, Y., Liu, H., et al. (2017a). The E3 ubiquitin ligase RNF185 facilitates the cGAS-mediated innate immune response. PLoS Pathog *13*.

Wang, X.-Y., Zhang, X.-H., Peng, L., Liu, Z., Yang, Y.-X., He, Z.-X., Dang, H.-W., and Zhou, S.-F. (2017b). Bardoxolone methyl (CDDO-Me or RTA402) induces cell cycle arrest, apoptosis and autophagy via PI3K/Akt/mTOR and p38 MAPK/Erk1/2 signaling pathways in K562 cells. Am J Transl Res *9*, 4652–4672.

Wang, Y., Serricchio, M., Jauregui, M., Shanbhag, R., Stoltz, T., Di Paolo, C.T., Kim, P.K., and McQuibban, G.A. (2015). Deubiquitinating enzymes regulate PARK2-mediated mitophagy. Autophagy *11*, 595–606.

Wang, Y.-Y., Yang, Y.-X., Zhe, H., He, Z.-X., and Zhou, S.-F. (2014). Bardoxolone methyl (CDDO-Me) as a therapeutic agent: an update on its pharmacokinetic and pharmacodynamic properties. Drug Des Devel Ther *8*, 2075–2088.

Wauer, T., Swatek, K.N., Wagstaff, J.L., Gladkova, C., Pruneda, J.N., Michel, M.A., Gersch, M., Johnson, C.M., Freund, S.M.V., and Komander, D. (2015a). Ubiquitin Ser65 phosphorylation affects ubiquitin structure, chain assembly and hydrolysis. EMBO J. *34*, 307–325.

Wauer, T., Simicek, M., Schubert, A., and Komander, D. (2015b). Mechanism of phospho-ubiquitin induced PARKIN activation. Nature *524*, 370–374.

Webster, N., Jin, J.R., Green, S., Hollis, M., and Chambon, P. (1988). The yeast UASG is a transcriptional enhancer in human hela cells in the presence of the GAL4 trans-activator. Cell *52*, 169–178.

Wenzel, D.M., Lissounov, A., Brzovic, P.S., and Klevit, R.E. (2011). UBCH7 reactivity profile reveals parkin and HHARI to be RING/HECT hybrids. Nature *474*, 105–108.

Wiborg, O., Pedersen, M. s., Wind, A., Berglund, L. e., Marcker, K. a., and Vuust, J. (1985). The human ubiquitin multigene family: some genes contain multiple directly repeated ubiquitin coding sequences. The EMBO Journal *4*, 755–759.

Wick, A.N., Drury, D.R., Nakada, H.I., Wolfe, J.B., and Grabowski, W. the technical assistance of B.B. and R. (1957). Localization of the Primary Metabolic Block Produced by 2-Deoxyglucose. J. Biol. Chem. *224*, 963–969.

Wiedemann, N., and Pfanner, N. (2017). Mitochondrial Machineries for Protein Import and Assembly. Annu. Rev. Biochem. *86*, 685–714.

Wilkinson, K.D., Urban, M.K., and Haas, A.L. (1980). Ubiquitin is the ATP-dependent proteolysis factor I of rabbit reticulocytes. J. Biol. Chem. *255*, 7529–7532.

Wong, Y.C., and Holzbaur, E.L.F. (2014). Optineurin is an autophagy receptor for damaged mitochondria in parkin-mediated mitophagy that is disrupted by an ALS-linked mutation. Proc Natl Acad Sci U S A *111*, E4439–E4448.

Wong, E.S.P., Tan, J.M.M., Wang, C., Zhang, Z., Tay, S.-P., Zaiden, N., Ko, H.S., Dawson, V.L., Dawson, T.M., and Lim, K.-L. (2007). Relative Sensitivity of Parkin and Other Cysteine-containing Enzymes to Stress-induced Solubility Alterations. J. Biol. Chem. *282*, 12310–12318.

Yagita, Y., Hiromasa, T., and Fujiki, Y. (2013). Tail-anchored PEX26 targets peroxisomes via a PEX19-dependent and TRC40-independent class I pathway. J Cell Biol *200*, 651–666.

Yamano, K., and Youle, R.J. (2013). PINK1 is degraded through the N-end rule pathway. Autophagy *9*, 1758–1769.

Yamano, K., and Youle, R.J. (2020). Two different axes CALCOCO2-RB1CC1 and OPTN-ATG9A initiate PRKN-mediated mitophagy. Autophagy *0*, 1–3.

Yamano, K., Fogel, A.I., Wang, C., van der Bliek, A.M., and Youle, R.J. (2014). Mitochondrial Rab GAPs govern autophagosome biogenesis during mitophagy. ELife *3*, e01612.

Yamano, K., Wang, C., Sarraf, S.A., Münch, C., Kikuchi, R., Noda, N.N., Hizukuri, Y., Kanemaki, M.T., Harper, W., Tanaka, K., et al. (2018). Endosomal Rab cycles regulate Parkin-mediated mitophagy. ELife *7*, e31326.

Yamano, K., Kikuchi, R., Kojima, W., Hayashida, R., Koyano, F., Kawawaki, J., Shoda, T., Demizu, Y., Naito, M., Tanaka, K., et al. (2020). Critical role of mitochondrial ubiquitination and the OPTN–ATG9A axis in mitophagy. J Cell Biol *219*.

Yang, J.-Y., and Yang, W.Y. (2013). Bit-by-bit autophagic removal of parkin-labelled mitochondria. Nature Communications *4*, 2428.

Yang, F., Teves, S.S., Kemp, C.J., and Henikoff, S. (2014). Doxorubicin, DNA torsion, and chromatin dynamics. Biochimica et Biophysica Acta (BBA) - Reviews on Cancer *1845*, 84–89.

Yang, K.-C., Ma, X., Liu, H., Murphy, J., Barger, P.M., Mann, D.L., and Diwan, A. (2015). TNF-Receptor Associated Factor-2 Mediates Mitochondrial Autophagy. Circ Heart Fail *8*, 175–187.

Yates, M.S., Tauchi, M., Katsuoka, F., Flanders, K.C., Liby, K.T., Honda, T., Gribble, G.W., Johnson, D.A., Johnson, J.A., Burton, N.C., et al. (2006). Pharmacodynamic characterization of chemopreventive triterpenoids as exceptionally potent inducers of Nrf2-regulated genes. Cancer Epidemiol Biomarkers Prev *15*, B88–B88.

Ye, Y., and Rape, M. (2009). Building ubiquitin chains: E2 enzymes at work. Nature Reviews Molecular Cell Biology *10*, 755–764.

Yim, W.W.-Y., and Mizushima, N. (2020). Lysosome biology in autophagy. Cell Discovery *6*, 1–12.

Yin, J., Guo, J., Zhang, Q., Cui, L., Zhang, L., Zhang, T., Zhao, J., Li, J., Middleton, A., Carmichael, P.L., et al. (2018). Doxorubicin-induced mitophagy and mitochondrial damage is associated with dysregulation of the PINK1/parkin pathway. Toxicology in Vitro *51*, 1–10.

Yonashiro, R., Ishido, S., Kyo, S., Fukuda, T., Goto, E., Matsuki, Y., Ohmura-Hoshino, M., Sada, K., Hotta, H., Yamamura, H., et al. (2006). A novel mitochondrial ubiquitin ligase plays a critical role in mitochondrial dynamics. EMBO J *25*, 3618–3626.

Yoo, Y.-S., Park, Y.-Y., Kim, J.-H., Cho, H., Kim, S.-H., Lee, H.-S., Kim, T.-H., Sun Kim, Y., Lee, Y., Kim, C.-J., et al. (2015). The mitochondrial ubiquitin ligase MARCH5 resolves MAVS aggregates during antiviral signalling. Nat Commun *6*.

Yoshii, S.R., Kishi, C., Ishihara, N., and Mizushima, N. (2011). Parkin Mediates Proteasome-dependent Protein Degradation and Rupture of the Outer Mitochondrial Membrane. J Biol Chem *286*, 19630–19640.

Yu, H., and Matouschek, A. (2017). Recognition of Client Proteins by the Proteasome. Annu. Rev. Biophys. *46*, 149–173.

Yue, W., Chen, Z., Liu, H., Yan, C., Chen, M., Feng, D., Yan, C., Wu, H., Du, L., Wang, Y., et al. (2014). A small natural molecule promotes mitochondrial fusion through inhibition of the deubiquitinase USP30. Cell Research *24*, 482–496.

Yun, J., Puri, R., Yang, H., Lizzio, M.A., Wu, C., Sheng, Z.-H., and Guo, M. (2014). MUL1 acts in parallel to the PINK1/parkin pathway in regulating mitofusin and compensates for loss of PINK1/parkin. ELife *3*.

Yusuf, M., Leung, K., Morris, K.J., and Volpi, E.V. (2013). Comprehensive cytogenomic profile of the in vitro neuronal model SH-SY5Y. Neurogenetics *14*, 63–70.

Zachari, M., and Ganley, I.G. (2017). The mammalian ULK1 complex and autophagy initiation. Essays Biochem *61*, 585–596.

Zachari, M., Gudmundsson, S.R., Li, Z., Manifava, M., Shah, R., Smith, M., Stronge, J., Karanasios, E., Piunti, C., Kishi-Itakura, C., et al. (2019). Selective Autophagy of Mitochondria on a Ubiquitin-Endoplasmic-Reticulum Platform. Developmental Cell *50*, 627-643.e5.

Zhang, C., Lin, M., Wu, R., Wang, X., Yang, B., Levine, A.J., Hu, W., and Feng, Z. (2011). Parkin, a p53 target gene, mediates the role of p53 in glucose metabolism and the Warburg effect. Proc Natl Acad Sci U S A *108*, 16259–16264.

Zhang, H., Bosch-Marce, M., Shimoda, L.A., Tan, Y.S., Baek, J.H., Wesley, J.B., Gonzalez, F.J., and Semenza, G.L. (2008). Mitochondrial Autophagy Is an HIF-1-dependent Adaptive Metabolic Response to Hypoxia. J. Biol. Chem. *283*, 10892–10903.

Zhang, J., Tripathi, D.N., Jing, J., Alexander, A., Kim, J., Powell, R.T., Dere, R., Tait-Mulder, J., Lee, J.-H., Paull, T.T., et al. (2015). ATM Functions at the Peroxisome to Induce Pexophagy in Response to ROS. Nat Cell Biol *17*, 1259–1269.

Zhao, Y.G., and Zhang, H. (2019). Autophagosome maturation: An epic journey from the ER to lysosomes. J Cell Biol *218*, 757–770.

Zhao, Q., Wang, J., Levichkin, I.V., Stasinopoulos, S., Ryan, M.T., and Hoogenraad, N.J. (2002). A mitochondrial specific stress response in mammalian cells. EMBO J *21*, 4411–4419.

Zhao, X., Heng, J.I.-T., Guardavaccaro, D., Jiang, R., Pagano, M., Guillemot, F., Iavarone, A., and Lasorella, A. (2008). The HECT-domain ubiquitin ligase Huwe1 controls neural differentiation and proliferation by destabilizing the N-Myc oncoprotein. Nature Cell Biology *10*, 643–653.

Zheng, N., and Shabek, N. (2017). Ubiquitin Ligases: Structure, Function, and Regulation. Annu. Rev. Biochem. *86*, 129–157.

Zheng, N., Wang, P., Jeffrey, P.D., and Pavletich, N.P. (2000). Structure of a c-Cbl–UbcH7 Complex: RING Domain Function in Ubiquitin-Protein Ligases. Cell *102*, 533–539.

Zhu, M., Li, Y., and Zhou, Z. (2017). Antibiotic ivermectin preferentially targets renal cancer through inducing mitochondrial dysfunction and oxidative damage. Biochemical and Biophysical Research Communications *492*, 373–378.

Zielonka, J., Sikora, A., Hardy, M., Ouari, O., Vasquez-Vivar, J., Cheng, G., Lopez, M., and Kalyanaraman, B. (2017). Mitochondria-Targeted Triphenylphosphonium-Based Compounds: Syntheses, Mechanisms of Action, and Therapeutic and Diagnostic Applications. Chem Rev *117*, 10043–10120.

Zimmerman, E.S., Schulman, B.A., and Zheng, N. (2010). Structural assembly of cullin-RING ubiquitin ligase complexes. Current Opinion in Structural Biology *20*, 714–721.

Zimmerman, M.W., Liu, Y., He, S., Durbin, A.D., Abraham, B.J., Easton, J., Shao, Y., Xu, B., Zhu, S., Zhang, X., et al. (2018). c-MYC drives a subset of high-risk pediatric neuroblastomas and is activated through mechanisms including enhancer hijacking and focal enhancer amplification. Cancer Discov *8*, 320–335.